Transactions of the ASME®

Technical Editor,
H. L. JULIEN (1998)
Associate Technical Editors
Advanced Energy Systems
M. J. MORAN (1996)
Fuels and Combustion Technologies
D. W. PACER (1994)
Gas Turbine
C. J. RUSSO (1995)
R. KIELB (1996)
S. SAMUELSEN (1996)
Internal Combustion Engine
W. CHENG (1996)
Nuclear Engineering
H. H. CHUNG (1996)
Power
P. H. GILSON (1996)

BOARD ON COMMUNICATIONS
Chairman and Vice-President
R. D. ROCKE

Members-at-Large
T. BARLOW, N. H. CHAO, A. ERDMAN,
G. JOHNSON, L. KEER, W. MORGAN,
E. M. PATTON, S. PATULSKI, R. E. REDER,
S. ROHDE, R. SHAH, F. WHITE,
J. WHITEHEAD

OFFICERS OF THE ASME
President, P. J. TORPEY
Exec. Director
D. L. BELDEN
Treasurer
R. A. BENNETT

PUBLISHING STAFF
Mng. Dir., Publ.
CHARLES W. BEARDSLEY
Managing Editor,
CORNELIA MONAHAN
Sr. Production Editor,
VALERIE WINTERS
Production Assistant,
MARISOL ANDINO

Transactions of the ASME, Journal of Engineering for Gas Turbines and Power (ISSN 0742-4795) is published quarterly (Jan., Apr., July, Oct.) for $150.00 per year by The American Society of Mechanical Engineers, 345 East 47th Street, New York, NY 10017. Second class postage paid at New York, NY and additional mailing offices. POSTMASTER: Send address changes to Transactions of the ASME, Journal of Engineering for Gas Turbines and Power, c/o THE AMERICAN SOCIETY OF MECHANICAL ENGINEERS, 22 Law Drive, Box 2300, Fairfield, NJ 07007-2300.
CHANGES OF ADDRESS must be received at Society headquarters seven weeks before they are to be effective. Please send old label and new address.
PRICES: To members, $40.00, annually; to nonmembers, $150.00.
Add $30.00 for postage to countries outside the United States and Canada.
STATEMENT from By-Laws. The Society shall not be responsible for statements or opinions advanced in papers or ... printed in its publications (B 7.1, para. 3).
COPYRIGHT © 1995 by The American Society of Mechanical Engineers. Authorization to photocopy material for internal or personal use under circumstances not falling within the fair use provisions of the Copyright Act is granted by ASME to libraries and other users registered with the Copyright Clearance Center (CCC) Transactional Reporting Service provided that the base fee of $3.00 per article is paid directly to CCC, Inc., 222 Rosewood Dr., Danvers, MA 01923.
Request for special permission or bulk copying should be addressed to Reprints/Permission Department.
INDEXED by Applied Mechanics Reviews and Engineering Information, Inc.
Canadian Goods & Services Tax Registration #126148048

Journal of Engineering for Gas Turbines and Power

Published Quarterly by The American Society of Mechanical Engineers
VOLUME 117 • NUMBER 1 • JANUARY 1995

TECHNICAL PAPERS

Advanced Energy Systems

2 The Performance Optimization of a Gas Turbine Cogeneration/Heat Pump Facility With Thermal Storage
M. R. von Spakovsky, V. Curti, and M. Batato

10 Gas Turbine Bottoming Cycles: Triple-Pressure Steam Versus Kalina
C. H. Marston and M. Hyre

16 A Methane–Steam Reformer for a Basic Chemically Recuperated Gas Turbine
S. T. Adelman, M. A. Hoffman, and J. W. Baughn

24 Reduction of Combustion Irreversibility in a Gas Turbine Power Plant Through Off-Gas Recycling
S. P. Harvey, K. F. Knoche, and H. J. Richter

Gas Turbines: Aircraft

31 Design Considerations of a Versatile Simulator for High-Bypass Turbofans (93-GT-14)
C. Balan

38 Simulating Indirect Thrust Measurement Methods for High-Bypass Turbofans (93-GT-335)
J. D. Stevenson and H. I. H. Saravanamuttoo

Gas Turbines: Closed Cycles

47 Applying Combined Pinch and Exergy Analysis to Closed-Cycle Gas Turbine System Design
V. R. Dhole and J. P. Zheng

Gas Turbines: Cogeneration

53 Multi-objective Optimization in Unit Sizing of a Gas Turbine Cogeneration Plant
R. Yokoyama and K. Ito

60 Optimal Operation of Cogeneration Plants With Steam-Injected Gas Turbines
K. Ito, R. Yokoyama, and Y. Matsumoto

67 The Compression of Fuel Gas for Turbines, Engines, and Boilers in Cogeneration Plants
I. M. Arbon

74 The Design, Selection, and Application of Oil-Free Screw Compressors for Fuel Gas Service
K. D. Lelgemann

81 The Design, Selection, and Application of Oil-Injected Screw Compressors for Fuel Gas Service
S. Tsutsumi and J. Boone

88 The Design, Selection, and Application of Reciprocating Compressors for Fuel Gas Service
D. Hough

Gas Turbines: Combustion and Fuels

94 Mathematical Modeling of an Annular Gas Turbine Combustor (93-GT-339)
K. Y. Sokolov, A. G. Tumanovskiy, M. N. Gutnik, A. V. Sudarev, Y. I. Zakharov, and E. D. Winogradov

100 The Importance of the Nitrous Oxide Pathway to NO_x in Lean-Premixed Combustion (93-GT-342)
D. G. Nicol, R. C. Steele, N. M. Marinov, and P. C. Malte

112 Computation of Turbulent Evaporating Sprays: Eulerian Versus Lagrangian Approach (93-GT-333)
M. Hallmann, M. Scheurlen, and S. Wittig

120 Effects of Oxygen and Additives on the Thermal Stability of Jet Fuels (93-GT-130)
S. P. Heneghan, C. R. Martel, T. F. Williams, and D. R. Ballal

125 Degradation of a Jet A Fuel in a Single-Pass Heat Exchanger (93-GT-334)
E. G. Jones, W. J. Balster, and M. E. Post

132 Comparison of Coriolis and Turbine-Type Flowmeters for Fuel Measurement in Gas Turbine Testing (93-GT-70)
J. D. MacLeod and W. Grabe

Gas Turbines: Electric Utilities

138 Comparative Evaluation of Combined Cycles and Gas Turbine Systems With Water Injection, Steam Injection, and Recuperation (93-GT-57)
O. Bolland and J. F. Stadaas

Gas Turbines: Manufacturing and Materials

146 High-Temperature Coatings for Protection Against Turbine Deterioration (93-GT-200)
W. Tabakoff, M. Metwally, and A. Hamed

152 Coatings for the Protection of Turbine Blades From Erosion (93-GT-291)
P. N. Walsh, J. M. Quets, and R. C. Tucker, Jr.

156 Processing Methods for High Reliability Silicon Nitride Heat Engine Components (93-GT-319)
V. K. Pujari and D. M. Tracey

(Contents Continued on Page 1)

Downloaded 03 Jun 2010 to 171.66.16.159. Redistribution subject to ASME license or copyright; see http://www.asme.org/terms/Terms_Use.cfm

161 Soft Computing in Design and Manufacturing of Advanced Materials (93-GT-1)
K. J. Clos, G. Y. Baaklini, and A. Vary

166 A Novel Method for Refurbishing Used Hot Section Gas Turbine Blades (93-GT-281)
A. Kempster and N. Czech

Gas Turbines: Marine

172 Digital Control System Development for an Intercooled Recuperated Gas Turbine (93-GT-326)
R. J. Carlson, P. M. West, and D. E. Azouz

Gas Turbine: Structures and Dynamics

176 Active Vibration Control of Rotating Machinery Using Piezoelectric Actuators Incorporating Flexible Casing Effects (93-GT-293)
T. S. Barrett, A. B. Palazzolo, and A. F. Kascak

188 Magnetic Bearing Control of Flexible Shaft Vibrations Based on Multi-access Velocity-Displacement Feedback (93-GT-294)
G. Petela and K. K. Botros

198 Exploring How Shroud Constraint Can Affect Vibratory Response in Turbomachinery (93-GT-285)
M.-T. Yang and J. H. Griffin

207 Eigenvector Derivatives of Generalized Nondefective Eigenproblems With Repeated Eigenvalues (93-GT-340)
Y.-Q. Zhang and W.-L. Wang

Gas Turbines: Vehicular Gas Turbines

213 Blade Erosion in Automotive Gas Turbine Engine (92-GT-344)
M. Metwally, W. Tabakoff, and A. Hamed

ANNOUNCEMENTS

9 Change of address form for subscribers

219 Errata on a previously published paper by X. Sun, W. G. Wang, R. M. Bata, and X. Gao

220 Information for authors

Downloaded 03 Jun 2010 to 171.66.16.159. Redistribution subject to ASME license or copyright; see http://www.asme.org/terms/Terms_Use.cfm

The Performance Optimization of a Gas Turbine Cogeneration/Heat Pump Facility With Thermal Storage

M. R. von Spakovsky

V. Curti

Laboratoire d'énergétique industrielle,
École Polytechnique Fédérale
de Lausanne (EPFL),
CH-1015 Lausanne, Switzerland

M. Batato

Département Engineering,
Nestlé, S.A.,
CH-1800 Vevey, Switzerland

With the push for greater energy conservation, the need for heating and/or power production is being filled by cogeneration facilities. Thus, the search for the best performance at the least cost for such multipurpose plants is made much more difficult by the fact that such facilities must meet differing goals or demands. Such a facility exists at the École Polytechnique Fédérale de Lausanne (EPFL) and has been studied in order to find the optimum modes of operation as a function of time for variations in both the heating and electrical demands this facility must meet. The results of this study are presented here. The plant itself provides heat and electricity for both the EPFL and the University of Lausanne and is projected to supply electricity to the exterior utility grid provided it can be shown to be economically viable. The plant's primary components include two gas turbines, a heat recovery system, two heat pumps, a set of heat storage tanks, and both medium and low-temperature district heating networks. In order to find the optimum mode of operation, a mixed-integer linear programming approach was used, which balances the competing costs of operation and minimizes these costs subject to the operational constraints placed on the system. The effects of both the cost of the fuel and the costs of electricity sold and bought on the best performance of the system are evaluated. In addition, the important features of the modeling process are discussed, in particular the heat storage tanks, which complicate the optimization of the series of steady-state models used to model the overall quasi-steady-state behavior of the system.

Introduction

As energy conservation becomes increasingly important due to the depletion of our natural resources and concerns for the environment, more and more cogeneration facilities are being used in order to get the most out of each single unit of fuel consumed. However, unlike more conventional plants, which have a single purpose (for example, to produce power or heat but not both) and can, thus, be operated according to the type of load placed on them, the picture for multipurpose units is less clear since they must meet mutually conflicting loads. Knowing how to produce both power and heat simultaneously so that the costs of operation for varying levels of demand are minimized requires some way of knowing at exactly what level and with what mix the sources of power and heat in the system should be maintained. Unless this can be done, the attractiveness of cogeneration diminishes due to the inability to meet the demands on the system effectively.

One way of minimizing the costs is mathematically to model and then optimize a system's thermodynamic and economic operation. The type of approach taken depends on how much detail and how much flexibility is needed in order to model a cycle's performance characteristics. The more detail and the more flexibility, the more nonlinear the model is and the more difficult to solve. However, if the goals of the modeling process are sufficiently limited (such as simply wanting to know the most economic levels and mixes of power and heat production in the system at each instance of time as opposed to all the thermodynamic state points and dissipations as well), then a linear model solved by any number of appropriate linear programming algorithms may be sufficient.

The goal of our study is limited in just this way. By developing a *linear* model of the cogeneration/heat pump facility studied here, it was possible to determine the best hourly and seasonal modes of operation for the plant. In particular, a Mixed Integer *Linear* Programming (MILP) (Reklaitis et al., 1983; Kuester and Mize, 1973) approach was utilized since a purely linear programming method would not account for the on/off behavior required of the different pieces of equipment in the plant in order to meet the demands on the system optimally. The work presented here was inspired by two appli-

Contributed by the Advanced Energy Systems Division for publication in the JOURNAL OF ENGINEERING FOR GAS TURBINES AND POWER. Manuscript received by the Advanced Energy Systems Division October 1, 1993; revision received June 13, 1994. Associate Technical Editor: M. J. Moran.

Copyright © 1995 by ASME

Downloaded 02 Jun 2010 to 171.66.16.102. Redistribution subject to ASME license or copyright; see http://www.asme.org/terms/Terms_Use.cfm

cations of this type presented by Ito et al. (1990) and Akagi et al. (1986) who in one of these analyzed a gas turbine-waste heat boiler plant, determining the most economic modes of operation of the plant consistent with the local price of electricity and fuel at the time. Since the completion and then initial publication of our work (von Spakovsky et al., 1992), three additional applications of this type have appeared in the literature, including two that deal with heat storage devices (Ito et al., 1991, 1992; Yokoyama and Ito, 1993).

In our study, an MILP approach was applied to a cogeneration/heat pump facility, which in addition to the heat pumps also includes two gas turbines, a heat recovery system, a set of heat storage tanks, and both medium and low-temperature district heating networks. This type of approach was then used to balance the competing costs of operation and minimize these costs subject to the operational constraints placed on the system. The effects of both the cost of the fuel and the costs of electricity sold and bought on the best performance of the plant were evaluated and the results are presented below. In addition, some of the important features of the modeling process are discussed, in particular the heat storage tanks, which complicate the optimization of the series of steady-state models used to approximate the overall quasi-steady-state behavior of the system.

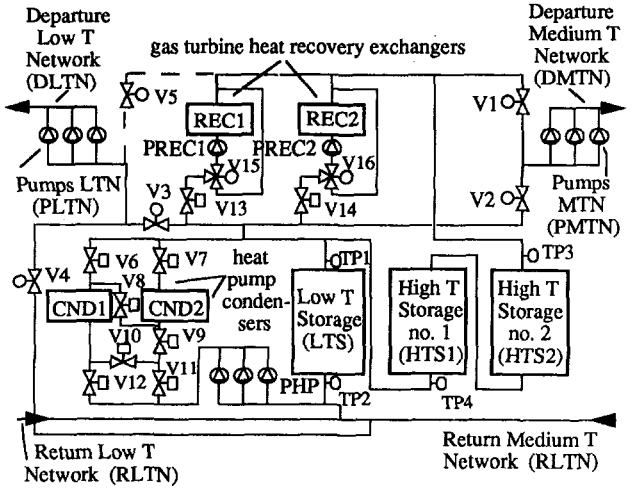

Fig. 1 General layout of the heating circuit for the cogeneration/heat pump facility with thermal storage at the EPFL

Description of the Plant

The cogeneration/heat pump facility at the École Polytechnique Fédérale de Lausanne (EPFL) provides both heat and electricity (Laboratoire d'Énergétique Industrielle, 1986). Hot water all year round and heat during the winter are supplied to the EPFL and the University of Lausanne while electricity is only provided to help cut peak demands in the outside utility grid or to meet the electricity demand for the technical institute (EPFL) and the university when outages occur in the outside grid. Future projections are for this facility also to supply electricity to the outside grid and to meet all the electrical demands for both the institute and the university provided that it can be shown to be economically viable.

As can be seen in Fig. 1, the energy used for heating is transported by two networks, a medium-temperature network (MTN) with a departure temperature ranging from 45 to 65°C, and a low-temperature network (LTN) with a departure temperature ranging from 35 to 50°C. The sources of heat include two vapor-compression heat pumps using ammonia as the working fluid and providing a total of 7 MWth, two fuel oil gas turbines providing a total of 12 MWth through the recovery of heat from the combustion gases, and three heat storage water tanks with a total capacity of 320 m^3 corresponding to a total thermal energy of 66 GJ.

The electric power needed to satisfy the demands of the institute, the university, and the internal operation of the plant itself is provided by either the outside utility grid or the two gas turbines. The latter provide a total of 7 MWe. The internal electrical demands of the plant include those of the heat pump compressors as well as those of the circulating pumps for the recuperators (turbine exhaust gas heat recovery units), the district heating networks, and the heat pump condensers. As was

Nomenclature

a = some fixed fraction
$\dot{C}^{\$}$ = total monetary cost rate of operation (objective function), sfr/s
D = $-1/+1$ integer variable expressing the directions of the mass flow rates for the high and low-temperature heat storage
$\dot{E}$ = electrical power, MWe
g = inequality constraint function
h = equality constraint function
I = number of operation variables
J = number of equality constraints
K = number of inequality constraints
$\dot{M}$ = mass flow rate, kg/s
p, q, r, s = parameters related to the performance characteristics of each piece of equipment
$\dot{Q}$ = heat rate, MWth
t = time
T = temperature, °C
T_1 = entry temperature at $V1$ in Fig. 2, °C
T_2 = entry temperature at $V2$ in Fig. 2, °C
T_3 = entry temperature at $V3$ in Fig. 2, °C
T_4 = entry temperature at $V4$ in Fig. 2, °C
$T_{3/4}$ = the average of T_3 and T_4, °C
$\mathbf{x}$ = operation (independent) variable vector
δ = zero-one integer variable expressing the on/off status of a piece of equipment
Φ = unit costs

Subscripts

BUY, B = relative to the electric power bought
CH = charging
CND1, CND2, CND = condenser relative to heat pump 1, 2, or both
CHP1, CHP2, CHP = compressor relative to heat pump 1, 2, or both
D = electric energy demand
DCH = discharging
DLTN = departure to the LTN

Downloaded 02 Jun 2010 to 171.66.16.102. Redistribution subject to ASME license or copyright; see http://www.asme.org/terms/Terms_Use.cfm

mentioned earlier, future projections call for selling any excess electrical production to the outside utility grid. As a consequence, this feature has been included in the analysis.

Looking once again at Fig. 1, it is apparent that both the heat pumps through their condensers (CND1 and CND2) and the gas turbines through the recuperators (REC1 and REC2) provide heat directly to the MT district heating network; but that only the heat pumps supply the LT network directly. The dotted line on either side of valve 5 ($V5$) in the figure indicates that a direct supply of heat from the turbines for the LT network is presently inoperable. Supplemental heating, however, for the LTN is provided by water returning from the MT network.

Presently, each heat pump is able to heat the water flowing through the condensers up to 50°C. The heat pumps are currently turned on when the outlet water temperature in the upper part of the low-temperature heat storage device (LTS) is smaller than the departure temperature of the MT network. The heat pumps first provide the thermal energy needed for the district heating networks and then feed the LTS. They are turned off when the temperature in the bottom part of the LTS is high enough. The LTS is then discharged to provide the necessary energy for the networks.

The gas turbines, on the other hand, are turned on when high heating demands occur. They can also be turned on if the heat pumps are out of order or when there is an electricity demand that for some reason cannot be provided by the outside utility grid. In this case and if the heating demand is low enough, the heat recovered from the combustion gases is stored in the high-temperature heat storage devices (HTS1 and HTS2). As soon as these reach their maximum capacity, the combustion gases are directly bypassed to the atmosphere.

Unfortunately, the mode of operation just described limits the possible modes of usage of the heat storage devices (LTS, HTS1, and HTS2) in conjunction with the heat pumps and gas turbines and does not fully take into account the electricity produced by the gas turbines. The latter can prove a benefit to the system in cases where it is cheaper to produce electricity than to buy it or in cases where a profit can be gained by selling any excess electricity produced. Thus, it would behoove the operators of the plant to be able to predict what the best or optimum mode of operation is when both heat and electrical demands are taken into account simultaneously.

Complicating this picture even further is a consideration of all the possible modes of heat storage tank operation not presently implemented by the operators of the facility. These storage devices, which are always either being charged or discharged with charge or without charge, can act either dependently or independently of the devices that charge them, depending on the mode of operation that they are in at the time, i.e., in a state of charge or discharge. For example, the heat pumps must be functioning when the LTS is in a state of charge and likewise for the gas turbines, which are tied to the HTS1 and HTS2. However, when these storage devices are discharging with or without a charge, they act independently of whether or not the heat pumps and/or the gas turbines are in fact running.

Thus, in order to resolve the scenarios and difficulties just posed, it was necessary to model the system mathematically and find an overall optimum mode of operation for each distinct time interval during a representative twenty-four hour period. Let us, therefore, proceed with a discussion of the mathematical model developed.

Mathematical Model

To start with, the objective of minimizing the operational costs of the system subject to the thermodynamic and operational constraints placed on the system can be expressed in general mathematical terms by the following expressions:

$$\text{minimize } \dot{C}^{\$} = \Phi_{\text{elec}(B)}\dot{E}_{\text{BUY}} - \Phi_{\text{elec}(S)}\dot{E}_{\text{SELL}} + \Phi_{\text{fuel}}(\dot{M}_{\text{FGT1}} + \dot{M}_{\text{FGT2}}) \quad (1)$$

$$\text{subject to } h_j(\mathbf{x}) = 0 \quad j = 1, \ldots, J \qquad g_k(\mathbf{x}) \geq 0 \quad k = 1, \ldots, K \quad (2)$$

where

$$\mathbf{x} = \{x_i\} \quad i = 1, \ldots, I \quad (3)$$

$$\Phi_{\text{elec}(B)} = f_{\text{elec}(B)}(t) \quad (4)$$

$$\Phi_{\text{elec}(S)} a \Phi_{\text{elec}(B)} \quad (5)$$

and $\dot{C}^{\$}$ is a monetary cost rate. The function f that appears

Nomenclature (cont.)

DMTN = departure to the MTN
elec = relative to the electric power
EXT = exterior
FGT1, FGT2, FGT = fuel for gas turbine 1, 2, or both
fuel = relative to the fuel oil for the gas turbines
GT1, GT2, GT = gas turbine 1, 2, or both
HP1, HP2, HP = heat pump 1, 2, or both
HTS1, HTS2, HTS = high-temperature storage device 1, 2, or both
L = lower limit
LOSS1, LOSS2, LOSS = relative to exhaust gas heat loss of gas turbine 1, 2, or both
LTN = low-temperature network (district heating)
LTS = low-temperature storage device
MTN = medium temperature network (district heating)
PHP = circulatory pumps for the heat pumps
PLTN = low-temperature network pumps
PMTN = medium-temperature network pumps
PREC1, PREC2, PREC = pumps for heat recovery exchanger 1, 2, or both
REC1, REC2, REC = heat recovery exchanger (recuperator) 1, 2, or both
RLTN = return from the LTN
RMTN = return from the MTN
SELL, S = relative to the electric power sold
$TP1$, $TP2$, $TP3$, $TP4$ = temperature probe 1, 2, 3, or 4
U = upper limit
$V1$, $V2$, $V3$, $V4$ = global points of heat exchange with the district heating networks (Fig. 2)
$V1$, $V2$, $V3$, $V4$ = regulated two-way duct valves (Fig. 1)
$V5$, $V7$ through $V13$ = regulated two-way duct valves (Fig. 1)
$V15$, $V16$ = regulated three-way duct valves
$V6$ through $V14$ = on/off valves

Superscripts

DLT = low-temperature heat demand
DMT = medium-temperature heat demand

Downloaded 02 Jun 2010 to 171.66.16.102. Redistribution subject to ASME license or copyright; see http://www.asme.org/terms/Terms_Use.cfm

in Eq. (4) expresses the time variation of the unit price of electricity bought during the day and "a" in Eq. (5) some fixed fraction. The equality constraints for the system given by the h_j represent the various mass and energy balances for the system (shown graphically in Fig. 2) and the component performance characteristics. The inequality constraints given by the g_k express any additional constraints on the system, which, for example, might be dictated by any physical limitations that must be placed on certain modes of the plant's operation. An illustration of the latter is constraining the heat pumps and/or gas turbines to be in operation any time their corresponding heat storage tanks are in a state of charge.

The only remaining parameter above is $\mathbf{x}$, which is a vector of all the operation variables used during the minimization process. These include any mass flow rates, heat transfer rates, and electrical energy consumptions or productions that are varied during the minimization in order to arrive at the optimum modes of operation for the site. Also, note that since the MILP method used to solve the system of equations, Eqs. (1), (2), and (3), is a *linear* programming method, the objective function (Eq. (1)) and all the constraint equations (Eqs. (2) and (3)) must be linear.

For the system depicted in Fig. 2, the equality constraints comprise the mass balances for the water in the heating circuit, the local heat balances at the system boundaries or from system heat sources, and the electrical balance for the system as a whole. The overall mass balance for the heating circuit can be written as

$$0 = \dot{M}_{\mathrm{CND1}} + \dot{M}_{\mathrm{CND2}} + \dot{M}_{\mathrm{LTS}} D_{\mathrm{LTS}} - \dot{M}_{\mathrm{REC1}} - \dot{M}_{\mathrm{REC2}} - \dot{M}_{\mathrm{HTS}} D_{\mathrm{HTS}} - \dot{M}_{V2} - \dot{M}_{V3} - \dot{M}_{V4} \quad (6)$$

where D_{LTS} and D_{HTS} represent integer variables external to the MILP, which are used to change the direction of mass flow for the low and high-temperature heat storage devices. Their values ($+1$ or -1) depend on the various possible scenarios in which the plant can be operated.

The overall balance for the electrical energy produced, bought, sold, and consumed by the system is given by

$$0 = \dot{E}_{\mathrm{SELL}} - \dot{E}_{\mathrm{BUY}} + \dot{E}_D + \dot{E}_{\mathrm{PLTN}} + \dot{E}_{\mathrm{PMTN}} + \dot{E}_{\mathrm{CHP1}} + \dot{E}_{\mathrm{CHP2}} + \dot{E}_{\mathrm{PHP}} + \dot{E}_{\mathrm{PREC1}} + \dot{E}_{\mathrm{PREC2}} - \dot{E}_{\mathrm{GT1}} - \dot{E}_{\mathrm{GT2}} \quad (7)$$

The local heat balances at the system boundary or from system heat sources are the ones associated with the heat recovered from the turbine exhaust gases by the heating circuit, i.e.,

$$\dot{Q}_{GT1} = \dot{Q}_{\mathrm{REC1}} + \dot{Q}_{\mathrm{LOSS1}} \quad (8)$$

$$\dot{Q}_{GT2} = \dot{Q}_{\mathrm{REC2}} + \dot{Q}_{\mathrm{LOSS2}}, \quad (9)$$

the heat demanded from the heating circuit to meet the heating demands placed on the system by the users of the district heating network, i.e.,

$$\dot{Q}^{\mathrm{DMT}} = \dot{Q}_{V1} + \dot{Q}_{V2} \quad (10)$$

$$\dot{Q}^{\mathrm{DLT}} = \dot{Q}_{V3} + \dot{Q}_{V4} \quad (11)$$

and the heat represented by the heat pumps and heat storage tanks, i.e.,

$$\dot{Q}_{\mathrm{CND}} = \dot{Q}_{\mathrm{CND1}_{\mathrm{source}}} + \dot{Q}_{\mathrm{CND2}_{\mathrm{source}}} \quad (12)$$

$$\dot{Q}_{\mathrm{LTS}} = \dot{Q}_{\mathrm{LTS}_{\mathrm{source/sink}}} \quad (13)$$

$$\dot{Q}_{\mathrm{HTS}} = \dot{Q}_{\mathrm{HTS1}_{\mathrm{source/sink}}} + \dot{Q}_{\mathrm{HTS2}_{\mathrm{source/sink}}} \quad (14)$$

These last three equations actually add nothing new as constraints since the heat contributions originating from these sources are handled as single enthalpies, which, along with their corresponding mass flow rates, arrive at points $V1$ through $V4$ in Fig. 2. The enthalpy drops that then occur across each of these points are associated with each of the heat transfers in Eqs. (10) and (11) used to satisfy the demands of the district heating networks.

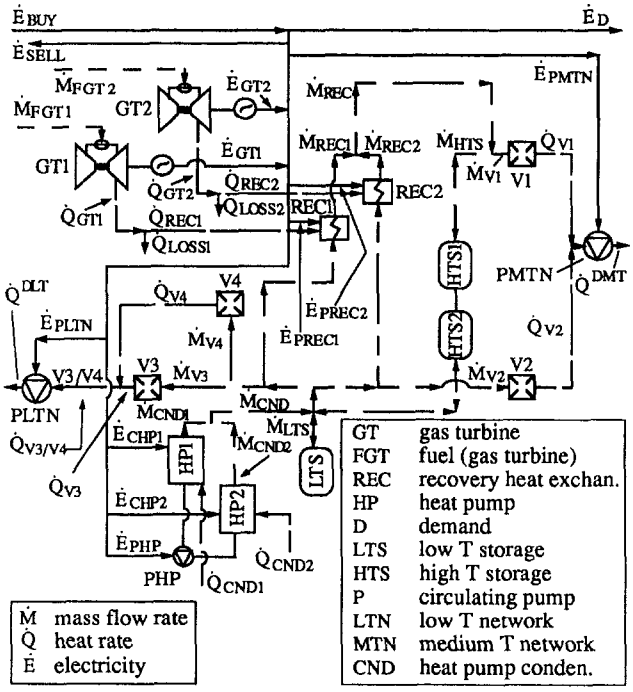

Fig. 2 Schematic representation of the mass and energy balance constraints used in the optimization of the system in Fig. 1

The terms $\dot{Q}_{\mathrm{REC1}}$, $\dot{Q}_{\mathrm{REC1}}$, $\dot{Q}_{V1}$, $\dot{Q}_{V2}$, $\dot{Q}_{V3}$, $\dot{Q}_{V4}$, $\dot{Q}_{\mathrm{LTS}}$, $\dot{Q}_{\mathrm{HTS}}$, and $\dot{Q}_{\mathrm{CND}}$ are the heat flows directly associated with the internal mass flows of the heating circuit. The relationship between these terms and their corresponding mass flow rates is established through a set of linear equations representing the performance characteristics of the components in the cycle. In the case of the gas turbine, the heat transfer is represented by a set of linear equations, which vary with the exterior temperature. This set poses no difficulties since it does not represent any nonlinearities with respect to the optimization. However, sets of linear performance equations used for the recuperators and for the heat pumps, which transfer heat to the heating network, and for the overall exchange of heat directly from the network to the user sites, represent nonlinear behavior with respect to the optimization, since there are variations in both the mass flow and temperature difference across each component. Such variations must be handled externally to the MILP algorithm (see discussion after Eq. (30) below) and, thus, represent one of the limitations imposed by a linear as opposed to nonlinear programming approach.

For the heat storage devices, there is no explicit component performance equation. For each, the times to charge and discharge are held constant, thus fixing their corresponding mass flow rates. The temperatures of charging and discharging, which are varied, are taken into account indirectly by the temperature drops across $V1$ through $V4$. The amount of heat stored in these devices depends on the amount of heat delivered by the gas turbines or the heat pumps and this amount depends on the current optimization (charging), on the prior optimization (discharging with charge), or on neither (discharging without charge, a condition which applies only to the HTS1 and HTS2). Thus, the rate of heat discharge is a constant and independent of the current optimization, while the rate of charge is a variable and, thus, a part of this optimization. Charging and discharging must, therefore, be handled externally to the MILP.

These characteristic equations represent additional equality constraints over and beyond those associated with the balance equations, Eqs. (6) through (11). Examples of these characteristic equations for the component heat transfer just discussed are written as follows:

Downloaded 02 Jun 2010 to 171.66.16.102. Redistribution subject to ASME license or copyright; see http://www.asme.org/terms/Terms_Use.cfm

$$\dot{Q}_{GT1} = r_{GT1}\dot{M}_{FGT1} + s_{GT1}\delta_{GT1} \quad (15)$$

$$\dot{Q}_{REC1} = r_{REC1}\dot{M}_{REC1} \quad (16)$$

$$\dot{Q}_{CND1} = r_{HP1}\dot{M}_{CND1} \quad (17)$$

$$\dot{Q}_{V1} = r_{V1}\dot{M}_{V1} \quad (18)$$

where, as discussed above, the coefficients in Eq. (15) vary with exterior temperature and those for Eqs. (16) through (18) vary with the temperature drops across each device. Similar equations for the second turbine, recuperator, heat pump, and other heat exchangers are found in von Spakovsky et al. (1992). The δ (0 or 1) variable in Eq. (15) is used by the MILP algorithm to simulate the on and off behavior of the gas turbines. This is done by using the delta variable as it appears in Eq. (15) and by placing it on the upper and lower limits of its corresponding mass flow rate (part of the inequality constraints given below). A similar set of δ's appears on the limits for the heat production associated with the heat pumps.

The only remaining equality constraints are those component characteristic equations associated with the electrical energy balance given in Eq. (7). They represent the electrical production by the gas turbines and the electrical consumption of the heat pump compressors and pumps, the recuperator pumps, and the circulating pumps for the heating networks. They are found in their entirety in von Spakovsky et al. (1992). Some examples are as follows:

$$\dot{E}_{GT1} = p_{GT1}\dot{M}_{FGT1} + q_{GT1}\delta_{GT1} \quad (19)$$

$$\dot{E}_{CHP1} = p_{CHP1}\dot{M}_{CND1} \quad (20)$$

$$\dot{E}_{PHP} = p_{PHP}\dot{M}_{CND} \quad (21)$$

$$\dot{E}_{REC1} = p_{REC1}\dot{M}_{REC1} \quad (22)$$

$$\dot{E}_{PLTN} = p_{PLTN}\dot{M}_{LTN} \quad (23)$$

Note that as with the heat transfer rates for the heat pumps, Eq. (20) actually represents a set of linear performance equations for the electric energy consumption of the heat pump compressors. A constant coefficient of performance of about 4.26 has been assumed.

To complete the definition of the mathematical model, the inequality constraints must be specified. These fall into two categories: bounds on all operation variables $\mathbf{x}$ and inequality constraints required to ensure that there are no contradictory or nonfeasible solutions produced by the MILP algorithm and that the heat storage devices operate in a way that is consistent with the operation of the gas turbines and heat pumps. With respect to $\mathbf{x}$, the following upper and lower bounds were placed directly on four of these variables, namely the heat rates relative to the condensers of the heat pumps and the fuel mass flow rates relative to the consumption of the gas turbines:

$$\dot{Q}_{L_{CND1}}\delta_{HP1} \le \dot{Q}_{CND1} \le \dot{Q}_{U_{CND1}}\delta_{HP1} \quad (24)$$

$$\dot{Q}_{L_{CND2}}\delta_{HP2} \le \dot{Q}_{CND2} \le \dot{Q}_{U_{CND2}}\delta_{HP2} \quad (25)$$

$$\dot{M}_{L_{FGT1}}\delta_{GT1} \le \dot{M}_{FGT1} \le \dot{M}_{U_{FGT1}}\delta_{GT1} \quad (26)$$

$$\dot{M}_{L_{FGT2}}\delta_{GT2} \le \dot{M}_{FGT2} \le \dot{M}_{U_{FGT2}}\delta_{GT2} \quad (27)$$

As was noted earlier, the delta variables in these expressions, along with those in Eqs. (15) and (19), simulate the on/off behavior of the corresponding pieces of equipment. Note that no bounds were placed directly on any of the other mass flow rates since they all depend on the fuel and heat pump condenser mass flow rates.

The fuel mass flow rates and the heat rates at the heat pump condensers are two of a total of twelve operation (or independent) variables used directly in the MILP algorithm during the optimization of the plant. These variables are

$$\mathbf{x} = \{\dot{Q}_{CND2}, \dot{Q}_{CND2}, \dot{M}_{FGT1}, \dot{M}_{FGT2}, \dot{Q}_{LOSS1}, \dot{Q}_{LOSS2}, \dot{E}_{BUY}, \dot{E}_{SELL}, \delta_{HP1}, \delta_{HP2}, \delta_{GT1}, \delta_{GT2}\} \quad (28)$$

The MILP algorithm automatically ensures 0 or 1 values for all the delta variables. The remaining variables are explicitly constrained to be greater than or equal to zero such that

$$\dot{Q}_{LOSS1}, \dot{Q}_{LOSS2}, \dot{E}_{BUY}, \dot{E}_{SELL} \ge 0 \quad (29a, b, c, d)$$

Of course, in addition to the variables explicitly used in the optimization algorithm, there are the implicit variables represented by

$$T_1(\text{at } V1),\ T_2(\text{at } V2),\ T_3 = T_2(\text{at } V3),\ T_4 = T_{RMTN}(\text{at } V4)$$
$$T_{3/4} = f(T_3, T_4)(\text{at } V3/V4),\ \dot{M}_{V4} = f(T_3, T_4, \dot{M}_{V3}) \quad (30)$$

Of these six additional variables, only the first two, T_1 and T_2, are independent. Taken in conjunction with the explicit variables, these variables introduce, as was mentioned earlier, nonlinearities into the optimization problem. Thus, they are handled independently of the MILP algorithm and are not optimized per se but are varied within reasonable limits in order to determine the best mix of temperatures within those limits.

The remaining inequality constraints are those belonging to category two above. They are presented by von Spakovsky et al. (1992) and ensure that the water mass flow rates for the recuperators are not negative, that the gas turbines and heat pumps are functioning when their respective heat storage devices are in a state of charge, that the water mass flow rates passing through the heat pump condensers or bypassing the low-temperature heat storage device are sufficiently large to be the source of all other mass flows in the heating circuit and that the mass flow rates feeding the medium-temperature heating network are sufficiently large to satisfy the mass flow rate passing by $V4$. This latter flow rate is an extraction flow from the flow returning from the MT network and is actually not extracted at the point shown in Fig. 2. Physically it is extracted as shown in Fig. 1. The representation appearing in Fig. 2 is its equivalent.

The only remaining equations needed in order to complete our presentation are the functions defining the hourly demands of each district heating network, the hourly changes in price of the electricity bought and sold, and the hourly variations in the return temperature for each district heating network. These appear in graphic form in the following section.

Procedures and Results

The MILP algorithm used is called ZOOM and was developed by Marsten (1985). It employs a tiered approach by first solving the problem as a linear program and then using a pivot and complement heuristic to find an initial integer feasible solution. A branch-and-bound search is then employed to find improved solutions and to verify optimality. In this way, the algorithm tries to ensure that the optimum found is more than just an inflection point or local optimum.

The choice of implicit variables, Eq. (30), is handled by our own algorithm as are the charging and discharging operations of the high and low-temperature heat storage devices. In fact, it is these components that ultimately dictate what the optimum structure and operation of the overall system will be at each time interval during a given 24-hour period, time intervals that are themselves determined (see von Spakovsky et al., 1992) by the charging and discharging behavior of these devices. For the optimization results that follow, a 24-hour period typical of a winter day in January in Switzerland was chosen.

Table 1 lists the fixed parameters; those that vary only as a function of time and are, thus, not optimized appear in Figs. 3 and 4. The latter include the return temperatures T_{RLTN} and T_{RMTN} (with $T_{RLTN} = T_{RMTN}$) for the district heating networks, the average temperature of the exterior T_{EXT}, and the heating demands of the medium and low-temperature user sites. The unit costs of electricity bought and sold and that of fuel are

Downloaded 02 Jun 2010 to 171.66.16.102. Redistribution subject to ASME license or copyright; see http://www.asme.org/terms/Terms_Use.cfm

Table 1 Fixed parameters

heat storage devices' charging and discharging times: $t_{LTS_{CH}} = 2000$ s $t_{LTS_{DCH}} = 2500$ s $t_{HTS_{CH}} = 6500$ s $t_{HTS_{DCH}} = 7500$ s	limits on the gas turbines' fuel mass flow rates and the heat pumps' condenser heat flow rates to the heating network: $\dot{M}_{LFGT1} = \dot{M}_{LFGT2} = 0.1028$ kg/s $\dot{M}_{UFGT1} = \dot{M}_{UFGT2} = 0.331$ kg/s $\dot{Q}_{LCND1} = \dot{Q}_{LCND2} = 0.01$ MWth $\dot{Q}_{UCND1} = \dot{Q}_{UCND2} = 4.0$ MWth
total heat storage capacities and mass flow rates used: $V_{LTS} = 106.7$ m^3 $V_{HTS} = 42.7$ m^3 $\dot{M}_{LTS_{CH}} = -53.34$ kg/s $\dot{M}_{LTS_{DCH}} = +42.67$ kg/s $\dot{M}_{HTS_{CH}} = -6.56$ kg/s $\dot{M}_{HTS_{CH}} = +5.69$ kg/s	coefficients and constants of the characteristic performance equations for the gas turbines and for the circulating pumps of the heating network and heat pumps: $p_{GT1} = p_{GT2} = 14.76$ $q_{GT1} = q_{GT2} = -1.1135$ $p_{PMTN} = p_{PLTN} = 4.286e\text{-}4$ $p_{PHP} = 2.813e\text{-}4$ electrical demand on the system $\dot{E}_D = 5.0$ MWe

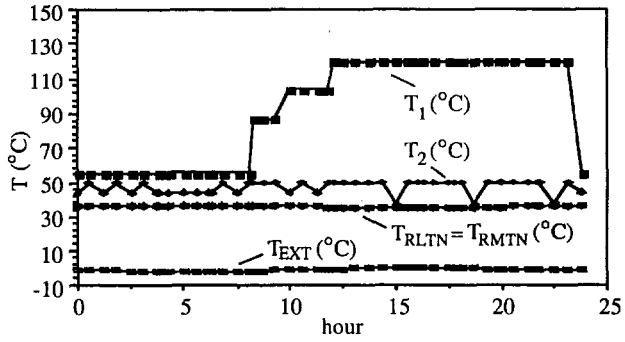

Fig. 3 Parameter as well as optimum temperature variations

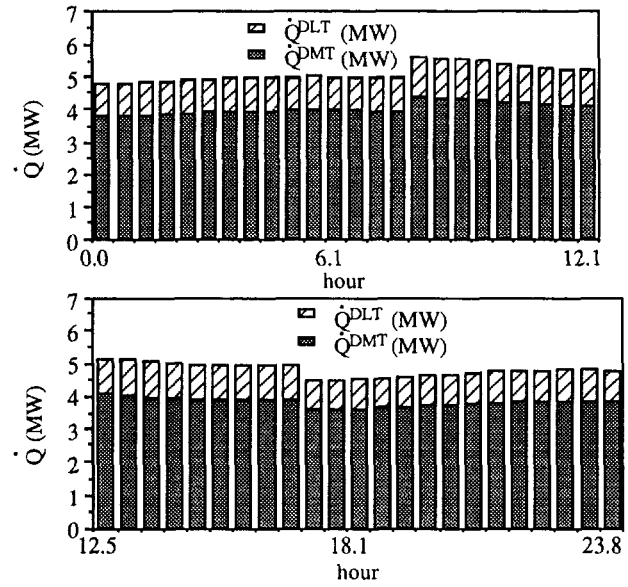

Fig. 4 Heating demands for the district heating networks

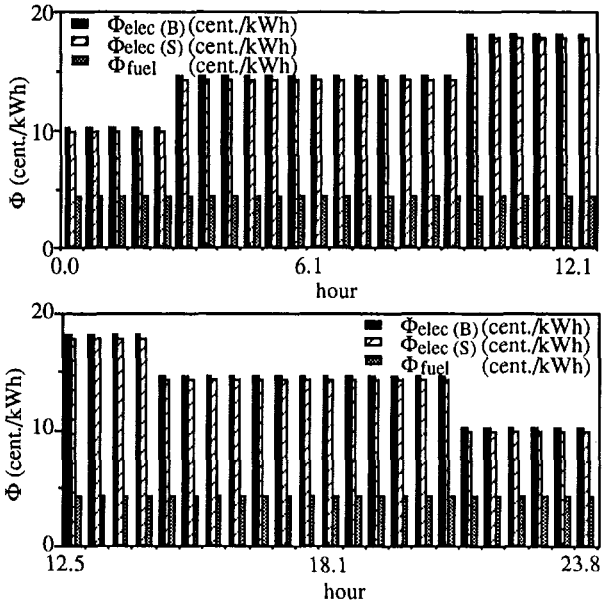

Fig. 5 Unit cost variations of electricity and fuel

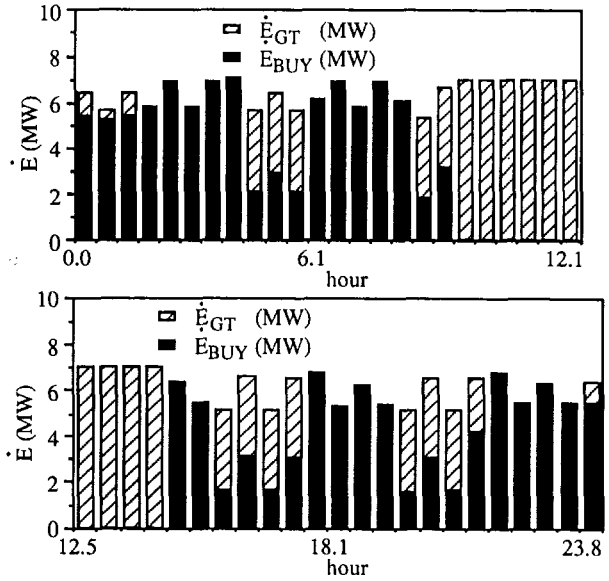

Fig. 6 Optimum amount of electricity bought and produced

also a function of time and are given in Fig. 5. The coefficients for the performance characteristic equations for the gas turbines and pumps are also found in Table 1 with the exception of those for Eqs. (15) and (22). The latter was not included in our model and the former's coefficients vary with the exterior temperature (see von Spakovsky et al., 1992). In addition, the volume given in Table 1 for the high-temperature storage devices represents only one fifth of their total capacity. Only part of the capacity was used since the remaining exceeds (based on the times to charge and discharge used here) that required to meet the demands of the district heating networks. Furthermore, it was assumed that there is significant stratification at only one moving point within both the LTS and HTS devices so that a well-defined temperature front between high and low temperatures exists. This, in fact, is known to be physically the case.

Complete results of the optimization are found in von Spakovsky et al. (1992). Some of the results appear in the following figures. They reflect not only the optimum at each time interval resulting from an MILP optimization of the mathematical model presented here but also the best and/or only feasible optimum solution among a set of such solutions at each time interval. The latter is based on a systematic search for the best temperature mix within the system.

Turning to Fig. 6, which shows the optimum amount of electricity bought and produced by the gas turbines over a 24-hour period, one can see that buying instead of producing in order to meet internal demands predominates in the early and late hours, but that the exact opposite trend is seen for the middle hours of the day. This is partly explained by the relatively high value of the unit price of electricity sold to that

Downloaded 02 Jun 2010 to 171.66.16.102. Redistribution subject to ASME license or copyright; see http://www.asme.org/terms/Terms_Use.cfm

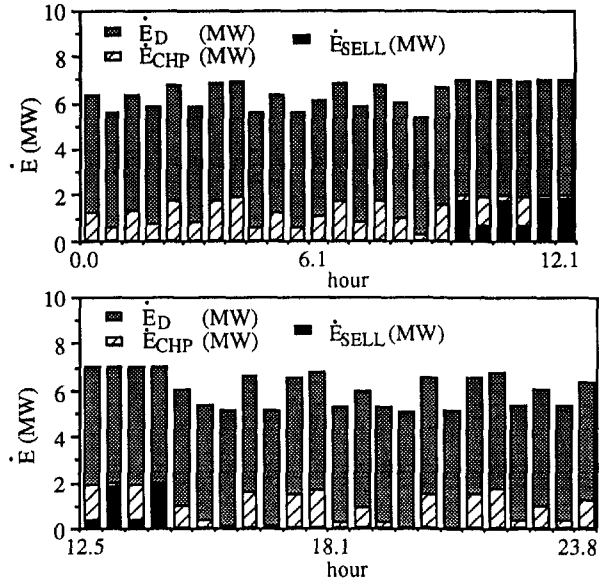

Fig. 7 Some internal electrical demands and the optimum electricity sold

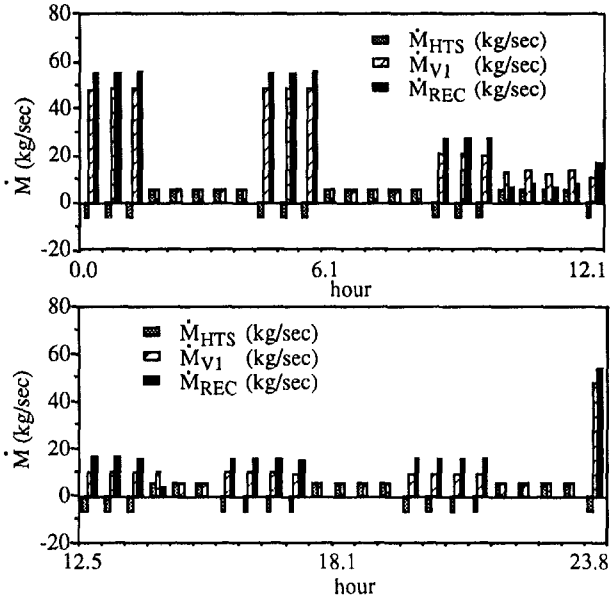

Fig. 9 Optimum heat recovery and HTS mass flow rates

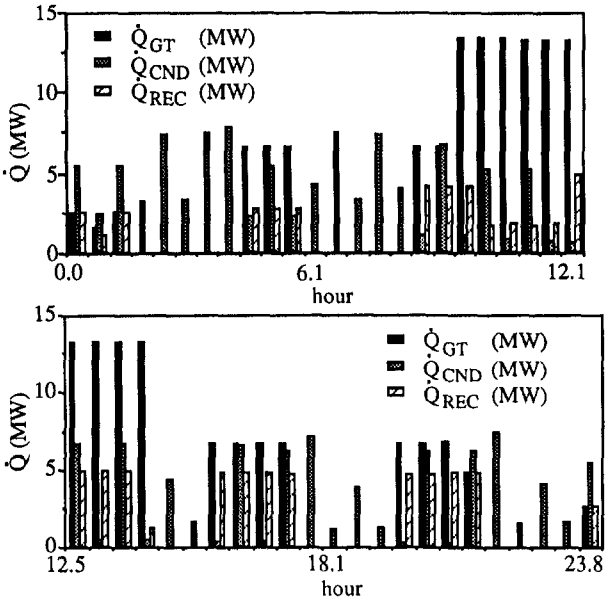

Fig. 8 Optimum turbine, heat pump, and recuperator heat rates

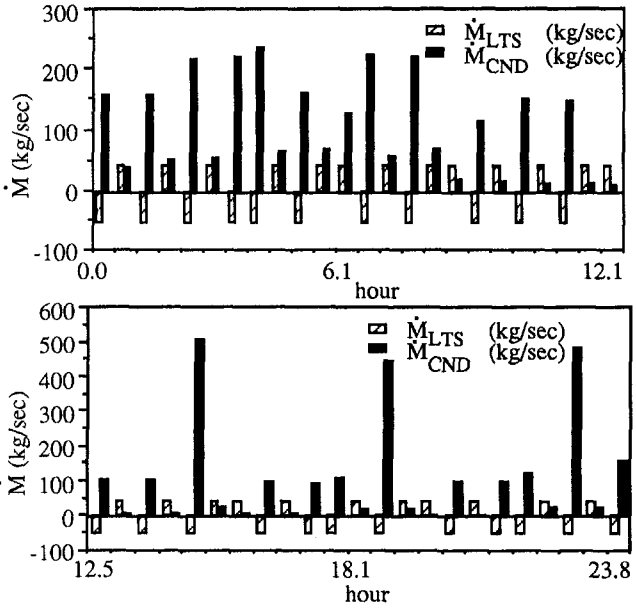

Fig. 10 Optimum mass flow rates for the heat pumps and LTS device

bought and by the rise in the unit price of electricity sold toward the noon hours (Fig. 5). This is verified in Fig. 7 where one can see that it becomes profitable to sell electricity to the outside utility grid during these hours.

Figure 8 shows the optimum heat rates for the turbines, heat pumps, and recuperators. The temperatures at which these are delivered are shown in Fig. 3. This figure indicates that within the limits placed on the optimization, the ideal temperature of heat recuperation combined with that of high-temperature heat storage or heat discharge varies between about 54 and 120°C. In contrast, the combination of heat delivered by the heat pumps and that of the low-temperature heat storage or heat discharge varies between about 37 and 50°C. At first glance, some of the lower heat recovery temperatures and of heat delivery by the heat pumps seem rather surprising. However, taken in the context of the changing structure of the system (such as the charging and discharging of the heat storage devices) and the varied constraints placed on the operation of the system, these rather low temperatures are the ones that at given intervals provide the lowest cost of overall operation and/or the only feasible solution.

Finally, the optimum mass flow rates for the system at each interval during the 24-hour period are seen in Figs. 9 and 10 and in von Spakovsky et al. (1992). In fact, Figs. 9 and 10 show the charging and discharging behavior of the high and low-temperature heat storage devices. The negative flow rates indicate when these devices are in a state of charge while positive values indicate discharge. Also, the three large spikes in the latter half of the day in Fig. 10 are due to the constraints placed on the mass flow rates of the heat pump condensers (see von Spakovsky et al., 1992) and on the mass flow rates delivered to the MT heating network (see von Spakovsky et al., 1992) and to the past history of the system's operation during the day, indicating that at these intervals these flows provide the lowest cost of overall operation and/or the only feasible solution.

Downloaded 02 Jun 2010 to 171.66.16.102. Redistribution subject to ASME license or copyright; see http://www.asme.org/terms/Terms_Use.cfm

Conclusions

The task of determining the optimum mode of operation for complex facilities such as the cogeneration/heat pump facility at the EPFL is a difficult if not impossible task if based solely on the experience of the engineers and operators running the plant and, particularly, if the plant must meet conflicting goals or demands. However, this task can be solved provided some mathematical approach is used that can simulate the facility's changing structure and operation and simultaneously take into account the complex interactions of a large number of operational variables, arriving at an optimum mode of operation for each set of conditions the facility may have to meet. Such a mathematical approach acts as a compliment to the engineer's and the operator's experience, and one such approach has been presented here.

The MILP approach used has certain advantages in that it can simulate the changing structure of the plant, i.e., the on/off operation of a system's components. Provided that the primary goal is to optimize the overall operation of a system without gleaning much in terms of the internal details of its operation, then such a linear approach suffices. The problem arises when a greater amount of detail is desired, such as, for example, the thermodynamic states at different points within the cycle or when the characteristic performance equations are no longer linear or must be represented by a set of linear performance equations. In such a case, the MILP approach is no longer adequate. Either a nonlinear approach must be used; or as was done for the specific problem presented here, a separate algorithm must be used in conjunction with the MILP to simulate the changing component characteristics.

Finally, a further complication arises if heat storage devices are used by the facility. By virtue of the fact that they store and discharge energy, their operation actually represents two separate problems, which in the context of the changing operation of the plant during the day, need to be viewed as a single problem. The MILP algorithm is unable to do this; and, thus, such devices must, as with the nonlinearities discussed above, be handled in a separate algorithm.

References

Akagi, S., Yokoyama, R., and Ito, K., 1986, "Optimal Operation of an Energy Saving Combined Plant for LNG Carriers," *Proceedings of the Japan-USA Symposium on Flexible Automation*, pp. 811–817.

Ito, K., Yokoyama, R., Akagi, S., and Matsumoto, Y., 1990, "Influence of Fuel Cost on the Operation of a Gas Turbine-Waste Heat Boiler Cogeneration Plant," ASME JOURNAL OF ENGINEERING FOR GAS TURBINES AND POWER, Vol. 112, pp. 122–128.

Ito, K., Yokoyama, R., and Shiba, T., 1991, "Optimal Operation of a Cogeneration Plant in Combination With Electric Heat Pumps," *Proceedings of the 1991 ASME Cogen Turbo V*, Budapest, pp. 371–378.

Ito, K., Yokoyama, R., and Shiba, T., 1992, "Optimal Operation of a Diesel Engine Cogeneration Plant, Including a Heat Storage Tank," ASME JOURNAL OF ENGINEERING FOR GAS TURBINES AND POWER, Vol. 114, pp. 687–694.

Kuester, J. L., and Mize, J. H., 1973, *Optimization Techniques With Fortran*, McGraw-Hill, New York.

Laboratoire d'Énergétique Industrielle, 1986, "La centrale de chauffage de l'EPFL CCT," internal report, École Polytechnique Fédérale de Lausanne (EPFL), Lausanne, Switzerland.

Marsten, R., 1985, *User's Manual for Zero/One Optimization Methods (ZOOM)*, University of Arizona, USA.

Reklaitis, G. V., Ravindran, A., and Ragsdell, K. M., 1983, *Engineering Optimization Methods and Applications*, Wiley, New York.

von Spakovsky, M. R., Curti, V., and Batato, M., 1992, "The Performance Optimization of a Cogeneration/Heat Pump Facility," *Proceedings of the Conference on Efficiency, Costs, Optimization and Simulation of Energy Systems (ECOS'92)*, Zaragoza, Spain.

Yokoyama, R., and Ito, K., 1993, "Optimal Operational Planning of Cogeneration Systems With Thermal Storage by the Decomposition Method," *Proceedings of the 1993 ASME Cogen-Turbo Power*, Bournemouth, United Kingdom.

Downloaded 02 Jun 2010 to 171.66.16.102. Redistribution subject to ASME license or copyright; see http://www.asme.org/terms/Terms_Use.cfm

Gas Turbine Bottoming Cycles: Triple-Pressure Steam Versus Kalina

C. H. Marston
Villanova University,
Villanova, PA 19085

M. Hyre
Massachusetts Institute of Technology,
Cambridge, MA 02139

The performance of a triple-pressure steam cycle has been compared with a single-stage Kalina cycle and an optimized three-stage Kalina cycle as the bottoming sections of a gas turbine combined cycle power plant. A Monte Carlo direct search was used to find the optimum separator temperature and ammonia mass fraction for the three-stage Kalina cycle for a specific plant configuration. Both Kalina cycles were more efficient than the triple pressure steam cycle. Optimization of the three-stage Kalina cycle resulted in almost a two percentage point improvement.

Introduction

The Kalina cycle (El-Sayed and Tribus, 1985a; Kalina, 1984; Kalina and Leibowitz, 1990; Marston 1990a; Park and Sonntag, 1990) is a power plant cycle that utilizes a binary working fluid, most often ammonia and water. When such a mixture is heated, the more volatile ammonia tends to vaporize first and at lower temperature than pure water. As the ammonia concentration of the remaining liquid decreases, saturation temperature rises, providing a better match to a hot gas heat source such as a gas turbine exhaust than the constant-temperature evaporation of a pure substance (water/steam). The working fluid is split into streams with different concentrations, providing a great deal of flexibility with which to optimize heat recovery and allowing condensation at a pressure greater than atmospheric.

This study (Hyre, 1991) was aimed at providing a comparison of a multi-pressure Rankine steam cycle and two variants of the Kalina cycle as the bottoming part of a high-efficiency gas turbine combined cycle. The fully reserved cost of electricity was considered in evaluating the steam plants but such data were, of course, not yet available for the Kalina cycle plant. The question as to whether the potential increase in efficiency is dramatic enough to justify the capital cost increases associated with the cycle is only partially addressed here.

Code Development

The simulation code developed to model the gas turbine topping cycle includes a thermodynamic properties generation code plus a configuration-specific driver program and a set of component modules.

Thermodynamic Data

More than 750 species, in gaseous, liquid, and solid phases, are included in the thermodynamic data base. These species include most of the constituents of bottom ash and fly ash so that gas, coal, and oil-fired topping cycles can be modeled.

The NASA PAC program (McBride and Gordon, 1967) was applied to molecular constant data from Robie and Waldbaum (1968) and from the JANAF *Thermochemical Tables* (1971). The least-squares technique of Zeleznik and Gordon (1961) was used to generate polynomial equations in temperature for heat capacity, enthalpy, and entropy. A new set of polynomials was needed because PAC combines sensible enthalpy and energies of chemical and physical changes into one numerical value and the distinction is important. Also, the zero reference for enthalpy and entropy in the new code was set at 0°C rather than 25°C in order to be consistent with the steam tables.

For most condensed species, the thermodynamic functions were also taken from the JANAF *Tables*. Additional thermochemical data for some ash species (Robie and Waldbaum, 1968) were added to complete the coefficient database. Thermodynamic properties of steam were generated from equations in the *ASME Steam Tables* (Meyer et al., 1967).

The code was checked against the ASPEN (JSD, 1989) code and another proprietary thermodynamic code and was found to be in excellent agreement. The code used for the thermodynamic properties of ammonia–water mixtures was developed by Marston (1990a) based on the work of El-Sayed and Tribus (1985b) and extended to 2800 psi by Dayan (1989) and Marston.

The combustor module assumes ideal gases and complete combustion with air (21 percent O_2, 79 percent N_2). All hydrogen and carbon in the fuel is oxidized to H_2O and CO_2. Nitrogen is assumed to pass through the process unchanged chemically. Results are expressed in terms of Lower Heating Value unless otherwise noted.

Since combustion in a gas turbine takes place at elevated pressures (between 10 and 30 atm) the accuracy of the ideal gas and complete combustion assumptions was checked against more sophisticated models (JSD, 1989; Gordon and McBride, 1976). Agreement was within 1 percent on temperature and within less than 0.1 percent on composition.

Contributed by the Advanced Energy Systems Division for publication in the JOURNAL OF ENGINEERING FOR GAS TURBINES AND POWER. Manuscript received by the Advanced Energy Systems Division October 4, 1993; revision received May 10, 1994. Associate Technical Editor: M. J. Moran.

Copyright © 1995 by ASME

Downloaded 02 Jun 2010 to 171.66.16.102. Redistribution subject to ASME license or copyright; see http://www.asme.org/terms/Terms_Use.cfm

Gas Turbine Rankine Combined Cycle

The configurations in this study are natural gas fired. They have a net output of about 240 MWe, no supplemental firing, and a forced circulation HRSG.

Gas Turbine Specification. Gas turbines have reached firing temperatures up to 2300°F (1260°C) with corresponding exhaust temperatures of about 1110°F (599°C). Combined cycle heat rates have fallen to a range of about 7000–8000 Btu/kWh (Jeffs, 1990). Most utilities have ordered plants without supplemental firing and with total outputs in the 100–250 MWe range (Edison Electric Institute, 1986). Natural gas is probably the most desirable fuel because it is clean and is readily available.

Performance and operating parameters of an advanced gas turbine (EPRI, 1987) were used for the analysis. Ambient temperature was taken to be 59°F (15°C). Turbine exhaust conditions were 1050°F (566°C), 800 lbm/s (363 kg/s) with a power output of 175 MWe.

Heat Recovery Steam Generator. Most heat recovery steam generators (HRSGs) in the USA use natural circulation. Natural circulation units may be easier to operate because of the absence of the circulation pumps, but forced circulation units are smaller and can be started up faster. In Europe forced circulation units have operated successfully at very high efficiencies over a wide range of gas turbine loads and exhaust characteristics, so forced circulation was assumed.

Number of Boiler Pressure Levels: Single-, double-, and triple-pressure steam bottoming plants were considered. With a single-pressure HRSG, steam generator output is only about 30 percent of the total plant output because the amount of heat recovered is limited by the pinch point in the boiler. A dual-pressure cycle can increase the power output of the steam cycle by up to 10 percent and an additional 3 percent can result by going to a triple-pressure cycle. Most of the additional power from the latter comes from the increase in average exergy of the steam rather than a further increase in the amount of actual energy transferred.

In multi-pressure cycles the temperatures versus duty curves are better matched. However, the resultant decreases in log mean temperature difference cause an increase in the capital cost of the HRSG because of the increase in the amount of required heat transfer area. Gas turbine exhaust pressure also rises, and more feedwater pumps, drum level controls, safety valves, steam turbine admission systems, etc., are required. The boiler must be capable of sliding pressure operation during startup, part load, and cycling because the temperature of the gas leaving the high-pressure evaporator is independent of load, while the heat removed by the high-pressure economizer is directly proportional to load.

Reheat. The reheater is assumed to be in series rather than in parallel with the superheater. This minimizes the problems associated with the flue gas distribution but makes it somewhat more difficult to ensure uniform initial and reheat steam temperatures under all load conditions.

Primary Steam Pressure. A limit on primary steam pressure is the moisture content in the last stage of the steam turbine. Turbine manufacturers consider 13 percent to be about the limit for long-term operation. If pressure exceeds 1500 psig (10.3 MPa), boiler feedwater treatment requirements become much more stringent and higher cost double casing turbines are required, so current steam bottoming cycles generally operate below this limit. The pressure levels shown in Table 1 were chosen because they have frequently been selected for recently ordered units.

Table 1 Boiler inlet pressures (psia)

Configuration	HP	IP	LP
Single-Pressure	815	---	---
	1015	---	---
	2415	---	---
Double-Pressure	815	---	50
	1015	---	110
	2415	---	110
Triple-Pressure	815	285	25
	1015	285	25
	2415	500	40
Triple-Pressure (with reheat)	815	340	25
	1015	340	25
	2415	700	25

Feedwater Heating and Deaeration. For gas turbine combined cycles, temperature limits in the compressor and gas turbine preclude air preheat, so all of the usable gas turbine exhaust heat can be transferred to the steam cycle. Following recent practice (Czermak and Wunsch, 1982), feedwater heating occurs only in the deaerator. Extraction deaerators are effective at all loads and this is especially important when operating off-design or when steam is being used in the topping cycle for NO_x control.

Stack Temperature. The absence of acidic species in the flue gas of natural gas fired units makes water condensation in the economizer acceptable. The only limit on stack temperature was the need to maintain plume buoyancy.

Steam Plant Economic Tradeoffs. Economic analysis was based on a fully reserved cost of electricity (FRCOE) study conducted by Bechtel Group (1988) using data updated to 1990 dollars. A reserved cost of electricity takes into account cost penalties for the loss of availability and for increased uncertainty due to complexity introduced by plant improvement schemes.

Capital costs were estimated for four cost blocks consistent with the Bechtel study: Gas Turbine, HRSG, Steam Turbine, and Adjustments. Gas turbine and HRSG unit cost was based on the Bechtel study. Steam turbine cost was taken from an advanced combined cycle power plant study (EPRI, 1987) by subtracting the cost of the gas turbine and HRSG. For each additional pressure level above a single-pressure HRSG, an allowance of 25 percent of the steam plant cost was included to account for increased operating complexity and lack of operating experience. A capacity factor of 0.90 was chosen on the assumption that the plant would be used in the baseload operations and not strictly for peaking or cycling. Levelizing factors were those suggested by EPRI for 1990.

Nomenclature

ASPEN = Commercial Systems Code
COE = Cost of Electricity
DCSS = Distillation Condensation Subsystem (the heat recovery and heat rejection part of the Kalina cycle)
EPRI = Electric Power Research Institute
FRCOE = fully reserved cost of electricity (cost estimates adjusted for differences in complexity and availability)
HRSG = Heat Recovery Steam Generator
JANAF = Joint Army Navy Air Force (Thermochemical Tables)

Downloaded 02 Jun 2010 to 171.66.16.102. Redistribution subject to ASME license or copyright; see http://www.asme.org/terms/Terms_Use.cfm

Table 2 COE, FRCOE, and adjusted overall system availability for the gas turbine/steam combined cycles

No. of Press. Levels	Avail	Heat Rate (Btu/kWh) (HHV)	COE (mills/kWh)	FRCOE
1	0.971	7795	69.04	70.21
2	0.958	7526	67.52	69.56
3	0.947	7456	67.16	69.33
3(Rht)	0.939	7407	66.71	69.24

note: Historical availability was 0.960

Table 3 Final steam plant configuration and unit costs

Number of Pressure Levels	3 w/reheat
Throttle Pressure:	
Economic evaluation	1015 psia
Final performance	1200 psia
Condenser Back Pressure	1 in. Hg
BFP to Turbine Inlet delta P	20%
Pinch Points	30 F°
Superheater Approach	50 F°
Economizer Approach	30 F°
Circulating Water Delta T	30 F°
Pump Efficiencies	0.80
Turbine Efficiencies	
Single Stage	0.87
High Pressure	8.835
Intermediate Pressure	0.905
Low Pressure	0.840
Gas Turbine	$215/kW
HRSG	$7.50/sq ft
Steam Turbine	$775/kW
Capital Charge	0.175
Levelization Factor	1.75
Natural Gas Fuel	$4.50/MBtu
O&M Fixed Charge	$6.60 kW/yr
O&M Incremental Charge	1.5 mills/kWhr

Operating and maintenance (O&M) costs were taken directly from data for the same advanced combined cycle unit on which steam turbine cost was based. O&M procedures are not standard and may determine the level of plant complexity that is acceptable to a specific utility.

Availability. A recent study by Brown and Gardner (1982) of the availability of 16 utility combined cycle power plants formed the basis for detailed estimates of multi-pressure steam plant availability. The plants in the EPRI study were built 10 to 15 years ago so availability factors were also adjusted to reflect recent improvements.

Availability of the complete steam cycle was taken as the product of the individual availabilities for each system/component as detailed by Hyre (1991). However, added pressure levels would not be expected to cause a doubling of failures so exponents of 1.8 and 2.5 for two-pressure and three-pressure cycles were used. The overall availability factors are shown in Table 2.

Utility and site-specific conditions may have a significant impact so conclusions based on this FRCOE analysis are, at best, a rough guide. With that disclaimer Table 2 also summarizes results for the three steam plants. The triple-pressure cycle with reheat appears to offer the best plant performance and best FRCOE. Cycle configuration is essentially that built at Utrecht (Jeffs, 1990).

While heat rate and COE decrease with increasing steam pressure, FRCOE is higher for the 2415 psig (16.6 MPa) cycle. The increase results from lack of combined cycle experience at this pressure level and requirements for more complex feedpumps and double case steam turbines.

Steam Plant Selection. Of those cycles considered in the economic evaluation, the 1015 psia (6.9 MPa) triple-pressure single reheat cycle was selected. Final performance evaluation of the triple-pressure steam cycle was based on a turbine inlet pressure of approximately 1200 psia (1500 psig at boiler feed pump exit). The higher pressure resulted in a more efficient plant and is more representative of turbine combinations offered commercially. The change was judged to be small enough not to significantly affect the conclusions from the economic evaluation. A series of perturbation studies established other parameters, such as pinch point and condenser back pressure. Data for the selected plant are shown in Table 3. Applicable values were used for both steam and Kalina plants.

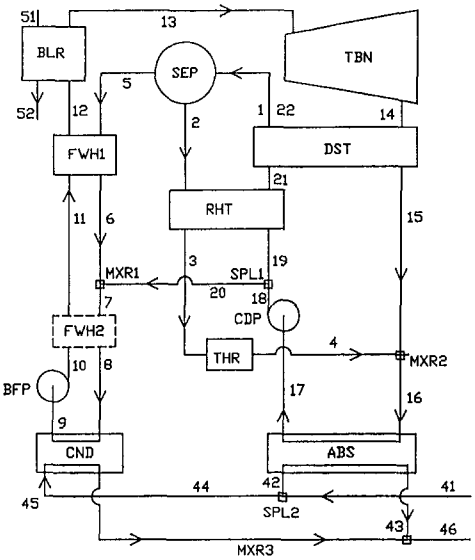

Fig. 1 System diagram for the simplified Kalina cycle

Kalina Bottoming Cycle

In the Kalina cycle a mixture of ammonia and water (approximately 70/30 by mass) is passed through a once-through boiler in counterflow with a hot gas heat source. The vapor is ammonia-rich so as evaporation proceeds the boiling temperature of the remaining liquid rises, resulting in a better heat transfer match to the heat source (Marston, 1990a). Downstream of the turbine exit an ammonia-depleted stream is mixed with the 70/30 mixture in a spray-type absorber to decrease the ammonia concentration to about 40 percent, so condensation, again in counterflow heat exchange, occurs above atmospheric pressure. The additional independent variable (composition) in the Distillation Condensation Subsystem (DCSS) provides a great deal of flexibility for maximizing heat recovery. Potential gains in performance over conventional steam cycles are thus attributable to:

- A better match to the thermal input as a result of vaporization at continuously increasing temperature (though a multipressure steam cycle has a roughly similar advantage).
- Lower effective heat rejection temperature because counterflow heat exchangers can be used.
- Effective heat recovery in the variable composition DCSS.

Configurations

Figure 1 is a flow diagram of the simplified cycle studied by Marston (1990a). The key to the DCSS is the flow path of fluid circulating between the separator and the absorber, states 2-3-4-16-17-1-2, plus the connection, 18-20-7, which dilutes the nearly pure vapor, 6, to the working fluid composition. The three-stage cycle proposed by Kalina and Leibowitz (1990) shown in Fig. 2 has exactly the same flow topology but it takes advantage of some of the possibilities for minimizing exergy loss by judicious use of additional heat exchangers. This includes a "recooler" to transfer thermal energy from the in-

Downloaded 02 Jun 2010 to 171.66.16.102. Redistribution subject to ASME license or copyright; see http://www.asme.org/terms/Terms_Use.cfm

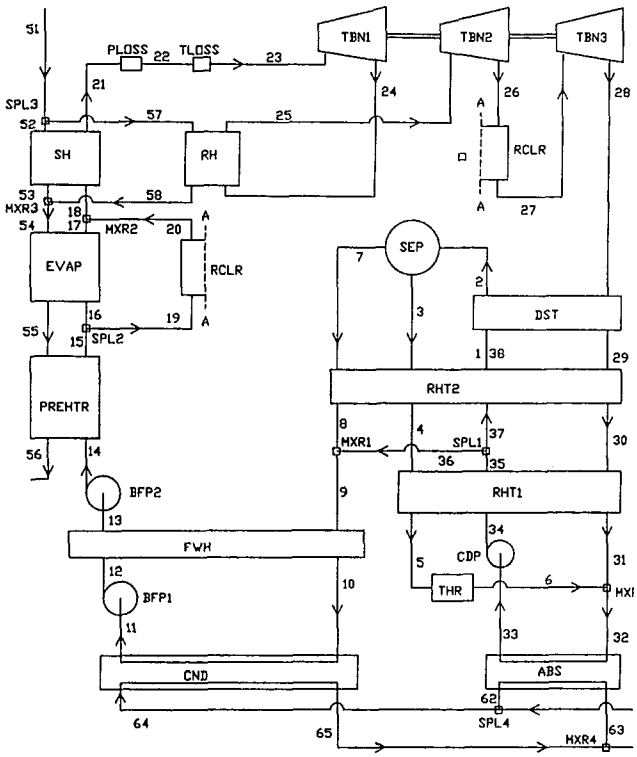

Fig. 2 System diagram for the three-stage Kalina cycle

Table 4 State points for the optimized three-stage Kalina cycle

State	p (kPa)	T (C)	X (-)	h (kJ/kg)	s (kJ/kg-K)	$\dot{m}$ (kg/s)
1	104	155	.4500	91.9	0.285	890
2	101	172	.4500	149.2	0.378	890
3	101	172	.3478	50.5	0.208	751
4	98	95	.3478	-31.7	0.069	751
5	95	80	.3478	-47.7	0.040	751
6	31	80	.3478	-47.7	0.040	751
7	101	172	.9637	645.3	1.230	139
8	98	115	.9637	583.1	1.134	139
9	98	126	.7500	327.2	0.693	241
10	95	109	.7500	280.1	0.613	241
11	92	70	.7500	-32.5	0.038	241
12	1306	74	.7500	-26.4	0.040	241
13	1266	116	.7500	20.7	0.126	241
14	1520	117	.7500	21.9	0.127	241
15	1140	256	.7500	197.7	0.407	241
16	1140	256	.7500	197.7	0.407	198
17	1140	420	.7500	797.0	1.161	198
18	1140	420	.7500	797.0	1.161	241
19	1140	256	.7500	197.7	0.407	43
20	1140	420	.7500	797.0	1.161	43
21	1140	905	.7500	1169.9	1.496	241
22	1140	905	.7500	1169.9	1.496	241
23	1140	905	.7500	1169.9	1.496	241
24	619	788	.7500	1095.7	1.509	241
25	600	905	.7500	1176.7	1.573	241
26	113	578	.7500	974.2	1.594	241
27	110	395	.7500	866.2	1.483	241
28	34	227	.7500	780.4	1.506	241
29	33	160	.7500	578.7	1.194	241
30	32	115	.7500	397.9	0.895	241
31	31	80	.7500	321.0	0.758	241
32	31	96	.4500	46.0	0.223	991
33	30	70	.4500	-64.5	0.014	991
34	101	70	.4500	-64.2	0.014	991
35	98	100	.4500	-32.1	0.073	991
36	98	100	.4500	-32.1	0.073	102
37	98	100	.4500	-32.1	0.073	890
38	104	155	.4500	98.1	0.295	890

termediate pressure (IP) turbine exhaust to thermal input. Both versions of the Kalina cycle were treated as the bottoming section of a gas turbine combined cycle. State point data for the three-stage cycle (optimized as discussed below) are presented in Tables 4 and 5.

While preliminary data from the Exergy, Inc., demonstration power plant (Leibowitz and Zervos, 1992; Leibowitz, 1993) are encouraging there are still design uncertainties. Countercurrent flow must be achieved in the heat exchangers with small temperature differences and with phase changes on both sides. Liquid and vapor phases must be well mixed since separation can result in a distortion of the boiling/condensing temperature profiles and a consequent reduction in heat transfer rate. Also, physical locations of the bubble point and the dew point in a once-through HRSG (as opposed to a drum type) are difficult to determine, and integrating a recooler into the cycle may be a problem.

Limited Optimization

Kalina cycle models have frequently used a boiler working fluid of ammonia mass fraction of 0.7, but the optimum composition is a function of many design parameters. The Monte-Carlo direct search method was applied to optimization of working fluid composition and separator temperature[1] of the three-stage configuration.

Other parameters, which represent conditions currently judged by utilities to be effective in terms of cost and performance, were held constant to provide a consistent basis of comparison with the triple-pressure Rankine cycle. The optimization was made for a specific plant configuration with preset gas turbine exhaust conditions and vapor turbine inlet pressure/temperature. Pressure drops are accounted for and

[1]Separator temperature varies approximately as the inverse of separator mass flow rate, nearly independent of turbine inlet composition (Marston, 1990a). Temperature as the independent variable is easier to work with analytically than flow rate but in practice one controls flow rates.

Table 5 Combustion gas and cooling water state points for the optimized three-stage cycle

State	p (kPa)	T (°C)	h (kJ/kg)	$\dot{m}$ (kg/s)
	Combustion Gas			
51	15	1006	298.7	1216
52	15	1006	298.7	694
53	15	520	169.1	694
54	15	672	208.7	1216
55	15	294	111.3	1216
56	14	155	76.5	1216
57	15	1006	298.7	522
58	15	869	261.3	522
	Cooling Water			
61	36	60	28.1	6131
62	36	60	28.1	3566
63	14	89	58.1	3566
64	36	60	28.1	2564
65	14	89	58.1	2564
66	14	89	58.1	6131

pumping power, including cooling water circulation pumps, has been included. Heat exchangers have not been sized but approach temperatures measured in the three MWe demonstration plant have been better than design specifications (Leibowitz and Zervos, 1992).

Two general approaches to optimization are "gradient" and "direct search." The gradient method was rejected because it was not feasible to derive explicit expressions for derivatives. Finite differences can be used to approximate derivatives, but then truncation error might affect the outcome and/or cause the solution scheme to converge slowly or not at all.

Direct search methods do not use derivatives but instead generate a sequence of improving approximations. Direct search is not restricted to continuous, well-behaved, monotonic functions. There are no formal optimality conditions, only successively improved solutions.

Downloaded 02 Jun 2010 to 171.66.16.102. Redistribution subject to ASME license or copyright; see http://www.asme.org/terms/Terms_Use.cfm

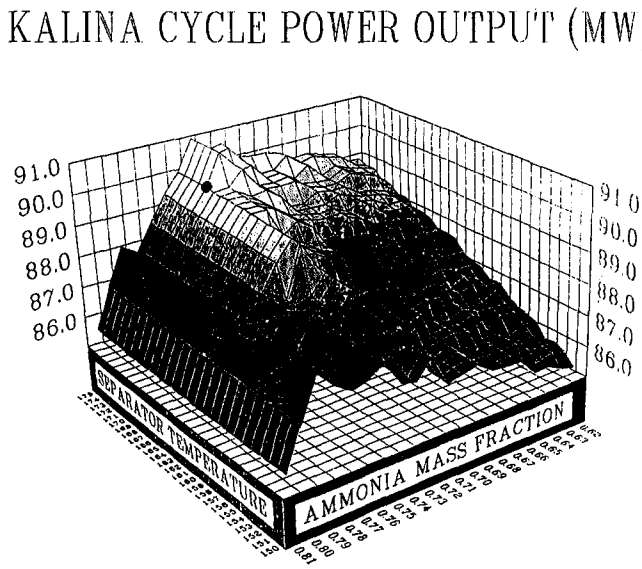

Fig. 3 Optimization of power output from the three-stage Kalina cycle. Vertical scale is MWe, separator temperature range is 150 to 175°F, NH_3 mass fraction range is from 0.62 to 0.81. Black dot shows practical optimum.

The Monte Carlo form of direct-search proposed by Luus and Jaakola (1973) was used. A number of trial points are generated at random. The best feasible of these is taken to be the minimum for that iteration, the search region is reduced around the selected point, and the random trial begins again. The method will generally converge to the global optimum and is not sensitive to irregularities in the objective function or to the existence of a multimodal objective function.

The optimization code was used as a driver to the model developed by Marston (1990b). Checks were placed throughout the cycle to ensure that approach temperature and pinch point constraints were not violated. When the search region became smaller than 0.001 for the ammonia mass fraction and smaller than 0.1 for the separator temperature, the optimization process was assumed to have converged. These tolerances resulted in a somewhat irregular performance surface, but convergence to the same optimum resulted starting from three different points. Convergence to a global maximum regardless of the number of local maxima was important since power output as a function of separator temperature and turbine inlet mass fraction is not monotonic.

The optimization process identified but did not reject violations of the 25°F (14°C) combustion gas pinch point. Thus, in Fig. 3, the useful optimum is the highest of those points on the power output surface that satisfies the combustion gas pinch point.

Computation time was typically 12 to 14 hours on an IBM 486 PC. Original and optimized cycle parameters are given in Table 6.

Results and Conclusions

Table 7 summarizes results for three gas turbine combined cycle power plants: triple-pressure steam, simplified single-stage Kalina, and optimized three-stage Kalina. Even the single-stage Kalina cycle generates slightly more power than the triple-pressure steam cycle and the three-stage version with limited optimization offers a gain in output of 9 MWe from a nominal 240 MWe plant. If costs associated with the additional surface area in the HRSG and with the additional equipment included in the DCSS are not excessive, the COE for a Kalina cycle may prove to be lower than that for a conventional steam cycle.

Table 6 Effects of limited optimization

	Original	Optimized
Ammonia Mass Fraction at Turbine Inlet	0.70	0.75
Separator inlet	0.4203	0.4500
Separator Temperature (°F)	160.0	172.0
Mass Flow Rate (lbm/s	230.5	241.1
Evaporator Pinch Point (F°)	30.0	30.0
Exhaust Gas Exit T (°F)	170.64	154.99
Cycle Efficiency	0.3141	0.3159
Net Cycle Output excluding circ water pump (MWe)	87.91	90.00

Table 7 Comparison of gas turbine combined cycle plants: triple-pressure Rankine, one-stage Kalina, and optimized three-stage Kalina

TOPPING CYCLE	
Compressor input (kW)	210,330
Gas Turbine output (kW)	369,445
Net Output (kW)	159,114

BOTTOMING CYCLE Inputs (kW)	Tri-Pressure Steam Rankine	1-Stage Kalina	Optimized 3-Stage Kalina
Boiler Feed Pump	843.1	1675.0	1,535.3
Aux. Blr Feed Pump			321.5
HP Boiler Circ Pump	88.6		
IP Boiler Circ Pump	3.3		
LP Boiler Circ Pump	41.5		
Condensate Pump	16.8	200.9	278.5
Circ. Water Pump	491.7	513.0	451.7
Total Input	1,485.0	2,188.9	2,587.0
Outputs (kW)			
HP Turbine	15,783.0	84,298.4	18,852.8
IP Turbine	19,453.0		51,472.3
LP Turbine	46,461.2		21,817.7
Gross Output	81,697.2	84,298.4	92,142.8
Net Output	80,212	81,909	89,556

OVERALL PLANT SUMMARY			
Power Output (kW)			
Topping Cycle	159,115	159,115	159,115
Bottoming Cycle	80,212	81,909	89,555
Total	239,327	241,024	248,670
Fuel Flow (lbm/s)	21.1	21.1	21.1
Fuel HHV (Btu/lbm)	23,861	23,861	23,861
Fuel LHV (Btu/lbm)	21,503	21,503	21,503
Energy Input (kW)			
HHV	531,862	531,862	531,862
LHV	479,302	479,302	479,302
Plant Efficiency			
HHV	45.00	45.31	46.75
LHV	49.93	50.29	51.88

Optimization was made for a specific plant configuration with preset gas turbine exhaust conditions and turbine inlet conditions (other than the inlet ammonia mass fraction). The cycle does not represent the maximum power output the Kalina cycle could achieve, but rather represents the maximum power output based on parameters that were judged to be favorable for current utility plant design.

References

Bechtel Group, 1988, EPRI Report AP-5815, May.

Brown, H., and Gardner, N. J., 1982, EPRI Report AP-2536, Aug.

Czermak, H., and Wunsch, A., 1982, "The 125 MW Combined Cycle Power Generator 'Korneuburg-B'," presented at the 27th International Gas Turbine Conference and Exhibit, London, United Kingdom, Apr. 18-22.

Dayan, A., 1989, private communication.

Edison Electric Institute, 1986, *Statistical Yearbook of the Electric Utility Industry*.

El-Sayed, Y. M., and Tribus, M., 1985a, ASME AES-Vol. 1, pp. 97-102.

El-Sayed, Y. M., and Tribus, M., 1985b, ASME AES-Vol. 1, pp. 89-95.

Downloaded 02 Jun 2010 to 171.66.16.102. Redistribution subject to ASME license or copyright; see http://www.asme.org/terms/Terms_Use.cfm

EPRI, 1987, Technical Assessment Guide, Report P-4463-SR, May.
Gordon, S., and McBride, B., 1976, NASA SP-273.
Hyre, M. R., 1991, "Gas Turbine Bottoming Cycles: Triple Pressure Steam versus Kalina," Master's Thesis, Villanova University, PA.
JANAF, 1971, *Thermochemical Tables*, 2nd ed, NSRDS-NBS 37.
Jeffs, E., 1990, "Utrect 225 MW Combined Cycle Certified at 52% Efficiency," *Gas Turbine World*, Jan.-Feb.
JSD Simulation Service Company, 1989, ASPEN/SP.
Kalina, A. I., 1984, ASME JOURNAL OF ENGINEERING FOR GAS TURBINES AND POWER, Vol. 106, pp. 737-742.
Kalina, A. I., and Leibowitz, H. M., 1990, ASME Paper No. 87-GT-35.
Leibowitz, H. M., and Zervos, N., 1992, *Proc. 27th IECEC*, Vol. 3, pp. 3.35-3.42.
Leibowitz, H. M., 1993, "Operating Experiences With the 3 MW Kalina Cycle Demonstration Plant," *Proc. American Power Conference*, Apr.
Luus, R., and Jaakola, T. H. I., 1973, *AIChE Journal*, Vol. 19, No. 4, pp. 760-766.
Marston, C. H., 1990a, ASME JOURNAL OF ENGINEERING FOR GAS TURBINES AND POWER, Vol. 112, pp. 107-116.
Marston, C. H., 1990b, *Proc. 25th IECEC*, Vol. 2, pp. 160-165.
McBride, B., and Gordon, S., 1967, NASA TN D-4097.
Meyer, C. A., et al., 1967, *ASME Steam Tables*.
Park, Y. M., and Sonntag, R. E., 1990, *Int. Jour. of Energy Res.*, Vol. 14, pp. 153-162.
Robie, R. A., and Waldbaum, R., 1968, Geol. Survey Bull. 1259.
Zeleznik, F. J., and Gordon, S., 1961, NASA TN D-767.

Downloaded 02 Jun 2010 to 171.66.16.102. Redistribution subject to ASME license or copyright; see http://www.asme.org/terms/Terms_Use.cfm

A Methane-Steam Reformer for a Basic Chemically Recuperated Gas Turbine

S. T. Adelman

M. A. Hoffman

J. W. Baughn

Department of Mechanical and Aeronautical Engineering, University of California, Davis, CA 95616

Several illustrative designs are presented for a methane-steam reformer (MSR) that is used as a chemical recuperator in a Basic Chemically Recuperated Gas Turbine power cycle (a "Basic" CRGT is defined as one without intercooling or reheat). In this cycle, an MSR, heated by the turbine exhaust flow, converts a methane-steam mixture into a hydrogen-rich fuel that powers the gas turbine. A computer code was developed to calculate the size and performance characteristics of counterflow reformers. The code consists of a one-dimensional marching scheme that integrates the chemical, thermodynamic, and geometric variables along the heat exchanger/reformer tubes. The calculated designs were selected to give near-minimum catalyst volumes. These designs show that maintaining a high reformer gas temperature, using combustion-side heat transfer augmentation techniques, and using a catalyst of high reactivity are critical to obtaining a compact reformer design.

Introduction

With many steam power plants reaching the end of their life cycles, there is currently much interest in finding efficient and cost-effective baseload electrical power generation systems. Kesser (1991) analyzed four possible gas turbine cycles to determine their thermal efficiency. The results showed that the combined cycle (CC) has the highest thermal efficiency, followed by the Basic Chemically Recuperated Gas Turbine (a Basic CRGT is defined as one without intercooling or reheat, as shown in Fig. 1), the steam-injected gas turbine (STIG), and the simple gas turbine cycle. The Basic CRGT cycle currently exists only as a thermodynamic model (Janes, 1990; Lloyd, 1991; Kesser, 1991).

Kesser's results indicate that a Basic CRGT might make an attractive demonstration power plant for testing the chemically recuperative concept at a relatively low cost compared to advanced CRGT cycles being proposed. The present research was undertaken to determine the size of the methane-steam reformer (MSR) required for a Basic CRGT. The designs were selected using the criterion of near-minimum catalyst volume, since it is likely that this will be close to the minimum capital cost.

Figure 1 shows the Basic CRGT cycle with the reformer flow parameters from Kesser's (1991) Reference Case 2 (with a compressor pressure ratio of 15). In the cycle, air is compressed, burned with the hydrogen-rich fuel from the methane-steam reformer (MSR), and expanded through the turbine. The combustion gas exiting the turbine is sent through three heat exchangers in a counterflow arrangement. Water enters the economizer and is heated to the saturation temperature. It is then boiled in the evaporator and mixed with methane at the evaporator exit. This methane-steam mixture is then heated in the third heat exchanger, which is the MSR, and converted into the hydrogen-rich combustor fuel. Only the MSR performance and size are evaluated in the present study.

Previous Models

In the CRGT models used by Lloyd (1991) and Kesser (1991), the reformer performance was calculated by specifying a reformer approach temperature difference at the exit, ΔT_{app}, a chemical-equilibrium approach temperature difference, ΔT_{eq}, and the cold and hot-side fractional pressure drops. The reformer approach temperature difference specifies the difference between the turbine exit temperature and the reformer cold-side exit temperature ($\Delta T_{app} = T_{hi} - T_{co}$; see Fig. 1). The ΔT_{eq} temperature difference is a measure of how closely the methane-steam reaction has approached equilibrium. Although this simple, approximate reformer model used by Kesser (1991) and others calculates the approximate reformer outlet conditions, it does not give any indication of the physical size of the reformer.

Several reformer models have been introduced to calculate the size of the large furnace-type reactors of the petrochemical industry. These include Oblad (1967), Grover (1970), Hyman (1968), Singh and Saraf (1979), Murty and Krishna Murthy (1988), and Alatiqi et al. (1989). Common to all of these models is the use of a one-dimensional marching scheme to calculate the length and performance of the reformer tubes.

Murray and Snyder (1985) modeled the methane-steam reforming of hydrogen-rich feed gas for fuel cells. In their MSR, the reformer tubes were heated by hot combustion gases flow-

Contributed by the Advanced Energy Systems Division for publication in the JOURNAL OF ENGINEERING FOR GAS TURBINES AND POWER. Manuscript received by the Advanced Energy Systems Division July 12, 1993; revision received May 11, 1994. Associate Technical Editor: M. J. Moran.

Copyright © 1995 by ASME

Downloaded 02 Jun 2010 to 171.66.16.102. Redistribution subject to ASME license or copyright; see http://www.asme.org/terms/Terms_Use.cfm

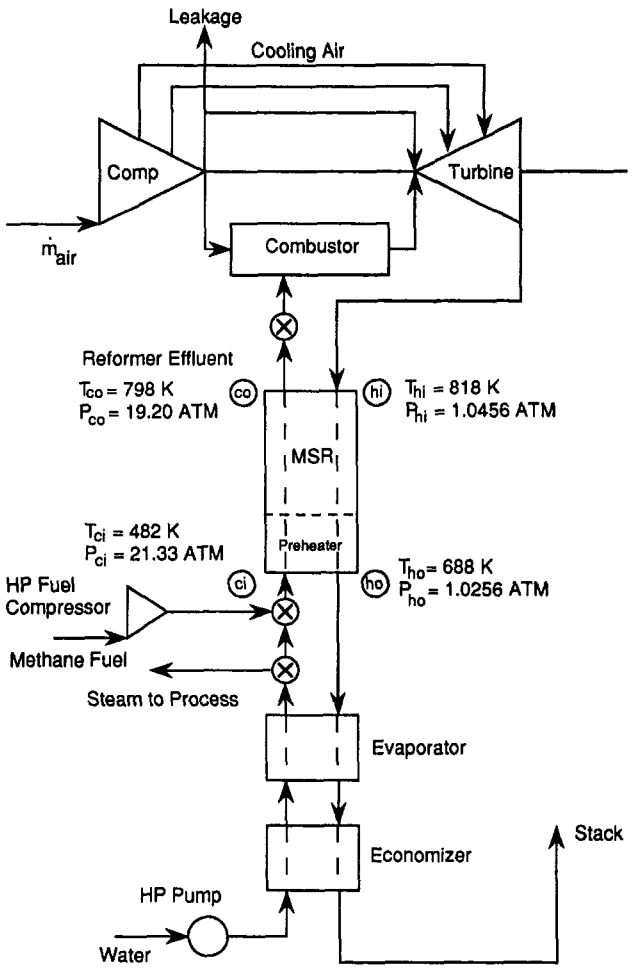

Fig. 1 The Basic Chemically Recuperated Gas Turbine Cycle (CRGT) for Reference Case 2 (Kesser, 1991). Key parameters are π_c = 15, $T_{comb.outlet}$ = 1498 K, $\dot{m}_{fuel}/\dot{m}_{air}$ = 0.157, and the cycle thermal efficiency = 47.3 percent based on the lower heating value (LHV). The methane-steam reformer (MSR) inlet and outlet conditions for this case are shown on the figure.

ing on the shell side. The Murray and Snyder model most closely satisfied the requirements for modeling an MSR for gas turbine heat recovery. For this reason, its basic assumptions and methods were adopted as the basis of the present model. However, three major modifications were necessary to satisfy the requirements of a CRGT MSR. First, Murray and Snyder modeled a reformer with laminar flow on the combustion side.

Table 1 Reformer concept summary

Concept	Preheater	Fins on Preheater and Reformer	Roughened Surfaces	ΔP_h	Catalyst Reactivity	% Catalyst of Concept A Required
A	No	No	No	0.02 atm	Rostrup-Nielsen (b)	100 %
B	Yes	No	No	0.04 atm	Rostrup-Nielsen (b)	96.5 %
C	Yes	No	No	0.02 atm	Rostrup-Nielsen (b)	89.3 %
A-E	No	No	Yes	0.02 atm	Rostrup-Nielsen (b)	76.6 %
B-E	Yes	No	Yes	0.02 atm	Rostrup-Nielsen (b)	74.4 %
C-E	Yes	No	Yes	0.02 atm	Rostrup-Nielsen (b)	69.2 %
C-FIN1	Yes	Yes	No	0.02 atm	Rostrup-Nielsen (b)	27.6 %
C-FIN2	Yes	Yes	No	0.02 atm	GIAP-3	11.3 %
C-EFIN1	Yes	Yes	Yes	0.02 atm	Rostrup-Nielsen (b)	24.5 %
C-EFIN2	Yes	Yes	Yes	0.02 atm	GIAP-3	9.0 %

The CRGT reformer model requires the simulation of turbulent flow along the reformer tube bundle. Second, Murray and Snyder did not include catalyst bed pressure drop calculations. The method of Hyman (1968) was added to the present model for this calculation. Third, the packed bed heat transfer correlation used by Murray and Snyder was replaced with a more accurate correlation (see Adelman, 1992, Appendix A). These modifications resulted in an MSR model capable of simulating Basic CRGT conditions.

MSR Model Description

A computer code called UCDMSR was developed to model the MSR. In this model, a unit cell contains a reformer tube surrounded by the appropriate combustion-side flow area. The reformer tubes are assumed to be arranged in an equilateral triangular pattern. The combustion-side flow area may also contain rectangular fins of high aspect ratio that run longitudinally along its length. The reformer tube is filled with nickel catalyst pellets and the cold-side fuel gases flow through this packed bed.

Some of the many different reformer concepts examined are summarized in Table 1, and a typical set of code inputs is listed in Table 2. Note that the mass flow rate inputs in Table 2 are for a unit cell.

Heat Transfer

The heat transfer coefficient on the combustion gas side is adequately represented by the Dittus–Boelter equation for fully turbulent flow along unfinned tubes. When external longitudinal fins are employed on the tubes, the heat transfer coefficient is adjusted for the additional fin area, A_{fin}.

On the inside of the reformer tube, the catalyst bed has a strong effect on the local heat transfer coefficient. The empirical correlation for a cylindrical-particle packed bed from Li and Finlayson (1977) was used in the present study:

Nomenclature

A = flow area or surface area, m^2
C = methane concentration, $kmol/m^3$
C_p = specific heat, J/kg-K
D = diameter, m
EA = Energy of Activation, J/kmol
h = heat transfer coefficient, W/m^2-K
k_g = gas conductivity, W/m-K
k_o = activity factor, kmol/h-atm
L = tube length, m
$\dot{m}$ = mass flow rate, kg/s
n = chemical species concentration, moles/initial moles of CH_4
P = pressure, atm
ΔP = pressure loss, atm
P/D = tube pitch to tube outer diameter ratio
r = kinetic rate, $kmol/h\text{-}m^3$
Re = Reynolds number
T = temperature, K
u = reformer gas velocity, m/s
X = chemical conversion, moles of species/initial moles of species
v = catalyst bed void factor
z = axial distance along heat exchanger, m

Subscripts

c = cold side (tube side)
ci = cold side inlet
co = cold side outlet
eq = specifies equilibrium condition
h = hot side (shell or combustion side)
hi = hot side inlet
ho = hot side outlet
o = specifies initial condition
p = catalyst particle
ti = tube inner wall
to = tube outer wall

Downloaded 02 Jun 2010 to 171.66.16.102. Redistribution subject to ASME license or copyright; see http://www.asme.org/terms/Terms_Use.cfm

Table 2 UCDMSR unit cell input parameters for reformer Concepts A, B, C, A-E, B-E, and C-E. Each column contains the inputs for a concept and its enhanced tube version. The inputs for each of these two concepts are the same except for the pitch-to-diameter ratio.

Inputs	Concept A & A-E	Concept B & B-E	Concept C & C-E
Preheater			
Geometry			
D_{to} (mm)	N/A	50.80	19.05
t_{wall} (mm)	N/A	3.05	2.11
k_{wall} (W/m K)	N/A	28.00	28.00
P/D smooth tube	N/A	1.280	3.400
P/D enhanced tube	N/A	1.355	3.500
Tube Side			
T_{co} (K)	N/A	550.00	650.00
T_{ci} (K)	N/A	482.10	482.10
P_{ci} (atm)	N/A	21.33	21.33
K_{in}	N/A	1.5	1.5
K_{out}	N/A	0.0	1.5
m_h/m_c	N/A	7.2952	7.2952
Fluid Species			
CH_4 (mol/mol)	N/A	0.1390	0.1390
H_2O (mol/mol)	N/A	0.8610	0.8610
Shell Side			
T_{ho} (K)	N/A	687.74	687.74
P_{ho} (atm)	N/A	1.0256	1.0256
m_h (kg/sec)	N/A	0.02	0.02
K_{in}	N/A	0.0	0.0
K_{out}	N/A	1.5	1.5
Fluid Species	Combustion Gas	Combustion Gas	Combustion Gas
Reformer			
Geometry			
D_p (mm)	8.20	8.20	8.20
v	0.28	0.28	0.28
D_{to} (mm)	50.80	50.80	50.80
t_{wall} (mm)	3.05	3.05	3.05
k_{wall} (W/m K)	28.00	28.00	28.00
P/D smooth tube	1.280	1.280	1.280
P/D enhanced tube	1.355	1.355	1.355
Catalyst			
k_o (kmol/hr atm)	200940	200940	200940
EA (J/kmol)	8.368E7	8.368E7	8.368E7
Tube Side			
T_{ci} (K)	482.10	from preheater	from preheater
P_{ci} (atm)	21.33	from preheater	from preheater
K_{in}	1.5	0.0	1.5
K_{out}	1.5	1.5	1.5
m_h/m_c	7.2952	7.2952	7.2952
Fluid Species	from preheater	from preheater	from preheater
Shell Side			
T_{ho} (K)	687.74	from preheater	from preheater
P_{ho} (atm)	1.0256	from preheater	from preheater
T_{hi} (K)	818.28	818.28	818.28
m_h (kg/sec)	0.02	0.02	0.02
K_{in}	1.5	1.5	1.5
K_{out}	1.5	0.0	1.5
Fluid Species	from preheater	from preheater	from preheater

$$h_c = 1.26 \left(\frac{k_{g_c}}{D_{ti}}\right) \mathrm{Re}_p^{0.95} \exp\left(\frac{-6D_p}{D_{ti}}\right) \tag{1}$$

Murray and Snyder (1985) calculated the packed bed heat transfer coefficient with a similar equation by Leva from Smith (1970). Leva's equation was used in the UCDMSR code only for the validation of the present model against Murray and Snyder's results.

Murray and Snyder compared limited internal Westinghouse data on the packed bed heat transfer coefficients to those predicted by Leva's equation. The Westinghouse data predicted a heat transfer coefficient twice that of Leva's equation. Murray and Snyder concluded that this higher heat transfer coefficient led to more accurate results than Leva's equation. This work by Murray and Snyder supports the use of Eq. (1) in UCDMSR, since doubling the heat transfer coefficient predicted by Leva's equation results in heat transfer coefficients that agree closely with Eq. (1) (see Adelman, 1992, Appendix A.4).

The UCDMSR code can simulate a reformer tube that has fully roughened outer surfaces. A General Electric study (Anon., G. E., 1977) showed that this enhancement method can roughly double the heat transfer coefficient with a resulting threefold increase in the friction factor. When modeling roughened unfinned or finned tubes, the UCDMSR code simply multiplies the heat transfer coefficient and friction factor by these multipliers.

Pressure Losses

The total pressure drop was calculated for each control volume by summing the friction and acceleration contributions. Inlet contraction and outlet expansion minor losses were included in the pressure drop calculations using K_{loss} factors. The Ergun equation (Ergun, 1952) was used to calculate the pressure drop in the catalyst bed.

Thermodynamic Properties

All thermodynamic properties used in the UCDMSR code are calculated using the STANJAN chemical equilibrium code that was developed at Stanford University by Reynolds (1986). This code is used as a subroutine in UCDMSR to calculate mixture compositions and thermodynamic properties at each unit cell control volume interface. The STANJAN source code was modified to use the steam table equations of Irvine and Lily (1984) for the water vapor. This modification eliminates errors introduced near the saturation curve by the ideal gas approximation for steam.

Chemical Kinetics

UCDMSR assumes the following equations to be the governing reactions within the reformer (Akers and Camp, 1955; Allen et al., 1975; Rostrup-Nielsen, 1975; Murray and Snyder, 1985):

$$CH_4 + 2H_2O = CO_2 + 4H_2 \tag{2}$$

$$CO_2 + H_2 = CO + H_2O \tag{3}$$

The reaction of Eq. (2) is kinetically controlled while the reaction of Eq. (3) has been shown to proceed fast enough to be considered equilibrium controlled (Murray and Snyder, 1985). Equation (3) has the effect of redistributing the products of Eq. (2). Carbon coking is not considered here because a high steam-to-carbon ratio prevents such formations (Murray and Snyder, 1985).

Equation (4) (Murray and Snyder, 1985) was chosen to model the rate of the demethanation reaction (Eq. (2)) because it is reasonably accurate and includes the equilibrium partial pressure of CH_4 explicitly:

$$-r_{CH_4} = k_o e^{-EA/RT} \left(P_{CH_4} - P_{CH_{4(Eq)}}\right) \tag{4}$$

Different combinations of the catalyst frequency, k_o, and energy of activation, EA, can represent a wide range of catalyst reactivities.

The UCDMSR code, following Murray and Snyder (1985), defines the normalized chemical conversion coefficients for the nonequilibrium methane concentration, the equilibrium methane concentration, and the equilibrium carbon dioxide concentration as:

$$X_{CH_4} = \frac{u_o C_o - uC}{u_o C_o} \tag{5}$$

$$X_{CH_{4(Eq)}} = \frac{n_{o(CH_4)} - n_{CH_{4(Eq)}}}{n_{o(CH_4)}} \tag{6}$$

$$X_{CO_2} \equiv X_{CO_{2(Eq)}} = -\frac{X_{CH_{4(Eq)}} - n_{CO_{2(Eq)}}}{X_{CH_{4(Eq)}}} \tag{7}$$

Downloaded 02 Jun 2010 to 171.66.16.102. Redistribution subject to ASME license or copyright; see http://www.asme.org/terms/Terms_Use.cfm

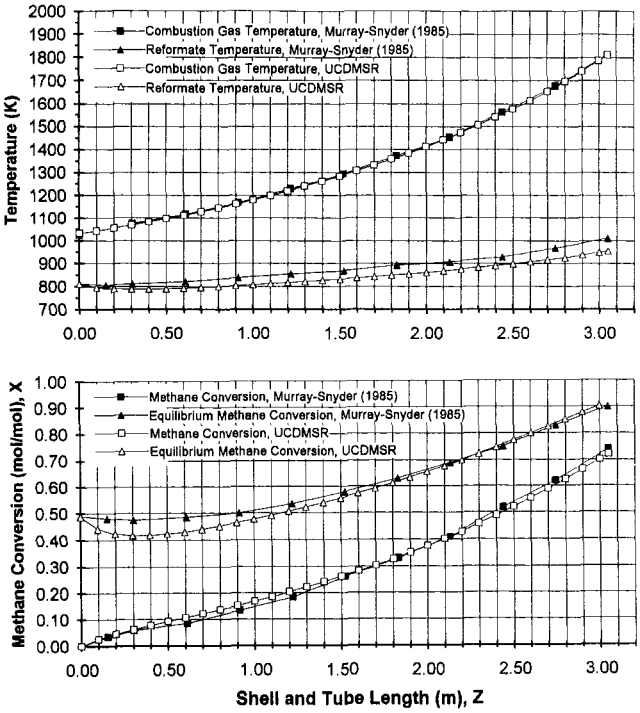

Fig. 2 Comparison of the results predicted by the UCDMSR Code and the model developed by Murray and Snyder (1985) for a convectively heated counterflow reformer

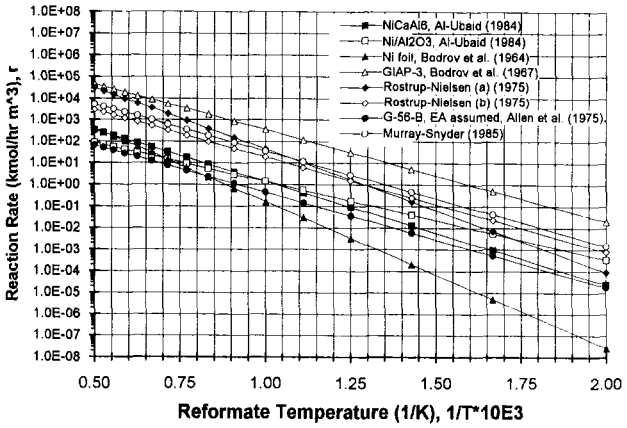

Fig. 3 Plots of the first-order reaction rate equation: $r = k_o \exp(-EA/RT)$ for combinations of values of the activity factor, k_o, and the Energy of Activation, EA, found in the literature for different commercial and experimental catalysts. Note that the Rostrup-Nielsen (b) values were used for the reference catalyst in the present study, while the GIAP-3 values were used to represent an advanced catalyst.

The parameter u in Eq. (5) is the reformer gas velocity, C is the methane concentration, and the product uC is the methane flux through the reformer tube cross section. The zero subscript in the equations indicates an initial value. The carbon dioxide conversion represented by Eq. (7) is obtained by making STANJAN equilibrium calculations. The resulting equilibrium species concentrations enable the equilibrium methane conversion and carbon dioxide conversions to be calculated for later use in the rate equation (Eq. (10)).

The demethanation rate in Eq. (4) can be rewritten in terms of the methane flux for the flow in a reformer tube:

$$-r_{CH_4} = \frac{d(-uC)}{dz} \tag{8}$$

and then the rate of methane conversion is obtained by dividing through Eq. (4) by $u_o C_o$:

$$\frac{dX_{CH_4}}{dz} = \left(\frac{k_o e^{-EA/RT}}{u_o C_o}\right)(P_{CH_4} - P_{CH_4(Eq)}) \tag{9}$$

Equation (9) can be rewritten in terms of the total pressure, the initial species concentrations, and the equilibrium and nonequilibrium methane concentrations only:

$$\frac{dX_{CH_4}}{dz} = \left(\frac{P_{tot} k_o e^{-EA/RT}}{u_o C_o}\right) \times \left(\frac{n_{o(CH_4)}(1 - X_{CH_4})}{n_{o(tot)} + 2X_{CH_4} n_{o(CH_4)}} - \frac{n_{o(CH_4)}(1 - X_{CH_4(Eq)})}{n_{o(tot)} + 2X_{CH_4(Eq)} n_{o(CH_4)}}\right) \tag{10}$$

Equation (10) is now written in terms of the single independent unknown, the normalized nonequilibrium methane concentration, X_{CH_4}.

UCDMSR Code Validation

The UCDMSR code was validated against the previous work of Hyman (1968) and Murray and Snyder (1985). The agreement with Hyman was reasonably good; while the reformate temperatures were only within about 40°C at the exit, the methane conversion was within about 3 percent. The pressure drops were almost exactly the same (see Adelman, 1992). The temperature and conversion profiles for the counterflow reformer design of Murray and Snyder are shown in Fig. 2 along with the predictions of the UCDMSR code. This figure demonstrates that the UCDMSR code is in good agreement with Murray and Snyder's calculations.

A Methane-Steam Reformer for the Basic CRGT

Kesser's Reference Case 2 (Fig. 1) models a CRGT cycle that contains a heavy-duty (industrial type) gas turbine (HGT) with a compressor pressure ratio of fifteen. The turbine exhaust temperature of this HGT is 818 K. A temperature of 818 K is high enough to produce a reasonable equilibrium methane conversion (approximately 35 percent). Some of the many different reformer concepts for Reference Case 2 that were examined in an attempt to minimize catalyst volume are summarized in Table 1. (See Adelman, 1992, for details on all the concepts.)

Kesser's UCDCRGT Reference Case 2 gives the temperatures, pressures, and chemical species at the hot-side outlet and cold-side inlet for his counterflow MSR. The UCDMSR code then integrates along the reformer until Kesser's hot-side inlet conditions are reached. In order to reduce the number of variables in this preliminary design study, a reformer tube outer diameter of 50.8 mm and a pitch-to-diameter ratio of 1.2 were selected based on industry standards (Janes, 1990). The catalyst pellet effective diameter was calculated for a 9.525 mm × 6.35 mm (3/8″ × 1/4″) cylindrical pellet, a common size employed by the industry for low-temperature reforming (Barton, 1991).

Figure 3 shows a summary of the different reaction rates used for modeling different catalysts found in the literature. The values of Rostrup-Nielsen (b) (1975), shown by the open diamonds in Fig. 3, were chosen to represent a practical reference catalyst reactivity. For several reformer concepts, the reported catalyst performance values for GIAP-3 were employed as an upper limit. This larger reactivity was used to investigate the effect of a higher performance catalyst on the MSR design.

Basic CRGT Reformer Results

MSR Concept A. The Concept A MSR is a pure counterflow reformer with catalyst filling the entire reformer tube

Downloaded 02 Jun 2010 to 171.66.16.102. Redistribution subject to ASME license or copyright; see http://www.asme.org/terms/Terms_Use.cfm

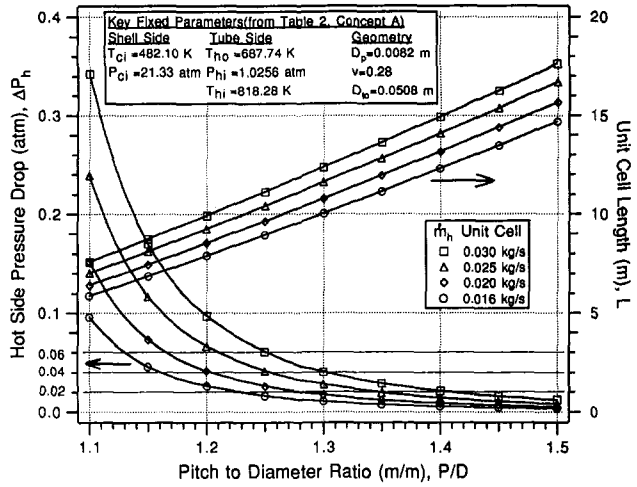

Fig. 4(A) Variation of the tube length, L, and the shell, hot-side pressure drop, ΔP_h, versus the pitch-to-diameter ratio, P/D_{to}, for MSR Concept A for four different hot-side mass flow rates, $\dot{m}_h$. All other input parameters are fixed at the values listed in Table 2.

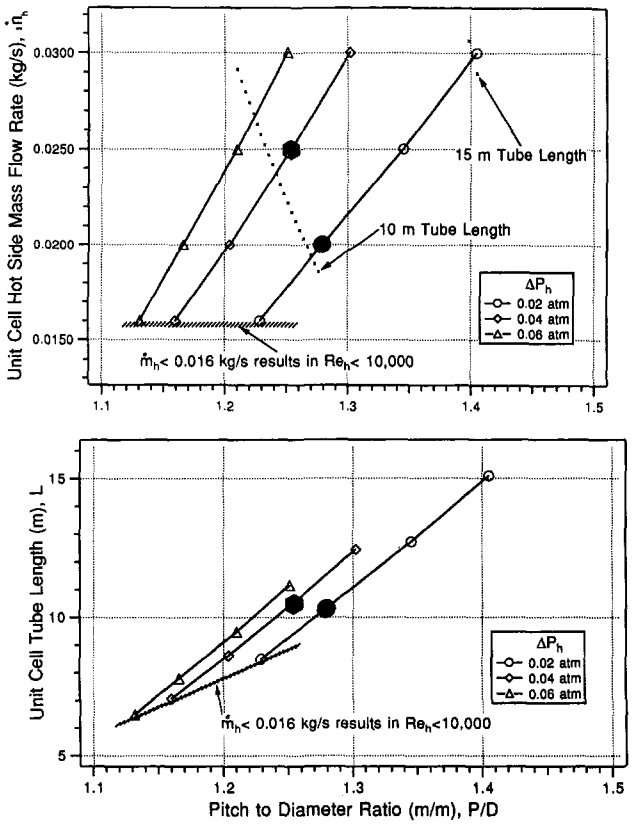

Fig. 4(B) Cross-plots of hot-side mass flow rate (upper figure) and the tube lengths (lower figure) of Fig. 4(A) for three values of the hot-side pressure drop. The large black circle is the design point selected for the hot-side pressure drop of 0.02 atm of Reference Case 2. The large black hexagon is an alternate design point if the hot-side pressure drop can be increased to 0.04 atm.

length. (The tubes are smooth and unfinned; the additional complexities of fins and heat transfer enhancement were added with later concepts.) The reference catalyst reactivity of Rostrup-Nielsen (b) used for Concept A (and for all but two of the cases in Table 1) has values of $k_o = 200{,}940$ kmol/h-atm and $EA = 8.368 \times 10^7$ J/kmol.

A parametric study of this concept was conducted in which all parameters were fixed at the values listed in Table 2 (Concept

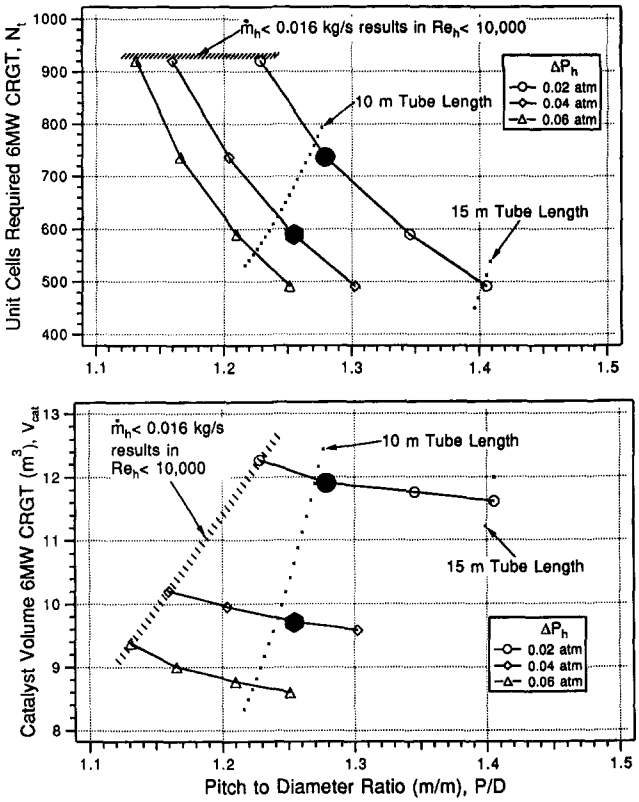

Fig. 4(C) Values for the number of reformer tubes (unit cells), N_t (upper figure), and the catalyst volume, V_{cat} (lower figure) required for a methane-steam reformer (MSR) for a 6 MW Basic CRGT for the four hot-side mass flow rates and the three hot-side pressure drops of Figs. 4(A) and 4(B)

A), except for the pitch-to-tube-outer-diameter ratio (P/D) and the hot-side mass flow rate ($\dot{m}_h$). The effect of these two variables on the reformer tube length (L) and hot-side pressure drop (ΔP_h) was determined. The cold-side mass flow rate, $\dot{m}_c$, is maintained at 0.1371 $\dot{m}_h$, which is the reformer hot to cold-side mass flow rate ratio for UCDCRGT Reference Case 2.

The results of this parametric study are shown in Fig. 4. The curves of Fig. 4(A) show that ΔP_h decreases with increasing P/D, and L increases almost linearly with increasing P/D. Figure 4(B) shows cross-plots of Fig. 4(A) for three values of the hot-side pressure drop (where Kesser's Reference Case 2 used $\Delta P_h = 0.02$ atm). These curves show that as the allowable hot-side pressure drop increases, the P/D and L can be decreased for a specified $\dot{m}_h$. As the mass flow rate is increased, the tube length and pitch-to-diameter ratio must increase in order to maintain the same hot-side pressure drop. For all curves, as the mass flow rate decreases, the limiting hot-side Reynolds number of 10,000 (minimum Re_h for fully turbulent flow) occurs at an $\dot{m}_h$ of about 0.016 kg/s.

Figure 4(C) shows the number of tubes (N_t) and the catalyst volume (V_{cat}) required for a 6 MW basic CRGT cycle using a HGT (heavy-duty gas turbine). A 6 MW power output was chosen somewhat arbitrarily; however, this approximates the output of a small industrial gas turbine such as the Allison 501-KH STIG operating at peak electrical efficiency. The turbine-exhaust mass flow rate for a 6 MW Basic CRGT cycle (14.72 kg/s), calculated from the specific shaft power of UCDCRGT Reference Case 2, was used to determine the number of tubes (N_t).

The selected design point for Concept A is shown on Fig. 4 as a large black circle (the design point inputs are given in Table 2 and the outputs are in Table 3A). This point was chosen on the 0.02 atm curve to match the UCDCRGT Reference Case 2 specifications, as mentioned above. The design point was

Downloaded 02 Jun 2010 to 171.66.16.102. Redistribution subject to ASME license or copyright; see http://www.asme.org/terms/Terms_Use.cfm

Table 3(A) UCDMSR unit cell output parameters for reformer Concepts A, B, and C. The tube count (N_t), tube bundle diameter (D_{tb}), catalyst volume, and thermal power transferred in the preheater and reformer sections all correspond to a 6 MW CRGT cycle.

Outputs	Concept A	Concept B	Concept C
Preheater			
Geometry			
L (m)	N/A	14.10	8.35
N_t	N/A	736	736
D_{tb} (m)	N/A	1.85	1.85
Total ΔP_C (atm)	N/A	0.00002	0.00342
Shell Side			
T_{hi} (K)	N/A	709.66	735.45
P_{hi} (atm)	N/A	1.0460	1.0272
Total ΔP_h (atm)	N/A	0.02036	0.00156
Thermal Power (MW)	N/A	0.40	0.88
Reformer			
Geometry			
L (m)	10.30	9.94	9.20
N_t	736	736	736
D_{tb} (m)	1.85	1.85	1.85
Catalyst Volume (m^3)	11.90	11.48	10.63
Tube Side			
T_{co} (K)	803.98	804.05	804.09
Total ΔP_C (atm)	0.39916	0.39142	0.36979
X_{CH_4}	0.2761	0.2763	0.2763
CAT (K)	5.06	5.00	5.00
Shell Side			
T_{ho} (K)	687.74	709.66	735.45
P_{ho} (atm)	1.0256	1.0460	1.0272
P_{hi} (atm)	1.0457	1.0630	1.0459
Total ΔP_h (atm)	0.02005	0.01701	0.01875
Thermal Power (MW)	2.44	2.04	1.56

Table 3(B) UCDMSR unit cell output parameters for reformer Concepts A-E, B-E, and C-E. The tube count (N_t), tube bundle diameter (D_{tb}), catalyst volume, and thermal power transferred in the preheater and reformer sections all correspond to a 6 MW CRGT cycle.

Outputs	Concept A-E	Concept B-E	Concept C-E
Preheater			
Geometry			
L (m)	N/A	13.97	5.01
N_t	N/A	736	736
D_{tb} (m)	N/A	1.96	1.90
Total ΔP_C (atm)	N/A	0.00002	0.00222
Shell Side			
T_{hIN} (K)	N/A	709.66	735.43
P_{hIN} (atm)	N/A	1.0532	1.0272
Total ΔP_h (atm)	N/A	0.02756	0.00164
Thermal Power (MW)	N/A	0.40	0.88
Reformer			
Geometry			
L (m)	7.89	7.66	7.13
N_t	736	736	736
D_{tb} (m)	1.96	1.96	1.96
Catalyst Volume (m^3)	9.11	8.85	8.23
Tube Side			
T_{cOUT} (K)	804.95	805.08	805.08
Total ΔP_C (atm)	0.30686	0.30237	0.28686
X_{CH_4}	0.2744	0.2747	0.2747
CAT (K)	6.70	6.65	6.62
Shell Side			
T_{hOUT} (K)	687.74	709.66	735.43
P_{hOUT} (atm)	1.0256	1.0532	1.0272
P_{hIN} (atm)	1.0456	1.0709	1.0459
Total ΔP_h (atm)	0.02001	0.01769	0.01862
Thermal Power (MW)	2.44	2.04	1.56

also chosen to give a reasonable reformer tube length of about 10.3 m with near-minimum catalyst volume. This also gives a reasonable pitch-to-diameter ratio of about 1.28.

Kesser (1991) showed that the thermal efficiency of the Basic CRGT cycle was not highly sensitive to ΔP_h. For example, Kesser found that the thermal efficiency of the Basic CRGT was reduced by about 0.4 percentage points when ΔP_h was doubled to 0.04 atm. If ΔP_h is doubled (moving from the large black circle to the large black hexagon on Fig. 4), the catalyst volume can be reduced by about 20 percent, keeping the tube length about the same. The number of tubes is reduced by about 20 percent (to 590), while the P/D is only reduced a small amount (from 1.28 to 1.255).

MSR Concept B. Analysis of the temperature and conversion profiles for Concept A revealed that negligible methane conversion took place over the first meter of the reformer tube. The temperature of the reforming gases coming out of the evaporator and into the reformer was not high enough to promote the methane-steam reaction. This observation led to a modification of the UCDMSR code that allowed the modeling of a preheater. In Concept B, the reformate gas temperature is raised in a preheater before it enters the reformer tube. The preheater tube contains no catalyst, and in Concept B it is simply an extension of the reformer tube with the same diameter. (See Table 2 for the inputs.)

The results listed in Table 3(A) show that Concept B does reduce the required catalyst volume of Concept A from 11.9 m^3 to 11.48 m^3, a 3.5 percent reduction. However, it requires a 14 m preheater tube to raise the fuel gas temperature from 487 K to 550 K, while the reformer tube in Concept A accomplished this in approximately one half of a meter. This is clearly a poor preheater design and several improvements are possible.

MSR Concept C. Concept C attempts to improve upon Concept B by using smaller preheater tubes of 19.05 mm outer diameter (instead of 50.8 mm of Concept B) to improve the heat transfer and result in less pressure drop. The improved heat transfer allows the preheater to raise the cold-side temperature to the much higher value of 650 K with reasonable tube lengths of about 8.35 m before the reformer gases reach the catalyst bed. The higher cold-side inlet temperature results in a reformer that is over a meter shorter than the reformer in Concept A. The volume of the catalyst is reduced by 10.7 percent over Concept A, and Concept C still meets the hot-side pressure drop requirements of 0.02 atm. A comparison of the sizes of Concepts A and C is given in Fig. 5.

MSR Concepts A-E, B-E, and C-E. Calculations for Concepts A, B, and C were repeated for tubes with enhanced heat transfer due to roughening on the hot combustion gas side for both the preheater and the reformer. The inputs for these concepts were identical to those of the smooth tube concepts, except for the pitch-to-diameter ratio. Values for the pitch-to-diameter ratio were found for concepts A-E and C-E such that these two enhanced tube concepts gave the same hot-side pressure drop of 0.02 atm as the smooth tube concepts.

Comparing Concept C-E to Concept C, the catalyst volume is reduced another 19.9 percent and is now only 69.2 percent of Concept A (See Table 1). A size comparison of these two concepts also appears in Fig. 5. A summary of the key results for all three enhanced tube MSR concepts appears in Table 3(B).

MSR Concepts C-FIN. Concepts C-FIN1 and C-FIN2 were created to size a type C preheater-reformer combination that employs longitudinally finned tubes. In this case, sixteen 1 mm thick × 15 mm high fins were assumed to be on the 19.05-mm-dia preheater tube, and twenty-four 1 mm × 12 mm fins were assumed on the 50.8-mm-dia reformer tube. (Higher fin densities should be investigated since they may be beneficial.) The "1" and "2" in the concept names designate different catalyst

Downloaded 02 Jun 2010 to 171.66.16.102. Redistribution subject to ASME license or copyright; see http://www.asme.org/terms/Terms_Use.cfm

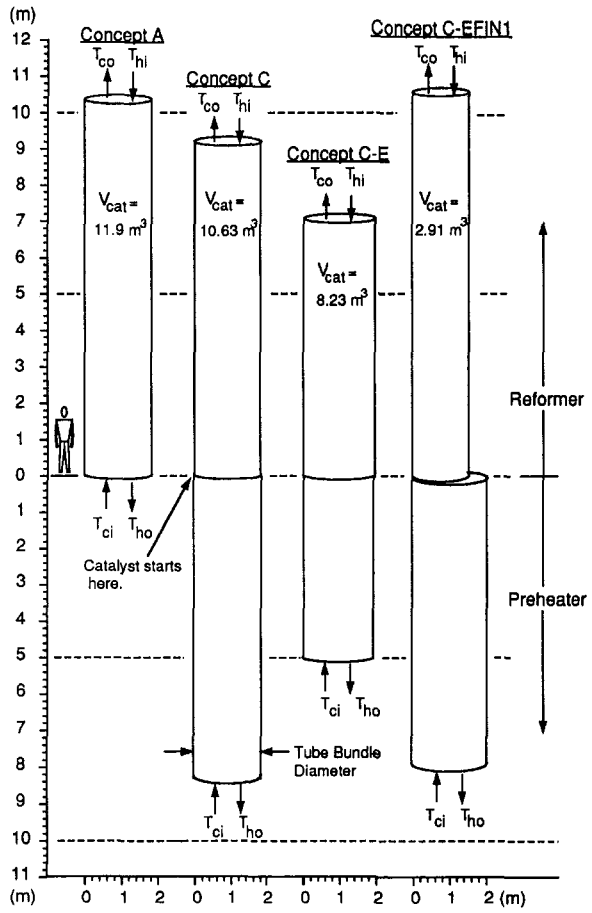

Fig. 5 Comparison of the sizes of the smooth tube methane-steam reformer (MSR) Concepts A and C with the enhanced (fully roughened) tube Concept C-E and the enhanced finned tube Concept C-EFIN1 for a 6 MW Basic CRGT. Concepts A, C, and C-E all require 736 tubes. Concept C-EFIN1 requires only 295 preheater tubes and 175 reformer tubes due to the improved heat transfer using the roughened fins.

reactivities: "1" is for the Rostrup-Nielsen (b) reactivity and "2" is for the GIAP-3 reactivity.

The increase in mass flow rates reduces the number of tubes required in the reformer and preheater sections of the C-FIN Concepts (keeping $\Delta P_h = 0.02$ atm by adjusting the pitch-to-diameter ratio). The positive results of all these adjustments is that the reformer tube count decreases from 736 tubes for Concepts A through C-E to only 175 tubes for C-FIN1 and C-FIN2. The catalyst volume required by C-FIN1 is only 27.6 percent of Concept A. Additionally, the improved hot-side heat transfer in the finned preheater allows the preheater cold-side exit temperature to be raised to 750 K without a large penalty in tube length (9.54-m-long tubes are required in the preheater). The resulting higher reformer inlet temperature of 750 K increases the catalyst efficiency.

The increased catalyst reactivity of Concept C-FIN2 has a large effect on the catalyst volume. If the larger reactivity of the GIAP-3 catalyst can be achieved, then the MSR of Concept C-FIN2 would have 59 percent less catalyst then C-FIN1 and only 11.3 percent of the catalyst required for Concept A. As expected, a compact design may be possible with extended surfaces and an advanced catalyst with high reactivity.

MSR Concepts C-EFIN. Next, Concepts C-EFIN1 and C-EFIN2 were created to size a type C preheater-reformer combination that employs longitudinally finned tubes enhanced with fully roughened surfaces on the hot combustion gas side. The same tube and fin geometry and mass flow rates as the two C-FIN concepts were used. The "1" and "2" in the concept names again designate the two different catalyst reactivities.

The roughened fins improve the overall heat transfer coefficient, but the improvement over Concepts C-FIN1 and C-FIN2 was small, as shown in Table 1. The added cost of manufacturing roughened finned tubes may not be justified by these small reductions in the required catalyst volume.

A size comparison of MSR Concept C-EFIN1 to Concepts A, C, and C-E is presented in Fig. 5. Note that Concept C-FIN1 was only slightly larger than Concept C-EFIN1 and hence was not shown in Fig. 5. Also note that the three unfinned concepts with their lower mass fluxes required 736 tubes per bundle, while Concepts C-FIN1 and C-EFIN1 require only 295 preheater tubes and 175 reformer tubes.

Other MSR Concepts. A promising concept involves the periodic distribution of the catalyst in the reformer tubes such as was studied by Solar Turbines, Inc. (Knox and Duffy, 1991) for the California Energy Commission. Preliminary calculations (Adelman, 1992) suggest that this concept deserves further study.

Summary and Conclusions

The UCDMSR code was developed in order to predict the performance and size of methane-steam reformers (MSRs) when used as heat recovery devices in a Basic CRGT power plant (a gas turbine power plant with no intercooling or reheat). The code has been used for the preliminary design of a variety of reformer concepts, some of which are summarized in Table 1. The size characteristics of four key designs for a 6 MWe Basic CRGT are sketched in Fig. 5. The evolution of the designs depicted in Fig. 5 was motivated by the objective to obtain near-minimum catalyst volume, and the results can be summarized by two important trends. First, the results indicate that a high reforming gas temperature is critical for efficient use of the catalyst. This can be accomplished by using a preheater that superheats the methane-steam gas mixture before it enters the reformer. Second, increasing the combustion-side heat transfer coefficient results in a more compact MSR.

The authors were surprised by the large size of the preheater and the methane-steam reformer required for a relatively small 6 MWe Basic CRGT. Of all the preliminary reformer design concepts examined, the C-EFIN concept (using fully roughened fins on the hot combustion gas side) is the best design based on obtaining near-minimum catalyst volume. However, it remains to be seen if this concept will result in the minimum cost of electricity for the Basic CRGT power plant. In order to determine whether this concept (or any of the other concepts) is practical, a detailed cost study of the entire CRGT power plant must be performed.

Acknowledgments

We wish to thank the University Energy Research Group of the University of California, which partially funded the research for this paper. We also thank the California Energy Commission for their encouragement, Professor W. C. Reynolds (Stanford University) for making available the source code for the chemical equilibrium solver STANJAN and Dr. Thomas Snyder (Westinghouse) for making some report material available to us and for several invaluable suggestions.

References

Adelman, S. T., 1992, "A Methane-Steam Reformer for a Basic Chemically Recuperated Gas Turbine," Master of Science Thesis, Department of Mechanical, Aeronautical and Materials Engineering, University of California, Davis, CA.

Akers, W. W., and Camp, D. P., 1955, *AIChE J.*, Vol. 4, p. 471.

Alatiqi, I. M., Meziou, A. M., and Gamelseed, G. A., 1989, "Modelling,

Downloaded 02 Jun 2010 to 171.66.16.102. Redistribution subject to ASME license or copyright; see http://www.asme.org/terms/Terms_Use.cfm

Simulating, and Sensitivity Analysis of Steam-Methane Reformers," *International Journal of Hydrogen Energy*, Vol. 14, No. 4, pp. 241–256.

Allen, D. W., Gerhard, E. R., and Likens, M. R., Jr., 1975, *Ind. Eng. Chem. Process Des. Dev.*, Vol. 14, p. 256.

Al-Ubaid, A. S., 1984, "Methane Steam Reforming Activity, Stability and Characterization of Nickel Supported Catalysts," Doctoral Thesis, University of Notre Dame, p. 19.

Anon, General Electric Co., 1977, *Heat Transfer Data Book*, Section 503.7 (now published by Genium Publishing Corp., Schenectady, NY).

Barton, I., 1991, I.C.I. Katalco Corp., personal telephone communication.

Bodrov, N. M., Apel'baum, L. O., and Temkin, M. I., 1964, *Kinet. Katal.*, Vol. 5, No. 4, p. 696.

Bodrov, N. M., Apel'baum, L. O., and Temkin, M. I., 1967, *Kinet. Katal.*, Vol. 8, No. 4, p. 821.

Ergun, S., 1952, "Fluid Flow Through Packed Columns," *Chemical Engineering Progress*, Vol. 48, No. 2, pp. 89–94.

Grover, S. S., 1970, *Hydrocarbon Process*, Vol. 49, No. 4, p. 109.

Hyman, M. H., 1968, "Simulating Methane Reformer Reactions," *Hydrocarbon Process*, Vol. 47, No. 7, pp. 131–137.

Irvine, T. F., and Liley, P. E., 1984, *Steam and Gas Tables With Computer Equations*, Academic Press, Inc., Orlando, FL.

Janes, J., 1990, "Chemically Recuperated Gas Turbine," California Energy Commission Draft Staff Report, P500-90-001.

Kesser, K., 1991, "Analysis of a Basic Chemically Recuperated Gas Turbine Power Plant," Masters Thesis, Department of Mechanical, Aeronautical, and Materials Engineering, University of California, Davis.

Knox, C. S., and Duffy, T. E., 1991, "Once Through Methane/Steam Reformer Design Evaluation for Chemically Recuperated Gas Turbine," Final Report for the California Energy Commission, Report No. SR90-R-6016-01.

Li, C., and Finlayson, B. A., 1977, "Heat Transfer in Packed Beds—A Reevaluation," *Chemical Engineering Science*, Vol. 32, pp. 1055–1066.

Lloyd, A., 1991, "Thermodynamics of Chemically Recuperated Gas Turbines," Master's Thesis, The Center for Environmental Studies, Princeton University, Princeton, NJ.

Murray, A. P., and Snyder, T. S., 1985, "Steam–Methane Reformer Kinetic Computer Model With Heat Transfer and Geometry Options," *Industrial Engineering Chemical Process Design and Development*, Vol. 24, No. 2, pp. 286–294.

Murty, C. V. S., and Krishna Murthy, M. V., 1988, "Modeling and Simulation of a Top-Fired Reformer," *Ind. Eng. Chem. Res.*, Vol. 27, pp. 1832–1840.

Oblad, A. G., 1967, *Oil Gas J.*, Vol. 54, No. 16, p. 164.

Reynolds, W. C., 1986, "The Element Potential Method for Chemical Equilibrium Analysis: Implementation in the Interactive Program STANJAN, Version 3," Department of Mechanical Engineering, Stanford University.

Rostrup-Nielsen, J. R., 1975, *Steam Reforming Catalysts*, Danish Technical Press, Inc., Copenhagen, pp. 85–105.

Singh, C. P. P., and Saraf, D. N., 1979, "Simulation of Side-Fired Steam-Hydrocarbon Reforms," *Ind. Eng. Chem. Process Des. Dev.*, Vol. 18, No. 1, p. 1.

Smith, J. M., 1970, *Chemical Engineering Kinetics*, 2nd ed., McGraw-Hill, New York, pp. 493–547.

Downloaded 02 Jun 2010 to 171.66.16.102. Redistribution subject to ASME license or copyright; see http://www.asme.org/terms/Terms_Use.cfm

Reduction of Combustion Irreversibility in a Gas Turbine Power Plant Through Off-Gas Recycling

S. P. Harvey
Thayer School of Engineering,
Dartmouth College,
Hanover, NH 03755

K. F. Knoche
University of Aachen (RWTH),
Aachen, Germany

H. J. Richter
Thayer School of Engineering,
Dartmouth College,
Hanover, NH 03755

Combustion in conventional fossil-fueled power plants is highly irreversible, resulting in poor overall energy conversion efficiency values (less than 40 percent in many cases). The objective of this paper is to discuss means by which this combustion irreversibility might be reduced in gas turbine power cycles, and the conversion efficiency thus improved upon. One such means is thermochemical recuperation of exhaust heat. The proposed cycle recycles part of the exhaust gases, then mixes them with fuel prior to injection into a reformer. The heat required for the endothermic reforming reactions is provided by the hot turbine exhaust gases. Assuming state-of-the-art technology, and making a number of simplifying assumptions, an overall efficiency of 65.4 percent was attained for the cycle, based on the lower heating value (LHV) of the methane fuel. The proposed cycle is compared to a Humid Air Turbine (HAT) cycle with similar features that achieves an overall efficiency of 64.0 percent. The gain in cycle efficiency that can be attributed to the improved fuel oxidation process is 1.4 percentage points. Compared to current high-efficiency gas turbine cycles, the high efficiency of both cycles studied therefore results mainly from the use of staged compression and expansion with intermediate cooling and reheating, respectively.

Introduction

In conventional fossil-fueled power plants, the combustion is highly irreversible and thus is, in part, responsible for the low overall efficiency of the total energy conversion from chemical to electrical energy. In a steam power plant, heat transfer in the steam generator contributes to a further decrease in efficiency.

Different tools are available to study energy conversion cycles in detail. In this paper we will focus on cycle *exergy losses* as the tool for analysis. Power plant exergy losses can be reduced in a number of ways. A fairly widespread example of high-efficiency power generation technology is the combined cycle configuration, which allows the waste heat content of a gas turbine cycle to be put to use to supply the heat input of a bottoming cycle. The most common bottoming cycle is a conventional steam Rankine cycle (Bolland, 1991), and the most efficient plant on-line at the present time achieves a thermal efficiency of 53 percent (Hamann and Joyce, 1989). Other more advanced bottoming cycles have been proposed such as the Kalina cycle (Kalina, 1983, 1984), which employs a high-temperature gas turbine cycle and a binary fluid (ammonia-water) bottoming cycle. The variable temperature boiling property of this binary fluid allows the shape of the power cycle heat addition temperature curve to match that of the sensible heat decrease of the combustion products more closely. Thus, the overall exergy losses are reduced, and the efficiency is therefore increased. The claimed overall thermal efficiency for a combined cycle using a Kalina bottoming cycle is 57 percent (Kalina and Tribus, 1992). The main problem with combined cycle configurations is their relative complexity, which implies high equipment costs and poor adaptability to partial load operating conditions.

The main reason for the poor exergetic efficiency of conventional fuel oxidation is the very nature of the process in which fuel and oxygen are brought into direct contact, resulting in a very disorganized release of high-energy combustion products in a hot flame. The efficiency of a power generating cycle might therefore be improved if immediate contact of fuel and oxygen is prevented and intermediate reactions are supported (Richter and Knoche, 1983).

Building on these thoughts, the combustion of natural gas (methane) can be made less irreversible if the fuel is first brought into contact with recycled exhaust gases (Knoche, 1990) consisting predominantly of CO_2, H_2O, and N_2. The CO_2 and H_2O components of these gases can be considered as oxygen carriers. The methane fuel is reformed in this endothermic process and oxidized partially to CO and H_2 by reducing some of the oxgyen-containing components in the recycled exhaust gases.

Contributed by the Advanced Energy Systems Division and presented at the ASME Winter Annual Meeting, Anaheim, California, November 8-13, 1992; revision received June 1, 1993. Associate Technical Editor: M. J. Moran.

Copyright © 1995 by ASME

Downloaded 02 Jun 2010 to 171.66.16.102. Redistribution subject to ASME license or copyright; see http://www.asme.org/terms/Terms_Use.cfm

The subsequent completion of the fuel oxidation process remains highly irreversible due to the temperature limitations of the turbines in which the combustion gases expand. However, the overall exergy losses are reduced, the useful work produced by the process is increased and less waste heat is released into the environment.

The new process proposed here is similar to a regenerative gas turbine cycle with intercooling and reheating. The process involves a single cycle, with no bottoming cycle. The heat recovered from the turbine exhaust is used to drive an endothermic reforming reaction in which the fuel is partially oxidized by the oxygen-containing components of the recycled exhaust gases. Before each turbine stage, substoichiometric amounts of air are injected into the reformed fuel stream and reheating is achieved by partial combustion.

The water vapor in the exhaust stream is partially liquefied in the condenser. After each compression stage intercooling is accomplished by injection of this water such that the gas stream is cooled to the wet bulb temperature.

In this paper, we will present two energy conversion processes. The first process, outlined above, uses recycled exhaust gases (CO_2, H_2O, and N_2) as oxygen carriers. Air is injected into the combustion chambers, supplying the oxygen necessary to complete the oxidation process and thus raise the gas stream temperature to the maximum allowable value at the inlet of the next turbine stage. With this process, an overall thermal efficiency of 65.4 percent (LHV) was obtained assuming reasonable turbomachinery efficiencies and temperature differences in the heat exchangers. The second process, presented for reference purposes, is a humid air gas turbine cycle incorporating some of the key features of the first process but without the reformer. The LHV thermal efficiency of this reference cycle is 64.0 percent. We conclude that the exhaust gas reforming process increases the cycle efficiency by 1.4 percentage points compared to a cycle with similar features but without fuel reforming prior to combustion. Thus, the gain due to the improved fuel oxidation mechanism, although far from negligible, is less than might have been expected. Much of the improvement in cycle efficiency compared to other high-efficiency gas turbine cycles discussed in the literature can be attributed to the use of staged compression and expansion with intermediate intercooling and reheat, respectively.

It should be clearly emphasized at this point that the intent of this paper is to provide thermodynamic analysis of a possible gas turbine cycle. The paper contains many simplifications, notably that of ignoring pressure drop losses in many of the cycle components and reaction kinetics of the reforming process. Also, important issues such as equipment costs associated with key cycle components are not discussed at this stage. These important issues will be the focus of a subsequent design phase.

As mentioned in the introduction, the key characteristics of the first energy conversion process considered in this paper is that part of the turbine exhaust gases (predominantly CO_2,H_2O, and N_2) are recycled. The gases containing oxygen (i.e., CO_2 and H_2O) are used as oxygen carriers. The proposed cycle is similar to a gas turbine cycle with intercooling, reheating, and a regenerator. The main difference is that in this cycle the regenerator does not simply preheat the combustion air; instead a reforming process occurs in which the fuel is partially oxidized by the recycled steam and carbon dioxide. In this section we will examine the cycle in detail. We will also present the results of an extensive optimization process undertaken using Aspen Plus™ process simulation software (Aspen, 1991) as a tool.

Cycle Description. The process flowsheet diagram of the cycle is shown in Fig. 1. In this section, we will briefly describe the features of the main cycle components.

Fuel Reforming Heat Exchanger. Heat from the hot exhaust stream leaving the final turbine set (stream 7 in Fig. 1) is used to preheat a pressurized mixture of recycled exhaust gases containing CO_2, N_2, and H_2O (stream 16) and fuel (methane). The energy levels reached during this operation are sufficient to enable endothermic reforming of CH_4, producing CO and H_2. The nitrogen can be considered for all practical purposes as behaving like an inert gas.

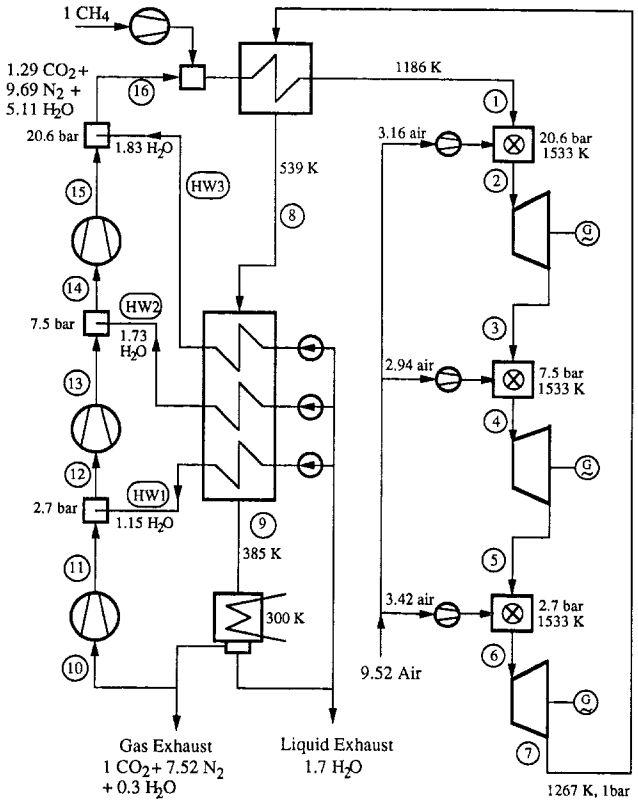

Fig. 1 Gas turbine cycle with recycled exhaust gases: flowsheet diagram

Expansion Process. The gas expansion (points 1 through 7 in Fig. 1) involves three stages with a reheat combustion chamber located between each turbine stage. In the first two combustion chambers, substoichiometric amounts of air are injected to partially combust the incoming gas stream containing CO and H_2. The fuel oxidation is completed in the final combustion chamber.

Exhaust Heat Recovery. As discussed previously, the hot turbine exhaust gases are used to supply the heat required by the endothermic reforming reactions. Further heat recovery is achieved by preheating the three water streams used in the injection coolers located in the compression section of the cycle.

Compression. A three-stage compression process is implemented with water injection cooling in between stages (points 10 through 16 in Fig. 1). The water is preheated to ensure that the temperatures reached after injection are above the saturation temperature for the mixture (HW1, 2, and 3 in Fig. 1).

Condenser. After all possible heat has been recovered, the exhaust stream enters the condenser (point 9 in Fig. 1) where it is cooled down to environmental temperature (300 K). The vapor stream leaving the condenser (containing CO_2,N_2, and the equilibrium quantity of water vapor) is then split, enabling part of the stream to be recycled. The remainder is discharged from the cycle since the stoichiometry of the overall reaction is:

$$CH_4 + 2\ O_2 + 7.52\ N_2 => CO_2 + 2H_2O + 7.52\ N_2 \qquad (1)$$

We see from this reaction equation that the gases discharged from the cycle must contain CO_2 and N_2 in a 7.52:1 ratio. The recycled gas stream must therefore contain CO_2 and N_2 in the

Downloaded 02 Jun 2010 to 171.66.16.102. Redistribution subject to ASME license or copyright; see http://www.asme.org/terms/Terms_Use.cfm

same ratio. When searching for optimal cycle parameters, the quantities of CO_2 and N_2 cannot be varied independently. 1 CO_2, 7.52 N_2, and the corresponding equilibrium quantity of H_2O are discharged in vapor form. Similarly, the liquid phase leaving the condenser (essentially pure liquid H_2O) is divided into two streams. The amount of liquid discharged from the cycle is such that the overall amount of H_2O leaving the process is as defined in reaction (1). The remainder of the water is fed into the water heater where it is preheated for injection cooling purposes.

Optimization Process Using Aspen Plus™. The proposed cycle was studied in detail using Aspen Plus process simulation software (Aspen, 1991). Aspen Plus is an engineering tool that may be used to model processes in chemical and petrochemical industries, petroleum refining, oil and gas processing, power generation, pharmaceuticals, biotechnology, etc. Based on a flowsheet model, Aspen Plus can be used to simulate the process fully. The code is capable of generating complete thermodynamic data for all streams in a process, which enables easy implementation of second law analysis. Built-in costing and optimization capabilities are also included. The results generated by Aspen Plus were verified using other codes, manual calculation methods, and standard tabular data. The cycle outlined in the previous section was studied with an aim to maximizing the net work output of the cycle per unit of supplied methane fuel. In order to make proper exergetic analysis, the efficiency should be referred to the exergy of the fuel. But this exergy is usually close to the heating value. Thus, to simplify comparisons with other high-efficiency cycles reported in the literature, we compute the thermal efficiency based upon the lower heating value (LHV) of the fuel even though most of the H_2O is condensed. The LHV of methane is approximately 802 MJ/kmol at 1 bar and 300 K.

A brief summary of the optimization procedure follows, based on the "monotonicity analysis" method suggested by Papalambros and Wilde (1988). A qualitative analysis of the cycle reveals the following properties:

- For given pressure values, the net work output of the cycle increases as the turbine inlet temperatures are increased. The turbine inlet temperatures are constrained not to exceed levels dictated by materials limitations and we conclude that the air quantities injected into the first two combustion chambers should be such that the maximum allowable temperature is attained. The temperature attained in the last combustion chamber cannot be controlled in this manner since the overall reaction is that specified by Eq. (1), and the total amount of air injected is therefore fixed. Predictably, the optimal values of the other design variables will be such that the maximum allowable temperature is reached in the last combustion chamber as well.
- Pressure is clearly a key design variable. We note that the only pressure value that can be varied independently is the cycle high pressure. The intermediate pressures are set such that the pressure ratios for all turbines and compressors are equal. This choice is based on the minimization of entropy generation for an ideal gas process.
- The overall efficiency of the cycle must increase as more heat is extracted from the turbine exhaust stream in the reformer. The limit to this heat recovery process is imposed by the minimum allowable pinch point temperature difference in the heat exchanger. The heat duty of the reformer was therefore chosen such that pinch point temperature difference was at its lowest allowable value.
- The compression intercooling is obtained by injection of recycled process water. The quantities and heat contents of the injected water streams are chosen such that saturation conditions (i.e., the dew point) are obtained after each injection. Further cooling would result in water droplet formation, which could in turn cause damage to the downstream compressor blades. The objective is to minimize the compressor work. We may consider the pump work to be essentially negligible and therefore as much water as possible should be injected in the last two stages since much less work is required to pump H_2O to a given pressure as a liquid than to compress it as a vapor. To inject larger amounts of water at the high-pressure level, it is necessary to preheat the water as much as possible, recovering as much heat as possible from the exhaust stream. Again, the limits of this heat recovery are dictated by the required minimal pinch point temperature differences in the different water heater sections.

The procedure outlined above maximizes the net work output of the cycle for a given amount of recycled CO_2 and N_2 by searching for the optimal high pressure, heat exchanger heat duties, distribution of air injected into the combustion chambers, amount of recycled H_2O and distribution of recycled H_2O between the three injection cooling processes. To find the fully optimal cycle, it is necessary to try different amounts of recycled CO_2 and N_2. The results and corresponding parameter values are presented in the following section.

Table 1 Technical parameter values

Polytropic Efficiencies, All Turbomachinery	0.9
Maximum Turbine Inlet Temperature	1533 K (1260°C)
Minimum ΔT, Reformer	25 K
Minimum ΔT, Water Heater	25 K

Results and Discussion. Before presenting the results, we will first discuss the choice of the main technical parameters for the cycle. These parameters are presented in Table 1. The polytropic efficiencies are reasonable values for modern high-performance axial compressors and turbines (Wilson, 1984). The turbine inlet temperature is representative of temperatures attained by state-of-the-art turbines (Day and Rao, 1993). In high-temperature metal turbines, blade cooling is usually achieved by circulating cooling air through the blade, then injecting this air into the expanding stream. For this cycle, this is a problem since injecting air into the partially combusted gas stream would result in combustion and heat release. However, other alternatives for high-temperature gas turbine operation are currently being investigated. These included closed-circuit high-pressure stream cooling (Matsuzaki et al., 1992) and ceramics. Ceramic technology offers the potential for uncooled operation at temperatures up to 1675 K (Parks et al., 1991). Therefore, assuming a turbine inlet temperature of 1533 K for an uncooled turbine stage is not unreasonable when considering a future baseload gas turbine power cycle. The temperature difference at the pinch point in the various heat exchangers is 25 K in all cases. For the water heaters, this value could feasibly be lowered to values as low as 10 K (Kalina et al., 1991; Bolland, 1991). For the reformer, both streams are gas streams and the heat transfer characteristics are therefore poor. To restrict the overall size of the reformer heat exchanger, it might be desirable in practice to increase the temperature difference between the two gas streams. For both cycles discussed in this paper, the effect of increasing the reformer ΔT up to 100 K is studied. In both cases, the impact on thermal efficiency is significant, but not prohibitive. Finally, we note that the temperature levels at the hot end of the reformer unit are very high, exceeding 1200 K. This poses a considerable technological challenge, especially when the high pressure difference between hot and cold streams is considered. Metal heat exchangers that can withstand the high temperatures involved here are currently on the market (e.g., Bavaria Anlagenbau Gmbh, 1990), but manufacturing a heat exchanger that can withstand high temperatures together with large pressure differences is a yet unresolved technological challenge.

Table 2 presents the main characteristics of the optimized

Downloaded 02 Jun 2010 to 171.66.16.102. Redistribution subject to ASME license or copyright; see http://www.asme.org/terms/Terms_Use.cfm

Table 2 Optimal cycle parameters and characteristics (all entries per kmol of fuel)

Exhaust Recycle Quantities	1.29 CO_2 + 5.11 H_2O + 9.69 N_2
High Pressure	20.61 bar
Heat Duties	
Condenser	351.9 MJ
Reformer	696.3 MJ
Water Heater	131.8 MJ
Work Characteristics	
Turbine Expansion Work	759.4 MJ
Recycled Exhaust Compressor Work	144.3 MJ
Air Compressor Work	78.1 MJ
Fuel Compressor Work	12.1 MJ
Pump Work	0.1 MJ
Net Work	524.8 MJ
η_{th} [LHV]	65.4 %

cycle. We first note that the recycled gas quantities are similar to the quantities of air used in a standard gas turbine cycle operating with excess air to ensure temperature levels that are compatible with the temperature resistance of the turbine blades. The pressure level is comparable to levels encountered in current aeroderivative gas turbine technology. We also note the relatively large size of the reformer heat exchanger (1.33 MJ of heat exchanged per MJ of net work produced, with a pinch point temperature difference of 25 K). The overall thermal efficiency is a very promising result when compared to values attained by other high-efficiency configurations such as the Kalina bottoming cycle process. This is even more true if the relative simplicity of the proposed cycle is considered together with the fact that the cycle uses only existing hardware components and technology, with the possible exception of the reformer heat exchanger, as discussed previously. A further advantage of the proposed cycle is that no excess air is introduced into the cycle and that the amounts of NO_x compounds produced therefore remain very low. In practice, nitrogen oxides appear only at the very end of the expansion process. Using a chemical equilibrium code written by NASA (Gordon and McBride, 1976), the equilibrium model fractions of the NO_x compounds at the exit of the last combustion chamber were found to be: $[NO] = 1.68^{*}10^{-5}$, $[NO_2] = 2.54^{*}\ 10^{-9}$, and $[N_2O] = 2.10^{*}\ 10^{-9}$. The mole fractions of all other NO_x compounds are less than 10^{-10}. The kinetics of further reactions involving the formed NO_x compounds are known to be slow, and the NO_x levels in the discharged exhaust stream can be assumed to be close to those at the exit of the final combustion chamber. Therefore, the NO_x content of the exhaust stream is remarkably low: less than 17 ppm of NO oxides.

The claim in this paper is that recycling exhaust gases to be used as oxygen carriers improves the efficiency of the cycle by reducing the irreversible entropy production of the fuel oxidation. The key component in this process is the reformer. In Fig. 2, we show the evolution of the equilibrium cold stream composition in the reformer as a function of total heat exchanged per kmol of fuel. The evolution of the N_2 composition is not shown since it remains essentially constant and equal to 7.52 kmol per kmol of fuel. Note that reaction kinetics are not accounted for in this diagram. However, extensive experience with industrial reforming reactors shows that at the exit temperatures and pressures considered here, it is reasonable to assume that chemical equilibrium composition has been reached at the reactor exit (Rostrup-Nielsen, 1983).

We first note that all of the fuel has been reformed at the exit of the heat exchanger and that the reforming operation is therefore complete. We also note that the CO_2 quantities vary less than the quantities of H_2O. We conclude that the dominant oxygen carrier in this case is H_2O. This confirms observations made in industry whereby when both steam and carbon dioxide

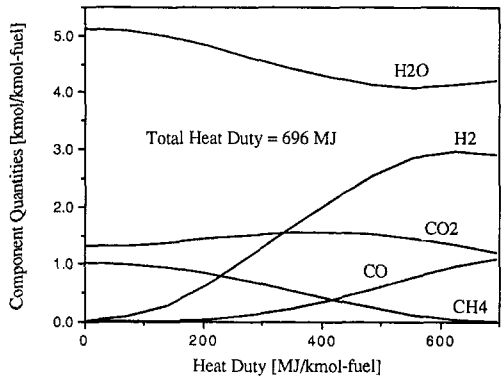

Fig. 2 Reforming process: cold stream composition versus heat duty (all quantities per kmol of fuel; N_2 stream not shown)

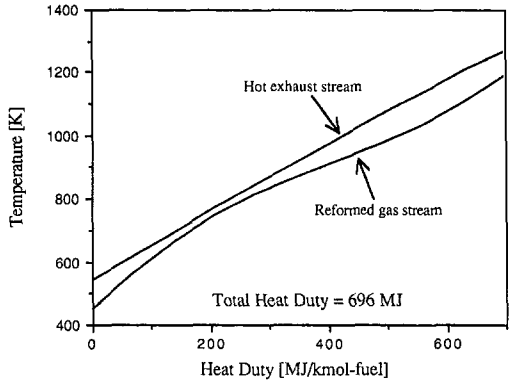

Fig. 3 Reforming process: temperature versus heat duty

are present in a reformer feed stream, the steam reforming reaction tends to dominate, and little or no carbon dioxide reforming is observed (Rostrup-Nielsen, 1983). The reformed gas stream contains approximately 3 kmol of H_2 and 1 kmol of CO. It is also interesting to observe the evolution of the heating curve (i.e., temperature versus heat exchanged in the reformer) of both streams. These curves are shown in Fig. 3.

The pronounced curvature of the cold-stream temperature profile in this diagram clearly illustrates the endothermic nature of the reforming process. It is also apparent that the reforming process is essentially finished at the exit of the reformer, and this is the reason why the slope of the reformed stream heating curve beings to increase again at the exit of the reformer. Similarly, the preheating operation at the cold end of the reformer can also be observed. At approximately 700 K, the slope of the curve changes, indicating that the endothermic reactions have begun. At this point it is appropriate to discuss the effect of reaction kinetics in the reformer. Reforming reaction kinetics have been studied in great detail in industry (see, for example, Rostrup-Nielsen, 1983). The key result to these studies is that for practical reforming operation, it is necessary to use a catalyst, usually nickel-based. Most commercial catalysts will ensure the product gases to be close to the thermodynamic equilibrium for exit temperatures higher than 1000–1050 K. However, even with a catalyst, the product stream composition is very different from the equilibrium composition at lower temperature levels. This will affect the cycle behavior considerably, since the reformer pinch point occurs in the region where reaction kinetics are low. The result of this will be to decrease the pinch point temperature difference significantly for a given reformer heat duty and fixed inlet and outlet temperatures, and this will have a negative impact on the cycle efficiency since the potential for exhaust heat recovery is thereby effectively reduced. However, in this paper, the effects of reaction kinetics will not be discussed further, and thermodynamic equilibrium composition will be assumed throughout the reformer.

Downloaded 02 Jun 2010 to 171.66.16.102. Redistribution subject to ASME license or copyright; see http://www.asme.org/terms/Terms_Use.cfm

Table 3 Sensitivity analysis: recycled exhaust gas (CO_2 and N_2) quantities

kmol [CO_2 + N_2] per kmol fuel	η_{th} - LHV [%]	Optimal H_2O recycle quantity [kmol/kmol-fuel]	Optimal cycle high pressure [bar]
5.48	65.307	5.40	64.44
6.48	65.383	5.33	49.40
7.48	65.426	5.28	39.05
8.48	65.435	5.23	31.62
9.48	65.440	5.18	26.25
10.48	65.442	5.14	22.23
10.98	65.442	5.11	20.61
11.48	65.442	5.09	19.17
12.48	65.441	5.05	16.76

Sensitivity Analysis: Recycled Exhaust Gas Quantities. The cycle is particularly insensitive to recycled exhaust gas quantities. The results are summarized in Table 3. Listed in the table are the LHV-based thermal efficiencies of the optimized cycle for given quantities of recycled exhaust gases together with the corresponding values of the optimal cycle high pressure and optimal recycle H_2O quantities. The most remarkable result of this sensitivity analysis is the fact that the process is very insensitive to the amount of exhaust gas recycled. For different quantities of recycled CO_2 and N_2 we note a slight variation in the optimal recycled quantity of H_2O, the main oxygen carrier for the reforming reactions. However, the optimal pressure varies considerably. The true maximum efficiency occurs at the reasonable cycle high pressure of 20.61 bar. The relative insensitivity to recycled exhaust quantities is useful. For example, if less exhaust gases are recycled, the optimal pressure increases, and as a result the exhaust temperature at the exit of the last turbine decreases. This in turn lowers the temperature levels at the hot end of the reformer, which could have significant impact on cost and feasibility of the reformer. The impact on overall cycle efficiency is however negligible.

Sensitivity Analysis: Turbine Inlet Temperature and Pinch Point ΔT in Reformer. Figure 4 shows the results of a preliminary parameter sensitivity analysis, in which the effects of two key parameters (namely the turbine inlet temperature and the reformer pinch point temperature difference) on the thermal efficiency of the optimized cycle are shown. Note that since the cycle overall efficiency is relatively insensitive to the quantity of recycled exhaust gas, the level of recycled CO_2 and N_2 was kept constant and equal to the optimal level for the cycle with turbine inlet temperatures equal to 1533 K and a reformer pinch point temperature difference of 25 K, i.e., 1.29 kmol CO_2 and 9.69 kmol N_2 per kmol of CH_4. So far in this paper, we have assumed that the temperature at the inlet of the turbines is the maximum temperature sustainable by a modern state-of-the-art turbine, namely 1533 K. This is obviously a very high temperature, and the cost of such a turbine will be considerable. Consequently, it is important to examine the impact of lowering this temperature on the overall efficiency. Furthermore, we have already pointed out that the reformer is a crucial part of the proposed process. The size of this reformer will be considerable, as will be the technical challenges associated with its construction. The physical size of the reformer is a function of the total heat to be transferred and the average temperature difference between the two gas streams. A larger temperature difference will mean better heat transfer characteristics, but higher irreversible entropy production, and thus a lower overall efficiency. In this paper, we have supposed a relatively small temperature difference (25 K at the pinch point), which might lead to an unacceptably large and expensive reformer. We furthermore pointed out above that when reaction kinetics are accounted for, the true pinch point temperature difference will be significantly less than the 25 K value computed based on thermodynamic equilibrium

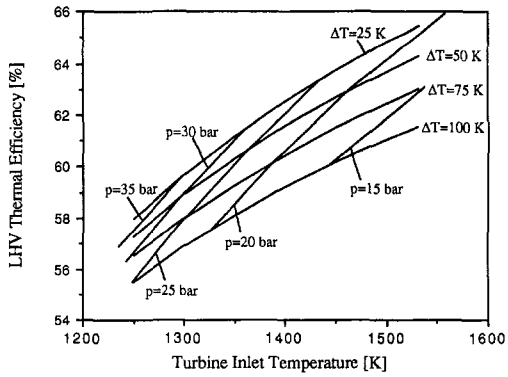

Fig. 4 Thermal efficiency as a function of maximum turbine inlet temperature and reformer pinch point ΔT

calculations for the reformed stream. The effects of these two parameters (i.e., turbine inlet temperature and reformer pinch point ΔT) on the thermal efficiency of the optimized cycle are shown in Fig. 4. The figure shows the LHV thermal efficiency as a function of turbine inlet temperature for different reformer pinch point ΔT values. The constant pressure lines give an indication of how the optimal pressure evolves for different values of the two variable parameters. Using the diagram we see for example that if the turbine inlet temperature is set at 1400 K (the maximum temperature that can presently be achieved with uncooled metal turbines) and the pinch point in the reformer is set at 100 K, the thermal efficiency drops to 59.2 percent and the optimal pressure is 16.6 bar, which is an acceptable pressure for aeroderivative gas turbine technology.

To conclude this section of results and discussion, Table 4 shows the results of a detailed exergy loss analysis of the cycle. The exergy loss of a component is computed according to:

$$\text{Exergy loss} = \Sigma(H_{in} - H_{out}) - T_0\Sigma(S_{in} - S_{out}) - W_{act} \quad (2)$$

where W_{act} is the actual work output of the component and $(H_{in} - H_{out})$and $(S_{in} - S_{out})$ refer respectively to the enthalpy and entropy variations associated with flow through the component. The summation sign Σ reflect the possibility of multiple streams, if applicable. The environmental temperature T_0 is assumed to be equal to 300 K.

The main result of this analysis is the fact that the exergy losses due to irreversible entropy production in the combustion chambers are still a very large portion of the overall exergy losses, despite the fact that exhaust gas recycling reduces the overall exergy losses attributable to the fuel oxidation process. At this point it is appropriate to investigate how effective the fuel reforming process actually is. We might therefore ask how effective the cycle would be with no reforming. In order to examine this question we will present a reference cycle that is a regenerative gas turbine cycle with staged intercooled compression and staged expansion with staged fuel injection. In this reference cycle, the heat recovered from the exhaust stream is used to preheat the incoming compressed combustion air. No reforming takes place during this preheating operation. This cycle will be presented in the following section.

Gas Turbine Cycle With Regeneration and Staged Fuel Injection

The cycle discussed in the previous section exploited the possibility of recycled exhaust gases used as oxygen carriers, chemical heat recovery, and staged expansion and compression to improve the net cycle work output and hence the thermal efficiency. For reference, we will examine the results obtained with a gas turbine cycle with similar characteristics.

Cycle Description. The flowsheet diagram of the cycle is shown in Fig. 5, and is in essence a variation of the humid air turbine (HAT) cycle that has been proposed recently by a

Downloaded 02 Jun 2010 to 171.66.16.102. Redistribution subject to ASME license or copyright; see http://www.asme.org/terms/Terms_Use.cfm

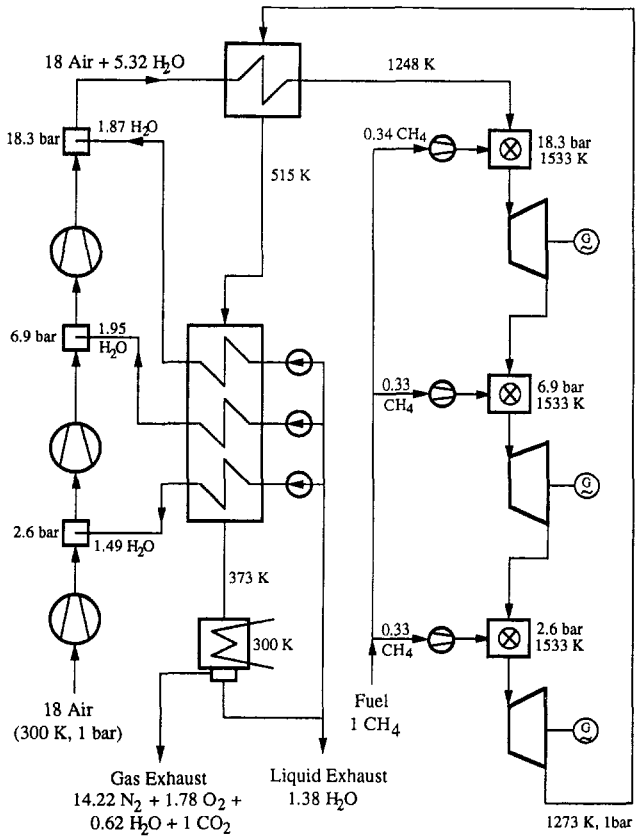

Fig. 5 Humid air turbine: flowsheet diagram

number of researchers as a viable alternative to combined cycle technology for high efficiency power generation using natural gas fuel (e.g., Day and Rao, 1993). Air enters the cycle and is compressed in a three-stage compressor section. Intercooling is achieved after each compressor set by injection preheated water such that the compressed gas stream is cooled down to the wet bulb temperature. The humid air is then preheated using the hot exhaust gas stream before entering the expansion section, which contains three turbine sets and three combustion chambers. The exhaust gas is used to preheat the combustion air and the injection cooling water. The figure shows a condenser. In practice, it might be preferable to dispose of the entire exhaust stream in a conventional manner and to inject fresh water into the cycle. This would avoid the costs associated with a condenser, but would require availability of large volumes of fresh water, which might need significant cleaning before being fed into the cycle. The technical data (turbine and compressor polytropic efficiencies, maximum turbine inlet temperatures, and minimum pinch point temperature differences in the heat exchangers) are assumed to be equal to the values presented in the previous section. By an optimization process similar to that discussed previously, we may determine the optimal values of the main cycle parameters, namely the cycle high pressure, the fuel distribution between the three combustion chambers, the excess air quantity, the air preheater heat duty, the water heater heat duty, the injected water quantity and the distribution of water between the three injection cooling points.

Results and Discussion. Again using the same technical parameters listed in Table 1, we obtain the following results for the fully optimized cycle (Table 5). As for the previous cycle, the overall efficiency is very insensitive to the amount of excess air supplied per kmol of fuel, and the optimal cycle configuration does not correspond to a pronounced maximal thermal efficiency. As before, the resulting optimal pressure varies considerably with changing excess air quantities.

Table 4 Second law analysis: summary of component exergy losses (all entries per kmol of fuel)

Components	Exergy Loss [MJ/kmol-fuel]
Reformer (incl. fuel injection)	28.8
Combustion Chambers	167.5
Turbines	18.1
Compressors & Pumps	16.7
Water Heater	9.9
Water Injectors	17.2
Condenser	31.0
TOTAL	289.1

Table 5 Optimal cycle parameters and characteristics (all entries per kmol of fuel)

Air Flow	18.0 kmol (189.1% of Theoretical Air)
Water Flow	5.32 kmol
High Pressure	18.26 bar
Heat Duties	
Regenerator - Air Preheater	651.6 MJ
Water Heater	109.3 MJ
Condenser (optional)	349.5 MJ
Work Characteristics	
Turbine Expansion Work	729.1 MJ
Air Compressor Work	208.2 MJ
Fuel Compressor Work	7.1 MJ
Pump Work	0.1 MJ
Net Work	513.64 MJ
η_{th} [LHV]	64.0%

Table 6 Second law analysis: summary of component exergy losses (all entries per kmol of fuel)

Components	Work-Loss [MJ/kmol-fuel]
Combustion Chambers	185.8
Regenerator	23.0
Turbines	17.4
Compressors and Pumps	16.4
Injection Cooling	23.7
Water Heater	8.4
Condenser	31.3
TOTAL	305.9

This cycle can be viewed as a practical implementation of the Carnot cycle in which we approximate isothermal compression and expansion by compressing and expanding the gas streams in stages with intercooling or reheat. A Carnot cycle run between a hot thermal reservoir at 1533 K and a cold heat sink at 300 K would have an efficiency of 80.4 percent. Thus, the 64.0 percent efficiency obtained with this gas turbine cycle is an encouraging result. This case demonstrates the potential high efficiencies that can be attained by implementing a cycle with multistaged intercooled compression and multistaged expansion with reheat combustors. We may now compare this cycle to the fuel reforming cycle discussed previously. To facilitate the comparison, Table 6 shows the results of the second law analysis for the cycle.

As mentioned above, this table shows that the exergy losses associated with the combustion chambers are higher than for the reforming cycle as a result of direct combustion (185.8 MJ compared to 167.5 MJ for the cycle with fuel reforming). However, this gain is partly offset by higher exergy losses in the heat recovery heat exchanger 28.8 MJ for the reforming cycle compared to 23.0 MJ for the HAT cycle). The combined losses of the heat recovery heat exchanger and the combustion chambers amount to 208.8 MJ for the reference HAT cycle and 196.3 MJ for the reforming cycle. The losses associated with the injection cooling process are greater for the HAT

Downloaded 02 Jun 2010 to 171.66.16.102. Redistribution subject to ASME license or copyright; see http://www.asme.org/terms/Terms_Use.cfm

cycle (23.7 MJ compared to 17.2 MJ for the reforming cycle). This is due to the larger gas flowrate in the compression section of the cycle. The combined exergy losses for all other cycle components are comparable for the two cycles (75.7 MJ for the reforming cycle and 73.4 MJ for the HAT cycle). Compared to the reference HAT cycle, the reduction in overall exergy loses for the reforming cycle amounts to 16.8 MJ/kmol-fuel. This reduction can be attributed mostly to reduced losses in the heat recovery heat exchanger and combustion chambers (12.5 MJ/kmol-fuel) and in the injection cooling process (6.5 MJ/kmol-fuel). The combined losses for all other cycle components are 2.3 MJ/kmol-fuel higher for the reforming cycle.

Finally, a parameter sensitivity analysis reveals results similar to those obtained for the reforming cycle. Increasing the pinch point temperature difference from 25 to 100 K and decreasing the turbine inlet temperature from 1533 K to 1400 K decreases the efficiency by 5.7 percentage points to 58.3 percent, compared to a 6.3 percentage point decrease for the reforming cycle.

We conclude from this comparison that the cycle using recycled exhaust gases and fuel reforming does allow the overall reversibility of the fuel oxidation process to be reduced through improved use of the heat content of the exhaust stream. However, this improvement is not as significant as hoped for, since the gain in efficiency amounts only to 1.4 percentage points. The comparison with the advanced HAT cycle shows clearly that much of the improvement in cycle efficiency over other high-efficiency gas turbine cycles discussed in the literature can be attributed to the staged compression with injection cooling and staged expansion with reheat combustion.

Conclusions

In this paper, we have discussed the possibility of improving energy conversion efficiencies by preventing direct contact between fuel and oxygen and relying upon intermediate reactions. Specifically, a new gas turbine cycle was proposed and discussed in which the exhaust gases are mixed with the fuel, then fed into a reformer reactor in which the heat required by the endothermic reforming reactions is provided by the hot exhaust gas stream. Thus, exhaust heat is recovered and used to drive a chemical reaction rather than to preheat combustion air as is the case in a normal regenerative gas turbine cycle. Assuming state-of-the-art cycle components, we computed that a fully optimized cycle could theoretically yield a thermal efficiency of 65.4 percent (LHV). A first-order economical analysis (Schäfer, 1991) suggests that the cost per installed kWh of the proposed fuel reforming cycle is similar to those reported for other high-performance power generation cycles. For comparison purposes, we also presented an advanced humid air turbine cycle incorporating many of the features of the proposed reforming cycle, but in which the exhaust gases are used to preheat a mixture of steam and combustion air prior to entry into the combustion chamber. Making similar assumptions about the cycle components' performance, we computed a theoretical thermal efficiency of 64.0 percent. We concluded that the reforming cycle does effectively reduce the exergy losses due to fuel oxidation compared to a similar cycle with conventional fuel combustion. However, the gain that can be attributed directly to the improved fuel oxidation mechanism is low, on the order of 1.4 percentage points. The analysis of the HAT cycle showed clearly that much of the improved efficiency over current high efficiency gas turbines can be attributed to the staged injection-cooled compression and the staged expansion with reheat combustion. These concepts are not new, but are rarely implemented in current cycles for economic or technical reasons. This study also underlines the high potential of the humid air turbine cycle, which affords very high efficiencies, yet is considerably simpler than combined cycle technology.

As stated in the introduction, the theoretical analysis of both cycles discussed in this paper is based upon a number of simplifying assumptions, notably neglecting pressure drop losses and reaction kinetics. Further work is necessary to examine a more realistic design in greater detail.

Finally, this study underlines the potential of powerful process simulation codes such as Aspen Plus™, without which this work would have been impossible.

Acknowledgments

The authors are grateful to the Electric Power Research Institute's Exploratory Research Program for making this research possible. Our particular thanks go to Dr. John S. Maulbetsch at EPRI for his support, interest, and suggestions.

References

Aspen, 1991, ASPEN PLUS™ Chemical Process Simulation Code, Aspen Technology Inc., Ten Canal Park, Cambridge MA.

Bavaria Anlagenbau Gmbh, Fürstenfeldbruck, Germany, 1990, BAVEX® plate type hybrid heat exchanger, company marketing documentation.

Bolland, O., 1991, "A Comparative Evaluation of Advanced Combined Cycle Alternatives," ASME JOURNAL OF ENGINEERING FOR GAS TURBINES AND POWER, Vol. 113, pp. 190–197.

Day, W. H., and Rao, A. D., 1993, "FT4000 HAT With Natural Gas Fuel," *Turbomachinery International*, Jan./Feb., pp. 22–29.

Gordon, G., and McBride, B. J., 1976, "Computer Program for Calculation of Complex Chemical Equilibrium Compositions, Rocket Performance, Incident and Reflected Shocks, and Chapman-Jouguet Detonations," NASA Sp-273, NASA Lewis Research Center.

Hamann, B., and Joyce, J. S., 1989, "World's Largest Gas Turbines for Ambarli Combined Cycle," *Modern Power Systems*, May, pp. 61–74.

Holt, N., 1991, "Gasification Power Plants: Highly Efficient Advanced Cycles," *EPRI Journal*, Apr.–May, pp. 40–43.

Kalina, A. I., 1983, "Combined Cycle and Waste-Heat Recovery Power Systems Based on a Novel Thermodyanmic Energy Cycle Utilizing Low-Temperature Heat for Power Generation," ASME Paper No. 83-JPGC-GT-3.

Kalina, A. I., 1984, "Combined Cycle System With Novel Bottoming Cycle," ASME JOURNAL OF ENGINEERING FOR GAS TURBINES AND POWER, Vol. 112, pp. 107–116.

Kalina, A. I., 1991, "Kalina Cycles and System for Direct-Fired Power Plants," ASME *Second Law Analysis—Industrial and Environmental Applications*, ASME AES-Vol. 25/HTD-Vol. 191, pp. 41–47.

Kalina, A. I., Leibowitz, H. M., Markus, D. W., and Pelletier, R. I., 1991, "Further Technical Aspects and Economics of a Utility-Size Kalina Bottoming Cycle," ASME Paper No. 91-GT-365.

Kalina, A. I., and Tribus, M., 1992, "Advances in Kalina Cycle Technology (1980–1991), " presented at the Florence World Energy Research Symposium, Florence, Italy, June.

Knoche, K. F., 1990, Visiting Professor at Thayer School of Engineering, Dartmouth College, personal communication.

Matsuzaki, H., Shimomura, K., Fukuyama, Y., Araki, T., Ishii, J., Yamamoto, M., Shibuya, S., and Okuhara, I., 1992, "New Advanced Cooling Technology and Material of the 1500°C Class Gas Turbine," ASME Paper No. 92-GT-240.

Papalambros, X. X., and Wilde, Y. Y., 1988, *Principles of Optimal Design*, Cambridge University Press.

Parks, W. P., Jr., Ramey, R. R., Rawlins, D. C., Price, J. R., and Van Roode, M., 1991, "Potential Applications of Structural Ceramic Composites in Gas Turbine," ASME JOURNAL OF ENGINEERING FOR GAS TURBINES AND POWER, Vol. 113, pp. 628–634.

Richter, H. J., and Knoche, K. F., 1983, "Reversibility of Combustion Processes," *Efficiency and Costing, Second Law Analysis of Processes*, R. A. Gaggioli, ed., ACS Symposium Series 235, pp. 71–86.

Rostrop-Nielsen, J. R., 1983, "Catalytic Steam Reforming," *Catalysis: Science & Technology*, J. R. Anderson and M. Boudart, eds., Springer-Verlag, Berlin, Vol. 5, Ch. 1, pp. 1–117.

Schäfer, B., 1991, "Energy Conversion Process," B. E. Thesis, Thayer School of Engineering, Dartmouth College, NH.

Wilson, D. G., 1984, *The Design of High-Efficiency Turbomachinery and Gas Turbines*, MIT Press, Cambridge, MA.

Downloaded 02 Jun 2010 to 171.66.16.102. Redistribution subject to ASME license or copyright; see http://www.asme.org/terms/Terms_Use.cfm

Design Considerations of a Versatile Simulator for High-Bypass Turbofans

C. Balan
GE Aircraft Engines,
Evendale, OH 45215

The continuing requirement for performance improvement of higher thrust turbofans is met by increased bypass ratios. The trend toward higher bypass ratios and relatively large-diameter low-pressure-ratio fans requires innovative design approaches, which include shorter inlets, slimmer nacelles, shorter fan ducts and exhaust systems, and possible elimination of thrust reverser. The success of this new generation of high-bypass ducted turbofans depends on understanding the acoustic impact from reduced treatment areas, inlet-fan coupling and operability, as well as overall system performance. To achieve these goals a versatile scale model propulsion simulator large enough to operate as a fan rig, yet small enough to be installed in a wind tunnel for evaluating overall acoustic, operability, and system performance, was developed. The criteria of designing such a simulator and its capabilities are discussed in this paper.

Introduction

The trend in increased volume of air traffic experienced over the past decades is expected to continue well into the future. The potential benefit of continuous improvements in the propulsion system and airframe performance is further amplified by this increase in air traffic volume. In order to concentrate the research objectives toward improved propulsion system performance, it is essential to understand the performance attributes. In the early days of civil aviation the performance attributes were limited to speed and reliability. This was later modified to include efficiency of the overall system, as well as acoustic considerations, and the challenge was met by changing from turbojets to turbofans of moderate bypass ratios. In the last few years, further improvement in propulsion system efficiency was accomplished by the technically successful counterrotating open rotor systems of significantly higher bypass ratio than the current engines. The need for evaluating the performance under simulated flight conditions, along with the requirements to address the noise concerns of the open rotor systems, led to the development of scale model simulators of reasonable size and power capable of being tested in wind tunnels and free jet anechoic facilities. These simulators provided the foundation for the research and development work carried out on the open rotor systems.

The increased volume of air traffic mentioned in the beginning is being met by larger aircraft powered by higher thrust engines to reduce traffic congestion. The increased global emphasis on environmental issues requires that these engines address concerns related to acoustics and emissions, while retaining or, if possible, improving the propulsion system performance.

This paper discusses some of the design considerations that were addressed in the development of a test bed for future research requirements in acoustics and performance of large turbofans. Although the propulsion simulator described here was initially aimed at large-size turbofans with fan diameter in the range of 300 cm or higher, it can be easily used for smaller size propulsion systems.

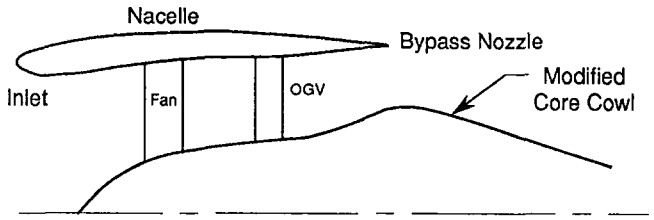

Fig. 1(*a*) Simulator with one stream

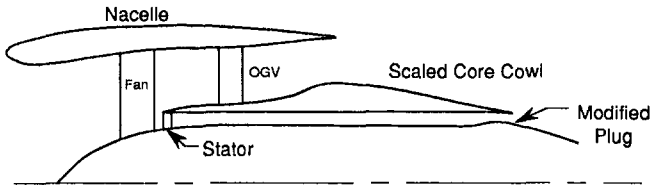

Fig. 1(*b*) Simulator with two streams

Contributed by the International Gas Turbine Institute and presented at the 38th International Gas Turbine and Aeroengine Congress and Exposition, Cincinnati, Ohio, May 24–27, 1993. Manuscript received at ASME Headquarters February 12, 1993. Paper No. 93-GT-14. Associate Technical Editor: H. Lukas.

Copyright © 1995 by ASME

Downloaded 02 Jun 2010 to 171.66.16.102. Redistribution subject to ASME license or copyright; see http://www.asme.org/terms/Terms_Use.cfm

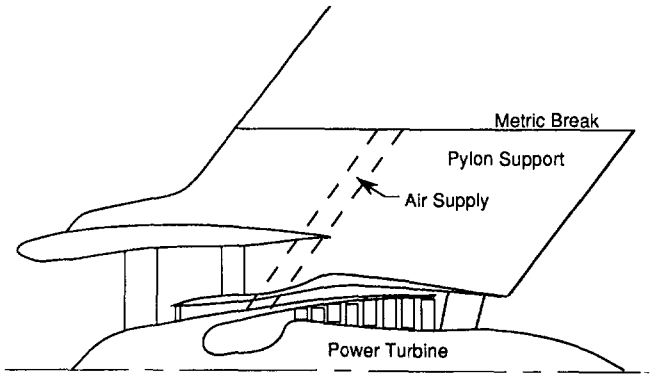

Fig. 2 Schematic of a pylon-mounted simulator

Simulator Configuration Considerations

The overall objective was to design a simulator capable of providing acoustic, aero, and operability data on high-bypass ducted fans. To this end, the primary components that need to be simulated are the inlet, nacelle, fan, outlet guide vanes (OGV), and bypass nozzle. The basic configuration of the simulator is illustrated in Fig. 1(*a*). This configuration is similar to the Turbine Powered Simulators, TPS, used in evaluating the installation effects during engine–airframe integration. The significant difference between the simulator for engine airframe integration and the simulator for fan performance evaluation is the difference in size and geometry of the fan. Normally, the TPS uses a generic small-scale fan to produce the correct scaled inlet flow and fan pressure ratio at the full-scale operating point under investigation. The TPS does not reproduce the fan performance as their objective is only to pump the required flow at the correct fan pressure ratio. The primary question on this configuration is regarding the core flow. If the core flow is not modeled as a part of the inlet flow, then the fan nozzle and core cowl downstream of the bypass stream exhaust nozzle would have to be distorted relative to the engine configuration. If the core flow is treated as a part of the fan flow to enable modeling of the entire fan, then the fan duct, OGV, core cowl, and fan nozzle would have to be distorted relative to the full-space engine. Another choice of fully modeling the core flow and core nozzle, as illustrated in Fig. 1(*b*), reduces the problem to a modified core nozzle and core plug, while all of the bypass stream components and inlet-nacelle would be fully representative of the engine system to be modeled. From the overall bypass stream simulation point of view, the configuration identified in Fig. 1(*b*) is ideal, inasmuch as it included a specially designed stator vane downstream of the fan hub at core inlet. Significant acoustic interaction, as well as operability concerns, especially in the case of variable pitch ducted fans, could require simulation of the booster-core inlet stator vanes, as well as the first stage of the booster rotor. The overall design would be more complex with the booster rotor included, but it would be a closer representation of the real engine at an increase in associated design complexity, manufacturing costs, and power requirements of the simulator.

The final configuration selected for the simulator included the booster. Even though the configuration without the booster rotor would have met most of the fan aerodynamic performance assessment objectives, the need for verifying successful booster design for acoustic cut-off and elimination of forward radiated booster rotor interaction tones required that the booster rotor be simulated.

This discussion is related to the propulsion system to be modeled. There is yet another consideration before the final simulator configuration can be arrived at. This involves the relative location of the power turbine and the model support system. Ideally a simulator that is pylon mounted, similar to the engine mount on the airframe, and a turbine located under the core cowl would be chosen. Such a simulator is illustrated in Fig. 2. The metric break of such a simulator would be located in the pylon support with the simulator force balance located in the pylon support. However, such a configuration would require a flow-through balance. Even though flow-through balances have been used successfully, the requirement of significantly higher turbine drive air temperature and associated thermal concerns on the balance accuracies excluded such a configuration as a viable option.

The configuration finally selected is illustrated in Fig. 3 and was similar to the successful counter rotating propulsion simulator (Delaney et al., 1986). The fan nacelle module was sting mounted off a separate turbine drive and the whole simulator was supported off the turbine housing using a strut. This configuration required two separate balances: one for the rotating components, i.e., fan and booster, and another for all the metric static nacelle components. Thermal concerns were not considered to be a problem as the hot air did not cross any of the balances. The pylon-mounted configuration illustrated in Fig. 2 would also have required two balances. To obtain accurate fan performance, a separate torque meter would have been needed, in addition to the pylon balance, to measure the power input to the robots.

Scale Factor and Model Size Considerations

The second most important decision made after the basic configuration to be simulated was the selection of scale factor and model size. The actual model size influences the choice of test facilities and the program cost, while the scale factor determines the level of uncertainty in scaling the model data to the full-scale engine.

A smaller model size requires low drive turbine air flow due to reduced fan power. Also the overall program cost will be lower. However, this leads to lower scale model Reynolds numbers and larger corrections to the measured data. In addition, a smaller model can require specialized instrumentation to reduce rake blockage. From an acoustic point of view, even a scale factor of 20 percent can lead to data processing requirements for frequencies in the range of 100 kHz, as the full scale frequencies of interest are limited to 20 kHz. At such high frequencies, data recording, microphone

Nomenclature

A = area
D = diameter
F = thrust
F = full space
HL = nacelle highlight
M = Mach number
n = net
P = pressure
O = free stream
Re = Reynolds number
p = propulsive
SHP = shaft horsepower
S = scale model
V = velocity
r = radius
η = efficiency

Subscripts

C = blade chord

Downloaded 02 Jun 2010 to 171.66.16.102. Redistribution subject to ASME license or copyright; see http://www.asme.org/terms/Terms_Use.cfm

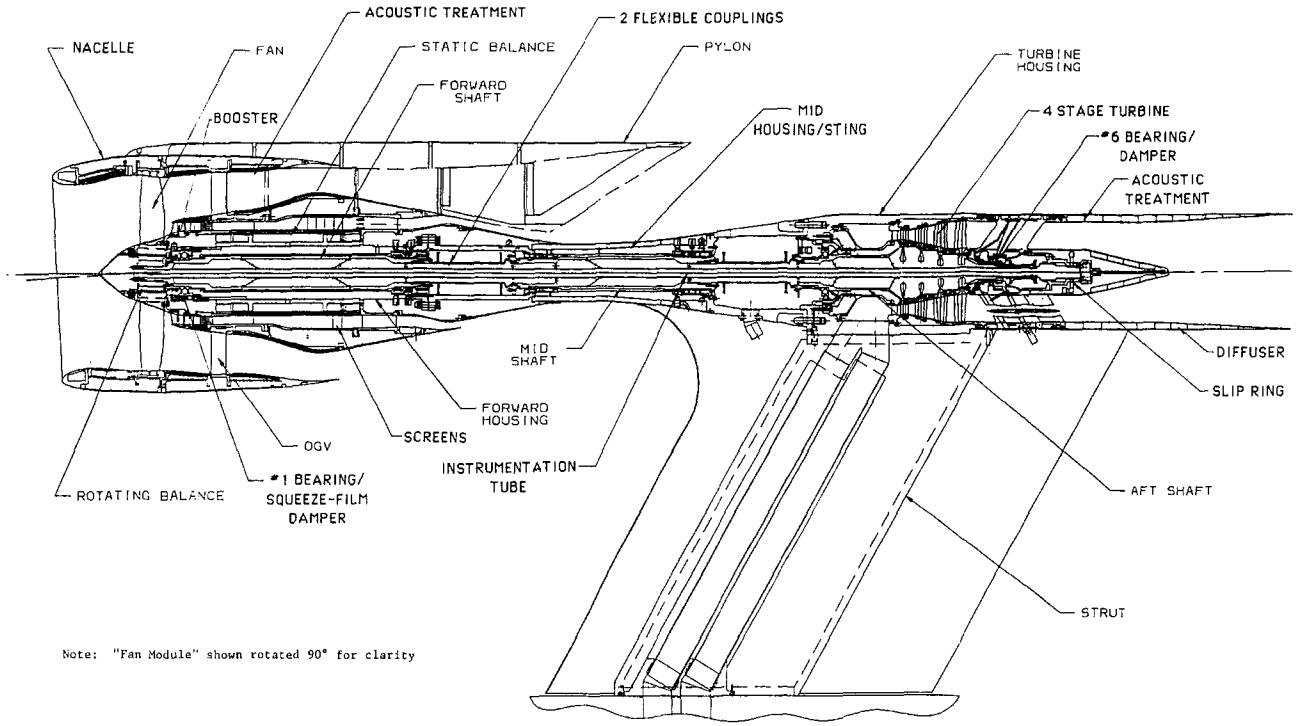

Fig. 3 Final simulator configuration

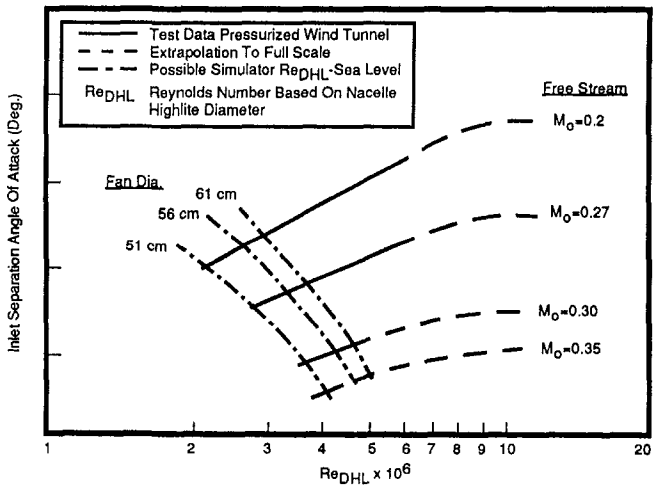

Fig. 4 Effect of Reynolds number on inlet separation

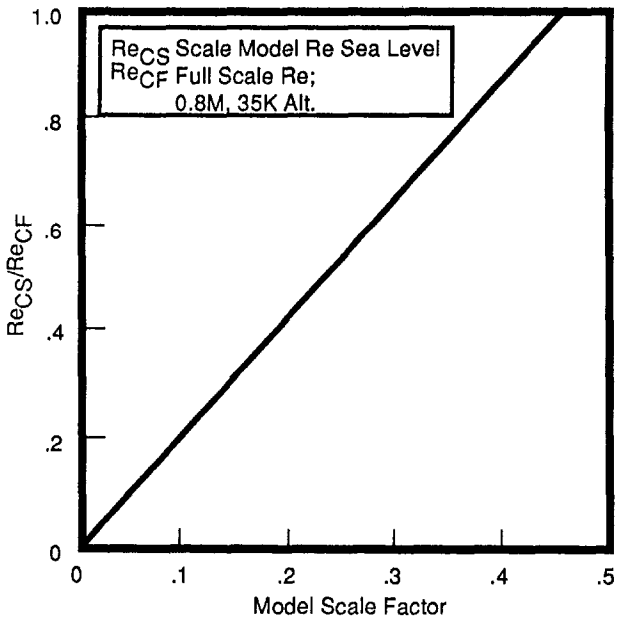

Fig. 5 Variation of sea level model to cruise full-scale Reynolds number ratio with scale factor

response, and ambient attenuation of the measured noise data are critical problems that need to be addressed. Scaling of the acoustic treatment for evaluating treatment suppression effectiveness can also be a problem. The frequency response of the aeromechanical data system for health monitoring can also be a consideration. Even though not all of these problems are common to all test facilities, it is necessary to choose a large enough scale factor such that test facility data processing limitations do not hinder the test. Additional problems related to small-scale factors and model sizes include effect of manufacturing tolerances on measured data, and inability to scale operating clearances.

Choice of a large-scale factor, on the other hand, can lead to excessive power requirements, which manifests itself as either large turbine drive air flow or higher turbine drive air pressure and temperature. The large-scale model also requires fairly large test facilities, i.e., the free jet size in the case of anechoic chambers to ensure no entrainment of shear layer into the fan inlet flow at high angle of attacks and to reduce wall interference and test section blockage in the case of wind tunnels.

The scale model Reynolds number affects both the nacelle external and internal separation at high angle of attack, as well as losses associated with flow path and fan. Most of the subscale component testing during the course of an engine development program is designed to address these problems separately, and provide the required data on full-scale engine component performance. In general, the nacelle-inlet through-flow scale models are tested in a pressurized wind tunnel to evaluate the high angle of attack low-speed inlet-

Downloaded 02 Jun 2010 to 171.66.16.102. Redistribution subject to ASME license or copyright; see http://www.asme.org/terms/Terms_Use.cfm

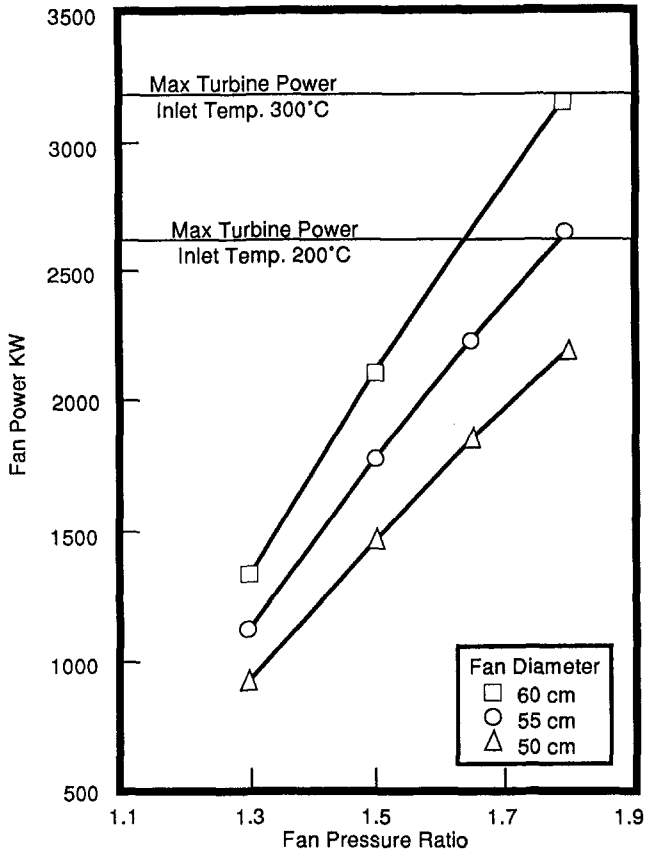

Fig. 6 Effect of fan pressure ratio on power requirement

nacelle performance. A typical plot of the effect of Reynolds number on angle of attack at which inlet separation occurs is shown in Fig. 4. It can be observed that even in a pressurized wind tunnel, unless a much larger scale model is used, some extrapolation is required to evaluate full-scale performance. The scale model Reynolds numbers of the propulsion simulator operating in a sea level free jet facility are also plotted in Fig. 4. It can be seen that with reasonable fan sizes in the propulsion simulator, scale model Reynolds numbers comparable to inlet models in pressurized tunnels can be achieved. In addition, the propulsion simulator can yield more valuable information on the inlet distortion characteristics, including the effect of inlet–fan coupling on inlet distortion and inlet–fan compatibility.

The corrections to the fan and OGV performance are applied as a function of Reynolds number based on their respective airfoil chord lengths. Along the sea level operating line, model to full-scale Reynolds number ratio is directly proportional to the scale factor. On the other hand due to the difference in sea level and altitude ambient conditions, the blade chord Reynolds number of a subscale fan operating along the cruise operating line, at sea level inlet conditions, is closer to the full-scale Reynolds number. The ratio of scale model to full-scale blade chord Reynolds number as a function of scale factor is presented in Fig. 5, for cruise operating line. For this plot the scale model is at sea level static inlet conditions. It can be seen that with scale factor of 0.4 no correction need to be made to the cruise operating line data of the fan rig. However, such a scale factor is impractical for full-scale fans of large diameters and normally corrections of the order of one half to three quarter points in efficiency to the measured fan performance will need to be applied to the subscale fan data, for scale factors in the range of 0.2.

It can be seen from this discussion that in general for very large turbofans, it is not feasible to avoid Reynolds number correction to the measured data. However, the scale factor should be chosen to avoid large corrections to the measured data. In the case of the current simulator, a scale factor that kept the corrections to the measured fan data to a minimum, while yielding scale model Reynolds numbers similar to the inlet models in a pressurized wind tunnel, and at the same time permit reasonable geometric similitude between the fan components was selected. The scale factor was in the neighborhood of 0.2 and the fan diameter was 56 cm.

Table 1 Turbine design parameters

Number of stages	4
Maximum rpm	17,000
Power	3150 kW
Inlet pressure	14 bar
Inlet temperature	300°C
Mass flow	12.7 kg/s
Housing diameter	33 cm

Table 2 Balance capabilities

Rotor balance	
Axial force	900 kg
Torque	210 kg-m
Stator Balance	
Axial force	900 kg
Normal force	725 kg
Side force	725 kg
Pitch moment	635 kg-m
Yaw moment	635 kg-m
Roll moment	210 kg-m

Turbine Design Considerations

The turbine design is directly related to the choice of scale model size and test facility capabilities. The power requirement of the turbine is determined by the fan size and characteristics, while the maximum power that can be produced by the turbine is decided by the test facilities air supply capabilities. In general, most test facilities can supply either low mass flows at very high pressure or high mass flows at moderate pressures. Based on a survey of available test facilities, the air supply limitation was estimated to be 12.7 kg/s at 20 atm. Allowing for losses through supply piping and control valves, the maximum air pressure measured at the turbine inlet was considered to be 14 atm.

Figure 6 is a plot of fan design point power requirements at sea level static inlet condition as a function of fan pressure ratio for three different size fans. Hub-to-tip radius ratio of 0.3, fan efficiency of 0.9, and average fan face Mach number of 0.65 were assumed for the evaluation. The maximum possible power output of the turbine at nominal turbine total to static efficiency for two different inlet temperatures is also plotted in the same figure. In reality one must have enough margin on the power requirement for off-design conditions. The true fan power requirement is the highest at the highest flow and pressure ratio to be tested and is a function of the fan characteristics. The choice of high inlet temperature can require specialized materials for both turbine and air supply piping. Ideally a maximum operating temperature of 400°C is an acceptable limit for conventional materials. For the current simulator power turbine, the maximum turbine inlet temperature of 300°C was selected. At the turbine inlet condition of 300°C and 14 atm, with a maximum drive air mass flow of 12.7 kg/s, the turbine can generate approximately 3150 kW. This capability enables the simulator to test fans of nominally 60 cm in diameter and design pressure ratios as high as 1.8. A maximum turbine speed of 17,000 rpm was selected based on fan tip speed requirements. Fan corrected tip speeds of up to 550 m/s are possible depending on ambient temperatures and fan size.

Downloaded 02 Jun 2010 to 171.66.16.102. Redistribution subject to ASME license or copyright; see http://www.asme.org/terms/Terms_Use.cfm

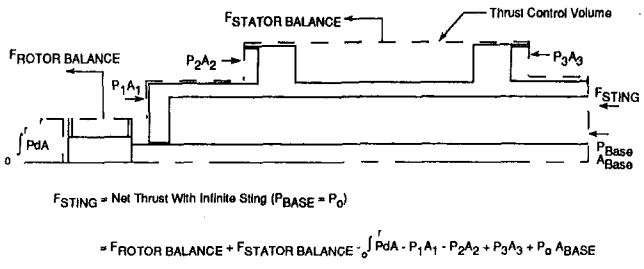

Fig. 7 UPS measured force schematic

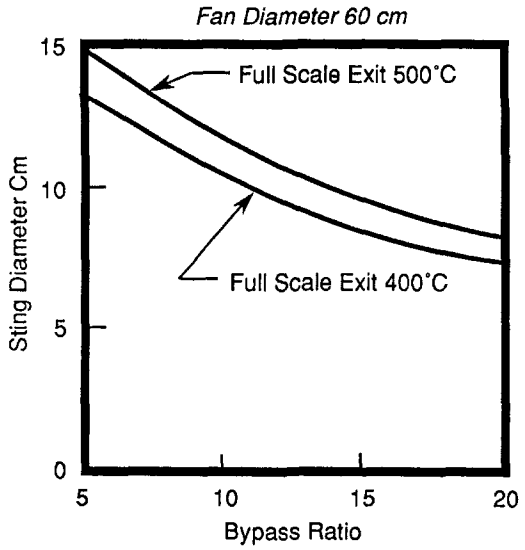

Fig. 8 Effect of bypass ratio on sting diameter

Additional considerations in the turbine design consisted of aerodynamic interference and acoustics. The proximity of the turbine housing to the fan-nacelle module was the primary aerodynamic concern. The potential field propagating forward from the turbine housing changes the local static pressure around the nacelle (Krynytzky, 1988). The correction to the measured forces due to this potential field is normally known as the buoyancy correction. As a simple rule the smaller the turbine housing and the longer the distance between the nacelle and turbine housing, the smaller will be the magnitude of the correction.

The acoustic consideration addressed was related to the aft radiated turbine noise on the measured fan noise. This problem was given special consideration and the measures taken to alleviate the problem included proper selection of blade vane count for acoustic cutoff, bulk absorber treatment of the turbine exhaust duct and the plug, and addition of the exhaust diffuser to reduce the turbine exit Mach number and the associated jet noise. The addition of the 1.6 area ratio exhaust diffuser also helped in improving the maximum power capability of the turbine by lowering the turbine exit static pressure.

The final turbine configuration selected is given in Table 1.

Balance and Instrumentation Considerations

As explained earlier, the basic configuration chosen was a sting-mounted fan-nacelle module with two balances. The metric fan and booster were mounted off a single rotating two-plane radial spoke force balance capable of measuring both the rotor thrust and torque (Delaney et al., 1986). The static nacelle balance that supported the static fan and core flow path components was a six-component balance, the six components being the axial, normal, and side forces relative to the model axis, and the pitch, yaw, and roll moments relative to the model axis. The side and normal forces, and the associated yaw and pitching moments, were only measured to account for the interaction of these components on the measured axial force to improve the accuracy. These components by themselves do not account for all of the forces acting on the engine mount and cannot be used directly to evaluate the engine mount loads. The basic balance capabilities are listed in Table 2.

This configuration of the balances was carefully chosen to enable the net axial force evaluation using a simple control volume approach. The basic schematic of the various forces acting on the control volume and the net system thrust definition is given in Fig. 7. This approach required that only a very small pressure area correction need to be made to the measured balance forces. From the measured sting force F_{sting}, the overall net thrust F_n is obtained by applying the appropriate buoyancy correction.

The advantages of the force balances to measure the thrust and torque are many. Without going through the detailed definitions and procedures for accounting for the booster performance, the overall advantages are listed below:

1 The measurement of direct power input to the bypass stream improves the accuracy of the temperature rise evaluation across the fan. This is of significant importance in estimating the fan efficiency, especially in the case of low pressure ratio fans, where the temperature rise across the fan is small.
2 The overall measured net thrust is useful in evaluating the acoustic data, as the acoustic testing is normally carried out with no instrumentation for directly measuring the fan pressure ratio.
3 The overall measured net thrust and the power input can be used to define a propulsive efficiency

$$\eta_p = \frac{F_n \cdot V_o}{\text{SHP}}$$

This propulsive efficiency includes the effect of inlet losses, nacelle drag, fan duct losses, and exhaust nozzle performance. This enables direct comparison of measured performance between various configurations, as well as effect of a given change in the configuration with reference to a baseline configuration.

The primary consideration in improving the force measurement accuracy is related to the number of instrumentation lines crossing the metric break of a fully instrumented model. Although the relative stiffnesses of the instrumentation lines are negligible compared to the balance flexures, they can contribute significantly to the hysteresis and inaccuracies in the low end of the balance measurements. The fully instrumented fan-nacelle measurements consisted of both analog and steady-state data. The analog data included Kulites for acoustics, fan tip flow field evaluation and inlet distortion measurements, strain gages for monitoring rotor and stator blade stresses, accelerometers for measuring system dynamics, and vibration levels. The steady-state data included balance measurements, static pressures and total pressures in the fan duct and flow path, and total temperature measurements in the fan and core flow paths. Of these, the analog data had to be routed to data monitoring, processing, and recording stations directly and the problem of routing the instrumentation lines across the metric break could not be avoided. However, a reduction in the number of lines crossing the metric break to acquire the steady-state pressures and temperatures was achieved by model-mounted electronic pressure scanners and millivolt scanner modules. Such a configuration reduced the lines that are needed to

Downloaded 02 Jun 2010 to 171.66.16.102. Redistribution subject to ASME license or copyright; see http://www.asme.org/terms/Terms_Use.cfm

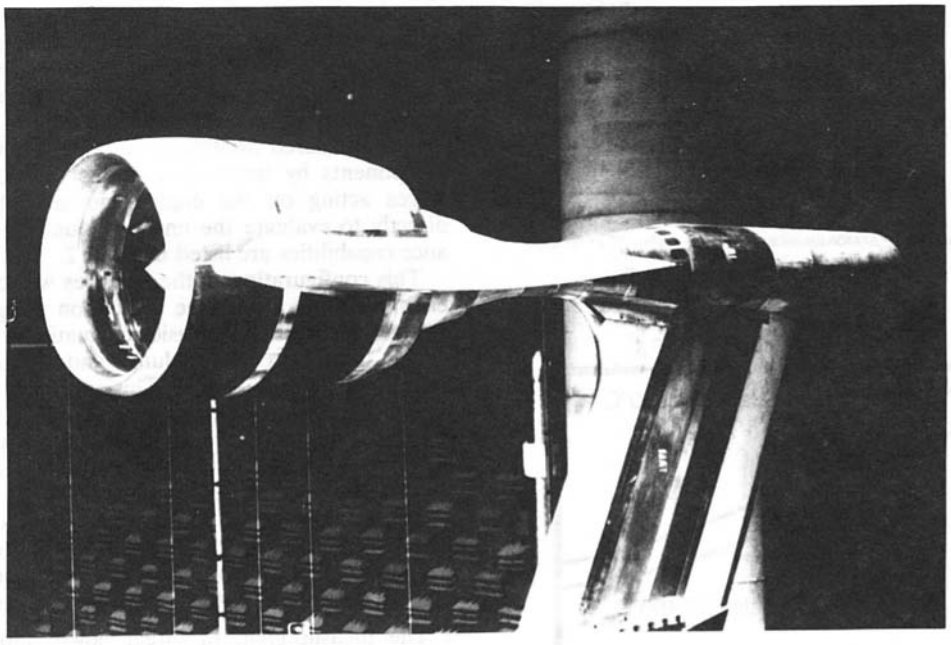

Fig. 9 Photograph of the high-bypass turbofan simulator

cross the metric break for steady-state data acquisition to the control and calibration pressure lines for the pressure scanner modules, multiplexed data, excitation and address cables to service the scanner modules and the reference junctions to the thermocouples used for temperature measurement. The number of reference junction lines crossing the metric break was further reduced to a minimum by using a common reference junction for groups of thermocouples. All of the rotating balance data were acquired through slip rings. Although the overall instrumentation routing and data acquisition explained here are simple in concept, considerable time and effort were spent in realizing a fully operational system since the instrumentation routing and data acquisition are fairly complex in terms of details. The overall system proved to be excellent in terms of data quality and data acquisition time, in spite of the waiting period needed to achieve thermal stability of the onboard modules.

Core Flow Path and Sting Design Considerations

The ideal sting for a sting-mounted model is infinitely long and small. In reality, the sting has to be of sufficient strength to support the cantilevered fan nacelle module and the loads associated with high angle of attack operation. Adequate room must also be available to route the instrumentation and service lines. As explained earlier, a reasonable attempt was made to reduce the number of instrumentation lines crossing the metric break, which also helped in reducing the sting size. Another factor that alleviated the effect of the sting on fan module performance is the reduced temperature of core flow relative to full-scale engine. The core nozzle exit total pressure and mass flow were maintained to simulate correct nozzle exit Mach number and bypass ratio. The flow area occupied by the scale model core stream tube is significantly smaller than the full-scale engine stream tube due to the temperature difference. This difference in stream tube areas is inversely proportional to the square root of the full-scale and the scale model exit temperature ratio. Figure 8 is a plot of the ideal finite sting that will yield the same core flow outermost streamline for various bypass ratios and two different full scale core nozzle exit temperatures. However, the overall requirements could not meet the ideal sting diameter, and the final sting diameter was much larger. Some of the effects of the sting were eliminated by redesigning the core nozzle and plug in the presence of the sting to provide the same ideal pressure distribution on the core cowl as the full-scale design. This was also verified by separate dual flow nozzle tests with a simulated sting and turbine housing. The final sting was 16 cm in diameter.

The simulator core nozzle exit total pressure was matched to the full-scale engine conditions by means of pressure drop screens installed in the core duct flow path as shown in Fig. 3.

Mechanical Design Considerations

The basic requirements of the mechanical design are the same as for any full-scale engine. The extreme requirements imposed by the simulator operating in a wind tunnel are related to safety and mechanical integrity and the need to change the configuration of the test hardware in an efficient manner to reduce wind tunnel test time and costs. Due to the considerable length of the simulator, the drive shaft was divided into three parts, each supported by two bearings and connected by flexible couplings. Additional mechanical details involve squeeze film dampers at number 1 and number 6 bearing locations to reduce bearing loads under possible blade-out conditions, and provision for field balancing the fan rotor assembly.

Final Simulator Configuration and Tests

The various components of the simulator are illustrated in Fig. 3 and a photograph of the simulator installed in an anechoic free jet test facility is given in Fig. 9. The final simulator configuration consisted of removable hard wall and acoustically treated panels in the bypass stream flow path, interchangeable bellmouth and inlet, interchangeable bypass stream exhaust nozzles including a variable exhaust area mechanism, and easily removable fan blades. The original design required that the bypass stream OGV to rotor spacing be variable. This was not deemed necessary to meet the objectives of the configuration tested. The simulator was successfully tested and data were acquired on many configurations up to 30 degrees angle of attack and Mach 0.25, over a period of 150 hours of simulator operation. The overall

Downloaded 02 Jun 2010 to 171.66.16.102. Redistribution subject to ASME license or copyright; see http://www.asme.org/terms/Terms_Use.cfm

data obtained consisted of fan mapping, acoustics, and operability on three different fan blade designs of 56 cm diameter.

Conclusions

Some of the key design considerations that dictated the design of a versatile scale model for bypass stream performance of a high-bypass turbofan have been discussed. The final simulator was successful in meeting the design objectives and provided the necessary performance data. This simulator is versatile enough to be useful in meeting future research requirements of performance improvement and noise reduction of a wide variety of high-bypass turbofans.

Acknowledgments

The author wishes to acknowledge the contributions of many participants from the General Electric Aircraft Engines, Evendale, Ohio, and the Boeing Company, Seattle, Washington, to the success of the program.

References

Delaney, B. R., et al., 1986, "A Modal Propulsion Simulator for Evaluating Counterrotating Blade Characteristics," SAE Paper No. 861715.

Krynytzky, A. J., 1988, "Mach Number Corrections for a Two Foot Propeller Rig in Solid and Slotted Test Sections," AIAA Paper No. 88-2056.

Downloaded 02 Jun 2010 to 171.66.16.102. Redistribution subject to ASME license or copyright; see http://www.asme.org/terms/Terms_Use.cfm

Simulating Indirect Thrust Measurement Methods for High-Bypass Turbofans

J. D. Stevenson[1]

H. I. H. Saravanamuttoo
Professor.
Fellow ASME

Department of Mechanical and Aerospace Engineering,
Carleton University,
Ottawa, Ontario, Canada

As yet, there is no known reliable method for directly measuring the thrust of a turbofan in flight. Manufacturers of civil turbofans use various indirect thrust measurements to indicate performance of an engine to the flight deck. Included among these are: Engine Pressure Ratio (EPR), Integrated Engine Pressure Ratio (IEPR), Fan mechanical speed (N_1), and various Turbine Gas Temperatures such as ITT or EGT. Of key concern is whether these thrust indicators give an accurate account of the actual engine thrust. The accuracy of these methods, which is crucial at take-off, may be compromised by various types of common engine deterioration, to the point where a thrust indicator may give a false indication of the health and thrust of the engine. A study was done to determine the effect of advanced engine cycles on typical values of these parameters. A preliminary investigation of the effects of common kinds of turbofan deterioration was conducted to see how these faults can affect both actual engine performance and the indirect thrust indicators.

Introduction

Although jet engines have been used commercially for 40 years, there is still no direct method of measuring thrust in flight. Indirect methods of indicating thrust are used, based on pressure measurements or rotational speeds. The use of engine pressure ratio (EPR), which is defined as the ratio of total exhaust pressure over total inlet pressure, became dominant in early turbojet engines where there was a direct relationship between EPR and thrust. A problem arose with the introduction of high-bypass turbofans, where a substantial portion of the total net thrust is provided by the cold or bypass stream; EPR considered only the core engine pressure ratio and hence the thrust contribution from the hot stream. One alternative was to use integrated engine pressure ratio (IEPR), which is based on an area-weighted average of the bypass and core nozzle pressure ratios. Another approach was to use fan rotational speed (N_1) to indicate thrust.

Advanced cycle turbofans may operate at significantly higher values of bypass ratio (BPR) and overall pressure ratio (OPR), which may influence the choice of parameter for indicating thrust. The effects of in-service deterioration may also be important in selecting the most suitable parameter.

This paper analyses the performance of a typical high-performance turbofan in the hope of providing objective data for comparing the usefulness of various thrust setting parameters.

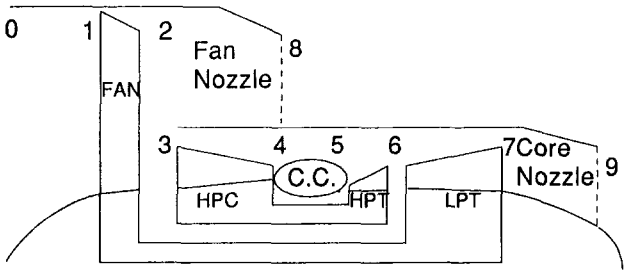

Fig. 1 Twin-spool turbofan station numbering

The Origins of EPR

It is instructive to consider the basis of EPR as a means of indicating the thrust of a simple, fixed nozzle turbojet:

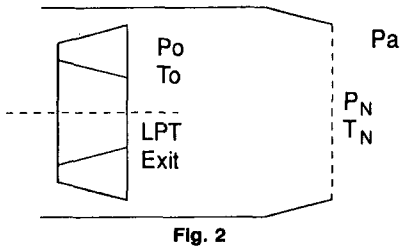

Fig. 2

For a choked nozzle,

$$F = mC_N + A(p_N - p_a), \quad \text{and} \quad \frac{p_N}{p_0} = \left(\frac{2}{\gamma + 1}\right)^{\frac{\gamma}{\gamma - 1}} \quad (1)$$

[1]Present address: GasTOPS Ltd., Gloucester, Ontario, Canada.

Contributed by the International Gas Turbine Institute and presented at the 38th International Gas Turbine and Aeroengine Congress and Exposition, Cincinnati, Ohio, May 24–27, 1993. Manuscript received at ASME Headquarters March 17, 1993. Paper No. 93-GT-335. Associate Technical Editor: H. Lukas.

Copyright © 1995 by ASME

Downloaded 02 Jun 2010 to 171.66.16.102. Redistribution subject to ASME license or copyright; see http://www.asme.org/terms/Terms_Use.cfm

Also:

$$m = \rho_N A C_N; \quad \rho_N = \frac{p_N}{RT_N}; \quad C_N^2 = 2C_p(T_0 - T_N)$$

Hence,

$$F = \rho_N A C_N^2 + A(p_N - p_a) \tag{2}$$

$$= \frac{p_N}{RT_N} A \cdot 2C_p(T_0 - T_N) + A(p_N - p_a)$$

$$= 2\frac{\gamma}{\gamma - 1} A \left(\frac{p_N}{p_0}\right)\left(\frac{p_0}{p_a}\right) p_a \left(\frac{T_0}{T_N} - 1\right) + A p_a \left(\frac{p_N}{p_0} \cdot \frac{p_0}{p_a} - 1\right) \tag{3}$$

Substituting the value of $\frac{p_N}{p_0}$:

$$\frac{F}{Ap_a} = \left[2\frac{\gamma}{\gamma - 1} \cdot \left(\frac{2}{\gamma + 1}\right)^{\frac{\gamma}{\gamma - 1}} \left(\frac{p_0}{p_a}\right)\left(\frac{\gamma + 1}{2} - 1\right)\right] + \left[\left(\frac{2}{\gamma + 1}\right)^{\frac{\gamma}{\gamma - 1}} \frac{p_o}{p_a} - 1\right] \tag{4}$$

This gives

$$\frac{F}{Ap_a} = \frac{p_0}{p_a}\left[\left(\frac{2}{\gamma + 1}\right)^{\frac{\gamma}{\gamma - 1}} (\gamma + 1)\right] - 1 \tag{5}$$

It follows that

$$\frac{F}{Ap_a} = K\left[\frac{p_o}{p_a}\right] - 1 \quad \text{where} \quad K = f(\gamma) \tag{6}$$

This can be extended to work with EPR instead, and noting that

$$\frac{p_{07}}{p_a} = \frac{p_{07}}{p_{01}} \cdot \frac{p_{01}}{p_a} \quad \text{i.e., nozzle } PR = EPR \times RPR$$

Then,

$$\boxed{\left(\frac{F}{Ap_a} + 1\right)/RPR = K(EPR)} \tag{7}$$

(where $K = 1.2594$ for $\gamma = 1.333$).

Thus, for a fixed nozzle turbojet, the ideal thrust can readily be found from the EPR. In the case of a turbofan, however, the EPR will depend on both the bypass ratio and fan pressure ratio since both of these have an effect on the total pressure of the LP turbine exhaust, and there is no longer a direct relationship between total net thrust and EPR. The concept of IEPR attempts to include the substantial thrust contribution from the fan or bypass nozzle through an area-weighted average defined as follows:

$$IEPR = \frac{p_{02} \cdot A_c + p_{07} \cdot A_h}{p_{01}(A_c + A_h)} \tag{8}$$

This requires extensive pressure measurements in the fan duct but appears to be a more logical way to indicate the thrust of a high-bypass turbofan.

The thermodynamic derivation of EPR is straightforward, but to pilots, EPR may appear to be an abstract concept that does not give an instinctive "feel" for thrust developed. Rotational speeds, such as N_1, can readily be related to thrust; anyone who has ever driven a car equipped with a tachometer can readily recognize red line limits and instinctively keeps within them.

Choice of Design Point

Modern high-bypass turbofans are designed around several flight conditions or design points, and not just the Sea Level Static (SLS) condition, as was perhaps the common design point in early engines when adequate take-off thrust was the primary concern. Current modern designs are usually optimized around three common flight conditions (Philpot, 1992):

1 Sea Level Static (SLS) Takeoff: Usually at ISA + 15° C, to allow a flat rated take-off thrust up to some hot ambient temperature condition (Hot Day Take-off, or

Nomenclature

A = area
bl = HP turbine cooling bleed (percent core massflow)
C = airflow velocity
c_p = specific heat (at constant pressure)
m = massflow
N_1, N_2 = mechanical LP and HP spool speeds
p, T = static pressure, temperature
p_a, T_a = ambient pressure, temperature
ΔP_b = combustion pressure drop (percent CDP)
p_0, T_0 = total pressure, temperature
p_N, T_N = nozzle plane static pressure, temperature
Q = nondimensional massflow parameter
γ = specific heat ratio
δ = corrected pressure = $p_0/1.01325$, p_0 in bars
η_∞ = polytropic efficiency
η = isentropic efficiency
Θ = corrected temperature ($T_0/288.16$, T_0 in K)

Abbreviations

BPR = bypass ratio
CDP = HP compressor delivery total pressure
EPR = engine pressure ratio
EGT = LP turbine exhaust gas total temperature
FPR = fan pressure ratio
GG = gas generator (core of turbofan)
HDTO = hot day take-off (ISA + 15° C at SLS)
HPC, HPT = high-pressure compressor, turbine
IEPR = integrated engine pressure ratio
ISA = international standard atmosphere
ITT = interturbine total temperature
LPC, LPT = low-pressure compressor (boosters), turbine
OPR = overall pressure ratio
PR = pressure ratio
RPR = ram pressure ratio
SLS = sea level static
TIT = HP turbine inlet total temperature
TOC = top of climb (Mach 0.8@35,000 ft)

Subscripts and Station Numbering

a = air
c = cold (fan or bypass)
cc = combustion chamber
g = gas
h = hot (core)
i = intake
mech = mechanical
N = nozzle plane

Downloaded 02 Jun 2010 to 171.66.16.102. Redistribution subject to ASME license or copyright; see http://www.asme.org/terms/Terms_Use.cfm

HDTO). Most modern engines automatically control the take-off fuel flow to prevent the TIT from exceeding a specified safety limit. In practical terms, the Inter-turbine Temperature (ITT) is used as the limiter due to difficulties with directly measuring the high TITs common in modern turbofans. The HDTO condition is important, limiting the maximum allowable TIT and hence influencing the ultimate thermodynamic cycle choice. Note that the ITT is sometimes called the gas generator Exhaust Gas Temperature (EGT) by many engine manufacturers. In this paper, EGT will be used to denote the LP turbine exhaust temperature.

2 Cruise: A majority of the fuel burned during a typical civil airliner flight will be during cruise, especially for long range. It is essential to have an excellent Specific Fuel Consumption (SFC) while allowing high cruising speed (i.e., maximizing Ca/sfc). The choice of engine cycle conditions (FPR, BPR, OPR, and cruise TIT) is optimized around this goal. Various airliners have different optimum cruise conditions owing to differing flight characteristics, but the most common standard cruise conditions used are Mach 0.8 to 0.85 at 35,000 ft altitude. The Mach 0.8 cruise condition has been used in this study.

3 Top-of-Climb (TOC): This condition is also called Maximum Climb, and for high-bypass engines it is the point of maximum pressure ratio within the engine. For this reason, the TOC condition sets the maximum Overall Pressure Ratio, and also the fan conditions (FPR, corrected massflow Q_1, and corrected LP spool speed). This point is commonly used as the Aerodynamic Design Point of the engine.

For fixed geometry nozzles, which will most certainly be the case with modern high-bypass turbofans, the choice of design point has a marked effect on off-design performance. This is especially true when the TOC and SLS conditions are compared, since both nozzles (fan and core) will be choked at the TOC, but may be unchoked at SLS. The off-design calculation method based on twin-spool matching is highly dependent on an accurate estimate of the fixed nozzle areas, as well as accurate determinations of the design point aerodynamic characteristics of the fan, compressor, and turbines. For the purposes of this paper, the TOC condition was used as the design point, as this gave the most reasonable results for off-design performance and provided good agreement with actual engines, which are of similar type to the generic twin-spool design that was analyzed. Note, however, that careful selection of the TOC spool speeds was essential to obtaining reasonable off-design performance.

Computer Simulation Methods Used

(a) On-Design Model. The off-design performance calculation procedure used required detailed knowledge of several design point parameters of the chosen engine cycle, particularly the engine cycle parameters such as FPR, BPR, OPR, and TIT, and fixed nozzle areas. A straightforward thermodynamic cycle calculation was used based on LP and HP spool work balances, polytropic compression and expansion processes, and separate nozzles. While the precise simulation of a particular engine was not the aim of this study, reference was made to manufacturers' information on similar high-bypass designs so that reasonable on-design performance could be simulated. This, in general, required a number of iterations since many of the design parameters (such as component efficiencies) are essentially educated guesses, especially since TOC engine cycle parameters are rarely quoted.

(b) Off-Design Simulation Model. The off-design simulation procedure used in this study was the twin-spool turbofan matching procedure based on the use of component characteristics or performance maps. This straightforward procedure is outlined only briefly below; a more detailed description can be found in *Gas Turbine Theory* (Cohen et al., 1987).

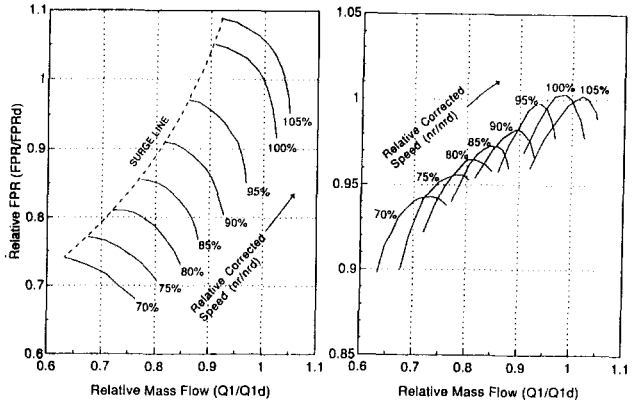

Fig. 3 Generalized fan map

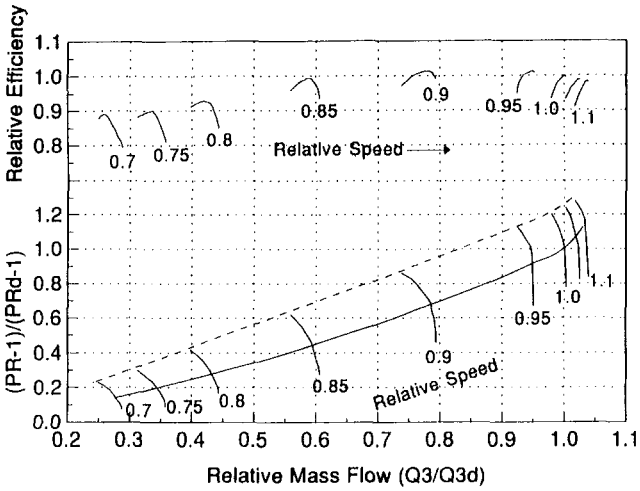

Fig. 4 Generalized HPC characteristic

The twin-spool matching method is an iterative procedure, which uses component characteristics for the fan and compressor. Fundamental to the procedure used is the assumption that the LP turbine remains choked. This is certainly the case for the flight conditions studied in this paper (it can be shown that the LP turbine only becomes unchoked near idle conditions). LP turbine choking fixes the operating point of the HP turbine due to flow compatibility between the two turbines. This assumption restricts the operation on the HP compressor to a single operating line, which greatly simplifies the matching calculations.

The fan and HP compressor were simulated using generalized characteristic curves, which were scaled by the design-point operating values for each component as defined in the on-design matching procedure. The generalized fan and HPC chics used are shown in Figs. 3 and 4. The fan chic is a nondimensionalized version of the fan map for the JT15D (Boyd, 1987). The HPC chic is the map of the LM2500 compressor, nondimensionalized based on the known design-point operation of this compressor (AN, GE Brochure, 1980). For practical computer usage of these maps, each of the nondimensional speed lines was divided into 10 points, and the three parameters for each point (relative nondimensional massflow, PR, and efficiency) were digitized into data files in tabular form; this method allows additional speed lines to be interpolated as needed.

The twin-spool matching procedure assumes separate (unmixed) nozzles of fixed area, and the iteration procedure is

Downloaded 02 Jun 2010 to 171.66.16.102. Redistribution subject to ASME license or copyright; see http://www.asme.org/terms/Terms_Use.cfm

Table 1 Design data for advanced cycle turbofan

Intake Efficiency	95%
Polytropic Efficiencies	90% (Fan, Boosters, HPC, HPT, and LPT)
Nozzle Efficiencies	99%
Spool/bearing Efficiencies	99%
Combustion Efficiency	99%
Combustion Pressure Drop	5% of CDP
HPT Cooling Bleed Flow	10% Total (5% Stators, 5% Rotors)
Cycle Conditions @ TOC Design Point	
Fan Pressure Ratio	1.7
Bypass Ratio	5.4
Overall Pressure Ratio	35.0
Turbine Inlet Temperature	1400 K
Design Air Flow	175 kg/s
Spool Mechanical Speeds	N_1 = 95%, N_2 = 96%
Nozzle Areas (m^2)	Cold = 1.023 Hot= 0.321

conducted for a specified fan speed and flight condition until the calculated core nozzle is the same as the fixed nozzle area within a specified error range, or until an impossible matching situation prevents a successful match for the flight condition specified. The bypass and core nozzles were simulated by using compressible flow relations, which can be simplified for converging nozzles, yielding analytical expressions for nozzles (Wittenberg, 1976). The use of these analytical relations avoids the need to use nozzle chics, and greatly simplifies the computerized calculation procedure.

Since advanced turbofan cycles were to be simulated in this study, it was necessary to include the effect of turbine cooling. Individual engines use unique (and increasingly complex) cooling configurations. In order to simulate overall trends, a simplified method was assumed whereby a certain percentage of HPC delivery air bypassed the combustion chamber and was introduced back at the HPT nozzle and rotor. This "bleed" air was assumed to be completely returned after the HPT. The simulation of this cooling bleed was accomplished by modifying the HP spool work balance to the form:

$$m_h C_{pa}(T_{04} - T_{03}) = m_h(1 - bl)C_{pg}(TIT - T_{06})\eta_{\text{mech}} \quad (9)$$

where bl is the percentage of HPC air used for rotor cooling.

Choice of Engine Cycle

A typical high-bypass turbofan was used as the basic engine modeled in this study. The details of this engine are shown in Table 1.

Since the cycle parameters chosen for this generic advanced cycle were very similar to the current CFM56-5 family of engines, calculated performance was compared with published engine data to verify that the computer model gave reasonable results. (AN, CFM56 Family of Engines Brochure, 1990).

The Effect of Different Engine Cycles

High BPR engines have reduced specific thrust (for the same TIT and OPR) and thus larger engines are needed for the same net thrust, as more and more of the cruising thrust is derived from the bypass nozzle. Higher FPR and TIT have more or less the opposite effect, though there is a limit to FPR due to the energy extraction limit for the LP turbine, when the amount of net thrust obtained from the bypass nozzle approaches 100 percent. The FPR is also limited to a maximum of about 1.8 (at TOC) for reasons of minimizing weight and noise. Also, high BPR designs (with take-off BPRs of around 5–6) derive about 70–75 percent of their take-off thrust from the bypass nozzle, while the percentage of TOC or cruise thrust for the same engine is slightly lower, ranging from 60–70 percent.

For the same core conditions (OPR and TIT), BPR and FPR have a marked effect on two thrust indicators, EPR and IEPR. Higher FPR (and BPR) means more energy must be extracted at the LPT, giving lower hot nozzle pressure. In extreme cases (very high BPRs and FPRs) it can be shown that EPRs of less than 1.0 can result due to the RPR effect. For current high-BPR designs (BPR of 5–6), EPR at take-off will typically be around 1.5, with FPRs from 1.55 to 1.65. TOC values of EPR are likely to be higher since OPR will tend to increase with altitude.

The impact of different cycle conditions (BPR and FPR) on IEPR is less severe than EPR due to the averaged nature of this indicator. Higher BPR results in lower IEPR, but increased FPR in general results in higher IEPR except for very high BPRs (8.0 and up). For typical modern turbofans with similar cycle parameters as given in Table 1, the IEPR at TOC will vary from about 1.6 to 1.75, and the equivalent engine will have IEPRs ranging from 1.55 to 1.65 at take-off (SLS) conditions.

The effect of cycle choice on spool speeds is more difficult to quantify, since the choice of "design" speeds in modern engines is very much a process of finding a compromise between the rotational speeds of the various aerothermal components. The method of control (either N_1 based or EPR based) will also have an effect. Thus, two very similar engines (with similar engine cycle parameters at take-off) could have quite different combinations of spool speeds at different operating points. In this paper the TOC condition was used as the overall design point of the engine, but it is noted that the mechanical speeds for the LP and HP spools are not 100 percent. The combination of spool speeds given for TOC is such that the spool speeds at the HDTO condition (used as the flat-rated take-off thrust condition) will both be approximately 100 percent. Thus 100 percent mechanical speed may be interpreted as the "design limit" rather than the "design point." The interplay between the two spool speeds will be elaborated on when off-design performance is discussed.

Nominal Off-Design Performance

The off-design performance was simulated for the turbofan design detailed in Table 1 by running the engine at a variety of flight conditions. The initial simulations were conducted over a range of flight speeds and altitudes to determine how this engine behaves during a typical take-off, climb, and cruise mission. It was necessary to use a climb profile (Mach number and true airspeed versus altitude) typical for a modern airliner. Figure 5 shows the climb profile used. The LP mechanical speed had to be specified at each flight condition to use the fan chic. For general purposes, N_1 was assumed to be 100 percent for take-off, 95 percent during climb, and then 90 percent for cruise. Using 100 percent N_1 at ISA take-off is seen to provide thrusts of over 100 percent of the flat-rated thrust.

(a) Typical Climb Performance. The variation of net thrust for this engine over a typical climb is shown in Fig. 6. The simulator appears to predict the correct trend, a gradual

Downloaded 02 Jun 2010 to 171.66.16.102. Redistribution subject to ASME license or copyright; see http://www.asme.org/terms/Terms_Use.cfm

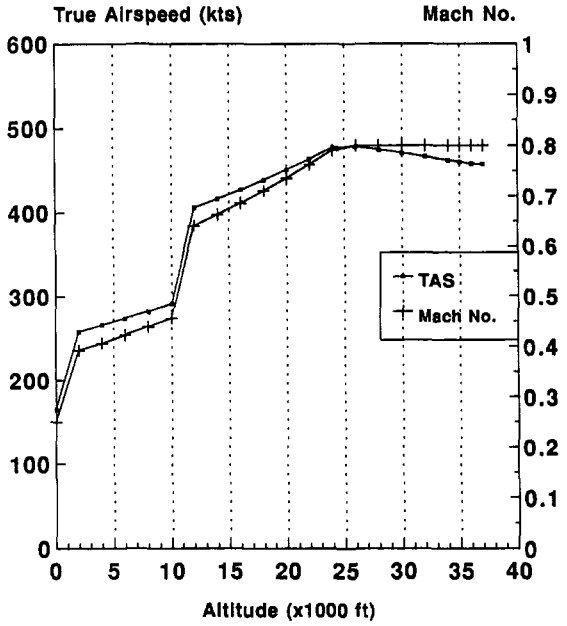

Fig. 5 Typical climb profile for modern airliner

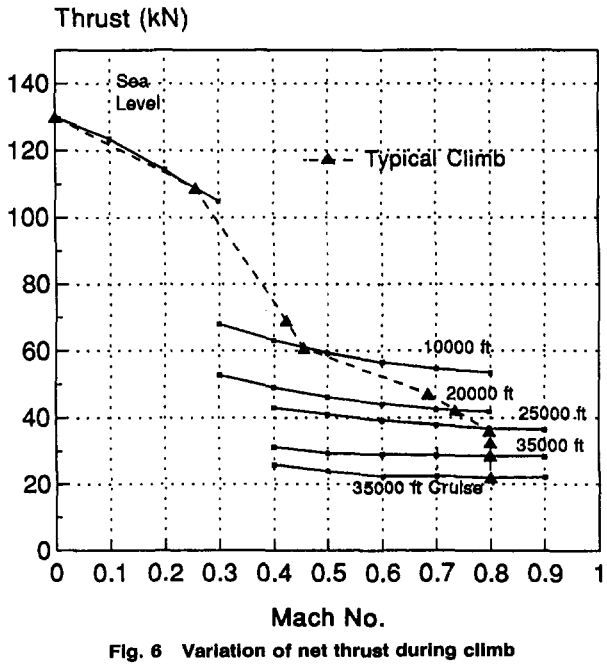

Fig. 6 Variation of net thrust during climb

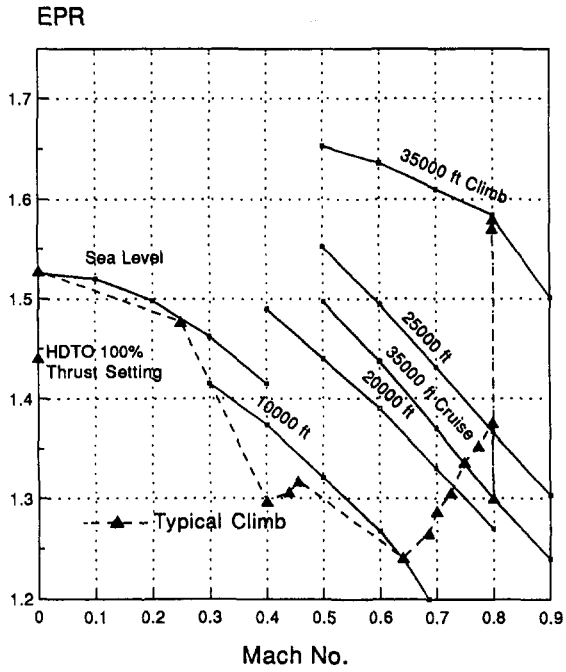

Fig. 7 Variation of EPR during climb

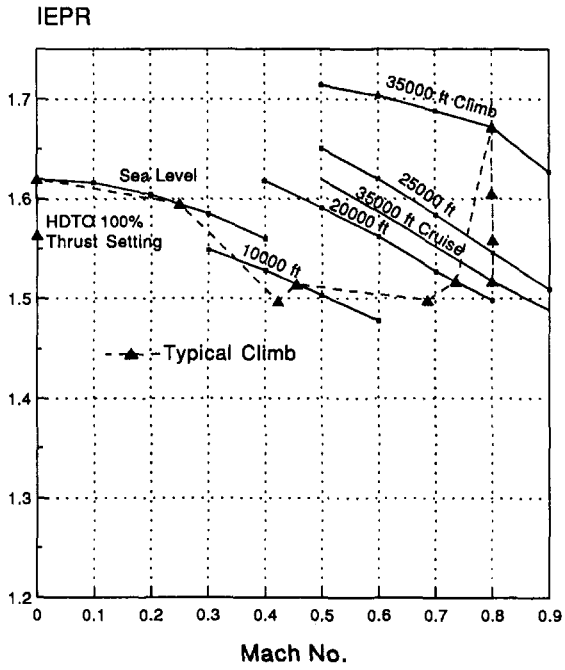

Fig. 8 IEPR variation during climb

decrease in delivered thrust with increasing Mach number and altitude. It also predicts a relatively flat thrust variation at high altitude. Note the effect of throttling back from 95 to 90 percent at 35,000 ft; this simulates the transition from TOC to cruise thrust.

Figures 7 and 8 show the variation of EPR and IEPR over the same set of flight conditions. Both show that these two thrust indicators exhibit the same trend; as forward speed increases, EPR and IEPR decrease (due to increases in the RPR). However, increasing altitude appears to have the opposite effect, and begins to dominate about 10,000 ft (where both indicators appear to be at their minimum value). From 10,000 ft to 27,000 ft, both indicators increase, but are still below the initial take-off values. Above 27,000 ft (when a constant Mach number is maintained) the increase in EPR and IEPR is more rapid, exceeding the take-off values at the TOC condition. Throttle-back to the cruise thrust level causes both to decrease sharply, to values below the take-off values. Note that the variation in IEPR is in general much slighter.

While a constant LP spool speed was used, it is interesting to note how N_2 changes during climb. Figure 9 shows the predicted variations of N_1 and N_2 during a typical climb. Following take-off (when N_1 is assumed to be 100 percent), the fan speed is reduced to 95 percent, with N_2 dropping to 97 percent at 2000 ft. With N_1 kept constant during climb N_2 drops, eventually reaching a value of 93 percent at about 25,000 ft. From this altitude to the top of climb altitude of 35,000 ft, the simulator predicts that N_2 will remain more or less constant. When N_1 is throttled back at cruise, it can be seen that N_2 drops by a similar amount, such that a cruise N_1 of 90 percent gives a HP spool speed of 88 percent.

Downloaded 02 Jun 2010 to 171.66.16.102. Redistribution subject to ASME license or copyright; see http://www.asme.org/terms/Terms_Use.cfm

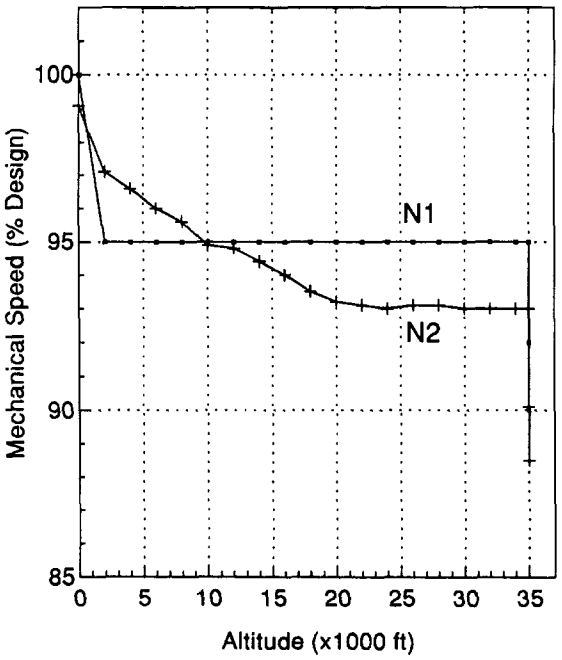

Fig. 9 Variation of spool speeds during climb

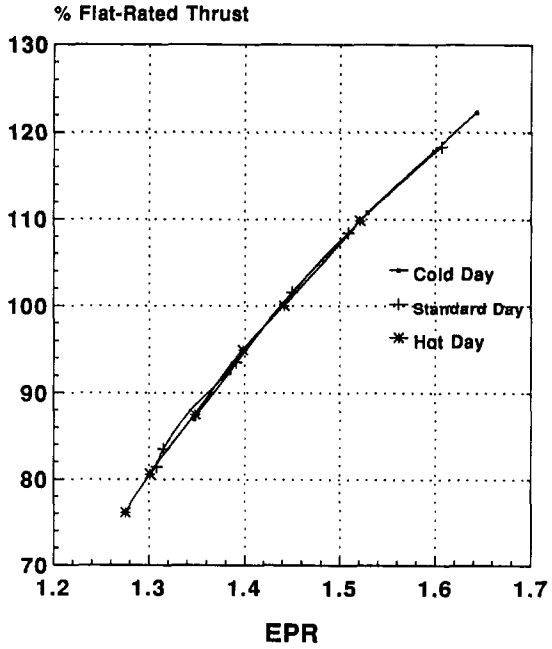

Fig. 11 Thrust versus EPR for a range of SLS conditions

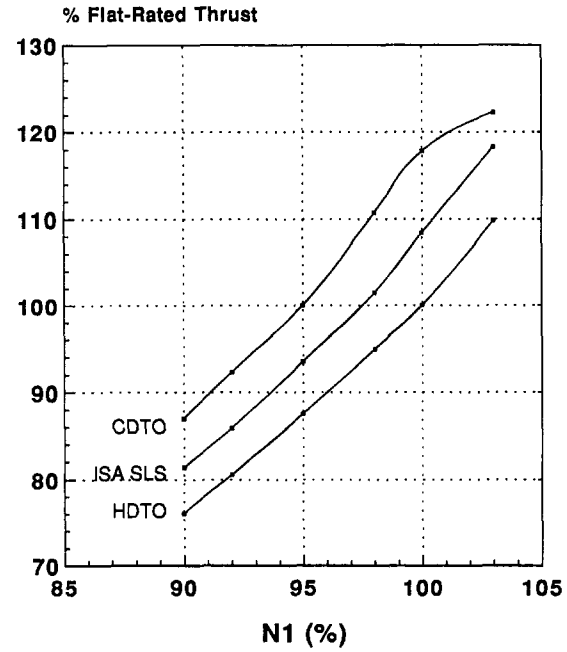

Fig. 10 Thrust versus N_1 for a range of SLS conditions

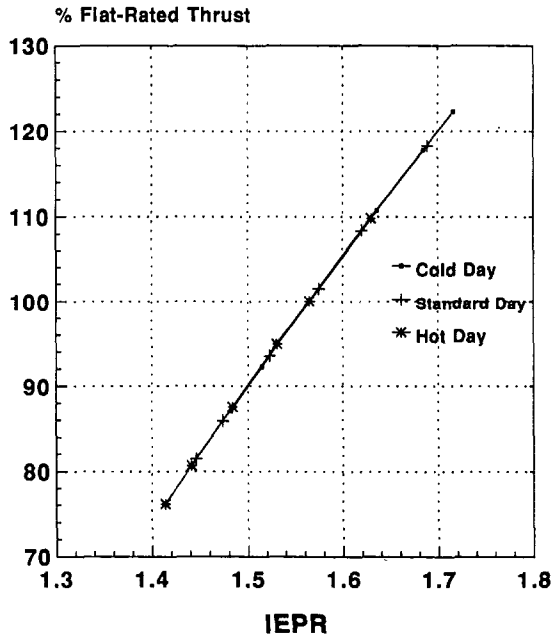

Fig. 12 Thrust versus IEPR for a range of SLS conditions

(b) Take-off Thrust and Thrust Indicators. Since performance at take-off is critical for safe operation, various SLS conditions were examined in greater detail to determine nominal trends. To simulate the concept of flat-rating, various fan mechanical speeds (N_1) were used at a given take-off condition. Three types of take-offs were used; a cold day take-off simulated by using ISA-15° C ambient conditions, a standard take-off using ISA conditions at sea level, and a hot day take-off (HDTO) simulated by using ISA + 15° C ambient conditions.

For almost all modern turbofans, the SLS thrust is held constant by a control system up to some limiting ambient temperature (ISA + 15° C is typical). This control is usually accomplished by automatic control of the fuel flow into the engine, most likely through sensing the GG exhaust temperature (ITT), which in turn controls the speed at which the engine runs. This can be simulated with the present model by adjusting N_1 to hold thrust constant for a wide range of SLS ambient temperature. Figure 10 shows how net thrust varies with fan speed for a range of SLS conditions. Note that the HDTO thrust at a fan speed N_1 = 100 percent was used as the flat-rated thrust. From this graph, the speed setting needed to obtain 100 percent thrust can be determined. On a cold day N_1 = 95 percent is required, whereas on a standard (ISA) day N_1 = 98 percent is needed to produce the flat-rated thrust. A 100 percent N_1 setting will yield thrusts over 100 percent for ambient take-off conditions of less than ISA + 15° C.

It is interesting to compare Fig. 10 with Figs. 11 and 12, which show the variation of net thrust when EPR and IEPR

Downloaded 02 Jun 2010 to 171.66.16.102. Redistribution subject to ASME license or copyright; see http://www.asme.org/terms/Terms_Use.cfm

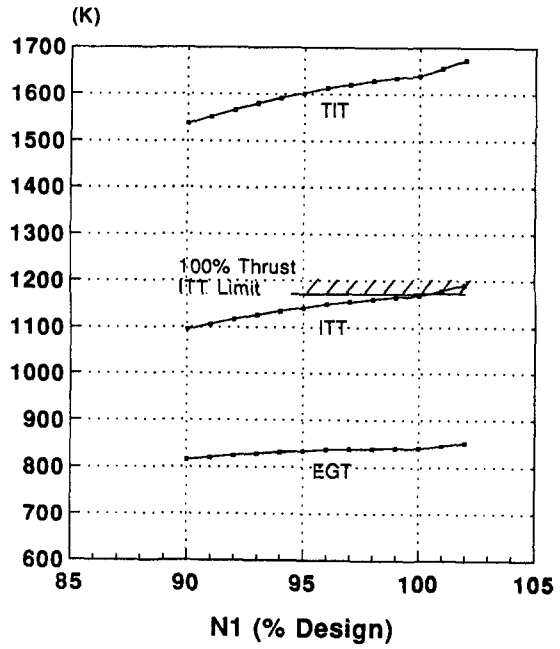

Fig. 13 Variation of cycle temperatures with N_1 for HDTO conditions

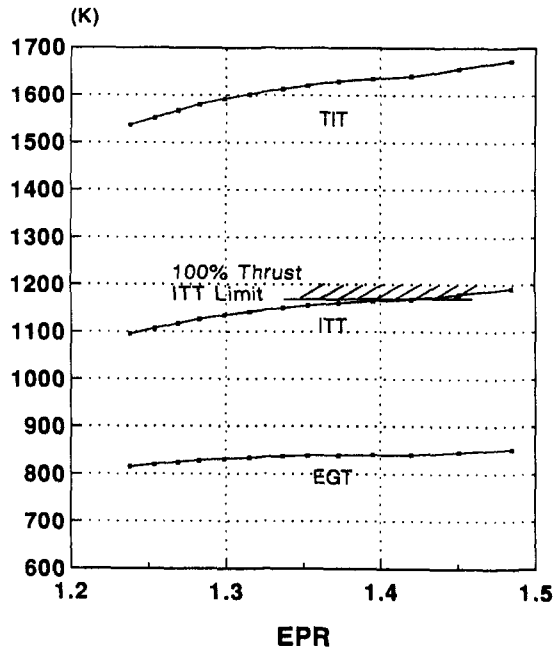

Fig. 14 Variation of cycle temperatures with EPR for HDTO conditions

are used as the thrust setting parameter. Unlike N_1, both of these parameters appear to have the unique property of giving the same thrust at a given setting, over the range of SLS conditions used. Thus, an EPR of approximately 1.44 should give 100 percent of the flat-rated thrust, while an IEPR of 1.56 will provide 100 percent flat-rated take-off thrust for the range of SLS conditions studied.

(c) Variation of Cycle Temperatures at Take-off. The most critical cycle temperature is the Turbine Inlet Temperature (TIT), which must be limited so that the thermal limit of the HP turbine rotor material is not exceeded. In practice, TIT is difficult to measure, so the gas generator exhaust gas temperature (called ITT in this paper) is usually used instead. Results from off-design simulation of the advanced cycle used in this study at various SLS conditions indicate that there is in general a good correlation in the variations of ITT and TIT. Figures 13 and 14 show the variation of the three hot end cycle temperatures (TIT, ITT, and EGT) plotted against fan mechanical speed and EPR for the HDTO case. The results for ITT will be used extensively in the next section on engine faults.

Simulation of Engine Faults

(a) Main Faults Simulated. A preliminary analysis was performed on a generic advanced cycle to determine the effects of various types of deterioration on delivered performance and thrust indication systems. Recall that a constant polytropic efficiency of 90 percent was used for the fan, HPC, HPT, and LPT during nominal on-design simulations. Given the wide variety of engine faults that could be simulated, for purposes of this study three key faults were investigated:

1 Fan foreign object damage (FOD)
2 HP compressor deterioration
3 HP turbine deterioration

Faults in these components can be approximated by changes in efficiency. Additional faults such as fouling may be simulated by changing flow rates (Aker and Saravamuttoo, 1989) and design pressure ratios could also be affected. The precise changes in component performance parameters due to typical engine faults are not known definitively as yet, so for this preliminary study the faults listed above were simulated by changing the polytropic efficiencies of the components while holding all other design-point values constant.

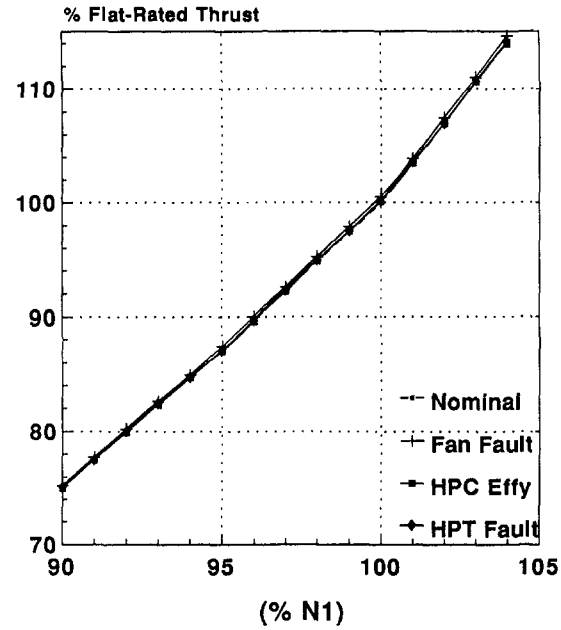

Fig. 15 Change in HDTO net thrust versus N_1 for faulted turbofan

(b) Results at Various T.O. Conditions. The most crucial operating point from both a safety and performance standpoint is take-off. The simulator was run for the three take-off conditions used earlier (cold day, standard day, and HDTO), and for the three faults noted above. For comparisons between different faults, a standard deterioration of 2 percent was used.

Initial results from the simulation were rather unusual, especially when it was noticed that fan or HPC deterioration simulations yielded increased thrust at the same take-off conditions and fan speed settings. Figure 15 shows the net thrust noted for HDTO conditions, plotted against the me-

Downloaded 02 Jun 2010 to 171.66.16.102. Redistribution subject to ASME license or copyright; see http://www.asme.org/terms/Terms_Use.cfm

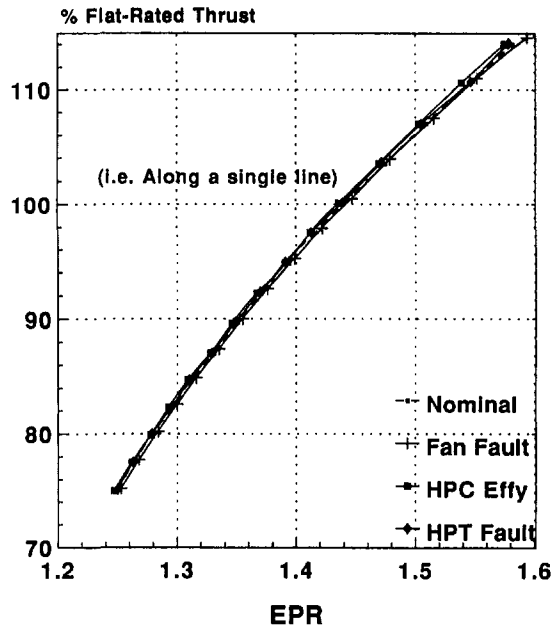

Fig. 16 Change in HDTO net thrust against EPR for faulted turbofan

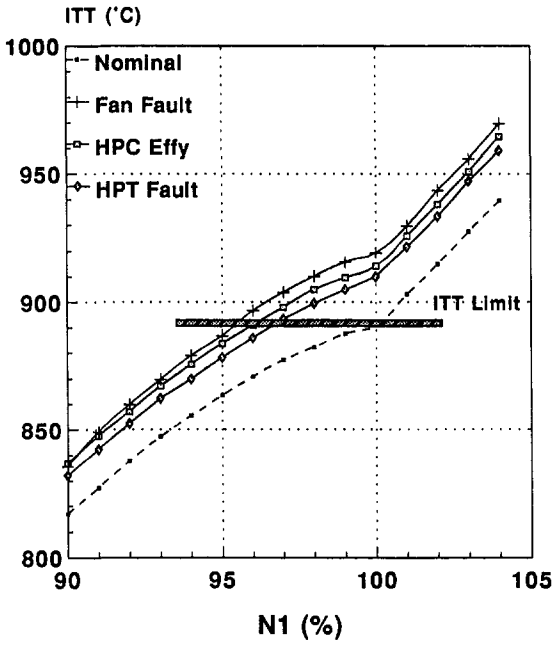

Fig. 17 ITT against N_1 for faulted turbofan at HDTO

chanical fan speed. Figure 16 shows the same information, but plotted against EPR.

The changes in performance are quite small for the deteriorations used, especially when N_1 is used as the thrust setting parameter. When EPR is used, the changes are more apparent. However, before discussing these effects, it is important to consider the role of temperature limit control in actual turbofan operation.

(c) Temperature Limit Control. At first glance, an increase in net delivered thrust with a drop in the efficiency of a particular component may appear odd. However, such results can be explained quite simply when one examines what happens with the cycle temperatures inside the engine, especially TIT. In the case of fan or HP compressor efficiency drops, the exit temperatures are going to increase; this has the net effect of increasing TIT and the hot end temperatures that follow (ITT and EGT). Increased TIT in general results in more thrust but at the penalty of increased fuel burn and decreased engine life. To show this phenomenon, the variation of the ITT for the HDTO condition has been plotted in Fig. 17 (against N_1) and Fig. 18 (against EPR).

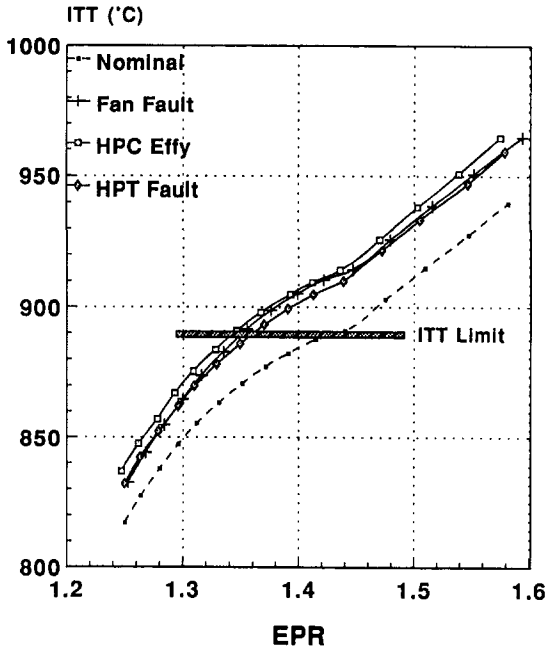

Fig. 18 ITT against EPR for faulted turbofan at HDTO

Table 2 Mean ITT increases with faults at HDTO

Fault	Increase (°C) over Nominal HDTO ITT at Constant N_1	Increase (°C) over Nominal HDTO ITT at Constant EPR
Fan $\eta\infty$ -2%	+25	+22.5
HPC $\eta\infty$ -2%	+20	+25
HPT $\eta\infty$ -2%	+15	+18.8

The increases in ITT that are predicted ignore the effect of automatic control of certain cycle temperatures. If the 100 percent thrust at HDTO is used as the limiting ITT value, then it is clear that the increased thrust performance due to increased ITT will not be realized. In fact, ITT will be controlled by adjusting fuel flow, resulting in a slower fan speed. The results for the three faults simulated are summarized in Table 2.

It is apparent that when N_1 is used to set thrust, fan deterioration has a slightly greater effect than HPC deterioration. This appears to be reversed when EPR is used, with HPC deterioration having the higher ITT rise for a constant EPR setting. When the ITT is limited to the HDTO 100 percent thrust rating, the effects of maximum available take-off thrusts are as follows:

HP Compressor Deterioration. HPC faults have a major effect on both TIT and ITT. With ITT limiting, the fan speed would be restricted to a maximum of 96 percent, which would deliver about 90 percent of take-off thrust. If EPR is used as the thrust setting parameter, the corresponding maximum EPR setting would be 1.345, which would provide 89 percent thrust. This difference is caused by EPR itself being affected by drops in component efficiencies.

HP Turbine Deterioration. HP turbine deterioration has a

Downloaded 02 Jun 2010 to 171.66.16.102. Redistribution subject to ASME license or copyright; see http://www.asme.org/terms/Terms_Use.cfm

minor effect on thrust. However, there is an effect on hot end cycle temperatures. If the ITT limit is applied N_1 will be restricted to a maximum of 96.7 percent, delivering a maximum of 91.5 percent of the flat-rated thrust. If EPR is used, a maximum EPR = 1.36 will apply, providing 92.5 percent take-off thrust.

Fan Deterioration. Fan deterioration causes an increase in ITT of approximately 25° C against a constant N_1 setting. For the same EPR setting, ITT increases 22.5° C. With ITT limiting applied, a maximum N_1 setting of 96 percent will deliver 89.8 percent take-off thrust. For EPR, a maximum setting of 1.352 would apply, providing a take-off thrust level of 90.3 percent.

It is important to note that while N_1 appears to be independent of any efficiency drops in the engine components, EPR is directly affected by them since changes in component efficiencies will cause changes in the LPT exhaust pressure. This is the main reason for the differences in net thrust when ITT limiting is applied. Similar results were noted when the thrust and ITT variance with IEPR was examined.

(d) Effect of Faults on Cruise Fuel Flow. Of secondary importance is the effect that faults have on the accuracy of setting cruise thrust using one of the indirect thrust setting parameters. The matter of sufficient cruise thrust is not necessarily one of safety, but economics. Simulation of various cruise flight conditions with faults indicates that the effect on overall delivered thrust is very minor when set against constant N_1, EPR or IEPR, with a maximum error of about 2 percent. If fuel flow is used to set thrust, the effect appears to be more pronounced, with all faults resulting in lowered thrust for the same FF. ITT limiting is not expected to be a concern at cruise.

FF is rarely used as a primary thrust setting parameter but is monitored to give an indication of engine health and cruise economy. If seen from the point of view of maintaining the same thrust (based on another indicator) more fuel will be required depending on the severity of fault. This is summarized in Table 3.

Table 3 Effect of faults on cruise fuel flow

Fault Type	Changes in Cruise FF at Constant Thrust	
	(kg/hr)	% Increase
Fan $\eta\infty$ -2%	+40	+3.2
HPC $\eta\infty$ -2%	+35	+2.8
HPT $\eta\infty$ -2%	+20	+1.6

Table 4 Maximum HDTO thrust with ITT limits

Fault Type	Maximum Thrusts Permitted (% Flat-rated Thrust)			
	Max N_1 (%)	Max Thrust	Max EPR	Max Thrust
No Fault	100	100	1.44	100
Fan $\eta\infty$ -2%	96	89.8	1.352	90.3
HPC $\eta\infty$ -2%	96	89.8	1.345	89
HPT $\eta\infty$ -2%	96.7	91.5	1.36	92.5

Conclusions

Recognizing that advanced cycle turbofans obtain most of their take-off thrust (typically over 70 percent) from the bypass nozzle, a comparative study was carried out to investigate the use of different thrust setting parameters.

A preliminary assessment of likely engine faults showed that the HP compressor and fan were the most important components regarding hot section temperature increases. Assuming a control limit on ITT, the choice of thrust setting parameter influences the thrust available from a deteriorated engine. Predictions of the maximum HDTO thrust obtained when using either N_1 or EPR are summarized in Table 4.

Meanwhile, faults appear to have little effect on the accuracy of IEPR when used to set take-off thrust. This seems to indicate that it is (theoretically) the best indicator. However, it is difficult to implement, requiring extensive pressure measurements in the fan bypass duct.

Fuel flow is not used as a primary thrust-setting parameter at take-off, but is of primary concern during cruise. The three component faults simulated appear to result in increased fuel flow to maintain the same cruise thrust level, with fan deterioration having the greatest impact.

It appears that there is no major difference between the three most popular thrust indicators. It is suggested, however, that N_1 gives a better intuitive appreciation of thrust level. Although EPR only indicates thrust due to the hot nozzle, it appears to give a good indication of overall thrust. The choice of parameter will be strongly influenced by the previous experience of the engine manufacturer.

Acknowledgments

The authors would like to express their thanks to the Natural Sciences and Engineering Research Council for financial support, which made this study possible. Mr. Stevenson was the recipient of an NSERC Scholarship, while Prof. Saravanamuttoo was supported by an NSERC Operating Grant.

References

AN, Snecma Sales Brochure, 1990, "CFM56 Family of Engines."

Aker, G. F., and Saravanamuttoo, H. I. H., 1989, "Predicting Gas Turbine Performance Degradation Due to Compressor Fouling Using Computer Simulation Techniques," ASME JOURNAL OF ENGINEERING FOR GAS TURBINES AND POWER, Vol. 111, pp. 343–350.

Borger, J. G., 1981, "The Well Tempered Transport Aircraft Engine," *Aeronautical Journal*, Nov.

Boyd, D. I., 1987, "Development of a New Technology Small Fan Jet Engine," *Canadian Aeronautics and Space Journal*, Vol. 33, No. 2, June.

Cohen, H., Rogers, G. F. C., and Saravanamuttoo, H. I. H., 1987, *Gas Turbine Theory*, 3rd ed., Longman Scientific and Technical.

GE Product Brochure, 1980, "General Electric LM2500 Industrial Gas Turbine System," GEA-10523C, 4/80 (5M).

Mirza-Baig, F. S., and Saravanamuttoo, H. I. H., 1991, "Off-Design Performance of Turbofans Using Gasdynamics," ASME Paper No. 91-GT-389.

Peacock, N. J., and Sadler, J. H. R., 1989, "Advanced Propulsion Systems for Large Subsonic Transport," AIAA Paper No. 89-2477.

Philpot, M. G., 1992, "Practical Considerations in Designing the Engine Cycle," AGARD Lecture Series LS-183, Paper 2.

Saravanamuttoo, H. I. H., 1972, "A Rapid Matching Procedure for Twin-Spool Turbofans," *Canadian Aeronautics and Space Journal*, Oct.

Saravanamuttoo, H. I. H., and MacIsaac, B. D., 1983, "Thermodynamic Models for Pipeline Gas Turbine Diagnostics," ASME JOURNAL OF ENGINEERING FOR GAS TURBINES AND POWER, Vol. 105, pp. 875–84.

Shevell, R. S., 1989, *Fundamentals of Flight*, 2nd ed., Prentice-Hall, Inc.

Wittenberg, H., 1976, "Prediction of Off-Design Performances of Turbojet and Turbofan Engines," *Proceedings on Performance Prediction Methods*, AGARD CP-242-76.

Downloaded 02 Jun 2010 to 171.66.16.102. Redistribution subject to ASME license or copyright; see http://www.asme.org/terms/Terms_Use.cfm

Applying Combined Pinch and Exergy Analysis to Closed-Cycle Gas Turbine System Design

V. R. Dhole[1]

J. P. Zheng

Centre for Process Integration,
University of Manchester
Institute of Science and Technology,
Manchester, United Kingdom

Pinch technology has developed into a powerful tool for thermodynamic analysis of chemical processes and associated utilities, resulting in significant energy savings. Conventional pinch analysis identifies the most economical energy consumption in terms of heat loads and provides practical design guidelines to achieve this. However, in analyzing systems involving heat and power, for example, steam and gas turbines, etc., pure heat load analysis is insufficient. Exergy analysis, on the other hand, provides a tool for heat and power analysis, although at times it does not provide clear practical design guidelines. An appropriate combination of pinch and exergy analysis can provide practical methodology for the analysis of heat and power systems. The methodology has been successfully applied to refrigeration systems. This paper introduces the application of a combined pinch and exergy approach to commercial power plants with a demonstration example of a closed-cycle gas turbine (CCGT) system. Efficiency improvement of about 0.82 percent (50.2 to 51.02 percent) can be obtained by application of the new approach. More importantly, the approach can be used as an analysis and screening tool for the various design improvements and is generally applicable to any commercial power generation facility.

Introduction

Pinch technology involves a combination of thermodynamic analysis tools and simple and practical design rules. The overall approach consists of two main stages, targeting and design. Targeting involves use of analysis and screening tools, and identifies the most promising options and quantifies their benefits ahead of design. In the design stage, these options are further developed as detailed designs. In this paper, we will maintain the pinch technology tradition of targeting followed by design. We will develop the tools for targeting based on the combination of pinch and exergy analysis. The promising options identified during targeting can then be developed into detailed designs/simulations. We will demonstrate the approach in a stepwise manner on a CCGT system.

Combined Pinch and Exergy Analysis

Basic pinch analysis employs "composite curves" (CC) and "grand composite curves" (GCC) to set targets for design improvements (Linnhoff et al., 1982). The CC set targets for energy recovery and heat exchange capital cost. The GCC are used for selecting appropriate external utilities and setting targets for their heat loads and temperatures. Both CC and GCC employ a temperature–enthalpy scale. Starting from a base case system design, the engineer constructs the curves (CC and GCC) based on the heating and cooling information of the system and sets energy and capital cost targets for the various design modifications.

The energy targets set by the CC and the GCC are mainly in terms of *heat loads*. Many systems, however, involve heat as well as power, for example power plants, refrigeration systems, etc. For such systems we employ exergy composite curves (ECC) (Umeda et al., 1979; Linnhoff and Dhole, 1992) and the exergy grand composite curve (EGCC) (Linnhoff and Dhole, 1992) to set targets in terms of *heat and power*. The ECC and the EGCC are obtained by replacing the vertical temperature axis of the CC and the GCC with the Carnot factor. Exergy is defined as the "ideal shaftwork equivalent" of a system or stream. An important feature of the ECC and EGCC is that the areas on these curves gain direct proportionality to shaftwork or power (Dhole, 1991; Linnhoff and Dhole, 1992). Based on this feature, for heat and power systems, the changes in the shaftwork can be directly targeted for any modifications in the system. The ECC and EGCC still retain all the energy and capital targeting capabilities of CC and GCC; in addition, they can set *shaftwork targets*. In this paper, the ECC and EGCC are termed the combined pinch and exergy representations (CPER).

We now illustrate the applications of the shaftwork targeting concept with an example of a low temperature system. Figure 1(*b*) shows an EGCC of a low-temperature process serviced by a refrigeration system (Dhole, 1991; Dhole and

[1]Current address: Linnhoff March Ltd., Knutsford, Cheshire, United Kingdom.

Contributed by the International Gas Turbine Institute and presented at the International Cogen-Turbo Power Congress and Exhibition, Bournemouth, United Kingdom, September 21–23, 1993. Manuscript received at ASME Headquarters June 1993. Associate Technical Editor: H. Lukas.

Copyright © 1995 by ASME

Downloaded 02 Jun 2010 to 171.66.16.102. Redistribution subject to ASME license or copyright; see http://www.asme.org/terms/Terms_Use.cfm

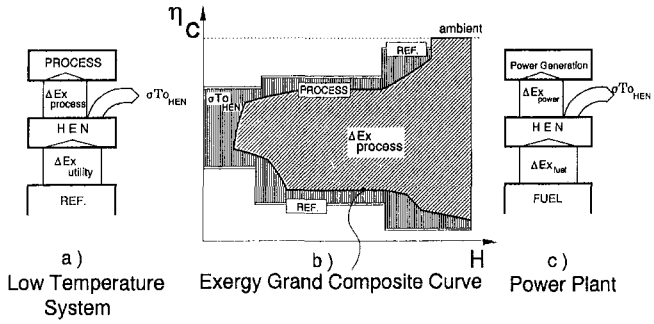

Fig. 1 Combined pinch and exergy representation using exergy grand composite curve and the analogy between a low-temperature process and a power plant

Linnhoff, 1993). The refrigeration system provides the net exergy (or shaftwork) requirement of the overall system (termed ΔEx_{ref}, proportional to the sum of the vertical and diagonally shaded areas). Part of this exergy is lost in the heat exchanger network (HEN) (termed σT_{oHEN}, proportional to the vertically shaded areas), while the remainder is supplied to the process (termed as $\Delta Ex_{\text{process}}$, proportional to the diagonally shaded area). The changes in the exergy areas are directly proportional to the changes in actual refrigeration shaftwork (Dhole, 1991; Linnhoff and Dhole, 1992). Therefore for any change in the process, the HEN, or the refrigeration system, we can evaluate the ΔEx_{ref} area. From this evaluation, we can directly predict or *target* for the changes in the refrigeration shaftwork ahead of design, thus setting *shaftwork targets*.

We will now consider the application of the shaftwork targeting concept to power plants (Fig. 1*c*). The application is analogous to the low-temperature system example (Figs. 1*a* and 1*b*). The fuel provides for the net exergy requirement of the power plant (ΔEx_{fuel}, analogous to ΔEx_{ref}—the vertical and the diagonally shaded area in Fig. 1*b*). A part of this exergy is lost in heat exchange (σT_{oHEN}—the vertical shaded area in Fig. 1*b*) while the remaining exergy is supplied for power generation (ΔEx_{power}, analogous to $\Delta Ex_{\text{process}}$—the diagonally shaded area in Fig. 1*b*). Again, the exergy areas are proportional to "actual" shaftwork or power generation (Dhole and Linnhoff, 1992).

If we *fix* the fuel input to the power plant (constant ΔEx_{fuel}), then any *reduction* in σT_{oHEN} will result in an equal *increase* in ΔEx_{power}. This means a proportional *increase* in the power generation and in the cycle efficiency. These changes can be identified from the exergy areas of the CPER. The CPER can be based on an ECC or an EGCC representation of the power plant. Thus, for a fixed fuel input into the power plant, a reduction in the σT_{oHEN} area of the CPER, due to any modification in the system, will provide a direct evaluation of the increase in the power generation and in the system efficiency, *ahead of detail design or simulation*. In essence, we are able to set *targets for improvements* in power generation and in cycle efficiency.

Table 1 Base case design information

Stream \ Data	Temperature (°C)	Pressure(kPa)
1	565.6	3431.0
2	27.0	3.5
3	28.5	20960.1
4	350.6	19856.9
5	358.5	18478.0
6	567.9	17099.0
7	336.7	3637.9
8	26.7	1382.4
9	338.8	6912.0
10	843.3	6687.9
11	530.5	2711.4
12	843.3	2624.1
13	618.5	1412.7
Mass Flow Rate (kg / hr)	Gas Cycle	Steam Cycle
	472566.0	531164.375

Before we discuss the application of this new approach to our CCGT system example, let us first understand the design of the base case CCGT system.

Base Case CCGT System Design

Figure 2 shows a schematic of a coal-fired CCGT system design (Kinney and Wright, 1978). The system employs Helium (He) as a working fluid for the CCGT and uses a pulverized coal-fired furnace. An important feature of the design is that none of the products of the direct coal combustion pass through the gas turbine. The calculated combined cycle thermodynamic efficiency is 50.2 percent (net power generated to heat from fuel), which is significantly higher than conventional steam cycle efficiency of 44–45 percent. The power generation involves two cycles: the CCGT cycle (using He) and a steam turbine cycle (with a single reheat). Heat transfer is mainly carried out in the furnace and the He exchanger. The furnace is used for He heating, steam generation, and steam reheating. The He exchanger transfer heat from He exhaust of the CCGT to steam generation and superheating. Table 1 provides the temperature, pressure, and mass flow information for the base case design. The system is designed for maximum He temperature of 843°C, steam generation at 17,100 kPa with superheating up to 568°C and reheating up to 566°C.

Nomenclature

CC = composite curves
CPER = combined pinch and exergy representation
CCGT = closed-cycle gas turbine
ECC = exergy composite curves
EGCC = exergy grand composite curve
FGC = flue gas composite
GCC = grand composite curve
He = helium
HEN = heat exchanger network
Ref. = refrigeration system
T_o = ambient temperature
T_f = flame temperature
T_{air} = air preheat temperature
T_{dew} = acid dew point temperature of flue gas
ΔT = temperature difference
ΔEx_{fuel} = exergy supplied by the fuel
ΔEx_{power} = exergy of power generation
$\Delta Ex_{\text{process}}$ = exergy supplied to the process
ΔEx_{ref} = exergy supplied by the refrigeration system
η_c = Carnot factor = $1 - T_o/T$
σT_{oHEN} = exergy loss in the HEN

Downloaded 02 Jun 2010 to 171.66.16.102. Redistribution subject to ASME license or copyright; see http://www.asme.org/terms/Terms_Use.cfm

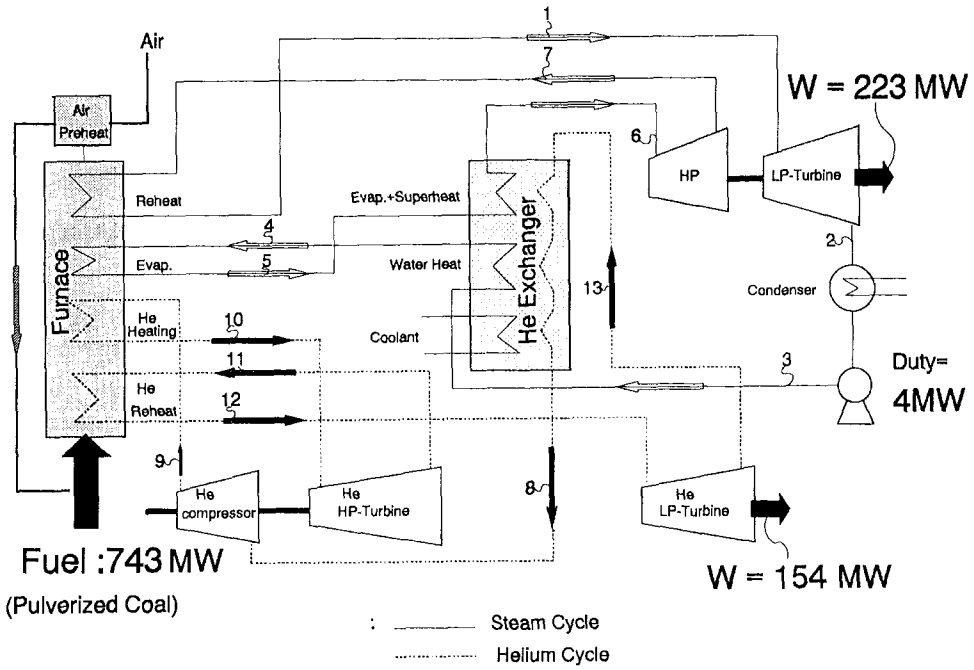

Fig. 2 Base case CCGT system configuration

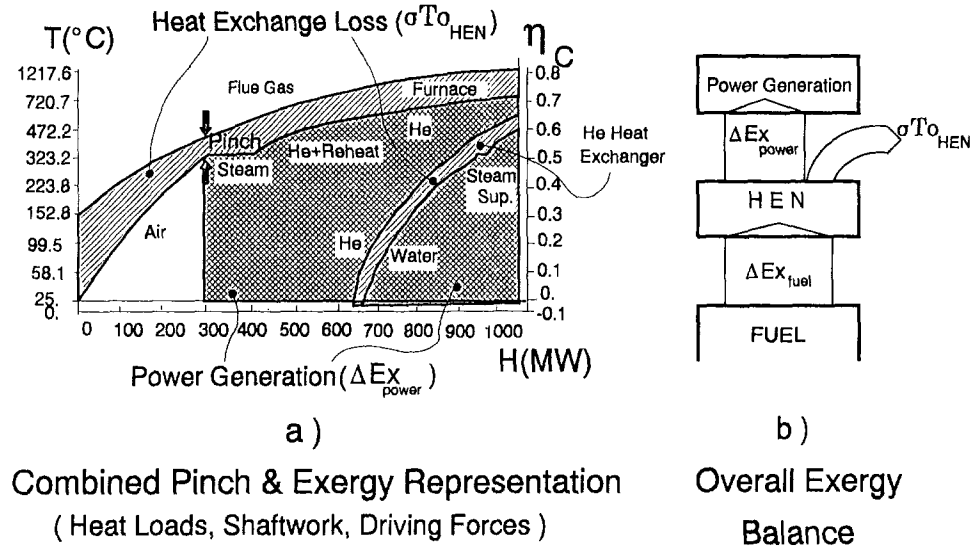

Fig. 3 Combined pinch and exergy representation (CPER) of the base case system

The authors are aware that the above-mentioned CCGT system is still in its research phase. However, the purpose of the article is to demonstrate the application of the principles of combined pinch and exergy analysis rather than to improve the competitive advantage of the CCGT system over other cycles. The authors believe that the approach that emerges out of this application can be generally used for design improvements in any power generation facility.

Applying Combined Pinch and Exergy Analysis to CCGT System

Base Case Combined Pinch and Exergy Representation. Figure 3(*a*) shows a combined pinch and exergy representation (CPER) of the base case CCGT system based on the ECCs of the furnace and the He exchanger. The ECCs have been shown separately but on the same diagram to retain a design integrity between the furnace and the He exchanger. The σT_{oHEN} and ΔEx_{power} areas are indicated in the CPER. The CPER also shows the available temperature driving forces in the furnace and the He exchanger. The CPER therefore simultaneously depicts distribution of heat loads, shaftwork, and driving forces in the system.

Figure 3(*b*) shows the exergy balance for the CCGT system (same as Fig. 1*c*). As discussed earlier, in order to improve the system efficiency, we need to identify modifications that will reduce the σT_{oHEN} area and therefore increase the power generation for a given fuel input. In order to identify these modifications, in addition to CPER, we will use another pinch technology tool called the "flue gas composite" as reviewed in the next section.

The Concept of Flue Gas Composite. The flue gas composite (FGC) (Hall, 1989; Hall et al., 1992) is useful in identifying opportunities for design improvements in the interface between the furnace and the remaining system. The fuel consumption of a cycle and the associated furnace de-

Downloaded 02 Jun 2010 to 171.66.16.102. Redistribution subject to ASME license or copyright; see http://www.asme.org/terms/Terms_Use.cfm

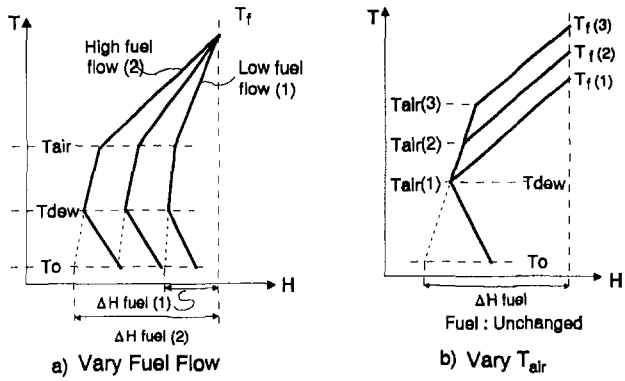

Fig. 4 Flue gas composite (FGC) representation

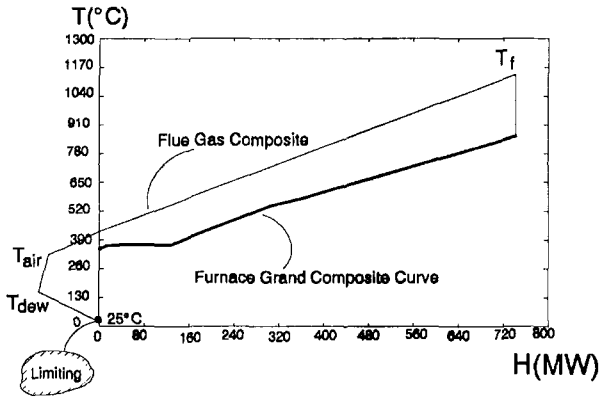

Fig. 5 Placement of FGC for the base case design

sign hinges on flue gas characteristics such as flow rates, temperatures, and the degree of air preheat. The FGC provides a concise representation of all these parameters enabling the designer to understand the interactions between them clearly. Figure 4 illustrates the construction and use of the FGC. The FGC is constructed as a composite profile of flue gas and air preheating duties and provides net heat available from furnace fuel as a function of temperature. The FGC therefore starts from the flame temperature (T_f) and shows "kinks" at the air preheat temperature (T_{air}) and the acid dew point temperature (T_{dew}) and ends at ambient air temperature (T_o) as shown in Fig. 4. Above T_{dew}, the FGC is a net heat source while below T_{dew} it is a net heat sink.

Changes in the fuel consumption affect the shape of the FGC as shown in Fig. 4(a). As we decrease the fuel consumption, the FGC envelope shrinks and shifts to the right as shown. The intercept on the enthalpy axis is directly proportional to the fuel consumption as shown in the figure. The lowermost end of the FGC (at T_o) also moves to the right as we decrease the fuel consumption.

Figure 4(b) shows the effect of variation in air preheat temperature (T_{air}) on the FGC. As we increase T_{air}, the top section of the FGC shifts upward proportionately, thus increasing T_f. The fuel consumption will remain unchanged.

Identifying Cycle Modification. In this section, we will use the concept of FGC and the CPER to suggest modifications in the base case design. Figure 5 shows the FGC placed against the GCC of the furnace (constructed from all the heating and cooling duties in the furnace section) for the base case CCGT system. In order to reduce the fuel consumption, we need to shift the FGC to the right (refer to Fig. 4a). However, the lowermost point of the FGC provides a constraint. Since the FGC is a net heat sink below T_{dew}, we need an additional heat source in order to satisfy this heat sink, thereby allowing the FGC to move to the right.

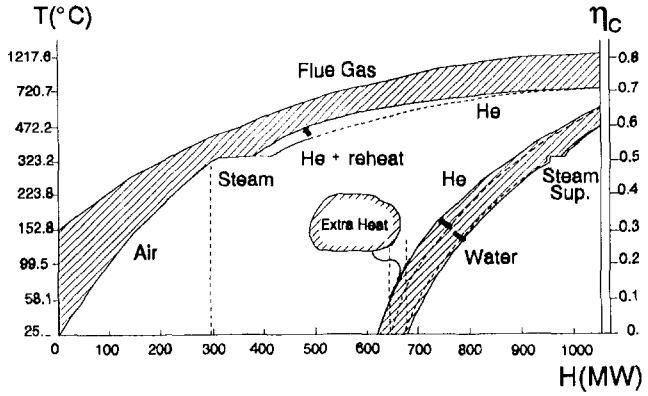

Fig. 6 System modification to generate an additional "heat source"

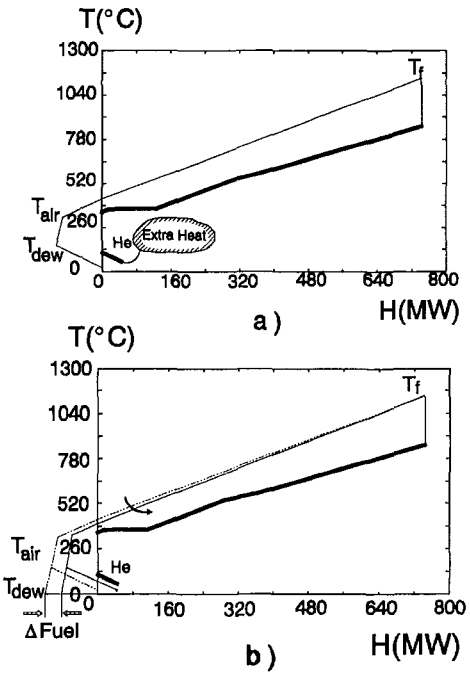

Fig. 7 Using the additional heat source for fuel saving

Figure 6 shows one of the possibilities for generating an additional "heat source" in the system. It involves increasing the He flow rate and proportionately reducing the steam flow rate in order to maintain the base case fuel consumption. Dotted lines show the system prior to modification, while solid lines show the system after modification. The increased He flow rate will result in "extra heat" available between 107°C and 57°C as shown in the figure. The figure also shows that the heat exchange losses will decrease in the furnace and increase in the He exchanger.

Figure 7(a) shows the GCC of the furnace after including the "extra heat" from He (as shown in Fig. 6) in its construction. The "extra heat" manifests itself as an additional heat source in the furnace GCC. This creates an opportunity to reduce the fuel consumption as shown in Fig. 7(b). The FGC envelope can move to the right with the extra heat from He partly satisfying the heat sink section of the FGC. This implies using He for air preheating!

To summarize, the modification involves a new exchanger between He and furnace air. The remaining air preheat duty will be against flue gas.

Downloaded 02 Jun 2010 to 171.66.16.102. Redistribution subject to ASME license or copyright; see http://www.asme.org/terms/Terms_Use.cfm

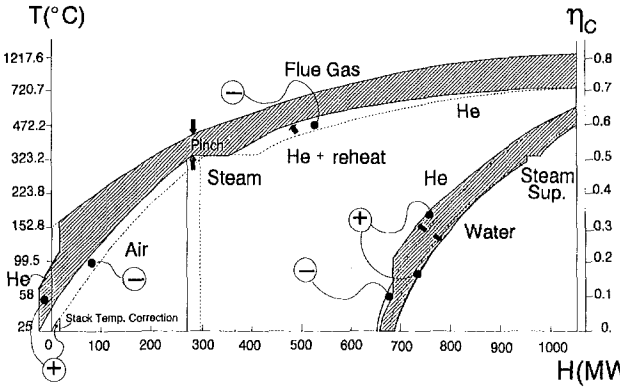

Fig. 8 Using the CPER to analyze and set targets for improvement in the overall system

Analyzing and Setting Targets for the Modification Using CPER. The effect of the modification on the overall system is shown in Fig. 8 with a CPER. We will now analyze the modification and set targets for the corresponding efficiency improvement using the CPER. The overall scale of the CCGT system has been adjusted to maintain the base case fuel consumption (as discussed in the earlier section). Any reduction in the σT_{oHEN} area will therefore result in an equal increase in the ΔEx_{power} area provided the net exergy of streams entering and leaving the system remains unchanged (exergy balance). Since the flue gas stack temperature has slightly increased compared to the base case, we need to take the corresponding exergy change into account. This correction is shown in Fig. 8 (in terms of equivalent σT_{OHEN} area). The negative changes in the σT_{oHEN} area imply an increase in the power generation and vice versa for the positive σT_{oHEN} changes. Thus, the *net* reduction in the σT_{oHEN} area equals the overall increase in ΔEx_{power}. The power generation and the cycle efficiency will also increase proportionately.

Based on the reduction in the σT_{oHEN} area from the CPER in Fig. 8, the increase in the power generation is predicted to be 6.4 MW with a corresponding efficiency improvement of 0.86 percent (i.e., from 50.2 to 51.06 percent). These are *targets* based on the CPER. They bypass the effort of detailed simulation of the furnace, the heat exchangers, and the turbine system.

The detailed simulation of the system shows an increase in the power generation by 6.1 MW with an efficiency improvement of 0.82 percent.

Table 2 compares the targets based on the CPER with the detailed simulation results. The resulting error is 4.7 percent, which indicates a good accuracy for all practical purposes. The targets provide a quick assessment of the impact of the modification.

The CPER in Fig. 8 also indicates the effect of the modification on the temperature driving forces and therefore on heat exchanger capital cost in the system. ΔT at the "pinch" in the convection section of the furnace decreases from 88°C to 54°C. This may adversely affect the capital cost and the overall economics of the modification. In the following section, we will discuss the possibilities for restoring the driving forces at the convection section pinch to the base case conditions.

Re-adjusting Driving Forces. Figure 9 provides two possibilities to restore the driving forces to the base case conditions (i.e., 88°C). The first alternative involves increasing T_{air} by 34°C (Fig. 9*a*). This will increase the T_f by 31°C while the fuel consumption will remain unchanged (also see Fig. 4*b*).

Figure 9(*b*) shows an alternate scheme to restore the temperature driving force at the pinch. We can "swap" part

Table 2 Comparing the targets based on the CPER with the detailed simulation results

	Targets based on CPER	Detailed Simulation	% Error
Increase in power generation	6.4MW	6.1MW	4.7%
Δ Efficiency	0.86%	0.82%	

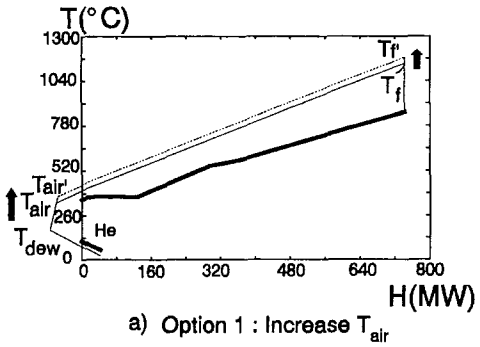

a) Option 1 : Increase T_{air}

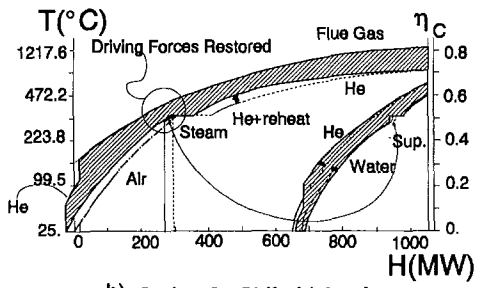

b) Option 2 : Shift driving forces

Fig. 9 Restoring temperature driving forces in the furnace

of the water heating duty (23 MW) from the He exchanger with the evaporation duty in the furnace, as shown in the figure. This will restore the driving forces at the pinch in the furnace while the driving forces in the He exchanger will decrease. In the base case design, the He exchanger constitutes only 1.3 percent of the total capital cost while the furnace constitutes 21 percent (Kinney and Wright, 1978). Therefore, although the capital cost of the He exchanger will increase, the *overall* capital cost will stay close to the base case conditions. In addition, the increase in the He flow initially increased the driving forces in the He exchanger (see Fig. 6). Thus, we *preferentially shift* the driving forces from the He exchanger to the furnace.

Capital–Energy Trade-off. The design modification discussed in the paper results in an efficiency improvement of 0.82 percent by increasing the He flow by 10 percent. An efficiency improvement of 1.2 percent is possible by increasing the He flow by 20 percent; however, the corresponding re-adjustment in the driving forces (as shown in Fig. 9*a*) involves an increase in T_{air} by 60°C. In general, such an efficiency improvement needs to be *optimized* with respect to capital and energy costs with due consideration for materials of construction constraints, etc.

Using the CPER (as in Fig. 8), it is possible to set targets for the capital cost of the heat exchange elements and indeed carry out a capital–energy optimization in a *targeting mode* ahead of detailed simulation (Linnhoff and Ahmed, 1989). However, due to the difficulties involved in obtaining the

Downloaded 02 Jun 2010 to 171.66.16.102. Redistribution subject to ASME license or copyright; see http://www.asme.org/terms/Terms_Use.cfm

appropriate capital cost correlations, in this paper, these targets have not been evaluated.

Overall Approach

The combined pinch and exergy approach for design improvements in power plants can be summarized in four steps as follows:

1 Obtain CPER for the base case system.
2 Identify modification options using CPER, available pinch technology tools (such as FGC), or ideas from other sources.
3 Analyze and set targets for efficiency improvement and capital cost changes using CPER on a fixed fuel basis. If new options are identified return to step 2.
4 Develop detailed designs for options that show promise in step 3.

The most important feature of the approach is the ability to analyze the system quickly and set targets ahead of detailed design. Targeting speeds up the process of overall design improvement. In addition, the analysis (based on CPER) generates ideas for alternative options for design improvement.

Conclusion and Significance

The paper provides a methodology for systematic improvement in the design of power plants based on a combined pinch and exergy approach. The CPER provides a simultaneous "picture" of heat load distribution, shaftwork, and temperature driving forces in the system, resulting in a powerful analysis tool. The analysis provides targets for design improvements and suggestions for alternative modifications in the system. In the current paper, we demonstrated the application of the new approach on a CCGT system. The approach can be applied for design improvements in other power generation cycles.

References

Kinney, C., and Wright, D. E., 1978, "Advanced Coal-Fueled Combustor/Heat Exchanger Technology Study," Division of Power Systems, Department of Energy USA, Contract No. EF-77-C-01-2612.

Dhole, V. R., 1991, "Distillation Column Integration and Overall Design of Subambient Plants," PhD thesis, UMIST, Manchester, United Kingdom.

Dhole, V. R., and Linnhoff, B., 1992, "Total Site Targets for Fuel, Co-generation, Emissions and Cooling," presented at ESCAPE II conference, Toulouse, France; also *Computers and Chemical Engineering*, 1993, Vol. 17, Suppl., pp. s101–s109.

Dhole, V. R., and Linnhoff, B., 1993, "Overall Design of Low Temperature Processes," presented at ESCAPE III Conference, Graz, Austria; also *Computers and Chemical Engineering*, Vol. 18, Suppl., 1994, pp. S105–S111.

Hall, S. G., 1989, "Targeting for Multiple Utilities in Pinch Technology," PhD thesis, UMIST, Manchester, United Kingdom.

Hall, S. G., Parker, S. J., Linnhoff, B., 1992, "Process Integration of Utility Systems," presented at IEA workshop on Process Integration, Gothenburg, Sweden, organized by CADDET/CASU.

Linnhoff, B., et al., 1982, "User Guide on Process Integration for the Efficient Use of Energy," Institution of Chemical Engineers, Rugby, United Kingdom.

Linnhoff, B., and Ahmed, S., 1989, "Supertargeting: Optimal Synthesis of Energy Management Systems," ASME *Journal of Energy Resources Technology*, Vol. 111, pp. 131–136.

Linnhoff, B., and Dhole, V. R., 1992, "Shaftwork Targets for Low Temperature Process Design," *Chem. Eng. Sci.*, Vol. 47, No. 8, pp. 2081–2091.

Umeda, T., Niida, K., and Shiroko, K., 1979, "A Thermodynamic Approach to Heat Integration in Distillation Systems," *AIChE Journal*, Vol. 25, No. 3, pp. 423–429.

Downloaded 02 Jun 2010 to 171.66.16.102. Redistribution subject to ASME license or copyright; see http://www.asme.org/terms/Terms_Use.cfm

R. Yokoyama
Associate Professor.
Mem. ASME

K. Ito
Professor.
Mem. ASME

Department of Energy
Systems Engineering,
University of Osaka Prefecture,
1-1, Gakuen-cho,
Sakai, Osaka, 593 Japan

Multi-objective Optimization in Unit Sizing of a Gas Turbine Cogeneration Plant

An optimal planning method for cogeneration plants proposed earlier is extended to the case with multiple optimization criteria. Equipment capacities and utility maximum demands are determined so as to minimize both the annual total cost and the annual primary energy consumption in consideration of plants' operational strategies for energy demand requirements. This problem is considered as a multi-objective optimization one, and a discrete set of Pareto optimal solutions is derived numerically by the weighting method. Through a numerical study on a simple cycle gas turbine cogeneration plant used for district heating and cooling, a trade-off relationship between the economic and energy-saving properties is clarified.

Introduction

Cogeneration plants have been introduced increasingly for commercial and public purposes in Japan. In order to utilize their high economic and energy-saving potentials, planners and operators are urged to propose good plans for the fundamental design and operation. For example, it is important for planners to determine equipment capacities and maximum utility demands rationally, especially capacities of prime movers and a maximum demand of purchased electricity. This is because underestimation of capacities of prime movers has the effect of introducing a relatively small amount of cogeneration and contrarily overestimation brings a reduction in the availability of prime movers. However, this problem is difficult to solve since it is necessary to take account of plants' operational strategies for seasonal and hourly variations of electricity and thermal energy demands estimated at the planning stage.

An optimal planning method has been proposed to determine equipment capacities and utility maximum demands rationally in consideration of plants' operational strategies (Yokoyama et al., 1991). Its extension to the case of multistage expansion planning has also been proposed (Matsumoto et al., 1992). In these papers, equipment capacities and utility maximum demands have been determined so as to minimize the annual total cost only from the economic viewpoint. However, their optimal values obtained on the basis of economy may not be suitable from other viewpoints, e.g., viewpoints of energy saving or environmental protection. In a numerical study of the previous paper, in fact, the optimization on the basis of economy has resulted in disposal of a large amount of exhaust heat, which has not been preferable from the energy saving viewpoint (Yokoyama et al., 1991). This result shows that the optimal solution only from the cogenerator side does not necessarily coincide with that from the global viewpoint. Considering the global energy or environmental problems at issue in recent years, it is necessary to propose good plans not only for profitable cogenerators but also for contributing to solving global problems. This needs optimal design and operation of cogeneration plants.

The objective of this paper is to propose a multi-objective optimization method in unit sizing of cogeneration plants and to clarify a trade-off relationship between the criteria from the cogenerator side and more global viewpoints. The economic and energy-saving properties are adopted as the criteria. A numerical study is carried out on a simple cycle gas turbine cogeneration plant used for district heating and cooling. The trade-off relationship between the economic and energy-saving properties is investigated through a parametric study with respect to energy rates.

Multi-objective Optimization in Unit Sizing

Outline of Optimal Planning Model. In this paper, the annual total cost and the annual primary energy consumption are adopted as objective functions to be minimized from the economic and energy-saving viewpoints, respectively. The annual total cost is evaluated as the sum of the annual capital cost and annual running cost on the basis of the annualized cost method (Witte et al., 1988). The annual capital cost of each piece of equipment is considered as a function of its capacity. The annual running cost of each utility is the sum of the customer/demand charges and energy charge. The demand charge is calculated from the plants' operational strategy. The annual primary energy consumption is also obtained from the plant's operational strategy.

The annual operational hours in a year are discretized by setting D representative days and by dividing each day into

Contributed by the International Gas Turbine Institute for publication in the JOURNAL OF ENGINEERING FOR GAS TURBINES AND POWER. Manuscript received by the International Gas Turbine Institute December 31, 1993. Associate Technical Editor: A. Scalzo.

Copyright © 1995 by ASME

Downloaded 02 Jun 2010 to 171.66.16.102. Redistribution subject to ASME license or copyright; see http://www.asme.org/terms/Terms_Use.cfm

H time periods, and the annual operational hour for the hth time period on the dth representative day is designated by T_{dh}. Energy demands are estimated for each time period on each representative day, and the operational strategy is assessed correspondingly. In addition to average energy demands, peak energy demands in summer and winter should be considered for equipment to supply energy during the peak periods. Then, the first objective function J_1, annual total cost, is expressed by

$$J_1 = F(x) + \sum_{d=1}^{D} \sum_{h=1}^{H} V_{dh}(\mathbf{x}, \mathbf{y}_{dh}, \mathbf{z}_{dh}) T_{dh}, \quad (1)$$

where F is the sum of the annual capital cost and the annual customer/demand charges, and it is a function of the vector composed of equipment capacities and utility maximum demands $\mathbf{x}$. The function V_{dh} is the hourly energy charge, and it is a function of $\mathbf{x}$, and the continuous variable vector $\mathbf{y}_{dh}$ and binary variable vector $\mathbf{z}_{dh}$, which express, respectively, energy flow rates and on/off status of operation of equipment for the corresponding time period (Ito et al., 1990). Similarly, the second objective function J_2, annual primary energy consumption, is expressed by

$$J_2 = \sum_{d=1}^{D} \sum_{h=1}^{H} P_{dh}(\mathbf{x}, \mathbf{y}_{dh}, \mathbf{z}_{dh}) T_{dh}, \quad (2)$$

where P_{dh} is the hourly primary energy consumption.

As constraints, it is necessary to consider performance characteristics of each piece of equipment and energy balance relationships of each energy flow for each time period on each representative day. Here, since performance characteristics of equipment change with the capacities, they should be considered as functions of the capacities. These constraints are expressed by

$$\mathbf{C}_{dh}(\mathbf{x}, \mathbf{y}_{dh}, \mathbf{z}_{dh}) = \mathbf{0}, \quad (d = 1, \ldots, D;\ h = 1, \ldots, H), \quad (3)$$

where $\mathbf{C}_{dh}$ is the vector composed of constraint functions.

Unknown variables are composed of the vector expressing equipment capacities and utility maximum demands $\mathbf{x}$, and the vectors expressing the operational strategy $\mathbf{y}_{dh}$ and $\mathbf{z}_{dh}$. Although the capacity of each piece of equipment is selected from a set of discrete values in the practical design, it is regarded as a continuous variable in this paper.

Hierarchical Optimization Algorithm. In order to solve the above-mentioned problem efficiently, a hierarchical optimization algorithm proposed for the single-objective optimal planning is employed here: Equipment capacities and maximum utility demands are determined in the unit sizing problem at the upper level; the operational strategy is assessed in the operational planning problem at the lower level; both levels are interconnected with each other by a penalty method. This hierarchical optimization procedure is shown in Fig. 1.

Optimal Unit Sizing. At the upper level, the optimal unit sizing problem is formulated as a nonlinear programming one, in which optimal values of equipment capacities and utility maximum demands $\mathbf{x}$ are searched so as to minimize the annual total cost J_1 and the annual primary energy consumption J_2. In this phase, the constraints of Eq. (3) are not taken into account explicitly, and only the constraints are considered that force virtual energy flows not to arise. The weighting method is employed for solving this multi-objective optimization problem (Cohon, 1978), and the two objective functions are combined to form a single objective function J_s as follows:

$$J_S = w_1 \frac{J_1}{J_1^0} + w_2 \frac{J_2}{J_2^0} \quad (w_1 + w_2 = 1), \quad (4)$$

where J_1 and J_2 are normalized by the corresponding values for a conventional energy supply plant without cogeneration J_1^0 and J_2^0, respectively. The weights w_1 and w_2 express the comparative importance of the corresponding objective functions J_1 and J_2, respectively. The combined objective func-

Nomenclature

$\mathbf{C}_{dh}$ = vector composed of constraint functions
D = number of representative days per year
E = electric power, MWh/h
$\bar{E}_{GT}$ = capacity (electrical output at rated load status) of gas turbine generator, MW
F = sum of annual capital cost and customer/demand charges, \$/y
H = number of time periods per day
J_{Odh} = objective function in optimal operational planning problem
J_S = combined objective function in optimal unit sizing problem
J_1 = first objective function in optimal unit sizing problem (annual total cost), \$/y
J_2 = second objective function in optimal unit sizing problem (annual primary energy consumption), MWh/y
J_1^0, J_2^0 = reference values for J_1 and J_2, respectively, \$/y, MWh/y
P_{dh} = hourly primary energy consumption, MWh/h
Q = heat flow rate, MWh/h
T_{dh} = annual operational hour, h/y
V_{hh} = hourly energy charge, \$/h
w_1, w_2 = weights for objective functions J_1 and J_2, respectively
$\mathbf{x}$ = vector composed of continuous variables for equipment capacities and utility maximum demands
$\mathbf{y}_{dh}$ = vector composed of continuous variables for energy flow rates
$\mathbf{z}_{dh}$ = vector composed of binary variables for on/off status of operation of equipment
α = unit cost ratio of energy charge for natural gas
η_e = generating efficiency at rated load status of gas turbine generator
η_h = waste heat recovery efficiency at rated load status of gas turbine generator plus waste heat recovery boiler
$\varphi_{gas}, \hat{\varphi}_{gas}$ = unit costs of energy charge for natural gas for assumed and currrent rate structures, respectively

Subscripts

buy = purchased electricity
d = index for representative day
disp = heat disposal
h = index for time period

Equipment Symbols (subscripts)

BA = gas-fired auxiliary boiler
BW = waste heat recovery boiler
EP = equipment for purchasing electricity
GT = gas turbine generator
PC = pump for space cooling
RE = electric compressor refrigerator
RS = steam absorption refrigerator

Downloaded 02 Jun 2010 to 171.66.16.102. Redistribution subject to ASME license or copyright; see http://www.asme.org/terms/Terms_Use.cfm

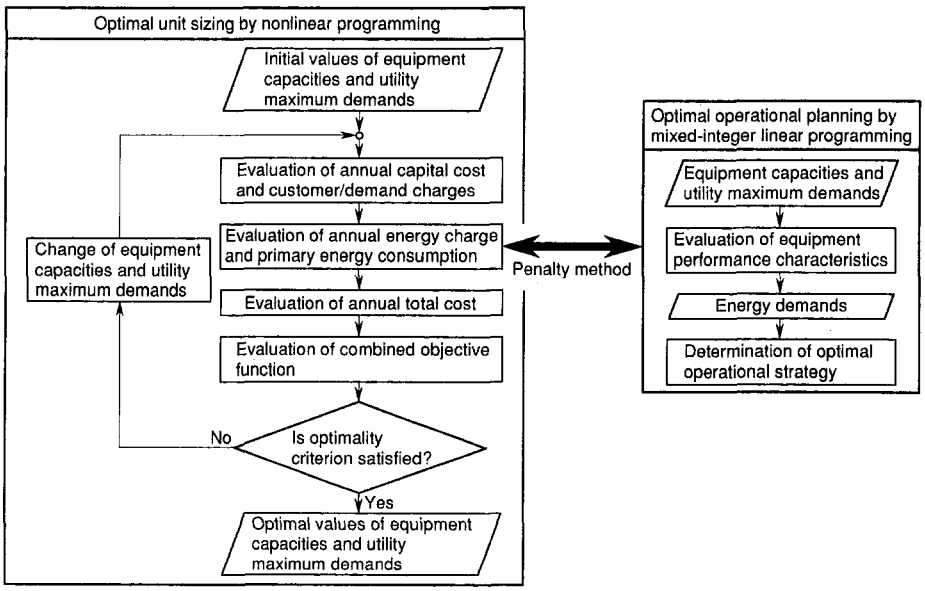

Fig. 1 Hierarchical optimization algorithm for unit sizing and operational planning

Table 1 Annual total and hourly maximum values of energy demands

	Annual total value GWh/y	Hourly maximum value MWh/h
Electricity	73.29	20.56
Space cooling	27.28	31.54
Steam	31.24	28.84

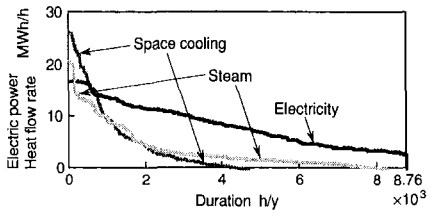

Fig. 2 Load duration curves for energy demands

tion J_s is minimized by changing the values of weights w_1 and w_2, and a discrete set of Pareto optimal solutions is derived numerically. The sequential linear programming method is adopted as a solving method of the nonlinear programming problem (Cheney and Goldstein, 1959).

Optimal Operational Planning. At the lower level, for a plant with the equipment capacities and utility maximum demands given at each searching step, the operational strategy is assessed, and the annual energy charge and primary energy consumption are evaluated. In this paper, the operational strategy is assessed using an optimal operational planning method proposed by the authors (Ito et al., 1990). If the value of $\mathbf{x}$ is given at the upper level, the overall optimization problem can be divided into $D \times H$ optimal operational planning problems, in which the values of $\mathbf{y}_{dh}$ and $\mathbf{z}_{dh}$ are determined independently for each time period on each representative day.

In the single-objective optimal planning only from the economic viewpoint, the hourly energy charge has been adopted as the objective function to be minimized in the optimal operational planning problem. This objective function has been consistent with that in the optimal unit sizing problem, and the resulting operational strategy has contributed directly to the minimization of the annual total cost. Similarly, in the multi-objective optimal planning considered here, the objective function in the optimal operational planning problem should be defined so that it is consistent strictly with that in the optimal unit sizing problem of Eq. (4). In order to minimize J_s for some value of $\mathbf{x}$, it is necessary to adopt

$$J_{Odh} = w_1 \frac{V_{dh}}{J_1^0/8760} + w_2 \frac{P_{dh}}{J_2^0/8760} \quad (d = 1, \ldots, D; \quad h = 1, \ldots, H) \quad (5)$$

as the objective function for each optimal operational planning problem.

In this phase, the constraints of Eq. (3) are taken into account explicitly. Additionally, virtual energy flows are added to the energy flows existing actually for any plant given at each searching step to satisfy the energy demands. The virtual energy flows play the role that they supply energy additionally only if the plant is too small to satisfy the energy demands. For that purpose, a penalty cost is imposed on the occurrence of virtual energy flows. At the upper level, given information about the occurrence of virtual energy flows, the design variables change automatically so as not to cause the virtual energy flows, or so as to satisfy the energy demands.

The optimal operational planning problem is formulated as a mixed-integer linear programming problem, and it is solved by the branch and bound method (Garfinkel and Nemhauser, 1972). The specific algorithm adopted here is based on the Land–Doig method (1960).

Numerical Study on Simple Cycle Gas Turbine Cogeneration Plant

The effectiveness of the proposed method is investigated through a numerical study on a simple cycle gas turbine cogeneration plant used for district heating and cooling.

Input Data

Energy Demands. In the district considered here, four office buildings and two hotels are to be constructed. The total floor area is about 384,000 m^2. For simplicity, it is assumed that the plant begins to supply energy to all buildings at the same time. Table 1 gives the annual total and hourly maximum values of electricity, space cooling, and steam demands. Figure 2 shows the load duration curves

Downloaded 02 Jun 2010 to 171.66.16.102. Redistribution subject to ASME license or copyright; see http://www.asme.org/terms/Terms_Use.cfm

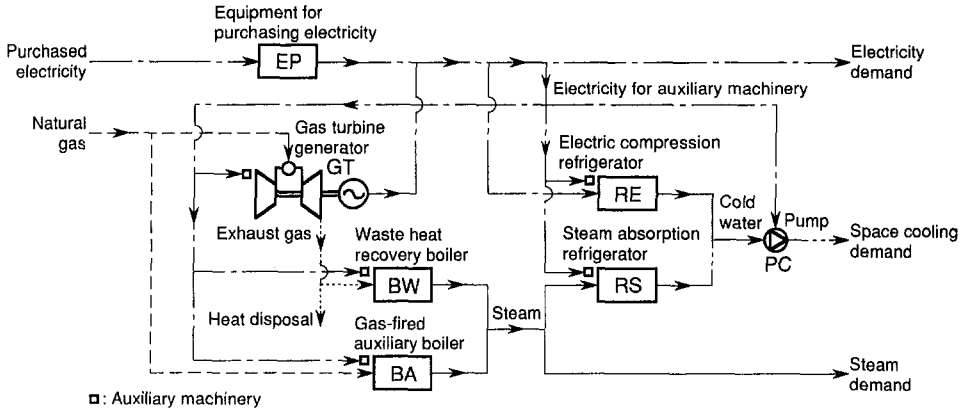

Fig. 3 Configuration of a simple cycle gas turbine cogeneration plant

Table 2 Performance characteristic values and initial capital costs of equipment

Equipment	Performance characteristic value		Initial capital cost
Gas turbine generator plus waste heat recovery boiler	Generating efficiency Waste heat recovery efficiency	Eq. (6) Eq. (7)	1760×10^3 \$/MW
Gas-fired auxiliary boiler	Thermal efficiency	0.90	53×10^3 \$/MW
Electric compression refrigerator	Coefficient of performance	3.60	172×10^3 \$/MW
Steam absorption refrigerator	Coefficient of performance	1.20	413×10^3 \$/MW
Equipment for purchasing electricity	—		450×10^3 \$/MW
Pump	Electricity consumption rate	0.025 MW/MW	—

indicating the annual variations of hourly energy demands. Here, a weekday, a Saturday, and a holiday are considered as representative days for each month; i.e., the operational strategy is investigated on 36 representative days throughout a year. Hourly energy demands are given as input data for each representative day. In addition to these average energy demands, peak energy demands in summer and winter are also given by multiplying the average energy demands on a weekday in August and January by 1.2, respectively.

Plant Configuration. Figure 3 shows schematically the configuration of a simple cycle gas turbine cogeneration plant investigated in this study. Although only one unit is illustrated for each kind of equipment, there may be several units. Solid lines, dot-dash lines, two dots-dash lines, dotted lines, and broken lines denote the flows of steam, electricity, cold water, exhaust gas, and natural gas, respectively.

Electricity is supplied to users by operating gas turbine generators and by purchasing electricity from an outside electric power company. Electricity is used to drive electric compression refrigerators, pumps, and other auxiliary machinery in the plant. Exhaust heat generated by the gas turbines is recovered by waste heat recovery boilers, and it is reused for several kinds of thermal energy in a cascaded way. Surplus exhaust heat is disposed of through exhaust gas dampers. Shortage of steam is supplemented by gas-fired auxiliary boilers. Cold water for space cooling is supplied by electric compression and steam absorption refrigerators. Steam is used for space heating and other miscellaneous purposes.

In this study, it is assumed that two units of gas turbine generator and waste heat recovery boiler are installed, and that one unit is installed for other kinds of equipment. The capacities of each kind of equipment except the pumps are determined optimally together with the maximum demands of purchased electricity and natural gas. It is assumed that the capacity of equipment for purchasing electricity is equal to the maximum demand for purchased electricity.

Performance and Cost Data. Performance characteristics and initial capital costs of equipment are given as functions of their capacities. Nonlinear curve fitting is adopted for the performance characteristics of units of gas turbine generator plus waste heat recovery boiler. For example, the generating efficiency at the rated load η_e tends to increase with the capacity, and conversely the waste heat recovery efficiency at the rated load η_h tends to decrease. These values can be approximated by

$$\eta_e = 0.211\bar{E}_{GT}^{0.15} \tag{6}$$

and

$$\eta_h = 0.555\bar{E}_{GT}^{-0.04}, \tag{7}$$

where $\bar{E}_{GT}$ is the capacity (electrical output at the rated load status) of a gas turbine generator. Variations in these efficiencies at part-load status are also taken into account. Linear curve fitting is adopted for performance characteristics of other kinds of equipment. Linear functions are used to express the relationship between initial capital cost and capacity for all kinds of equipment. The representative values of performance characteristics and initial capital costs are given in Table 2.

The rates for purchased electricity and natural gas adopted in this study are standard ones used in Japan, and they are given in Table 3. In evaluating the annual total cost, it is assumed that the life of equipment is 15 y, the salvage value of equipment is zero, and the interest is 0.1. In evaluating the primary energy consumption, it is assumed that the thermal efficiency of purchased electricity is 0.388.

Results and Discussion

Fundamental Study. First, a numerical study has been carried out on the assumptions stated above. Figure 4 shows the trade-off relationship between the two objective functions J_1 and J_2 for a discrete set of Pareto optimal solutions. The reference values of the objective functions J_1^0 and J_2^0 have been determined for a conventional energy supply plant composed of an equipment for purchasing electricity, a gas-fired auxiliary boiler, and a steam absorption refrigerator. A

Downloaded 02 Jun 2010 to 171.66.16.102. Redistribution subject to ASME license or copyright; see http://www.asme.org/terms/Terms_Use.cfm

Table 3 Rates for purchased electricity and natural gas

Utility	Unit cost		
	Customer charge	Demand charge	Energy charge
Purchased electricity	—	13.92×10^3 \$/(MW·month)	86.16 (Jul.~Sep.) \$/MWh 78.32 (Other months)
Natural gas	288 \$/month	9.6 (Apr.~Oct.) \$/(m³/h·month) 25.6 (Other months)	0.247 \$/m³

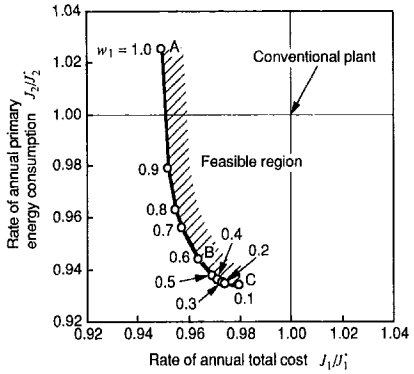

Fig. 4 Trade-off relationship between two objective functions for current rate structures

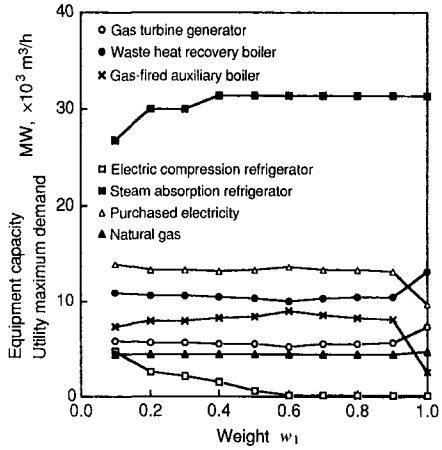

Fig. 5 Optimal values of equipment capacities and utility maximum demands for current rate structures

trade-off curve is drawn through the discrete points. The region on the right and upper sides of this curve corresponds to feasible solutions. This curve shows that the two objective functions conflict with each other. That is, we cannot improve one objective function without making the other one worse, which is the property of Pareto optimal solutions.

Solution A with the weight $w_1 = 1.0$ results from the minimization of annual total cost only from the economic viewpoint. This solution has a 5.1 percent decrease in annual total cost as compared with the conventional plant. However, it has a 2.6 percent increase in annual primary energy consumption, and this result is not preferable from the energy-saving viewpoint. This is because, as indicated in the introduction, gas turbine generators of a large capacity are selected, and a large amount of exhaust heat must be disposed of. Solution B with the weight $w_1 = 0.6$ has a 1.6 percent increase in annual total costs as compared with solution A, while it has an 8.0 percent decrease in annual primary energy consumption, and the values of both objective functions are smaller than those for the conventional plant. This result shows that we can improve the energy-saving property drastically at a small sacrifice of the economic property. The situation like this emerges for solutions whose tangents for the trade-off curve have large or small slopes. Solution C with the weight $w_1 = 0.1$ has an additional decrease in annual primary energy consumption as compared with solution B. However, it has an increase in annual total cost. Therefore, it is preferable only from the global viewpoint, and is not advantageous to the cogenerator.

Figure 5 shows the optimal values of equipment capacities and utility maximum demands for the above-mentioned discrete set of Pareto optimal solutions. In the vicinity of $w_1 = 1.0$, the capacities of gas turbine generators and waste heat recovery boilers become large, and correspondingly the capacity of gas-fired auxiliary boiler and the maximum demand of purchased electricity become small. This result is due to the rate structures of purchased electricity and natural gas, and the performance characteristics of gas turbine generators. That is, the unit cost of energy charge for natural gas is relatively lower than that for purchased electricity, and the value of exhaust heat is also low. In addition, the generating efficiency of gas turbine generators tends to increase with capacity as expressed by Eq. (6). Therefore, gas turbine generators of a large capacity are selected in spite of a possibility of causing a large amount of heat disposal. However, in the range of $w_1 = 0.9 \sim 0.1$, the capacity of gas turbine generators becomes smaller than that in the case of $w_1 = 1.0$. This is because the introduction of the energy-saving property into the evaluation criteria makes the value of exhaust heat higher.

Figures 6(a–c) show the load duration curves for electricity supply and exhaust heat utilization corresponding to solutions A to C, respectively. In these figures, E_{GT1} and E_{GT2} are the electric power generated by the two gas turbine generators, E_{buy} is the electric power purchased from an outside electric power company, Q_{BW1} and Q_{BW2} are the flow rates of exhaust heat utilized by the two waste heat recovery boilers, and Q_{disp1} and Q_{disp2} are the flow rates of exhaust heat disposed of. For all the solutions, the first gas turbine generator operates mainly, and the second one operates additionally only at peak demand periods. For solution A, both the gas turbine generators operate at the rated load status, and consequently about half of exhaust heat is disposed of. This is because the generating efficiency of gas turbine generators at the rated load status is higher than that at part-load status, in addition to the reasons stated above. For solution B, the capacity of gas turbine generators decreases, and their annual operational hours also decrease. This reduces the amount of heat disposal. Nevertheless, both the gas turbine generators operate at the rated load status. For solution C, both the gas turbine generators operate at part-load status so as not to dispose of exhaust heat. This is because the energy-saving property is more important than the economic property in the evaluation.

Parametric Study. The optimal design and operation determined from the economic viewpoint depend significantly on the rate structures of purchased electricity and natural gas. It is important to investigate the effect of the rate structures on the multiobjective optimization in unit sizing and operational planning. Next, a parametric study has been carried out by changing the unit cost of energy charge for

Downloaded 02 Jun 2010 to 171.66.16.102. Redistribution subject to ASME license or copyright; see http://www.asme.org/terms/Terms_Use.cfm

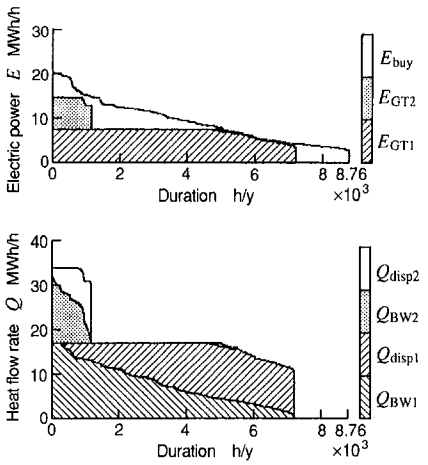

Fig. 6(*a*) Solution *A* ($w_1 = 1.0$)

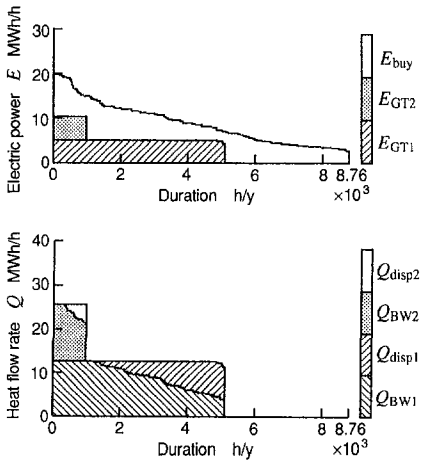

Fig. 6(*b*) Solution *B* ($w_1 = 0.6$)

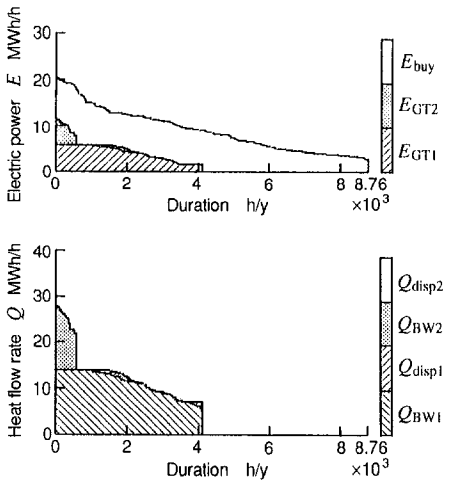

Fig. 6(*c*) Solution *C* ($w_1 = 0.1$)

Fig. 6 Load duration curves for electricity supply and exhaust heat utilization

natural gas. Here, we have introduced the unit cost ratio α defined by

$$\alpha = \varphi_{gas}/\hat{\varphi}_{gas}, \tag{8}$$

where $\hat{\varphi}_{gas}$ is the current unit cost of energy charge for natural gas, and φ_{gas} is the value assumed in this parametric study.

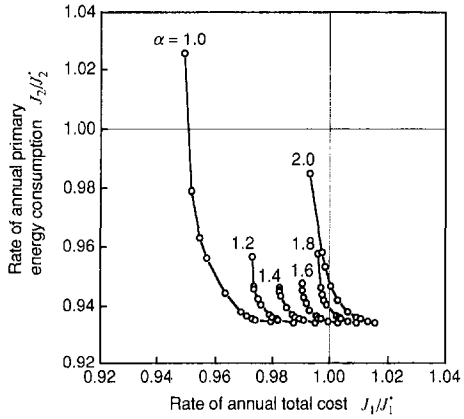

Fig. 7 Trade-off relationships between two objective functions for various rate structures

Figure 7 shows the trade-off relationships between the two objective functions J_1 and J_2 corresponding to the discrete sets of Pareto optimal solutions for several values of the unit cost ratio α. In the case of $\alpha = 1.0$, the values of both the objective functions J_1 and J_2 range widely for the solutions in the range of $w_1 = 1.0 \sim 0.1$. However, in the cases of $\alpha = 1.2 \sim 1.8$, the value of the annual primary energy consumption J_2 changes within a narrow range for the solutions in the range $w_1 = 1.0 \sim 0.1$. This feature shows that the minimization of the annual total cost only from the economic viewpoint brings almost simultaneously that of the annual primary energy consumption. This is because the unit cost ratio of purchased electricity to natural gas is almost equal to the ratio of coefficients that are used to convert purchased electricity and natural gas consumptions into primary energy ones. These rate structures of purchased electricity and natural gas give an incentive to improve the energy-saving property even by adopting the design and operation from the cogenerator side, although the economic property becomes worse with an increase in unit cost of energy charge for natural gas. In the case of $\alpha = 2.0$, the values of both the objective functions range widely again. This is because the unit cost of energy charge for natural gas is relatively higher than that for purchased electricity, and the introduction of cogeneration is disadvantageous to the cogenerator even from the economic viewpoint. As a result, a conventional plant without cogeneration or a small-scale cogeneration plant becomes preferable.

Figures 8(a, b) show the optimal values of equipment capacities and utility maximum demands for the discrete sets of Pareto optimal solutions in the cases of $\alpha = 1.4$ and $\alpha = 2.0$, respectively. In both the cases, the capacity of gas turbine generators decreases with an increase in the weight w_1. In the case of $\alpha = 2.0$, the change is remarkable, and the capacity of gas turbine generators becomes zero at the point of the weight $w_1 = 1.0$.

Conclusions

A multi-objective optimization approach has been proposed to the unit sizing of cogeneration plants in consideration of their operational strategies. The economic and energy-saving properties have been adopted as multiple optimization criteria from both the cogenerator side and more global viewpoints. A discrete set of Pareto optimal solutions has been derived numerically by the weighting method. A simple cycle gas turbine cogeneration plant used for district heating and cooling has been investigated as an example. The trade-off relationship between the annual total cost and annual primary energy consumption has been clarified, and the effect of importance for these objective functions on the

Downloaded 02 Jun 2010 to 171.66.16.102. Redistribution subject to ASME license or copyright; see http://www.asme.org/terms/Terms_Use.cfm

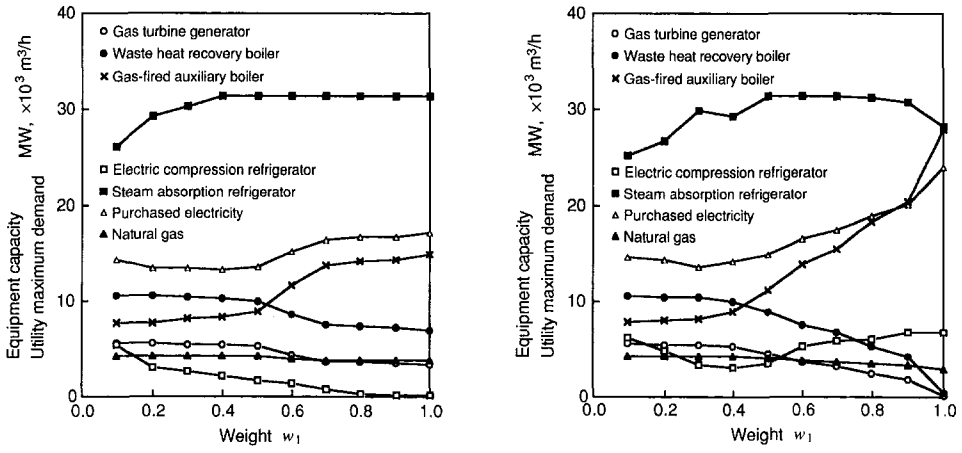

Fig. 8(a) $\alpha = 1.4$ **Fig. 8(b)** $\alpha = 2.0$

Fig. 8 Optimal values of equipment capacities and utility maximum demands for various rate structures

design and operation has also been clarified. This study has shown that although the solution only from the economic viewpoint is not preferable from the energy saving viewpoint, we can improve the energy-saving property greatly at a small sacrifice of the economic property. A parametric study has also been carried out to investigate the effect of rate structures of purchased electricity and natural gas. This study has shown which rate structures give an incentive to improve the energy-saving property even by adopting the design and operation only from the cogenerator side.

The paper has dealt with a numerical study only on a simple cycle gas turbine cogeneration plant. The proposed method can be applicable to cogeneration plants including other prime movers with different performance characteristics. As a subsequent subject, it will be important to carry out these case studies.

References

Cheney, E. W., and Goldstein, A. A., 1959, "Newton's Method for Convex Programming on Tchebycheff Approximation," *Numerical Mathematics*, Vol. 1, pp. 253–268.

Cohon, J. L., 1978, *Multiobjective Programming and Planning*, Academic Press, New York, p. 13.

Garfinkel, R. S., and Nemhauser, G. L., 1972, *Integer Programming*, Wiley, New York, pp. 5–7.

Ito, K., Yokoyama, R., Akagi, S., and Matsumoto, Y., 1990, "Influence of Fuel Cost on the Operation of a Gas Turbine-Waste Heat Boiler Cogeneration Plant," ASME JOURNAL OF ENGINEERING FOR GAS TURBINES AND POWER, Vol. 112, pp. 122–128.

Land, A. H., and Doig, A. G., 1960, "An Automatic Method of Solving Discrete Programming Problems," *Econometrica*, Vol. 28, pp. 497–520.

Matsumoto, Y., Yokoyama, R., and Ito, K., 1992, "Optimal Multistage Expansion Planning of a Gas Turbine Cogeneration Plant," *Proceedings of the 6th Congress and Exposition on Gas Turbines in Cogeneration and Utility, Industrial and Independent Power Generation*, pp. 43–49.

Witte, L. C., Schmidt, P. S., and Brown, D. R., 1988, *Industrial Energy Management and Utilization*, Hemisphere Publishing, Washington, DC, pp. 68–69.

Yokoyama, R., Ito, K., and Matsumoto, Y., 1991, "Optimal Sizing of a Gas Turbine Cogeneration Plant in Consideration of Its Operational Strategy," *Proceedings of the 5th International Symposium and Exposition on Gas Turbines in Cogeneration, Repowering and Peak-Load Power Generation*, pp. 363–370.

Downloaded 02 Jun 2010 to 171.66.16.102. Redistribution subject to ASME license or copyright; see http://www.asme.org/terms/Terms_Use.cfm

K. Ito
Professor.
Mem. ASME

R. Yokoyama
Associate Professor.
Mem. ASME

Department of Energy Systems Engineering,
University of Osaka Prefecture,
1-1, Gakuen-cho,
Sakai, Osaka 593, Japan

Y. Matsumoto
Manager,
Technical Research Center,
Kansai Electric Power Co., Inc.,
3-11-20, Nakoji,
Amagasaki, Hyogo 661, Japan

Optimal Operation of Cogeneration Plants With Steam-Injected Gas Turbines

The effect of introducing steam-injected gas turbines into cogeneration plants is investigated from economical and energy-saving aspects on the basis of a mathematical programming approach. An optimal planning method is first presented by which the operational strategy is assessed so as to minimize the hourly running cost. Then, a case study is carried out on a plant used for district heating and cooling. Through the study, it is ascertained that the proposed method is a useful tool for the operational planning of steam-injected gas turbine plants, and that these plants can be attractive from economical and energy-saving viewpoints as compared with both simple-cycle gas turbine plus waste heat boiler plants and conventional energy supply ones.

Introduction

In recent years, district heating and cooling systems have been introduced positively in Japan into redeveloped areas in many cities. Under these circumstances, gas turbine cogeneration plants are expected to play important roles because of their economical and energy-saving advantages compared with conventional energy supply plants. Simple cycle gas turbine plus waste heat boiler plants (simple cycle plants) are adopted for most cogeneration plants installed currently into district heating and cooling systems. However, these plants cannot change the ratio of heat output to electrical output (heat to power ratio) flexibly corresponding to the change of both electricity and thermal energy demands. This becomes one of the weak points of cogeneration plants for commercial and public purposes, because the demand ratio of thermal energy to electricity varies widely hourly, daily, and seasonally. Thus it is strongly urged for planners of cogeneration plants to raise the plants' flexibility regarding the heat-to-power ratio.

Steam-injected gas turbine (STIG) units are expected to give a solution to this subject, and their performance characteristics are evaluated by several authors (Fraize and Kinney, 1979; Brown and Cohn, 1981; Larson and Williams, 1987). These units aim to increase electrical output and generating efficiency by injecting superheated steam into combustors of gas turbines, and it becomes possible to change the heat-to-power ratio flexibly by adjusting the amount of steam injection. Additional flexibility regarding the heat-to-power ratio can be obtained by adjusting supplemental firing with duct burners of waste heat boilers. Thus the high operational flexibility of cogeneration plants with STIG units gives a potential for economical and energy-saving aspects higher than those of simple-cycle plants.

It is an important theme to execute plants' operation rationally as well as to raise their operational flexibility by hardware. In the past, the thermal- or electric-following strategies have been adopted as conventional operational strategies for cogeneration plants. According to them, prime movers are operated to follow the demand for thermal energy or electricity, respectively. These strategies have the disadvantage that the surplus or shortage of supplies of electricity or thermal energy occur very often against their demands because of the lack of operational flexibility. The adoption of these strategies for STIG cogeneration plants may spoil their high flexibility regarding the heat-to-power ratio. In order to make positive use of their high operational flexibility and to realize the above-stated potential for high economical and energy-saving aspects, it is necessary to introduce an intelligent and flexible operational strategy. Some papers were presented on the optimal operation of STIG units (Maher et al., 1987; Baken and Haspel, 1988). However, the papers describe the operational strategy only for one STIG unit, and not for a total cogeneration plant with multiple STIG units.

The purpose of the present paper is to propose a planning method for the optimal operation of total cogeneration plants with STIG units. Using a mathematical programming approach, the authors have already proposed such a planning method for simple-cycle plants (Ito et al., 1988, 1990), and combined gas and steam turbine cycle plants (Ito et al., 1987). The present paper describes an extension of this method to the case of STIG cogeneration plants. First, performance characteristics of STIG units are formulated in detail. Second, the formulation of the plants' operational planning problem is summarized. Last, a case study is carried out on a plant used for district heating and cooling. Throughout the study, the

Contributed by the International Gas Turbine Institute for publication in the JOURNAL OF ENGINEERING FOR GAS TURBINES AND POWER. Manuscript received by the International Gas Turbine Institute October 13, 1993. Associate Technical Editor: H. L. Julien.

Copyright © 1995 by ASME

Downloaded 02 Jun 2010 to 171.66.16.102. Redistribution subject to ASME license or copyright; see http://www.asme.org/terms/Terms_Use.cfm

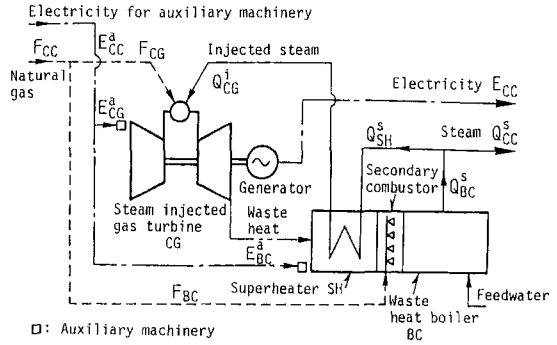

Fig. 1 Structure of STIG unit

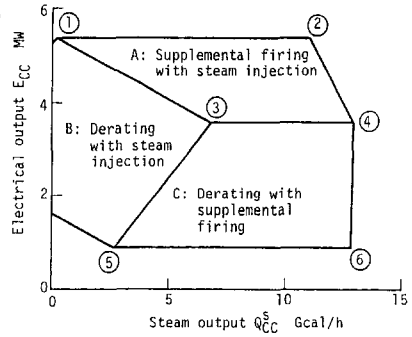

Fig. 2 Operating region of STIG unit

optimal operational strategy is assessed concretely, and the economical and energy-saving aspects are evaluated.

Plant Structure

Figure 1 illustrates the structure of a STIG unit. In this figure, solid, broken, and one dot-dash lines indicate flows of steam, natural gas, and electricity, respectively. As well as a simple-cycle gas turbine unit, this unit is equipped with a gas turbine generator and a waste heat boiler. Electrical output can be increased by injecting superheated steam into a combustor of the gas turbine. Steam output can also be increased by supplemental firing with duct burners of the waste heat boiler. As shown in Fig. 2, the unit can operate within a wide range of electrical and steam outputs by adjusting the amounts of steam injection and supplemental firing. In this figure, region *A* shows supplemental firing with steam injection, region *B* does derating with steam injection, and region *C* does derating with supplemental firing, respectively.

Figure 3 illustrates the structure of the total cogeneration plant investigated in the present paper. Here, we investigate the plants that include not only STIG units but also simple-cycle gas turbine units. In this figure, the two dots-dash line indicates the flow of cold or hot water. Electricity is supplied to users by the parallel running of gas turbine generators and purchasing electricity from an outside electric power company. Electricity is also used to drive electric compression refrigerators, pumps, cooling towers, and other auxiliary machinery in the plant. This plant has the possibility to sell the electricity generated by gas turbine generators to the outside electric power company. Steam generated by waste heat boilers in cogeneration units is used for several purposes in a cascade way. Surplus steam is disposed of through steam dumping, and it is taken into account as heat disposal in Fig. 3. The shortage of steam is supplemented by auxiliary boilers. Electric compression and steam absorption refrigerators are installed to supply cold water for space cooling, and heat exchangers to supply hot water for space heating and other miscellaneous purposes. Although only one unit is illustrated for each kind of equipment in Fig. 3, there may be several units.

Optimal Operational Planning

The cogeneration plant in Fig. 3 has many alternatives concerning the operational strategy to satisfy energy demands, because the supply and demand of both electricity and thermal energy are connected to each other very closely and complexly. For example, the heat-to-power ratio of STIG units can be changed flexibly by steam injection and supplemental firing. In addition, the operation of electric compression refrigerators for space cooling increases electricity demand. Thus the high flexibility of STIG units and the complex energy supply-demand relationships in the plant make it very difficult to determine the operational strategy rationally. The authors have already proposed a planning method for the optimal operation of simple-cycle plants, and combined gas and steam turbine cycle plants. Using this method, the operational strategy for each piece of constituent equipment can be determined so as

Nomenclature

Energy quantities

E = electric power, MWh/h
F = natural gas consumption, m^3/h*
Q = heat flow rate, Gcal/h
W = feedwater consumption, m^3/h

Other symbols

J = objective function (hourly running cost), yen/h
p, q, r, s, t = parameters related to performance characteristics of each piece of equipment
α = reduction rate of annual running cost, percent
β = annual rate of energy saving, percent
γ = reduction rate of annual total cost, percent
δ = binary variable expressing on/off status of each piece of equipment
$\underline{(\ )}, \overline{(\ )}$ = lower and upper bounds, respectively

Equipment symbols (subscripts)

BA = auxiliary boiler
BC, BW = waste heat boilers
CC = steam-injected gas turbine unit
CE, CS = cooling towers
CG = steam-injected gas turbine generator
GT = simple-cycle gas turbine generator
HE = heat exchanger
PC, PE, PH, PS, PW = pumps
RE = electric compression refrigerator
RS = steam absorption refrigerator
SH = superheater

Superscripts

a = electricity for auxiliary machinery
i = steam injection
m = status without steam injection
s = steam

*Measured at standard conditions.

Downloaded 02 Jun 2010 to 171.66.16.102. Redistribution subject to ASME license or copyright; see http://www.asme.org/terms/Terms_Use.cfm

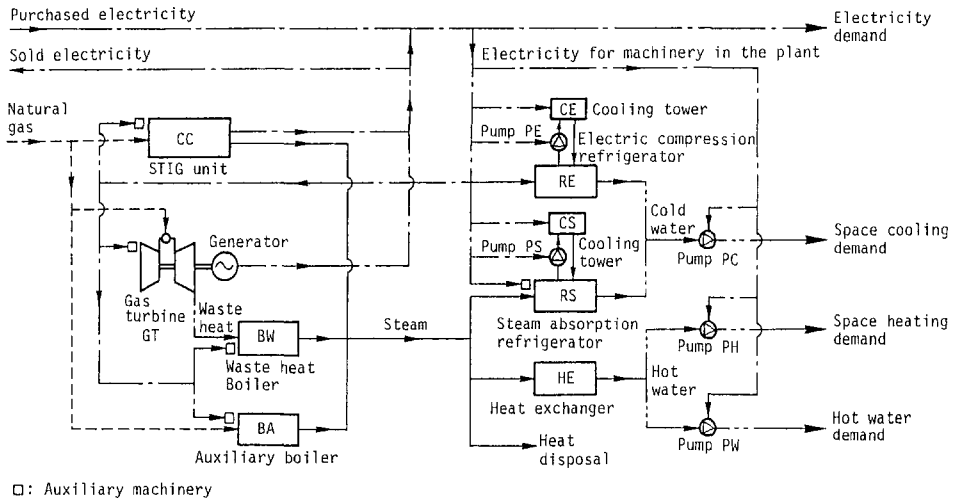

Fig. 3 Structure of total cogeneration plant

to minimize the hourly running cost. In the present paper, the above-described method is extended to the case of cogeneration plants with STIG units.

Performance Characteristics of STIG Unit. Prior to the formulation of the total cogeneration plant, the performance characteristics of the STIG unit in Fig. 1 are formulated in detail.

For a simple-cycle gas turbine generator, the relationship between electrical output and natural gas consumption is approximated accurately enough by a linear equation. Similarly, the performance characteristics of the STIG generator are expressed by

$$E_{CC}=p_{CG}F_{CG}+q_{CG}Q^i_{CG}+r_{CG}\delta_{CG}, \tag{1}$$

where E_{CC} is the electrical ouptut, F_{CG} is the natural gas consumption, and Q^i_{CG} is the heat of injected steam. The natural gas consumption is the sum of basic consumption without steam injection F^m_{CG} and additional consumption with steam injection F^i_{CG}; i.e.,

$$F_{CG}=F^m_{CG}+F^i_{CG}. \tag{2}$$

The capacity of the gas turbine limits the basic consumption by its lower bound $\underline{F}^m_{CG}$ and upper one $\overline{F}^m_{CG}$. This limitation is given by

$$\underline{F}^m_{CG}\delta_{CG}\le F^m_{CG}\le\overline{F}^m_{CG}\delta_{CG}. \tag{3}$$

In Eqs. (1) and (3), δ_{CG} is the binary variable that expresses the on(δ_{CG} = 1)/off(δ_{CG} = 0) status of operation of the STIG generator. A proportional relationship between Q^i_{CG} in Eq. (1) and F^i_{CG} in Eq. (2) is taken into account as follows:

$$F^i_{CG}=s_{CG}Q^i_{CG}. \tag{4}$$

In addition, Q^i_{CG} is limited by an upper bound $\overline{Q}^i_{CG}$ as follows:

$$0\le Q^i_{CG}\le\overline{Q}^i_{CG}\delta^i_{CG}, \tag{5}$$

where δ^i_{CG} is the binary variable that expresses the on(δ^i_{CG} = 1)/off(δ^i_{CG} = 0) status of steam injection.

The performance characteristics of the waste heat boiler are expressed by the following linear equation:

$$Q^s_{BC}=p_{BC}F_{CG}+q_{BC}Q^i_{CG}+r_{BC}\delta_{CG}+s_{BC}F_{BC}, \tag{6}$$

where Q^s_{BC} is the steam output, and F_{BC} is the natural gas consumption for supplemental firing. The sum of the first three terms denotes the heat recovered from exhaust gas, and the fourth term is the heat generated by supplemental firing. The natural gas consumption F_{BC} is also limited by an upper bound $\overline{F}_{BC}$ as follows:

$$0\le F_{BC}\le\overline{F}_{BC}\delta_{BC}, \tag{7}$$

where δ_{BC} is the binary variable that expresses the on(δ_{BC} = 1)/off(δ_{BC} = 0) status of supplemental firing. In addition, since the upper bound on Q^s_{BC} is affected by steam injection, the following inequality is taken into account:

$$Q^s_{BC}\le p^s_{BC}Q^i_{CG}+q^s_{BC}\delta_{CG}. \tag{8}$$

Furthermore, several relationships must be considered in the formulation. The following energy balance relationship is obtained regarding the heat generated by the waste heat boiler:

$$Q^s_{BC}=Q^s_{SH}+Q^s_{CC}, \tag{9}$$

where Q^s_{SH} is the heat sent to the superheater for steam injection, and Q^s_{CC} is the heat supplied to the outside of the STIG unit. As the performance characteristic of the superheater, a proportional relationship between Q^i_{CG} and Q^s_{SH} is also taken into account; i.e.,

$$Q^i_{CG}=p_{SH}Q^s_{SH}. \tag{10}$$

At a part-load status of the STIG unit, steam injection and supplemental firing are not executed simultaneously. This condition is satisfied by

$$\delta^i_{CG}+\delta_{BC}\le\delta_{CG}+F^m_{CG}/\overline{F}^m_{CG}. \tag{11}$$

The electricity to drive auxiliary machinery of the STIG generator and the waste heat boiler, E^a_{CG} and E^a_{BC}, is approximated by

$$E^a_{CG}=p^a_{CG}F_{CG}+q^a_{CG}\delta_{CG} \tag{12}$$

and

$$E^a_{BC}=p^a_{BC}Q^s_{BC}+q^a_{BC}\delta_{CG}, \tag{13}$$

respectively. The total consumption of natural gas F_{CC} and that of electricity E^a_{CC} are given by

$$F_{CC}=F_{CG}+F_{BC} \tag{14}$$

and

$$E^a_{CC}=E^a_{CG}+E^a_{BC}, \tag{15}$$

respectively. The feedwater consumption W_{BC} can be related with the heat of injected steam Q^i_{CG} as follows:

$$W_{BC}=t_{CG}Q^i_{CG}. \tag{16}$$

These equations express the performance characteristics of each operating region A to C in Fig. 2 by adopting the three binary variables. Independent variables to be determined are the natural gas consumption of the STIG generator F_{CG}, the heat of injected steam Q^i_{CG}, and the natural gas consumption for supplemental firing F_{BC}. Other variables are considered as dependent variables.

Downloaded 02 Jun 2010 to 171.66.16.102. Redistribution subject to ASME license or copyright; see http://www.asme.org/terms/Terms_Use.cfm

Planning Model for Total Plant. A summary is described on the operational planning model for the total cogeneration plant in Fig. 3. First, the performance characteristics of each piece of constituent equipment are formulated in the same way as stated in the previous section. Next, energy balance and supply-demand relationships are formulated for each energy flow in Fig. 3. These relationships are considered as constraints to be satisfied in the present optimization problem. The objective function to be minimized is the hourly running cost given by

J = (Energy charge of natural gas) + (Energy charge of purchased electricity) − (Income from sold electricity) + (Charge of feedwater), (17)

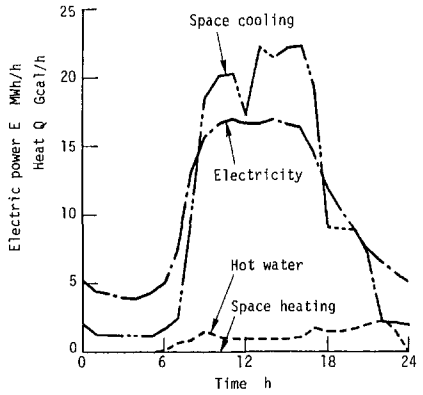

Fig. 4 Energy demand pattern on representative weekday in August

Table 1 Alternatives concerning plant structures

Table 1(*a*) STIG plants

Number of gas turbine units: Steam injected		1	1	2	1	2	3
Number of gas turbine units: Simple cycle		0	1	0	2	1	0
Number of gas turbine units: Total		1	2		3		
Number of auxiliary boilers		3	2		2		
Number of refrigerators: Absorption type	Number of refrigerators: Compression type						
6	0	C1G0E0	C1G1E0	C2G0E0	C1G2E0	C2G1E0	C3G0E0
4	2	C1G0E2	C1G1E2	C2G0E2	C1G2E2	C2G1E2	C3G0E2

Table 1(*b*) Simple-cycle plants and conventional energy supply plants

Number of simple cycle gas turbine units		1	2	3	4	5	0
Number of auxiliary boilers		3	2	2	1	1	3
Number of refrigerators: Absorption type	Number of refrigerators: Compression type						
6	0	G1E0	G2E0	G3E0	G4E0	G5E0	G0E0
4	2	G1E2	G2E2	G3E2	G4E2	G5E2	–

where it is necessary to include the fourth term in the objective function, because the feedwater used for steam injection must be treated with chemicals in advance, its price is relatively high, and it cannot be reused. Unknown variables to be determined by the optimization calculation include binary and continuous variables that correspond to the on/off status and load level of equipment, respectively.

This optimization problem results in a mixed-integer linear programming problem (Garfinkel and Nemhauser, 1972), and it can be solved using an algorithm based on the branch and bound method (Land and Doig, 1960).

Evaluation of Economics and Energy Saving. The long-term economics of plants are evaluated on the basis of the annualized costs method (Witte et al., 1988); i.e., the annual total cost is adopted as an evaluation criterion. The annual total cost is calculated as the sum of the annual capital and running costs. The annual capital cost is determined by multiplying the initial capital cost of equipment by a capital recovery factor calculated from a life of equipment and an interest rate. A salvage value of equipment may be included in this evaluation. The annual running cost is calculated by summing up each hourly running cost through one year, and by adding the demand charge of purchased electricity and natural gas. The energy saving is evaluated from the annual consumption of primary energy.

Case Study

A case study is carried out on STIG plants used for district heating and cooling. Here, several properties of the plants are investigated by comparing them with those of simple-cycle plants and conventional energy supply ones.

Input Data. The energy supplied area consists of four office buildings and two hotels. A weekday, a Saturday, and a holiday are considered as representative days for each month; i.e., the operational strategy is investigated for 36 representative days throughout one year. Hourly energy demand is given as input data for each representative day. For example, Fig. 4 shows the energy demand pattern estimated on the weekday in August.

Tables 1(*a*) and 1(*b*) show several alternatives concerning the structures of STIG plants, and simple-cycle plants or conventional energy supply plants, respectively. In the case names, *C*, *G*, and *E* denote the numbers of STIG units, simple-cycle gas turbine units, and electric compression refrigerators, respectively. According to these numbers, the numbers of auxiliary boilers and steam absorption refrigerators are also determined. As shown in this table, several cases are investigated by changing the number of gas turbine units, and the combination of both electric compression and steam absorption refrigerators. Table 2 shows the performance characteristics of a STIG unit using the data for each operating point

Table 2 Performance characteristics of a STIG unit

Operating point				①	②	③	④	⑤	⑥
Electrical output		E_{GC}	MW	5.388	5.388	3.562	3.562	0.890	0.890
Electric power for auxiliary machinery	Gas turbine	E^{a}_{GG}	MW	0.150	0.150	0.143	0.143	0.102	0.102
	Waste heat boiler	E^{a}_{BC}	MW	0.032	0.094	0.039	0.073	0.016	0.073
	Total	E^{a}_{CC}	MW	0.182	0.244	0.182	0.216	0.118	0.175
Injected steam		Q^{I}_{GG}	Gcal/h	6.726	6.726	0.0	0.0	0.0	0.0
Steam input to superheater		Q^{S}_{SH}	Gcal/h	5.465	5.465	0.0	0.0	0.0	0.0
Steam output from waste heat boiler		Q^{S}_{BC}	Gcal/h	5.660	16.376	6.830	12.815	2.732	12.816
Steam output from unit		Q^{S}_{CC}	Gcal/h	0.195	10.911	6.830	12.815	2.732	12.816
Natural gas consumption	Gas turbine	F^{B}_{GG}	$\times 10^3$Nm^3/h	1.136	1.136	1.136	1.136	0.555	0.555
		F^{I}_{GG}	$\times 10^3$Nm^3/h	0.090	0.090	0.0	0.0	0.0	0.0
		F_{GG}	$\times 10^3$Nm^3/h	1.226	1.226	1.136	1.136	0.555	0.555
	Waste heat boiler	F_{BC}	$\times 10^3$Nm^3/h	0.0	1.115	0.0	0.623	0.0	1.050
	Total	F_{GC}	$\times 10^3$Nm^3/h	1.226	2.342	1.136	1.758	0.555	1.605

Downloaded 02 Jun 2010 to 171.66.16.102. Redistribution subject to ASME license or copyright; see http://www.asme.org/terms/Terms_Use.cfm

① to ⑥ in Fig. 2. For other kinds of equipment, the performance characteristics are omitted, and only their capacities are given in Table 3.

For each alternative stated above, two cases are investigated; i.e., one is the case where selling electricity is accepted, and the other is the case where selling electricity is forbidden. The tariff of utilities used in the study is shown in Table 4. Two kinds of tariff are used concerning purchased electricity. Tariff I is based on the time-of-use pricing. According to tariff II, the electricity price is constant except for the summer season. If selling electricity is accepted, the price of sold electricity is assumed to be equal to that of purchased electricity by considering that an electric power company operates the cogeneration plant. In evaluating the annual capital cost of equipment, the life and salvage value are assumed as 15 years and zero, respectively. In the evaluation of the annual primary energy consumption, the overall thermal efficiency of purchased electricity is assumed as 35 percent.

Results and Considerations. As far as no special remark is given, the following result corresponds to the case where only steam absorption refrigerators are installed, selling electricity is forbidden, and tariff II is adopted for purchased electricity.

Operational Patterns. Figure 5 shows the optimal operational pattern of electricity supply on the representative weekday in August for the case C2G0E0. Figures 5(*a*) and 5(*b*) correspond to tariffs I and II, respectively. In these figures, E_{CC1} and E_{CC2} are the electric power generated by the first and the second STIG generators, respectively, and E_{buy} is the purchased electric power. Tariff I keeps both of the STIG generators shut down at night, because the price of purchased electricity is very low during the period. On the other hand, tariff II keeps one of the STIG generators operating even at night, because the price of purchased electricity is constant through the day. In both cases, STIG generators operate at the rated load level without steam injection during the period with high thermal energy demand. However, during the period with low thermal energy demand, they increase electrical output by steam injection so as not to produce any surplus steam.

Table 3 Capacities of constituent equipment

Equipment		Capacity
Gas turbine generator	Steam injected	5.39 MW (With steam injection)
	Simple cycle	3.45 MW
Auxiliary boiler		8.09 Gcal/h
Refrigerator		4.84 Gcal/h

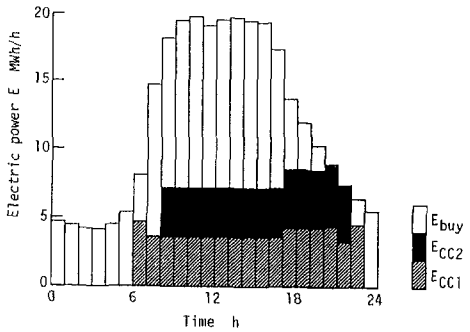

Fig. 5(*a*) Tariff I adopted

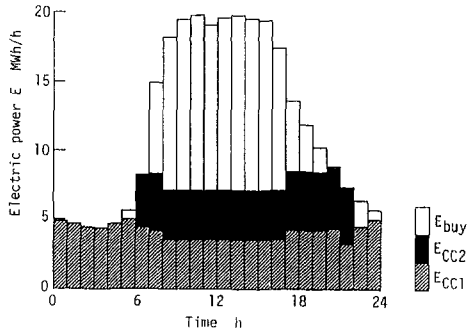

Fig. 5(*b*) Tariff II adopted

Fig. 5 Optimal operational pattern of electricity supply on representative weekday in August for case C2G0E0

Figure 6 shows the operating points of the first STIG unit for the case C2G0E0. Figures 6(*a*) and 6(*b*) correspond to the cases where selling electricity is accepted or forbidden, respectively. In these figures, Q^{s}_{CC1} is the steam output of the first STIG unit. A circle whose area is proportional to the annual operational hour is drawn on each operating point. Figure 6(*a*) shows that the unit operates almost at the rated load status with or without steam injection because it is possible to sell surplus electricity to an outside electric power company. On the other hand, Fig. 6(*b*) shows that the unit sometimes operates at part-load status with steam injection so as to satisfy the required energy demands without selling surplus electricity.

Annual Total Results. Figure 7 shows a comparison among several cases with respect to the reduction rate of annual running cost α. The reduction rate of annual running cost is calculated by

$$(\text{Reduction rate}) = \frac{\left(\begin{matrix}\text{Value of}\\ \text{conventional plant}\end{matrix}\right) - \left(\begin{matrix}\text{Value of}\\ \text{cogeneration plant}\end{matrix}\right)}{\left(\begin{matrix}\text{Value of}\\ \text{conventional plant}\end{matrix}\right)} \times 100. \quad (18)$$

Table 4 Tariff of utilities

Utility		Customer charge	Demand charge	Energy charge
Natural gas		36×10^3 yen/month	1.50×10^3 yen/(Nm³/h·month) (Apr.~Oct.) 3.72×10^3 yen/(Nm³/h·month) (Other months)	34.34 yen/Nm³
Purchased electricity	Tariff I	–	1.827×10^3 yen/(kW·month)	17.045 yen/kWh (Period A*1) 12.815 yen/kWh (Period B*2) 7.300 yen/kWh (Period C*3)
	Tariff II	–	1.827×10^3 yen/(kW·month)	11.550 yen/kWh (July~Sept.) 10.500 yen/kWh (Other months)

*1 Period A: 10~17 h on weekdays and Saturdays in July~Sept.
*2 Period B: 8~22 h on weekdays and Saturdays except period A
*3 Period C: except periods A and B

Downloaded 02 Jun 2010 to 171.66.16.102. Redistribution subject to ASME license or copyright; see http://www.asme.org/terms/Terms_Use.cfm

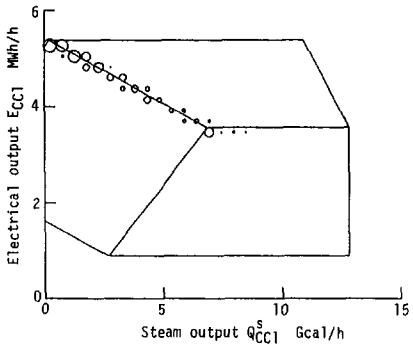

Fig. 6(*a*) Selling electricity accepted

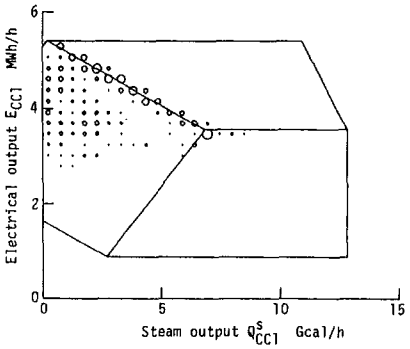

Fig. 6(*b*) Selling electricity forbidden

Fig. 6 Operating points of the first STIG unit for case C2G0E0

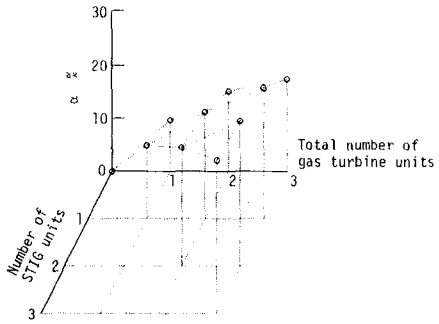

Fig. 7 Relationship between reduction rate of annual running cost α and number of gas turbine units

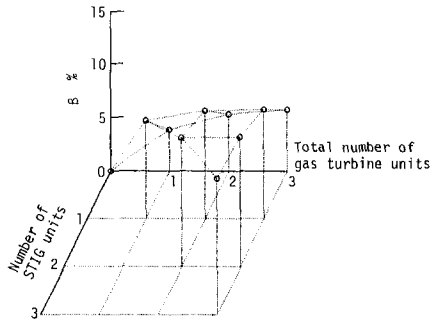

Fig. 8 Relationship between annual rate of energy saving β and number of gas turbine units

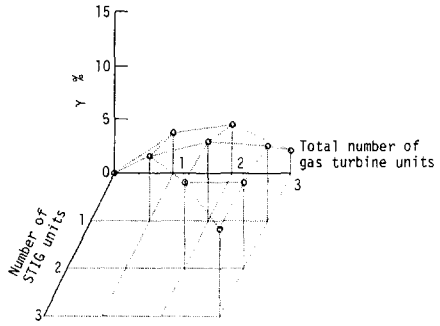

Fig. 9(*a*) Corresponding to Fig. 7 and Fig. 8

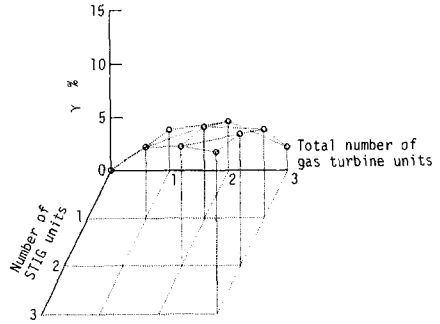

Fig. 9(*b*) Selling electricity accepted

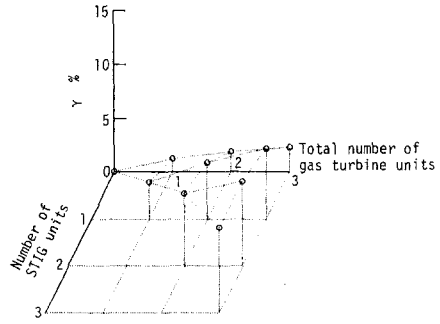

Fig. 9(*c*) Two electric compression refrigerators installed

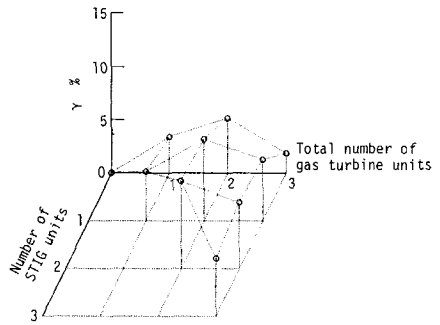

Fig. 9(*d*) Tariff I adopted

Fig. 9 Relationship between reduction rate of annual total cost γ and number of gas turbine units

Thus the reduction rate means how the cogeneration plant is superior as compared with the conventional plant. In Fig. 7, the origin corresponds to the conventional plant, and the points with zero STIG unit correspond to the simple cycle plants. As the number of gas turbine units increases, the operational flexibility becomes higher, and consequently the annual running cost is reduced. The introduction of STIG units gives more reduction in the annual running cost because of their high flexibility regarding the heat to power ratio. Figure 8 shows a comparison among several cases with respect to the annual rate of energy saving β. The annual rate of energy saving is defined as the reduction rate of annual primary energy consumption, and it is also calculated by Eq. (18). Similarly, the effectiveness of introducing STIG units is shown in Fig. 8.

Figure 9 shows a comparison among several cases with re-

Downloaded 02 Jun 2010 to 171.66.16.102. Redistribution subject to ASME license or copyright; see http://www.asme.org/terms/Terms_Use.cfm

spect to the reduction rate of annual total cost γ. The annual total cost of the conventional plant is about 1.80×10^9 yen/y. The minimum value of the annual total cost among all cases is about 1.51×10^9 yen/y for the case C3G0E0 in Fig. 9(*b*). If selling electricity is forbidden, the minimum value of the annual total cost is about 1.64×10^9 yen/y for the case C3G0E0 in Fig. 9(*a*). As stated above, in the case of STIG plants, the annual total cost is minimized by installing three gas turbine units. On the other hand, in the case of simple cycle plants, the annual total cost is minimized by installing only two gas turbine units. For example, the annual total cost is about 1.70×10^9 yen/y for case G2E0 in Figs. 9(*a*) and 9(*b*). This is because the increase in the annual capital cost dominates the decrease in the annual running cost as the number of gas turbine units increases. Figure 9(*c*) corresponds to the cases with two electric compression refrigerators and four steam absorption ones, and it shows a different situation as compared with Fig. 9(*a*). Figure 9(*d*) corresponds to the cases where tariff I is adopted. The annual total cost is minimized by installing two STIG units, and its minimum value is 1.66×10^9 yen/y for the case C2G0E0. This is because the price of purchased electricity is very low at night, and consequently the over-installation of STIG units leads only to the increase in the capital cost.

Conclusions

An optimal planning method on the basis of the mixed-integer linear programming has been proposed to determine the operational strategy for cogeneration plants with steam-injected gas turbines. Using the method, a case study has been carried out on a plant used for district heating and cooling. Through the study, the economical and energy-saving aspects of steam-injected gas turbine plants have been evaluated by comparing them with those of simple-cycle gas turbine plus waste heat boiler plants and conventional energy supply ones. The following main results have been obtained:

1 Steam-injected gas turbine plants have high flexibility regarding the heat to power ratio. In order to make positive use of this superiority, it is necessary to introduce an intelligent operational strategy. The method proposed in the present paper enables us to determine their operational strategy rationally and easily.

2 The economical and energy-saving aspects of cogeneration plants for district heating and cooling are affected by energy demands, plant structures, utility tariff, etc. The present case study shows that steam-injected gas turbine plants can be attractive from economical and energy saving viewpoints as compared with both simple-cycle gas turbine plus waste heat boiler plants and conventional energy supply ones.

Acknowledgments

The authors would like to thank Mr. H. Abe, an engineer of Takenaka Corporation, for his contribution to the present research.

References

Baken, J. A. M., and Haspel, B. van den, 1988, "Optimised Operation of Steam-Injected Gas Turbine Cogeneration Units," *Proc. of the 2nd International Symposium on Turbomachinery, Combined-Cycle Technologies and Cogeneration (1988 ASME COGEN-TURBO II)*, pp. 259-265.

Brown, D. H., and Cohn, A., 1981, "An Evaluation of Steam Injected Combustion Turbine Systems," ASME JOURNAL OF ENGINEERING FOR POWER, Vol. 103, pp. 13-19.

Fraize, W. E., and Kinney, C., 1979, "Effects of Steam Injection on the Performance of Gas Turbine Power Cycles," ASME JOURNAL OF ENGINEERING FOR POWER, Vol. 101, pp. 217-227.

Garfinkel, R. S., and Nemhauser, G. L., 1972, *Integer Programming*, Wiley, New York, pp. 5-7.

Ito, K., Yokoyama, R., Horii, S., Matsumoto, Y., and Akagi, S., 1987, "An Optimal Operational Planning Model for Gas Turbine Cogeneration Plants," *Proc. of the 1987 Tokyo International Gas Turbine Congress*, Vol. I, pp. 97-104.

Ito, K., Yokoyama, R., Yamaguchi, T., Matsumoto, Y., and Akagi, S., 1988, "Optimal Operational Planning of a Gas Turbine Combined Heat and Power Plant Based on the Mixed-Integer Programming," *Proc. of the IFAC International Symposium on Power Systems Modelling and Control Applications*, pp. 13.4.1-13.4.7.

Ito, K., Yokoyama, R., Akagi, S., and Matsumoto, Y., 1990, "Influence of Fuel Cost on the Operation of a Gas Turbine-Waste Heat Boiler Cogeneration Plant," ASME JOURNAL OF ENGINEERING FOR GAS TURBINES AND POWER, Vol. 112, pp. 122-128.

Land, A. H., and Doig, A. G., 1960, "An Automatic Method of Solving Discrete Programming Problems," *Econometrica*, Vol. 28, pp. 497-520.

Larson, E. D., and Williams, R. H., 1987, "Steam-Injected Gas Turbines," ASME JOURNAL OF ENGINEERING FOR GAS TURBINES AND POWER, Vol. 109, pp. 55-63.

Maher, K. J., Ehmke, H. J., and Gibson, D. C., 1987, "Optimum Operation of a Steam Injected Gas Turbine," presented at USSR/Australia Workshop on Advanced Energy Technologies.

Witte, L. C., Schmidt, P. S., and Brown, D. R., 1988, *Industrial Energy Management and Utilization*, Hemisphere Publ., Washington, DC, pp. 68-69.

Downloaded 02 Jun 2010 to 171.66.16.102. Redistribution subject to ASME license or copyright; see http://www.asme.org/terms/Terms_Use.cfm

The Compression of Fuel Gas for Turbines, Engines, and Boilers in Cogeneration Plants

I. M. Arbon
Caledonian Compressors Limited,
Glasgow, United Kingdom

The proliferation of gas-fired cogeneration plants in recent years had led to many installations being located on sites remote from high-pressure gas pipelines. Since it is often impractical or not cost effective to provide a dedicated high-pressure gas supply, such installations are often based close to alternative sources of fuel, such as small natural gas wells, landfill sites, or sewage digester plants. This paper will look at typical gas sources and composition, requirements of the fired equipment, the types of fuel gas compressors normally used, methods of compressor capacity control, and the development of synthetic and semi-synthetic lubricants for fuel gas compression duty.

Typical Gas Source and Composition

Natural Gas Wells. There are still enormous natural gas resources within the earth's crust. In the case of large gas fields, it is cost effective to gather gas from numerous wells and transport it by pipeline (or as LNG) to the two major areas of consumption, namely North America and Western Europe. Smaller fields, however, are more suited to the installation of a local user of the gas, e.g., a cogeneration or CHP (combined heat and power) plant.

Presently, natural gas is mainly obtained directly from wells drilled into natural gas rock strata. A major secondary source is "associated" gas, which is gas stripped from flowing crude oil coming from oil wells. In the past, this gas was often wasted by flaring, but now, to an ever-increasing degree, this is being avoided by using the gas as fuel or feedstock. This "associated" gas is processed as follows: (*a*) removal of natural gas liquids; (*b*) dehydration; (*c*) desulfurization and use.

For typical gas analyses, see Fig. 1(*a*).

Town Gas Mains. Although traditional "coal gas" is rarely used nowadays in the developed world, in certain parts of the world, notably Japan, the gas available in some town mains is still derived from the naphtha cracking process. In other parts, particularly Western Europe, and to an increasing extent in Japan, the former coal gas mains have been converted for use with natural gas. In either case, the gas pressure available in the main is insufficient for injection into gas turbines, although it may be adequate for gas reciprocating engines.

Typical gas analyses are shown in Fig. 1(*a*).

Refinery Waste Gas. For many years, waste gases, off gases, tail gases, etc., in refineries and petrochemical plants have been wasted by flaring, despite the fact that they are usually high in hydrocarbons and often have high calorific values. There is now a growing interest in utilizing these gases as a fuel for use in boilers, gas engines, and gas turbines. In most cases, this requires compression from around atmospheric pressure up to the required injection pressure for the fired equipment.

One of the main characteristics of this type of duty is that various different gas streams are combined and the composition, molar mass, and isentropic exponent of the gas will vary considerably. This means that the only practical compressor that can be used is the positive displacement type, due to the severe operational problems variation in molar mass causes for dynamic compressors.

In this application, gas compositions vary enormously, but some examples are shown in Fig. 2(*a*).

Landfill Sites. The indiscriminate dumping of refuse on land is an age-old practice still widely followed, particularly in small communities. However, the unsightliness of dumping grounds and the unavoidable presence of flies, rats, smoke, and odors led to the development of more efficient and sanitary methods. The most common method, known as "sanitary landfill" was a procedure first introduced in England in 1912. The traditional way of building a landfill site, on flat land, is the trench method shown in Fig. 3. It is increasingly common, however, for landfill sites to be located against a hillside, as shown in Fig. 4, and it is largely this type that is described in the remainder of this section, although the same principles apply to either.

Sanitary landfill makes use of the natural fermentation brought about by micro-organisms in the putrescible portion of the refuse. Usually the refuse is deposited in shallow layers, compacted, and covered within 24 hours with com-

Contributed by the International Gas Turbine Institute and presented at the International Cogen-Turbo Power Congress and Exhibition, Bournemouth, United Kingdom, September 21–23, 1993. Manuscript received at ASME Headquarters June 1993. Associate Technical Editor: H. Lukas.

Copyright © 1995 by ASME

Downloaded 02 Jun 2010 to 171.66.16.102. Redistribution subject to ASME license or copyright; see http://www.asme.org/terms/Terms_Use.cfm

	UK	TX,USA	D(1)	D(2)	I	E	J(naptha)	J(LNG)
CH_4	92.8	49.2	82.5	82.0	93.8	89.9	89.5	28.7
C_2H_6	2.8	17.7	5.5	3.3	2.4	4.5	9.7	4.6
C_3H_8	0.6	7.5	4.5	0.6	0.6	1.1	0.3	0.8
C_4H_{10}	0.2	7.0	2.5	0.3	0.2	0.4	0.2	0.2
C_5+	0.1	12.5	2.0	-.-	0.1	0.2	-.-	-.-
CO_2	0.4	1.5	.75	1.2	0.5	0.7	-.-	15.1
CO	-.-	-.-	-.-	-.-	-.-	-.-	-.-	3.4
N_2	3.1	2.5	-.-	12.6	2.4	3.2	0.3	7.9
O_2	-.-	-.-	-.-	-.-	-.-	-.-	-.-	1.9
H_2	-.-	-.-	.5	-.-	-.-	-.-	-.-	37.4
H_2S	tr.	tr.	.25	-.-	-.-	-.-	-.-	-.-
H_2O	50. ppm	2.1	1.5	sat.	sat.	sat.	sat.	sat.

Fig. 1(*a*) Typical natural gas compositions (fuel gas service)—worldwide sites

	Phil., PA	L.A. County, CA		Blanchet	Ham	Bray	Cagliostro	Elzy
		Puente Hills	B.K.K.					
CH_4	54.0	36.6	32.1	44.0	47.5	50.0	53.4	50.0
C_xH_x					0.3		0.17	
CO_2	45.0	36.6	28.2	34.2	47.0	35.0	34.3	42.5
CO					0.1		0.005	
N_2	--	14.5	29.9	20.8	3.7	13.0	6.2	5.4
O_2	--	3.8	4.6	1.0	0.8	1.7	0.05	0.2
H_2					0.1		0.005	1.9
N_2O_2	1.0	trace						
H_2S	--	--	trace	0.75	0.01	0.3	0.005	-.-
H_2O	sat.	sat.	sat.					

These gases also contain traces of a large variety of salts, bromides, benzenes and numerous other chemicals.

Fig. 1(*b*) Typical landfill gas compositions

GAS	UK	SPAIN	LIBYA	AL,USA	MI,USA
CH_4	11.93	21.9	1.8	15.80	11.81
C_2H_6	0.43	25.5	7.6	5.90	5.91
C_3H_8	0.63	10.6	38.2	6.40	2.95
C_4H_{10}	1.21	4.4	37.7	7.21	1.96
C_5+	0.69	1.5	12.9	2.94	-.-
CO	-.-	0.1	-.-	-.-	-.-
CO_2	-.-	0.1	1.5	51.23	68.90
H_2	69.53	28.3	-.-	-.-	-.-
O_2	-.-	0.5	-.-	-.-	-.-
N_2	-.-	5.9	0.1	0.42	1.97
NH_3	1.66	-.-	-.-	-.-	-.-
H_2S	13.49	1.2	-.-	10.10	4.92
H_2O	0.43	sat.	0.2	sat.	1.58

Fig. 2(*a*) Typical refinergy waste gas compositions

	City of Los Angeles California, USA	City of Seoul Korea	City of Chicago Illinois, USA
Pressure (abs.)	0.98 bar	1.01 bar	not known
Temperature	32°C (90°F)	35°C	not known
Relative humidity	saturated	saturated	saturated
Constituent	**Percent by Volume**		
CH_4	60-64%	60%	57%
CO_2	36-35%	35%	33%
H_2O	4-1%	sat.	5.5%
H_2	--	3%	1%
N_2	--	--	3%
O_2	--	1%	--
C_nH_n	<1,000 ppm	--	--
H_2S	<3,500 ppm	500ppm	0.5%
Trace Elements ($\mu g/m^3$)	Cl <10 Zn <3 Na <80 Ca <10 K <18 Mg <8 V <40 Cu <4 Pb <20 Cd <3 Fe <10 As <80		

Fig. 2(*b*) Typical digester gas compositions

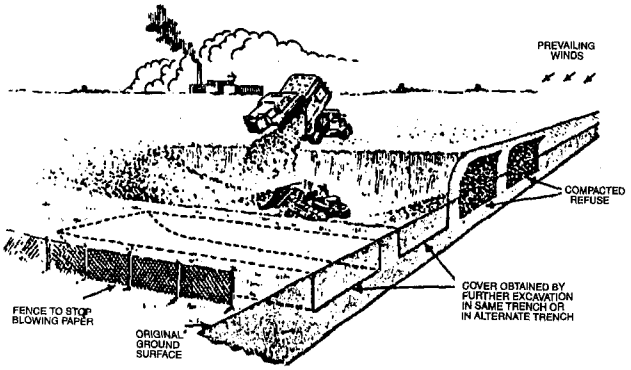

Fig. 3 Trench method of sanitary landfill used to dispose of refuse in a flat land area

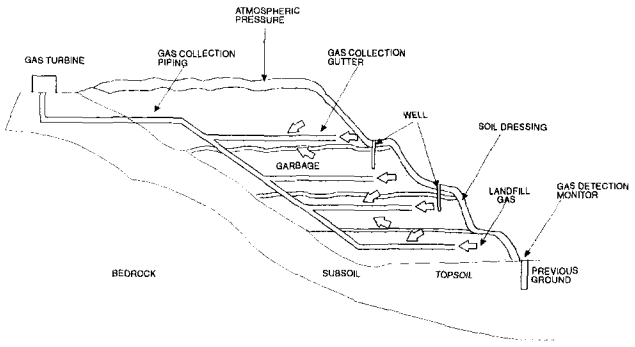

Fig. 4 Typical hillside landfill site with gas recovery system

pacted earth or other chemically inert material to form an effective seal. Mechanical equipment such as a bulldozer is used to grade, compact, and cover the refuse.

Sanitary landfill is still far and away the most popular method of waste disposal in the USA. According to the EPA, there are currently about 10,000 such facilities in public use in the United States.

Landfill uses a procedure that ensures effective use of the land. When a refuse truck arrives, it can unload only at a designated spot. This is the working face and is the only area of the landfill where refuse is exposed during a working day. Although varying in size, a typical working face is about 12 m

Downloaded 02 Jun 2010 to 171.66.16.102. Redistribution subject to ASME license or copyright; see http://www.asme.org/terms/Terms_Use.cfm

(40 ft) high and 30 m (100 ft) wide. At the end of the working day, the exposed refuse is covered again.

As the refuse decays, a gas (LFG) is produced, predominantly methane and carbon dioxide, which, if not collected, can lead to explosions in the landfill; historically, the LFG had to be flared, which can lead to environmental pollution. On the other hand, because of the high methane content of LFG (see typical analyses in Fig. 1*b*), making it similar to natural gas, it can be used as a fuel in gas turbines, reciprocating engines, or boilers.

Following a decision to use LFG as a fuel, and before the landfill site is begun, suitable gas collection piping must be laid throughout the whole site. These pipes are connected, as headers, to mesh "gutters," which are embedded in the refuse layers. As the refuse is dumped, it is spread around and over the gutters until the predetermined depth of the layer is reached. The refuse layer is then covered with a layer of ground soil and the whole process is repeated several times, until a cross section through the landfill will resemble a multilayer sandwich (see Fig. 4). Gas gutters and collection pipes are incorporated in each layer of refuse and connected together to provide a supply network for the gas that forms through a natural anaerobic biological reaction as the refuse decomposes. In some cases, this natural reaction may be accelerated by the use of suitable catalysts.

Since most landfill sites are relatively small, reciprocating engines have more commonly been used in the past, although there is now a significant number of installations using gas turbines, particularly in the USA.

Obviously, the most important consideration for compression of such gases is that the materials of construction can withstand the corrosive characteristics of the trace elements in the landfill gas. For this reason, oil-injected compressors are often preferred due to the protective effect of the oil film coating all surfaces in such compressors. The oil is almost totally removed (< 1 ppm remaining) from the gas in a separator system before the gas is injected into the engine or turbine.

Sewage Digester Plants. Sewage sludge is the accumulated settled solids deposited in tanks or basins and containing a varying amount of water to form a semiliquid mass. The various sludges are: primary sludge, chemically precipitated sludge, trickling filter secondary sludge, excess activated sludge, and digested sludge.

Sludge may be hauled or pumped to sea, dewatered on vacuum filters, and incinerated or sold for fertilizer immediately after removal from the sewage-treatment process, or it may be digested by micro-organisms under controlled conditions to reduce the organic content prior to ultimate disposal. Digestion tanks are usually circular, with diameter as required and 5 m to 8 m deep. They are usually heated to about 35°C (95°F), the optimum temperature for the micro-organisms that decompose the organic matter. A standard design provides for 0.05–0.08 m^3 (2–3 ft^3) of heated digestion tank per person contributing to the sewers; twice that volume is required for unheated tanks. About 30 days is normally needed for complete digestion in a heated tank.

In the process of digestion the micro-organisms produce, for each person contributing to the sewers, from 0.015 to 0.035 m^3 (0.5 to 1.3 ft^3) of carbon dioxide and methane per day. This gas may be collected and used to heat the digestion tanks and buildings and/or in gas engines/turbines that drive generators, sewage pumps, and air compressors.

Rotary sliding-vane gas compressors have proved ideal for anaerobic digester gas mixing because of their ability to handle corrosive gases. In most cases, the compressor is used to raise the gas pressure to the level needed to overcome the total depth of the sludge. The compressor discharges the gas into the draft tube at the bottom of the digester, thus allowing the gas to circulate and permeate through the sludge to the top of the digester. This often allows a plant to increase the sludge capacity by increasing bacterial activity without an increase in physical plant size.

Sliding-vane gas compressors may also be used as boosters for reciprocating engine fuel gas systems or as the first-stage compressor in a two-stage gas turbine fuel gas system. A typical compression process P & I diagram for a two-stage system is shown in Fig. 5.

The system illustrated in Fig. 5 uses a sliding-vane compressor to draw the gas, under vacuum conditions, through the primary scrubber system and then exhaust the gas at an absolute pressure of 3–4 bar (40–60 psia) through the secondary scrubber. The gas is usually cooled in a shell-and-tube heat exchanger before the secondary scrubber to remove any condensable constituents. The second-stage compressor is an oil-injected screw-type, which raises the gas to a suitable pressure (in this case 21 bar) for injection into a gas turbine. The compressor thus converts low-pressure digester gas into a usable fuel for gas engines or turbines for on-site generation of electrical power. Generally enough power is produced to operate almost all process equipment and to provide heat and light.

Digested sludge or activated sludge filter cake can be dehydrated in heat dryers and then bagged or sold in bulk as organic fertilizer. All sludge cake can be incinerated and there is usually sufficient heat value in the sludge to carry on the incineration process without further addition of fuel, once the incinerator has been brought to operating temperature. Sludge may be hauled to dumping grounds, or pumped to suitable areas at sea.

Some typical digester gas compositions are shown in Fig. 2(*b*).

Requirements of Fired Equipment

As already discussed, there are three main items of gas-fired equipment used in cogeneration and CHP plants:

Gas Turbines. Many cogeneration and CHP systems use a gas turbine generator at the heart of the system. As described in Section A, the gas supply for the turbine is usually from a low-pressure source, and since gas turbines have typical required injection pressures of 15–25 bar (industrial gas turbines) or 30–45 bar (aeroderivative gas turbines), a gas compressor is required to raise the pressure from close to atmospheric up to injection pressure. Although most compressor types have been tried in this application, the majority of such applications nowadays use rotary screw (particularly oil-injected) or reciprocating compressors.

Historically, one of the major concerns with the oil-injected compressors has been that any carry-over of oil into the turbine could lead to local ignition of the oil in the gas stream with the result that, at best, carbon deposition would lead to deteriorating performance of the turbine, and at worst, could cause hot spots in the combusters, leading to turbine "burn-out." Two significant developments over the past decade have reduced these concerns to a negligible level:

(*a*) The development of high-efficiency separator/filtration systems, which can reduce oil carryover to < 1 ppmv. This topic is not covered in detail in this paper.

(*b*) The development of synthetic and semisynthetic lubricants, which, in addition to their low miscibility with the process gas, have greatly suppressed ignition characteristics, and are even nonflammable in some cases. These lubricants are dealt with in some detail in a later part of this paper.

Gas Engines. There are two types of reciprocating en-

Downloaded 02 Jun 2010 to 171.66.16.102. Redistribution subject to ASME license or copyright; see http://www.asme.org/terms/Terms_Use.cfm

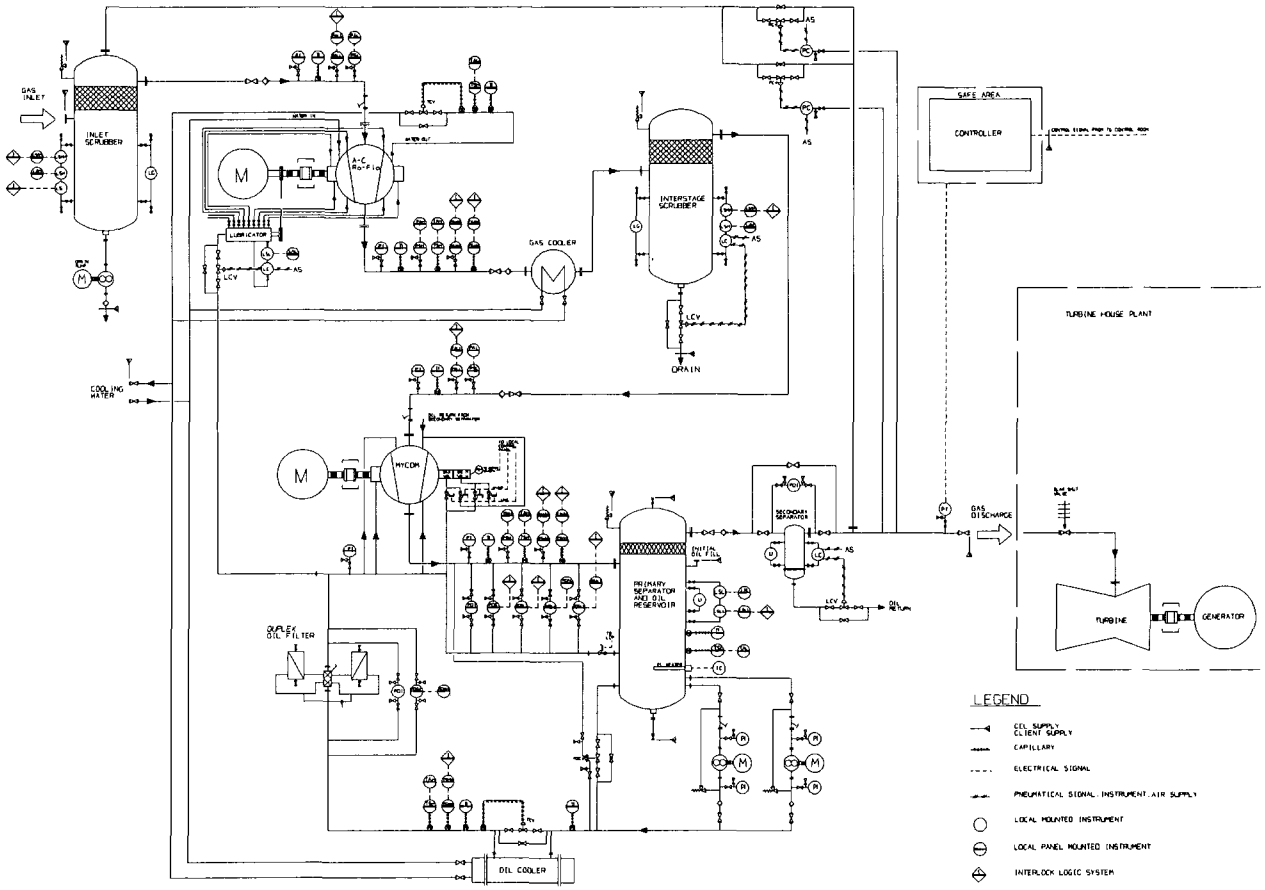

Fig. 5 P & I diagram of typical two-stage fuel gas compressor system using landfill gas

gine for gaseous fuel: the compression-ignition dual fuel engine and the spark ignition engine. The dual fuel engine operates on either gas and oil or diesel fuel and can change fuel while running. The spark ignition engine runs only on gas. Turbocharging and gas injection at pressure give higher thermal efficiencies in a spark ignition engine but the cost must be weighed against that of the cheaper naturally aspirated engine. Gas engines tend to give less clean combustion than gas turbines; while exhaust gas cleaning can be used, this is always an extra cost.

Fuel gas can be supplied to a gas engine at three different pressure levels:

- at just above atmospheric pressure, in a spark-ignited engine, with gas/air mixing prior to any turbocharging;
- at absolute pressures of 4–5 bar, for gas/air mixing after the turbocharger;
- at 250–300 bar, by direct injection into the cylinder of larger engines (the "gas diesel" technology).

The most commonly applied of these methods in cogeneration plants having > 1 MW power output is the second. In recent times, however, there have been important developments in the high-pressure injection method. Following the successful operation of several pilot plants, commercial scale installations of increasing size have been commissioned. A plant with a 3×5.4 MW electrical output was installed in the USA in 1990 and a 7.2 MW plant in Sweden in 1992. The largest plant to date is currently being installed at a United Kingdom site and uses British Natural Gas (for typical gas analysis see Fig. 1*a*) in two reciprocating engines, which each have an electrical output of 16 MW. Each engine is supplied with fuel gas at 275 bar by a five-stage reciprocating compressor.

Gas-Fired Boilers. Most gas-fired boilers available today are suitable for use with most of the gases referenced in this paper. The only real concern is with trace elements in some of the gas compositions and materials of construction of boilers and burners should be checked for compatibility.

The required gas supply pressure to the boiler is determined by the burner nozzle type and design and can vary from slightly above atmospheric up to about 10 bar; many of these applications fall in the range of 3 to 4 bar and, in the case of natural gas, compressors are rarely required. However, landfill gas and sewage digester gas will almost always require some form of compression even in low-pressure boilers; again, a rotary sliding vane is commonly used in this service.

Overview of Compressor Types Normally Used

As mentioned previously, the majority of fuel gas applications require the supply of gas at a constant pressure over a wide range of flow rates. The gas source can also vary significantly in terms of composition and molar mass. This means that the dynamic type of compressor, e.g., centrifugal, is often not suitable for this service, and this paper will only consider the use of positive displacement compressors. There are four main types of p.d. compressors used for fuel gas applications:

(*a*) Reciprocating compressors, which are particularly suitable for high compression ratio applications.

Downloaded 02 Jun 2010 to 171.66.16.102. Redistribution subject to ASME license or copyright; see http://www.asme.org/terms/Terms_Use.cfm

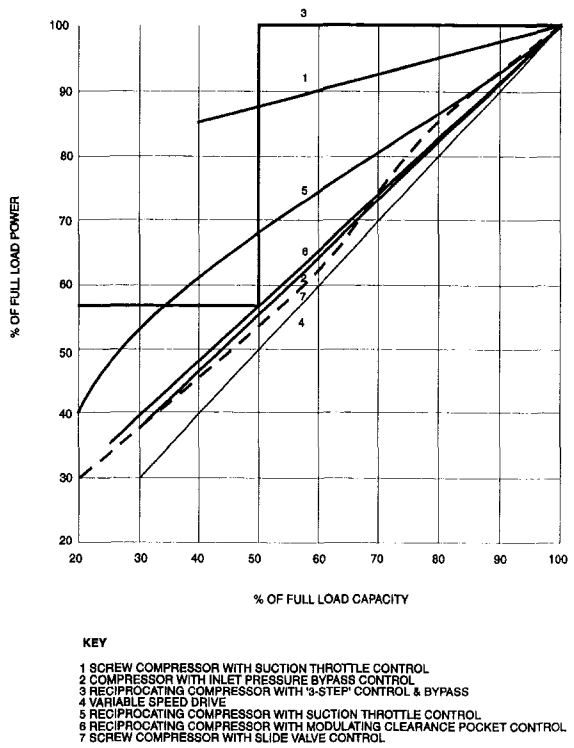

Fig. 6 Comparison of various methods of capacity control

(*b*) "Oil-free" screw compressors, suited to medium compression ratio applications, particularly with "dirty," contaminated or explosive gases.

(*c*) "Oil-injected" screw compressors, suited to medium compression ratio applications, particularly with "sour," "wet," and/or corrosive gases.

(*d*) Rotary, sliding vane compressors, which are particularly suitable for low compression ratio duties.

The application of each of these compressor types in cogeneration service is not considered further here.

Methods of Compressor Capacity Control

Since all of the compressor types under consideration are positive displacement machines, careful consideration must be given to the control system in order to take full advantage of this type of compressor. The various methods of capacity control are shown on a power versus capacity diagram in Fig. 6.

Speed Variation. Speed variation is the most efficient capacity control method for positive displacement compressors. It provides good capacity matching and a power reduction, which follows the reduction in capacity fairly exactly.

With *reciprocating compressors*, particularly if a large speed range is required, care must be taken to provide sufficient flywheel inertia and lubricating oil pump capacity for the lower end of the speed range. Also there is the possibility of mechanical resonances occurring somewhere in the speed range.

Oil-free screw compressors are also best controlled by speed variation; this is usually achieved by using a steam turbine drive, although gas turbines have also been used on occasion.

As with all other compressor types, there is a growing usage of variable-speed electric motors to achieve the same result. At present the capital cost of speed control equipment for electric motors is high and the payback period may not be acceptable.

Discharge Gas Bypass. By this method any excess capacity is diverted from the discharge back to the compressor suction via a suitable aftercooler or bypass cooler. It is a very common method for gas compressor installations and is a relatively inexpensive and effective modulating control system if the operating conditions are relatively stable. A very significant drawback, however, is that the absorbed power of the compressor remains unchanged even if most of the gas is being recirculated. Obviously, if variable conditions exist, this is not the most economical control method.

Suction Throttling. This fully modulating control system comprises a suction throttle valve, which reduces the inlet pressure in response to a reduction in capacity requirement. Although this is a relatively inexpensive and simple system, it suffers from the fact that power reduction is not directly proportional to capacity reduction. Typically, 55 percent inlet capacity corresponds to approximately 70 percent of full load power.

Inlet Gas Bypass. This system allows gas that has been drawn into the compressor to be returned to the suction until the correct capacity is achieved, before compression begins. This reduced capacity is then compressed and discharged in the usual way. This is one of the most efficient methods of capacity control since positive displacement compressors absorb power in proportion to capacity at any given discharge pressure. Available control systems can provide stepless capacity adjustment from 100 down to 10–15 percent with virtually proportional power saving.

The *oil-injected screw compressor* customarily uses this system in its slide-valve capacity control valve. Unlike turbocompressors, screw compressors are not liable to surge and instability in certain operating ranges, and the capacity control slide valve permits operation of the compressor between 10 and 100 percent of the full flow rate. Any of a number of process variables such as suction or discharge pressure can be used to control the slide valve actuator. One compressor manufacturer has also produced an *oil-free screw compressor* with similar slide-valve control, but there have apparently been some operating difficulties due to the lack of lubrication between slide valve and rotors.

Figure 6 shows the effect on volume flow and absorbed power of the operation of the capacity control slide valve. It can be clearly seen that, with this type of compressor, volume flow can be controlled over a very wide range (approximately 10–100 percent), at fixed speed and with power saving almost proportional to the reduction in capacity. Actuation of the slide-valve is usually by a hydraulic piston, although electric servomotors are sometimes used.

The *reciprocating compressor* employs a system often referred to as SRF (stepless reverse flow) control, which performs a similar function to the slide valve down to 15 percent of full load. The delivered gas volume is reduced by holding the suction valve open for a controlled and variable proportion of the delivery stroke, thus modifying the indicator diagram. The volume and power reductions are virtually directly proportional. The system provides stepless capacity control to meet any demand while maintaining constant pressures. Other advantages are constant pressure ratios across all stages, irrespective of capacity, providing better control of temperatures, smaller piping and surge bottles, extended valve life, and extended equipment life in general. Although the initial cost is higher than simple bypass control, savings can be substantial where part load running is required.

Clearance Pocket Regulation (Reciprocating Compressor Only). Volumetric efficiency, the ratio of intake volume to swept volume, is determined by the expansion of gas trapped in the cylinder clearance volume. For a given pressure ratio

Downloaded 02 Jun 2010 to 171.66.16.102. Redistribution subject to ASME license or copyright; see http://www.asme.org/terms/Terms_Use.cfm

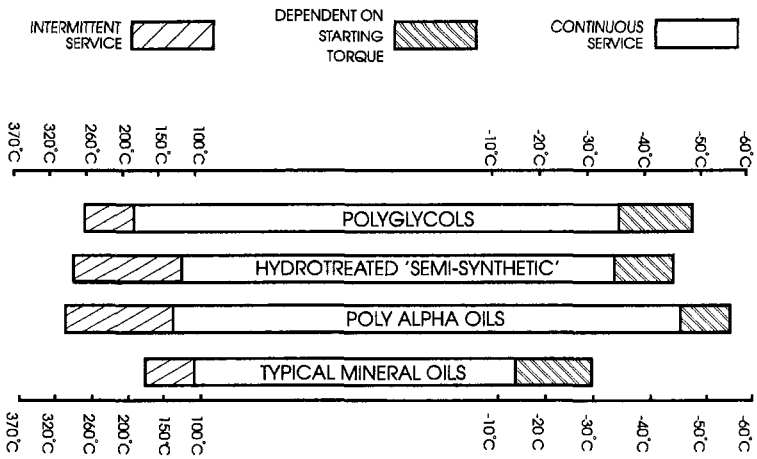

Fig. 7 Comparative temperature limits of mineral oil and synthetic lubricants

an increase in the clearance volume will reduce the volumetric efficiency and hence the capacity of the compressor. Additional clearance is provided in the form of clearance pockets, which are opened or closed by the control system to vary capacity and maintain constant pressure.

In a variation of the design, stepless capacity reduction is achieved by varying the length of time for which the clearance pocket is connected to the cylinder during the compression and expansion periods. Power savings are less than with SRF control but are still significant. This method of capacity control is relatively inexpensive, with good turndown capabilities.

Step Control. This method is used predominantly with reciprocating compressors, although a similar method can be applied to oil-injected screw compressors. In the *reciprocating compressor*, it involves unloading cylinder ends in sequence to reduce capacity. Double-acting reciprocating compressors usually have two or three steps, although in some cases five steps are possible. It is rarely used for gas applications.

Some *oil-injected screw compressors* have the stepless slide-valve control replaced with a sequence of lift valves (usually solenoid operated) located at intervals along the compression length of the compressor casing. Operation of these valves can provide unloading to say, 70 and 40 percent of capacity. Another method uses a piston valve, which covers and uncovers slots in the compressor casing, which permit recycling of the suction gas as described in "Inlet Gas Bypass" above.

Development of Synthetic and Semisynthetic Lubricants

There are often considerable benefits to be obtained by the injection of oil in compressors. The oil, injected into the compression space, has the effect of:

1 *sealing* the clearances between moving and stationary parts, thereby improving efficiency;
2 *cooling* the compressor by absorbing much of the heat of compression, resulting in relatively low discharge temperatures;
3 *lubricating* all moving parts and preventing any danger of metal-to-metal contact;
4 *protecting* all metal parts of the compression space against corrosion by the process gas;
5 acting as a *sound-damping* agent, resulting in relatively low noise levels.

However, not all types of gas are compatible with conventional mineral oils and close attention must be paid to the suitability of the oil selected for a particular gas application. The lubricant must satisfy not only the basic lubrication requirements but also:

(*a*) resist chemical breakdown;
(*b*) resist dilution;
(*c*) prevent chemical corrosion;
(*d*) lubricate under extremes of temperature;
(*e*) be compatible with elastomers used within the compressor.

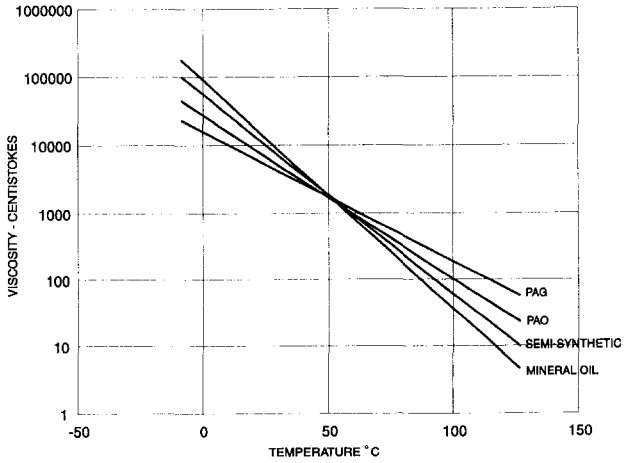

Fig. 8 Comparative viscosity / temperature curves

Conventional mineral oils are a complex mixture of naphthenic and paraffinic compounds, containing nitrogen, oxygen, and sulfur as well as aromatic and other unsaturated hydrocarbons. Some of these compounds are susceptible to thermal, chemical, and oxidative breakdown, which results in sludge, varnish, and polymerization leading to compressor failure. There are, nowadays, many readily available synthetic lubricants that can be applied to solve these problems; the most commonly used synthetic lubricants are: polyalphaolefins (PAOs), polyalkylene-glycols (PAGs), silicones, and "semisynthetic" or "hydrotreated" fluids. The temperature limitation of each of these oil types is shown in Fig. 7 and the effects of each on viscosity in Fig. 8.

The largest group of gases for fuel applications is the "hydrocarbons," which, in addition to normal olefins, etc., is taken to include: natural gas, wellhead gas, associated gas, vapor recovery gas, digester gas, landfill gas. For relatively pure and clean hydrocarbons, such as methane, ethylene, or

Downloaded 02 Jun 2010 to 171.66.16.102. Redistribution subject to ASME license or copyright; see http://www.asme.org/terms/Terms_Use.cfm

ethane, conventional mineral oils are used; for "heavier" gases, such as butane or hexane, PAGs are normally required, with propane/propylene (MW = 44) being the normal crossover point for lubricant selection. Contaminated hydrocarbons, such as natural gas or landfill gas, particularly when compressed for use as fuel in a gas turbine or engine, usually require a non-petroleum-based lubricant; in these cases PAGs are again recommended. For "sour" hydrocarbon gas applications, where hydrogen sulfide is present, especially with moisture content, synthetic lubricant is essential; in these cases PAGs are most often used, although PAOs are also widely used in such applications.

Probably the most difficult group of gases to deal with are chemically hostile "reactive gases." These include: methyl chloride, hydrogen chloride, sulfur dioxide, ammonia, carbon dioxide (with contaminants including water), chlorinated hydrocarbons, and gases containing trace mineral acids. When these gases are compressed, not only is the compression equipment subject to corrosion, but the lubricant itself is susceptible to chemical attack. In such applications, the ideal lubricants have proved to be PAOs, although in some instances semisynthetics may be used without difficulty (particularly when special silicones are blended in for added corrosion protection).

Effect of Process Gas Contamination

Particulate Contamination. Some gases contain hard particulate entrained in the gas stream. In most cases the gas is at least partly cleaned at the source, although it may be necessary to install a separator upstream of the compressor inlet.

Other gases contain soft particulate entrained in the gas; in some cases, this combines with any injected liquid to form a sludge, which can lead to blockages. It is usually advisable to avoid the use of liquid injection with this type of gas.

Nominally clean, dry gases also need careful evaluation: Permanent inlet gas filters may be needed where products of corrosion of preceding equipment can be carried forward or where catalyst dust may be present.

Droplets in Suspension. Liquid droplets present in the incoming gas can cause erosion, particularly of moving parts. To avoid erosion, a droplet separator should be provided, upstream of the compressor, with an effective cutoff size rating of 50–100 μm.

Although, with the use of synthetic lubricants, it is no longer difficult to compress fully saturated gases in oil-injected compressors, care must be exercised in maintaining discharge temperature well above dew point to avoid condensation of water leading to possible emulsification of the lubricant.

Molar Mass Variation. Wide variations in molar mass have little effect on positive displacement compressors, which is why they are often applied for duties where wide variations are expected.

Compressibility Variation. Operation close to the saturation line presents few problems for oil-injected compressors, subject to the comments already made above.

Gas Solution in Lubricant. In an oil-injected compressor, the deliberate injection of oil into the gas stream almost invariably leads to some solution of gas in the oil. This is usually perfectly acceptable, within limits, but will require careful evaluation of the characteristics of the lubricant selected (see above), to ensure that solution can be held within these acceptable limits.

Conclusions

Since cogeneration is a growth industry, the application of fuel gas compressors with an ever-increasing variety of gas compositions is also growing. The positive displacement type of compressor has proved to be extremely reliable and ideally suited to this service. As stated elsewhere, each of the four compressor subtypes mentioned in this paper has a specific field of application, but in many cases any of the four can cover required fuel gas duties. It has not been the purpose of this paper to select a particular compressor type but to provide information on certain features of currently available compressors.

In most of the compressors considered in this paper, the lubricant, to a greater or lesser degree, comes in contact with fuel gas, and the development of synthetic lubricants has to be seen as one of the major breakthroughs in this industry. Gases that even a decade ago were regarded as impossible, or not cost effective, to compress are now being readily utilized to produce power, particularly in cogeneration plants.

The increasing influence of the environmentalist lobby and its opposition to flaring or otherwise wasting byproduct gases is also good news for the cogeneration industry and we can anticipate a steady increase in the number of small electrical generating plants utilizing gases such as landfill gas, sewage digester gas, and refinery offgases.

Downloaded 02 Jun 2010 to 171.66.16.102. Redistribution subject to ASME license or copyright; see http://www.asme.org/terms/Terms_Use.cfm

The Design, Selection, and Application of Oil-Free Screw Compressors for Fuel Gas Service

K. D. Leigemann
MAN Gutehoffnungshütte AG,
Oberhausen, Federal Republic of Germany

Fuel gas compressors installed in cogeneration systems must be highly reliable and efficient machines. The screw compressor can usually be designed to meet most of the gas flow rates and pressure conditions generally required for such installations. To an ever-increasing degree, alternative sources are being found for the fuel gas supply, such as coke-oven gas, blast-furnace gas, flare gas, landfill gas, and synthesis gas from coal gasification or from pyrolysis. A feature of the oil-free screw compressor when such gases are being considered is the isolation of the gas compression space from the bearing and gear lubrication system by using positive shaft seals. This ensures that the process gas cannot be contaminated by the lubricating oil, and that there is no risk of loss of lubricant viscosity by gas solution in the oil. This feature enables the compressed gas to contain relatively high levels of particulate contamination without danger of "sludge" formation, and also permits the injection of water or liquid solvents into the compression space, to reduce the temperature rise due to the heat of compression, or to "wash" any particulate matter through the compressor.

Introduction

Natural gas is usually the most common fuel used in thermal energy processes. However, alternative gases are now being increasingly employed, such as coke-oven gas, blast furnace gas, flare gas, landfill gas, and synthesis gas obtained from coal gasification or from pyrolysis.

These gases are usually not as easy to process as natural gas and present special problems to most compressor designs.

The principle of operation of the screw compressor has been known since 1878, the year in which a patent was issued to Heinrich Kriegar.

The first operational compressor of this type was designed and constructed in 1934 by the Swedish engineer Lysholm.

SRM (Svenska Rotor Maskiner AB), the owner of the master patents, has developed this product to its present level of marketability in cooperation with licensed manufacturers throughout the world.

Operating Principle

A screw compressor (Fig. 1) comprises two rotors, one of which is called the male and the other a female. Each rotor has a number of profiled lobes, which are designed to mesh with each other. The male rotor has a similar function to that of a piston in a reciprocating compressor and provides induction, compression, and discharge by means of purely rotary motion.

This means that the operating principle of the screw compressor is that of a positive-displacement machine. Consequently there is no danger of surging as in the turbocompressor.

The machine has a stable characteristic with a rise in the pressure ratio hardly causing any drop in volume flow. It has no valves that could become defective, and no component parts subject to mixed friction and wear.

Thanks to the purely rotary motion, no free inertial forces

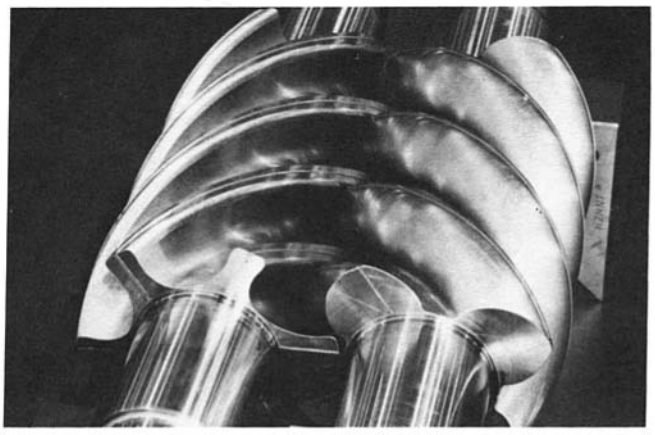

Fig. 1 Screw compressor

Contributed by the International Gas Turbine Institute and presented at the International Cogen-Turbo Power Congress and Exhibition, Bournemouth, United Kingdom, September 21–23, 1993. Manuscript received at ASME Headquarters June 1993. Associate Technical Editor: H. Lukas.

Copyright © 1995 by ASME

Downloaded 02 Jun 2010 to 171.66.16.102. Redistribution subject to ASME license or copyright; see http://www.asme.org/terms/Terms_Use.cfm

are produced that would necessitate special foundations or could excite vibration of neighboring components.

The machine has, in relation to its weight and dimensions, a high specific performance.

Design Principle

Of course, the induction, compression, and discharge operations can only be performed when the rotors are housed in a casing that allows proper admission to the rotor profiles through an aerodynamically shaped inlet port and is provided with an outlet port of similar design (Fig. 2). The inlet port is at the top and the outlet port at the bottom.

The required pressure ratio determines the built-in volume ratio (V_i) for a particular fuel gas, and this in turn governs the size and configuration of the discharge port. The volume ratio determines the amount of compression work prior to discharge.

In order to achieve the highest possible efficiency, the built-in volume ratio should be as close as possible to the volume ratio determined by the actual pressure ratio.

The rotors are radially and axially supported in sturdy bearings outside the compression space. Process-gas screw compressors are supported exclusively in sleeve-type radial bearings with a hydrodynamic film. These have a life expectancy of a very high order.

Since the rotors in an oil-free screw compressor are not in contact with each other, some means of keeping them separated and in phase in required. This is achieved by means of a pair of timing gears usually adjusted with zero backlash to ensure that the design tolerances are maintained and the rotors are properly synchronized when running. Only about 10 percent of the power input to the male rotor is transmitted to the female rotor.

The male rotor, whose lobes mesh with the flutes of the female rotor, causes displacement and ejection of the gas.

The bearings ensure that an exactly defined clearance is maintained between the rotor circumference and the casing as well as between the end face of the rotor profile body and the casing. The rotor profile clearances are established by precise manufacture. The timing gears ensure that intermeshing of the rotors takes place without any contact between the profiles.

Therefore, the rotors of the process-gas screw compressors do not need any lubrication in the compression space since there is no contact between the rotors. Consequently there is no danger of lubricant deterioration by gas or gas constituents or of any lubricant portions entering downstream systems.

Tip Speed

Influence of Volumetric Efficiency η_v and Dynamic Losses η_d With Regard to the Sonic Velocity of the Gas Handled. In oil-free screw compressors (Fig. 3) the effect of oil viscosity in the profile body due to lubricant injection does not exist. As this effect causes the efficiency to be markedly reduced at high speeds, screw compressors with lubricant injection should not be operated at tip speeds in excess of 50–60 m/s.

The tip speed of an oil-free screw compressor is mainly determined by the sonic velocity of the gas to be compressed.

While the asymmetric profiles almost exclusively applied today have led to an improvement in efficiency thanks to the smaller size of the so-called "blowhole," the clearances needed for operation of the machine cannot be eliminated.

These running clearances allow part of the gas under compression to return, at sonic velocity, from the interlobe space at higher pressure to that at lower pressure. There is thus a constant backflow of part of the gas being compressed.

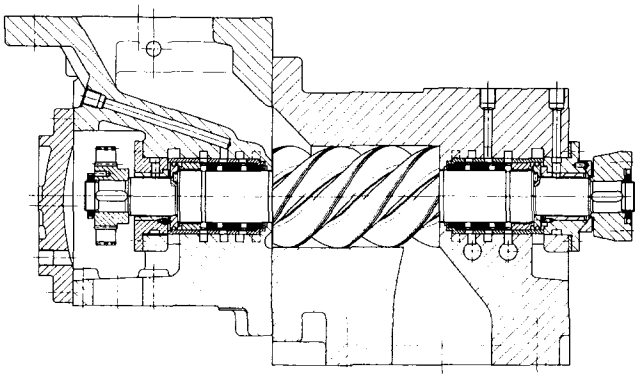

Fig. 2 Vertical cross section of a typical "oil-free" process-gas screw compressor

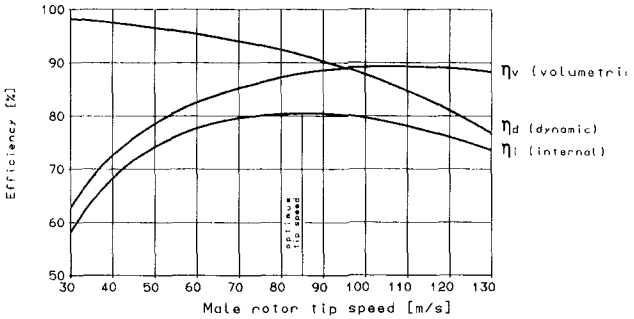

Fig. 3 Efficiency curves for oil-free screw compressor

This also occurs to a lesser extent in a screw compressor with lubricant injection, but here the high viscosity of the lubricant has a certain sealing effect at the running clearances so that high volumetric efficiencies are attained, even at low tip speeds.

The process-gas screw compressor is operated at higher tip speeds in order to improve the ratio of actual gas delivery and leakage backflow and thus to attain high volumetric efficiencies.

As, for a given compressor size, the clearances are determined on the basis of the operating temperature and are constant, and as the sonic velocity in a defined gas is also constant, the rate of leakage backflow is constant as well.

If a compressor thus defined is operated at ever higher tip speeds, the volumetric efficiency η_v at first improves more and more until the point is reached where, owing to deterioration of the ratio of rotor tip speed to sonic velocity in the gas, the interlobe spaces are filled to a lesser degree. There is also a rise in the dynamic losses η_d due to gas friction between the fast-moving surfaces and the gas.

From these two parameters the resultant overall volumetric efficiency η_i is obtained for a given inlet design condition.

As can be seen from the graph, an optimum range of tip speeds can be assigned to every gas handled by an oil-free screw compressor. However, as the curve is almost flat within a relatively large range, a certain deviation from the optimum leads to only a slight decrease in efficiency.

Roughly speaking, for gases with a molecular weight of 60–80 kg/kmol the optimum tip speed is in the range from 30 to 60 m/s.

For gases with a molecular weight of 20–40 kg/kmol it is 70 to 120 m/s.

With very light gases a tip speed of 150 m/s may not even be the optimum.

The idea of these somewhat elaborate considerations is to dispel the frequently expressed prejudice that an oil-free screw compressor runs too fast.

Downloaded 02 Jun 2010 to 171.66.16.102. Redistribution subject to ASME license or copyright; see http://www.asme.org/terms/Terms_Use.cfm

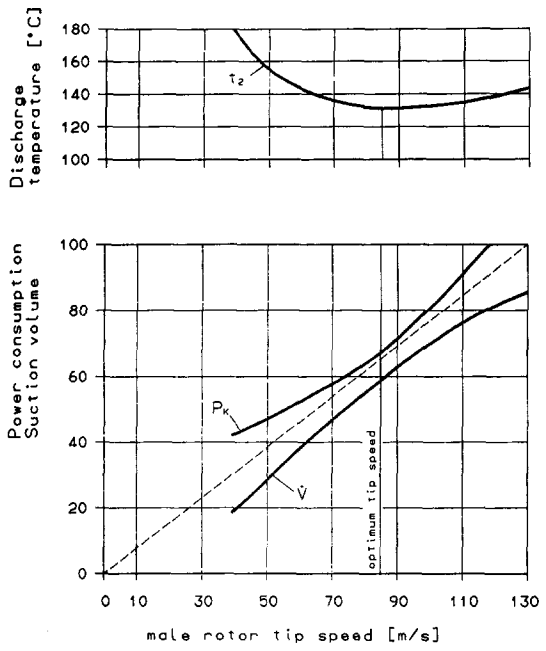

Medium: HC-Gas
Pressure ratio: 3
Molecularweight: 30

Fig. 4 Curves showing effect of speed variation for oil-free screw compressors

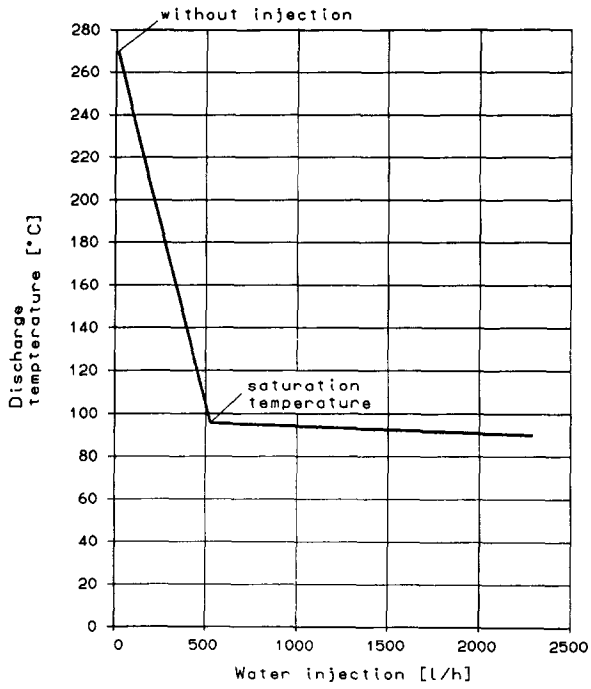

Lime kiln gas
p_1 = 0,9 bar t_1 = 40°C
p_2 = 4,5 bar $\dot{V}_1$ = 6000 m³/h

Fig. 5 Effect of water injection on discharge temperature for oil-free screw compressors

The process-gas screw compressor generally runs at a tip speed three times that of a screw compressor with lubricant injection. This means, for identical rotor sizes, the flow rate is three times greater.

However, compared to a turbocompressor, the tip speed is only about $^1/_3$. This explains why the process-gas screw compressor is not as sensitive to the presence of dust in the gas as in the turbocompressor.

In principle, dust entrained in the gas causes abrasion also in a screw compressor without injection, but here the progress of wear is much slower for the same dust content and consistency.

Volume Flow Control by Speed Variation

Screw compressors have a constant torque at a constant pressure ratio (Fig. 4). This means that with a speed-controlled screw compressor an excellent part-load response is obtained. Admittedly, a negative effect is produced by the previously described influences, such as a drop in volumetric efficiency on reduction of the tip speed due to a constant leakage backflow.

However, there is also a decrease in the dynamic losses already referred to, so that proper control by speed variation is possible within a relatively wide range. Here again the sonic velocity in the gas is an important factor. The graph shows a screw compressor without injection, which handles a gas with a molecular weight of 30 kg/kmol.

The performance is such that operation away from the optimum speed is best achieved by means of variable-speed drive.

The drop in volumetric efficiency at low speed causes the discharge temperature of the compressor to rise.

Heavy gases with a low sonic velocity allow speed variation within an even wider range, as at low speed the volumetric efficiency drops to a lesser degree.

With light gases the range of speed adjustment is limited for screw compressors without injection and allows flow variation by about 30 percent only.

Oil-Free Screw Compressors With Liquid Injection

The oil-free screw compressor (Fig. 5) has already been referred to several times as a machine without injection. It has also been mentioned in the preface that the specific features of the oil-free screw compressor can still be improved by providing additional facilities.

One important step for improvement is to inject liquids. This differs from the lubricant-injected screw compressor in that the liquid injected is not expected to lubricate the rotors and the bearings at the same time and is recirculated in a closed-circuit oil system, but can be selected for the specific gas and the particular requirements of the process.

One generally distinguishes between two kinds of injection:

(A) Injection for Reduction of the Compression Temperature. Compression is known to be a more or less isentropic process. The compression temperature results from the pressure ratio, the C_p/C_v factor of the gas to be compressed, and an allowance for the loss in efficiency.

As the operating temperature of an oil-free screw compressor is restricted by the selection of the construction materials and the coefficients of expansion of these, i.e., their thermal expansion, the discharge temperature must be limited to about 200°C or a maximum of 250°C for each compressor stage. The running clearances referred to in section 2 may cease to exist if the discharge temperature is too high, and this may result in damage to the machine.

Liquid injection is very helpful where the gas to be compressed permanently changes its molecular weight and thus the C_p/C_v factor.

An example of such gases is flare gas.

If the gas mixture is heavy, the C_p/C_v factor is small; for instance, at a pressure ratio of 6 a single-stage compressor can be operated with a relatively low discharge temperature.

If the gas mixture becomes lighter, the C_p/C_v factor

Downloaded 02 Jun 2010 to 171.66.16.102. Redistribution subject to ASME license or copyright; see http://www.asme.org/terms/Terms_Use.cfm

increases considerably and the discharge temperature of the compressor rises abruptly above the allowable level.

In this case a small quantity of liquid, such as petrol, is injected into the compressor stage and the vaporization heat of this absorbs the heat of compression. The compressor can safely be kept running.

Compressors for gases with changes in molecular weight between 9 and 44 kg/kmol are already in existence.

Other compatible liquids can also be used. It is only necessary to ensure that vaporization takes place without any residues and that the liquid injected does not cause any erosion or corrosion problems. The danger of erosion and corrosion can also be eliminated by selection of suitable materials for the compressor.

However, the gas may also necessitate limitation of the compression temperature. For instance, all acetylene-containing mixed gases decompose in an explosion-like manner when no oxygen is present. Styrene-containing gases polymerize and butadiene-containing gases form rubber.

This example shows that injection of a liquid may be very important.

The quantities of liquid injected for temperature reduction are relatively small compared to the weight of the compressed gas, as the heat is removed with the aid of the vaporization heat of the liquid.

This thermal limitation allows single-stage compressors to be applied in cases where normally two-stage machines would be needed.

In addition, variable-speed control is possible within a wide range.

(B) Injection for Cooling and Washing. If a quantity of liquid greater than the vaporization quantity is injected, a two-phase mixture is discharged at the compressor outlet port. This liquid causes a reduction of the compression temperature to prevent polymerization or reactions in the gas handled.

The compression process is almost isothermal.

In addition, the liquid present in the gaps also causes a slight improvement in volumetric efficiency.

There is also a washing effect.

Considerable quantities of partly undesirable constituents of the gas are transferred to the injected liquid if the undesirable constituents have an affinity to the liquid.

Consequently the reluctance to use these gases with gas turbines is rapidly diminishing.

Among these is coke-oven gas, the NH_3, H_2S, and HCN contents of which are considerably reduced.

Another example is low-caloric blast furnace top gas, where the contents of chloride and also of dust are reduced.

There are oil-free screw compressors that handle gas containing up to 300 mg/m^3 if dust without any noticeable abrasion effect. This is explained by the fact that the liquid injected covers all internal surfaces of the machine with a film by which the dust is kept off.

However, the material selected for the compressor must be of a kind that does not allow erosion to be caused by the medium injected.

The injection of large quantities of liquid into oil-free screw compressors also allows landfill gas to be handled by these machines. With this gas one never knows for sure what aggressive constituents and in what quantities have been added to the base gas in the course of time.

As the injection liquid is incompressible, it is necessary to limit its quantity according to the rotor profile chosen and to the built-in volume ratio. Normally injection quantities up to 3 percent by volume referred to the suction flow rate of the compressor stage do not present any problem if the liquid is distributed in the form of droplets. This applies particularly to machines where the liquid is already contained in the gas handled, as with two-phase compressors.

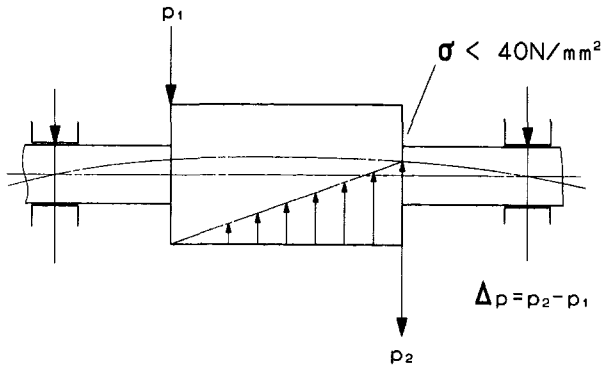

Fig. 6 Pressure distribution and rotor bending forces for a downward discharge screw compressor

Abrupt accumulation of large quantities of liquid may cause destruction of a screw compressor (liquid hammer).

As the intake port is at the top and the outlet port at the bottom, liquids automatically run out of the compression space when the machine is at a standstill.

However, the intended cleaning of the gas stream from undesirable gas constituents does not allow frequent utilization of the injection liquid in the compressor. The contaminants accumulate and the liquid gradually loses its ability to absorb them. A point of saturation is reached.

In addition, liquids with a high concentration of acid constituents start attacking the materials of the compressor system. Therefore it is necessary to remove injection liquid in good time and to replace it by a clean liquid.

Some injection liquids are used only once, which shows that the desired cleaning of the main gas stream is not achieved without consequences, as the liquid removed has to be discarded.

This compression process also allows single-stage compressors with high pressure ratios to be provided and to operate these machines within wide speed variation ranges.

Mechanical Features of the Oil-Free Screw Compressor

Compression takes place only in an exactly defined sealed triangular area of the rotor pair on one side, i.e., the discharge side (see Fig. 6). This means that the opposite, or suction side, of the rotor pair is either exposed to no pressure or inlet suction pressure.

As a result, the rotor pair is subjected both radially and axially to forces produced by the difference between the gas pressures. This is entirely different from the turbocompressor.

These features lead to certain specific requirements.

In the first place, rotor material of appropriate strength has to be chosen. This is necessary because of the fact that the stress that arises and the deflection of the rotors are determined by the bearing spacing and the residual rotor shaft diameter together with the gas load. However, the small rotor profile clearances do not allow any major deflection.

As the rotors are rotating bodies, the rotor shaft stress is an alternating stress.

The ratio of actual stress to allowable stress has to be checked in every particular case.

Depending on the material, a stress of up to about 40 N/mm^2 is allowed. This value is relatively low, but the notch effect in the fillet between rotor profile body and rotor shaft as well as any possible corrosive attack on the shaft surfaces by the gas have to be taken into account.

Downloaded 02 Jun 2010 to 171.66.16.102. Redistribution subject to ASME license or copyright; see http://www.asme.org/terms/Terms_Use.cfm

The bearing span results from the length of the profile body and the length needed for shaft sealing.

The residual rotor shaft diameter results from the profile chosen and is usually the most significant single factor affecting rotor deflection.

Small numbers of profile lobes, such as with the $^3/_4$ combination, result in small residual rotor shaft diameters.

Large numbers of profile lobes, such as with the $^4/_6$ combination, result in larger residual rotor shaft diameters and consequently stiffer rotors.

A typical length/diameter ratio of the rotor profile body in an oil-free screw compressor is 1.65, although models with an L/D ratio of 1.2 are also available.

However, scope for development has not yet come to an end and the innovation potential is far from being exhausted.

Larger lobe numbers and smaller L/D ratios are already under consideration with a view to developing screw compressors for higher pressure differences.

There are also other essential distinguishing features compared to turbocompressors.

The necessary high rotor stiffness with respect to deflection and rotor shaft stress automatically leads to lateral critical speeds above the operating speeds.

The separation margin of 20 percent over the maximum allowable operating speed as required under API 619, para. 2.7.1.4, is exceeded in most cases.

For a machine with variable-speed control this means that operation at any desired speed within the adjusting range is possible. Any necessary uprating later on can also be achieved in most cases by just increasing the speed.

The bearings have to absorb both the radial and axial forces resulting from the difference between the gas pressures.

These forces are much higher than those arising with turbocompressors, where generally only the rotor weight has to be supported. Therefore the bearings of screw compressors are provided with much larger faces.

The allowable load for radial bearings is maximum 5 N/mm^2 and for axial bearings maximum 2 N/mm^2.

The relatively high bearing load in a screw compressor is always applied in the same direction. Therefore no oil whip can occur as in the turbocompressor, where this is prevented by providing bearings of special shape (polygon shape, lemon shape, tilting pad). The bearings used by my company for screw compressors are sleeve-type radial bearings and tapered-land axial bearings.

While with turbocompressors the mechanical bearing loss is about 1 percent of the compressor power requirement, this loss may be up to 6 percent in the case of a screw compressor.

Of course, the higher power losses are partly due to the fact that two rotors have to be supported and there are twice as many bearings.

This disadvantage does, however, provide a desirable beneficial feature.

Thanks to the previously mentioned high rotor stiffness, a rigid connection between the rotating rotors and the stiff casing is established with the aid of the high bearing forces. This allows any irregular condition with respect to unbalance to be exactly measured with an accelerometer to API 678.

As the machine is run at subcritical speed, dynamic balancing of the rotors is never done in the contract casing, so that there is no need for vibration measurement in a second plane or for mounting a keyphasor. Of course, installation of vibration probes to API 670 is possible. However, these do not provide any more safety of compressor operation.

For measurement of the bearing condition, thermocouples to API 670 are provided both radially and axially in the load-supporting areas of the bearing faces.

As the rotors intermesh in the profile body and there are only small clearances, a thermocouple embedded in the axial bearing responds to an axial rotor movement due to a bearing defect more quickly and with more reliability than an axial position probe to API 670.

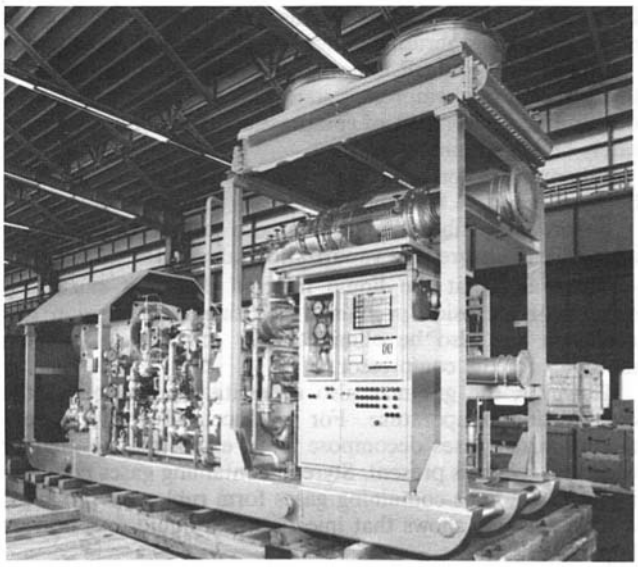

Fig. 7 Process-gas screw compressor

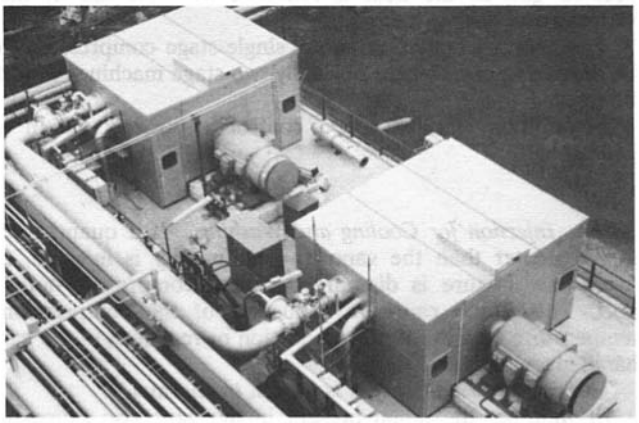

Fig. 8 Flare-gas compressor

Therefore, installation of axial position probes to API 670 can be dispensed with.

Of course, installation of axial position probes to API 670 is possible. However, these do not provide any more safety of compressor operation as they only respond when an axial bearing is defective and the compressor has already been shut down by the axial-bearing temperature monitoring system.

For radial vibration measurement it is also important to know that the lobes on the male rotor cause a radial vibration, as each lobe meshing with the corresponding flute on the female rotor and causing a pulselike gas ejection performs an operation that corresponds to that of the compression stroke of a reciprocating compressor.

This compression stroke of the male-rotor lobe produces a reaction vibration in a radial direction on the rotor and the casing.

This reaction vibration caused by the gas pulsation is insignificant for a qualitative assessment of the running smoothness of the machine to VDI 2056 "Criteria for assessing mechanical vibrations of machines" and has therefore to be filtered out at the monitor.

This also applies to the low-frequency vibrations as other-

Downloaded 02 Jun 2010 to 171.66.16.102. Redistribution subject to ASME license or copyright; see http://www.asme.org/terms/Terms_Use.cfm

Table 1 Typical screw compressor sizes and performance data

L/D ratio 1.65			
Rotor dia. mm	Suction flow at 60-130 m/s m3/h	Differential pressure bar	Max. disch. pressure bar abs.
321	5610 - 11390	11.0	17.0
408	9180 - 18700	10.0	12.0
510	14280 - 28560	9.0	11.0
643	22865 - 45560	7.5	9.0
816	36720 - 73100	6.0	7.0

L/D ratio 1.65			
Rotor dia. mm	Suction flow at 60-130 m/s m3/h	Differential pressure bar	Max. disch. pressure bar abs.
102	350 - 1050	8.0 - 14.0	41.0
127	570 - 1700	8.0 - 14.0	41.0
163	980 - 2800	8.0 - 14.0	41.0
204	1600 - 4400	8.0 - 14.0	41.0
255	2600 - 7000	8.0 - 14.0	41.0
321	4400 - 11800	8.0 - 14.0	41.0
408	9180 - 18700	8.0 - 14.0	41.0

L/D ratio 1.2			
Rotor dia. mm	Suction flow at 60-130 m/s m3/h	Differential pressure bar	Max. disch. pressure bar abs.
102	260 - 770	10.0 - 17.0	41.0
127	420 - 1200	10.0 - 17.0	41.0
163	710 - 2000	10.0 - 17.0	41.0
204	1150 - 3200	10.0 - 17.0	41.0
255	1900 - 5100	10.0 - 17.0	41.0
321	3100 - 8100	10.0 - 17.0	41.0
408	6500 - 13360	10.0 - 17.0	41.0

wise vibrations produced in the vicinity of the compressor may cause compressor shutdown.

The vibration amplitude produced by the compression stroke of each rotor lobe may be up to four times that produced by the rotation of the rotor (rotors).

A portable real-time analyzer allows occasional checking of the entire vibration spectrum.

The relatively high bearing losses in a screw compressor also have a further advantage that should not remain unmentioned.

This is the high damping effect with respect to torsional critical speeds, because in drivers with a relative uniform torque, such as squirrel-cage motors, steam or gas turbines, the damping forces in the rotating system are so high that even torsional forces excited at the first torsional critical speed cannot produce surface stresses that are a danger to the system.

This is particularly important with variable-speed control ranges between 50 and 100 percent, where the first critical speed is frequently passed.

Of course, for drivers with an irregular torque the transient torsional vibration analysis required under API 619, para. 2.7.1.11, is performed.

Shaft Seals

It is necessary to provide an absolutely tight sealing between the gas-handling portion of the machine and the lubricated hydrodynamic bearings, as no contact between the gas and the lubricant is allowed.

This is the only way to achieve the long inspection intervals of 24,000 service hours for the compressor units, demanded today for applications in refineries, power generation and petrochemical plants, and to obtain a high availability.

Labyrinth seals in a variety of materials can be provided. These seals require a buffer gas or gas extraction system.

Most of the oil-free screw compressors with liquid injection as described in the section "Injection for Cooling and Washing" are provided with liquid-film seals whose sealing liquid is the same as the medium injected into the machine.

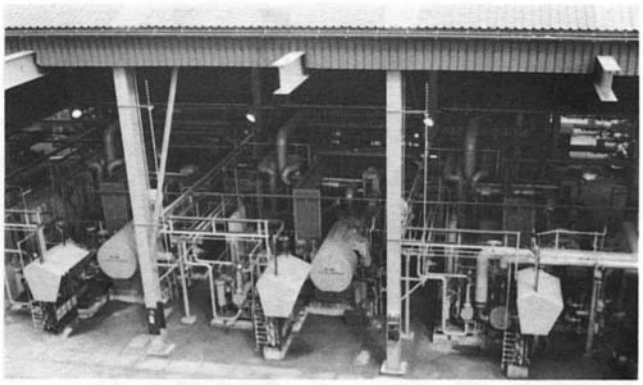

Fig. 9 Fuel-gas compressors

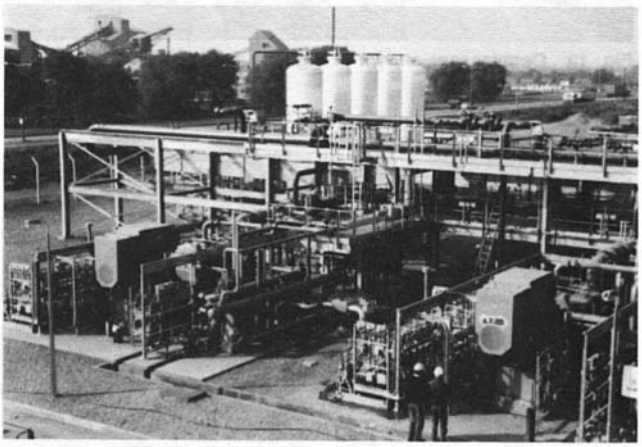

Fig. 10 Molecular sieve

Fig. 11 Process-gas screw compressor

Downloaded 02 Jun 2010 to 171.66.16.102. Redistribution subject to ASME license or copyright; see http://www.asme.org/terms/Terms_Use.cfm

Fig. 12 Compressor shown in Fig. 11, mounted on offshore platform

Fig. 13 Blast furnace

Most oil-free screw compressors are equipped with mechanical (contact) seals. These are cooled by the oil system of the compressor. With this type of sealing, buffer gas is needed in very rare cases only. However, buffer gas can be additionally provided where difficult or toxic gases are compressed. This seal is gas-tight not only during operation of the machine but also during stand-still periods, even if the seal oil supply should fail.

Leakage oil is generally discarded.

With currently available material combinations for mechanical seals, such as silicon carbide, mechanical seals are no longer regarded as wearing parts.

The most appropriate sealing system is agreed upon between the user and the manufacturer.

Examples of Application and Design

Figure 7 shows a process-gas screw compressor completely assembled at the manufacturer's works as a packaged unit for installation directly at a well-head (gas gathering) without needing a foundation. The unit is protected against ingress of drifting sand. Cooling of the lube and seal oil for the mechanical seal is by an air-blast cooler as the compressor is used in a desert area. It compresses 3950 m^3/h of "associate" gas from 1.03 bar to 3.44 bar.

Figure 8 shows a flare-gas compressor with accessible noise enclosure in a refinery.

Two two-stage process-gas screw compressors are mounted on a single table-top foundation. All auxiliary equipment is installed under the table-top.

Each individual compressor is equipped with liquid-film seals. The same liquid used for sealing is injected into the compression spaces to prevent polymerization of the heavy hydrocarbons. Compression is almost isothermal. Each unit compresses 11,000 m^3/h of flare gas from 1.01 bar to 7.0 bar.

Figure 9 shows fuel-gas compressors in a refinery.

Three two-stage process-gas screw compressors (two driven by electric motor, one with steam turbine drive) as packaged units, mounted on concrete slabs, for fuel gas supply to a gas turbine.

The compressors are equipped with mechanical seals. Each unit compresses 2500 m^3/h of fuel gas from 3.5 bar to 17.5 bar.

In Fig. 10 a molecular sieve is charged with coke-oven gas for hydrogen extraction.

Two two-stage process-gas screw compressors are packaged units mounted on concrete slabs, outdoors.

Each individual compressor is equipped with liquid-film seals. The same liquid used for sealing is injected into the compression spaces to prevent polymerization of the heavy hydrocarbons. Compression is almost isothermal. Each unit compresses 4800 m^3/h of coke-oven gas from 1.03 bar to 9.0 bar.

Figures 11 and 12 show a process-gas screw compressor completely assembled at the manufacturer's works as a single-lift package for direct mounting on the deck of an offshore oil production platform. The machine compresses 5650 m^3/h of "associate" gas from 1.37 bar to 6.85 bar.

This compressor stage has mechanical seals.

Figure 13 shows injection of coke-oven gas into blast furnaces to substitute coke and to accelerate reduction.

Two two-stage process-gas screw compressors are individually mounted on table-top foundations. All auxiliary equipment is installed under the table tops. The gas/water coolers and the water/air coolers are located adjacent to the foundations. Each individual compressor is equipped with liquid-film seals. The same liquid used for sealing is injected into the compression spaces to prevent polymerization of the heavy hydrocarbons. Compression is almost isothermal. Each unit compresses 40,700 m^3/h of coke-oven gas from 1.01 bar to 11.0 bar.

Downloaded 02 Jun 2010 to 171.66.16.102. Redistribution subject to ASME license or copyright; see http://www.asme.org/terms/Terms_Use.cfm

The Design, Selection, and Application of Oil-Injected Screw Compressors for Fuel Gas Service

S. Tsutsumi

J. Boone

NV Mycom Europe SA,
Zaventem, Belgium

Fuel gas compressors installed in cogeneration systems must be highly reliable and efficient machines, like the other main components, such as gas turbines, gas engines, etc. In the range of gas flow rate and pressure conditions generally required for such systems, the oil-injected screw compressor is often the most suitable compressor type for these requirements. Advantages of oil injected screw compressors are: improved compression efficiency; low discharge gas temperature; high reliability; simple mechanical construction; which all result from injection of lubricant into the compressor. Injected lubricant is discharged together with compressed gas on the high-pressure side but the oil is separated by a fine oil separation system down to a level that causes no problems for the downstream combustion equipment. The oil-injected screw compressor is equipped with an integral stepless capacity control by means of a slide valve, which makes part-load operation possible with reduced power consumption and improves overall system efficiency. As cogeneration systems, which are energy efficient and environmentally sound, are now increasing in number, so oil-injected screw compressors are expected to be used more widely.

Background and Development of Oil-Injected Screw Compressor

Installation of industrial localized electric power generation plants, such as cogeneration systems, is rapidly increasing worldwide. When the engines use a gaseous fuel, the available fuel gas pressure is not sufficiently high, and a fuel gas compressor is required. In the case of gas turbine cogeneration systems, where a rotary-type main engine is used, which reduces manpower and maintenance costs, oil-injected screw compressors are widely selected and used as being the most reliable and efficient rotary machines for the required conditions.

MYCOM installed its first fuel gas compressor for such a system in 1983, for Japan's first continuous operation gas turbine cogeneration plant. Since 1983, more than 100 fuel gas compressors have been supplied, compressing not only natural gas or city gas but also landfill gas, sewage digester gas, waste gas from refinery, petroleum field gas, etc., including aggressive components and heavy hydrocarbon gases successfully.

The basic idea for the screw compressor can be regarded as having developed from the theory of gears by the German engineer Heinrich Kriger in 1878, more than 100 years ago. Academic gear theories were also introduced around 1928 by the Japanese Dr. Naruse of Tohoku University and by the Russian Dr. Novikov, but these theories were not realized in practical compressor technology at the time. The world's first successful industrial screw compressor was developed in 1934 by Dr. Lysholm of SRM (Svenska Rotor Maskiner AB) in Sweden. This was patented worldwide and opened up the development of screw compressors. In 1938, a British company HOWDEN started manufacturing industrial oil-free screw compressors, applying them in air and gas applications. The oil-free screw compressor must run at relatively high speeds to obtain a reasonable efficiency, as the compressed gas is likely to leak from the high-pressure to the low-pressure side through the clearances between the rotors, and between rotors and casing, with a maximum compression ratio of only 3 to 4. The mechanical construction of the oil-free screw compressor is complex, using timing gears and transmission gears for high speed. It must be designed to prevent problems caused by high compression temperature and thermal expansion. Sealing of lube oil from the compression chamber is also very difficult and requires expensive design (four seals per compressor stage) and materials. Since these characteristics were regarded as disadvantages, a liquid injection system for oil-free screw compressors was researched and an oil-injected screw compressor for air was developed around 1955 to 1958. This was also applied as an industrial refrigeration compressor from 1963, and can be regarded as the start of practical modern oil-injected screw compressors.

Significant advantages have been found in oil-injected screw compressors for the compression of nonrefrigerant gases, and since 1974, these compressors have been applied to many different gases, e.g., chlorine, helium, hydrogen chloride, methyl chloride, hydrogen, and various hydrocarbons.

One disadvantage of the oil-injected screw compressor was

Contributed by the International Gas Turbine Institute and presented at the International Cogen-Turbo Power Congress and Exhibition, Bournemouth, United Kingdom, September 21-23, 1993. Manuscript received at ASME Headquarters June 1993. Associate Technical Editor: H. Lukas.

Copyright © 1995 by ASME

Downloaded 02 Jun 2010 to 171.66.16.102. Redistribution subject to ASME license or copyright; see http://www.asme.org/terms/Terms_Use.cfm

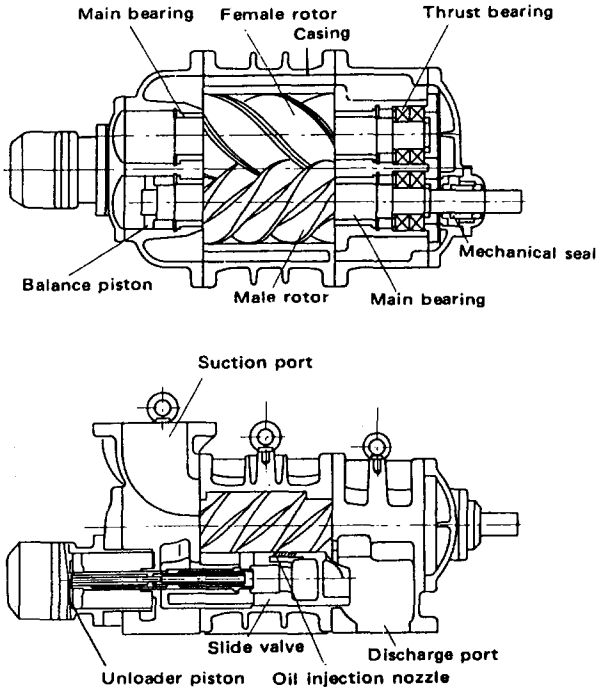

Fig. 1 Sectional view of oil-injected screw compressor

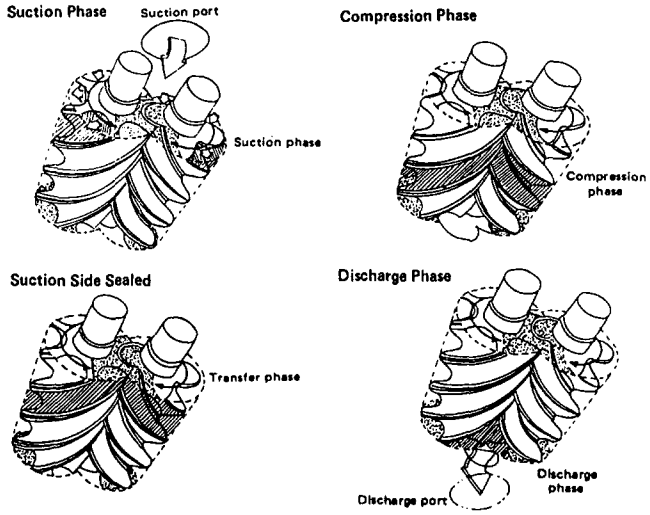

Fig. 2 Gas compression mechanism of screw compressor

that the downstream equipment in an open-cycle gas process cannot normally accept gases contaminated by lube oils. However, the development of fine oil separation systems has improved the technology. Another problem was that certain process gases could have impurities or aggressive components causing unforeseen damage to the compressor and lube oil. This led to the development of compressor materials and the blending of suitable lube oils and synthetic lubricants. Due to these efforts and achievements, the use of oil-injected screw compressors for process gas service is now established for all gases except oxygen, giving advantages that are difficult to obtain from other types of compressors.

Basic Design Features of Oil-Injected Screw Compressors

The screw compressor is classified as a positive displacement-type rotary compressor. This type employs a rotating section to compress and eject the gas, although the effect is the same as that of a reciprocating compressor. As shown in Fig. 1, the functional heart of the compressor is two mating, helically lobed rotors supported by bearings at either end of the compressor casing. The rotor with four convex lobes is called the male rotor, while the one with six concave lobes is the female rotor.

The compressor driver is direct-coupled to the male rotor by means of a flexible coupling. A two-pole electric motor is normally preferred, with rotating speed of 2950 rpm at 50 Hz or 3550 rpm at 60 Hz, but speeds from 1500 to 4500 rpm are possible with a suitable driver, depending on the conditions. The female rotor is driven through the oil film between it and the male rotor, and does not require timing gears as in an oil-free screw compressor.

The suction phase starts when a pair of lobes unmesh at the suction gas intake port. Gas flows into the increasing volume formed between the lobes and casing until the lobes are completely unmeshed. The trapped pocket is isolated from the inlet and outlet ports, moved circumferentially at constant suction pressure. When remeshing starts at the end of the gas intake, the trapped volume starts decreasing, the charge is gradually moved helically, while being compressed simultaneously toward the discharge end as the lobe mesh point moves along axially. Discharge starts when the compressed volume has been moved to the axial port at the discharge end of the machine and continues until the trapped volume is completely released by the rotation of the rotors.

The amount of internal compression, which occurs before release, is a characteristic that can be designed by the sizing of the discharge port to suit a particular duty. This feature is known as the "Built-in volume ratio" and is given the symbol "Vi." The relationship between Vi and compression ratio is as shown below:

$$Vi = \frac{\text{Volume of trapped gas when compression begins}}{\text{Volume of same amount of gas when discharge begins}} \quad (1)$$

$$(Vi)^k = CR = Pd/Ps \quad (2)$$

where:

Vi = built-in volume ratio
CR = compression ratio
k = specific heat ratio (Cp/Cv) of the gas
Pd = discharge pressure
Ps = suction pressure

All manufacturers supply compressors with a choice of several Vi values so that a compressor may be selected closely approximates the requirements of the intended pressure conditions. It should be chosen according to the actual operating conditions so that the compressor can operate at maximum volumetric and power efficiency. Standard built-in Vi values of MYCOM compressors are:

$$L = 2.6,\ M = 3.6,\ H = 5.8.$$

If the operating pressure ratio is very high, for example $CR > 10$, two-stage compound compressors are also recommended in order to obtain much better efficiency.

Male and female rotors are supported by generously sized sleeve-type journal bearings with large oil pockets to ensure that oil films are created under all conditions.

The considerable axial thrust force developed across the rotors is countered by a pair of angular contact antifriction ball bearings on each rotor. The use of ball bearings also minimizes the gas leakage since minimum end clearance between rotors and casing can be maintained at the discharge end. A balance piston is incorporated on the NDE of the male rotor, which uses oil pressure to offset the axial force and relieve the bearings of full load. Thus thrust bearings can be provided with a long life expectancy.

Downloaded 02 Jun 2010 to 171.66.16.102. Redistribution subject to ASME license or copyright; see http://www.asme.org/terms/Terms_Use.cfm

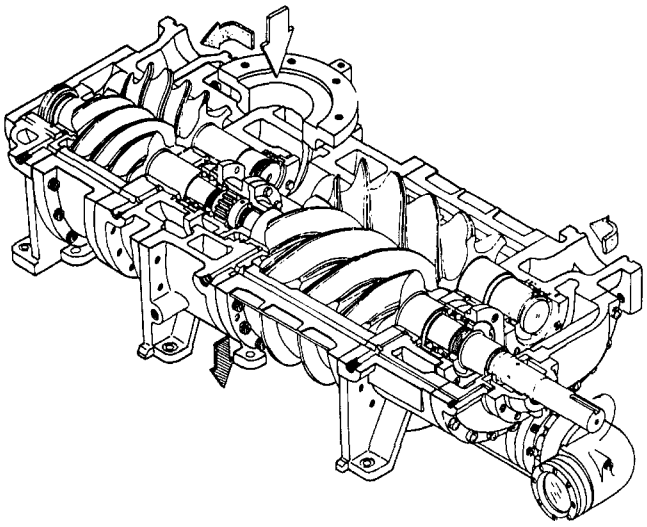

Fig. 3 Cutaway view of compound two-stage compressor

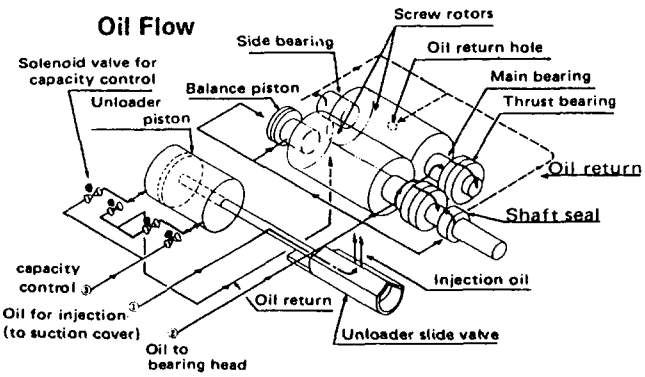

Fig. 4 Lubricant flow direction of oil-injected screw compressor

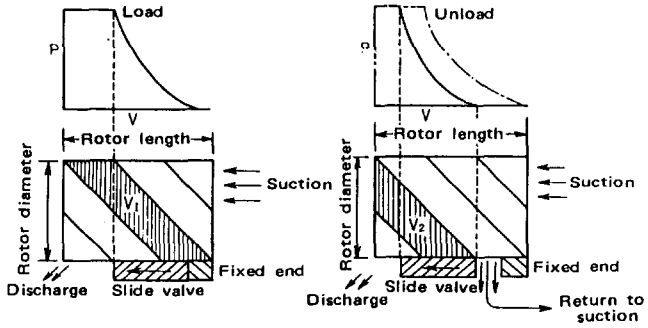

Fig. 5 Slide valve capacity control mechanism

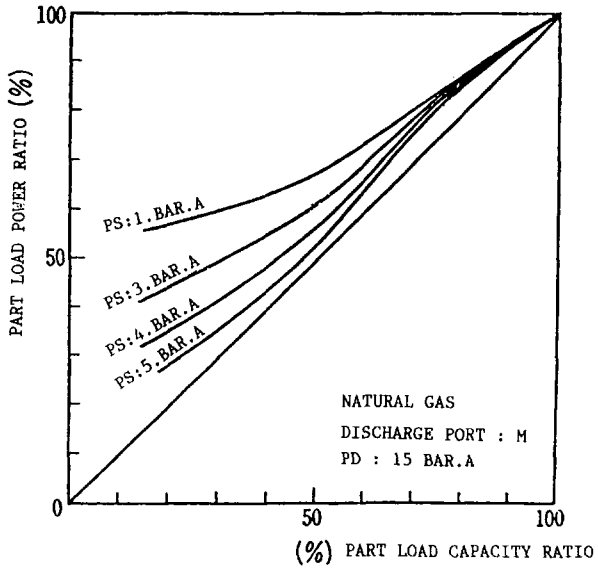

Fig. 6 Typical part-load performance curve

Only one shaft seal, which is a mechanical type, is required to isolate the pressure in the compressor casing from the atmosphere, at the driven side male rotor end. The shaft seal is always lubricated by the injection and the bearing lubrication oil. The seal oil returns into the compressor casing and a separate seal oil circuit is not necessary. The seal chamber is always flooded with oil so that the process gas never leaks to atmosphere.

The lubrication oil of oil-injected screw compressors gives many effective features and their importance to its higher reliability and efficiency is summarized below.

1 Lubrication. An oil film is formed on all the internal surfaces of the compressors and prevents metal-to-metal contact of rotating parts. The female rotor is driven by the male rotor via the oil film on the contact surface, providing very long rotor life.

2 Sealing. The clearances between male and female rotors and between rotors and casing are effectively sealed by the injection oil, which minimizes gas leakage from the high-pressure to the low-pressure zone. This also enables a high volumetric efficiency over a wide range of compression ratios.

3 Cooling. The power required to compress the gas from suction to discharge pressure appears as heat, which increases the discharge temperature. In an oil-injected screw compressor, a small amount of injection oil can lower the discharge temperature to between 70 and 80°C where oil-free compression would easily exceed 180°C. Lower discharge temperature minimizes the thermal expansion of the rotors, which makes it possible to set the clearances as small as possible and employ common material and simple mechanical construction.

4 Noise. Because of the damping effect of the injected oil, the sound pressure level of the compressor noise can be reduced considerably.

5 Corrosion Resistance. The presence of oil on all exposed metallic surfaces provides excellent resistance to corrosive attack of the metals. Thus, wet CO_2, which forms carbonic acid, and requires stainless steel to be used for construction in oil-free compressors, can be readily compressed in oil-injected machines using completely standard materials such as carbon steel and grey cast iron.

Compressor Design Feature Relevant to Fuel Gas Services

A particular advantage of the oil-injected screw compressor for fuel gas service is its capacity control feature, which is by the built-in slide valve mechanism. This slide valve moves parallel with the rotor, axially in the bottom of the rotor casing, and controls the flow rate by altering the effective length of the rotors being used for the compression. The movement of the slide valve toward the unloading direction opens a bypass for the gas trapped between the rotors and casing at suction, which flows back into the suction chamber before the compression begins.

The movement of the slide valve is accomplished by feeding oil to either side of a double-acting hydraulic piston in a cylinder. The oil flow direction and its flow quantity are controlled by on/off switching of the solenoid valves. Figure 6 shows a typical part-load performance curve for oil-injected screw com-

Downloaded 02 Jun 2010 to 171.66.16.102. Redistribution subject to ASME license or copyright; see http://www.asme.org/terms/Terms_Use.cfm

pressors. As can be seen, the power reduction in the uppermost region is almost proportional to the reduction of the capacity. This means that when the system load and gas consumption are decreasing, the oil-injected screw compressor does not consume unnecessary power.

Another feature for fuel gas service is to select a suitable lubricant, which is effective and important for the mechanism of an oil-injected screw compressor. In cases where the fuel gas is typical methane-rich natural gas, LNG, or inert and lighter hydrocarbons that do not include aggressive impurities, conventional mineral oils can be used successfully. Lube oil can be selected according to its viscosity, which is the basic parameter required by the compressor for reliable operations. In cases where the fuel gas includes heavier hydrocarbons such as petroleum field gas, refinery gas, etc., solubility of the gas in the lubricant is much higher, and also condensation of the gas in the compression chamber may occur. These gases create dilution of lubricant, which significantly lowers the original viscosity of the neat lubricant. If dilution is severe enough, the viscosity of the lubricant may be reduced to a level where it is no longer sufficient for adequate lubrication, which will lead to compressor failure.

In such a case, it is desirable to select synthetic lubricants, which have less solubility with hydrocarbons. Certain synthetic lubricants are capable of 10–20 percent saturation of hydrocarbons, which is the maximum dilution possible even with hydrocarbons heavier than C_4, while maintaining necessary viscosity of the lubricant even in the critical operating conditions.

If the gas contains aggressive and corrosive components such as H_2O vapor, wet CO_2, H_2S, etc., as is common in landfill gas or petroleum field gases, selection of the lubricant must be discussed with experienced and knowledgeable manufacturers. Many synthetic lubricants have been developed recently that can be used in oil-injected screw compressors for aggressive process gases or heavy hydrocarbons.

To summarize, several options are available for oil-injected screw compressors to meet the special conditions and requirements of fuel gas service:

1 Casing and Rotor Materials. As the fuel gas is flammable, casing and/or rotors are sometimes required to be made of steel. Although the standard screw compressor materials are grey cast iron casing and nodular cast iron rotors, cast carbon steel casing and/or forged carbon steel or chromium-molybdenum steel rotors are available as an option.

2 Journal Bearings. In the case of corrosive gases, a special material for journal bearing coating can be offered instead of the standard white metal (babbitt) lining.

3 Thrust Bearings. In critical operating conditions, tilting-pad thrust bearings can be offered in order to avoid the "life" component of angular contact ball bearings.

4 Shaft Seal. Depending on the application, type of gas, and pressure conditions, different types of mechanical seal and also materials of the contact surface are available.

Sizing, Pressure/Flow Characteristics of Compressor Relating to Turbine/Engine

The oil-injected screw compressor is normally driven by a commercially available two-pole electric motor (either 50 Hz or 60 Hz), as it can be operated at relatively low speeds with high efficiency. The standard swept volume of MYCOM screw compressors at a nominal 3000 rpm are approximately 100 to 5000 m^3/h; this is called the "theoretical displacement," which is the trapped volume between two rotors and the casing used for gas compression in one hour.

One of the characteristics of a screw compressor is that it needs a minimum clearance in the casing, which has a distinct

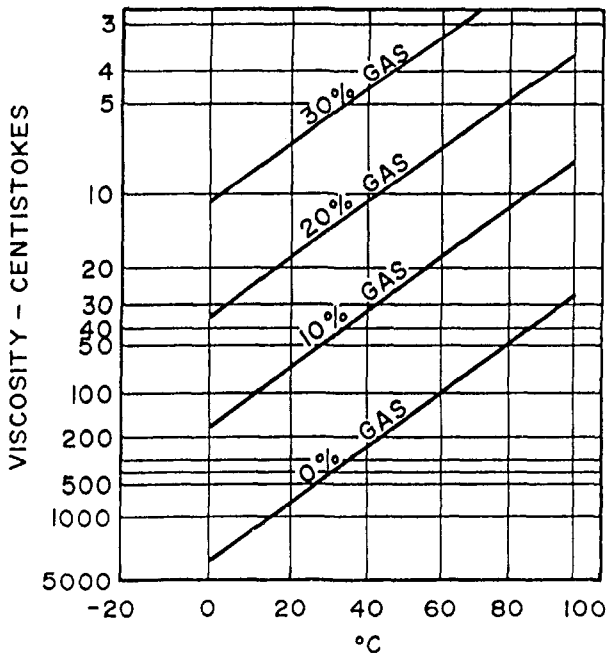

Fig. 7 Typical effect of dilution on viscosity of hydrocarbon gas/oil mixture

influence on the efficiency performance, particularly for smaller sized machines. It should be noted that, for capacities of less than 100 m^3/h, the reciprocating compressor has better performance character. On the other hand, very large screw compressors have problems in production, maintenance accessibility, inferior performance, and are not practically economical. For very high flow rate requirements, compact, high-speed, centrifugal compressors are the recommended solution.

As described, the optimum capacity range for screw compressors is in medium flow rates, which also covers the required flow rate of most existing gas turbines/gas engines (500 to 10,000 Nm^3/h at various gas supply pressures) for industrial and individual cogeneration systems (electric power output of 1 to 20 MW).

The formula to calculate the "nominal" flow rate [Vn] of compressor is, according to Boyle and Charles' law:

$$Vn = \frac{Vs \times Ps \times 273}{Ts \times 1.013},\quad QS = VTH \times Ev \tag{3}$$

where:

Vn = nominal flow rate, Nm^3/hr at 0°C, 1 atm
Vs = actual suction gas volume, m^3/h
Ps = suction pressure, bar•abs
Ts = suction temperature, K
VTH = theoretical compressor displacement
Ev = volumetric efficiency of compressor at required operating conditions

The required absolute inlet pressure of the gas for the gas turbine is normally 12 to 16 bar in smaller range, and 18 to 22 bar in larger machines. The available gas pressure of European natural gas distribution networks for industrial use is also normally in a wide range of 2 to 7 bar depending on the country and location. The compression ratio required for above varying suction and discharge pressure therefore has a very wide range between 1.5 to 11, so selection of a suitable Vi is as important as choosing the size of compressor model to suit the actual required flow rate.

In cases where the fuel gas is landfill gas or some other kind of waste gas, and available pressure is close to atmospheric pressure or even under vacuum conditions, very high compression ratios of 15 to 20 are required and the compound, two-

Downloaded 02 Jun 2010 to 171.66.16.102. Redistribution subject to ASME license or copyright; see http://www.asme.org/terms/Terms_Use.cfm

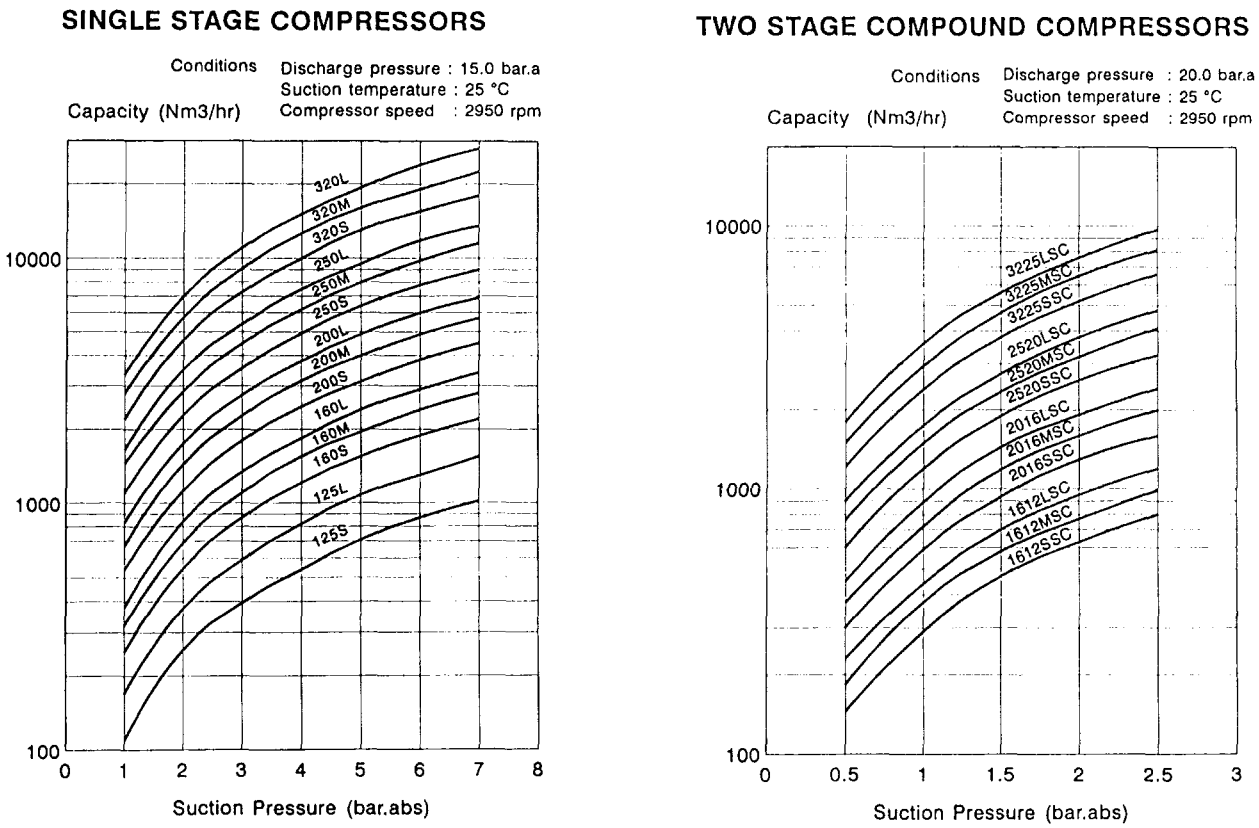

Fig. 8 Typical flow rate chart of MYCOM oil-injected screw compressors for natural gas service

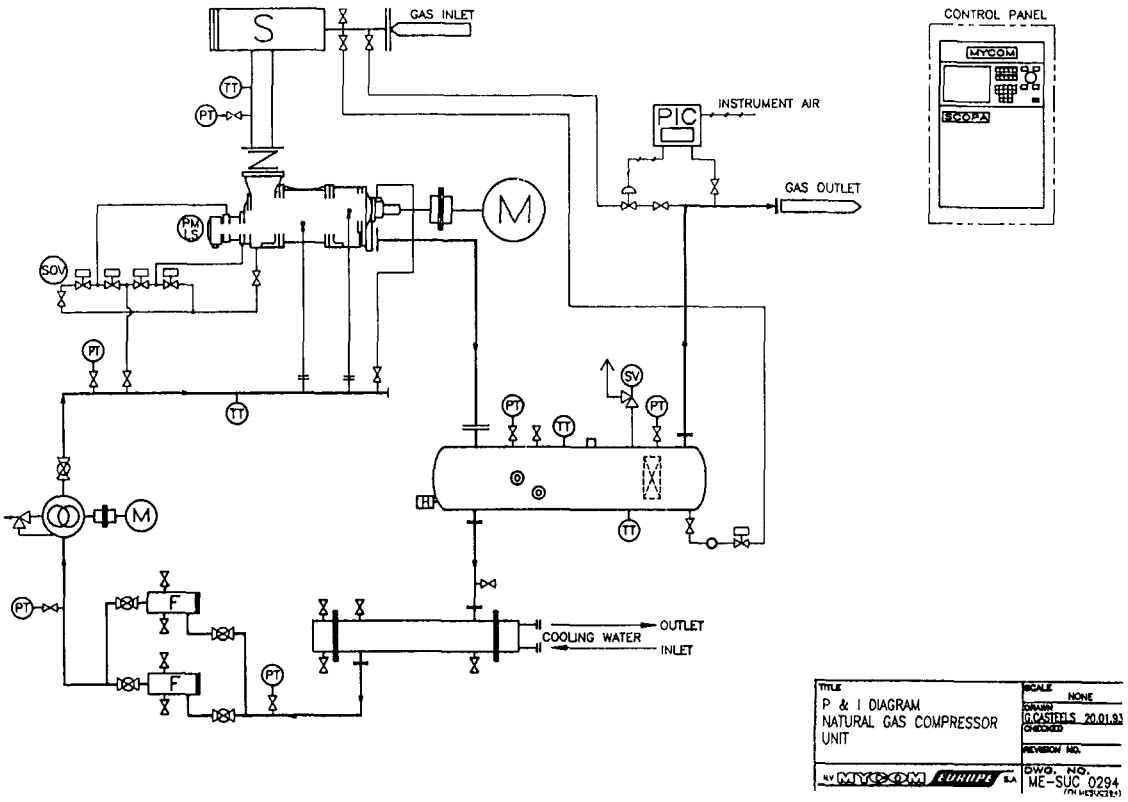

Fig. 9 Typical flow diagram of oil-injected screw compressor package unit

Downloaded 02 Jun 2010 to 171.66.16.102. Redistribution subject to ASME license or copyright; see http://www.asme.org/terms/Terms_Use.cfm

stage screw compressor is recommended as even at the maximum $Vi = 5.8$, the volumetric efficiency of a single-stage compressor will be relatively poor.

Compressor Package Features Relevant to Fuel Gas Application

Figure 9 shows a typical flow schematic diagram of an oil-injected screw compressor package unit. The various auxiliary components shown in the diagram are normally assembled with the compressor and driver on a rigid steel base; the package unit is completed in the factory, which simplifies installation. The fuel gas enters the suction gas strainer, which eliminates any scales and/or particles and then goes into the compressor.

Lubricant is also supplied into the compressor; during compression the oil and the gas mix freely and are discharged from the compressor outlet port. This mixture of gas and oil then enters the primary separator vessel. The lubricant is then separated from the gas, which continues through to the downstream process (e.g., a gas turbine). The lubricant collects in the reservoir, which forms the lower part of the separator vessel, and then passes through the oil cooler(s) and oil filter(s) and is pumped by oil pump(s) back to the compressor. In order to maintain the desired operating condition and safety, various pressure and temperature instruments and controls are installed in the gas line and the lube oil circuit.

Lubricant supply pressure is normally 2 to 3 bar higher than discharge pressure, as the whole oil circuit is under compressor discharge pressure, which is adjusted by the built-in relief valve of the oil pump. Positive displacement, screw, or gear-type pumps are normally used for this duty, assuring high reliability and efficiency.

The lubricant temperature is increased by the compression process to the same temperature as the discharge gas, and must be cooled down to the required oil supply temperature by the oil cooler in order to obtain suitable viscosity at the compressor. An oil temperature control valve is sometimes installed, to bypass the cooler under certain conditions.

One of the most important components in the package for fuel gas compressor service is the oil separator. Lubricant in the fuel gas must be removed as far as possible and the cleanliness of the gas must be maintained sufficiently to prevent any problems in the combustion equipment downstream. The most commonly used oil separator today is a horizontal format, cylindrical vessel with coalescing filters. This type of oil separator combines the primary and the secondary separation in one shell. The mixture of gas and oil discharged from the compressor is released into the end of the vessel and moves slowly in a large settling area with flow reversal devices providing a reduction of velocity allowing liquid droplets and particles of lube oil to be separated from the gas by natural gravitation. From this primary section, the gas flows into coalescing elements, which form the secondary fine separation section. Fine oil separation by coalescing filters is achieved by the highly efficient fine filter medium, which consists of a fibrous mass of "Borosilicate microfiber," employing several mechanisms such as direct interception, inertial impaction, and diffusion by Brownian motion. Liquid-phase lubricant and all but the finest of mists and aerosols can be removed, down to 0.01 mg/m^3, based on 7 bar air at 21°C with typical compressor lube oil. Liquids trapped by the filter will coalesce and form larger droplets, which gravitate within its cellular structure to form a "wet band" around the bottom of the filter and which drain to the bottom of the separator housing where the oil return is located.

Depending on the composition of the fuel gas, conventional types of vertical oil separator are also used with primary separation effect by demister or knitted wire mesh employing the principle of impingement. In this case, secondary fine oil separators, using the above-mentioned coalescing filters, must be

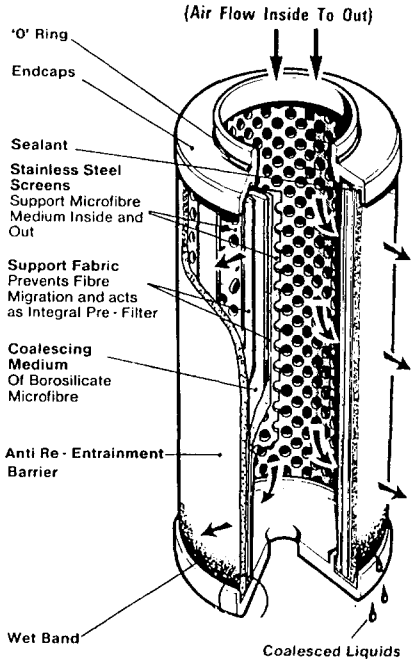

Fig. 10 Typical cutout view of coalescing filter

installed in series in order to achieve the required separation for fuel gas services.

Using the oil separation system described, experience shows that oil carryover in oil-injected screw compressor systems can be reduced successfully down to 5 to 10 ppmv, which is well within permitted levels for most existing gas turbines or engines. If further fine oil separation is required, multiple stages of fine separators and aftercoolers can also be installed in the compressor package unit to reduce oil carryover to lower than 1 ppmv.

Another feature of the compressor package unit for fuel gas service is its capacity control system. The slide valve in an oil-injected screw compressor provides stepless flow rate modulation during normal continuous operation. Flow rate control is normally arranged to maintain constant discharge pressure, moving the slide valve by a control signal, which is given from a discharge pressure sensor and controller. If the gas consumption decreases but compressor capacity remains the same, the discharge pressure will rise and the rise is sensed and signals to unload the slide valve. On the other hand, when gas consumption increases, the discharge pressure falls and the signal is given to load the slide valve, which increases the flow rate of the compressor.

However, the stroke speed of the slide valve is limited as it is governed by the action of the hydraulic mechanism, which depends on the oil supply to cylinder and piston. In some cases, the stroke speed of the slide valve is sometimes not quick enough to follow drastic gas flow changes such as emergency shut-down or immediate full loading. The stroke speed is also influenced by oil temperature and viscosity, suction and discharge pressure conditions, etc. The slide valve cannot move to the required position from 0 to 100 percent instantly and normally the full stroke takes 30 to 60 seconds or even longer depending on the conditions. If the moving speed is too fast, overshooting of the slide valve may occur, so that stable control cannot be obtained.

A possible solution to follow these drastic flow rate changes can be summarized as follows:

1 Installing an adequately sized accumulator between the compressor and the gas turbine, to provide a buffer to smooth out peaks and troughs of pressure.

Downloaded 02 Jun 2010 to 171.66.16.102. Redistribution subject to ASME license or copyright; see http://www.asme.org/terms/Terms_Use.cfm

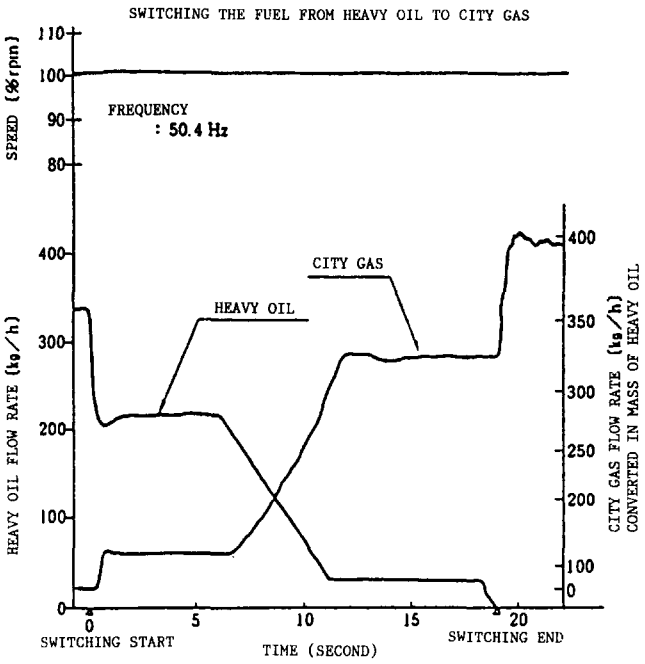

Fig. 11 Example of gas consumption chart of gas turbine during immediate full load charging

2 Installing a bypass pressure control valve from the compressor discharge to suction, which can compensate for the slow response of the slide valve under drastic flow rate changes. On emergency shut-down, the bypass valve recirculates high pressure gas to suction, until the slide valve has moved back to its 0 percent position, thus avoiding excessive discharge pressure. For full-load charging, the slide valve can be preset at a certain loaded position, and the compressor provided with auxiliary discharge pressure control by the bypass valve; as soon as the turbine starts to load, the bypass valve closes and the compressor can immediately supply the required gas flow to the turbine.

The two systems above should be selected and applied depending on the characteristics of the gas turbine and the operating load requirements of the installation.

As a summary of this paper, there follows a description of an example of oil-injected screw compressors applied with special features for cogeneration systems. Although oil-injected screw compressors are able to provide high efficiency at low speeds, they consume some of the electric power produced by the cogeneration plant. In the following example, the compressor is shaft-driven by the gas turbine-generator set, instead of by a separate electric motor, enabling the overall efficiency of the cogeneration system to be improved.

A Japanese manufacturer has developed a 1000 kW industrial gas turbine-generator set for cogeneration and assembled an oil-injected screw compressor on the same steel base frame, directly coupled to the antidriven tandem shaft of the electric generator. The compressor has been required to run, not at the same speed as the generator (1500 rpm) but at a higher speed, and to rotate in the same direction as the generator. MYCOM has developed a special screw compressor model 160SRT with built-in speed increasing gear and driven shaft, which turns in the opposite direction. The first of this in a cogeneration plant was in 1987; since then, more than 15 sets of the same type are in successful operation.

This is only an example of the special cases, but should show a remarkable capability of oil-injected screw compressors for better cogeneration systems.

Conclusion

The foregoing features and references show that oil-injected screw compressors can be applied successfully to provide the most suitable performance and reliability for all modern cogeneration systems. The contribution of cogeneration systems to major current topics of human concern, such as environmental protection and energy saving, should also be taken into consideration. Furthermore, the installation of even more cogeneration systems in the near future seems probable.

The fuel gas compressor is an indispensable item of major equipment in this application, which is expected to be utilized even more effectively and widely in future.

Although modern oil-injected screw compressor packages are adequate to fulfill all the requirements of cogeneration systems, there is a constant demand from the market to have further improvements in efficiency and development to improve the economics of both the main and the auxiliary equipment. The compressor industry should not be negligent in continuing its efforts to improve existing technology further.

References

Arbon, I. M., 1993, "An Introductory Guide to the Design and Application of Rotary Screw Compressors in the Oil & Gas Process Industry," MEP, United Kingdom.

Billet, C. T., and Fielding, R. M., 1984, "A Quantitative Method to Determine Oil Carryover From High Efficient Coalescing Filters," I.C.E.C., Perdue Univ., W. Lafayette, IN.

Dreksler, M. Y., and Scheel, L. F., 1976, "A Technique for Rotating Rotary Compressors," ASME Conference, Mexico City, Mexico.

Gauhar, M. A., 1988, "An Introduction to the Oil-Flooded Screw Compressors," Technical paper of MYCOM CORPORATION, Torrance, CA.

Kasahara, K., 1975, "Screw Compressor," *Journal of Refrigeration*, Japan, Vol. XX, pp. XX-OO.

Kohnosu, M., and Watanabe, A., 1983, "A Cogeneration System for High-Rise Building Using Dual Fuel Gas Turbine," GTSJ paper. I.G.T.C. Tokyo, Japan.

Tolfa, J. C., 1989, "Synthetic Lubricants Suitable for Use in Process and Hydrocarbon Gas Compressors," presented at the STLE National Meeting, Atlanta, GA.

Yamamoto, S., 1978, "Screw Type Compressors," *Journal of Refrigeration and Air-Conditioning Technology*, Japan, Vol. XX, pp. XX-OO.

Downloaded 02 Jun 2010 to 171.66.16.102. Redistribution subject to ASME license or copyright; see http://www.asme.org/terms/Terms_Use.cfm

The Design, Selection, and Application of Reciprocating Compressors for Fuel Gas Service

D. Hough
Belliss & Morcom,
Birmingham, United Kingdom

This paper describes the design and application of reciprocating compressors for fuel gas service. In fuel gas services and particularly power generation it is important to minimize all parasitic losses. Efficiency over a range of operating conditions requires sophisticated control systems and the paper describes the merits of each system and their effect on operating cost. Some of the important operational considerations are described together with major design features. The use of staging and the advantages of a modular approach to compressor design are also covered, which demonstrates the suitability of the reciprocating compressor for fuel gas service particularly when variation of inlet conditions cannot be avoided.

Introduction

Recently there has been increasing interest in the utilization of available gas sources for electricity generation. A fuel gas compressor is the essential interface between the energy source and the prime mover. The compressor raises the gas supply pressure to a controlled level suitable for use in an engine or, for larger installations, a gas turbine coupled to an electrical generator. The mass flow rate and pressure of the fuel gas supply must be adequate for all operating conditions. For maximum efficiency of power generation, careful selection of the compressor is most important. Common gaseous fuels used today are natural gas, biogas, and mine drainage gas having minimum net calorific values of 33.5, 21, and 13.6 MJ/Nm^3, respectively.

Fuel gas compressors fall into two groups. The first group covers dynamic machines such as centrifugal and axial compressors, generally used when gas flow conditions are large and within the compressors' operating characteristics. Although dynamic machines are available from 700 m^3/h, their use is usually limited to applications in excess of 2000 m^3/h. The second group covers positive displacement machines such as reciprocating and screw compressors capable of handling flows up to 70,000 m^3/h, although most applications are considerably below this figure, and in many instances no more than 12,000 m^3/h.

Figure 1 indicates operating ranges for positive displacement and dynamic machines.

This paper highlights some of the important features of reciprocating compressors and their effect on overall performance.

Fuel Gas Considerations

Engines have been run on a range of gases, but natural gas is most common. An important property of a fuel gas is its "methane number," which represents its anti-knock rating. A high methane number, ensuring controlled combustion, facilitates selection of compression ratio and combustion chamber shape for optimum performance and reliability. Most natural gases have methane numbers from 70 to 100

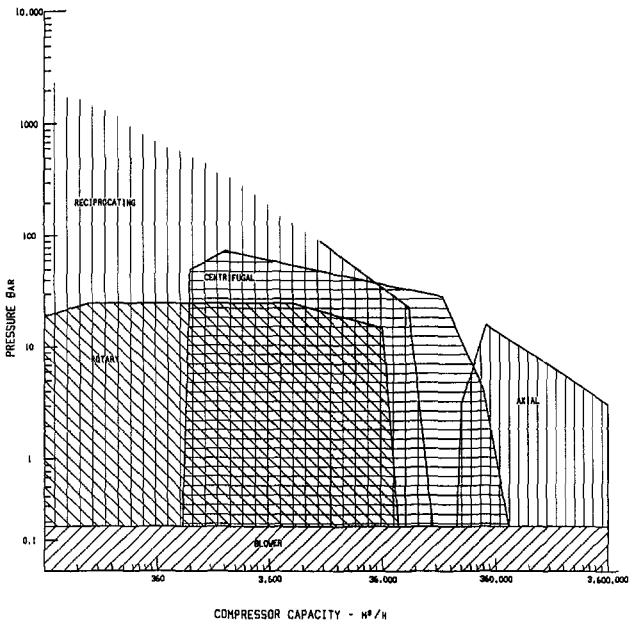

Fig. 1 Compressor types—approximate capacity and pressure limitations

Contributed by the International Gas Turbine Institute and presented at the International Cogen-Turbo Power Congress and Exhibition, Bournemouth, United Kingdom, September 21–23, 1993. Manuscript received at ASME Headquarters June 1993. Associate Technical Editor: H. Lukas.

Copyright © 1995 by ASME

Downloaded 02 Jun 2010 to 171.66.16.102. Redistribution subject to ASME license or copyright; see http://www.asme.org/terms/Terms_Use.cfm

and can be used in standard engines. Gases with methane numbers below 55 give rise to considerable design problems.

Methane numbers of selected gases are indicated below:

Gas type	*Methane number*
Hydrogen	0
Butane	10
Butadiene	12
Ethylene	15
Butylene	20
Propylene	18.6
Isobutylene	6
Propane	33.5
Ethane	43.7
Town gas	33
Carbon dioxide	75
Natural gas	77–78.5
Methane	100
Sewage gas	133.8

Note: Sewage gas possesses a methane number higher than that of methane since it contains a large volume of carbon dioxide, which acts as a buffer gas.

A gas engine requires clean, dry, noncorrosive gas. Corrosive gases considerably reduce engine life. Hydrogen sulfide content should not exceed 0.1 percent by volume and hydrogen content should be less than 20 percent by volume.

Considerations in assessing the suitability of a fuel gas include: composition, moisture content, and calorific value.

The following are typical compositions of fuel gases.

Natural gas

Methane	81.9–84	percent
Ethane	3.3–5.6	percent
Butane	0.6–0.7	percent
Butane	0.6–0.7	percent
Carbon dioxide	1.2–1.6	percent
Nitrogen	6.4–12.1	percent

Lower calorific value: 33.5 MJ/Nm^3

Landfill gas

Methane	63.8	percent
Carbon dioxide	33.6	percent
Nitrogen	2.3	percent
Oxygen	0.16	percent
Hydrogen	0.05	percent
Carbon monoxide	0.001	percent
Saturated hydrocarbons	0.003	percent
Unsaturated hydrocarbons	0.009	percent

Lower calorific value: 21.0 MJ/Nm^3

Sewage gas

Methane	60 percent
Carbon dioxide	35 percent
Nitrogen	5 percent

Lower calorific value: 21 MJ/Nm^3

Operational Considerations

The overriding requirements of any gas plant are safety of operation, reliability, and efficiency, all of which have to be allied to the commercial need to produce the equipment competitively. It is imperative that the following gas information be made available prior to selecting a compressor:

(*a*) Complete gas analysis, including variations.
(*b*) Amount of water present.
(*c*) Particulate matter content.
(*d*) Constituent gas vapor analysis for each major thermodynamic change.
(*e*) Variation in gas inlet condition.

Most biogases contain large amounts of carbon dioxide, which will combine with any water present to form carbonic acid, resulting in corrosion of most ferrous materials. Sulfur dioxide and nitrogen oxides are even more aggressive when wet. Sulfur-bearing gases are often present in landfill gas from the decomposition of sulfur compounds. Hydrogen sulfide reduces the fatigue strength of components, necessitating careful material selection and low design loadings. Landfills often contain volatile chlorinated solvents, which yield hydrogen chloride.

SINGLE STAGE

CAPACITIES:	FROM 240 M3/H TO 12600 M3/H
INLET PRESSURES:	SUB-ATMOSPHERIC TO 2.0 BAR G
DELIVERY PRESSURES:	2.4 BAR G TO 4.5 BAR G

HIGHER INLET/DELIVERY PRESSURES CAN BE ACCOMMODATED WITHIN THE COMPRESSION RATIO LIMITATIONS OF SINGLE STAGE COMPRESSION.

TWO STAGE

CAPACITIES:	UP TO 8400 M3/H
INLET PRESSURES:	SUB-ATMOSPHERIC TO ATMOSPHERIC
DELIVERY PRESSURES:	UP TO 17 BAR G

THREE STAGE

CAPACITIES:	UP TO 2500 M3/H
INLET PRESSURES:	SUB-ATMOSPHERIC TO ATMOSPHERIC
DELIVERY PRESSURE:	UP TO 27 BAR G

THE USE OF TWO OR THREE STAGES IS DEPENDENT UPON THE COMPRESSION RATIO.

Fig. 2 Typical range of duties for biogas applications

Even in trace amounts this causes pitting of cast iron and carbon steel and stress cracking in stainless steels. Aluminum alloy components are also attacked by chlorinated species. Consideration must also be given to galvanic corrosion.

Corrosive gases may be neutralized by scrubbing and dosing techniques. Failing complete neutralization, items like valves and gas cooler tubes should be in stainless steel and cast iron components should have a high nickel content.

Many gases are corrosive only if liquid water is present. This suggests two other approaches.

(*a*) *Predrying the gas:* This can be very expensive particularly with high inlet gas volumes. The associated pressure drop may also present problems.

(*b*) *Avoidance of Condensation:* The gas temperature is maintained above the dewpoint during compression. If this is not entirely possible, ensure all liquids are removed using a no gas loss system. For gas turbines, the gas must be dry and free from all particulate matter including oil. After gas cooling and liquid separation, the gas can be reheated to a temperature above the dewpoint in a gas-to-gas heat exchanger before final delivery. For reliability, build-up of residues in the compressor and pipework must be avoided by proper design of pipework, use of plain tube coolers, and coating of critical components.

Reciprocating Gas Compressors

The reciprocating compressor handles the medium to lower end of the inlet volume range. Figure 2 shows a typical range of duties for biogas applications. Oil-free gas compression, preferable for turbines, is readily provided.

They are simple in principle and can accept wide variations in suction and discharge conditions. Even larger duty changes can be accommodated by on-site modifications to the cylinder configuration.

Their flexibility is combined with the best specific power characteristics over the wide operating range and consequently they are widely used for fuel gas compression in power generation where power losses from ancillary equipment must be minimized.

The reciprocating gas compressor is usually a crosshead type with double-acting cylinders providing a compression cycle above and below the piston on alternate strokes. Figure 4 shows a typical indicator diagram for a reciprocating com-

Downloaded 02 Jun 2010 to 171.66.16.102. Redistribution subject to ASME license or copyright; see http://www.asme.org/terms/Terms_Use.cfm

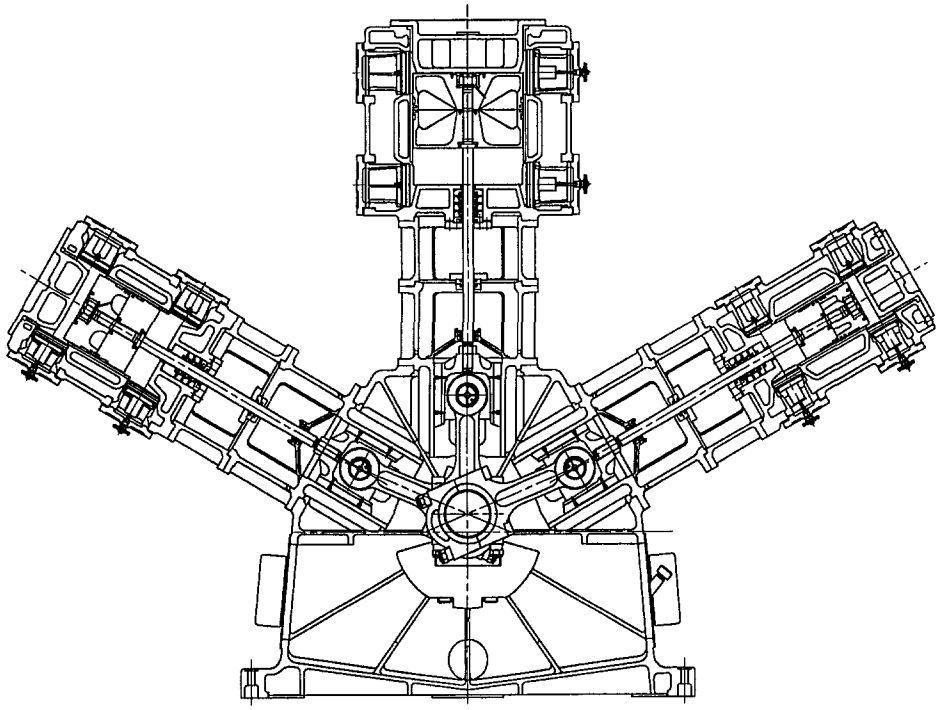

Fig. 3 Typical three-stage "*W*" compressor

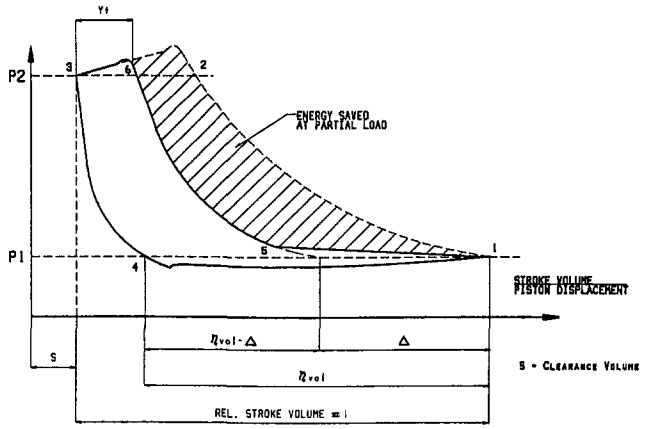

Fig. 4 Indicator diagram for operation at full load and partial load

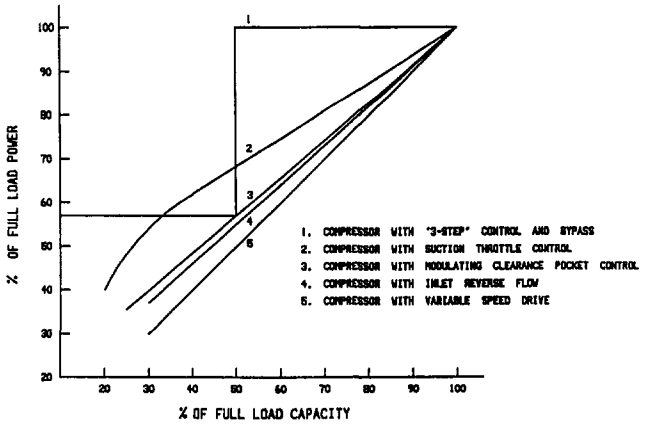

Fig. 5 Comparison of various methods of capacity control for reciprocating compressors

pressor. This theoretical PV diagram showing compression, discharge, and suction represents the amount of work done on the gas in one cycle.

The area above the line "2–3" represents the work done in moving the gas through the valves. The clearance volume indicated by "*s*" determines the mechanical volumetric efficiency, the actual value being equal to the ratio of clearance volume to swept volume. The actual volumetric efficiency will be influenced by inlet flow restrictions and preheating. The clearance volume does not however have any significant effect on power consumption since the pressurized gas in the clearance volume always re-expands to a point close to where compression would begin if the clearance volume was considered separately. The actual clearance volume is a function of the mechanical clearance volume, ratio of specific heats, and the ratio of the absolute discharge pressure to absolute suction pressure.

Since the suction and discharge valves operate by pressure difference, there are valve pressure losses. Consequently the volumetric efficiency is lower and the work done greater than theoretical. The pressure ratio is usually limited to obtain acceptable volumetric efficiency, discharge temperature, and piston loads.

The incorporation of the crosshead design ensures that piston ring loads are kept to a minimum, this being particularly important for nonlubricating operation.

Since the reciprocating compressor has reciprocating masses, the maximum allowable rod load is a function of the inertia loads and gas loads. Figure 6 shows a typical rod load diagram. These loads are cyclical and directly influence the design of the small end, big end, and main bearings. The combined loads on the main crankshaft vary according to angular position. Consequently the main bearing has a revolving load, whereas the load on the journal tends to oscillate within a 90 deg sector of one portion of the shaft. Figure 7 shows a typical torque diagram for a three-stage "*W*" compressor. The crosshead pins and cross head faces all require load reversal to ensure good lubrication and acceptable levels of reliability.

Reciprocating compressors exhibit primary out-of-balance forces, which in the case of a "vee" configuration are reduced

Downloaded 02 Jun 2010 to 171.66.16.102. Redistribution subject to ASME license or copyright; see http://www.asme.org/terms/Terms_Use.cfm

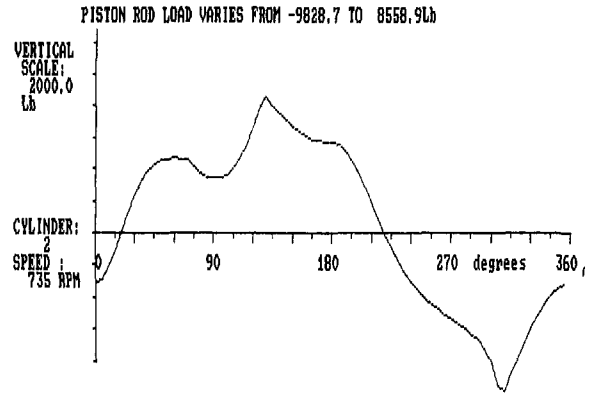

Fig. 6 Combined piston rod load diagram

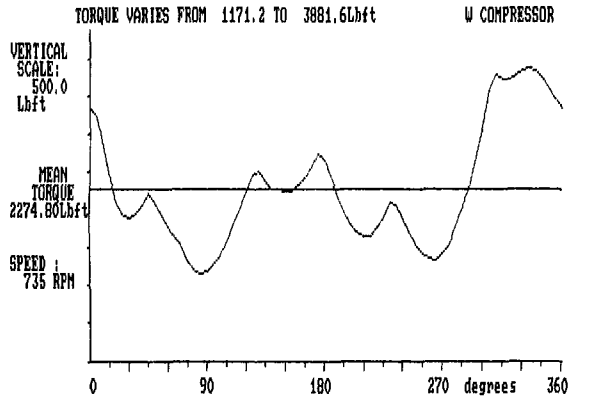

Fig. 7 Crankshaft torque diagram

to zero by introducing a suitably sized counterbalance weight. The secondary out-of-balance vertical component and secondary out-of-balance vertical couple are zero when the cylinder angles are positioned at 45 deg. The remaining secondary out-of-balance horizontal component and other remaining couples can be controlled and are relatively small in comparison to the total weight of the machine.

With multistage compressors the efficiency can be increased by introducing some form of cooling between the stages. Changes in suction and delivery pressure produce changes in interstage pressures. These changes can be accommodated, providing individual stage conditions do not exceed design limitation. Changes in interstage pressures affect the compressor intake flow rate, but the main factor in fuel gas compressors is probably suction pressure, as this directly affects gas density, hence mass flow.

Reciprocating gas compressors are designed for the maximum volume flow required, which usually occurs at minimum suction pressure. At higher suction pressures the mass flow rate will increase, resulting in higher power consumption. In these circumstances an effective control system is required to reduce volume flow to that required with corresponding reduction in power.

Reciprocating compressors for fuel gas applications are usually limited to three stages with piston speeds not exceeding 5 m/s. Modern materials technology gives average maintenance intervals at least equal to those of the prime mover. The number of compressor stages required, normally up to three, depends upon the particular site requirements. Relatively low inlet pressure, e.g., in landfill gas applications, normally require two or three stages if a gas turbine is used, but single-stage compression may be viable with a gas engine. Figure 3 shows a typical three-stage "*W*" configuration. However, the cylinders can also be arranged for single or two-stage operation.

General guidelines are as follows:

(*a*) *Single Stage*: This is usually used on the lower compression ratios (say up to 5). Fairly large capacities can be handled, although specific power tends to be inferior to multistage machines.

Other limitations become apparent with increasing compression ratio:

(*i*) Relatively rapid reduction in volumetric efficiency and consequently inlet capacity.
(*ii*) Relatively rapid increase in delivery temperature.
(*iii*) At the higher compression ratios mechanical load limitations may conflict with capacity requirements.

Even at lower compression ratios a two-stage machine may be a more viable proposition in some cases.

(*b*) *Two-Stage*: Compression ratios may be up to 22, although at the higher end this overlaps with the three-stage machines. The choice for optimum performance depends on the particular case.

The two-stage compressor is more expensive than the single-stage as it includes an intercooling system. Also, for a given number of cylinders the inherent inlet volume capacity is less. Advantages are that mechanical loads and delivery temperatures do not increase in proportion to the overall compression ratio.

Specific power is good over a wide range of conditions.

Two-stage compressors permit a high degree of optimization, not only to meet site performance requirements but also in the economical selection of components such as intercoolers and aftercoolers, etc.

(*c*) *Three-Stage*: Three-stage compressors are used for higher compression ratios, which occur with low inlet pressures as in landfill applications. They tend to be most expensive due to the more complex interstage arrangements and generally require a larger crankcase to accommodate the three cylinders. Again, specific power is good at conditions likely to be encountered in biogas applications.

Valves. The compressor valves operate on differential pressure and give the reciprocating compressor its high degree of flexibility and efficiency. A multi-stage machine becomes virtually self-regulating and can accommodate large variations in inlet and outlet pressure. Modern long-life valves and the latest design of valve chambers are the main contributing factors to the general performance and efficiency of this type of machine.

Volumetric Efficiency. This is the ratio of actual volume compressed to cylinder swept volume and is mainly determined by the cylinder clearance volume. Since the compression curve and the clearance volume expansion curve have similar characteristic, volumetric efficiency has virtually no effect on specific power consumption.

Gas Temperatures. Gas temperatures are readily controlled by using multiple stages with intercooling and thermostatically controlled water cooling circuits.

Balancing. Many configurations exist ranging from horizontally opposed cylinder designs taking up much floor space but little headroom and having no inertia or couple forces acting on the foundation to single-stage vertical designs requiring minimum floor space but being virtually unbalanced and therefore needing substantial foundations.

The "*V*" and "*W*" configurations are an accepted compromise. These are partially balanced, having only low-magnitude secondary inertia forces acting on the foundation, which may therefore be light and in some cases need only be

Downloaded 02 Jun 2010 to 171.66.16.102. Redistribution subject to ASME license or copyright; see http://www.asme.org/terms/Terms_Use.cfm

sufficient to bear the weight of the compressor. Floor space and headroom requirements are small.

Sealing and Oil Free Operation. The reciprocating mechanism has a simple yet highly effective self-adjusting system of sealing.

Piston rings and rod glands for nonlubricated cylinders are made from PTFE-based materials, which have advanced to a level where maintenance periods for large compressors match or exceed those of most prime movers. Compressor cylinders are separated from the crankcase by distance pieces, which are longer than the piston stroke. Should any lubricating oil pass the sealing rings in the crankcase, it cannot be carried up to the cylinder gas seal and contaminate the gas in the cylinder. A flinger collar is fitted to prevent oil from creeping up the piston rod.

Where it is important that air not mix with the gas, as might conceivably happen if the gas pressure in the cylinder is below atmospheric pressure during the suction stroke, the distance piece compartment is sealed and fed with inert gas at a small positive pressure.

Liquid Separation and Gas Pretreatment. Water-saturated gases and those containing liquids must pass through knockout vessels or separators before entering the compressor. Additionally, scrubbers and chemical dosing can be used to clean and neutralize the acidity of the gas.

Noise Control. A water-cooled reciprocating compressor is in itself fairly quiet, but noise from motors, cooling fans, or other ancillary equipment should be included in any assessment. Very effective acoustic enclosures can be designed and can incorporate hazard warning, fire control, and other systems. However, these represent very considerable capital cost. A compromise noise emission level can often be achieved by careful selection of fans and low noise motors.

Variation in Inlet Volume Flow. A gas engine or turbine requires a certain input of energy from the fuel gas represented by a particular mass flow requirement of gas of a given calorific value. To achieve this, the compressor must provide a consistent volume flow of gas measured in Nm^3/h. This is a volume referred to as NTP (usually taken as 1.013 bar a, 0° C, dry gas). Landfill gas, for example, is almost certainly saturated with water vapor, usually significantly above 0° C and possibly at a pressure below atmospheric. It will be evident from this that the actual inlet gas volume flow the compressor must handle will be appreciably larger than the reference flow corresponding to the mass flow. Furthermore, there will be day-to-day variations in the gas inlet conditions, which will result in variation of the inlet volume requirements.

The usual approach is to size the compressor for the maximum likely inlet volume requirement and to provide a control system to take care of the variations. Matching is facilitated by a modular approach to the design of the reciprocating compressor using a fixed number of crankcases of different power capabilities, each having a group of interchangeable cylinders, which can be used in any required combination. The modular approach allows optimization of efficiencies, speeds, temperatures, etc., for most economical operation at each particular site.

Although a somewhat drastic approach, the modular reciprocating gas compressor could be amenable to an on-site cylinder change to meet a significant change of duty. No other type of compressor has this total flexibility.

Variation in Overall Compression Ratio. It is quite usual to find that the gas supply pressure at the compressor inlet is subject to significant variation, which may be on a seasonal, daily, or even hour-to-hour basis. With a constant delivery pressure, the compressor is required to accommodate a fluctuating overall compression ratio. This of course would be most undesirable for any fixed ratio type of machine or, indeed, a dynamic machine with its relatively limited ratio variation capability. With these types any significant variation of compression ratio from the design value will result in less than optimum performance. In marked contrast, the reciprocating compressor is highly tolerant of overall compression ratio variation.

The likely limits of inlet pressure (and, if applicable, delivery pressure) are taken into account in selecting a cylinder arrangement to give good operating characteristics over the compression ratio range. At the same time all aspects resulting from a compression ratio variation such as volumetric efficiencies, stage delivery pressures and temperatures, and line loadings, must be considered so that adequate service margins are maintained, thus ensuring reliability and good overall performance.

Efficiency. Perhaps the most useful criterion to the user is the specific power consumption in kWs/m^3 of gas compressed.

It is difficult to generalize, but provided the gas is presented to the compressor clean and free from aggressive constituents, as is the case with natural gas, then the reciprocating compressor is generally accepted as having the highest efficiency because of its slow operating speed and high sealing capability.

However, there are circumstances when the gas contains a variety of aggressive species and large quantities of liquid.

In these applications when gas pretreatment cannot be considered for economic reasons, other compression techniques may have to be considered if acceptable levels of reliability are to be achieved.

Principal Features of the Reciprocating Compressor.

(*a*) Low overall power consumption.
(*b*) Ability to accommodate significant changes in inlet pressure and overall compression ratio.
(*c*) Large selection of cylinder combinations for optimum site performance.
(*d*) Large range of control systems.

Methods of Compressor Control for Reciprocating Compressors

Careful consideration must be given to the capacity control systems in order to take full advantage of the features of reciprocating compressors.

Step Control. This method involves unloading cylinder ends in sequence to reduce capacity. Double-acting reciprocating compressors usually have two or three steps, although in some cases seven steps are possible. This method of control is increasingly being offered as a means of obtaining economic capacity control.

Discharge Pressure Bypass. By this method any excess capacity is diverted from the discharge back to the compressor suction via a suitable aftercooler and bypass valve. It is a very common method for gas compressor installations and is a relatively inexpensive and effective modulating control system if the operating conditions are relatively stable. A very significant drawback, however, is that the absorbed power of the compressor remains unchanged even if most of the gas is being recirculated. Obviously, if variable conditions exist, this is not the most economical control method.

Inlet Reverse Flow. This system allows gas that has been drawn into the compressor to be expelled to the suction until the correct capacity is achieved, before compression begins.

Downloaded 02 Jun 2010 to 171.66.16.102. Redistribution subject to ASME license or copyright; see http://www.asme.org/terms/Terms_Use.cfm

This reduced capacity is then compressed and discharged in the usual way.

This is one of the most efficient methods of capacity control since positive displacement compressors absorb power in proportion to capacity at any given discharge pressure. Available control systems can provide stepless capacity adjustment from 100 percent down to 15 percent with virtually proportional power saving.

The reciprocating compressor employs a system often referred to as SRF (Stepless Reverse Flow) control. The delivered gas volume is reduced by holding the suction valve open for a controlled and variable proportion of the delivery stroke, thus modifying the indicator diagram. The volume and power reductions are virtually directly proportional. The system provides stepless capacity control to meet any demand while maintaining constant pressure. Other advantages are constant pressure ratios across all stages irrespective of capacity, providing better control of temperatures, smaller piping and surge bottles, extended valve life, and extended equipment life in general. Although the initial cost is higher than simple bypass control, savings can be substantial where part-load running is required. The payback period can be less than one year. The system is ideal for electrical generation schemes where parasitic losses must be minimized. Figure 4 indicates the power saving achievable.

Clearance Pocket Regulation. Volumetric efficiency, the ratio of intake volume to swept volume, is determined by the expansion of gas trapped in the cylinder clearance volume. For a given pressure ratio an increase in the clearance volume will reduce the volumetric efficiency and hence the capacity of the compressor. Additional clearance is provided in the form of clearance pockets, which are opened or closed by the control system to vary capacity and maintain constant pressure.

In a variation of the design, stepless capacity reduction is achieved by varying the length of time for which the clearance pocket is connected to the cylinder during the compression and expansion periods. Power saving is less than with SRF control but is still significant. This method of capacity control is relatively inexpensive, with good turndown capabilities.

Variable Speed Drive. Speed variation is the most efficient capacity control method for reciprocating compressors. It gives good capacity matching and a power reduction that follows the reduction in capacity fairly exactly.

With reciprocating compressors, particularly if a large speed range is required, care must be taken to provide sufficient flywheel inertia and lubricating oil pump capacity for the lower end of the speed range; also, there is the possibility of mechanical resonances occurring somewhere in the speed range.

At present the capital cost of speed control equipment for electric motors is relatively high and the payback period may not be acceptable to the customer.

Throttle Control. This fully modulating control system comprises a suction throttle valve, which reduces the inlet pressure in response to a reduction in capacity requirement. This relatively inexpensive and simple system suffers from the fact that power reduction is not directly proportional to capacity reduction. Typically, 55 percent inlet capacity corresponds to approximately 70 percent full-load power.

When the gas pressure is little, if any, above atmospheric pressure, the suction depression consequent on inlet throttling results in the ingress of air to the system. If critical air/gas ratios occur the installation could be a hazard in some circumstances.

A comparison of the various capacity control systems is shown in Fig. 5.

Appraisal of Reciprocating Compressor Features

The reciprocating compressor uses a crank and connecting rod linkage to convert rotary to translatory motion. The translatory speed is usually less than 5 m/s.

Light, compact, packaged compressors, easily installed and quickly put to use, requiring the lightest of foundations and little maintenance for long periods, are not features exclusive to rotary compressors. The reciprocating compressor may embody these features plus others, including:

(*a*) Exceptional adaptability to changing conditions.
(*b*) Wide range of capacities and pressure.
(*c*) Completely oil free compression, where necessary.
(*d*) Available in water or air-cooled versions.
(*e*) Above all, high efficiency.

In the reciprocating compressor it is usually possible to reduce the primary out-of-balance forces to an acceptable level and offset the smaller secondary forces. Consequently, it is possible to design the reciprocating compressor for foundations comparable with those for screw compressors.

The self-regulating valves of a reciprocating machine, which give it a high degree of flexibility and efficiency, can accommodate large changes in compression ratio without affecting overall efficiency.

Efficiency is the outstanding feature of the reciprocating compressor. It is achieved by good sealing, efficient valving, low pressure ratios per stage, intercooling, and low parasitic losses. In most circumstances the reciprocating gas compressor absorbs less power overall than other types of compressors.

For a gas turbine it is preferable although not essential that the gas supply be oil free. The reciprocating compressor delivers totally oil-free gas, usually in a cleaner condition than at the suction.

Gas compressors rarely run continuously on full load and great care is necessary in choosing the correct capacity control system. Overall, the inlet reverse flow system used on the reciprocating compressor is the most efficient.

Conclusions

Although there is no universal compressor, the reciprocating machine covers the widest range of duties due to its automatic adaptability to the changing pressures, facility for capacity control and, not least, high efficiency.

The modular construction of the reciprocating compressor allows a wide range of cylinder sizes, which can be optimized and changed to satisfy any future application and this versatility, coupled to a V belt pulley change, offers a wide range of capacities and pressures from a single frame size.

The ultimate choice of compressor depends on many factors, but running costs must be among the most important. The consistently lower specific power consumption of the reciprocating compressor continues to keep it to the forefront in energy-sensitive applications where efficient and reliable performance is required.

Acknowledgments

The author would like to thank the management of Belliss & Morcom, a business unit of Allen Power Engineering, for permission to publish this paper.

Downloaded 02 Jun 2010 to 171.66.16.102. Redistribution subject to ASME license or copyright; see http://www.asme.org/terms/Terms_Use.cfm

K. Y. Sokolov

A. G. Tumanovskiy

M. N. Gutnik

All-Russian Heat-Engineering Institute (VTI), Moscow, Russia

A. V. Sudarev

Y. I. Zakharov

E. D. Winogradov

Research and Technological Institute of Power Machine Building (VNITIEM), Saint Petersburg,Russia

Mathematical Modeling of an Annular Gas Turbine Combustor

A mathematical model for the description of axisymmetric swirled flow with diffusion combustion is based on numerical solution of the Reynolds equation with a k–W model of turbulence. The results of numerical and experimental investigations of local and general characteristics of flow, heat and mass transfer, combustion, and NO_x formation in an annular combustor with opposite swirled air jets are presented. Satisfactory agreement between calculations and experiments is obtained. The dependences of combustor characteristics versus geometric and operational parameters are generalized.

Introduction

Combustors in gas turbines (GT) are one of the main elements whose operational performance governs the reliability and efficiency of the GT itself. In order to make in-depth studies of the process in a combustor, including the formation of toxic substances, the stabilization of the flame, the mixing of the streams, and other phenomena occurring in them, mathematical models are used that make it possible to determine the local characteristics of the flow in a wide range of variation in structural and operational parameters and to describe the hydrodynamic, heat and mass transfer, and combustion of the fuel (Ustimenko et al., 1986; Khalil et al., 1975). These models can be used to optimize the design of the combustor and its elements and reduce the volume of experimental and tuning work.

Test Combustor

Methods of calculating the characteristics of flow, mass transfer, and combustion have been developed for the element of the front zone of the combustor of a GTN 25 gas turbine unit, in which there is microflame combustion of a gaseous fuel in a system of streams swirled in opposite directions.

This fuel-burning principle is a comparatively new one, which has not yet had sufficient experimental investigation, particularly as regards the effect of geometric parameters on the characteristics of the process. No individual ports for entry of secondary and cooling air into the chamber enable the flow to be regarded as axisymmetric, which considerably simplifies the calculation procedure.

The experimental combustor is an annular channel formed by two coaxial cylinders (H = 0.22 m, R = 0.35 m). At its inlet are two swirlers with the same height of vanes (0.075 m) and opposite swirl directions. They are separated by a stabilizer (B = 0.078 m) in which the end surface is perforated for admission of fuel gas (Fig. 1).

Mathematical Model

The study is based on the numerical solution of a system of Reynolds equations for axisymmetric (two-dimensional solution) flow with allowance for rotation (Khintse, 1963) averaged with respect to the Faure method. Turbulent viscosity was determined using an improvement of the k–W model of turbulence (Ilegbusy and Spalding, 1985). The Kolmogorov–Prandtl ratio $\eta_r = \rho k/W^{0.5}$ was introduced, while the values for the energy of turbulence k and the time-mean square vorticity fluctuation W were determined from a solution of appropriate transfer equations.

To calculate the distribution of the concentration m of a passive gas introduced into an isothermal air flow through the end surface of a stabilizer, a transfer equation was solved for m in fields of averaged velocity components and effective viscosity that had been previously calculated for this type of burner.

When calculating flows with combustion, it was assumed that the entire process is a diffusion combustion, i.e., the rate

Contributed by the International Gas Turbine Institute and presented at the 38th International Gas Turbine and Aeroengine Congress and Exposition, Cincinnati, Ohio, May 24–27, 1993. Manuscript received at ASME Headquarters March 17, 1993. Paper No. 93-GT-339. Associate Technical Editor: H. Lukas.

Copyright © 1995 by ASME

Downloaded 02 Jun 2010 to 171.66.16.102. Redistribution subject to ASME license or copyright; see http://www.asme.org/terms/Terms_Use.cfm

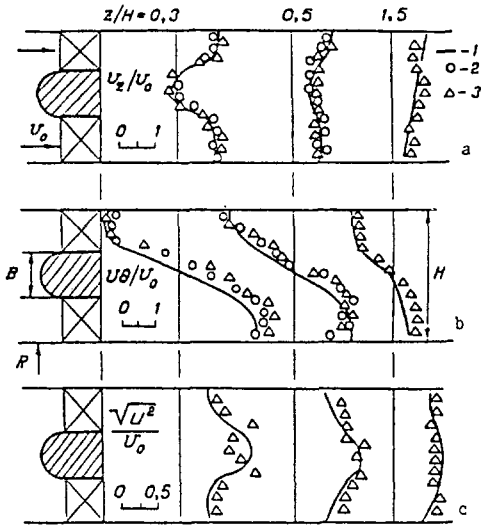

Fig. 1 Distribution of axial (*a*), and tangential (*b*) components of velocity and intensity of turbulence (c) ($\phi = \pm 60$ deg; $K_F = 0.35$); (1) measurement by Pitot probe, (2) measurement by hot-wire anemometer, (3) calculated data

of combustion depends only on the turbulent mixing of the fuel and the oxidizer.

From an examination of the one-stage reaction of the combustion of the methane

$$CH_4 + O_2 = CO_2 + H_2O$$

the Schwab-Zel'dowich scalar function was introduced, defined as

$$f = \frac{m_{CH_4} - m_{O_2}/S + m^{in}_{O_2}/S}{1 + m^{in}_{O_2}} \quad (1)$$

where m_{CH_4}, m_{O_2} are the mass concentrations of methane and oxygen at the point of the calculated zone examined; $m^{in}_{O_2}$ is the concentration of oxygen at the inlet to the channel; S is the stoichometric coefficient ($S = 4$).

To calculate fluctuations of concentration it was assumed that variation in f with time is described by the β-function of the distribution of probability density (Jones, 1980). Values of the functions $\tilde{f}$ and g (g is the square of fluctuation in function f) were found from the solution of transfer equations.

The averaged values of all scalar functions $\Phi(f)$ (temperature and concentrations of reagents) were calculated from the formula

$$\tilde{\Phi}(f) = \int_0^1 \Phi(f) P_\beta(f) df. \quad (2)$$

Density was averaged with time

$$\bar{\rho} = \frac{1}{\int_0^1 \frac{P_\beta(f)}{\rho(f)} df} \quad (3)$$

It is worth noting that in determination of instantaneous temperature, enthalpy fluctuation was assumed to depend on mixture component fluctuation only (Jones, 1980). In this case

$$c_{P_{mix}} T = \tilde{h} = \left(\tilde{h}^{in}_{CH_4} - \tilde{h}^{in}_a\right)\left(f - \tilde{f}\right) - m_{CH_4} H_{CH_4} \quad (4)$$

where $\tilde{h}^{in}_{CH_4}$, $\tilde{h}^{in}_a$ are the enthalpies of the methane and air at the inlet, $\tilde{h}$ is the averaged enthalpy at a given point, H_{CH_4} is the heat of combustion of methane; c_p is the specific heat of gas mixture.

To account for radiation effects the four-flux model of De Marco and Lockwood (1975) was used.

The continuum equation and equations of component momentum, enthalpy, functions f and g, turbulent characteristics of k and W, and radiation fluxes Rz and Rr were written in a canonical form and solved simultaneously:

$$\frac{\partial}{\partial z}\left(\rho U_z \tilde{\Phi}\right) + \frac{1}{r}\frac{\partial}{\partial r}\left(r\rho U_r \tilde{\Phi}\right) = \frac{\partial}{\partial z}\left(b_\phi \frac{\partial \tilde{\Phi}}{\partial z}\right) + \frac{1}{r}\frac{\partial}{\partial r}\left(r b_\phi \frac{\partial \tilde{\Phi}}{\partial r}\right) + \tilde{S}_\phi \quad (5)$$

Here $\Phi = U_z, U_r, rU_\theta, k, W, R_z, R_r, h, f$, and g.

Expressions for source terms S_Φ, coefficients b_Φ, and respective constants were taken from the works of Ilegbusy and Spalding (1985), Jones (1980), and Gosman et al. (1969).

The boundary conditions used were: in the inlet section, profiles of all dependent variables are assigned and are parameters of the problem; natural gas is distributed uniformly over the whole end surface of the stabilizer; at the outlet the longitudinal derivatives of all functions are equal to zero.

At solid boundaries adiabatic conditions were set for functions m, $\tilde{f}$, and g: derivatives along the normal to the wall were equal to zero. For hydrodynamic variables it was assumed that the so-called logarithmic "wall principle," which has been validated for swirl flows of the type looked at by Khalil and Spalding (1975), is satisfied. When calculating flow near the perforated surface of the stabilizer a correction was introduced to this principle that took account of the blowing in.

The wall temperature was determined assuming the balance of convective and radiant wall heat fluxes.

Nomenclature

B = height of stabilizer
c_p = specific heat
f = Schwab–Zel'dowich scalar function
g = square of fluctuation of function f
H = height of annular channel
h = enthalpy
H_{CH_4} = specific heat of combustion of methane
k = turbulence energy
$K_F = B/H$ = blockage factor
L = length of the recirculation zone
m = concentration of passive gas (admixture)
m_{O_2}, m_{CH_4} = mass concentration of CH_4 and O_2
P_β = β-function of the distribution of probability density
P_a = inlet air pressure
R = radius of internal cylinder
T, t = temperature in K and in °C
t_a = inlet air temperature
U_z, U_r, U_θ = axial, radial, and tangential components of the averaged velocity
U_0 = axial velocity of the swirlers inlet
U_{in} = axial velocity in annular channel inlet (before the swirlers and stabilizer)
W = time-mean square vorticity fluctuation
z, r = axial and radial coordinates
α = air–fuel equivalence ratio
η_z = fuel burnup value
ρ = density
τ = residence time
ϕ = swirl angle

Superscripts

~ = averaged value with respect to Faure method

Downloaded 02 Jun 2010 to 171.66.16.102. Redistribution subject to ASME license or copyright; see http://www.asme.org/terms/Terms_Use.cfm

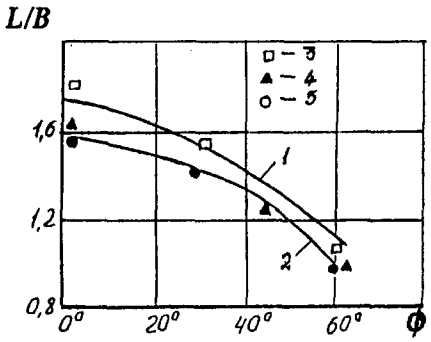

Fig. 2 Relative length of recirculation zone as a function of swirl angle and degree of blockage: (1, 2) calculation, (3–5) experiment, (1, 3) $K_F = 0.43$, (4, 6) $K_F = 0.35–0.37$

At the nodal points the special approach described by Maiorova et al. (1987) was used.

When calculating NO concentration the two-step Zel'dowich scheme was applied:

$$O + N_2 = NO + N$$

$$N + O_2 = NO + O$$

Assuming (Ramos, 1985) that monatomic oxygen is defined from

$$O + O + M = O_2 + M$$

and using the reaction constants of Newhall and Shahed (1971), we obtained the expression for instantaneous reaction rate:

$$R_{NO} = 1.58 \times 10^{14}\left(\frac{\rho m_{O_2}}{T}\right)^{0.5} m_{N_2} \cdot \exp\left(-\frac{67535}{T}\right)(s^{-1}) \tag{6}$$

Considering the possibility of presenting density, temperature, and mass concentrations of O_2 and N_2 as a function of f, the averaged reaction rate of NO, required for solving the NO transfer equation, may be calculated from

$$\tilde{S}_{NO} = \int_0^1 R_{NO}(f) P_B(f) df \tag{7}$$

The NO equation, Eq. (5), was solved using fields of basic variables calculated earlier.

The system of differential equations was solved by the finite difference method of Khalil et al. (1975) on a 31 × 31 grid.

Results and Discussion

Figure 1 shows the results of calculations compared with experimental data on profiles of axial U_z/U_0 and tangential U_θ/U_0 velocities and intensity and turbulence, which were obtained by measurements using a five-hole Pitot probe and hot-wire anemometers on a full-scale rig at VTI. They correspond to an angle of opposite swirl of ±60 deg and a factor of blockage by a stabilizer $K_F = B/H = 0.35$, relating to an internal cylinder radius of $R/H = 1.6$. According to recent research (Slobodyanyuk, 1987) the accuracy of measuring U_z and U_θ with a spherical Pitot probe outside and inside the recirculation zone were 5–10 and 40 percent, respectively. The accuracy of hot-wire measurements in the swirled flows with high intensity of turbulence was evaluated as in the Narinder and Chevray studies (1975) established as 10–20 percent for averaged velocities and 30–35 percent for fluctuating velocities.

It is clear from the diagram that the results of calculations and experiments agree within the limits of measurement error.

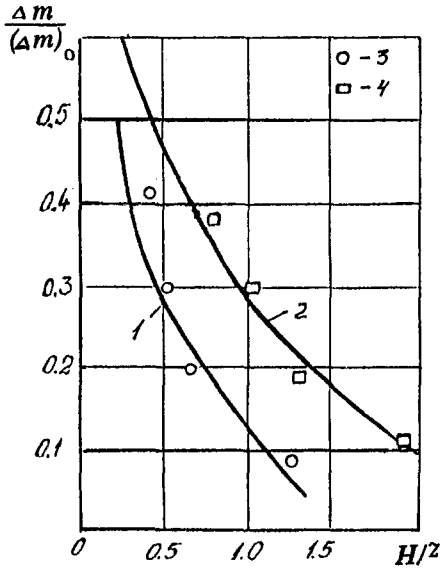

Fig. 3 Variation in relative nonuniformity of the concentration profile of a passive gas admixture along the channel: (1, 2) calculation, (3, 4) experiment, (1, 3) $\phi = \pm 60$ deg, (2, 4) $\phi = 0$ deg

Similar agreement is also observed with swirl values $\phi = 0$, ±30, ±45 deg, and blockage factor $K_F = 0.3–0.55$ (Fig. 2). Thus, the mathematical model used accurately describes the isothermal flow examined. The calculations show that when the degree of blockage in the channel is increased to 0.55–0.6, there is a rise in the relative length of the recirculation zone (L/B). When the angle of swirl increases the recirculation zone L/B diminishes (Fig. 2).

An increase in the angle of swirl also has a marked effect on intensity of turbulence, which at $\phi = \pm 60$ deg reaches almost 100 percent, while the maximum turbulence with a straight-stream flow does not exceed 30 percent.

It is worth noting that with $K_F = 0.35$ the pressure loss coefficient ($2\Delta P^*/\rho U_{in}^2$) for the unswirled flow ($\phi = 0$) was about 1, while at $\phi = \pm 45$ and ±60 deg it reaches 5 and 16, respectively.

Calculated and experimental data seem to agree in terms of mass and heat transfer characteristics. To investigate mass transfer in an isothermal flow, measurements were made of the distribution of concentration of methane, which was supplied without being ignited to the front of the combustor through the perforation in the stabilizer.

Figure 3 shows variations in the relative nonuniformity of the concentration profiles of a passive gas along the channel with flow swirl values $\phi = 0$ and ±60 deg and blockage factor $K_F = 0.35$. Here $\Delta m = (m_{max} - m_{min})$ is the nonuniformity of concentration profile in a given section; $\Delta m^0 = (m_{max} - m_{min})^{in}$ is the same value in the inlet section.

Figure 4 shows experimental and calculated distributions of gas temperature along combustor for three variants of the swirl angle: 0, ±45, ±60 deg; $K_F = 0.35$; $\alpha = 4$; $t_a = 200°C$. It is clear that in this case as well there is satisfactory agreement between the calculated and experimental data.

Large opposite swirl angles intensify the mixing process, causing the temperature profiles to be uniform along the channel. With ±60 deg and at $z/H = 3$ the profile nonuniformity is not in excess of 10 percent.

At swirl angles equal or above 45 deg the annular channel curvature also influences temperature distribution (Fig. 5) as follows: With smaller curvature radius the maximum temperature line tends to curve and at $R/H < 1$ the combustor outlet temperature maximum is found to be at the inner shell. In the calculations the equality of axial velocities at the exits of both swirlers were supposed. That is, air flow was

Downloaded 02 Jun 2010 to 171.66.16.102. Redistribution subject to ASME license or copyright; see http://www.asme.org/terms/Terms_Use.cfm

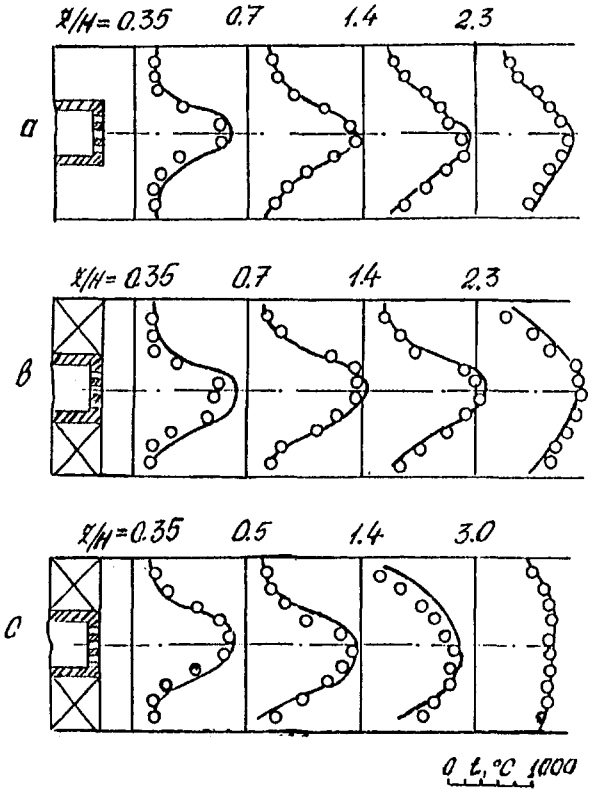

Fig. 4 Profiles of flame temperature along the channel ($\alpha \approx 4$, $t_a \approx 200$°C); (*a*) $\phi = 0$ deg; (*b*) $\pm$ 45 deg; (*c*) $\pm$ 60 deg; (1) calculation, (2) experiment

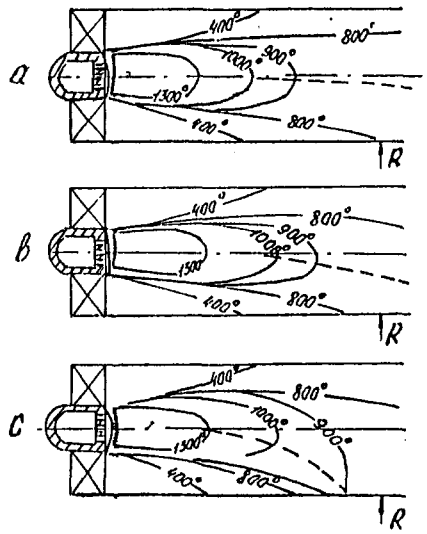

Fig. 5 Influence of a curvature radius on a combustor temperature distribution: (*a*) *R*/*H* = 4.0; (*b*) 1.6; (*c*) 0.5

distributed between swirlers in accordance with the passage area only.

Analysis of the calculated and experimental curves of fuel combustion along the channel (Fig. 6) shows that in operating conditions ($\alpha = 3.5$–6, $t_a = 100$–300°C) it is possible to use models of approximated diffusion combustion within a wide range of variation in structural parameters. In transient conditions with $\alpha > 7.5$ this model underestimates the unburned gas losses. To calculate these conditions a combustion model is required that takes into account the kinetics of the chemical reactions.

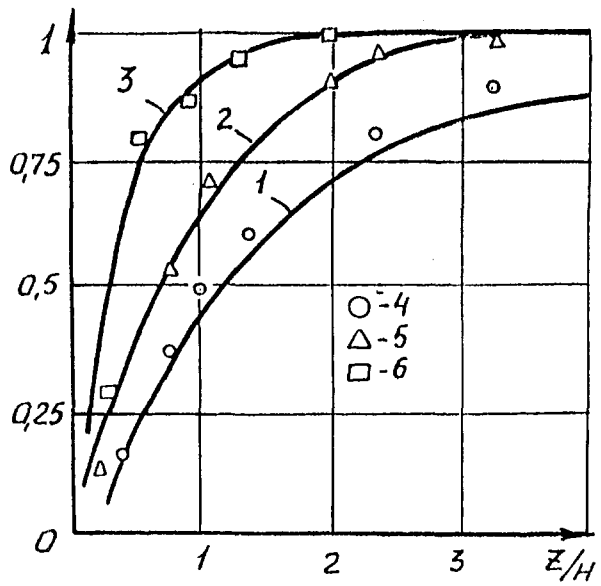

Fig. 6 Curves of fuel combustion along the channel ($\alpha' \approx 4$, $t_a \approx 200$°C): (1–3) calculation; (4–6) experiment; (1, 4) $\phi = 0$ deg; (2, 5) $\pm$45 deg; (3, 6) $\pm$60 deg

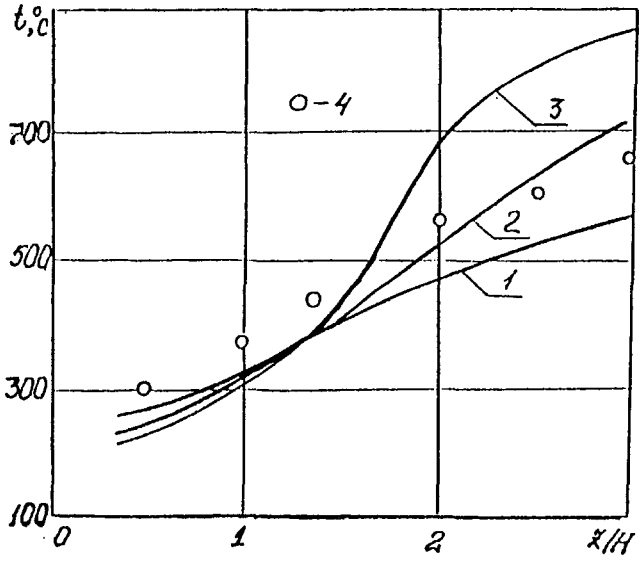

Fig. 7 Variation of the inner shell temperatures along the channel: (1–3) calculation; (4) experiment; (1) $\phi = 0$ deg; (2, 4) $\pm$45 deg; (3) 60 deg

Wall temperature variation along the channel is illustrated in Fig. 7.

Flow swirling results in higher heat transfer coefficient, thus causing some wall temperature reduction at the inlet section. However, due to intensive mixing because of opposite swirl, the downstream wall gas temperature increases and the wall temperature becomes higher as compared to the straight-stream flow. In this case, the outer shell has a lower temperature, which can be explained by a somewhat curving flame toward the inner shell under the action of mass forces.

Satisfactory agreement with experiments allowed calculations on the flame local characteristics to be applied for calculating NO concentration. Figure 8 shows variation of NO concentration along the channel axis at various geometric and flow conditions.

At large opposite swirl angles residence time for the combustor high-temperature zone decreases with decreasing

Downloaded 02 Jun 2010 to 171.66.16.102. Redistribution subject to ASME license or copyright; see http://www.asme.org/terms/Terms_Use.cfm

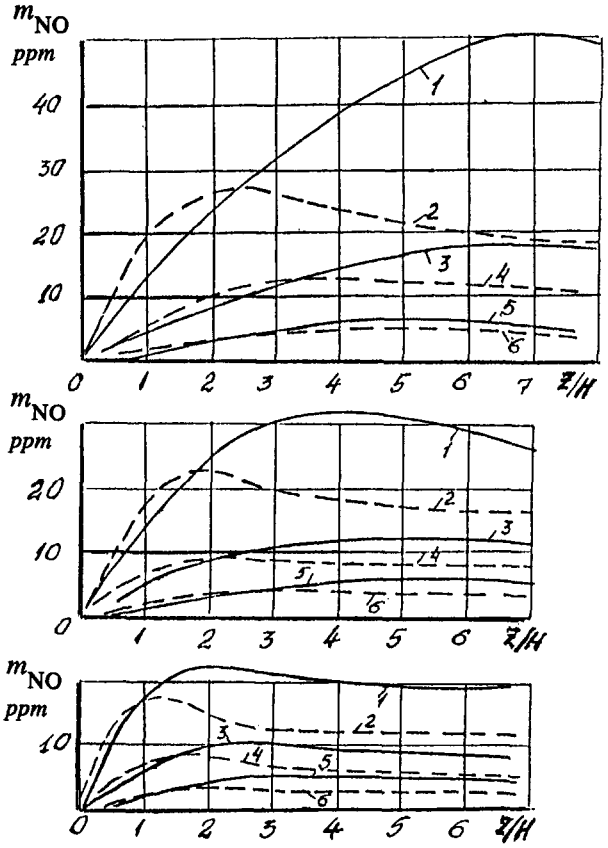

Fig. 8 NO concentration variation along the channel axis at various swirl angles, inlet air temperature and equivalence air–fuel ratio (U_0 = 20 m/c): (*a*) ϕ = 0 deg; (*b*) ± 45 deg; (*c*) ±60 deg; (1, 3, 5) t_a = 300°C; (2, 4, 6) 200°C; (1–3) α = 3.0; (4–6) α = 5.0

flame temperature and length; this leads to lower flame and outlet NO concentrations. Air temperature is a strong influence on NO formation (Fig. 8).

Combustor outlet NO concentration dependence versus air/fuel ratio at different air temperatures and swirl angles is given in Fig. 9 (K_F = 0.36, U_0 = 35 m/c).

Of practical interest is the generalization of data obtained in different calculations to account for the effect of geometries and flow conditions on the combustor outlet NO concentration. Since the rate of NO formation strongly depends on temperature, we may assume that the combustor outlet NO concentration is defined by the maximum rate of NO formation reaction (R_{NO}^{max}) with α = 1.1 and appropriate residence time. Thus we obtain

$$m_{NO} = R_{NO}^{max}\,\tau_{NO}$$

Here, τ_{NO} is mostly dependent on air–fuel equivalence ratio and mixing conditions. Using Eq. (6) for R_{NO}^{max} we arrive at:

$$R_{NO}^{max} \sim P_a^{0.5} \cdot \exp\left(-\frac{67535}{T_{a=1.1}}\right)$$

Finally, NO concentration within α = 2.5–8; t_a = 40–400°C; K_F = 0.25–0.6; ϕ = 0–60 deg; U_O = 10–40 m/c; H = 0.1–0.3 m can be generalized by:

$$m_{NO} = 9.4 \times 10^{16}\,\frac{1}{\alpha^n}\,\frac{1}{1+tg\phi}\left(\frac{K_F}{0.36}\right)^m \exp\left(-\frac{67535}{T_{a=1.1}}\right)\frac{H}{U_0}\,P_a^{0.5}\,[\text{ppm}] \qquad (8)$$

where n = 1.2–0.25$tg\phi$; m = 0.12 + 0.5$tg\phi$; P_a = air pressure, MPa.

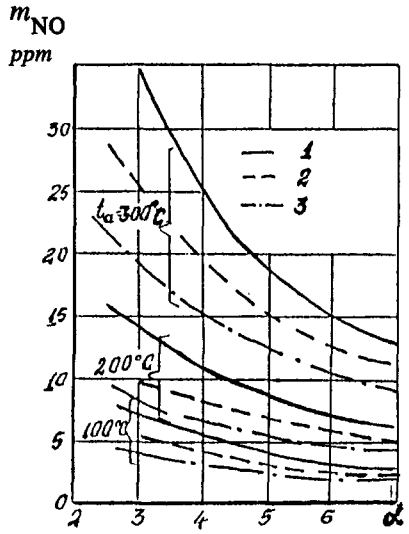

Fig. 9 Combustor outlet NO concentration dependence on swirl angle and air–fuel ratio: (1) ϕ = 0 deg; (2) ±45 deg; (3) ±60 deg

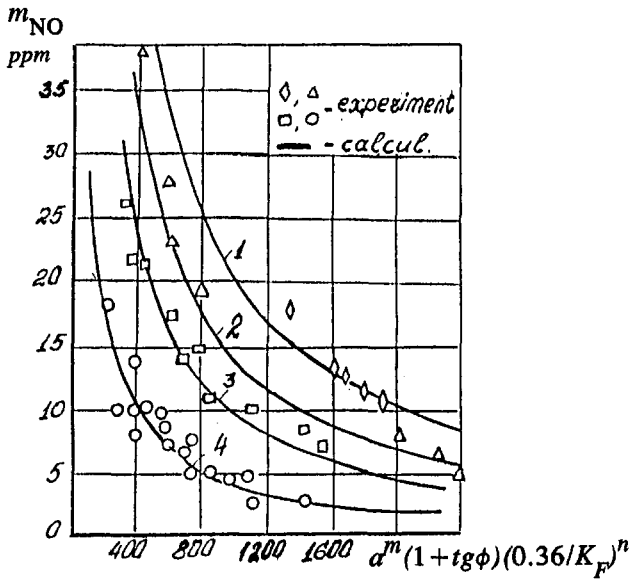

Fig. 10 Combustion outlet NO concentration dependence on a generalizing parameter of Eq. (8): (1) t_a = 300°C, (2) 250°C, (3) 200°C, (4) 100°C

Natural gas combustion temperature at the air–fuel equivalence ratio α = 1.1 can be calculating using:

$$T_{\alpha=1.1} = 2057 + 0.55\,T_a + 0.0001\,T_a^2$$

Figure 10 illustrates NO concentration dependence versus the generalizing parameter of Eq. (8) for several air temperatures and experimental data for P_a = 0.12–0.15 MPa.

The comparison shows good agreement between calculations and experiments for a considerable range of geometries and flow conditions.

Summary

The results of the numerical study proved the validity of the proposed mathematical model for comprehensive description of annular combustor processes.

The model allows adequate determination of combustion flow and heat and mass transfer characteristics for different geometries and flow conditions of a given annular combustor.

Downloaded 02 Jun 2010 to 171.66.16.102. Redistribution subject to ASME license or copyright; see http://www.asme.org/terms/Terms_Use.cfm

References

De Marco, A. G., and Lockwood, F.C., 1975, "A New Flux Model for the Calculation of Radiation in Furnaces," *La revista dei combustibili*, Vol. 29/5-6, pp. 184–190.

Gosman, A. D., Pan, V. M., Ranchel, A. K., et al., 1969, *Heat and Mass Transfer in Recirculating Flows*, Academic Press, New York.

Ilegbusi, J. O., and Spalding, D.B., 1985, "Improvement of k–W Model of Turbulence," ASME *Journal of Heat Transfer*, Vol. 107, pp. 63–68.

Jones, U., 1980, *Prediction Methods for Turbulent Flows*, Hemisphere Publishing Corporation, Washington, DC.

Khalil, E. E., Spalding, D. B., and Whitelaw, J. H., 1975, "The Calculation of Local Properties in Two Dimensional Furnaces," *International Journal of Heat and Mass Transfer*, Vol. 18, pp. 775–780.

Khintse, N. O., 1963, *Turbulence*, Fizmatgiz., Moscow.

Maiorova, A. I., Sviridenkov, A. A., and Sokolov, K. Yu., 1987, "Method of Calculation of Swirled Recirculating Flows," *Proceedings of ZIAM*, Vol. 1203, pp. 49–55.

Narinder, K. T., and Chevray, R., 1975, "Cross Wire Anemometry in High Intensity Turbulence," *Journal of Fluid Mechanics*, Vol. 71/4, pp. 785–790.

Newhall, H. K., and Shahed, S. M., 1971, "Nitrogen Oxides Formation in High Pressure Flames," *Proceedings of 13th Symposium (International) on Combustion*, Pittsburgh, PA, pp. 381–385.

Ramos, J. I., 1985, "A Numerical Study of Swirl Stabilized Combustor," *Journal of Non-equilibrium Thermodynamic*, Vol. 10, pp. 263–270.

Slobodyanyuk, L. I., 1987, "Accuracy of Flow Measurement Based on Using of Pitot Probes," *Izv. vuzov. Energetika*, Vol. 7, p. 97.

Ustimenko, B. P., Dzhakupov, K. B., and Krol', V. O., 1986, "Numerical Modelling of Aerodynamics and Combustion in Furnace and Industrial Units," Nauka, Alma-ata.

Downloaded 02 Jun 2010 to 171.66.16.102. Redistribution subject to ASME license or copyright; see http://www.asme.org/terms/Terms_Use.cfm

The Importance of the Nitrous Oxide Pathway to NO_x in Lean-Premixed Combustion

D. G. Nicol

R. C. Steele

N. M. Marinov

P. C. Malte

Department of Mechanical Engineering,
Combustion Laboratories,
University of Washington,
Seattle, WA 98195

This study addresses the importance of the different chemical pathways responsible for NO_x formation in lean-premixed combustion, and especially the role of the nitrous oxide pathway relative to the traditional Zeldovich pathway. NO_x formation is modeled and computed over a range of operating conditions for the lean-premixed primary zone of gas turbine engine combustors. The primary zone, of uniform fuel–air ratio, is modeled as a micromixed well-stirred reactor, representing the flame zone, followed by a series of plug flow reactors, representing the postflame zone. The fuel is methane. The fuel–air equivalence ratio is varied from 0.5 to 0.7. The chemical reactor model permits study of the three pathways by which NO_x forms, which are the Zeldovich, nitrous oxide, and prompt pathways. Modeling is also performed for the well-stirred reactor alone. Three recently published, complete chemical kinetic mechanisms for the C1–C2 hydrocarbon oxidation and the NO_x formation are applied and compared. Verification of the model is based on the comparison of its NO_x output to experimental results published for atmospheric pressure jet-stirred reactors and for a 10 atm. porous-plate burner. Good agreement between the modeled results and the measurements is obtained for most of the jet-stirred reactor operating range. For the porous-plate burner, the model shows agreement to the NO_x measurements within a factor of two, with close agreement occurring at the leanest and coolest cases examined. For lean-premixed combustion at gas turbine engine conditions, the nitrous oxide pathway is found to be important, though the Zeldovich pathway cannot be neglected. The prompt pathway, however, contributes small-to-negligible NO_x. Whenever the NO_x emission is in the 15 to 30 ppmv (15 percent O_2, dry) range, the nitrous oxide pathway is predicted to contribute 40 to 45 percent of the NO_x for high-pressure engines (30 atm), and 20 to 35 percent of the NO_x for intermediate pressure engines (10 atm). For conditions producing NO_x of less than 10 ppmv (15 percent O_2, dry), the nitrous oxide contribution increases steeply and approaches 100 percent. For lean-premixed combustion in the atmospheric pressure jet-stirred reactors, different behavior is found. All three pathways contribute; none can be dismissed. No universal behavior is found for the pressure dependence of the NO_x. It does appear, however, that lean-premixed combustors operated in the vicinity of 10 atm have a relatively weak pressure dependence, whereas combustors operated in the vicinity of 30 atm have an approximately square root pressure dependence of the NO_x.

Introduction

During the 1992 Gas Turbine and Aeroengine Congress, it was stated in more than one presentation that the nitrous oxide pathway is responsible for much of the NO_x formed in lean-premixed gas turbine engine combustors fired on natural gas. This possibility is examined in this study by using a simple chemical reactor model, and the recently published kinetic mechanisms of hydrocarbon oxidation and NO_x formation of Drake and Blint [1], Miller and Bowman [2], and Michaud et al. [3].

The benefits of this type of study are as follows:

1 It permits the determination of combustion conditions for which the nitrous oxide pathway should be considered, and for which the Zeldovich pathway alone is insufficient to explain the NO_x. It indicates the importance that should be given to including the nitrous oxide chemistry in fluid codes for gas turbine combustors.

2 It permits the NO_x trends for lean-premixed combustion to be studied, for example, the pressure dependence of the NO_x.

Contributed by the International Gas Turbine Institute and presented at the 38th International Gas Turbine and Aeroengine Congress and Exposition, Cincinnati, Ohio, May 24–27, 1993. Manuscript received at ASME Headquarters March 17, 1993. Paper No. 93-GT-342. Associate Technical Editor: H. Lukas.

Copyright © 1995 by ASME

Downloaded 02 Jun 2010 to 171.66.16.102. Redistribution subject to ASME license or copyright; see http://www.asme.org/terms/Terms_Use.cfm

3 It provides insight into combustor arrangements that have the potential to minimize the formation of NO_x.

This paper is arranged so that the chemical reactor model and chemical kinetic mechanisms are summarized first. This is followed by comparisons of the model predictions to the measurements of NO_x obtained for well-defined laboratory burners. This provides for the verification of the model. This is followed by the application of the model to the prediction of NO_x for lean-premixed combustion conditions.

The focus of this study is on the chemical kinetics of NO_x formation. Chemical pathways most likely to form the NO_x in lean-premixed combustors are determined. Results obtained with different chemical mechanisms are compared. The fluid mechanics of NO_x formation is not modeled in this study. That is left to other studies. However, inference can be drawn from the results obtained herein regarding the role fluid mechanics might play in minimizing the NO_x formation in lean-premixed combustors.

Chemical Reactor Model

The baseline chemical reactor model employed consists of a micromixed well-stirred reactor (WSR), followed immediately by a series of plug-flow reactors (PFR). Usually, the WSR is assigned the smallest volume that will permit reaction for a given mass flow rate of reactants. This is termed "incipient blowout." It is defined to be 101 percent of the volume for blowout of the WSR.

The WSR provides for the initiation and stabilization of the combustion process, and represents the flame zone. The PFR provides for the continuation of the combustion process, and given adequate mean residence time, permits the combustion process to approach completion. It represents the post flame zone. Together, the WSR and PFR, of uniform fuel–air equivalence ratio, are taken to simulate the complete lean-premixed combustion process.

A variation of the baseline model is used to assess the sensitivity of the NO_x to the fraction of the combustor volume assumed to be the WSR. In this variation, the WSR component is increased progressively until it comprises the complete combustor, at which point the PFR component is eliminated. In an actual combustor, this variation would require the inlet streams to penetrate increasingly deeper into the combustor, and thus, produce an increasingly larger region that is intensely mixed and is high in free radical concentrations. The effect of this, as shown later, is to increase the NO_x.

Another variation of the model involves removal of the WSR. Combustion stabilization is then accomplished by including one or more recycle zones, by which hot, burned gases are brought forward to the initial plug-flow reactor stage. In a previous study of lean-premixed combustion for gas turbine engines [4], this variation was found to cause little change in the NO_x compared to that predicted by the baseline model, and thus, is not reconsidered herein.

In order to validate the baseline model, and the WSR model alone, test cases were computed and compared to datasets for laboratory combustors. These datasets include atmospheric pressure jet-stirred reactor measurements from two laboratories, and porous-plate burner data for 10 atm. Following this phase of the study, the baseline model was applied to a range of lean-premixed gas turbine combustor operating conditions in order to determine the following:

1 The effect of varying the volume of the flame zone (i.e., the WSR) relative to the volume of the postflame zone (i.e., the PFR).
2 The effects of varying the combustor pressure (1, 10, and 30 atm) and inlet temperature (300, 600, and 800 K).

The NO_x Chemical Pathways

Zeldovich. The extended Zeldovich pathway is given below by reactions (1)–(3). Thermal NO_x refers to NO_x formed from the extended Zeldovich pathway when the O atom, H atom, OH radical, and O_2 are at chemical equilibrium concentrations. When these species have nonequilibrium concentrations, the NO_x formed is referred to as Zeldovich NO_x. Initiation occurs by the reverse rates of reactions (1) and (1*a*).

$$N + NO = N_2 + O \quad (1)$$

$$N + NO = N_2 + O(^1D) \quad (1a)$$

$$N + O_2 = NO + O \quad (2)$$

$$N + O_2 = NO + O(^1D) \quad (2a)$$

$$N + OH = NO + H \quad (3)$$

Note: $O(^1D)$ denotes the electronically excited singlet O atom; O denotes the ground state triplet O atom. Reactions (1*a*) and (2*a*) pertain only to the Michaud et al. kinetic mechanism [3].

Nitrous Oxide. The nitrous oxide pathway is given below by reactions (4)–(11). The mechanism is initiated by the reverse rates of reactions (4) and (4*a*), and the N_2O formed is then oxidized to NO mainly by reaction (5), but also forms by reactions (8), (10), and (11). The N_2O is reduced to N_2 by reactions (4), (4*a*), (6), (7), and (9).

$$N_2O + M = N_2 + O + M \quad (4)$$

$$N_2O + M = N_2 + O(^1D) + M \quad (4a)$$

$$N_2O + O = NO + NO \quad (5)$$

$$N_2O + O = N_2 + O_2 \quad (6)$$

$$N_2O + H = N_2 + OH \quad (7)$$

$$N_2O + H = NO + NH \quad (8)$$

$$N_2O + OH = N_2 + HO_2 \quad (9)$$

$$N_2O + CO = NO + NCO \quad (10)$$

$$N_2O + M = N + NO + M \quad (11)$$

Note: Reactions (4*a*) and (11) pertain only to the Michaud et al. kinetic mechanism [3].

Prompt. For the prompt mechanism, only the initiating reaction is listed. This is reaction (12) below. The balance of the prompt NO_x mechanism involves the oxidation of the HCN molecules and the N atoms, and the chemical recycle of NO to HCN by reaction with CH_x species. Under lean-premixed conditions, the HCN oxidizes to NO by the reaction sequence HCN => CN => NCO => NO. The N atom oxidizes mainly by reaction (2).

$$N_2 + CH = HCN + N \quad (12)$$

Nitrogen Dioxide. The NO formed by the three chemical pathways just described can oxidize to NO_2, mainly by reaction (13) listed below. Because of this, the mechanisms and results of this study are normally expressed as NO_x (the sum of NO and NO_2), rather than as NO.

$$NO + HO_2 = NO_2 + OH \quad (13)$$

Isolation of Pathways. In order to consider the NO_x contributed individually by these pathways, the following procedure can be used: (1) The Zeldovich NO_x is computed first by including only reactions (1–3) in the model. (2) This is followed by adding reactions (4–11) in order to give the sum of the Zeldovich NO_x and the NO_x contributed by the nitrous oxide pathway. (3) The concluding step involves the addition of the prompt NO_x pathway (i.e., reaction (12) and

Downloaded 02 Jun 2010 to 171.66.16.102. Redistribution subject to ASME license or copyright; see http://www.asme.org/terms/Terms_Use.cfm

all of the additional reactions involving the nitrogen chemistry), to give the total NO_x. The individual contributions are then determined by difference.

A similar procedure, which gives results identical to those obtained by the long procedure just described (within 4 percent), regardless of the order of application of the following steps, is used in this study. Starting from the full mechanism, the steps are as follows:

1 Prompt NO_x is eliminated by removing reaction (12). This reaction is the primary source of the N atoms and cyano molecules formed by the attack of hydrocarbons on N_2. (Other, less important reactions between hydrocarbons and N_2 are also eliminated, even though they do not contribute significantly.)
2 Zeldovich NO_x is eliminated by removing the reverse rates of reactions (1) and (1*a*). These are the only reactions that produce N atoms and NO by attack of O atoms on N_2.
3 The contribution of the nitrous oxide pathway to NO_x is eliminated by removing the reverse rates of reactions (4) and (4*a*). These are the only reactions that contribute significantly to the formation of N_2O from N_2.

The Chemical Kinetic Mechanisms

Three complete chemical kinetic mechanisms of hydrocarbon oxidation and NO_x chemistry are used in the present study. These three mechanisms are those of Drake and Blint [1], Miller and Bowman [2], and Michaud et al. [3].

The kinetic mechanism of Drake and Blint, hereafter referred to as the DB mechanism, has been used without deletions. Reaction (9), with rate data as estimated in [2], has been added to the DB mechanism; and the pressure sensitivities of reaction (4) and the CH_4 dissociation reaction have been extended from 20 to 35 atm. The rate data selected for reaction (12) are from [5], since these have been found to give the best overall agreement between the model results and the jet-stirred reactor and porous-plate datasets considered. The DB kinetic mechanism, which was developed from verification of laminar, premixed flame data taken at the burner surface, shows an enhanced importance of the prompt NO_x pathway [1].

The kinetic mechanism of Miller and Bowman, hereafter referred to as the MB mechanism, has been used without deletions. The dissociation reactions for C_2H_6, C_2H_5, C_2H_3, CH_4, and reaction (14) listed below, have been corrected for elevated pressure. The MB kinetic mechanism is the successor to the Glarborg et al. mechanism [5], which was based on jet-stirred reactor data.

$$CH_2CO + M = CH_2 + CO + M \qquad (14)$$

The kinetic mechanism of Michaud et al., hereafter referred to as the MWF mechanism, has been used without deletions. The dissociation reactions for C_2H_6, C_2H_5, C_2H_3, CH_4, reaction (14), as well as reactions (15) and (16) listed below, have been corrected for elevated pressure. The MWF kinetic mechanism was developed using porous-plate burner data and includes the addition of the singlet O atom chemistry to the Zeldovich and nitrous oxide pathways.

$$OH + NO_2 = HOONO \qquad (15)$$

$$N_2O + H = HNNO \qquad (16)$$

These three kinetic mechanisms have been selected for this study, since they represent recent developments in NO_x chemistry for combustion sources. The MB mechanism has been used in several studies, the DB mechanism provides enhanced prompt NO_x rates, and the MWF mechanism provides alternative possibilities regarding the O atom attack on N_2 and the formation of N_2O. These mechanisms cover a useful range of chemical kinetic possibilities for NO_x formation in gas-fired, high-pressure combustors.

Laboratory Reactor NO_x Measurements

In the next two sections of this paper, results for NO_x are shown and discussed for two distinctly different types of laboratory combustion reactors. Results obtained by the model applied to the conditions of these reactors are examined. The two types of reactor are jet-stirred reactors and a porous-plate burner.

Jet-stirred reactors, when operated at short residence times (of a few milliseconds) can approach the well-stirred reactor (WSR) condition. At this condition, the rate of mixing is fast compared to the rate of chemistry for the process being studied, which in this case is the formation of NO_x. The condition is characterized as zero dimensional. Results for NO_x are shown in the next section, which appear to satisfy the WSR condition. Results are also shown for jet-stirred reactors operated so that the mixing is not fast compared to the chemistry. In this situation, the finite mixing rate, together with wall heat loss, promotes gradients and structure within the reactor and influences the NO_x formation. Increases in NO_x because of these influences are shown. However, decreases in NO_x because of a finite mixing rate can also occur, and are shown.

The porous-plate burner, on the other hand, is essentially a one-dimensional plug-flow reactor (PFR). Although the initial region of burner requires backmixing and back-diffusion for stabilization of the flame (the model uses a WSR zone), under lean-premixed conditions only a relatively small amount of the NO_x emitted from the burner is formed in this region. This region generally has a short mean residence time compared to that of the overall burner. Thus, the NO_x is formed predominantly in the bulk of the burner, which is well modeled as a PFR.

Jet-Stirred Reactor NO_x

Jet-stirred reactors permit NO_x to be examined under conditions of intense recirculation of the burning gases into the fresh reactants. Furthermore, they provide databases for the development of NO_x mechanisms, e.g., see [5].

Published results on NO_x formation for lean, premixed, methane-fired jet-stirred reactors are reviewed and compared to the model predictions. The model predictions are based on the measured temperatures, pressures, mean residence times, and inlet reactant concentrations. The NO_x yields are in the low (< 10 ppmv) and modest (< 100 ppmv) ranges. The data are based on the actual O_2 (dry) concentrations. The reactor pressure is ambient, which is either 1.0 or 0.92 atm (depending on the elevation of the laboratory site). Three types of results are shown, including: (1) NO_x trends, (2) comparison to the model, and (3) NO_x pathways.

NO_x Trends

Trends in the rate of formation of NO_x are shown in Fig. 1. This rate is based on the NO_x measured for the reactor divided by the mean residence time of the reactor. These results are derived from [6]. The measurements were obtained at a pressure of $P = 0.92$ atm, a fuel–air equivalence ratio of $\phi = 0.75$, an inlet temperature of the reactants of $T_{in} = 295$ K, and an inlet air humidity ratio of 8×10^{-4} g H_2O/g dry air. The mean residence time was varied over a wide range, from $\tau = 6$ to 40 ms. The reactor temperature depended mainly on the mean residence time. That is, with increasing mean residence time, the reactor experienced increasing heat loss, which led to a decrease in temperature.

The main trends evident from Fig. 1 are as follows:

Downloaded 02 Jun 2010 to 171.66.16.102. Redistribution subject to ASME license or copyright; see http://www.asme.org/terms/Terms_Use.cfm

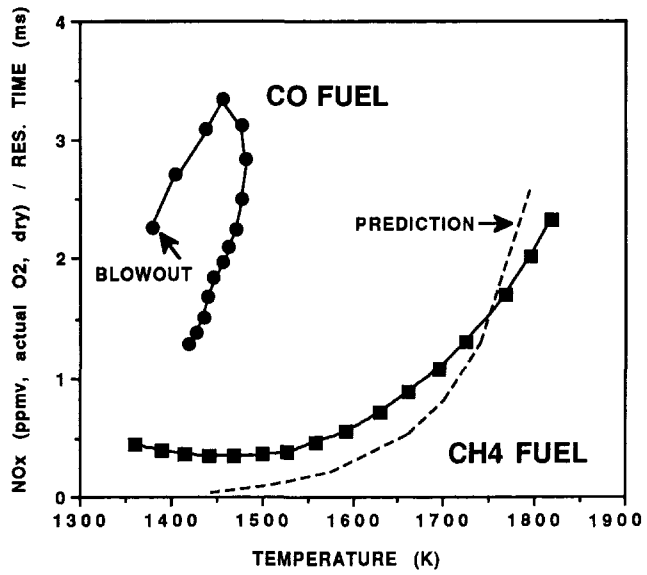

Fig. 1 Measured, overall rate of formation of NO_x, based on conditions of a dry sample at the actual O_2 concentration, versus temperature for a jet-stirred reactor operated at a pressure of 0.92 atm, an inlet temperature of 295 K, a fuel–air equivalence ratio of 0.75, and nominal mean residence times of 6 to 40 ms for the CH_4 fuel and 7 to 24 ms for the CO fuel, from [6]. Model predictions use the Miller and Bowman [2] chemical kinetic mechanism.

Table 1 Measured and predicted results for a jet-stirred reactor operated at 0.92 atm pressure and 295 K inlet temperature

FUEL	MEASUREMENTS			PREDICTIONS				
	T (K)	τ (ms)	NOx	Model	NOx	Prompt	Nitrous	Zeld.
CH4	1445	30.3	13.2	DB	1.51	1.23	0.24	0.04
				MB	1.03	0.31	0.68	0.04
				MWF	1.16	0.31	0.79	0.06
CH4	1661	11.5	9.4	DB	6.99	4.09	1.30	1.60
				MB	5.99	1.78	2.74	1.47
				MWF	7.27	1.78	3.56	1.93
CH4	1795	6.54	12.2	DB	18.13	6.52	2.74	8.87
				MB	16.79	3.86	4.82	8.11
				MWF	20.75	3.86	6.53	10.36
CO	1440	19.0	33.9	DB	5.20	0.02	4.80	0.33
				MB	18.19	0.0	17.90	0.29
				MWF	15.05	0.0	14.65	0.40
CO	1443	9.43	31.8	DB	3.95	0.02	3.67	0.26
				MB	13.54	0.0	13.30	0.24
				MWF	11.49	0.0	11.18	0.31

1 The importance of the nitrous oxide pathway to NO_x is demonstrated by the results for the combustion of the CO fuel. The nitrous oxide pathway contributed nearly all of NO_x. Furthermore, the rate of NO_x formation for the CO combustion was markedly greater than for the methane combustion (at similar temperatures). Because of the modest temperatures of the CO combustion, the Zeldovich pathway was weak. Model predictions indicate that less than 10 percent of the NO_x measured for the CO combustion was caused by the Zeldovich pathway (see Table 1). The CO combustion with the nearly dry air gave high O atom levels, which promoted N_2O formation by reaction (4 reverse), followed by N_2O oxidation to NO by reaction (5). The nitrous oxide was not destroyed by reaction (7), because of the low levels of the H atom. For the methane combustion, however, the O atom levels were lower, and the H atom levels were considerably greater. Thus, less N_2O was formed, and that which was formed was destroyed by reaction (7). Markedly less NO_x was formed.

An interesting additional aspect of the results for the CO combustion is the double-valued behavior of the NO_x. The lower part of the curve corresponds to the usual behavior of the reactor: i.e., the reactor temperature increased with decreasing mean residence time. The upper part of the curve, however, corresponds to the short mean residence times. The reactor was near blowout. The temperature (and free radical concentrations) increased with increasing mean residence time, resulting in the maximum in the NO_x formation rate at the temperature of about 1450K.

2 For the methane combustion, typical behavior is shown in Fig. 1 for temperatures greater than about 1600 K (corresponding to the shortest residence times run). That is, the rate of formation of the NO_x increased with increasing temperature, and the measured and modeled NO_x agree within a factor of about two. However, for temperatures below 1600 K, involving residence times of about 15 ms and greater, the reactor was significantly influenced by gradients caused by the finite mixing rate and the wall heat loss. The WSR is no longer a reasonable model. It significantly underpredicts the NO_x. It is interesting to note that at the lowest temperatures (and longest residence times) examined, the rate of NO_x formation measured actually increased with decreasing temperature. This is attributed to regions of elevated temperature in the center of the reactor. Because of the heat loss at the walls of the reactor, the temperatures in the center of the reactor, in the vicinity of the inlet jets, were hotter than the temperatures measured for the bulk of the reactor. This effect is explored in detail in [7].

Measured and modeled values for selected cases from Fig. 1 are given in Table 1. The predictions for the methane cases show that all the pathways contribute to the NO_x, except for a very weak Zeldovich contribution for the 1445 K case. As explained above, close agreement between the measured and modeled results is not expected for the methane cases because of the relatively long mean residence time run. On the other hand, the CO combustion more nearly satisfied the WSR condition, because of the modest temperatures and low H_2O concentrations. For these cases the lack of agreement between the measured and modeled results (using the MB and MWF mechanisms) is caused by uncertainty in the measured H_2O inlet air concentration. The CO combustion is very sensitive to changes in the H_2O content of nearly dry air. In [6], close agreement is obtained between the measured and modeled results for the NO_x when the measured O atom concentrations are used in a kinetic mechanism involving the nitrous oxide and Zeldovich pathways.

For the methane combustion, the DB, MB, and MWF mechanisms predict about the same total NO_x. The difference evident is the favoring by the DB mechanism of prompt NO_x over NO_x formed by the nitrous oxide pathway. For the CO combustion, the reduced prediction by the DB mechanism of the NO_x formed by the nitrous oxide pathway is significant. The MB and MWF mechanisms appear to offer the best representation of the nitrous oxide pathway.

Comparison to the Model

Figure 1 and Table 1 are useful primarily for the trends they show. The measurements considered now show very good agreement to the model predictions, and thus, are useful quantitatively. These are the results shown in Fig. 2.

In Fig. 2, results of Corr et al. [7], Bartok et al. [8], Malte et al. [9], and Singh et al. [10] are plotted. The fuel-rich data of [8] and [9] have not been included, and only single data points have been used from [7] and [10], since the remainder of their data were obtained in combustion gases diluted by an inert in order to maintain a constant temperature. Also, not all of the lean data of [8] are plotted, in order to show a relatively uncluttered figure.

Downloaded 02 Jun 2010 to 171.66.16.102. Redistribution subject to ASME license or copyright; see http://www.asme.org/terms/Terms_Use.cfm

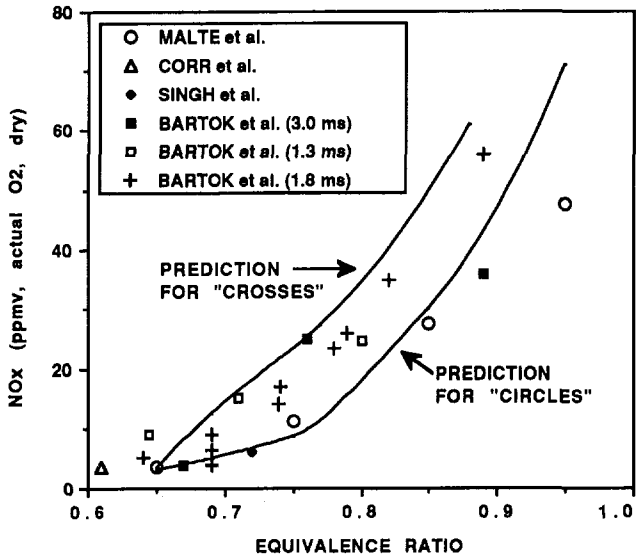

Fig. 2 Measured NO_x (dry, actual O_2) versus fuel–air equivalence ratio for jet-stirred reactors operated at ambient pressure and nominal mean residence times of 1.3 to 5 ms. Bartok et al [8] measurements for 464 K inlet temperature; other measurements (from [7, 9 and 10]) for 295 K. Model predictions use the Miller and Bowman [2] chemical kinetic mechanism.

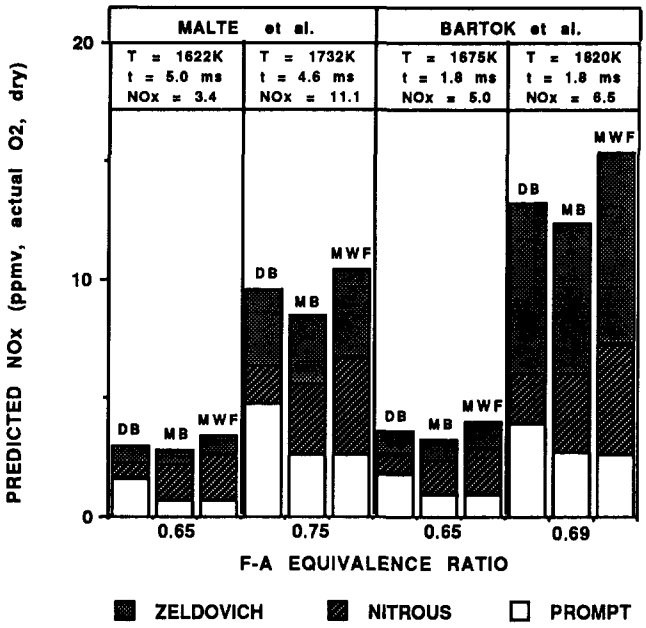

Fig. 3 Predicted contributions of the Zeldovich, nitrous oxide, and prompt chemical pathways to total NO_x using the Drake and Blint (DB), the Miller and Bowman (MB), and the Michaud et al. (MWF) kinetic mechanisms, and assuming a well-stirred reactor operating at the measured temperature and mean residence time, versus fuel-air equivalence ratio. Same conditions as for Fig. 2.

The range of ϕ is 0.60 to 0.95, and the range of τ is 1.3 to 5.0 ms. The pressure is 1 atm for [7] and [8], and 0.92 atm for [9] and [10]. The reactant inlet temperature is 464 K for [8], and 295 K (nominal) for the other data.

Because the temperatures of Malte et al [9] were measured by OH absorption and also by fine, coated, heat loss corrected thermocouples, these temperature data are assumed to be the most accurate of the datasets.

Figure 2 shows NO_x predictions using the MB mechanism, applied to the experimental conditions of Bartok et al. [8] at 1.8 ms mean residence time, and Malte et al. [9]. These cases have been selected for modeling because of the extensive database of [8] at 1.8 ms (and the use of [8] for kinetic mechanism development [5]), and the accurate temperatures of [9]. (In [4], comparison of all the measurements shown in Fig. 2 to the model with the DB mechanism was conducted.)

In Fig. 2 the agreement between the measured and predicted NO_x values is very good, especially for the conditions of Malte et al. [9] for $\phi < 0.90$. For $\phi > 0.90$, the rate of combustion was sufficiently rapid for the free radical concentrations (O, OH, and H) to relax toward equilibrium in the bulk of the reactor volume. Thus, as confirmed by direct measurement of OH, the free radical concentrations in the bulk of the reactor were less than the WSR-predicted values [9]. This, in turn, meant a decrease in the amount of NO_x formed by the Zeldovich and nitrous oxide pathways. This is an example of the influence of finite mixing causing a reduction in NO_x compared to the WSR condition. (This is in contrast to the behavior shown in Fig. 1 and discussed above, in which case the slow mixing led to increased NO_x compared to the WSR prediction.)

With respect to the results of Bartok et al. [8], two features are noted: (1) The NO_x is greater than that measured by Malte et al. [9] because of the higher inlet temperature. Also, the very short residence times of [8] led to enhanced free radial concentrations, and therefore, to greater NO_x yields. (2) The small differences noted between the modeled and measured values are assumed to be due to uncertainty in the measured temperature.

The generally good agreement noted in Fig. 2 between the modeled and measured NO_x is taken as verification of the model for lean-premixed combustion, at least for well-stirred combustion at atmospheric pressure.

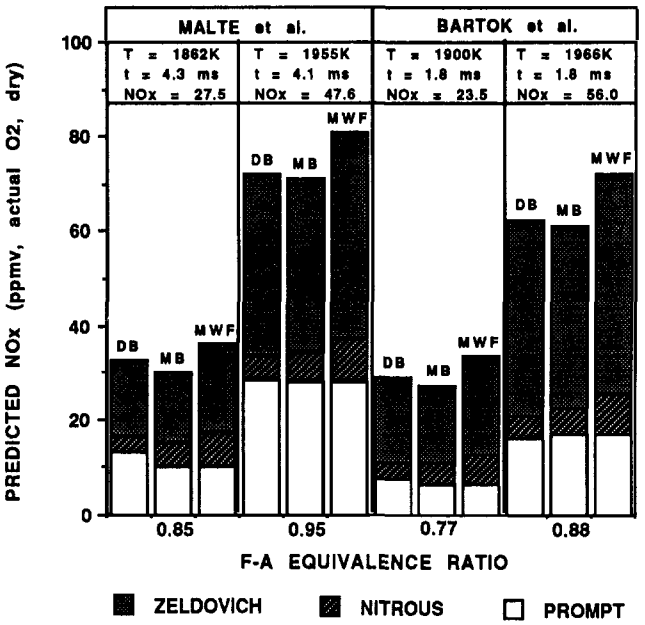

Fig. 4 Predicted NO_x contributions assuming a well-stirred reactor operating at the measured temperature and mean residence time versus fuel-air equivalence ratio. Similar to Fig. 3.

NO_x Pathways. Attention is now turned to the contributions of the different NO_x pathways for the cases of Fig. 2 modeled. These results are shown in Figs. 3 and 4. The experimental conditions for the cases of [8] and [9] treated are listed in the boxes near the tops of the figures. The following characteristics are found:

1 Especially for the results shown in Fig. 3, with ϕ between

Downloaded 02 Jun 2010 to 171.66.16.102. Redistribution subject to ASME license or copyright; see http://www.asme.org/terms/Terms_Use.cfm

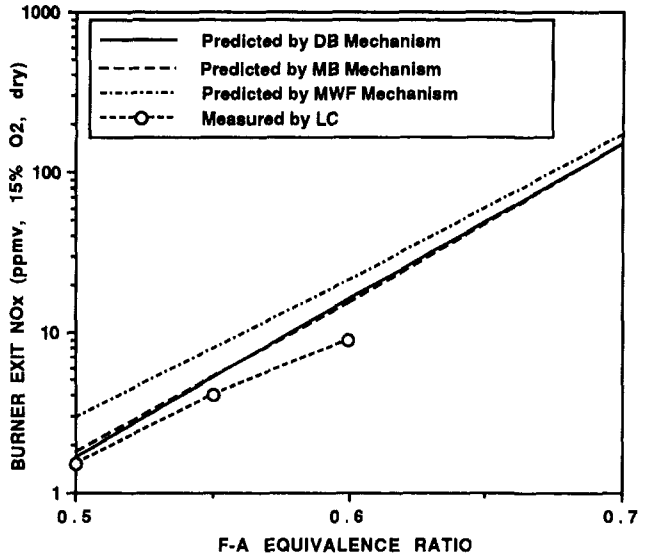

Fig. 5 Predicted and measured NO_x for a porous-plate burner operated at a pressure of 10.4 atm, and an inlet temperature of 616 K versus fuel–air equivalence ratio. Measurements are from Leonard and Correa [11]. Predictions are based on an adiabatic chemical reactor consisting of a WSR operating at incipient blowout, followed by a PFR.

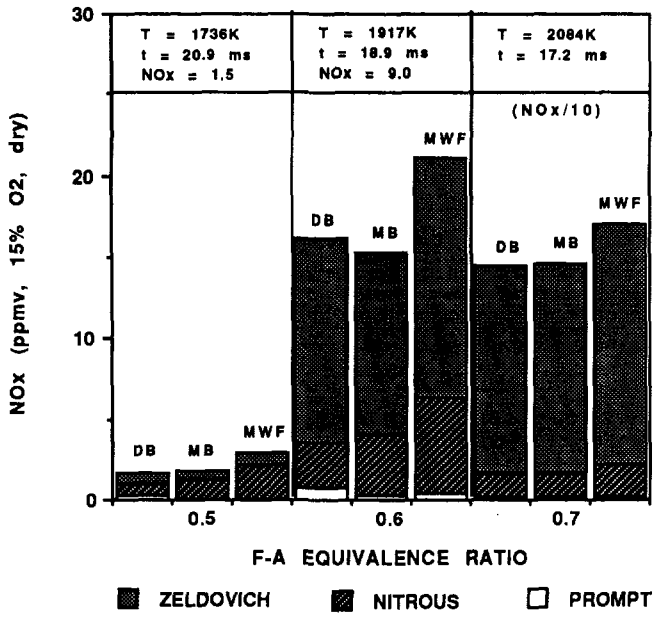

Fig. 6 Predicted NO_x contributions for the porous-plate burner versus fuel–air equivalence ratio. Same conditions as for Fig. 5. The NO_x results for the 0.7 equivalence ratio are divided by 10.

0.65 and 0.75, all three NO_x pathways are significant. None is negligible.

2 The total NO_x predicted is about the same for the different mechanisms, though, because of the inclusion of the singlet O atom chemistry, the MWF mechanism generally gives a slightly greater NO_x than the DB and MB mechanisms.

3 At the leanest (and lowest temperature) cases considered, the nitrous oxide and prompt pathways provide the majority of the NO_x. Furthermore, the mechanisms differ. For the DB mechanism, the greatest contributor is the prompt pathway; whereas for the MB and MWF mechanisms, the greatest contributor is the nitrous oxide pathway. (It should be noted, that the prompt NO_x portion of the MWF mechanism is based on the MB mechanism.)

From these results it is concluded that all three NO_x pathways must be considered for lean, premixed combustion, at least for well-stirred combustion at atmospheric pressure.

Porous-Plate Burner NO_x

Attention is now directed to the porous-plate burner operated at elevated pressure. The questions are (1) whether the model and chemical kinetic mechanisms are valid for this burner, and (2) whether the NO_x formation is similar to that for the jet-stirred reactor.

Experimental Conditions. The porous-plate burner data are from Leonard and Correa [11], hereafter termed measurements by LC. The fuel was methane, premixed with air. The burner pressure was 10.4 atm, and the mixture inlet temperature was 616 K. (Leonard and Correa also conducted experiments for lower pressures and mixture inlet temperatures. Those results were modeled previously by the present authors [4].) The length of the burner, i.e., the distance from the porous-plate to the sampling point, is 11.4 cm, and the burner diameter is 5 cm. This database considered covers a range of ϕ from 0.5 to 0.6.

Comparison to the Model. The burner is modeled by applying the baseline model (i.e., the WSR operating at incipient blowout, followed by the PFR). Adiabatic behavior is assumed.

In Fig. 5, the NO_x modeled by the three mechanisms is compared to the measurements. Results are shown for the experimental ϕ range of 0.5 to 0.6, as well as for assumed operation at ϕ up to 0.7. Over the ϕ range from 0.5 to 0.7, by the adiabatic assumption, the variation in the overall burner τ is 20.4 to 17.2 ms, and the variation in the burner exit temperature is 1736 to 2084 K (by all three mechanisms). The corresponding values predicted for the WSR zone operating at incipient blowout are $\tau = 0.25$ to 0.02 ms and $T = 1643$ and 1795 K (DB mechanism), and $\tau = 0.21$ to 0.03 ms and $T = 1611$ to 1860 K (by the MB and the MWF mechanisms).

For the leanest and coolest case considered ($\phi = 0.5$), good agreement is noted between the measured NO_x and the NO_x predicted by the model using the DB and MB mechanisms. Differences between the modeled and measured NO_x for the higher ϕ examined are attributed to heat loss from the burner, which is not considered in the model.

Michaud et al. [3] developed their mechanism through comparison to porous-plate burner data very similar to that examined here. In their study [3], the burner heat loss was accounted for, and good agreement between predicted and experimental data was claimed. For the present application, assuming adiabaticity, the predictions based on the MWF mechanism are a few parts per million greater than those obtained based on the DB and MB mechanisms.

With respect to the first question posed above, it appears, at least from the chemical kinetic standpoint, that the model is valid. The model agreement to the laboratory measurements is reasonable, and can be improved by computing the burner heat loss.

NO_x Pathways

In Fig. 6, the breakdown of the NO_x contributions is shown. These results are for the exit of the burner. Listed in the boxes near the top of the figure are the predicted adiabatic exit conditions, and the measured NO_x.

With respect to the prompt NO_x, the behavior is considerably different from that of the jet-stirred reactor cases stud-

Downloaded 02 Jun 2010 to 171.66.16.102. Redistribution subject to ASME license or copyright; see http://www.asme.org/terms/Terms_Use.cfm

ied above. At the leanest and coolest conditions examined the nitrous oxide pathway is predominant. The prompt NO_x is small to negligible. The Zeldovich NO_x is secondary. However, for ϕ greater than about 0.6, the Zeldovich NO_x is predominant. (The inclusion of heat loss in the model would shift the regime of Zeldovich predominance to slightly higher ϕ).

Thus, the second question posed above is also answered. The NO_x behavior of the porous-plate burner operated at elevated pressure is different from that of the jet-stirred reactors operated at ambient pressure. For lean-premixed combustion at low NO_x levels, the nitrous oxide pathway is predicted to be predominant in the porous-plate burner, whereas for the jet-stirred reactors, the predictions indicate that both the nitrous oxide and prompt pathways are important. There are at least three effects involved in this regard:

1 The elevated pressures promote the nitrous oxide pathway, because of the three-body recombination reaction (4 reverse), which initiates the pathway.

2 The elevated inlet temperatures (of the porous plate burner) diminish the prompt pathway.

3 Hydrocarbon free radicals (such as CH, which enters into the prompt NO_x initiating reaction (12)) are restricted to a narrow zone in the porous-plate burner. They are not dispersed throughout the burner, as is possible in the jet-stirred reactor operated at very intense mixing rates.

Comments on the Residence Time Distribution

The particle residence time distributions of the two types of laboratory reactors examined are much different, and cover the limiting possibilities. For the jet-stirred reactors, the individual particles have residence times from very short to very long compared to the mean residence time; whereas, for the porous-plate burner, all of the particles reside in the burner for approximately the mean residence time. It is noteworthy, as demonstrated above, that these distinctly different situations both exhibit good agreement between the measured and modeled NO_x. This provides confidence in the model and the chemical kinetics.

The lean-premixed primary zone of gas turbine engine combustors should have a particle residence time distribution that lies between the limiting distributions of the laboratory reactors. The tendency, however, may be toward a relatively narrow residence time distribution (centered around the mean residence time). This distribution is provided by the WSR/PFR baseline model (described above and used to simulate the porous-plate burner). In order to examine the effect a wider residence distribution has on the NO_x, the fraction of the combustion process treated as a WSR is enlarged (as described above). Although there is virtue in identifying a chemical reactor model that best simulates the actual combustor, the objective of this study regarding the importance of the nitrous oxide pathway is well met by applying the simple WSR/PFR model, and by varying the WSR to PFR ratio.

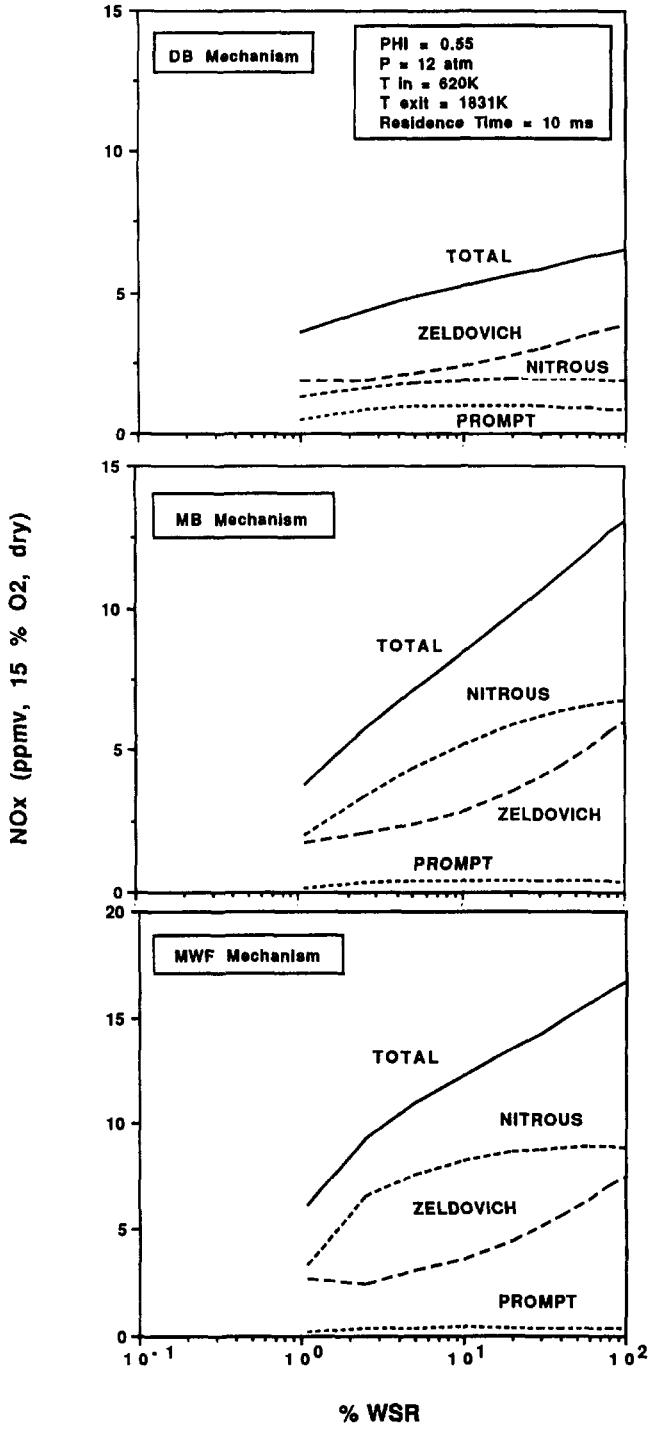

Fig. 7 Predicted NO_x contributions versus percentage of the combustor modeled as a WSR. Balance of combustor is a PFR. Total mean residence time of the combustor is fixed at 10 ms. Combustor pressure of 12 atm, inlet temperature of 620 K, and a fuel–air equivalence ratio of 0.55.

Lean-Premixed Combustion Modeled Results

The results modeled for the NO_x formed in the lean-premixed primary zone of the gas turbine combustor are now presented and discussed.

Effect of WSR Fraction. A decision in the type of modeling conducted here is the size (or fraction of the total primary zone combustor volume) chosen for the WSR. The remainder of the combustor is the PFR. The WSR is the region of elevated free radical concentrations. The baseline model assumes a WSR of size corresponding to incipient blowout. Elsewhere [3], the WSR size has been selected to be a constant value, corresponding to the size for blowout of the leanest mixture that can be burned at the P and T_{in} treated.

NO_x predictions for lean-premixed combustion are sensitive to the size of the WSR. This is shown in Figs 7, 8, and 9, for three assumed gas turbine combustor conditions. The results in Figs. 7 and 8 are for an intermediate pressure combustor (12 atm and 620 K combustor inlet temperature) having a primary zone ϕ of 0.55 and 0.65, respectively. Note

Downloaded 02 Jun 2010 to 171.66.16.102. Redistribution subject to ASME license or copyright; see http://www.asme.org/terms/Terms_Use.cfm

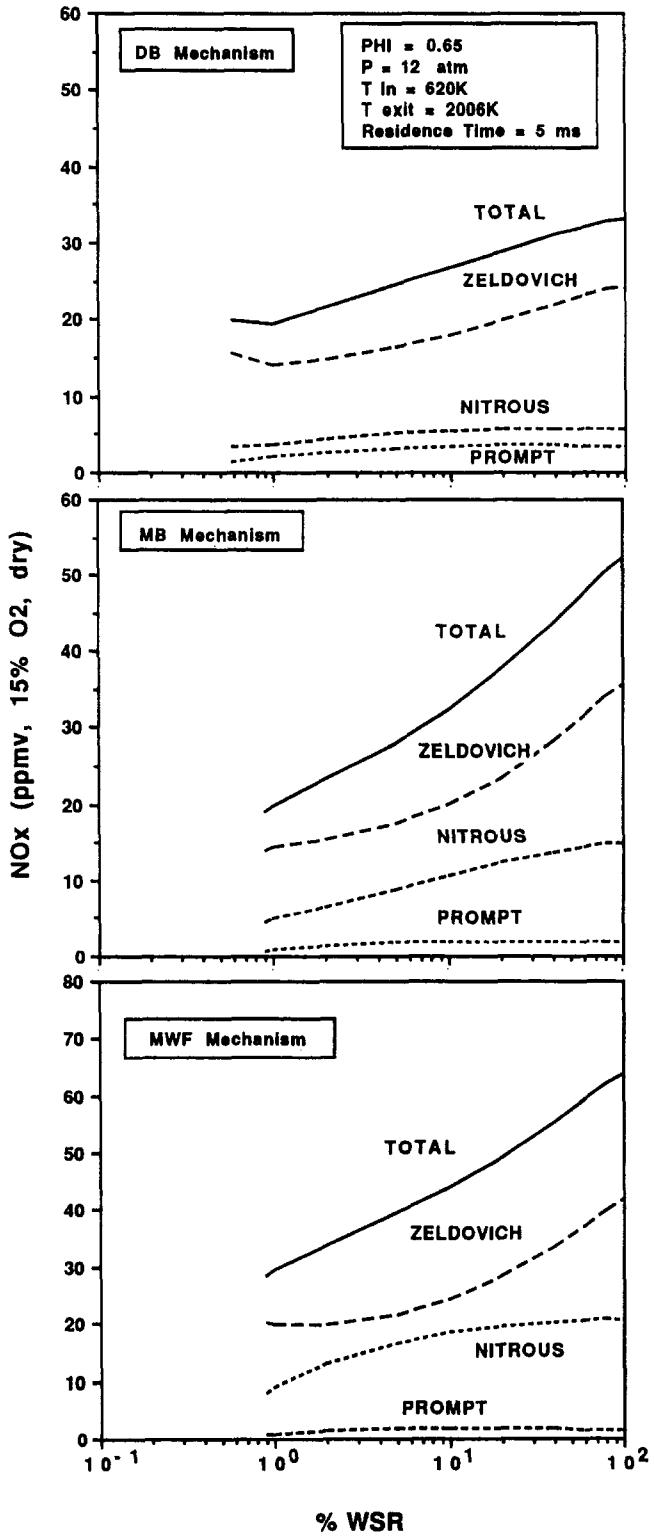

Fig. 8 Predicted NO_x contributions versus percentage of combustor modeled as a WSR. Balance of combustor is a PFR. Total mean residence time of the combustor is fixed at 5 ms. Combustor pressure of 12 atm, inlet temperature of 620 K, and a fuel–air equivalence ratio of 0.65.

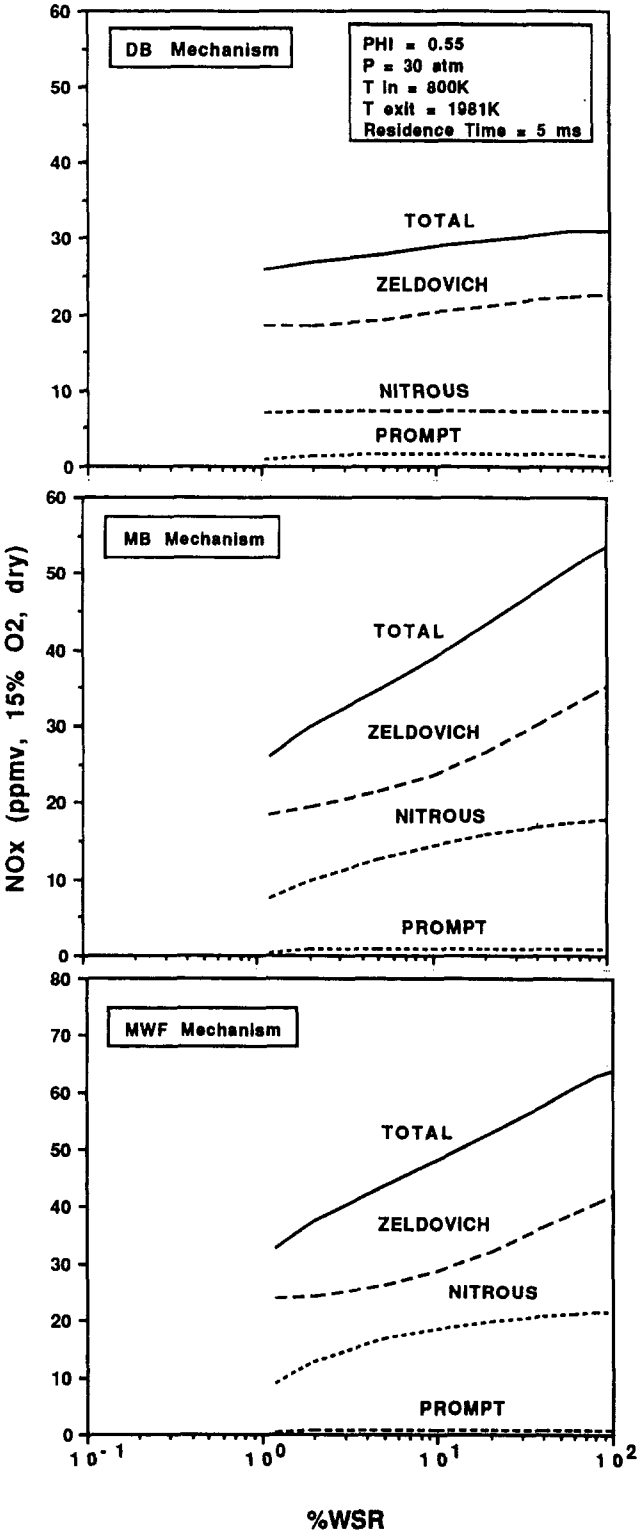

Fig. 9 Predicted NO_x contributions versus percentage of combustor modeled as a WSR. Balance of combustor is a PFR. Total mean residence time of the combustor is fixed at 5 ms. Combustor pressure of 30 atm, inlet temperature of 800 K, and a fuel air equivalence ratio of 0.55.

that the mean residence time of the $\phi = 0.55$ combustor has been increased to $\tau = 10$ ms (from the nominal value of 5 ms used herein, in order to overcome the lower temperature of this case and effect reasonable completion of combustion). In Fig. 9, the results are shown for a high pressure combustor (30 atm and 800 K combustor inlet temperature) operated at $\phi = 0.55$ and $\tau = 5$ ms.

For all of the cases treated, the percentage of the primary zone volume modeled as the WSR is increased from the blowout value (about 1 percent) to 100 percent. The major trends are summarized as follows:

1 In all cases the NO_x increases with increasing WSR size. The MB mechanism (followed closely by the MWF mech-

Downloaded 02 Jun 2010 to 171.66.16.102. Redistribution subject to ASME license or copyright; see http://www.asme.org/terms/Terms_Use.cfm

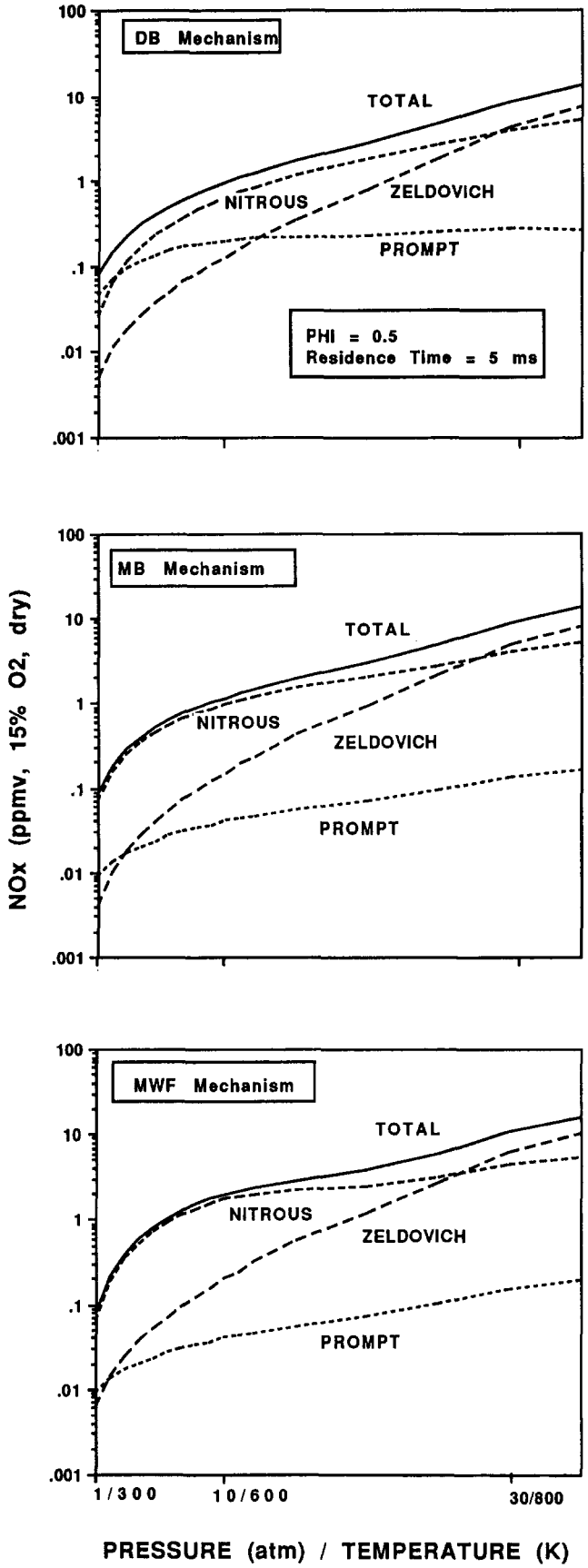

Fig. 10 Pressure and inlet temperature effects on NO_x predicted for a lean-premixed combustor modeled as a WSR operating at incipient blowout, followed by a PFR. The combustor inlet temperature is calculated assuming an engine compressor of 85 percent isentropic efficiency drawing standard air. The mean residence time is 5 ms and the fuel–air equivalence ratio is 0.5.

anism) shows the greatest sensitivity. The DB mechanism for the 30 atm combustor shows the least sensitivity.

2 The Zeldovich contribution shows the greatest sensitivity to the WSR percentage. The nitrous oxide contribution tends to level off above about 10 percent WSR percentage.

3 The MWF mechanism predicts the largest NO_x amounts.

4 The order of the NO_x contribution is Zeldovich > nitrous oxide > prompt. The exception is the 12 atm, $\phi = 0.55$ case, for which the order is nitrous oxide > Zeldovich > prompt, when the MB and MWF mechanisms are used.

5 The contribution of the prompt pathway is small to negligible. This is true even for the DB mechanism, which gives the highest prompt NO_x contribution. Even for the case of 100 percent WSR, the prompt NO_x is never as strong as the nitrous oxide contribution. This is different from the behavior noted in Fig. 3 for the atmospheric pressure jet-stirred reactors operated at $\phi = 0.65$, for which case the prompt NO_x predicted by the DB mechanism was predominant.

These results imply that the lean-premixed flame should be thin in order to effect minimum NO_x formation. That is, the flame should be designed to permit the free radicals to relax toward equilibrium as quickly as possible, after ensuring that the essential hydrocarbon oxidation steps are completed. A drawn-out zone of free radical chemistry, as obtained with large-scale recirculation, would appear to enhance the NO_x. (This situation is different from that of diffusion flames, for which long, slowly mixed flames have been found to reduce NO_x.)

Effects of Pressure and Inlet Temperature. The remainder of the results are for the baseline model (i.e., WSR at incipient blowout, and total residence time of 5 ms). The combined effect of pressure and combustor inlet temperature on NO_x is shown in Fig. 10 for $\phi = 0.5$. The pressure range is 1 to 35 atm. Pressure increments in regions of significant sensitivity to pressure are 1 atm; elsewhere the increments are 5 atm. The corresponding combustor inlet temperatures are approximately those at the exit of a gas turbine engine compressor of 85 percent isentropic efficiency inducting standard sea level air.

The pressure sensitivity of the NO_x (without the influence of the combustor inlet temperature) may be assessed by assuming that NO_x varies as pressure raised to the exponent n according to the equation:

$$NO_x(\text{ppmv}) \alpha P^n \tag{17}$$

Results for the exponent n are listed in Table 2 for the range of pressures and inlet temperatures considered herein. Conditions for which the inlet temperature is matched to the pressure by the engine compressor assumption used above are indicated by the bold typeface. The values of n are derived from logarithmic straight line fits to the computed results around 1, 10, and 30 atm. The traditional pressure exponent (for thermal NO_x and for Fenimore [12] prompt NO_x) is 0.5.

The results of Fig. 10 and Table 2 are summarized as follows:

1 As shown in Fig. 10, the greatest sensitivity of the NO_x to pressure (and inlet temperature) occurs in the range of approximately 1 to 8 atm pressure. The weakest sensitivity occurs in the range of approximately 10 to 13 atm. This range of weakest sensitivity is noted especially for the results obtained with the MWF mechanism.

2 In the 1 to 10 atm range, most of the NO_x sensitivity noted in Fig. 10 is caused by the response of the nitrous

Downloaded 02 Jun 2010 to 171.66.16.102. Redistribution subject to ASME license or copyright; see http://www.asme.org/terms/Terms_Use.cfm

Table 2 Pressure dependence of NO_x for lean-premixed combustion at a mean residence time of 5 ms

	DB Mechanism				MB Mechanism				MWF Mechanism			
Φ=0.5	T\P	1	10	30	T\P	1	10	30	T\P	1	10	30
	300	**0.42**	--	--	300	**0.50**	--	--	300	**0.50**	--	--
	600	0.13	**0.67**	1.13	600	0.26	**0.19**	0.00	600	0.21	**-0.13**	-0.44
	800	0.13	0.19	**0.62**	800	0.22	0.20	**0.30**	800	0.19	0.06	**0.14**
Φ=0.6	T\P	1	10	30	T\P	1	10	30	T\P	1	10	30
	300	**0.26**	0.80	0.70	300	**0.33**	0.31	-0.15	300	**0.28**	-0.15	-0.66
	600	0.18	**0.27**	0.57	600	0.26	**0.22**	0.28	600	0.23	**0.09**	0.14
	800	0.33	0.35	**0.52**	800	0.37	0.38	**0.48**	800	0.35	0.33	**0.44**
Φ=0.7	T\P	1	10	30	T\P	1	10	30	T\P	1	10	30
	300	**0.24**	0.45	0.80	300	**0.31**	0.24	0.08	300	**0.27**	0.00	-0.20
	600	0.40	**0.37**	0.51	600	0.44	**0.38**	0.47	600	0.41	**0.33**	0.42
	800	0.61	0.48	**0.51**	800	0.62	0.49	**0.50**	800	0.58	0.43	**0.44**

oxide pathway to changing pressure (and inlet temperature). Above approximately 10 atm, the response of the nitrous oxide pathway is relatively weak. This is noted especially for the MWF mechanism, in which case the response of the NO_x formed by the nitrous oxide pathway to increasing pressure (and inlet temperature) is almost flat above approximately 10 atm. For the highest pressures examined, the NO_x sensitivity is influenced by the response of the Zeldovich pathway to pressure (and inlet temperature, especially).

3 The results in Table 2 show that there is no universal pressure exponent for the NO_x formed in lean-premixed combustion.

4 The results in Table 2 show reasonable agreement between the DB, MB, and MWF mechanisms when the following conditions are true: $P = 1$ atm (all inlet temperatures and ϕ's considered); $P = 10$ atm and $T_{in} = 600$ K (all ϕ's considered except 0.5); $P = 10$ atm and $T_{in} = 800$ K (all ϕ's considered): $P = 30$ atm and $T_{in} = 600$ K ($\phi = 0.7$ only); $P = 30$ atm and $T_{in} = 800$ K (all ϕ's considered except 0.5). For the leanest ϕ's considered (i.e., 0.5) the agreement between mechanisms is poor, except when the pressure is low or the inlet temperature is high.

5 For a lean-premixed combustor operating at $P = 10$ atm, $T_{in} = 600$ K, and $\phi = 0.6$, the results in Table 2 indicate that the NO_x pressure exponent lies in the 0.1 to 0.3 range. As P, T_{in}, or ϕ increase, the exponent increases (toward approximately 0.5). On the other hand, as P, T_{in}, or ϕ decrease, the exponent becomes quite dependent on the mechanism selected, and no clear behavior is evident.

6 For a lean-premixed combustor operating at $P = 30$ atm, $T_{in} = 800$ K, and ϕ of either 0.6 or 0.7, the results in Table 2 indicate that the NO_x pressure exponent is approximately 0.5. For a leaner value of ϕ, the exponent becomes very dependent on the mechanism selected.

7 Although generally in this study the NO_x concentration predicted does not depend strongly on the mechanism selected, this tendency does not carry over to the pressure dependence of the NO_x for gas turbine engine conditions when ϕ is about 0.5 (and less). For the very lean fuel–air ratios, more study will be required in order to understand the pressure dependence of the NO_x.

The Nitrous Oxide Contribution

In Fig. 11, the percentage contribution of the nitrous oxide pathway to the total NO_x is plotted versus the absolute amount of the NO_x formed by this pathway. For gas turbine engine, lean-premixed combustor conditions, the minimum contribution is about 10 percent. A significant percentage contribution is noted when the absolute contribution to the NO_x is in the 1 to 10 ppmv (15 percent O_2 dry) range.

In Fig. 12, the percentage contribution of the nitrous oxide pathway is plotted versus the total NO_x. These results indicate that whenever the total NO_x emission is in the 15 to 30 ppmv (15 percent O_2, dry) range, the nitrous oxide pathway contributes 40 to 45 percent of the NO_x for a high pressure engine (30 atm) and 20 to 35 percent of the NO_x for an intermediate pressure engine (10 atm). For engines producing less than 10 ppmv (15 percent O_2, dry) total NO_x, the nitrous oxide contribution increases steeply and approaches 100 percent at the lowest total NO_x levels.

Conclusions

In this paper, total NO_x and the contributions of the nitrous oxide, Zeldovich, and prompt pathways in lean-premixed combustion have been presented. The kinetic mechanisms of Drake and Blint [1], Miller and Bowman [2], and Michaud et al. [3] have been compared over a range of operating conditions. The computer model has been compared to laboratory data. The modeled results for NO_x showed good agreement to the laboratory data for jet-stirred reactors operated at short mean residence times, and for the porous-plate burner operated at minimum heat loss conditions.

A comparison of the relative importances of the nitrous oxide, Zeldovich, and prompt pathways for gas turbine engine conditions shows that the three kinetic mechanisms considered give similar results for most of the conditions examined. All three mechanisms predict comparable total NO_x amounts. The DB mechanism consistently predicts the largest prompt NO_x contribution. The MB and the MWF mechanisms, which use identical hydrocarbon chemistry, pre-

Downloaded 02 Jun 2010 to 171.66.16.102. Redistribution subject to ASME license or copyright; see http://www.asme.org/terms/Terms_Use.cfm

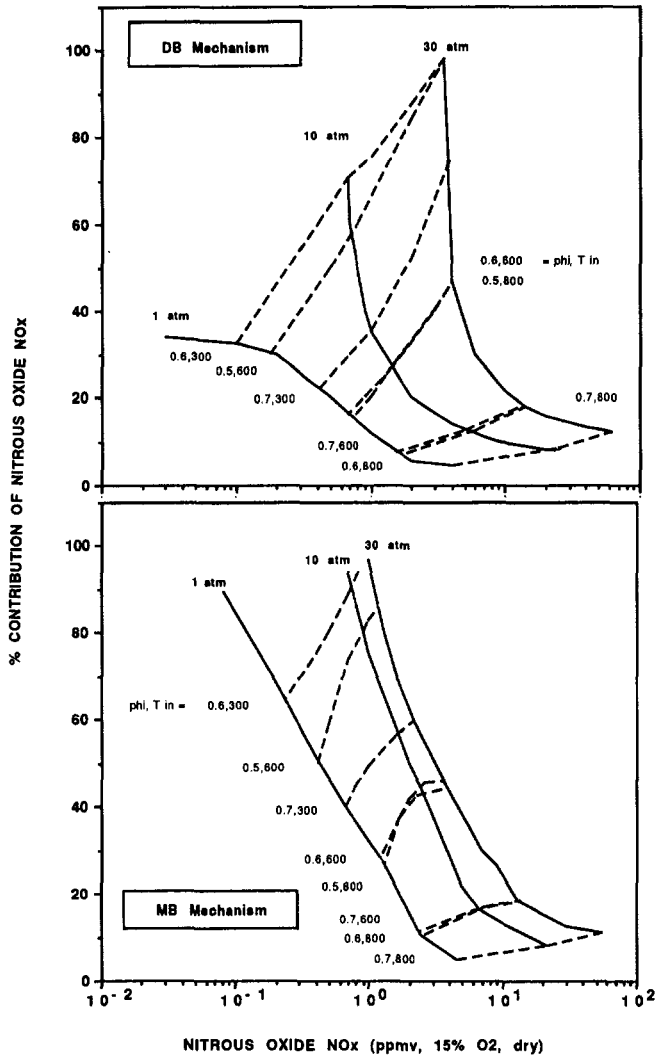

Fig. 11 Predicted percent contribution of nitrous oxide-NO_x versus absolute nitrous oxide-NO_x for a lean-premixed combustor modeled as a WSR operated at incipient blowout, followed by a PFR. Mean residence time equal to 5 ms.

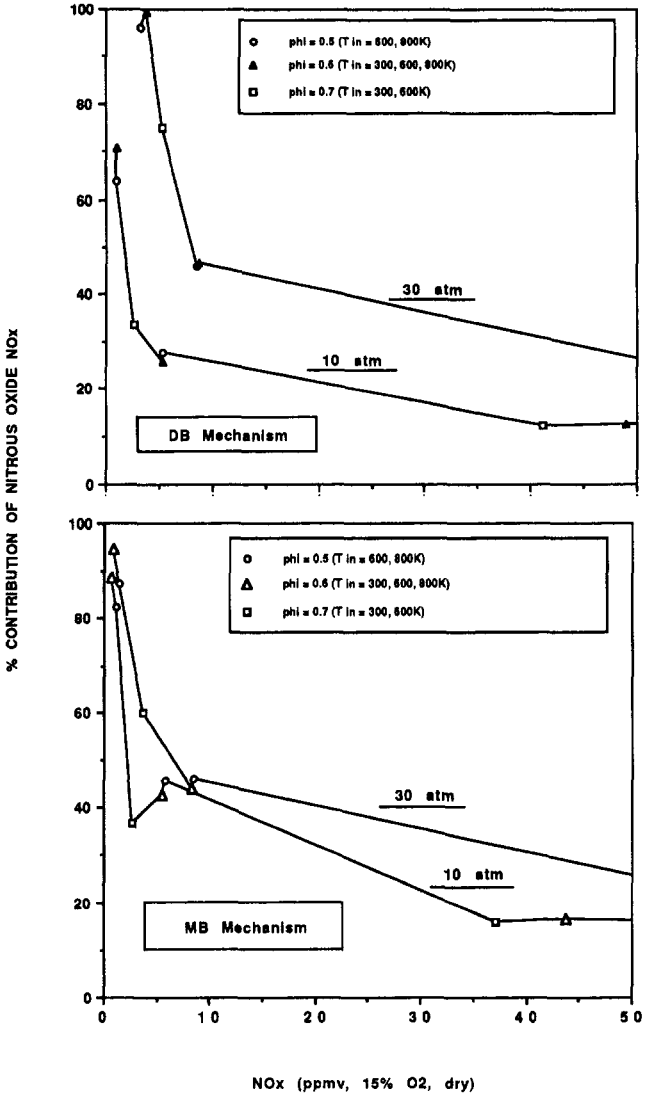

Fig. 12 Predicted percentage contribution of nitrous oxide-NO_x versus total NO_x for a combustor modeled as a WSR operated at incipient blowout, followed by a PFR. Mean residence time equal to 5 ms.

dict the same prompt NO_x contributions. The MWF mechanism consistently predicts greater nitrous oxide and Zeldovich NO_x, and hence, greatest total NO_x, because of the inclusion of the singlet O atom chemistry. The two areas of significant difference between the three mechanisms involve (1) the pressure dependence of the NO_x for the leanest cases examined (i.e., $\phi = 0.5$), and (2) the low nitrous oxide–NO_x predicted by the DB mechanism for the CO combustion experiments. These areas should receive further study.

Over the range of pressures, combustor inlet temperatures, and residence times considered, for the leanest conditions examined, the major source of the NO_x exiting the combustor is formed by the nitrous oxide pathway. At richer conditions, all three kinetic mechanisms show that the largest NO_x source is the Zeldovich pathway, but that the nitrous oxide pathway is an nonnegligible route.

The results indicate that whenever the total NO_x emission is in the 15 to 30 ppmv (15 percent O_2, dry) range, the nitrous oxide pathway contributes 40 to 45 percent of the NO_x for a high-pressure engine (30 atm) and 20 to 35 percent of the NO_x for an intermediate pressure engine (10 atm). For engines producing less than 10 ppmv (15 percent O_2, dry) total NO_x, as is the goal with ultra low NO_x combustors, the nitrous oxide contribution increases steeply and approaches 100 percent.

Although this study has examined NO_x formation from the chemical kinetic viewpoint, the results indicate that the fluid mechanics of the lean-premixed combustor should be arranged so that the flame zone(s) are as thin as possible. Broad zones of high-intensity, recirculating combustion are likely to carry elevated free radical concentrations, and thus, increase the NO_x formation.

References

1 Drake, M. C., and Blint, R. J., "Calculations of NO_x Formation Pathways in Propagating Laminar, High Pressure Premixed Methane/Air Flames," *Combust. Sci. and Tech.*, Vol. 75, 1991, p. 261–285.

2 Miller, J. A., and Bowman, C. T., "Mechanism and Modeling of Nitrogen Chemistry in Combustion," *Prog. in Energy and Combust. Science*, Vol. 15, 1989, pp. 287–338.

3 Michaud, M. G., Westmoreland, P. R., and Feitelberg, A. S., "Chemical Mechanisms of NO_x Formation for Gas Turbine Conditions," *Proceedings of the Twenty-fourth Symposium (International) on Combustion*, The Combustion Institute, Pittsburgh, 1992.

4 Nicol, D. G., Malte, P. C., Lai, J., Marinov, N. M., Pratt, D. T., and Corr, R. A., "NO_x Sensitivities for Gas Turbine Engines Operated on

Downloaded 02 Jun 2010 to 171.66.16.102. Redistribution subject to ASME license or copyright; see http://www.asme.org/terms/Terms_Use.cfm

Lean-Premixed Combustion and Conventional Diffusion Flames," Paper No. 92-GT-115, ASME, New York (1992).

5 Glarborg, P., Miller, J.A., and Kee, R. J., "Kinetic Modeling and Sensitivity Analysis of Nitrogen Oxide Formation in Well-Stirred Reactors," *Combust. and Flame*, Vol. 65, 1986, pp. 177–202.

6 Malte, P.C., and Pratt, D. T., "Measurement of Atomic Oxygen and Nitrogen Oxides in Jet-Stirred Combustion," *Proceedings of the Fifteenth Symposium (International) on Combustion*, The Combustion Institute, Pittsburgh, pp. 1061–1070.

7 Corr, R. A., Malte, P. C., and Marinov, N. M., "Evaluation of NO_x Mechanisms for Lean, Premixed Combustion," Paper No. 91-GT-257, ASME, New York (1991).

8 Bartok, W., Engelman, V. S., Goldstein, R., and del Valle, E. G., in: *AIChE Symp. Ser.*, No. 126, Vol. 68, 1972, p. 30.

9 Malte, P. C., Schmidt, S. C., and Pratt, D. T., "Hydroxyl Radical and Atomic Oxygen Concentrations in High-Pressure Turbulent Combustion," *Proceedings of the Sixteenth Symposium (International) on Combustion*, The Combustion Institute, Pittsburgh, 1977, pp. 145–155.

10 Singh, S., Grosshandler, W. L., Malte, P. C., and Crain, W. R., Jr., "Oxides of Nitrogen Formed in High-Intensity Methanol Combustion," *Proceedings of the Seventeenth Symposium (International) on Combustion*, The Combustion Institute, Pittsburgh, 1979, pp. 689–699.

11 Leonard, G., and Correa, S., "NO_x Formation in Premixed High-Pressure Lean Methane Flames," in: *Proceedings 2nd ASME Fossil Fuel Combustion Symposium*, New Orleans, Jan. 14–18, 1990.

12 Fenimore, C. P., "Formation of Nitric Oxide in Premixed Hydrocarbon Flames," *Proceedings of the Thirteenth Symposium (International) on Combustion*, The Combustion Institute, Pittsburgh, 1971, pp. 373–380.

Downloaded 02 Jun 2010 to 171.66.16.102. Redistribution subject to ASME license or copyright; see http://www.asme.org/terms/Terms_Use.cfm

M. Hallmann

M. Scheurlen

S. Wittig

Lehrstuhl und Institut für Thermische Strömungsmaschinen, Universität Karlsruhe (T.H.), Karlsruhe, Federal Republic of Germany

Computation of Turbulent Evaporating Sprays: Eulerian Versus Lagrangian Approach

A new Eulerian model for turbulent evaporating sprays is presented. It comprises droplet heating and evaporation processes by solving separate transport equations for the droplet's temperature and diameter. A Lagrangian approach, which we have discussed in detail on other occasions, is used in comparing the results of the new method. A comparison with experimental data shows that both approaches are successful in predicting the main features of turbulent evaporating sprays.

1 Introduction

The proper matching of the flow field with the fuel spray characteristics of the atomizer is a necessary condition for the optimum performance as well as for the reduction of emissions from high-intensity gas turbine combustors.

Experimental approaches within the developing process of new combustion chambers are often very cost and time consuming. In contrast, major advances in computer technology and computational fluid dynamics (CFD) led to the development of fast numerical codes allowing the verification of experimental data within a relatively short period of time. Additionally, experimental costs may be greatly reduced by "computational experiments" used for the investigation of different model configurations.

The present study is devoted to the development of a new Eulerian approach for the numerical simulation of turbulent evaporating sprays. Results of the new model are compared with both experimental data and another computational method, the well-known Lagrangian approach.

Eulerian methods for the prediction of turbulent two-phase flows have been used by various groups of researchers (e.g., Melville and Bray, 1979; Elghobashi et al., 1984; Chen and Wood, 1986; Krämer, 1988). They all dealt with questions concerning the dispersion of particles in parabolic flows neglecting heat and mass transfer between the two phases. Mostafa and Elghobashi (1985) as well as Mostafa and Mongia (1987) reported about Eulerian methods for the computation of turbulent jets with droplet vaporization. But also in these papers rather simplified assumptions were made. So the authors assumed isothermal flow conditions and a constant droplet (saturation) temperature. In addition, a simplified mass transfer model for the calculation of the droplet diameter was used. In contrast, the present study introduces a new model for the computation of fuel spray characteristics including droplet heating and evaporation by solving separate transport equations for the droplet's temperature and diameter. This model is applicable not only for parabolic flows but also for turbulent recirculating nonisothermal evaporating sprays, which are of dominant interest within the design process of real gas turbine combustors.

Based on the Lagrangian equations for the droplet's transport and evaporation, the new Eulerian model formulation is derived. The equations are solved numerically and tested against published experimental data as well as against numerical data computed by the Lagrangian approach.

2 Governing Equations

2.1 Gas Phase Equations. For the steady mean flow under consideration, the time-averaged continuity equation and the stationary Reynolds equations in conjunction with the standard k–ϵ turbulence model are solved numerically with a finite volume discretization method. The turbulent transport of enthalpy (h) and vapor concentration (c_α) is calculated via additional transport equations. The wall function method is used in the present study to eliminate the large number of grid points needed to resolve the laminar sublayer (Launder and Spalding, 1974). For more detailed information the reader is referred to Wittig et al. (1987a, b) and Noll et al. (1989).

2.2 Droplet Equations: Lagrangian Approach

Droplet Motion. The droplet velocity is obtained by solving the particle momentum equation as follows:

$$\frac{d\mathbf{u}_p}{dt} = \frac{3}{4}\frac{\rho}{\rho_p}\frac{c_D}{D_p}c_{\text{rel}}(\mathbf{u} - \mathbf{u}_p) + \mathbf{F} \tag{1}$$

with

$$c_{\text{rel}} = \|\mathbf{u} - \mathbf{u}_p\| \tag{2}$$

$$\text{Re}_p = \frac{D_p c_{\text{rel}}}{\nu} \tag{3}$$

Contributed by the International Gas Turbine Institute and presented at the 38th International Gas Turbine and Aeroengine Congress and Exposition, Cincinnati, Ohio, May 24–27, 1993. Manuscript received at ASME Headquarters March 17, 1993. Paper No. 93-GT-333. Associate Technical Editor: H. Lukas.

Copyright © 1995 by ASME

Downloaded 02 Jun 2010 to 171.66.16.102. Redistribution subject to ASME license or copyright; see http://www.asme.org/terms/Terms_Use.cfm

$$c_D = 0.36 + 5.48\,\mathrm{Re}_p^{-0.573} + \frac{24}{\mathrm{Re}_p} \tag{4}$$

The external forces acting on a particle, e.g., gravity, are denoted by **F** in Eq. (1) and are assumed to be negligible in the present investigations. The droplet location itself is given by

$$\frac{d\mathbf{x}_p}{dt} = \mathbf{u}_p \tag{5}$$

For turbulent flows, the particle motion is simulated by a stochastic or Monte Carlo approach. Therefore, the instantaneous gas phase velocity is split up into a mean and a fluctuating quantity:

$$\mathbf{u} = \bar{\mathbf{u}} + \mathbf{u}' \tag{6}$$

where $\bar{\mathbf{u}}$ is determined from the solution of the stationary Reynolds equations. The fluctuation $\mathbf{u}'$ is chosen randomly from an isotropic Gaussian distribution of the gas phase velocity with a standard deviation of

$$\sigma = \sqrt{\frac{2}{3}k} \tag{7}$$

The interaction time of a particle with the randomly sampled velocity field is determined by one or the other of the following possible events (Gosman and Ioannides, 1983):

1 The particle moves sufficiently slow relative to the gas to remain within the eddy during its whole lifetime t_e or
2 the relative velocity between gas and particle is sufficient to allow it to traverse the eddy in a transit time t_r shorter than t_e.

Consequently, the computation of the particle movement with randomly sampled gas phase velocities provides different particle trajectories for identical initial conditions. This causes the final results to be of a statistical nature. Therefore, a sufficiently large number of realizations of particle paths is required to reduce the sampling error. A detailed description of the method is given by Gosman and Ioannides (1983).

Droplet Heating and Evaporation. A detailed derivation of different models for droplet heating and evaporation is given by Faeth (1983) and Wittig et al. (1988). Using the so-called "Uniform Temperature Model" the balance equation for the droplet temperature is

$$\frac{dT_p}{dt} = \frac{6\,\mathrm{Nu}\,\mathrm{Fr}\,\lambda_{\mathrm{ref}}}{\rho_p c_{p,p} D_p^2}(T_\infty - T_p) + \frac{4}{D_p c_{p,p}}\Delta h_v \frac{dD_p}{dt} \tag{8}$$

and, assuming a constant liquid density, for the decreasing diameter of the droplet

$$\frac{dD_p}{dt} = -\mathrm{Fr}\frac{4\,M_v n_{\mathrm{ref}}\Gamma_{\mathrm{ref}}}{\rho_p D_p}\ln\left(\frac{1 - X_{v,\infty}}{1 - X_{v,p}}\right) \tag{9}$$

with

$$\mathrm{Nu} = 2\,\mathrm{Le}\ln\left(\frac{1 - X_{v,\infty}}{1 - X_{v,p}}\right)\left[\exp\left(\mathrm{Le}\ln\left(\frac{1 - X_{v,\infty}}{1 - X_{v,p}}\right)\right) - 1\right]^{-1} \tag{10}$$

$$\mathrm{Le} = \frac{\Gamma_{\mathrm{ref}} c_{p,v,\mathrm{ref}} n_{\mathrm{ref}}}{\lambda_{\mathrm{ref}}} \tag{11}$$

$$\mathrm{Fr} = 1 + 0.276\sqrt{\mathrm{Re}_p}\,\mathrm{Pr}^{1/3} \tag{12}$$

The model implies a uniform temperature distribution in the droplet assuming an infinite thermal conductivity. The calculation of the reference values and the mol fraction of the vapor is shown in the appendix.

2.3 Droplet Equations: Eulerian Approach. In comparison to the Lagrangian approach, the evaporating spray is

Nomenclature

A, B, C = coefficients of the Cox–Antoine vapor pressure equation
c_D = drag coefficient
$c_{p,p}$ = specific heat of the droplets, J/kg K
$c_{p,v}$ = molar specific heat of vapor, J/mol K
c_{rel} = relative velocity, m/s
D = diameter, m
c_α = vapor concentration, kg/kg
$\mathbf{F}$ = external forces, m/s^2
Fr = Frössling number
H = step height, m
h = specific enthalpy, J/kg
Δh_v = specific enthalpy of evaporation, J/kg
k = kinetic energy of turbulence, m^2/s^2
L_x = length scale of the k–ϵ model, m
Le = Lewis number
M = molecular weight, kg/mol
n = molar concentration, mol/m^3
nd = number of discrete drop-size classes
Nu = Nusselt number
Pr = Prandtl number
p = pressure, N/m^2
Re = Reynolds number
S = source term (equation dependent)
Sc = Schmidt number
T = temperature, K
t = time, s
t_e = eddy lifetime, s
t_r = transit time, s
U_0 = maximum measured velocity before step, m/s
u, v, w (u_i) = velocity components, m/s
$\dot{V}$ = volume flow rate, m^3/s
x, y, z (x_i) = Cartesian coordinates, m
v_c = volume fraction of the dispersed phase
X = mol fraction
Γ = diffusion coefficient, m^2/s
ϵ = turbulence energy dissipation rate, m^2/s^3
λ = thermal conductivity, W/(mK)
μ = dynamic viscosity, Ns/m^2
ν = kinematic viscosity, m^2/s
ρ = density, kg/m^3
σ = standard deviation of the gas phase velocity, m/s
τ = particle response (relaxation) time, s
ω = particle response frequency, s^{-1}

Subscripts

g = gas
l = liquid
p = particle, droplet
ref = reference values (1/3 rule)
s = droplet surface
t = turbulent
v = vapor
∞ = ambient

Superscripts

$\bar{(\,)}$ = time average
$()'$ = turbulent fluctuation

Downloaded 02 Jun 2010 to 171.66.16.102. Redistribution subject to ASME license or copyright; see http://www.asme.org/terms/Terms_Use.cfm

treated as an interacting and interpenetrating continuum. The equations describing continuity and momentum exchange of the liquid phase for laminar flow conditions can be derived from a mass and momentum balance at an infinitesimal small fluid volume:

$$\frac{\partial}{\partial x_i}(v_c\,\rho_p u_{i,p}) = S_{v_c} \tag{13}$$

$$\frac{\partial}{\partial x_i}(v_c\,\rho_p u_{i,p} u_{j,p}) = \frac{3}{4} v_c\,\rho \frac{c_D}{D_p} c_{\mathrm{rel}}(u_j - u_{j,p}) + F_j + S_{v_c} u_{j,p} \tag{14}$$

The mass source term due to droplet evaporation is obtained by

$$S_{v_c} = v_c\,\rho_p \frac{4}{D_p}\frac{dD_p}{dt} \tag{15}$$

where dD_p/dt is determined from Eq. (9). The term on the left-hand side of Eq. (14) represents the interia force per unit volume due to the droplet acceleration. The first term on the right-hand side represents the drag force due to the slip between the two phases, the second contains external forces like gravity, and the third takes into account momentum loss due to droplet evaporation. Pressure gradient terms for the dispersed phase are neglected.

A transport equation for the droplet temperature can be derived via an energy balance in the same manner as the momentum equation using the right-hand side of Eq. (8):

$$\frac{\partial}{\partial x_i}(v_c\,\rho_p u_{i,p} T_p) = v_c \frac{6\,\mathrm{Nu}\,\mathrm{Fr}\,\lambda_{\mathrm{ref}}}{c_{p,p} D_p^2}(T_\infty - T_p) + S_{v_c}\left(\frac{\Delta h_v}{c_{p,p}} + T_p\right) \tag{16}$$

In Eq. (16) the first term of the right-hand side represents droplet heating due to the temperature gradient between the two phases, the second droplet cooling due to droplet evaporation. The specific heat of the liquid $c_{p,p}$ is assumed to be constant.

Deriving a transport equation for the droplet diameter, we first write:

$$\frac{\partial}{\partial x_i}(v_c\,\rho_p u_{i,p} D_p) = D_p \frac{\partial}{\partial x_i}(v_c\,\rho_p u_{i,p}) + v_c\,\rho_p u_{i,p}\frac{\partial D_p}{\partial x_i} = D_p \frac{\partial}{\partial x_i}(v_c\,\rho_p u_{i,p}) + v_c\,\rho_p \frac{dD_p}{dt}$$

Including Eqs. (13) and (15) yields:

$$\frac{\partial}{\partial x_i}(v_c\;\rho_p\;u_{i,p}\;D_p) = \frac{4}{3} S_{v_c} D_p \tag{17}$$

For nonevaporating sprays Eqs. (13) and (17) are identical.

Turbulence Modeling. Turbulence effects are evaluated by introducing fluctuation quantities for the volume fraction and for the droplet's velocities, temperature, and diameter:

$$\Phi_p = \overline{\Phi}_p + \Phi'_p \tag{18}$$

$$\overline{\Phi}_p = \frac{1}{\Delta t}\int_t^{t+\Delta t} \Phi_p\,dt \tag{19}$$

Inserting Eq. (18) in the left-hand side of Eqs. (13), (14), (16), and (17), time averaging and using the following gradient hypothesis for the second-order correlations representing the turbulent fluxes of momentum, mass, and enthalpy:

$$-\rho_p \overline{v'_c u'_{j,p}} = \frac{\mu_{t,p}}{\mathrm{Sc}_{t,p}}\left(\frac{\partial v_c}{\partial x_j}\right) \tag{20}$$

$$-\rho_p v_c \overline{u'_{i,p} u'_{j,p}} = v_c\,\mu_{t,p}\left(\frac{\partial u_{i,p}}{\partial x_j} + \frac{\partial u_{j,p}}{\partial x_i}\right) \tag{21}$$

$$-\rho_p \overline{T'_p u'_{j,p}} = \frac{\mu_{t,p}}{\mathrm{Sc}_{t,p}}\left(\frac{\partial T_p}{\partial x_j}\right) \tag{22}$$

$$-\rho_p \overline{D'_p u'_{j,p}} = \frac{\mu_{t,p}}{\mathrm{Sc}_{t,p}}\left(\frac{\partial D_p}{\partial x_j}\right) \tag{23}$$

leads to a set of equations for turbulent evaporating sprays that can be easily cast in a form identical to commonly used gas phase equations:

$$\frac{\partial}{\partial x_i}(v_c\;\rho_p\;u_{i,p}) = \frac{\partial}{\partial x_i}\left(\frac{\mu_{t,p}}{\mathrm{Sc}_{t,p}}\frac{\partial v_c}{\partial x_i}\right) + S_{v_c} \tag{24}$$

$$\frac{\partial}{\partial x_i}(v_c\,\rho_p u_{i,p} u_{j,p}) = \frac{\partial}{\partial x_i}\left(v_c\,\mu_{t,p}\left(\frac{\partial u_{j,p}}{\partial x_i} + \frac{\partial u_{i,p}}{\partial x_j}\right)\right) + \frac{3}{4} v_c\,\rho \frac{c_D}{D_p} c_{\mathrm{rel}}(u_j - u_{j,p}) + F_j + S_{v_c} u_{j,p} \tag{25}$$

$$\frac{\partial}{\partial x_i}(v_c\,\rho_p u_{i,p} T_p) = \frac{\partial}{\partial x_i}\left(v_c \frac{\mu_{t,p}}{\mathrm{Sc}_{t,p}}\frac{\partial T_p}{\partial x_i}\right) + v_c \frac{6\,\mathrm{Nu}\,\mathrm{Fr}\,\lambda_{\mathrm{ref}}}{c_{p,p} D_p^2}(T - T_p) + S_{v_c}\left(\frac{\Delta h_v}{c_{p,p}} + T_p\right) \tag{26}$$

$$\frac{\partial}{\partial x_i}(v_c\,\rho_p u_{i,p} D_p) = \frac{\partial}{\partial x_i}\left(v_c \frac{\mu_{t,p}}{\mathrm{Sc}_{t,p}}\frac{\partial D_p}{\partial x_i}\right) + \frac{4}{3} S_{v_c} D_p \tag{27}$$

Triple correlations involving fluctuations in the liquid phase density (ρ_p v_c) are neglected.

The closure hypothesis Eqs. (20) and (21) for the turbulent mass flux and momentum transfer have been tested successfully by many workers (Chen and Wood, 1984; Elghobashi et al., 1984; Melville and Bray, 1979) and have been extended in the present study for turbulent heat and mass transfer in evaporating sprays (Eqs. (22), (23)). The turbulent viscosity $\mu_{t,p}$ of the dispersed phase is modeled using the approach of Melville and Bray (1979):

$$\mu_{t,p} = \mu_t \frac{\rho_p}{\rho}\frac{k_p}{k} \tag{28}$$

with

$$k_p = \frac{1}{2}\left(\overline{u'^2_p} + \overline{v'^2_p} + \overline{w'^2_p}\right) \tag{29}$$

The ratio of the turbulent kinetic energies of the dispersed and the gas phase is calculated following the approach of Krämer (1988):

$$\frac{k_p}{k} = \frac{1}{1 + \omega^2\tau^2} \tag{30}$$

Since in general the droplets do not follow the motion of the surrounding fluid from one point to another it is expected that the ratio k_p/k is different from unity and varies with the particle relaxation time τ and local turbulence quantities (Elghobashi et al., 1984). Krämer recommends the following equations for the frequency of the particle response:

$$\omega = \frac{1}{\tau}\left(\frac{\sqrt{\frac{2}{3}k}}{L_x}\tau\right)^{0.25} \tag{31}$$

$$\tau = \frac{1}{18}\frac{\rho_p}{\rho}\frac{D_p^2}{\nu}\frac{1}{1 + 0.133\,\mathrm{Re}_p^{0.687}} \tag{32}$$

with a characteristic macroscopic length scale of turbulence

Downloaded 02 Jun 2010 to 171.66.16.102. Redistribution subject to ASME license or copyright; see http://www.asme.org/terms/Terms_Use.cfm

Table 1 Coupling terms for the gas phase equations due to droplet transport and evaporation

EQUATION	COUPLING TERM
continuity	$-\sum_{k=1}^{nd}(S_{v_c})$
vapour concentration	$-\sum_{k=1}^{nd}(S_{v_c})$
momentum	$-\sum_{k=1}^{nd}\left(\frac{3}{4}\, v_c\, \rho\, \frac{c_D}{D_p}\, c_{rel}\, (u_j - u_{j,p}) + S_{v_c}\, u_{j,p}\right)$
enthalpie	$-\sum_{k=1}^{nd}\left(c_{p,p}\left(v_c\, \frac{6\, Nu\, Fr\, \lambda_{ref}}{c_{p,p}\, D_p^2}\, (T - T_p) + S_{v_c}\, (\frac{\Delta h_v}{c_{p,p}} + T_p)\right)\right)$

$$L_x = C_\mu^{0.75}\frac{k^{1.5}}{\epsilon} \tag{33}$$

For the turbulent Schmidt number $Sc_{t,p}$ of the dispersed phase Krämer suggests a value of 0.3. During this work this value was found to be too low, especially for small and medium-sized particles. Therefore, we recommend a value of $Sc_{t,p} \approx 2.5$ for problems treated in the next section.

Coupling With the Gas Phase Equations. The gaseous phase is affected by the dispersed phase due to momentum, heat, and mass exchange. An advantage of the new Eulerian model is now given by an easy way of coupling the two phases. Due to an identical mathematical formulation, the same term appears for both phases, simply with different sign. A drawing up of the coupling terms for the gas phase equations is given in Table 1.

The expressions are added up for all *nd* discrete drop-size classes. Turbulence quantities of the gas phase are assumed to be unaffected by the presence of the dispersed phase. A more detailed description of coupling effects between the two phases will be presented elsewhere (Wittig et al., 1993).

3 Solution Steps

3.1 Droplet Equations. In the Lagrangian approach the ordinary differential equations governing the behavior of each droplet are solved by forward numerical integration from the injection location, at which the initial conditions are prescribed (Gosman and Ioannides, 1983). In contrast, the partial differential equations of the Eulerian droplet model can be solved with the same numerical procedure as the gas phase equations, e.g., a finite volume discretization method in the present study.

3.2 Overall Solution Procedure. After calculating the droplet field with the prevailing values of the gas field properties, the gas field is recalculated with the coupling terms due to droplet transport and evaporation. This procedure is repeated until the coupling terms converge, i.e., both phases have statistically stationary values.

4 Results and Discussion

In contrast to a large number of experimental studies in particle-laden jets and channel flows, detailed experimental investigations of the particle-size-resolved dispersion in separated flows are rare. In addition, complete data sets including particle-size-resolved velocities and volume fractions for separated two-phase flows with evaporating droplets are not available. Due to these facts the new model has been tested against different experimental data.

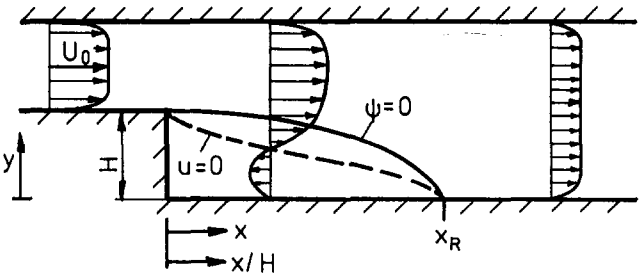

Fig. 1 Backward facing step geometry; $\psi = 0$ dividing streamline; $u = 0$ zero velocity line (Ruck and Makiola, 1988)

Ruck and Makiola (1988) measured particle velocities in a single-sided backward-facing step flow for particle diameters ranging from 1 to 70 μm, where the results for the minimum and maximum diameters are used to verify the two different theoretical approaches.

Measurements of a recirculating droplet charged air flow within a model combustor were presented by Himmelsbach (1987) and Wittig et al. (1988). These measurements are used to validate the new Eulerian evaporation model.

4.1 Particle Dispersion in a Single-Sided Backward Facing Step Flow. For the experimental study Ruck and Makiola (1988) used a test section made of glass with an expansion ratio of 1:2 and a step height of 25 mm (Fig. 1). Measurements considered here were performed with a Reynolds number of

$$\mathrm{Re}_H = \frac{U_0 H}{\nu} = 64 \times 10^3$$

In Fig. 2 streamwise velocities of very small oil droplets ($D_p \approx 1$ μm) in comparison to heavy starch particles with a medium diameter of 70 μm are shown for three different distances behind the step.

For the small oil droplets the predicted velocities of both approaches agree excellently with experimental data. In addition, the Eulerian calculations show identical results for the velocity components of the gas and the droplet phase. This is, following Fogt and Peric (1990), a special requirement if two fluids with nearly identical properties are investigated as a two-fluid mixture and, therefore, a test for the correctness of the model. The predicted reattachment length of the separation zone behind the step is $x/H = 8$ and also in excellent agreement with the measurements of Ruck and Makiola (1988).

Results for the heavy particles agree only in the upper half of the test section. Discrepancies occur in the recirculation zone, which has not been entered by particles in the Lagrangian approach. For the Eulerian method, due to the mathematical formulation (continuum assumption), results are obtained for the whole calculation domain. However, the volume fraction of the dispersed phase in the recirculation zone is at least three orders of magnitude lower than the volume fraction at the channels inlet and, therefore, not of practical interest.

Besides numerical or model problems, discrepancies between measured and predicted velocities for the starch particles may be caused by problems selecting monodispersed particles in the experiment. Often so-called "monodispersed" sprays contain a great number of very small particles, as well. In contrast to bigger particles, these small particles will easily reach the separated region and falsify the results of the measurements.

Detailed experimental data of the particle size distribution

Downloaded 02 Jun 2010 to 171.66.16.102. Redistribution subject to ASME license or copyright; see http://www.asme.org/terms/Terms_Use.cfm

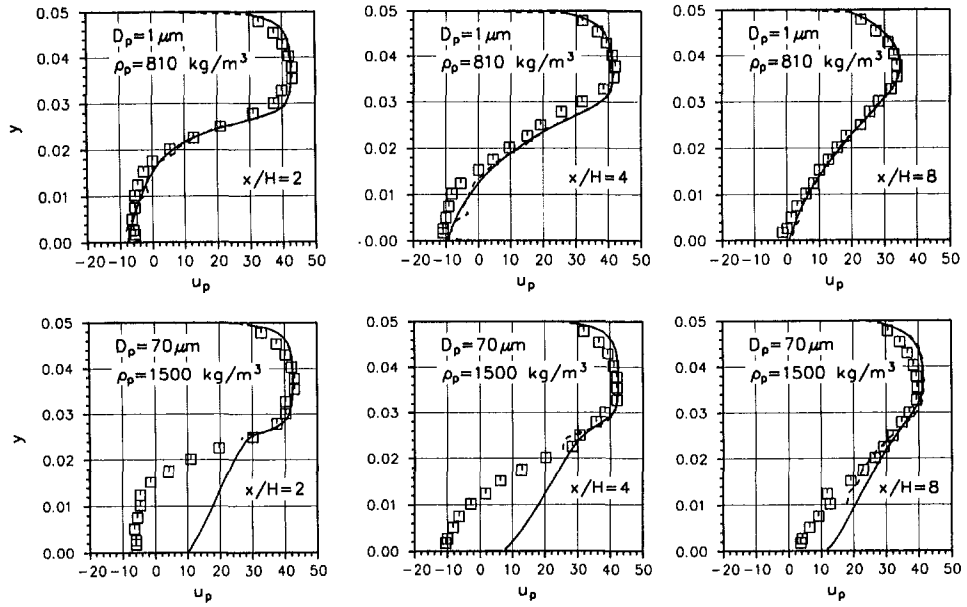

Fig. 2 Mean velocity profiles for 1 and 70 μm particles behind the backward facing step: □ measurements (Ruck and Makiola, 1988); —— Eulerian approach, ---- Lagrangian approach

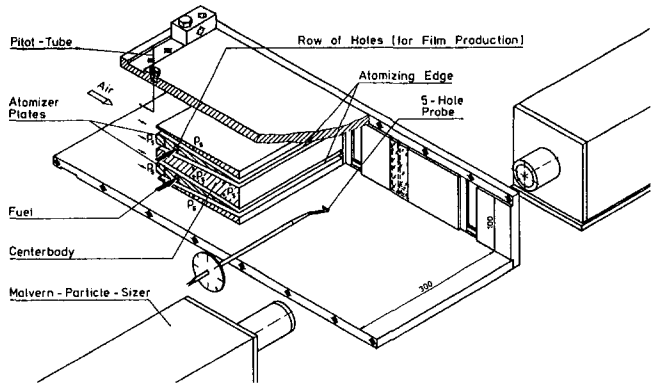

Fig. 3 Test section: two-dimensional combustor model (Wittig et al., 1988)

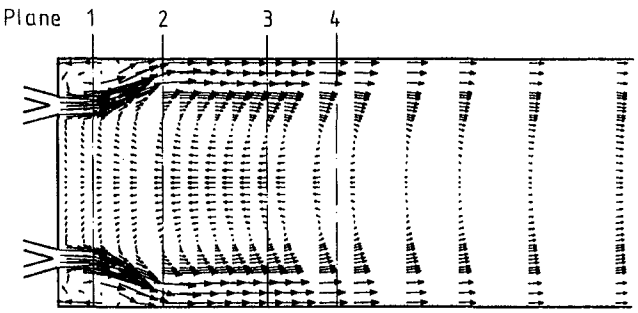

Fig. 4 Calculated flow field with axial locations of measuring planes; plane 1: x = 20 mm, plane 2: x = 60 mm, plane 3: x = 120 mm, plane 4: x = 160 mm (Wittig et al., 1988)

and the volume fraction of the dispersed phase are not available. On the other side it has been shown by computational experiments with a particle size distribution at the channels inlet containing some small particles, that much better agreement with the experiment for the particle velocities in the recirculation zone is obtained. Nearly identical results for oil and starch particles, especially for $x/H = 2$, also give a good reason that in the experiment not only 70 μm particles were measured.

Regarding the computations, it must be taken into account that in the Eulerian approach an over- or underprediction of the turbulent dispersion could lead to a misrepresentation of the velocities in the recirculation zone. Additional analyses for the prediction of turbulent particle dispersion in separated flows are the subject of current investigations and will be published soon (Wittig et al., 1993).

4.2 Evaporation of Fuel Droplets in Turbulent Combustor Flow. The test section used in our laboratory is shown in Fig. 3. It consists of a rectangular flow channel with a cross-sectional area of 100×300 mm^2. A prefilming two-dimensional airblast nozzle is incorporated into the test section. The airflow enters the channel through four slots. Two of these slots are charged with a liquid film. As reported earlier (Wittig et al., 1987), the symmetric flow field has a two-dimensional character and can be predicted with sufficient accuracy. Figure 4 shows the calculated flow field with the axial locations of four measuring planes.

The experimental studies were performed with ethanol at a gas temperature of 520 K. The inlet temperature of the liquid was 315 K and was determined by thermocouple measurements (Wittig et al., 1988). Droplet motion and evaporation were calculated for ten discrete drop-size classes. The initial conditions for the droplets were determined from elaborate studies of air-blast atomizers as a function of the operating parameters of the nozzle and the properties of the liquid. They can be discribed with the distribution parameters $D_{63,2} = 78$ μm and $N = 2$ in the Rosin–Rammler distribution (Sattelmayer, 1985; Kneer et al., 1990). Figures 5 and 6 show the predicted spatial distribution of two different drop sizes in the upper half of the model combustor for both numerical approaches. The excellent agreement of the two methods in all details is proof that the new Eulerian model yields adequate results for evaporating droplets. Fluctuations, which can be seen in the Lagrangian results, are due to the statistical nature of the Monte Carlo sampling method. They could be damped by increasing the number of particles used to evaluate mean droplet diameters.

Downloaded 02 Jun 2010 to 171.66.16.102. Redistribution subject to ASME license or copyright; see http://www.asme.org/terms/Terms_Use.cfm

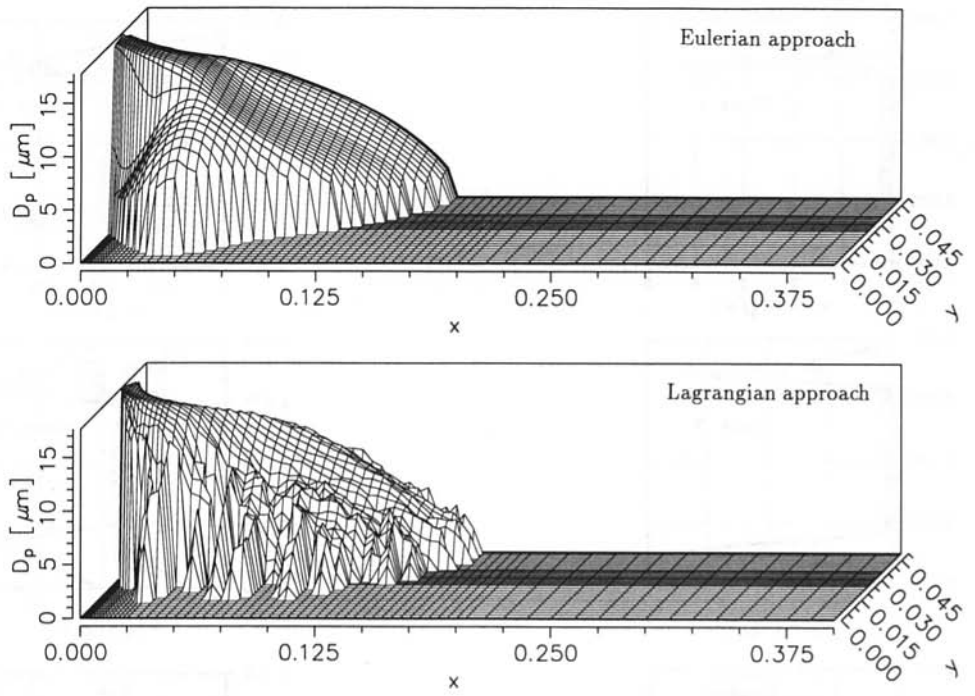

Fig. 5 Spatial distribution of the droplet diameter for a starting diameter of 17.67 mm

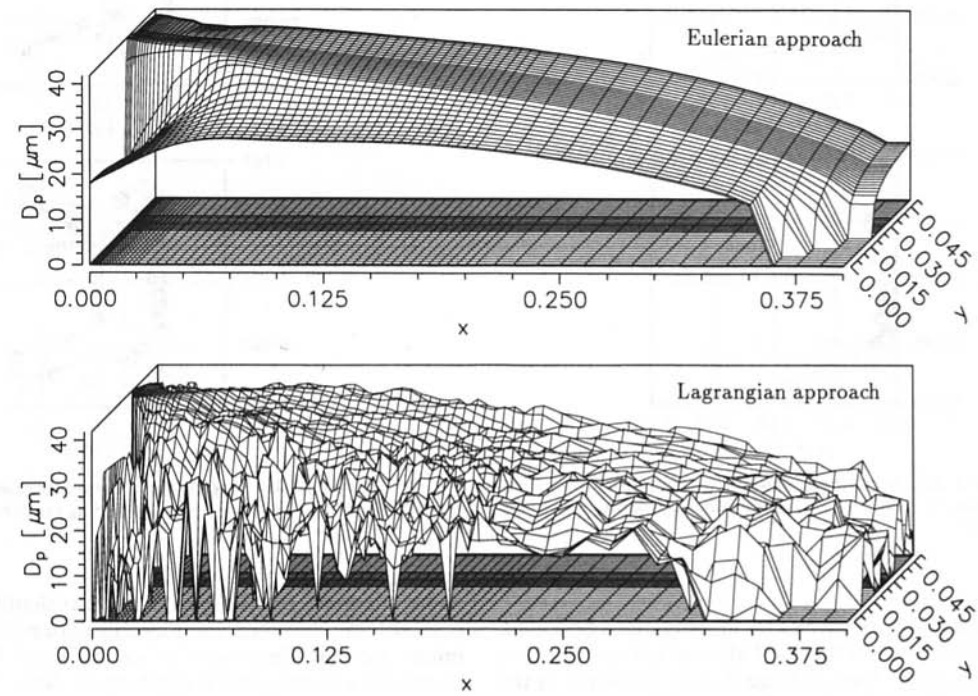

Fig. 6 Spatial distribution of the droplet diameter for a starting diameter of 41.84 mm

In Fig. 7 the calculated volume fraction of the liquid phase is plotted against experimental data given by Himmelsbach (1987). In the first three planes, the predicted values agree very well with the measurements. In the fourth plane, the measured volume fractions are slightly too high. This is due to a strong droplet/wall interaction between the second and the third measuring plane. In this region droplets are reflected partly into the flow field. These effects are not resolved by the numerical models at the moment.

Detailed results of the droplet diameter distribution of the evaporating spray can be seen in Fig. 8. The calculated characteristic diameters of the assumed Rosin–Rammler distribution agree very well with the experimental data of Wittig et al. (1988). Only in the first plane can small discrepancies

Downloaded 02 Jun 2010 to 171.66.16.102. Redistribution subject to ASME license or copyright; see http://www.asme.org/terms/Terms_Use.cfm

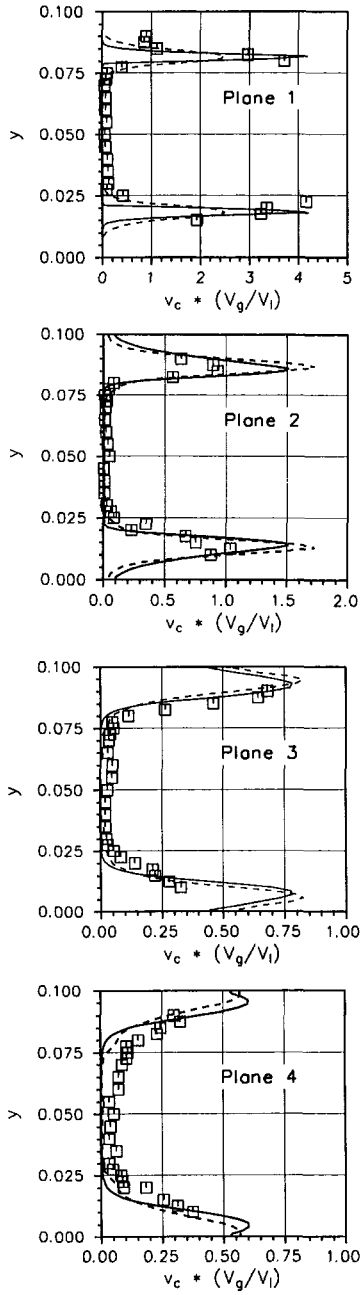

Fig. 7 Calculated and measured volume fractions; □ measurements (Himmelsbach, 1987), —— Eulerian approach, ---- Lagrangian approach

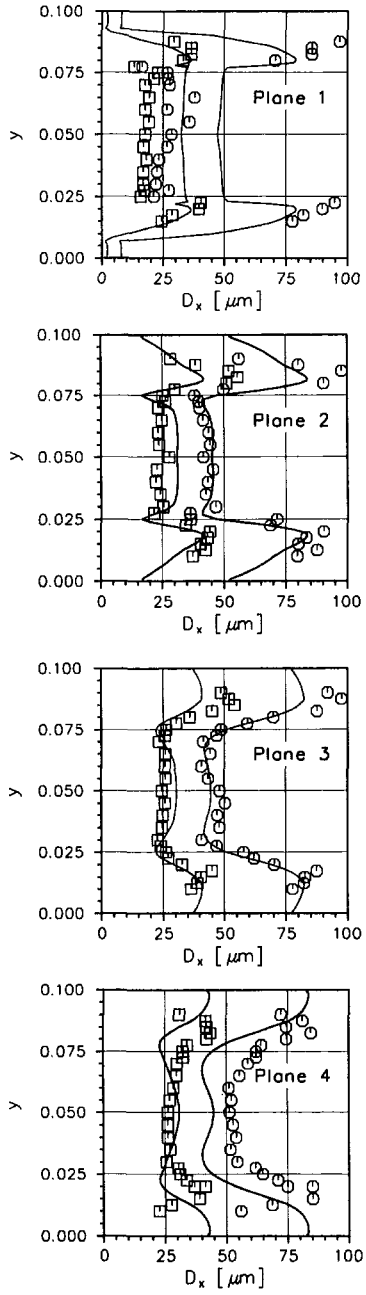

Fig. 8 Characteristic droplet diameters: measurements: □ D_{10}, ○ D_{50} (Wittig et al., 1988), —— Eulerian approach

between theoretical and experimental investigations be found. In this case, both experimental and theoretical results have to be analyzed in detail. Due to large density gradients in the gas phase, especially in the first plane, the optical measurements may be the source for the deviation.

5 Conclusions

A new Eulerian model for turbulent evaporating sprays has been developed. In contrast to former Eulerian approaches, it comprises transport equations for droplet heating and evaporation and is applicable for recirculating flows. Comparisons of the new model with Lagrangian calculations and experiments with respect to droplet velocities, diameter distributions, and concentrations revealed excellent agreement. The current performance of the new model is believed to be adequate for the purposes of evaluating high-intensity combustors. However, the physical understanding of the turbulent particle dispersion processes need further improvements for a more general application. Nevertheless, the similar structure of the transport equations obtained by the Eulerian approach with the commonly used gas phase equations offers scope for an incorporation of our new model in standard CFD codes.

Acknowledgments

The authors express their thanks to Mr. Roland Schmehl for doing the Lagrangian computations. This work was supported in part by the Arbeitsgemeinschaft Hochtemperatur Gasturbine (AG Turbo/Turboflam) and by a grant from the SFB 167 (High-Intensity Combustors) of the Deutsche Forschungsgemeinschaft.

Downloaded 02 Jun 2010 to 171.66.16.102. Redistribution subject to ASME license or copyright; see http://www.asme.org/terms/Terms_Use.cfm

References

Chen, C. P., and Wood, P. E., 1984, "Turbulence Closure Modeling of Two-Phase Flows," *Chemical Engineering Communications*, Vol. 29, pp. 291–310.

Chen, C. P., and Wood, P. E., 1986, "Turbulence Closure Modeling of the Dilute Gas-Particle Axisymmetric Jet," *AIChE Journal*, Vol. 32, No. 1, pp. 163–166.

Elgobashi, S. E., Abou-Arab, T. W., Rizk, M., and Mostafa, A., 1984, "Prediction of the Particle-Laden Jet With a Two-Equation Turbulence Model," *International Journal of Multiphase Flow*, Vol. 10, No. 6, pp. 697–710.

Faeth, G. M., 1983, "Evaporation and Combustion of Sprays," *Progress in Energy and Combustion Science*, Vol. 9, pp. 1–76.

Fogt, H., and Meric, M., 1990, "Finite Volume Approach to Two-Fluid Modelling of Two Phase Flows: Some Consistency Problems," *Proceedings of the 5th Workshop on Two-Phase Flow Predictions*, Erlangen, Mar. 19–22, pp. 130–139.

Gosman, A. D., and Ioannides, E., 1983, "Aspects of Computer Simulation of Liquid-Fueled Combustors," *Journal of Energy*, Vol. 7, No. 6, pp. 482–490.

Himmelsbach, J., 1987, "Experimentelle und numerische Untersuchungen zur Ausbreitung und Verdampfung flüssiger Brennstofftropfen in einer Heißgasströmung," Diplomarbeit, Institut für Thermische Strömungsmaschinen, Universität Karlsruhe (T.H.), Federal Republic of Germany.

Kneer, R., Benz, E., and Wittig, S., 1990, "Drop Motion Behind a Prefilming Airblast Atomizer: Comparison of Phase Doppler Measurements With Numerical Predictions," *Proceedings of the 5th International Symposium on Applications of Laser Technology to Fluid Mechanics*.

Krämer, M., 1988, "Untersuchungen zum Bewegungsverhalten von Tropfen in Turbulenter Strömung in Hinblick auf Verbrennungsvorgänge," Dissertation, Institut für Feuerungstechnik, Universität Karlsruhe (T.H.), Federal Republic of Germany.

Launder, B. E., and Spalding, D. B., 1974, "The Numerical Calculation of Turbulent Flows," *Computer Methods in Applied Mechanics and Engineering*, Vol. 3, No. 3, pp. 269–289.

Melville, W. K., and Bray, K. N. C., 1979, "A Model of the Two-Phase Turbulent Jet," *International Journal of Heat and Mass Transfer*, Vol. 22, pp. 647–656.

Mostafa, A. A., and Elghobashi, S. E., 1985, "A Two-Equation Turbulence Model for Jet Flows Laden With Vaporizing Droplets," *International Journal of Multiphase Flow*, Vol. 11, No. 4, pp. 515–533.

Mostafa, A. A., and Mongia, H. C., 1987, "On the Modeling of Turbulent Evaporating Sprays: Eulerian Versus Lagrangian Approach," *International Journal of Heat and Mass Transfer*, Vol. 30, No. 12, pp. 2583–2593.

Noll, B., Bauer, H.-J., and Wittig, S., 1989, "Gesichtspunkte der numerischen Simulation turbulenter Strömungen in brennkammertypischen Konfigurationen," *Zeitschrift für Flugwissenschaft und Weltraumforschung*, Vol. 13, pp. 178–187.

Ruck, B., and Makiola, B., 1988, "Particle Dispersion in a Single Sided Backward-Facing Step Flow," *International Journal of Multiphase Flow*, Vol. 14, No. 6, pp. 787–800.

Sattelmayer, T. F., 1985, "Zum Einfluß der ausgebildeten turbulenten Luft-Flüssigkeitsfilm-Strömung auf den Filmzerfall und die Tropfenbildung am Austritt von Spalten geringer Höhe," Dissertation, Institut für Thermische Strömungsmaschinen, Universität Karlsruhe (T.H.), Federal Republic of Germany.

Sparrow, F. M., and Gregg, J. L., 1958, "The Variable Fluid Property Problem in Free Convection," *Transactions of ASME*, Vol. 80, pp. 879–886.

Wittig, S., Bauer, H.-J., and Noll, B., 1987a, "On the Application of Finite-Difference Techniques for the Computation of the Flow Field in Gas Turbine Combustors With Complex Geometries," AGARD-CP-422.

Wittig, S., Klausmann, W., and Noll, B., 1987b, "Turbulence Effects on the Droplet Distribution Behind Airblast Atomizers," AGARD-CP-422.

Wittig, S., Klausmann, W., Noll, B., and Himmelsbach, J., 1988, "Evaporation of Fuel Droplets in Turbulent Combustor Flow," ASME Paper No. 88-GT-107.

Witting, S., Hallmann, M., Scheurlen, M., and Schmehl, R., 1993, "A New Eulerian Model for Turbulent Evaporating Sprays in Recirculating Flows," AGARD-CP-536.

APPENDIX

The reference values in the models presented are determined according to the 1/3 rule of Sparrow and Gregg (1958):

$$T_{\text{ref}} = \frac{2}{3}T_p + \frac{1}{3}T_\infty \tag{34}$$

$$X_{v,\text{ref}} = \frac{2}{3}X_{v,p} + \frac{1}{3}X_{v,\infty} \tag{35}$$

$$n_{\text{ref}} = n(T_{\text{ref}}) \tag{36}$$

$$\Gamma_{\text{ref}} = \Gamma(T_{\text{ref}}) \tag{37}$$

$$c_{p,v,\text{ref}} = c_{r,v}(T_{\text{ref}}) \tag{38}$$

$$\lambda_{\text{ref}} = \lambda(T_{\text{ref}}) \tag{39}$$

The vapor concentration at the droplet's surface

$$X_{v,p}(p_s) = \frac{p_s}{p} \tag{40}$$

is given by an exponential law following Cox–Antoine

$$p_s(T_p) = \exp\left(A + \frac{B}{T_p + C}\right) \tag{41}$$

where A, B, and C are specific values for the droplet liquid under consideration.

Downloaded 02 Jun 2010 to 171.66.16.102. Redistribution subject to ASME license or copyright; see http://www.asme.org/terms/Terms_Use.cfm

Effects of Oxygen and Additives on the Thermal Stability of Jet Fuels

S. P. Heneghan

C. R. Martel

T. F. Williams

D. R. Ballal

University of Dayton,
Research Institute,
Dayton, OH 45469-0140

A previously developed flowing single-pass heat-exchanger test rig (Phoenix rig) has been used to evaluate the effectiveness of various additives and the kinetic mechanism of both deposit formation and oxygen consumption. The Phoenix rig has been modified to include not just a heated single tube, but also a cooling test section and both hot and cold filters. The effects of flow conditions, antioxidants, and metal deactivator additives on the location and amount of the deposit are discussed. In general, antioxidants were effective at reducing the deposits on the hot test section, but almost invariably caused increased plugging of cool downstream filters. Downstream plugging of cool filters also increased with decreased temperatures in the heated section or with increased flow. Tests with both oxygen-saturated and oxygen-depleted fuels have shown that the solubility of oxygen is linearly related to the fraction of oxygen in a sparge gas, and that the amount of deposit is linearly related to the total quantity of dissolved oxygen passed. Finally, in contrast to initial modeling efforts, the consumption of oxygen is shown to be significantly more complex than a simple bimolecular, pseudo-first-order in oxygen, process. It is found to be much closer to pseudo-zero-order in the early stages, decaying to pseudo-first-order when the oxygen nears depletion.

Introduction

Commercial and military jet aircraft use jet fuel as a heat sink or working fluid for heat management. After absorbing heat, a fraction of the fuel is consumed in the engines; the remainder is returned to the storage tanks. Some current and planned aircraft use ram air-heat exchangers to cool aircraft jet fuels to acceptable temperatures before returning to the storage tanks. Jet fuels are known to degrade by thermal-oxidative pathways at temperatures approaching 450 K for times in the neighborhood of tens of seconds.

As discussed previously (Harrison, 1990), the problems associated with thermal degradation of jet fuels are expected to increase due to increased engine efficiency, higher heat loads, loss of ram air coolers, and lower quality fuel sources, particularly coal-derived JP fuels. To understand the kinetics of the thermal degradation process, evaluate the effectiveness of various additives, and assist in the development of effective models for the prediction of thermal deposition, we have developed the Phoenix rig (Heneghan et al., 1993).

After initial testing and evaluation of the Phoenix rig, we used this apparatus to identify critical features concerning the kinetics of deposit formation, including the evaluation of global rate constants for oxygen consumption and deposit formation. The objective of this was to develop a better understanding of the low-temperature oxidation process and to evaluate several antioxidant additives. In addition, we have studied the use of metal deactivators to inhibit deposition. Finally, a downstream cooling section and two downstream filters were installed to assess the relative importance of bulk-versus-wall reactions and the effects of product solubility on the deposition process.

This paper presents numerous results on the effectiveness of antioxidant and metal deactivator additives, describes new studies on low-temperature oxidation, and discusses current efforts to model these results.

Experimental Description

A flowing single-pass heat exchanger (Phoenix rig) was developed (Heneghan et al., 1993) to evaluate jet fuel ther-

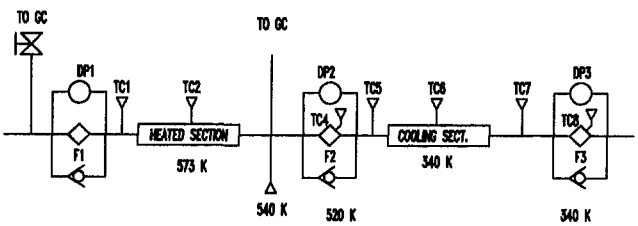

Fig. 1 Flow diagram of modified Phoenix rig test section showing relative location of thermocouples (TC), differential pressure gauges (DP), filters (F), and gas chromatograph sampler (GC). Listed temperatures are typical for 16 ml/min flow and 300°C (573 K) block temperature.

Contributed by the International Gas Turbine Institute and presented at the 38th International Gas Turbine and Aeroengine Congress and Exposition, Cincinnati, Ohio, May 24–27, 1993. Manuscript received at ASME Headquarters March 1, 1993. Paper No. 93-GT-130. Associate Technical Editor: H. Lukas.

Copyright © 1995 by ASME

Downloaded 02 Jun 2010 to 171.66.16.102. Redistribution subject to ASME license or copyright; see http://www.asme.org/terms/Terms_Use.cfm

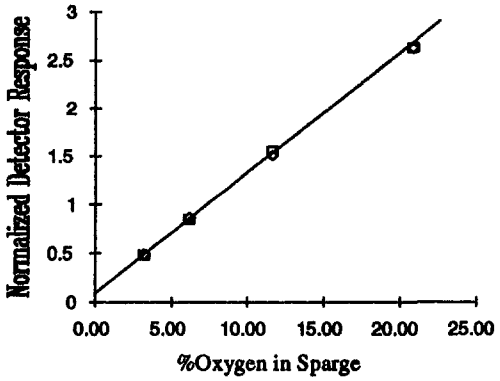

Fig. 2 Linearity of detector response and oxygen solubility to various sparge gas fractions of oxygen

mal stability. The Phoenix rig was modified slightly to include both heating and cooling test sections. In addition, 2 μm porosity stainless-steel filters were added after the heated (F2) and the cooled (F3) test sections. A block schematic of the test rig is shown in Fig. 1. F2 is maintained at a temperature usually about 50°C less than the block temperature, while the cool F3 is maintained at about 65°C.

Fuel-degradation products that form on the walls of heated and cooled tubes are measured by carbon burnoff. The products on the filters are measured both gravimetrically and by carbon burnoff. Tubes and filters are rinsed with hexane and dried under vacuum prior to measurement. The pressure drop across both F2 and F3 is monitored during the tests. Dissolved oxygen in the test fuel is controlled by sparging the fuel using a nitrogen/oxygen mixture. A gas chromatograph (GC) is used to measure the dissolved oxygen. The fuel is sampled both upstream and immediately downstream of the heated test section.

The partial pressure of oxygen is set by adjusting the nitrogen to oxygen ratio in a sparge gas. Figure 2 shows the chromatographic analysis of the fuel for oxygen content after 15 hours of sparging for different fractions of oxygen sparge. The excellent fit verifies the linear dependence of dissolved oxygen on fraction of oxygen in the sparge gas, and also shows that the detector response is in a linear regime.

The baseline test fuel is listed in Table 1 and its properties were described earlier (Heneghan et al., 1993). In addition to the baseline test fuel, three antioxidants (AO), a metal deactivator (MDA), and a jet fuel additive package (JFA-5) were studied. These items are also listed in Table 1. JFA-5, a DuPont product, is specified for addition to thermally stable jet fuel (MIL-T-25224) and MDA is approved for use in aviation turbine fuels.

Test Results—Deposits

Location. Figure 3 shows the magnitude and axial location of the deposits in the heated test section (608 K) for Jet-A fuel at three different flow rates. The higher flow rates at comparable times yield more deposits and the deposits have moved downstream. However, if the data are plotted versus time in the heated test section, it is easy to see (Fig. 4) that the deposits occur at very nearly the same time, independent of the flow rate. Similar results were obtained in the heated section for block temperatures of both 543 K and 573 K.

The other interesting location information relates the amounts of deposit on the hot (F2) and cold (F3) filters and in the hot and cold test sections as a function of the heater-block temperature and flow rate. Table 2 shows how these four values change for three different block temperatures, and three flow rates. Note that the amount of deposit increases with temperature for the hot test section, while this trend is reversed for the filters and the cold test section. Also, higher flow rates significantly increase the deposits on the filters at the lower block temperatures.

Total Flow and Oxygen. Figure 5 shows the normalized log of the total carbon deposit within the heated test section versus the log of volume of fuel for a six-hour experiment for three block temperatures. In general, the amount of deposits increased within increasing block temperature.

Table 1 Test material description

Item	Description
Jet-A	Stock feed jet fuel, not hydrotreated
JFA-5	Additive package for MIL-T-25224
AO-1	Tertiarybutylhydroquinone
AO-2	Proprietary sulfur/oxygen
AO-3	Proprietary phenol
MDA	N,N'-disalicylidene-1,2,-propanediamine

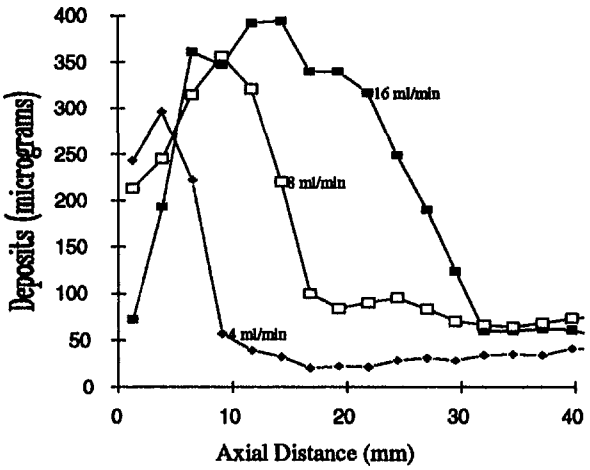

Fig. 3 Axial deposit location for Jet-A at three different flow rates

Nomenclature

A = pre-exponential
AMW = average molecular weight
E = activation energy
$f = [O_2]_t/[O_2]_o$
$[F]$ = concentration of fuel or a fuel component
g = grams
k = rate constant
L = liters
$[O_2]_t$ = concentration of oxygen at time t
R = universal gas constant
s = seconds
T = temperature
t = time
V = volume
α, β, γ = reaction orders
τ = residence time

Abbreviations

AO = antioxidant
GC = gas chromatograph
JFA-5 = jet fuel additive
MDA = metal deactivator
MIL = military specification
TD = total deposits

Downloaded 02 Jun 2010 to 171.66.16.102. Redistribution subject to ASME license or copyright; see http://www.asme.org/terms/Terms_Use.cfm

Table 2 Relative amount of deposits on four test sections

Hot Section (µg)	Cold Section (µg)	F2 (µg)	F3 (µg)	Block Temp (K)	Outlet Fuel Temp (K)	Flow Rate (ml/min)
3657	128	458	239	608	576	16
2615	160	238	467	608	573	8
1261	114	213	298	608	569	4
2909	210	3400	466	573	542	16
1209	142	1007	284	573		8
875	128	266	281	573	533	4
1234	1896	2660	25560	543	518	16
1031	177	809	2020	543	518	8
799	152	499	423	543	510	4

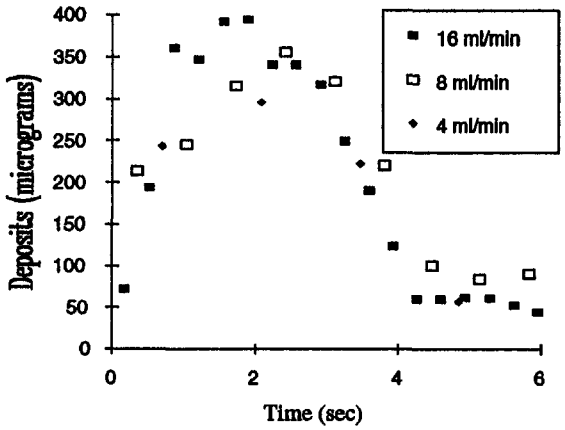

Fig. 4 Time location of deposits for Jet-A at three different flow rates

While it is true that the fuel flow rate has been increased for these experiments, the amount of dissolved oxygen flow has also been increased. To assess quantitatively the effects of dissolved oxygen, varying-flow experiments were repeated using a diminished initial oxygen concentration and a 573 K block temperature. The results at 573 K are summarized in Fig. 6. The line is drawn through the heated tube deposits only.

Additive Effects. The addition of antioxidants to Jet-A has a mixed effect on oxygen consumption. AO-1 and AO-2 tend to increase the temperature at which the fuel consumes oxygen, while JFA-5 (which contains an antioxidant as part of the overall package) tends to decrease this temperature. AO-3 caused severe plugging (measured as a large increase in the pressure drop) of F3 and necessitated termination of the test prior to completion.

Figure 7 compares the deposits measured in the hot section, on the hot filter, in the cold section, and on the cold filter, for the Jet-A, Jet-A +25 mg/L AO-2, and Jet-A + 6 mg/L MDA for a 12-hour 573 K block temperature, 16 ml/min test. The extra test length (12 versus 6 hours) resulted in significant buildup of deposits at F3, where essentially none was visible after six hours for the baseline Jet-A. The antioxidant did not substantially affect the hot deposits, but significantly reduced the cold deposits while the metal deactivator reduced both the hot and cold section deposits. The measured reduction in the cold section deposits occurred even though the pressure drop across the cold filter had risen dramatically for all the additives.

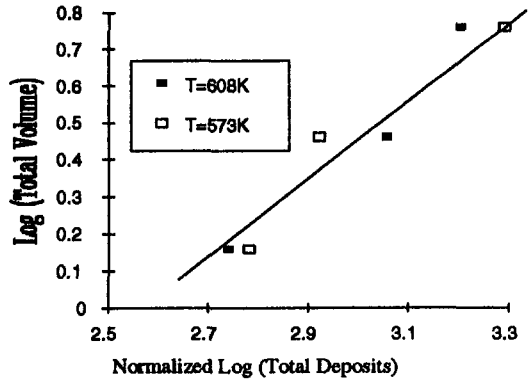

Fig. 5 Dependence of total deposits in hot section on volume flow

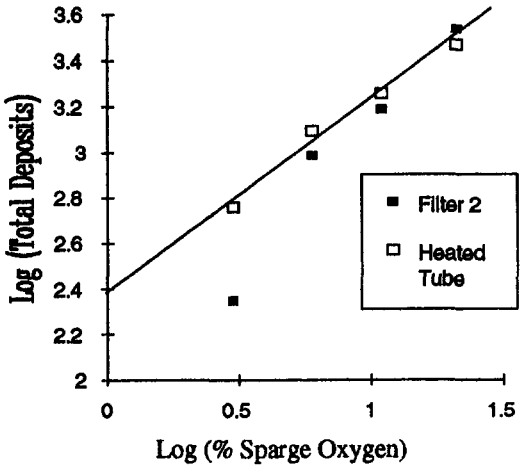

Fig. 6 Dependence of total deposits on oxygen concentration for constant flow at 573 K

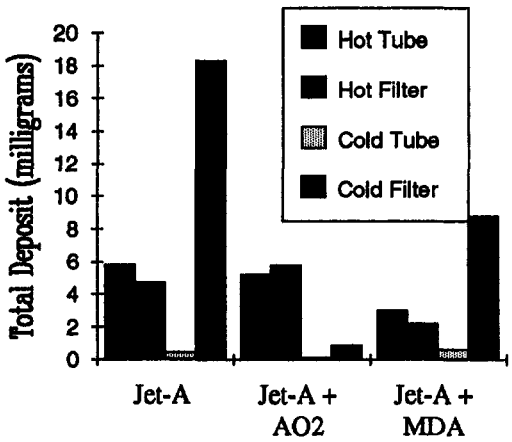

Fig. 7 Effectiveness of additives on deposits

Test Results—Oxygen Consumption

The diminished initial oxygen concentration allowed us to perform an interesting check on the order of oxygen-consumption. As described previously (Heneghan et al., 1993), the oxygen consumption experiments are run by varying the block temperature at a constant flow rate and measuring the dissolved oxygen concentration and the bulk fuel temperature at the outlet of the test section. The results of the oxygen depletion test are shown in Fig. 8. This figure shows the normalized detector response to dissolved oxygen as a function of the output bulk fuel temperature. The output fuel temperature is varied by increasing the block temperature while maintaining a constant flow rate. Four separate initial conditions are shown, each represented by the percentage of oxygen in the sparge gas.

Downloaded 02 Jun 2010 to 171.66.16.102. Redistribution subject to ASME license or copyright; see http://www.asme.org/terms/Terms_Use.cfm

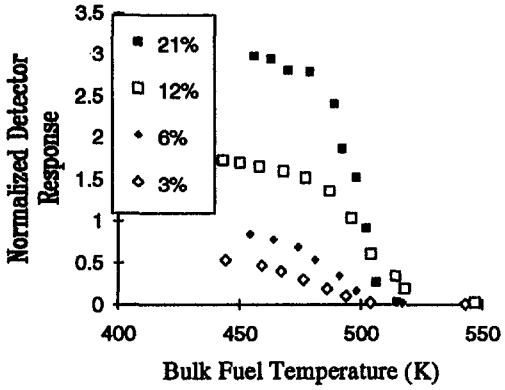

Fig. 8 Oxygen-consumption curves for various sparge percent oxygen

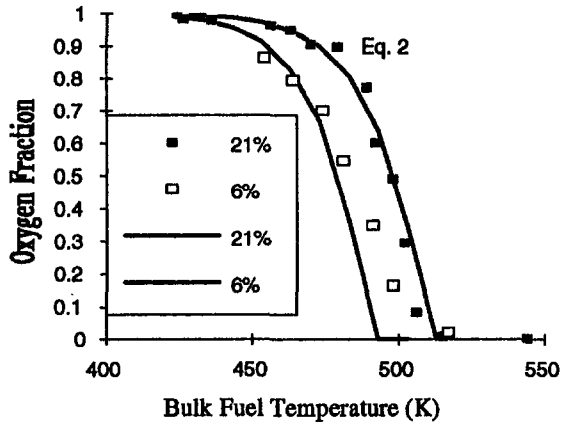

Fig. 9 Dependence of fraction of oxygen remaining on the output bulk temperature for two initial oxygen sparge conditions

Discussion

Kinetics of Oxygen Consumption. The results of the oxygen depletion tests were discussed by Heneghan et al. (1993) in terms of a pseudo-first-order reaction. (Pseudo-first-order means that the concentrations of all other reactants are large compared to oxygen and, therefore, can be treated as constants.) The equation used to fit the saturated (21 percent sparge or about 50 ppm) oxygen depletion data was:

$$\ln\left(\frac{[O_2]}{[O_2]_o}\right) = \frac{\tau}{(T_{\text{final}} - 300)} \int_{300}^{T_{\text{final}}} A \exp(-E/RT)dT \quad (1)$$

However, Heneghan and Zabarnick (1994) have recently shown that the oxidation of fuel may be zero-order in oxygen, first order in oxygen, or mixed order. Without inhibitors, the order is likely to start out as zero order and switch to first-order. Jones (1993) has shown, in a similar flowing system, that the reaction order for oxygen consumption follows zero-order kinetics, with significant acceleration due to autocatalysis.

From Eq. (1), if the concentration of oxygen is plotted in terms of fraction of oxygen ($[O_2]_t/[O_2]_o$) versus the output temperature (T_{final}), the resulting graph should be independent of the initial oxygen concentration. Figure 9 shows the fraction of oxygen remaining versus temperature for two different initial oxygen concentrations. This clearly shows that the oxygen consumption is different from the first-order process.

Following the reasoning similar to the one discussed by Heneghan et al. (1993) but assuming that the reaction is pseudo-zero-order in oxygen, the expression for oxygen fraction can be written as:

$$\left(\frac{[O_2]_t}{[O_2]_o}\right) = 1 - \frac{\tau}{[O_2](T_{\text{final}} - 300)} \int_{300}^{T_{\text{final}}} A \exp(-E/RT)dT. \quad (2)$$

Notice that the rate of decrease in the fraction of oxygen remaining depends on the initial oxygen concentration. In fact, as the initial concentration of oxygen is decreased, the rate of consumption of the fraction increases.

The two curves added to Fig. 9 are representative of zero-order behavior (as expressed in Eq. (2)). The curve for the saturated-oxygen level (21 percent sparge)) represents the expected concentration if the depletion were zero-order with an A factor of 10^{15} ppm/s and an activation energy of 30.5 kcal/mole. The curve for the diminished initial oxygen is shown using Eq. (2) and the same Arrhenius parameters as used for the saturated oxygen case. It is clear that the oxygen consumption process is very complicated.

Kinetics of Deposit Formation. The data in Fig. 5 suggest that the deposit formation at higher temperatures is linearly dependent on the volumetric fuel-flow rate. However, the information in that graph cannot distinguish the difference between total fuel and total oxygen. The dependence on oxygen is shown in Fig. 6.

A simple global kinetic relationship for the formation of deposits on the test section walls is given by

$$TD = k[O_2]^{\alpha}[F]^{\beta} t V^{\gamma} \text{AMW}, \quad (3)$$

where V is the total volume in liters; $[O_2]$, $[F]$ are concentrations in moles/L; α, β, γ are the reaction orders; k is the rate constant in $(\text{L/mole})^{\alpha+\beta-1}/\text{s}$; AMW is the average molecular weight of the deposit in g/mole; t is the time in seconds; and TD is the total deposit in grams.

AMW converts the molar quantities associated with concentrations and rate constants to weights. AMW can be eliminated if the concentrations are given in grams/liter (to the power $(\alpha + \beta - 1)$ per second.

To determine the reaction order, take the logarithm of both sides of Eq. (3) and vary one variable (volume, $[O_2]$). Then a plot of log (TD) versus the variable will have a slope equal to α, β, or γ. This is the reason we have chosen to present the deposit data of Figs. 5 and 6 as log–log plots. The slopes of the lines in Figs. 5 and 6 are both nearly unity. This indicates that the reaction order for the global rate equation is unit for V, the total flow volume, and the concentration of oxygen.

Finally, the product of volume and oxygen concentration is the amount of oxygen flowed. Interestingly, the amount of deposits is not dependent on the amount of fuel, but the amount of oxygen. Flowing twice the fuel at half the oxygen level will yield essentially no change in the amount of deposits.

Location. Figures 3 and 4 show that while the location of the deposit in terms of the axial distance traveled has changed with the increased flow, the time it takes to form deposits has not changed. Since the time for deposit formation is essentially constant, and it is known that deposit formation is temperature sensitive (Hazlett, 1991), the appearance of the deposits at a fixed time indicates that the heating rate of the fuel (°C/s) is independent of the flow conditions.

Further, it is interesting to note that the major portion of the deposit-forming reactions begins at a certain time/temperature and is concluded at a particular time/temperature. This points out a major difficulty in evaluating global rate constants for deposition (k_d). To evaluate k_d, it is necessary to use the correct time of the reactions. In this case, most of the reactions are complete within six seconds (for the 573 K

Downloaded 02 Jun 2010 to 171.66.16.102. Redistribution subject to ASME license or copyright; see http://www.asme.org/terms/Terms_Use.cfm

block temperature). This time is neither the residence time (τ) nor the experiment time (6 to 12 hours). If the behavior of oxygen or other limiting compounds versus time is well understood and its time-dependent concentration is used in the modeling, its disappearance will ensure that the rate of production of solids goes to zero at the appropriate time (see Eq. (3)). In that case, any sufficiently long period of time can be used to evaluate k_d. If initial or average values are used, the appropriate time must be selected in addition to good average values.

Finally, there is a significant increase in deposits downstream from the hot test section whenever the temperature in the hot section is lowered. The deposit in the downstream sections is also highly dependent on the flow velocity (for the lower block temperatures). For instance, at a block temperature of 543 K, the deposit in the cold filter increases 60-fold for a fourfold increase in flow rate.

It is not clear what causes these significant deposits in the downstream section at lower temperatures, but it is possible that at the lower temperatures or higher flow rates the concentration of peroxides exiting the heated section is increased (Hazlett et al., 1977). This is because peroxides are the initial result of low-temperature oxidation. At higher temperatures, decomposition of the peroxides occurs in the bulk fuel more rapidly. Higher fuel flows spend less time at high temperatures, while lower block temperatures and shorter residence times contribute to a lowering of the maximum fuel temperature. At the lower temperatures and shorter residence times, the residual peroxide concentration is expected to be maximized. Decomposition of these peroxides could be a surface-catalyzed reaction (Benson, 1960), possibly leading to the results observed here.

Additives. The addition of antioxidants to Jet-A was found to have limited success in reducing the deposits formed in the hot test section. In addition, the effect on the temperature at which oxidation occurred was minimal; and it is not clear whether changes in this temperature are desirable. It has been recognized for many years that nonhydrotreated fuels were not particularly susceptible to low-temperature oxidation. Therefore, the small changes in oxidation temperature for the nonhydrotreated fuels should not be surprising. In addition, the phenol-based antioxidant caused a serious deposit problem that precluded test completion.

The metal deactivator appeared to produce the best results—it reduced both hot and cold deposits. However, despite the diminished deposit in the cold filter, the pressure drop across that filter increased. This suggests that something blocks the filter, but washes away before the carbon measurement. Since the filter is washed with hexane and dried before weighing, the compound may be either low boiling or soluble in hexane. If it were soluble in hexane, it would likely be soluble in fuel. Further, all the antioxidants and the metal deactivator had the same effect; this suggests that these additives have somehow changed the chemistry. A full understanding of these results has not yet been realized.

The best results in the heated section have come from the JFA-5 additive package studied by Heneghan et al. (1993). JFA-5 is believed to contain a combination of antioxidant and metal deactivator. We still need to retest JFA-5 with the new system to evaluate the effect of this additive on the downstream filters and cooling section.

Conclusion

The Phoenix rig was modified to trap bulk particulates formed in the heated section and to study problems associated with cooling after heating. Quantitative data on the location of deposits within the entire system as well as the distribution of deposits within the heated section were obtained.

Studies involving the oxygen consumption at reduced oxygen levels revealed that the kinetics of the oxygen reactions appears to be more complex than first-order. While the kinetics for deposit formation is also likely to be complex, simple global equations can be used to show that a major limiting factor in the production of solids is the availability of oxygen. Further, the production is linearly dependent on the availability of oxygen. The ability to track the deposit formation in time is critical to the evaluation of global kinetic parameters.

The use of antioxidants in nonhydrotreated fuels was of little use in preventing total deposits. Metal deactivators show limited promise; however, there is significant promise from the use of packages, such as JFA-5.

Acknowledgments

This work was supported by the US Air Force Wright Laboratories, Wright-Patterson Air Force Base, Ohio, under Contract Nos. F33615-87-C-2767 and F33615-92-C-2207. W. M. Roquemore served as the Air Force Technical Monitor.

References

Benson, S. W., 1960, *Foundations of Chemical Kinetics*, McGraw-Hill, New York.

Harrison, W. E., III, 1990, "Aircraft Thermal Management: Report of the Joint WRDC/ASD Aircraft Thermal Management Working Group," WRDC TR-90-2021.

Hazlett, R. N., Hall, J. M., and Matson, M., 1977, "Reactions of Aerated *n*-Dodecane Liquid Flowing Over Heated Metal Tubes," *Ind. Eng. Chem. Prod. Res. Dev.*, Vol. 16, p. 171.

Hazlett, R. N., 1991, "Thermal Oxidation Stability of Aviation Turbine Fuels," ASTM, Philadelphia, PA.

Heneghan, S. P., and Zabarnick, S., 1994, "Oxidation of Jet Fuels and Deposit Formation," *Fuel*, Vol. 73, p. 35.

Heneghan, S. P., Martel, C. R., Williams, T. F., and Ballal, D. R., 1993, "Studies of Jet Fuel Thermal Stability in a Flowing System," ASME JOURNAL OF ENGINEERING FOR GAS TURBINES AND POWER, Vol. 115, pp. 480–485.

Jones, E. G., Balster, W. J., and Post, M. E., 1995, "Degradation of a Jet A Fuel in a Single-Pass Heat Exchanger," ASME JOURNAL OF ENGINEERING FOR GAS TURBINES AND POWER, Vol. 117, this issue, pp. 125–131.

Downloaded 02 Jun 2010 to 171.66.16.102. Redistribution subject to ASME license or copyright; see http://www.asme.org/terms/Terms_Use.cfm

Degradation of a Jet A Fuel in a Single-Pass Heat Exchanger

E. G. Jones

W. J. Balster

M. E. Post

Systems Research Laboratories, Inc.,
Dayton, OH 45440

The formation of bulk and surface insolubles in a Jet A fuel during a single pass through heated stainless-steel tubes has been studied. Low temperature and low flow rates were utilized to produce near-isothermal conditions. In a second series of experiments, depletion of oxygen in the fuel saturated with respect to room-temperature air was measured under identical isothermal conditions. At a wall/bulk-fuel temperature of 185°C, rates of surface deposition and oxygen depletion were correlated; the maximum in the surface-deposition rate was found to occur after the Jet A fuel was stressed sufficiently that the dissolved oxygen was totally consumed. Results are discussed in terms of the autoxidation of the Jet A fuel and the concurrent production of deleterious bulk and surface insolubles.

Introduction

The thermal oxidative stability of jet fuels is of major importance because of the use of fuel as the primary heat sink in military aircraft. Increased aircraft performance creates a greater heat load to be dissipated through heat exchangers into the aviation fuel. At elevated temperatures oxidative degradation of the fuel takes place with the concurrent formation of bulk insolubles and surface deposits, both of which can greatly reduce engine performance and lead to downtime or engine failure.

Knowledge of the mechanism and kinetics of fuel degradation can be used to improve aircraft performance through fuel selection, blending, or the introduction of additives. In addition, acquisition of kinetic parameters describing the degradation processes can be used in conjunction with global-modeling programs to predict surface fouling under conditions that may not be readily achieved in the laboratory. Recent modeling by Katta and Roquemore (1992) has been successful in predicting accumulated wall deposition in injector feed-arm rigs.

The goal of the current study was to select a typical aviation fuel, subject it to isothermal stress within stainless-steel tubing using a single-pass heat exchanger, study the rates of both oxygen consumption and surface deposition, and evaluate bulk-particle formation. Typically fuel deposition studies in flowing rigs have involved high temperature, high flow, and large variation in bulk-fuel and wall temperatures in attempts to approximate actual engine conditions (Marteney and Spadaccini, 1986; Giovanetti and Szetela, 1986; Kendall et al., 1987; Chin et al., 1992; Chin and Lefebvre, 1993). Achievement of isothermal conditions in the current study required the use of relatively low flow rates (< 2 cm^3 min^{-1}) and wall temperatures (< 205°C); however, the constancy of wall and bulk-fuel temperatures greatly simplified the kinetic analysis.

The particular aviation fuel chosen for this study was a straight-run distillate fuel, meeting all USAF specifications, obtained from Shell Oil and designated Jet A (SHELL) or POSF-2827. Previous USAF-funded studies (Jones et al., 1992; Heneghan et al., 1993) have shown this fuel to have a propensity for surface deposition; it was considered an ideal candidate for thermal-oxidative degradation studies.

Experimental

The Jet A (SHELL) had a breakpoint of 539 K from the Jet-Fuel Thermal-Oxidation Test (JFTOT) and a sulfur level of 0.079 percent (w/w). Kendall and Mills (1986) have shown that the presence of certain sulfur-containing compounds tends to inhibit oxidation, but at the expense of increased insoluble formation. A similar finding has been reported in static flask tests for the currently studied fuel (Jones et al., 1992). The Jet A (SHELL) fuel was used as received, without filtration.

All experiments were conducted inside stainless-steel (304) tubes using the isothermal heat exchanger shown in Fig. 1. The tubing (0.125-in. OD, 0.020-in. wall) was cleaned with 10 percent Blue Gold solution using ultrasound, followed by water and methanol rinses. Background surface carbon in 2-in. tube sections was typically 10–20 μg and varied slightly from batch to batch. A syringe pump (ISCO Model 500D) was employed to transfer the fuel in a single pass through a 32-in.-long heated section. As will be discussed later, a long heat exchanger is necessary for capturing a large fraction of the surface-depositing material. In fact, in some experiments it was necessary to pass the fuel through two lengths of heated section. This was accomplished by an external loop and a second pass through another groove in the heater block.

Contributed by the International Gas Turbine Institute and presented at the 38th International Gas Turbine and Aeroengine Congress and Exposition, Cincinnati, Ohio, May 24–27, 1993. Manuscript received at ASME Headquarters March 17, 1993. Paper No. 93-GT-334. Associate Technical Editor: H. Lukas.

Copyright © 1995 by ASME

Downloaded 02 Jun 2010 to 171.66.16.102. Redistribution subject to ASME license or copyright; see http://www.asme.org/terms/Terms_Use.cfm

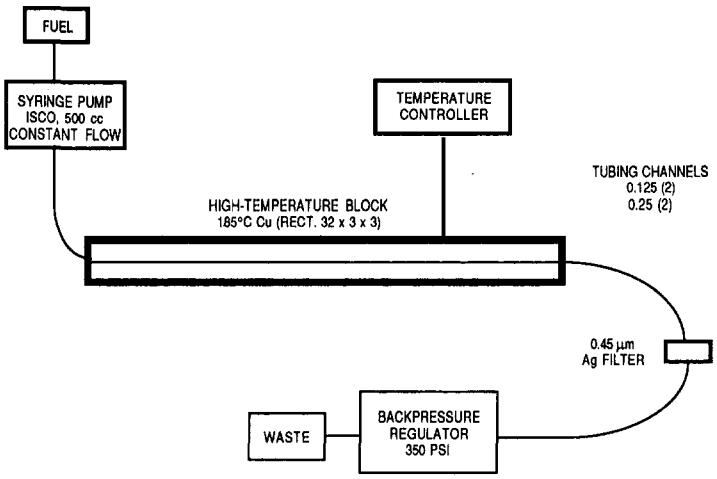

Fig. 1 Schematic diagram of isothermal heat exchanger

System pressure was maintained at 350 psi throughout the experiments to ensure a single phase. The fuel was stressed and then passed through an in-line 0.45-μm Osmonics silver-metal membrane filter. Deposition experiments were typically conducted over a 6-h time period, after which the tube was allowed to drain overnight and was then cut into sixteen 2-in. sections, which were rinsed with heptane and placed in a vacuum oven (115°C) for a minimum of 12 h. The filter was rinsed with heptane to remove residual fuel and was subjected to the same vacuum-oven conditions. Quantification of the total carbon in the filter and in the tube section was completed using a LECO RC-412 surface carbon analyzer. Deposits of this type generally contain ~ 80 percent carbon. Based on the nomenclature and heptane insolubility, the increased surface carbon was in the form of insoluble solids (*IS*) or insoluble gums (*IG*). Additional analyses of the filter deposits indicated that soluble gums (*SG*) were negligible and that the bulk particles were ~ 50 percent *IS* and ~ 50 percent *IG*.

Two basic experiments were conducted. In the first the fuel was passed through the tube at a fixed flow rate for 6 h, and the surface and bulk insolubles were quantified as described above. Initially the fuel was passed at room temperature until all the trapped air pockets were removed; then the desired fuel flow rate was set, and the copper-block heaters were turned on. Figure 2 shows the time required for the block to reach a setpoint of 185°C; the 10 min required to achieve equilibrium is considered negligible compared to the 360-min test duration. In the second type of experiment, the relative amount of dissolved oxygen present in the stressed fuel was measured using an in-line Hewlett-Packard gas chromatograph modified at the University of Dayton Research Institute (Rubey et al., 1992). In these experiments dissolved oxygen was evaluated for a series of flow rates, providing different stress intervals in the heated section. The data were represented as percent residual oxygen versus stress duration, with 100 percent corresponding to the amount

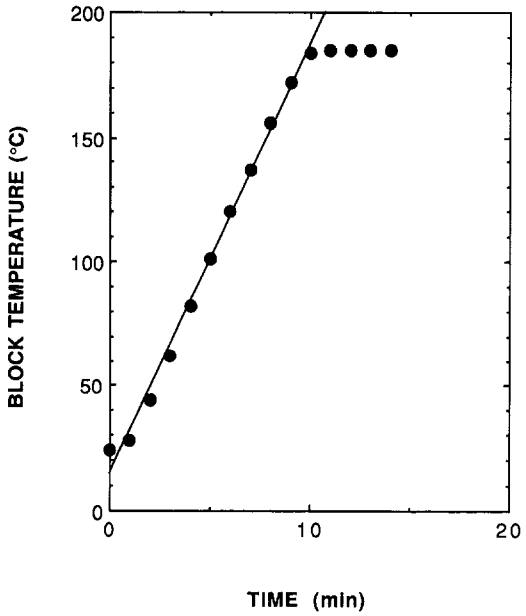

Fig. 2 Time required to achieve preset block temperature (185°C). Flow 1.0 cm^3 min^{-1}.

of oxygen in Jet A (SHELL) fuel saturated with respect to air at room temperature. Fuel was initially sparged with air under ambient conditions for 15 min to establish equilibrium air saturation. For some experiments where more dissolved oxygen was required, the fuel was initially sparged for 30 min with pure oxygen to achieve equilibrium levels of dissolved oxygen before the pump was filled. Similarly, for blank experiments where minimal oxygen was required, the fuel was sparged with helium for 30 min prior to the experiment. Although some residual dissolved oxygen remains after he-

Nomenclature

IS = Insoluble Solids (insoluble in heptane and acetone)
IG = Insoluble Gums (insoluble in heptane, soluble in acetone)
SG = Soluble Gums (soluble in heptane)
A = Arrhenius pre-exponential factor
E = Arrhenius activation energy
T = temperature (K)
R = gas constant
JFTOT = Jet-Fuel Thermal-Oxidation Test
t = fuel stress duration
t' = experimental test duration
s = distance along heated tube
v = fuel velocity
k = rate coefficient
USAF = United States Air Force

Downloaded 02 Jun 2010 to 171.66.16.102. Redistribution subject to ASME license or copyright; see http://www.asme.org/terms/Terms_Use.cfm

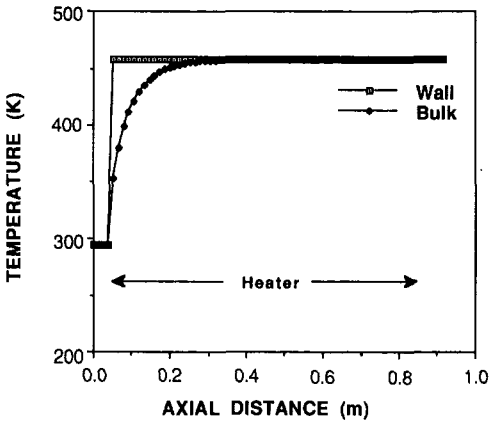

Fig. 3 Approach of bulk temperature to wall temperature. Flow 1.8 cm^3 min^{-1}, block temperature 185°C.

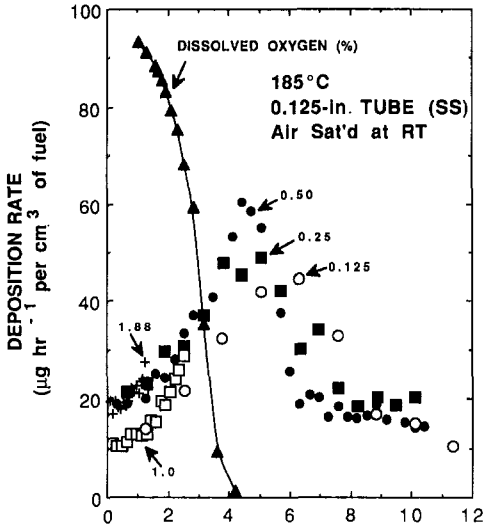

Fig. 4 Deposition from room-temperature air-saturated Jet A (SHELL) fuel at 185°C, 350 psi in 0.125-in. stainless-steel tubing as function of stress duration. Superimposed is dissolved oxygen (percent of air-saturated level at room temperature) as function of stress duration.

lium sparge, it is estimated to be < 5 percent of the air-saturated value and effectively serves as a comparison blank. The air-saturated dissolved oxygen is typically taken to be 50 ppm (w/w), although absolute measurements were not made. All signals were corrected for naturally occurring argon that is not chromatographically separated.

Results and Discussion

In this section the following subjects will be addressed:

- Approach to isothermal test conditions
- Reaction time frame and experimental time frame
- Deposition
- Mass balance
- Effects of buoyancy/gravity
- Oxygen consumption and Arrhenius parameters

The thermo-oxidative reactions of Jet A fuel over the temperature range studied are described generally as autoxidation. The pertinent reaction steps have been well addressed in many texts. Some of the major aspects are summarized in the appendix, based on the treatment of Walling (1957).

Approach to Isothermal Test Conditions. Isothermal conditions are achieved when the cold fuel reaches the same temperature as the tube walls or the copper block. Figure 3 shows the calculated (Katta, 1992) approach to isothermal conditions for the bulk fuel at room temperature passing through a tube maintained at 185°C at a flow rate of 1.8 cm^3 min^{-1}. It should be noted that for deposition studies discussed herein, 1.8 cm^3 min^{-1} represents a fast flow or a worst-case situation with respect to the achievement of isothermal test conditions. Clearly at least 75 percent of the tube experiences isothermal conditions at this flow rate.

Reaction Stress Duration and Experimental Test Time. In dynamic tests conducted isothermally, two distinct time frames are important. The first, or stress duration, is the time during which the fuel experiences the isothermal heated-block temperature. From a chemical standpoint, this represents the average time allotted for thermal-oxidative fuel degradation. At a fixed flow any position(s) along the tube is directly related to the reaction time or stress duration by the relation $t = s/v$. The average velocity, v, in turn, is directly proportional to the flow; and if an estimate is made for fuel expansion at 185°C (15 percent), the stress duration can be directly calculated from the flow and tube dimensions. In the current experiments this time frame is typically in the range 1–30 min.

The second time frame, t', is the test duration. For example, $t' = 6$ h represents a reasonable time for achieving deposits above the background levels. For other fuel types such as hydrotreated fuels having reduced amounts of heteroatoms and containing antioxidant additives, much longer experimental test times are necessary for achieving consistently measurable deposition.

Deposition. Surface carbon burnoff provides information on the quantity of carbon in the deposit collected in a 2-in. section of tube over a 6-h test period. A deposition rate (μg carbon per time in the tube section per cm^3 of fuel) is calculated by dividing the amount of carbon in the tube section by the residence time in the tube section and the total amount of fuel passed through the tube. The deposition rate is equivalent to micrograms of carbon per time per volume of tube section and can be converted to micrograms of carbon per time per unit area of the tube section by dividing by the surface-to-volume ratio. For example, Fig. 4 is a plot of deposition rate ($\mu g\ h^{-1}$ per cm^3 of fuel passed) as a function of time, where the time is the stress duration t, for five different flows ranging from 0.125 to 1.88 cm^3 min^{-1}.

Several important points should be made. First, at the highest flows, namely 1.88 and 1.0, the 32-in.-long tube encompasses only a small portion of the total profile since the fuel is passing through the tube so quickly that complete deposition is not possible. Presumably, a much longer tube, which would permit longer stress duration ($\sim$ 10 min), would encompass the entire deposition profile. This, in fact, is shown in the data at a flow of 0.5 cm^3 min^{-1}, where a second pass was required for collecting all the data points. Second, for the slower flows, deposition rates increase with time, pass through a maximum, and finally decrease to the baseline. This observation indicates completion of a reaction within 10 min. Since background carbon levels have not been subtracted from the raw data, the baseline in Fig. 4 is $\sim$ 10–20 $\mu g\ h^{-1}$ per cm^3 of fuel. Third, within the noise of the data, the deposition rates peak in the vicinity of 4–6 min.

The equilibrium level of dissolved oxygen is dependent upon the partial pressure of oxygen during sparging; hence, sparging the fuel with pure oxygen as opposed to air will produce about five times more dissolved oxygen. The deposi-

Downloaded 02 Jun 2010 to 171.66.16.102. Redistribution subject to ASME license or copyright; see http://www.asme.org/terms/Terms_Use.cfm

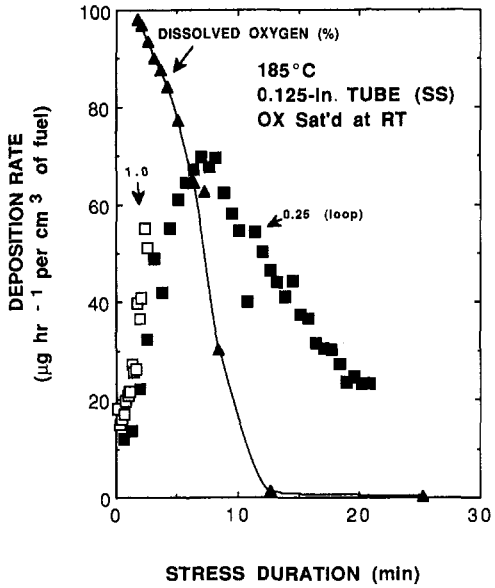

Fig. 5 Deposition from room-temperature oxygen-saturated Jet A (SHELL) fuel at 185°C, 350 psi in 0.125-in. stainless-steel tubing as function of stress duration. Superimposed is dissolved oxygen (percent of oxygen-saturated level at room temperature) as function of stress duration.

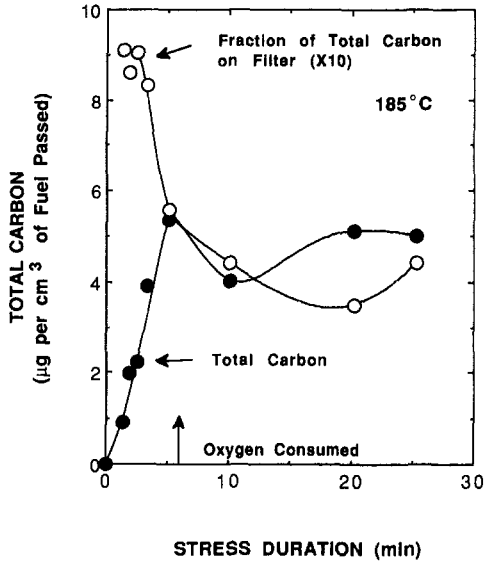

Fig. 6 Total carbon in surface deposits and bulk insolubles formed as function of stress duration. Superimposed is that fraction of total carbon measured on filter.

tion shown in Fig. 5 was obtained under the same conditions as those in Fig. 4; however, the plots in Fig. 5 were made with fuel saturated with respect to oxygen at room temperature. As noted above, the deposition rate increases from baseline, passes through a maximum, and slowly drops, approaching baseline. The data collected at a flow rate of 0.25 cm^3 min^{-1} were obtained in two complete heat-exchanger passes, i.e., 64 in. of stainless-steel tubing. The effects of additional oxygen are not manifested in significantly higher deposition rates but in a broadened deposition profile. The maximum shifts to ~ 7–8 min, and the total deposition remains incomplete after 21 min. Clearly, the total amount of deposit has increased. The quantification of the total surface deposit and the filter deposit will be discussed in the following section.

Mass Balance. Figure 4 shows that plotting the deposition rate as a function of stress duration brings the deposition peaks into near coincidence. It is not clear whether the small apparent differences in peak location are significant or whether the profiles are the same within experimental uncertainty. However, it should be obvious that when the flow rate is such that the stress duration is < 8 min, not all of the precursors to deposition will have a chance to deposit by diffusion to the walls. In other words, many deposition precursors will pass through the tube and be trapped on the filter, provided they can be stopped either by adsorption or filtration. In Fig. 6, the *total* amount of deposit evaluated by integrating all the surface-deposited carbon and adding the filtered carbon is plotted as a function of stress duration.

Note that the total carbon produced from 1 cm^3 of fuel increases with stress duration for ~ 5 min and remains nearly constant for the next 20 min. These data clearly show that there is a maximum amount of carbonaceous material that can be made in one cubic centimeter of fuel at 185°C. This value is ~ 5 $\mu g\ cm^{-3}$ for air-saturated fuel. If the data from Fig. 5 are used, with fuel saturated with respect to pure oxygen, the total is 25.1 $\mu g\ cm^{-3}$ or five times more than that for the air-saturated fuel. This factor represents the difference in the total amount of oxygen available for reaction and points to the crux of the observed deposition, namely, the quantity of dissolved oxygen.

Also plotted in Fig. 6 is the fraction of the total material present in the filter. As discussed above, for slow flows where the total deposition can be completed within the heat exchanger, the filtered bulk fraction is minimal (~ 40 percent of the total). At high flows where the deposition cannot be completed within the heat exchanger owing to its limited length, the deposition precursors are captured preferentially by the filter, and the fraction approaches 100 percent for the shortest stress duration or fastest flow. In summary, the total amount of carbonaceous material is being partitioned between the tube surface and the in-line filter.

It is important to note that some fraction of the bulk particles will not adhere to the tube walls. These are *IS* and *IG* formed in the bulk stressed fuel that are distinct from the deposition precursors. From Fig. 6 one can estimate that of the *total* 5 μg of carbon collected from each cubic centimeter of fuel, 40 percent, i.e., 2 μg, is obtained even when the maximum amount of deposition has occurred. These nondepositing bulk particles, as mentioned earlier, are present ~ 50 percent as *IS* and ~ 50 percent as *IG*. The remaining 3 μg of carbon is associated with deposition precursors and, after 10 min of stressing, will be deposited on the inner tube walls or, with shorter stress time, in part on the filter. Such precursors, when present on the filter, are acetone soluble, i.e., *IG*. In summary, at 185°C, given sufficient stressing (~ 5 min), one cubic centimeter of the Jet A (SHELL) fuel will produce 1 μg of nondepositing *IG*, 3 μg of deposition precursor in the form of *IG*, and 1 μg of a nondepositing *IS*. Stressing up to 25 min fails to produce additional insolubles because the insoluble-forming reactions are complete.

Despite the fact that the deposition precursor collected in the bulk is an *IG*, the deposit is subjected to up to 6 h of further heating after deposition occurs. As a result, surface deposits cure to become primarily *IS*.

Buoyancy/Gravity. The single-pass heat exchanger used to obtain the data in Figs. 4 and 5 was operated in a horizontal configuration. Concerns arise about the possible role of buoyancy or, more seriously, gravity in the observed deposition. The low flow rates and the near-equilibrium conditions would tend to reduce the significance of buoyancy; however, gravitational effects must be addressed. In some of the previous studies in this laboratory with flasks operated in

Downloaded 02 Jun 2010 to 171.66.16.102. Redistribution subject to ASME license or copyright; see http://www.asme.org/terms/Terms_Use.cfm

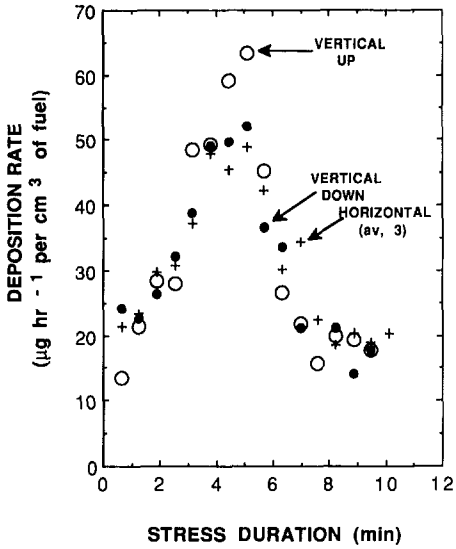

Fig. 7 Deposition measured using horizontal or vertical configuration of heat exchanger: buoyancy/gravity check. Flow 0.25 cm^3 min^{-1}.

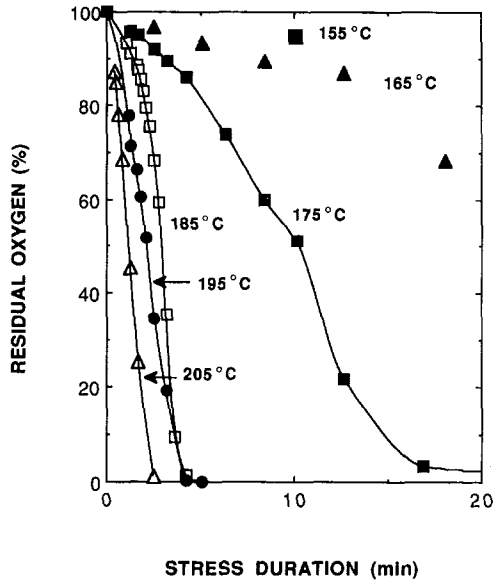

Fig. 8 Residual dissolved oxygen in Jet A (SHELL) fuel as function of fuel stress duration (100 percent corresponds to air saturation at room temperature)

a static mode, it was concluded that surface deposition follows pseudo-zeroth-order kinetics and that bulk insolubles (which are most influenced by gravity) do not contribute to surface deposition (Jones et al., 1992). In order to compare deposition on tubes with and without gravitational effects along the tube, the deposition was studied both horizontally and vertically. Also, deposition was studied for fuel passing upward and downward through the heat exchanger in the vertical configuration. The results, shown in Fig. 7, clearly demonstrate that under the current test conditions (namely, 185°C, slow flow, and 0.125-in. tubes), buoyancy/gravitational effects are negligible.

Oxygen Depletion and Arrhenius Parameters. The oxygen depletion measured in a separate experiment but under the same deposition conditions is also plotted in Figs. 4 and 5. The very close coupling between oxygen loss and surface deposition is obvious. In contrast, in a hydrotreated fuel where the dissolved oxygen is removed at faster rates, concomitant deposition at 185°C is not observed. Based upon the stress duration required for deposition and that required for oxygen depletion, the precursor to deposition must be an early and primary autoxidation product. This further explains the existence of a maximum in the deposition rate. Once the oxygen has been totally consumed, the deposition precursor soon forms and subsequently diffuses to the wall.

The importance of oxygen in determining the total amount of bulk or surface deposits is readily apparent in Fig. 6 where the total amount of bulk and surface deposits increases until the oxygen is totally consumed (~ 4 min) and then remains constant for up to 20 min of additional heat stressing. The close coupling of both surface deposits and bulk particles to the availability of oxygen is pronounced.

It is apparent from the oxygen loss depicted in Figs. 4 and 5 that the rate of oxygen consumption increases as the oxygen is consumed. This sigmoid behavior is well known in the autoxidation of hydrocarbons, particularly in the absence of an initiator, and it arises from autocatalysis (cf. appendix). It is beyond the scope of the current paper to address this area; however, hydroperoxides, ROOH, are a primary autoxidation product and when they are formed in abundance, the biomolecular reaction R(1) can occur

$$2\text{ROOH} \rightarrow \text{ROO}^{\bullet} + \text{RO}^{\bullet} + \text{H}_2\text{O} \qquad \text{R(1)}$$

This provides a lower energy free-radical initiation route, thereby increasing the overall oxygen consumption with ROOH production. Walling (1957) has discussed this area in detail.

The depletion of oxygen has also been monitored at 205, 195, 175, 165, and 155°C. A representation of most of the data is shown in Fig. 8. Because of the strong dependence of rate upon temperature, not all of the data can be visualized in a single plot. Significantly at temperatures such as 205 and 195°C where autocatalysis is less pronounced, it is clear from the linear oxygen loss that the reaction kinetics are zeroth order down to at least 20 percent residual oxygen and possibly lower. Recent data obtained using the Jet A (SHELL) fuel with an additive package have indicated that zeroth order describes the reaction down to < 10 percent residual oxygen (Jones and Balster, 1993). Under the experimental test conditions, results indicate reaction in an oxygen nonlimited regime. Clearly, at lower oxygen concentration the reactions must convert to oxygen-limited behavior when insufficient oxygen molecules are present to react with all the hydrocarbon free radicals. Reactions in flowing rigs with fuel saturated with respect to air are best described by oxygen nonlimited kinetics (i.e., zeroth order in oxygen). This explains the anomaly in Figs. 4 and 5 where five times more oxygen does not produce a significant increase in the deposition rate. It does produce five times more insolubles but much more time is required.

Assuming that the oxygen loss obeys Arrhenius kinetics, i.e., $k = A\exp(-E/RT)$, a plot of $\ln k$ versus $10^3/T$ has a slope E/R an an intercept A. The Arrhenius plot for the rate data is given in Fig. 9 over a 50-deg temperature range. It should be noted that experimental difficulties preclude extending this range significantly. At higher temperatures, oxygen consumption is so rapid that faster flows are needed, and these introduce large errors due to the time required to reach isothermal conditions. At low temperatures, relatively long times are required to establish equilibrium, and signal drift in the oxygen analyzer becomes significant.

The Arrhenius parameters best fitting the data are E = 35.8 kcal $mole^{-1}$ and $A = 2.2 \times 10^{11}$ mole $liter^{-1}$ s^{-1}. The units of A are consistent with zeroth-order oxygen loss. Heneghan et al. (1993) have reported Arrhenius parameters

Downloaded 02 Jun 2010 to 171.66.16.102. Redistribution subject to ASME license or copyright; see http://www.asme.org/terms/Terms_Use.cfm

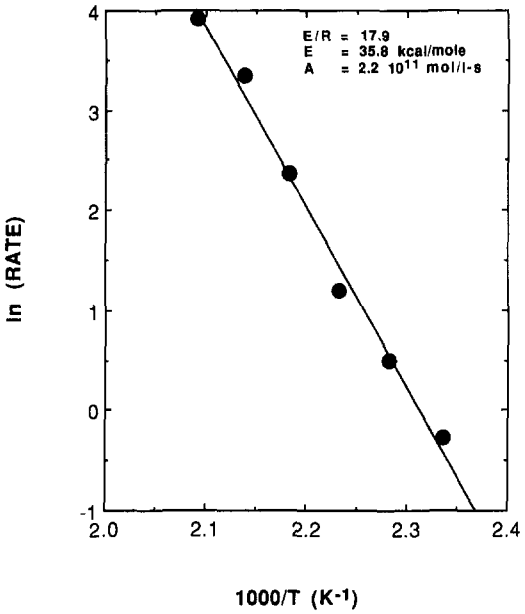

Fig. 9 Arrhenius plot for Jet A (SHELL) fuel over temperature range 155–205°C (units of rate are percent air saturation at room temperature per min)

for this fuel, which are calculated from deconvoluting oxygen loss over a broad temperature range, assuming first-order loss of oxygen. Despite the order difference, the activation energies are remarkably similar (compare 35.5 kcal mole^{-1}). The pre-exponential factors cannot be compared due to the order difference.

Conclusions

The thermo-oxidative behavior of a commercial Jet A fuel has been studied isothermally as a function of stress time at 185°C by monitoring the dissolved oxygen, the time-dependent surface deposition, and the total amount of bulk insolubles. All conclusions are based upon isothermal low-flow conditions that, by experimental design, are not representative of engine conditions. Turbulence under high-flow conditions tends to sweep deposition precursors and other insolubles downstream; these effects can be addressed only by global modeling. Modeling studies with the methods of Katta and Roquemore (1992) are currently under way using the fundamental chemical results reported herein. The following conclusions are drawn:

- All oxygen is consumed in 4 and 12 min, for room-temperature air- and oxygen-saturated fuel, respectively.
- Oxygen loss is characterized by zeroth-order kinetics, with autocatalysis occurring as oxygen is consumed. From 155 to 205°C the initial rate of oxygen loss is accurately described by the Arrhenius rate expression, with $A = 2.2 \times 10^{-11}$ mole liter^{-1} s^{-1} and $E = 35.8$ kcal mole^{-1}.
- Air-saturated fuel reacts in an oxygen nonlimited regime.
- As oxygen is depleted, deposition on the inner wall of the fuel lines increases, passes through a maximum, and then decreases to baseline, indicating the formation and consumption of a deposition precursor. In general, the occurrence of a maximum in deposition rate along a heated tube is ascribed to oxygen depletion.
- Deposition profiles are brought into near coincidence by plotting deposition rate as a function of stress duration.
- When one cubic centimeter of air-saturated fuel is stressed more than 5 min, insoluble products contain ~ 5 μg of carbon; 1 μg is ascribed to both *IS* and *IG*, which do not adhere to the tube, and 3 μg is assigned to a deposition precursor existing as an *IG*.
- The total quantity of insolubles is proportional to the dissolved oxygen.
- Low flow rates tend to focus the fouling problem near the heat source; high flow rates tend to sweep the deposition precursors and other bulk particles downstream and effectively change the location of the fouling problem.
- The close coupling between oxygen consumption and the observation of deposits is ascribed to the presence of deleterious sulfur compounds. For example, although a hydrotreated Jet A-1 fuel with diminished sulfur content reacts about three times faster than the Jet A (SHELL), it does not display significant deposition concurrent with oxygen consumption.

Acknowledgments

This work was supported by and performed at Wright Laboratory, Aero Propulsion and Power Directorate, Wright-Patterson Air Force Base, OH, under USAF Contract No. F33615-90-C-2033. The authors would like to thank Mr. Tim Gootee for performing the surface carbon analyses. The authors acknowledge valuable discussions with T. F. Williams and C. R. Martel concerning the heat-exchanger construction and with W. A. Rubey concerning oxygen analysis.

References

Chin, J. S., Lefebvre, A. H., and Sun, F. T.-Y., 1992, "Temperature Effects of Fuel Thermal Stability," ASME JOURNAL OF ENGINEERING FOR GAS TURBINES AND POWER, Vol. 114, pp. 353–358.

Chin, J. S., and Lefebvre, A. H., 1993, "Influence of Flow Conditions on Deposits From Heated Hydrocarbon Fuels," ASME JOURNAL OF ENGINEERING FOR GAS TURBINES AND POWER, Vol. 115, pp. 433–438.

Giovanetti, A. J., and Szetela, E. J., 1986, "Long Term Deposit Formation in Aviation Turbine Fuel at Elevated Temperature," AIAA Paper No. 86-0525.

Heneghan, S. P., Martel, C. R., Williams, T. F., and Ballal, D. R., 1993, "Studies of Jet Fuel Thermal Stability in a Flowing System," ASME JOURNAL OF ENGINEERING FOR GAS TURBINES AND POWER, Vol. 115, pp. 480–485.

Jones, E. G., Balster, W. J., and Anderson, S. D., 1992, "Formation of Insolubles in Jet Fuels: Effects of Oxygen," *Preprints Symposia—Structure of Jet Fuels III*, Division of Petroleum Chemistry, Inc., American Chemical Society, Washington, DC, Vol. 37, No. 2, pp. 393–402.

Jones, E. G., and Balster, W. J., 1993, to be published.

Katta, V. R., and Roquemore, W. M., 1992, "A Numerical Method for Simulating the Fluid-Dynamic and Heat-Transfer Changes in a Jet-Engine Feed Arm Due to Fouling," AIAA Paper No. 92-0768.

Katta, V. R., 1992, private communication.

Kendall, D. R., and Mills, J. S., 1986, "Thermal Stability of Aviation Kerosines: Techniques to Characterize Their Oxidation Properties," *I & EC Product Research and Development*, Vol. 25, pp. 360–366.

Kendall, D. R., Houlbrook, G., Clark, R. H., Bullock, S. P., and Lewis, C., 1987, "The Thermal Degradation of Aviation Fuels in Jet Engine Feed-Arms: Part 1—Results From a Full-Scale Rig," 30th International Gas Turbine Congress, Tokyo, Japan, Oct. 26–31.

Marteney, P. J., and Spadaccini, L. L., 1986, "Thermal Decomposition of Aircraft Fuels," ASME JOURNAL OF ENGINEERING FOR GAS TURBINES AND POWER, Vol. 108, pp. 648–653.

Rubey, W. A., Tissandier, M. D., Striebich, R. C., and Tirey, D. A., 1992, "In Line Gas Chromatographic Measure of Trace Oxygen and Other Dissolved Gases in Flowing, High-Pressure, Thermally Stressed Fuel," *Preprints Symposia—Structure of Jet Fuels III*, Division of Petroleum Chemistry, Inc., American Chemical Society, Washington, DC, Vol. 37, No. 2, pp. 371–376.

Walling, C., 1957, *Free Radicals in Solution*, Wiley, New York.

APPENDIX

Autoxidation

Initiated with trace amount of hydroperoxide (ROOH)

$$ROOH \rightarrow RO^{\bullet} + HO^{\bullet} \text{ (thermal)}$$

Downloaded 02 Jun 2010 to 171.66.16.102. Redistribution subject to ASME license or copyright; see http://www.asme.org/terms/Terms_Use.cfm

Initiated with large amounts of hydroperoxide

$$2ROOH \rightarrow ROO^{\bullet} + RO^{\bullet} + H_2O \text{ (autocatalysis)}$$

Propagation $RO^{\bullet} + RH \rightarrow ROH + R^{\bullet}$

$$HO^{\bullet} + RH \rightarrow H_2O + R^{\bullet}$$

$$R^{\bullet} + O_2 \rightarrow ROO^{\bullet}$$

$$ROO^{\bullet} + RH \xrightarrow{k_t} ROOH + R^{\bullet}$$

Termination $2ROO^{\bullet} \xrightarrow{k_t}$ nonradicals

Assuming steady state in $R^{\bullet}$ and $ROO^{\bullet}$, it can be shown that given sufficient dissolved oxygen,

$$-\frac{d[O_2]}{dt} = \frac{d[ROOH]}{dt} = k_p[RH]\left(\frac{R_i}{2k_t}\right)^{1/2}$$

where R_i is the rate of initiation.

Sulfur-containing fuel components react with $ROO^{\bullet}$, deplete the peroxy-radical concentration, and reduce the rate of oxygen consumption.

Downloaded 02 Jun 2010 to 171.66.16.102. Redistribution subject to ASME license or copyright; see http://www.asme.org/terms/Terms_Use.cfm

Comparison of Coriolis and Turbine-Type Flowmeters for Fuel Measurement in Gas Turbine Testing

J. D. MacLeod

W. Grabe

National Research Council,
Ottawa, Ontario, Canada

The Machinery and Engine Technology (MET) Program of the National Research Council of Canada (NRCC) has established a program for the evaluation of sensors to measure gas turbine engine performance accurately. The precise measurement of fuel flow is an essential part of steady-state gas turbine performance assessment. Prompted by an international engine testing and information exchange program, and a mandate to improve all aspects of gas turbine performance evaluation, the MET Laboratory has critically examined two types of fuel flowmeters, Coriolis and turbine. The two flowmeter types are different in that the Coriolis flowmeter measures mass flow directly, while the turbine flowmeter measures volumetric flow, which must be converted to mass flow for conventional performance analysis. The direct measurement of mass flow, using a Coriolis flowmeter, has many advantages in field testing of gas turbines, because it reduces the risk of errors resulting from the conversion process. Turbine flowmeters, on the other hand, have been regarded as an industry standard because they are compact, rugged, reliable, and relatively inexpensive. This paper describes the project objectives, the experimental installation, and the results of the comparison of the Coriolis and turbine-type flowmeters in steady-state performance testing. Discussed are variations between the two types of flowmeters due to fuel characteristics, fuel handling equipment, acoustic and vibration interference, and installation effects. Also included in this paper are estimations of measurement uncertainties for both types of flowmeter. Results indicate that the agreement between Coriolis and turbine-type flowmeters is good over the entire steady-state operating range of a typical gas turbine engine. In some cases the repeatability of the Coriolis flowmeter is better than the manufacturer's specification. Even a significant variation in fuel density (10 percent), and viscosity (300 percent) did not appear to compromise the ability of the Coriolis flowmeter to match the performance of the turbine flowmeter.

Introduction

In the accurate assessment of gas turbine performance, the establishment of correct fuel flow is important. Fuel flow is considered as a performance parameter on its own merits, but it also appears in the much specific fuel consumption function. Thus the measurement of fuel flow is critical to the certification of new engines and the acceptance testing of overhauled ones.

Largely prompted by the NRC's participation in the AGARD-sponsored Uniform Engine Testing Program, an examination of the measurement of fuel flow was initiated, with the purpose of improving accuracy and evaluating new methods of flow establishment. Although fuel flow, in aviation gas turbine testing, is evaluated in the form of mass flow, most measurements are being carried out using volume flowmeters, predominantly of the turbine type (Grabe, 1988). Traditionally, NRC had been using turbine-type flowmeters to measure fuel flow volumetrically, with appropriate conversion factors to calculate mass flow. Recently, interest in the direct measurement of mass flow, using Coriolis-type flowmeters, has emerged from field testing of gas turbines, in a steady-state mode, where access to correct volume-mass conversion is not always available.

The Coriolis-type flowmeters have been used for several years in the process industries to measure and control production of fluids and fluid/solid mixtures. The emphasis in this role was the necessity of a simple, reliable, and robust instrument to measure flow rate independently of temperature, density, or viscosity.

The use of Coriolis flowmeters to measure fuel flow rate in gas turbine testing is relatively recent. The advantages are

Contributed by the International Gas Turbine Institute and presented at the 38th International Gas Turbine and Aeroengine Congress and Exposition, Cincinnati, Ohio, May 24-27, 1993. Manuscript received at ASME Headquarters February 18, 1993. Paper No. 93-GT-70. Associate Technical Editor: H. Lukas.

Copyright © 1995 by ASME

Downloaded 02 Jun 2010 to 171.66.16.102. Redistribution subject to ASME license or copyright; see http://www.asme.org/terms/Terms_Use.cfm

obvious: direct measurement of mass flow of fuel, simplicity, and low maintenance. The disadvantages include possibly higher pressure losses (depending on internal tube configuration) and high intitial costs (Furness, 1991).

A limited comparison of the performance of turbine flowmeters and a Coriolis-type flowmeter was undertaken by NRC to get a better understanding of both types of flow measurement device. All tests were confined to steady-state operation.

Project Objectives

The objectives of this flowmeter comparison project were:

(*a*) to assess the strengths and weaknesses of both turbine and Coriolis flowmeters,
(*b*) to evaluate the Coriolis flowmeter as to its suitability for use in gas turbine testing under steady-state laboratory conditions,
(*c*) to comment on the suitability of the Coriolis flowmeter under field testing conditions,
(*d*) to verify accuracy claims of the Coriolis flowmeter,
(*e*) to examine the calibration methodology for a mass flowmeter.

Fuel Flow Measurement

Before comparing the performance of turbine and Coriolis-type flowmeters, it is important to understand fully the principles under which each device operates. The limitations and strengths of each flowmeter type obviously have a strong bearing on the usefulness and accuracy of the test results obtainable in both laboratory and field testing conditions. Included in this segment of this paper are brief descriptions of the operating principles of both types of flowmeters.

Turbine Flowmeters. The turbine flowmeter, as a measuring device for liquid and gaseous flow, has been in use for a considerable time, and, hence, its principles are generally well known among users. In brief, fluid flow is directed through a metering body with a finely machined cylindrical duct, in which a turbine rotor is placed, in line with the flow. Disregarding small effects, the turbine rotates in direct proportion to the velocity of the fluid flow through the meter. A magnetic or modulated carrier pickup detects the passage of each rotor blade tip and generates a pulse. Because of geometric peculiarities and fluid effects, each flowmeter must be calibrated for accurate flow measurement. This is done by correlating the pickup pulses with either known volumes of flow passing by the turbine rotor or with known liquid mass flows passing through the meter and being collected and weighed subsequently. An in-depth treatment of turbine flowmeter systems has been given by Zimmerman and Deery (1977).

Since the turbine flowmeter is a volume flow measuring apparatus, whereas fuel mass flows are rather needed in gas turbine testing, conversion from volume to mass is required. To do so, certain fluid properties must be established, and their accuracies are directly reflected in the final accuracy of the mass flow. The equation for fuel mass flow may take the form:

$$W_f = \frac{\text{FREQ} * 3.7816730 * RD_{T_f}}{C_T * K} \tag{1}$$

where:

W_f = observed fuel flow, kg/s
FREQ = flowmeter frequency, pulses/s, Hertz
3.7816730 = volume–mass conversion factor
RD_{Tf} = relative density (specific gravity) at fuel temperature
C_T = flowmeter thermal correction factor
K = flowmeter calibration factor, pulses/US gallon

A similar expression can be written for flow units of lb_m/h. Details of the flow equation derivation can be found in a report by Grabe (1988). It should be noted that the K factor has the basic form "pulses per unit volume"; the unit "US gallon" has been carried over, in this instance, from the original one of the ballistic flow calibrator, in use at the National Research Council in Ottawa.

To facilitate data comparison between different test and fuel conditions, it is customary to reduce observed flow data to standard values:

$$W_{f_{\text{cor}}} = \frac{W_f}{\delta\sqrt{\theta}} * \frac{NHC}{NHCR} \tag{2}$$

where:

W_{fcor} = fuel flow corrected to standard conditions, kg/h or lb_m/h
W_f = fuel flow at test conditions, kg/h or lb_m/h
δ = (engine inlet total pressure)/(standard day barometric pressure)
θ = (engine inlet total temperature)/(standard day temperature)
NHC = net heat of combustion, MJ/kg or BTU/lb_m
NHCR = reference net heat of combustion, MJ/kg or BTU/lb_m

The first part of the correction term yields a fuel mass flow corrected to standard day conditions, while the second part allows for variances in energy content in a certain fuel batch. In engine performance establishment, it is the energy input for a given thrust or power output that, ultimately, is of consequence.

Coriolis Flowmeters. A Coriolis mass flowmeter measures mass flow directly, using the Coriolis principle, which is based on the conservation of angular momentum, as it applies to the Coriolis acceleration of a given fluid. In principle, a Coriolis mass flowmeter consists of a tube with a fixed inlet and outlet, which is vibrated sinusoidally from the axis formed by the inlet and outlet ends. The tube may be either straight or omega shaped, and is vibrated using a drive coil attached at the axis. Electromagnetic sensors are mounted upstream and downstream of the drive coil to measure velocity signals from the vibrating tube. This means that liquid flow is measured by transferring vibrational energy from the meter tubing to the flowing liquid and back to the meter. To appreciate this principle, imagine a vibrating tube as shown in Fig. 1. If no liquid is flowing, the drive coil in the middle of the tube will cause both arms to vibrate in phase. Mass flowing into the tube starts to receive vibrational energy from the tube walls as it enters the first bend (Fig. 2). In this process, the tube loses the same amount of energy. The result is that the phase of the vibrational cycle lags at the upstream sensor location; the reverse will happen at the downstream location. The liquid is vibrating as it enters the bend, but transfers this energy to the pipe. The result is that the mass flow advances the vibrational phase at the downstream sensor location. When combined, these two changes in vibrational phase produce a twisting of the flow tube as shown in Fig. 3. The amplitude of this twist is directly proportional to the mass flow rate and is nearly independent of the temperature, density, or viscosity of the liquid involved.

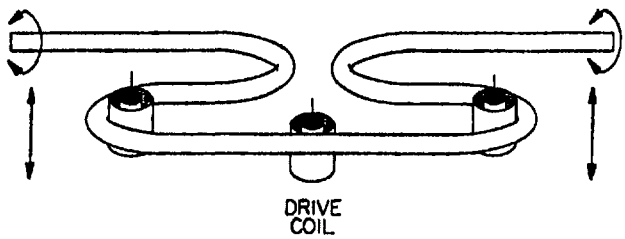

Fig. 1 Coriolis flowmeter configuration

Downloaded 02 Jun 2010 to 171.66.16.102. Redistribution subject to ASME license or copyright; see http://www.asme.org/terms/Terms_Use.cfm

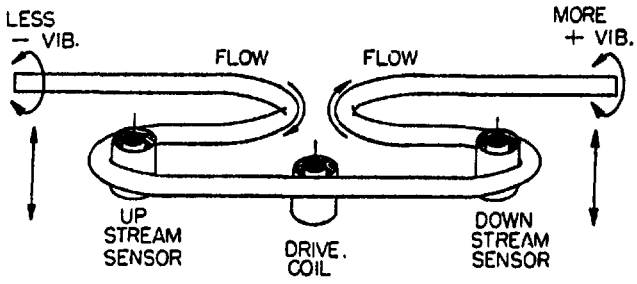

Fig. 2 Coriolis flowmeter: principles of operation

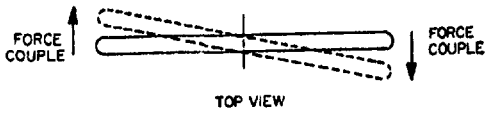

Fig. 3 Coriolis flowmeter: force couple generation

In practical application, a Coriolis mass flowmeter may contain two parallel tubes, but the principle outlined remains unchanged.

To compare the turbine and Coriolis flowmeters, the Coriolis meter was installed in series with two turbine meters in the fuel delivery system of a gas turbine engine. The evaluation procedures included observations of the installation and operation of the meters in general, and more specifically, a comparison of the flow measurements between the average of two turbine meters, and the Coriolis meter.

Installation Criteria. The test setup was designed to evaluate the flowmeters under various conditions to establish the effects of the following criteria:

(*a*) installation,
(*b*) fuel temperature,
(*c*) relative density (specific gravity),
(*d*) viscosity,
(*e*) noise and vibration, and
(*f*) flow range.

While most of the effects of these criteria on turbine meters are well documented (Grabe, 1988), the effects on the Coriolis meter are not.

To establish any installation effects on the Coriolis meter, the meter was installed in several configurations: fixed mounting, and flexible mounting. To analyze fuel temperature effects, tests were performed on different days with different inlet fuel temperatures.

For the investigation of relative density and viscosity effects, two fuel types were used, one 10 percent denser, and with 300 percent higher viscosity than the other. Noise and vibration effects were investigated by placing the Coriolis meter in close proximity to an afterburning turbofan engine producing noise levels up to 173 dB. Finally, the Coriolis meter was tested over a low and a high flow range using two different gas turbine engines. For low flow range testing (800–2400 lbm/hr) an Allison T56 turboprop engine was used, while for the high flow range (500–9000 lbm/hr), the flowmeter was measuring the core flow of a General Electric F404 afterburning turbofan engine.

Instrumentation Description. The fuel flow measurement system used for this study consisted of two turbine flowmeters, in series with a 1/2-in.-dia Coriolis mass flowmeter. For low flow range testing, two 1/2-in.-dia turbine meters were used, while for high flow range testing, one 3/4-in. and a 1-in. turbine meter were installed.

Data from the meters were recorded using a NEFF 620 data acquisition system controlled by a DEC Microvax II computer. For each installation, the gas turbine engine was operated over its entire power range. At various power settings, a five minute stabilization period was observed before two three-minute steady-state data scans were initiated. Typically, up to six power settings (12 data points) were recorded for each test.

A ballistic flow calibrator was used to assess the accuracy and calibration of the turbine flowmeters. A brief description of the calibrator and its principle is included.

Omnitrak Flow Calibrator. The Institute for Mechanical Engineering, National Research Council, is the custodian of an Omnitrak ballistic flow calibrator, Model OT-150, by Flow Technology, Inc. It calibrates a turbine flowmeter by correlating the pulses generated by its pick-off with a precise volume of fluid.

The Omnitrak ballistic calibrator incorporates a piston, which travels inside a honed cylinder, pushing the calibration fluid along its path, and farther downstream, through the flowmeter to be calibrated. A piston rod is connected to the piston, carrying a photoelectric sensor. The sensor, or encoder, slides over a finely etched glass rule, generating pulses from the etched markings. These pulses have been, through previous calibration, correlated with a specific volume; hence, a precise calibration volume can be determined from the encoder pulses. This correlation between encoder pulses and volume forms the basis of the calibration constant of the calibrator, also referred to as the K factor of the calibrator. As an indication of the fine resolution of the calibrator calibration, some 62,000 markings on the glass rule represent one US gallon.

A calibrator K factor for the flowmeter is being calculated from primary data through the relationship:

$$K = \frac{\text{No. FMP} * T\ \text{VOL}}{T\ \text{FMP} * \text{VOL}} \tag{3}$$

where:

K = calibration factor of the flowmeter, pulses/US gallon (or any other specified unit volume)
No. FMP = number of flowmeter pulses collected, pulses
T VOL = time required for the test volume to be displaced, s
T FMP = time required for collecting the flowmeter pulses, s
VOL = volume of fluid displaced, US gallon or fraction thereof (or any other specified unit volume)

A detailed description of the Omnitrak calibrator can be found in the manufacturer's manual (FTI, 1982).

Since the calibration factor of the flowmeter is derived from the calibration constant of the calibrator, which is based on reference conditions, the K factor must be corrected to the actual conditions, i.e., temperatures and pressures, prevailing at the time of calibration (Grabe, 1991).

Test Results

Before a comparison between the turbine and Coriolis flowmeters could be made, it was necessary to establish the repeatability of the two turbine meters used as the reference for the low flow range and high flow range testing. Previous work (MacLeod and Orbanski, 1992) determined that the agreement between the two 1/2-in. turbine flowmeters used with the Allison T56 engine was ±0.16 percent. For the higher flow range, the agreement between the 3/4-in. and 1-in. turbine flowmeters of the General Electric F404 testing was ±0.2 percent, as shown in Fig. 4.

Low Flow Range Testing. To evaluate the Coriolis mass flowmeter in the lower flow regime, the device was installed in series with existing turbine meters in the fuel delivery system of an Allison T56 turboshaft engine. The Coriolis mass flowmeter was installed in three different configurations. In the first one, the flow sensor was placed in the fuel line, halfway

Downloaded 02 Jun 2010 to 171.66.16.102. Redistribution subject to ASME license or copyright; see http://www.asme.org/terms/Terms_Use.cfm

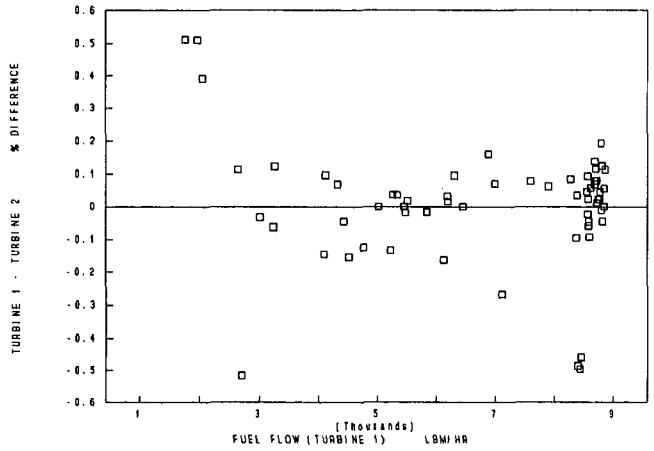

Fig. 4 Turbine flowmeter repeatability

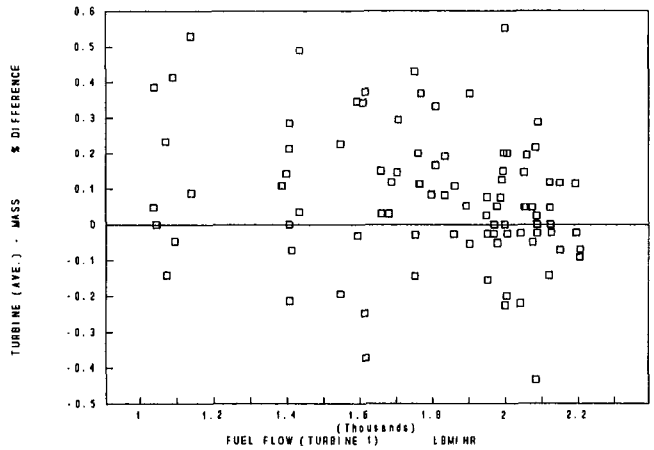

Fig. 5 Low flow range comparison

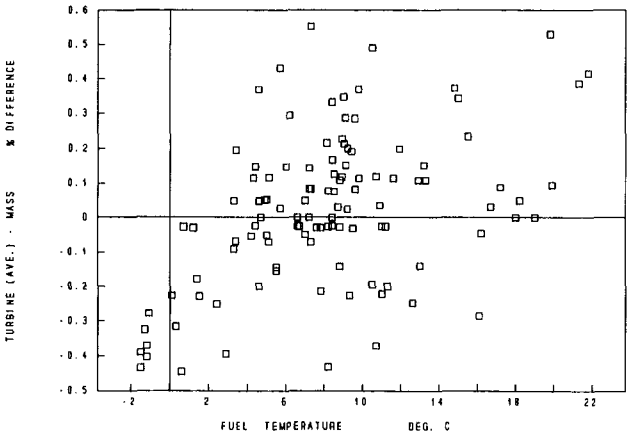

Fig. 6 Low flow range temperature effects

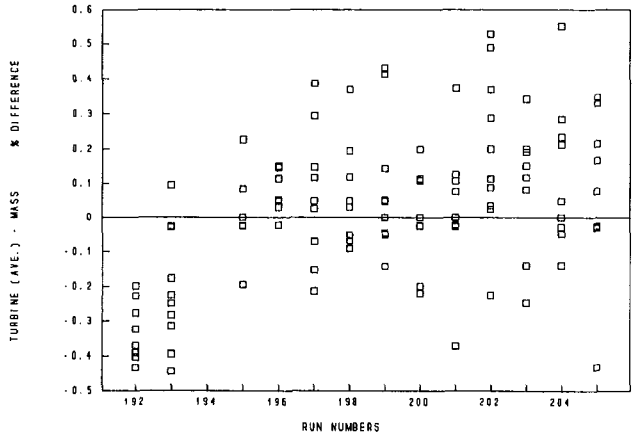

Fig. 7 Low flow range installation effects

between the engine fuel control and the facility turbine meters. Two lengths of approximately 2 m of flexible fuel line connected the Coriolis flow sensor to the engine and the turbine meters upstream. The flexible hoses were attached directly to the flanges of the sensor unit. For the second setup, the sensor was moved to a position 1 m upstream of the turbine meters. In both configurations, the sensor was placed on a foam pad sitting on the concrete floor. For the final configuration, the Coriolis flow sensor was rigidly bolted to the floor as described in the installation manual (Schlumberger, 1991).

A total of 14 steady-state test runs were performed with the Coriolis mass flowmeter installed in the fuel system. As shown in Fig. 5, the comparison between the turbine and Coriolis flowmeter is quite good, with 95 percent of the data falling within the ± 0.3 percent scatter band, over the tested flow range. The fuel temperature did not appear to have any influence on the test results as indicated in Fig. 6. This includes testing done with two different fuel types. The first fuel had a relative density of 0.763 and a viscosity of 1.194 centistokes at 15.56°C, while the second fuel had a relative density of 0.839 and a viscosity of 4.112 centistokes. As far as installation effects are concerned, there was no apparent correlation between the three configurations and the variation between the turbine and Coriolis meters, as can be seen from the plot against run numbers in Fig. 7. Configuration two was an attempt to see if the pressure fluctuations at the fuel control inlet were propagating upstream and affecting the Coriolis sensor. This was found not to be the case. The sensor, placed less than 2 m from the engine, did not experience any fluctuations as a result of noise, vibration, or electrical interference. Noise levels near the sensor were approximately 125 dBA.

High Flow Range Testing. To evaluate the Coriolis mass flowmeter in the higher flow regime, the device was placed in series with existing turbine meters in the fuel delivery system of a General Electric F404 afterburning turbofan engine. The Coriolis mass flowmeter was installed in two different configurations. In the first, the flow sensor was placed in the fuel line, halfway between the engine fuel control and the facility turbine meters, sitting loosely on the floor. Approximately 2 m of flexible fuel line were between the engine and the Coriolis flow sensor and between the sensor and the turbine meters upstream. For the second setup, the sensor was rigidly bolted to the floor as described in the installation manual (Schlumberger, 1991).

Six steady-state test runs were performed with the Coriolis mass flowmeter installed in the F404 fuel system. In Fig. 8, the comparison between the turbine and Coriolis flowmeter indicates a divergence between the two fuel meter types of up to 1.2 percent, over the tested flow range. In every test, the Coriolis meter always read a higher value than the average of the two turbine meters.

To isolate the possible causes of this divergence, the data were analyzed on a run-to-run basis. In Fig. 9, the results show an interesting trend. Run numbers 92, 95, and 96 were performed with the Coriolis meter sitting loosely on the floor, while runs 93, 94, and 97 were carried out with the meter bolted solidly to the floor. For the loose mounting tests, the data scatter is higher (0.5 to 0.7 percent), than for the solid mounting ones (0.25 to 0.35 percent). However, the solid mounting tests show a significant shift away from the averaged turbine meter values (up to 1.2 percent). It was discovered that the frequency output card used in the Coriolis flowmeter receiver was unstable, and would drift between runs. After run

Downloaded 02 Jun 2010 to 171.66.16.102. Redistribution subject to ASME license or copyright; see http://www.asme.org/terms/Terms_Use.cfm

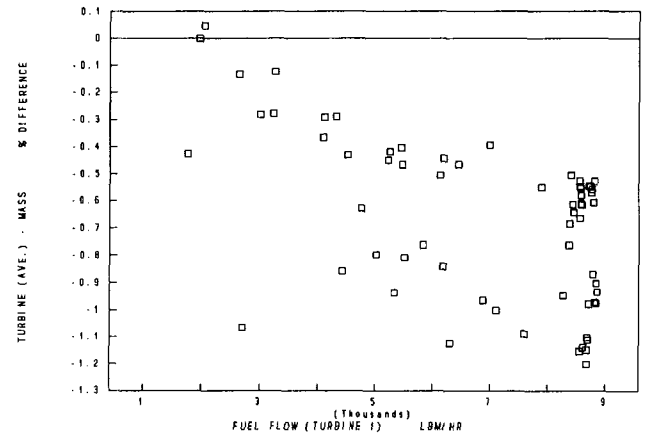

Fig. 8 High flow range comparison

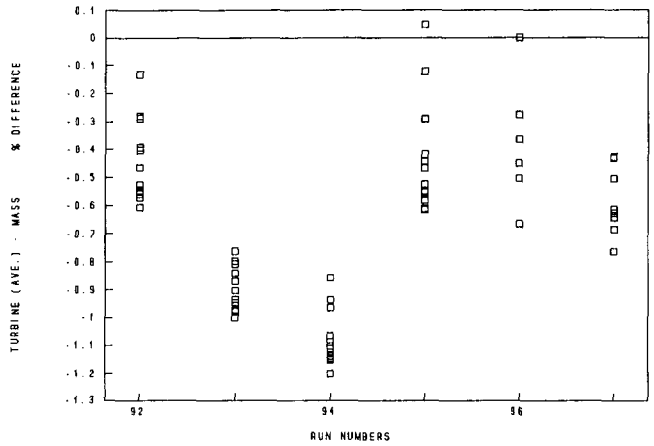

Fig. 9 High flow range installation effects

94 the frequency card was recalibrated, so that runs 95 and 96 start closer to zero. After run 97, the card was recalibrated after it was noticed that Coriolis meter readings were beginning to drift away again from the turbine meter readings. This frequency drifting is not related to the Coriolis method of flow measurement in any way; it is simply a poor quality frequency output card for the meter chosen for this test program. If undetected and uncorrected, the drifting can lead to significant measurement bias errors, and, hence, steps must be taken to prevent this problem.

Based on previous experience with Coriolis mass flowmeters (MacLeod, 1987) the sensitivity of the Coriolis flow tubes to noise and vibration is significant. In the tests discussed here, the effects of loose versus solid mounting were measurable. The divergence in the flow rate of the two meter types is speculated to be the result of airborne noise vibrating the Coriolis meter tubes. These vibrations would cause higher tube oscillations, indicating higher flow rates, as shown in Fig. 8. In addition, the deviation between the two meter types increases with flow rate, since the acoustic energy in the test cell also is increasing with engine power. Unfortunately, time constraints did not permit testing with an acoustic enclosure surrounding the Coriolis meter to verify this hypothesis.

Coriolis Meter Calibration. Any flowmeter has to be checked for its calibration, at the beginning of its service life and periodically thereafter. The calibration of turbine flowmeters is well established and documented. The calibration technique of mass flowmeters of the Coriolis type, with a ballistic calibrator, is less known, simply because these meters have only recently come into widespread use. It has been said that the accuracy of a Coriolis mass flowmeter is inherently superior to that of a ballistic calibrator, and, hence, a calibration by that apparatus would be meaningless. However, until that proposition has been proven valid, a technique has been developed at NRC by which mass flowmeters can be calibrated.

The mass flowmeter has a frequency output, in addition to a voltage one, which is proportional to the flow rate. Thus, the meter can be treated like a turbine flowmeter in a ballistic calibrator, with the output parameters being valid entities, viz. volume flow rate and K factor. The frequency, calculated in turbine flowmeter calibration, becomes now an input parameter. To obtain a mass flow calibration, however, some further steps are required. A mass flow has to be computed by the equation:

$$\dot{m} = \dot{V} \times RD \times 3.7816730 \text{ [kg/min]} \tag{4}$$

where:

m dot = mass flow at the fluid temperature, kg/min
V dot = volume flow rate through the meter, US gallon/min
RD = relative density of calibration fluid at fluid temperature
3.7816730 = volume–mass conversion, kg H_2O @15.56°C/US gallon

Knowing the mass flow rate of a calibration point, one can calculate a modified K factor for the meter in terms of "pulses per kg," instead of "pulses per US gallon" by:

$$K_m = \frac{\text{FREQ} \times 60}{\dot{m}} \text{ [pulses/kg]} \tag{5}$$

The question remains how best to evaluate the calibration. Two possibilities have been examined. One, the most logical one, has the mass flow plotted against frequency, on the basis that a direct proportionality supposedly exists between them. The other has the modified K factor, K_m, plotted against frequency. Since viscosity is said not to affect the flow measurement of a Coriolis meter, frequency does not have to be corrected for its effects. Examination of the two approaches shows that the latter one is superior in that it produces a far better resolution, and, hence, more accurate calibration evaluation. As an example, in one particular mass flowmeter calibration it was found that differences, between distinct calibration points and values obtained from curves, varied from 0.1 to 1.2 percent for the K_m approach and 0.1 to 4.5 percent for the straight mass flow one. The differences increased from high to low flows. This observation leads to the conclusion that, on account of the better resolution of its plotting scale, the calibration evaluation via the modified K factor yields more accurate results and should be preferred.

Uncertainty Analysis

Flow Measurement by Turbine Flowmeter. The uncertainty analysis of fuel flow measurement is rather complex and depends on many small contributors. An attempt has been made by Grabe (1988) to give a detailed error analysis of the whole fuel flow measuring system, which uses a turbine flowmeter. It was shown that the possible error depends, to a large degree, on the conditions under which the measurements are taken. In that analysis, two conditions were chosen: one severe, the other average. The severe condition, for example, would consider extreme fluid temperatures, low flow rates, which means a low meter frequency, and a method of relative density determination with a high reproducibility uncertainty. The average conditions were those more likely to be encountered in the field.

The contributing elements of an uncertainty analysis of observed fuel flow include such items as the turbine flowmeter frequency, the fluid relative density, the correction for flow-

Downloaded 02 Jun 2010 to 171.66.16.102. Redistribution subject to ASME license or copyright; see http://www.asme.org/terms/Terms_Use.cfm

meter thermal expansion, and the K factor; see Eq. (1). For the corrected fuel flow, inlet temperatures and pressures, as well as the fuel net heat of combustion, further add to the final uncertainty. Each of these items depends, in turn, on contributing elements of its own. For example, relative density, formerly called specific gravity, at measurement temperature, is a function of its relative density at reference temperature, the fuel temperature, and the fuel's critical temperature. The uncertainty of each of these contributors is created during measurement.

Taking all of these possible error contributions into account, it was found that, in a well-run system, where great care is taken at all steps in the chain, the following uncertainties may occur. The observed fuel flow, under average measurement conditions, could be expected to have an overall uncertainty of ± 0.4 percent. Under severe conditions, this uncertainty would nearly double to ± 0.7 percent. For corrected fuel flow, including corrections for the fuel net heat of combustion, the uncertainty would be ± 0.65 percent for average conditions and ± 1.0 percent for severe ones.

It must be borne in mind that these uncertainties are by no means guaranteed. Only if careful steps are taken along the fuel flow establishment path, can these rather tight uncertainties be achieved. Each element contributes, in some way, to the final accuracy of the fuel flow establishment. For example, if an average K factor were used for the whole flow range, instead of following the universal curve for accurate local values, the K-factor error contribution could amount to 0.5 percent, rather than a predicted 0.2 percent from the analysis (Grabe, 1988).

Flow Measurement by Coriolis Flowmeter. The contributing elements of an uncertainty analysis of observed fuel flow for a Coriolis flowmeter include such items as the drive coil frequency, the frequency response of the electromagnetic sensors, the thermal correction for flowmeter tube elasticity changes, zero stability, and the K factor. For the corrected fuel flow, inlet temperatures and pressures, and the fuel net heat of combustion, must be considered to determine the final uncertainty. Each of these items depends, in turn, on contributing elements of its own.

Taking all of these possible error contributions into account, it was found that the following uncertainties may occur. The observed fuel flow, under average measurement conditions, could be expected to have an uncertainty of ± 0.15 percent of reading $\pm$ zero stability. The zero stability can be as high as ± 0.5 percent of reading based on the test results shown here and in previously published work (Keita, 1989).

Summary and Conclusions

For accurate fuel flow measurement, certain precautions must be taken in installing and operating a flowmeter, be it a turbine or a Coriolis-type device. The turbine flowmeter is a relatively simple device measuring volumetric flow rate, which is affected by fuel temperature, relative density, and viscosity of the fluid. The Coriolis mass flowmeter indicates mass flow directly through reasonably complex procedure, with little or no influence from the properties of the fluid.

Comparison tests between the turbine and Coriolis flowmeters indicated good agreement of about ± 0.3 percent over the lower portion of the flow range of the Coriolis meter examined. At higher flow rates, the Coriolis flowmeter indicated flow rates approximately 0.5 percent higher than the two turbine meter in series with it. This divergence was attributed to noise and vibration emanating from the gas turbine. Fuel temperature, relative density or viscosity did not appear to influence the Coriolis flowmeter in any way. Installation effects on the Coriolis flowmeter were minimal, and the pressure losses were similar to that for the turbine flowmeters (depending on turbine meter diameter). Drifting in the electronic components of the Coriolis flowmeter required frequent adjustments of the frequency board to maintain close agreement with turbine flowmeter results. If undetected and uncorrected, these drifts could lead to substantial measurement errors.

Recommendations

Based on previous experience with Coriolis mass flowmeters (MacLeod, 1987) and the results of this study, the Coriolis flowmeter has shown to have the capability of accurately measuring fuel flow to a gas turbine, provided certain precautions are observed. It is recommended that Coriolis flowmeter be seriously considered for gas turbine testing, both in the laboratory and in field installations. However, because of the complexity of the electronic conditioning required to monitor the Coriolis flowmeter, the device should, for the time being, be used in series with a turbine flowmeter to detect any possible drift in the Coriolis meter readings.

References

FTI, 1982, "Installation, Operation and Maintenance Manual Omnitrak," Flow Technology, Inc., 4250 East Broadway Road, Phoenix, AZ 85040.

Furness, R. A., 1991, "BS7405: The Principles of Flowmeter Selection," *Flow Measurement and Instrumentation*, Vol. 2, Oct. pp. 233-242.

Grabe, W., 1988, "Fuel Flow Measurement in Gas Turbine Testing," Division of Mechanical Engineering, National Research Council, Ottawa, Ontario, TR-ENG-001 (NRC No. 29808).

Grabe, W., 1991, "Turbine Flowmeter Calibration," Institute for Mechanical Engineering, National Research Council, Ottawa, Ontario, CAT-ENG-013.

Keita, N. M., 1989, "Contribution to the Understanding of the Zero Shift Effects in Coriolis Mass Flowmeters," *Flow Measurement and Instrumentation*, Vol. 1, Oct. pp. 39-43.

MacLeod, J. D., 1987, "Evaluation of the EXAC Mass Flowmeter," Division of Mechanical Engineering, National Research Council, Ottawa, Ontario, CAT-ENG-002.

MacLeod, J. D., and Orbanski, B., 1992, "Turbine Rebuild Effects on Gas Turbine Performance," ASME Paper No. 92-GT-23.

Paik, J. S., Lim, K. W., Lee, K. B., 1990, "Calibration of Coriolis Mass Flowmeters Using a Dynamic Weighing Method," *Flow Measurement and Instrumentation*, Vol. 1, Apr. pp. 171-175.

Schlumberger Industries Inc., 1991, "M-dot Direct Mass Flowmeter With Datamate 2000 Operating and Maintenance Manual."

Zimmerman, R., and Deery, D., 1977, "Handbook for Turbine Flowmeter Systems," Flow Technology Inc., 4250 East Broadway Road, Phoenix, AZ 85040.

Downloaded 02 Jun 2010 to 171.66.16.102. Redistribution subject to ASME license or copyright; see http://www.asme.org/terms/Terms_Use.cfm

Comparative Evaluation of Combined Cycles and Gas Turbine Systems With Water Injection, Steam Injection, and Recuperation

O. Bolland

J. F. Stadaas

Norwegian Institute of Technology / SINTEF, Trondheim, Norway

Combined cycles have gained widespread acceptance as the most efficient utilization of the gas turbine for power generation, particularly for large plants. A variety of alternatives to the combined cycle that recover exhaust gas heat for re-use within the gas turbine engine have been proposed and some have been commercially successful in small to medium plants. Most notable have been the steam-injected, high-pressure aeroderivatives in sizes up to about 50 MW. Many permutations and combinations of water injection, steam injection, and recuperation, with or without intercooling, have been shown to offer the potential for efficiency improvements in certain ranges of gas turbine cycle design parameters. A detailed, general model that represents the gas turbine with turbine cooling has been developed. The model is intended for use in cycle analysis applications. Suitable choice of a few technology description parameters enables the model to represent accurately the performance of actual gas turbine engines of different technology classes. The model is applied to compute the performance of combined cycles as well as that of three alternatives. These include the simple cycle, the steam-injected cycle, and the dual-recuperated intercooled aftercooled steam-injected cycle (DRIASI cycle). The comparisons are based on state-of-the-art gas turbine technology and cycle parameters in four classes: large industrial (123–158 MW), medium industrial (38–60 MW), aeroderivatives (21–41 MW), and small industrial (4–6 MW). The combined cycle's main design parameters for each size range are in the present work selected for computational purposes to conform with practical constraints. For the small systems, the proposed development of the gas turbine cycle, the DRIASI cycle, are found to provide efficiencies comparable or superior to combined cycles, and superior to steam-injected cycles. For the medium systems, combined cycles provide the highest efficiencies but can be challenged by the DRIASI cycle. For the largest systems, the combined cycle was found to be superior to all of the alternative gas turbine based cycles considered in this study.

Introduction

Gas turbine development with respect to performance has mainly relied on increased turbine inlet temperature and improved blade cooling technology. These improvements have had a positive impact, especially on combined cycle performance. Today, using a combined cycle for power generation and cogeneration applications is probably the best way to utilize advanced gas turbine technology. Advanced gas turbine cycles with features like steam injection, intercooling, and recuperation have the potential of achieving high efficiencies, but have not gained the widespread acceptance that the combined cycle has enjoyed.

When analyzing gas turbine cycles, it has become more and more important to include the impact of turbine cooling on the turbine expansion path and on cycle performance, as turbine inlet temperatures have been raised. Different approaches have been taken in order to include turbine cooling in gas turbine cycle performance calculations. Rohsenow (1955) divided the turbine expansion path into a cooled and an uncooled portion. For the cooled portion a relation for heat transfer to cooled blades per unit of work ($\dot{Q}/\dot{W}$) was derived. This relation was based on the temperature difference between the hot gas and the wall, a defined loss factor, and an expression for maximum work per stage. At that time this was a unique type of solution to determine the quantity of heat rejected by cooling without using extensive heat transfer analysis. The Rohsenow method applies only to the case where heat is removed from the turbine blades and is rejected to a sink external to the turbine. Another method

Contributed by the International Gas Turbine Institute and presented at the 38th International Gas Turbine and Aeroengine Congress and Exposition, Cincinnati, Ohio, May 24–27, 1993. Manuscript received at ASME Headquarters February 12, 1993. Paper No. 93-GT-57. Associate Technical Editor: H. Lukas.

Copyright © 1995 by ASME

Downloaded 02 Jun 2010 to 171.66.16.102. Redistribution subject to ASME license or copyright; see http://www.asme.org/terms/Terms_Use.cfm

was proposed by Louis et al. (1983) intended for different types of cooling methods such as internal impingement and convection cooling, film cooling, and closed-loop cooling by water. In this model, internally cooled blades are treated as heat exchangers operating at constant metal temperatures and the coolant exit temperature is a function of the heat exchanger effectiveness. The coolant requirements and heat transfer with film cooling are determined using a correlation from Louis (1977). A single-stage model for the expansion path divided into three portions is used. In the first portion the coolant is mixed with the hot gas, resulting in a drop of stagnation temperature at constant stagnation pressure followed by a drop in stagnation pressure at constant stagnation temperature. The second portion is an adiabatic expansion with an isentropic efficiency, and the third portion is a repetition of the first one. The GASCAN code (Elmasri, 1986a) enables stage-by-stage calculations of the turbine based on the free-vortex design method. The cooling flows to each blade row are found from semi-empirical cooling effectiveness curves (Elmasri and Pourkey, 1986). A different approach is given by Elmasri (1986b) where a closed-form solution is used for the impact of cooling on cycle performance. This model is based on representing the turbine as an expansion path with continuous, rather than discrete, work extraction. However, the closed-form solution requires constant fluid properties. The model for cooled turbines presented in this paper is based on the work by Elmasri (1986b).

Gas Turbine Model

In principle, raising the turbine inlet temperature increases the efficiency and the specific work output of gas turbine cycles. The surfaces of the components exposed to the hot gas must be maintained below a certain safe working temperature, consistent with mechanical strength and corrosion resistance. As the turbine inlet temperature is raised, the temperature difference between the hot gas and the metal surfaces will increase. The cooling requirements will then increase both with respect to the amount of coolant for a given stage and to the proportion of the expansion path that has to be cooled. Cooling of stages in the expansion path counteracts the effect of increased inlet temperature. When, for a given level of cooling technology, the turbine inlet temperature is raised beyond a certain value, the cooling penalties are such that cycle efficiency falls.

In air-cooled turbines, mixing the cooling air into the main flow causes losses in both stagnation temperature and pressure. The thermodynamic penalty due to those losses is usually more substantial than that due to heat extraction from the expanding hot gas through the walls. Since those penalties increase with the flow rate of the cooling air, minimizing this flow rate is desirable. This is achieved by improving internal heat transfer between the coolant and the blade and by using the spent coolant to shield the blade from the hot gas, which essentially reduces the blade external heat transfer coefficient. Both of those effects could be achieved if practical transpiration cooling systems were developed. Today they are partially apparent in the technology on film cooling. The older technology of internal air cooling does not utilize the spent coolant to reduce the external heat transfer coefficient. Thus, its performance can be considered as a lower limit on film cooling, whereas transpiration cooling represents an upper limit. Other methods of reducing cooling air requirements are currently being developed. One such method being applied to some machines is to externally precool the cooling air going to the first row of stators. The use of other coolant fluids like steam or liquid water has also been proposed.

The objective for the development of a gas turbine model in the present work is to study gas turbine cycle performance. No attempt is made to do a detailed physical stage-by-stage analysis including features such as velocity triangles and prediction of stage efficiencies. Due to the large number of parameters influencing cooling losses, precise calculations can only be attempted for specific machines and conditions. Such computations can yield satisfactory predictions for the performance of a particular machine. To obtain a general understanding of the parameters governing cooling losses, and to compare different levels of machine technology and different gas turbine cycles with respect to performance, one often employs approximate models. Such models should not be simplified to a degree where satisfactory numerical results cannot be provided. In the present work a gas turbine model is developed that is sufficiently simplified to facilitate parametric studies of gas turbine cycle performance, while retaining an adequate level of detail to provide useful numeric results.

The turbine is treated as an expander whose walls continuously extract work. The stagnation temperature of the gas relative to those walls is approximated by a very-close-to-continuously-varying function, rather than the steplike variation of a real machine. This is depicted in Fig. 1, which shows that the assumed temperature profile underestimates the relative gas-to-surface temperature difference for a stator, while overestimating it for the rotor. The stage average, however, is essentially correct.

Nomenclature

A = area, m^2
B = blade axial breadth, m
C = degree of reaction factor
c_P = specific heat capacity, kJ/(kg K)
l = airfoil perimeter, m
L = blade height, m
$\dot{M}$ = mass flow rate, kg/s
Ma = Mach number
p = pressure, bar
Pr = Prandtl number
PRC = pressure ratio compressor
$\dot{Q}$ = heat flow, kW
r = recovery factor
R = gas constant, kJ/(kg K)
SP = blade circumferential spacing, m
St = Stanton number
T = temperature, K or °C
u = velocity, m/s
$\dot{W}$ = power, kW
Y = cooling air mixing loss factor
α = heat transfer coefficient, $kW/(m^2 K)$
δ = sum of the relative deviations
ϵ = heat exchanger efficiency
η = efficiency
κ = ratio of specific heats = c_P/c_v
ρ = density, kg/m^3
σ = technology level descriptor
ϕ = angle of coolant injection (see Fig. 3)
ω = specific work, kJ/kg air

Subscripts and Superscripts

a = ambient
ad = adiabatic
AUX = auxiliary
c = coolant, cooling air
CE = combustor exit
co = compressor
F = fuel
g = gas (hot gas expanding through the turbine)
GT = gas turbine
IC = intercooler
$M+G$ = mechanical and generator (efficiency η_{M+G})
P = polytropic
s = free-stream
ST = steam turbine
t = turbine
TE = turbine exit
w = wall

Downloaded 02 Jun 2010 to 171.66.16.102. Redistribution subject to ASME license or copyright; see http://www.asme.org/terms/Terms_Use.cfm

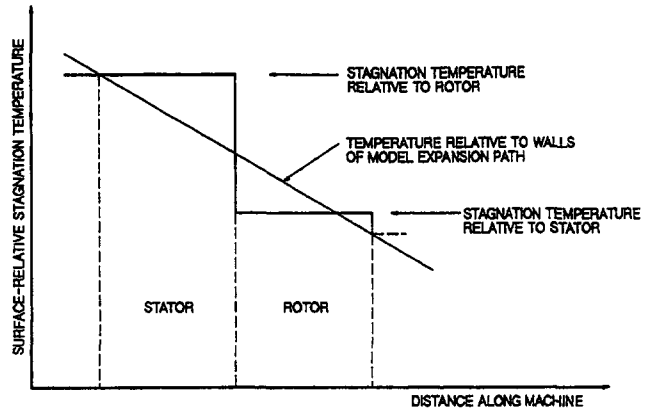

Fig. 1 Schematic representation of the temperature profile in the expansion path with continuous work extraction (after Elmasri, 1986b)

The connection between this idealized model of the expansion path and the real machine is accomplished by setting its work flux equal to the machine stage average (Elmasri, 1986b):

$$\frac{d\dot{W}}{dA_w} = \frac{\dot{W}_{\text{stage}}}{A_{w,\text{stage}}} \tag{1}$$

The stage work is proportional to the local gas-flow rate and the square of the pitchline velocity. That is

$$\dot{W}_{\text{stage}} = C\dot{M}_g u^2 \tag{2}$$

where the proportionality constant C depends on the stage geometry and velocity triangles, and is typically in the range $1.0 < C < 1.5$. An element of the expansion path is shown in Fig. 2. The heat flux is

$$\frac{d\dot{Q}}{dA_w} = \alpha(T_{ad} - T_w) \tag{3}$$

where T_{ad} is the adiabatic wall temperature. This temperature is close to the gas stagnation temperature, given by the "recovery factor" r,

$$r = \frac{T_{ad} - T_s}{T_g - T_s} \tag{4}$$

where T_s is the free-stream static temperature. For turbulent flow the recovery factor can be expressed as a function of the Prandtl number (Kreith and Black, 1980), i.e.,

$$r = \text{Pr}^{1/3}. \tag{5}$$

For a typical gas composition from a gas turbine combustor the recovery factor is close to one, and therefore the adiabatic wall temperature is assumed to be equal to the local stagnation temperature ($T_{ad} = T_g$). The heat flux through the wall will then be

$$\frac{d\dot{Q}}{dA_w} = \alpha(T_g - T_w). \tag{6}$$

Assuming that the heat transfer coefficient for the expansion path is the same as for the stage average, one may write

$$\alpha = \frac{\text{St}\, c_{P,g}\dot{M}_g}{A_g} \tag{7}$$

where the Stanton number is defined as

$$\text{St} = \frac{\alpha}{\rho u c_{P,g}} \tag{8}$$

The heat transfer through the blade wall can be expressed by the following equation:

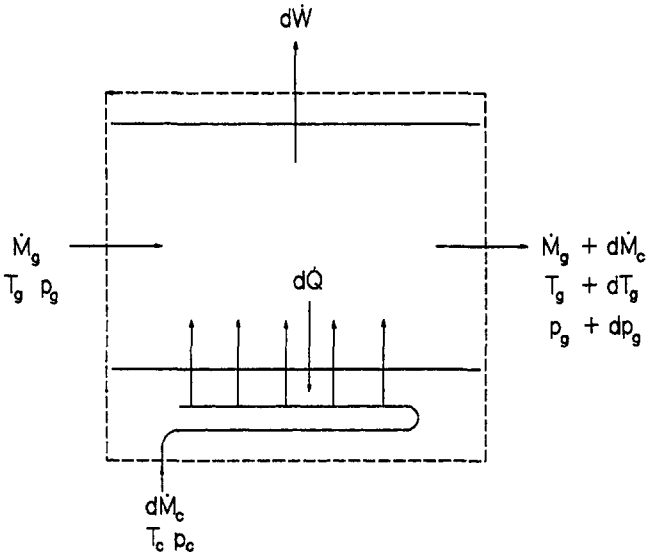

Fig. 2 Element of the cooled expansion path

$$d\dot{Q} = c_{P,c}\epsilon(T_w - T_c)d\dot{M}_c \tag{9}$$

where $d\dot{M}_c$ is the cooling air flow rate supplied at T_c, and ϵ is the heat exchanger effectiveness for an internally cooled blade, i.e.,

$$\epsilon = \frac{T_{c,\text{out}} - T_c}{T_w - T_c}. \tag{10}$$

$T_{c,\text{out}}$ in Eq. (10) is the temperature of the cooling air entering the gas path. Further, the work extracted through the walls is given by

$$d\dot{W} = -\dot{M}_g c_{P,g} dT_g. \tag{11}$$

dT_g is obtained from

$$\frac{dT_g}{T_g} = \left(\frac{p + dp}{p}\right)^{R\eta_{P,t}/c_P} - 1 \tag{12}$$

The efficiency ($\eta_{P,t}$) in Eq. (12) is the uncooled turbine polytropic efficiency. At this point it is possible to derive an expression that relates the required cooling air mass flow to the work extraction for an element of the expansion path. By combining Eqs. (1), (2), (6), (7), (9), and (11) the following relation is found:

$$\frac{d(\dot{M}_c c_{P,c})}{\dot{M}_g c_{P,g}} = \sigma \frac{dT_g}{T_a} \frac{(T_g - T_w)}{(T_w - T_c)} \tag{13}$$

where σ is

$$\sigma = \frac{\text{St}\dfrac{A_{w,\text{stage}}}{A_g}}{C(\kappa - 1)\text{Ma}^2\epsilon} \tag{14}$$

and where the Mach number is

$$\text{Ma} = \frac{u}{\sqrt{T_a \kappa R}}. \tag{15}$$

For a cascade, the ratio of wall area to gas flow path inlet area is

$$\frac{A_w}{A_g} = \frac{l}{SP} + \frac{2B}{L} \tag{16}$$

where l = airfoil perimeter, SP = blade circumferential spacing, B = axial breadth, and L = blade height. Typical value of A_w/A_g is around 4 for a row and 8 for a stage.

Downloaded 02 Jun 2010 to 171.66.16.102. Redistribution subject to ASME license or copyright; see http://www.asme.org/terms/Terms_Use.cfm

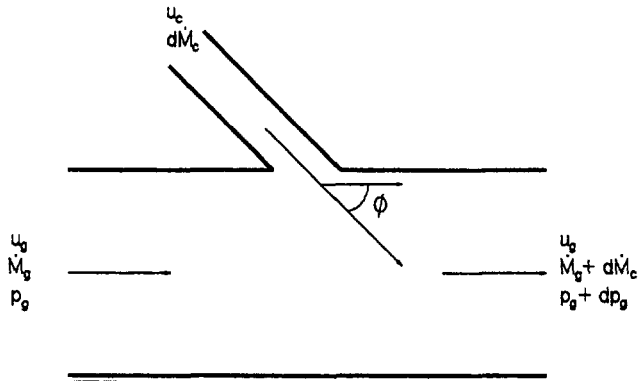

Fig. 3 Element of duct with gas injection

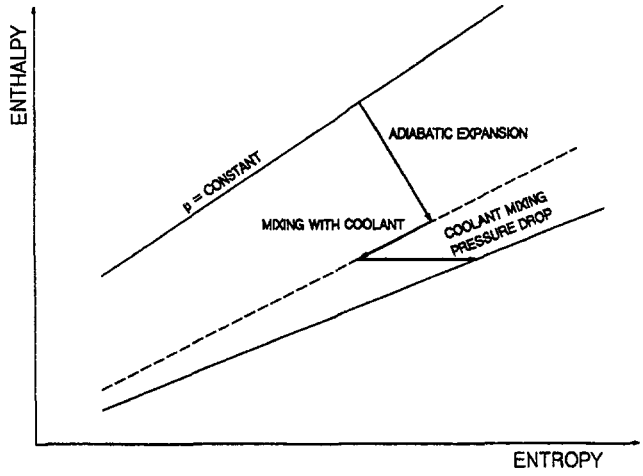

Fig. 4 Computational model for an element of the expansion path

Stanton numbers based on the cascade inlet area, according to Elmasri (1986b), are typically about 0.005. The Mach number, Ma, based on the pitchline velocity, is typically in the range of 0.6 to 0.85 for current gas turbines. With $\kappa = 1.4$ and $C = 1.2$, Eq. (14) gives the estimate of $\sigma \cdot \epsilon$ to be 0.12–0.26. Heat exchanger effectiveness, ϵ, depends on the cooling air delivery temperature and the blade internal heat transfer area, the heat transfer coefficient and the temperature difference. The value of ϵ by Louis et al. (1983) is assumed to be in the range of 0.3 to 0.5, where the lower value is typical for film-cooled blades with multiple compressor extractions, and the upper value is typical for internally cooled blades with cooling air taken from the compressor discharge. The parameter σ characterizes the relative heat to work loadings on the machine surfaces, and can be regarded as a descriptor of the level of technology for a cooled machine.

Mixing the cooling air with the hot gas results in an irreversible loss of stagnation pressure. Consider the flow in a duct between two sections an infinitesimal distance apart (Fig. 3). In this element of duct length, cooling air is injected with an angle ϕ into the gas stream at the flow rate $d\dot{M}_c$. To find the loss of stagnation pressure, a momentum balance is applied (Shapiro, 1953), and arranged in the following manner:

$$\frac{dp}{p} = -\frac{d\dot{M}_c}{\dot{M}_g}\kappa M^2 Y \tag{17}$$

The factor Y, when different from unity, permits other values for the mixing pressure loss than that of perpendicular mixing.

The model of one element of the expansion path is then described by Eqs. (11), (12), (13), and (17). The expansion path is divided into a large number of elements, and for each element those four equations are employed. Figure 4 shows the computational model of one element in an enthalpy/entropy diagram. The element is split into the following parts: adiabatic expansion (work extraction), mixing of hot gas and cooling air at constant pressure (loss of stagnation temperature), and mixing of hot gas and cooling air at constant enthalpy (loss of stagnation pressure).

The compression path is computed with a large number of stages in order to (1) take into account variable specific heat capacity due to temperature dependency and changes in air composition if an evaporative intercooler is used, (2) and have multiple cooling air bleeds. Considering stage "i" of the compression path, the following equations are used. The work equation is

$$\dot{W}_i = \dot{M}_i c_{P,i} \Delta T_i. \tag{18}$$

The ΔT_i is computed from the stage inlet temperature, T_i, and the stage inlet and outlet pressures, p_i and p_{i+1}, with the following equation:

$$\frac{\Delta T_i}{T_i}\left(\frac{p_{i+1}}{p_i}\right)^{R/\eta_{P,co}c_P} - 1. \tag{19}$$

The stage flow rate is the compressor inlet mass flow, $\dot{M}_{co,\text{inlet}}$, minus the cooling air mass flow, $\dot{M}_c$, extracted from stages at lower pressures than the present stage, plus the mass added in the evaporative intercooler, $\dot{M}_{IC}$, if the stage is at a pressure above the intercooler pressure. That is,

$$\dot{M}_i = \dot{M}_{co,\text{inlet}} - \sum_{n=1}^{i-1} \dot{M}_{c,n} + \dot{M}_{IC}. \tag{20}$$

The cooling air flow rate is determined by Eq. (13). For a given cooled turbine stage, the corresponding compressor stage at which cooling air is bled is selected in such a way that the pressure of the cooling air equals the pressure of the cooled turbine stage multiplied by a factor slightly larger than unity. If this required bleed pressure is larger than the compressor discharge pressure, cooling air is supplied from the compressor discharge. In the present work emphasis was placed on including precise calculation of thermophysical properties (Kunz, 1982; Olikara and Borman, 1975; Valland and Pedersen, 1988). For the combined cycle calculations, the computational model for the steam cycle was given by Bolland (1991).

Gas Turbine Characterization

In order to provide useful numeric results from the cycle analysis, efforts were made to employ the technology level of existing gas turbines. A selection of gas turbines was carried out. These machines were categorized in four classes: large industrial (A), medium industrial (B), aeroderivative machines (C), and small industrial (D). For each class of machines an "average" gas turbine was defined and used in the cycle analysis. The technology parameters, described in the previous section, for each gas turbine served as a basis when defining these average gas turbines. The data for the gas turbines were mainly based on the GTPRO (1992) database, and included air flow, compressor discharge temperature, power output, fuel flow, turbine exit temperature, and an estimate of the cooling air flow rate downstream of the first stator row of the turbine. To quantify representative technology parameters for each gas turbine, the parameters in the model (combustor exit temperature T_{CE}, turbine uncooled polytropic efficiency η_P, and the level of technology descriptor σ) were found such that the sum of relative deviations (δ) between the known machine data and those

Downloaded 02 Jun 2010 to 171.66.16.102. Redistribution subject to ASME license or copyright; see http://www.asme.org/terms/Terms_Use.cfm

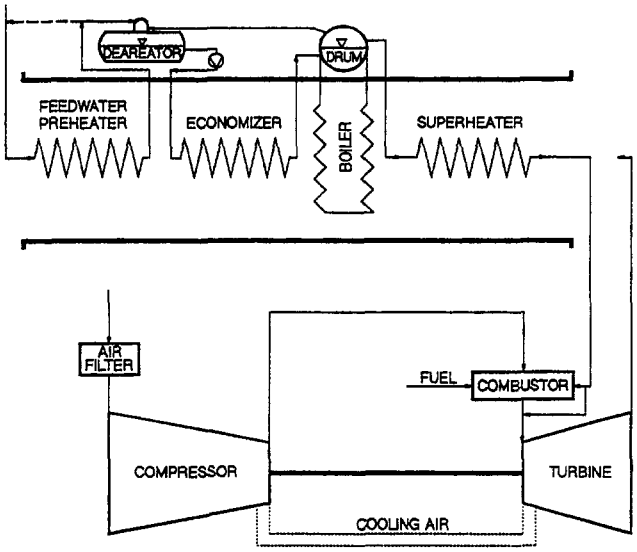

Fig. 5 Steam-injected gas turbine cycle

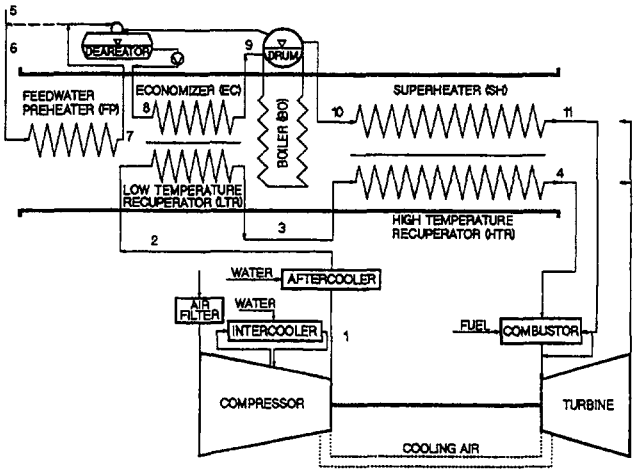

Fig. 6 Dual recuperated intercooled aftercooled steam injected cycle (DRIASI)

calculated by the model was minimized. A simplification was made by setting the cooling air mixing loss factor (Y) to unity because its significance with respect to gas turbine performance is much smaller compared to the other three parameters mentioned above. The minimization problem is then

$$\delta = \min\left\{\left|\frac{\dot{W}_{GT,\text{model}} - \dot{W}_{GT,\text{known}}}{\dot{W}_{GT,\text{known}}}\right| + \left|\frac{\dot{M}_{F,\text{model}} - \dot{M}_{F,\text{known}}}{\dot{M}_{F,\text{known}}}\right| + \left|\frac{T_{TE,\text{model}} - T_{TE,\text{known}}}{T_{TE,\text{known}}}\right|\right\}. \quad (21)$$

The results of the gas turbine characterization are given in Table 1. Only a few of the gas turbines listed in Table 1 are able to take steam injection flow rates substantially exceeding those used for NO_x control. Very few gas turbines are intended for or may easily be redesigned for compressor intercooling or recuperation (Thomas and Higson, 1985; Staudt et al., 1989). In the present work it is assumed that some modifications can be made to the gas turbines. These are: (1) allow a larger nozzle throat area for the turbine; (2) changes in the cooling air flow paths; (3) air can be taken out of the machine for recuperation and be put back.

Cycle Description

Four types of cycle were studied: simple cycle, steam-injected cycle, DRIASI (dual-recuperated intercooled aftercooled steam-injected) cycle, and combined cycle. The steam-injected and the DRIASI cycles are shown in Figs. 5 and 6, respectively. When comparing the simple cycle and the steam-injected cycle, the latter offers a higher efficiency mainly due to reduced cycle energy rejection temperature, and higher specific work due to the small compression work for liquid water compared to air. The increase in efficiency and specific power for a steam-injected cycle over a simple cycle is thermodynamically limited by a pinch-point restriction of the exhaust gas heat recovery process. Another method of increasing gas turbine cycle efficiency is to preheat the combustion air by a heat exchange from the turbine exhaust (recuperator). The increase in efficiency for a recuperated cycle over a simple cycle is thermodynamically limited by the heat exchanger effectiveness of the recuperator and the compressor discharge temperature. The idea behind the DRIASI cycle (Elmasri, 1988a, b; Bolland, 1990) is to combine steam injection, recuperation, and water injection into an effective gas turbine exhaust heat recovery scheme. Water injection into the compressor or/and after the compressor helps bring down the stack temperature, thus reducing the temperature of the cycle heat rejection. On the other hand, water and steam injection increases the loss of latent heat from the stack. Evaporative intercooling of the compressor with water increases the heat capacity of the turbine coolant and reduces the required coolant flow rate. By combining water injection with recuperation, a reduction of the temperature of heat addition to the process is avoided. The pinch-point limitation of the steam-injected cycle is canceled by locating a portion of the recuperator (LTR) below the pinch-point temperature of the heat recovery process. The water injection, together with the low-temperature recuperator, allows steam generation at temperatures below the pinch point because the water is vaporized at a partial pressure well below that of the gas turbine combustor. A visualization of the heat recovery process for the DRIASI cycle is given in Fig. 7, where the numbers correspond to those in Fig. 6. The combined cycle takes advantage of the high temperature of the cycle heat addition of the Brayton cycle and the low temperature of cycle heat rejection of the Rankine cycle. By using a dual or triple pressure steam Rankine cycle the heat transfer losses between the Brayton and Rankine cycles are rather small, as is the stack loss (Bolland, 1991). The cooling system of combined cycles for class A gas turbines is typically based on a direct water-cooled condenser, which allows the condenser pressure to be very low. For smaller combined cycles there is a tendency toward using cooling towers or air-cooled condensers. The condenser pressure for such cooling systems is higher. In the present work it is assumed that

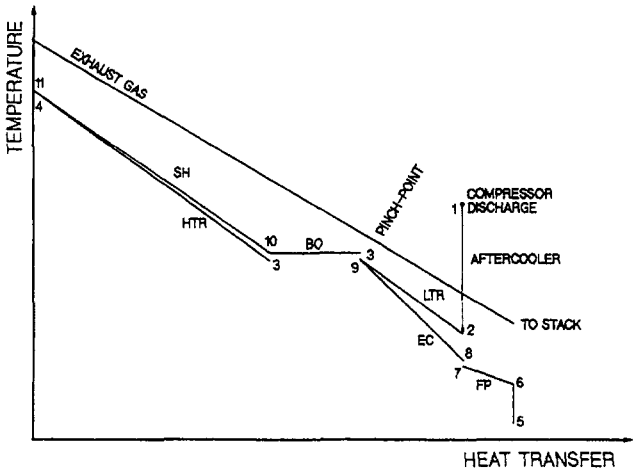

Fig. 7 Heat recovery diagram for the dual recuperated intercooled aftercooled steam-injected cycle

Downloaded 02 Jun 2010 to 171.66.16.102. Redistribution subject to ASME license or copyright; see http://www.asme.org/terms/Terms_Use.cfm

Table 1 Results from the characterization of gas turbines

Class	Types	[1]$\dot{W}_{GT}$ MW	[1]η_{GT} %	[1]T_{TE} °C	[1]PRC -	σ -	T_{CE} °C	$\eta_{P,t}$ %	$\eta_{P,c}$ %	[2]$\dot{M}_c$ %
A	Siemens V84.3 ABB GT13E GE 9171E GE 7221FA	141	35.0	550	14.2	0.41	1234	87.8	90.7	14.9
B	GE 6541B Siemens V64.3 ABB Type 8 West. 251 B12A	48.4	32.5	532	14.8	0.49	1203	86.2	89.7	15.6
C	LM 2500PE LM 5000PD LM 6000PA TPM FT8	30.2	37.6	471	23.4	0.40	1269	88.3	90.0	19.6
D	Ruston Typhon Ruston Tornado Solar Taurus Dresser R. DC990	4.6	28.8	487	12.2	0.63	1019	85.5	86.8	5.9

[1]Inlet/outlet pressure drop = 10 mbar, ambient temperature 15°C, relative humidity 60 percent, auxiliary power rquirement is here not taken into account. Efficiency based on fuel lower heating value and generator terminal output.
[2]The total amount of cooling air downstream of the combustor exit as percentage of the compressor inlet flow rate.

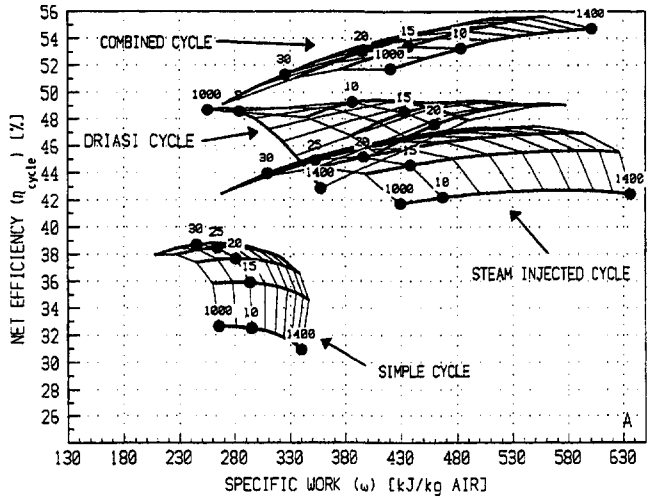

Fig. 8 Computational results for machine class A (large industrial)

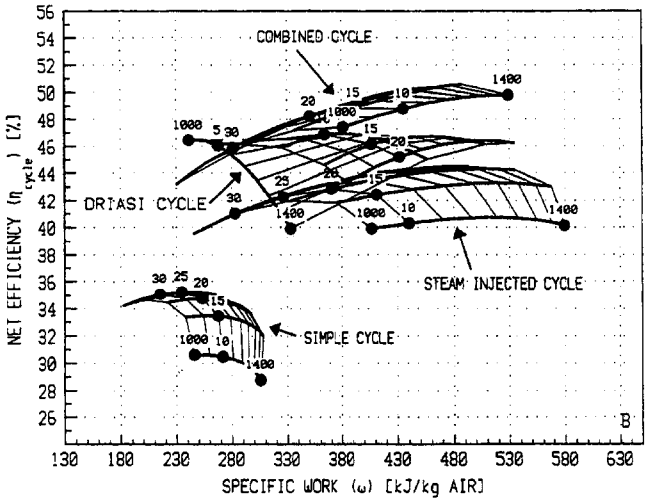

Fig. 9 Computational results for machine class B (medium industrial)

combined cycles with gas turbines of classes B, C, and D are using cooling towers with an increased condenser pressure, compared to combined cycles with class A gas turbines. The steam cycle level of technology, here meaning whether it is a triple pressure, dual pressure, or single pressure cycle, is in current design practice very dependent upon the power output of the steam cycle. This design practice is also reflected in the assumptions made for the present work, and is described in the appendix.

Results and Discussion

Parametric studies are presented over a broad range of cycle pressure ratios (PRC) and turbine inlet temperatures (T_{CE}), and the results for the four types of cycle are given in separate diagrams (Figs. 8 to 11) for each class of gas turbines. In each diagram the cycle efficiency (η_{cycle}) and specific work (ω) are given as functions of the pressure ratio and turbine inlet temperature. Different definitions of turbine inlet temperature exist, but in the present work the combustor exit (or first nozzle inlet) temperature is used. A list of computational assumptions is given in the appendix.

The definitions of cycle efficiency and specific work used in the present work are given in Eqs. (22) and (23):

$$\eta_{\text{cycle}} = \frac{\dot{W}_{GT}\eta_{M+G,GT} + \dot{W}_{ST}\eta_{M+G,ST} - \dot{W}_{\text{AUX}}}{\dot{M}_F \text{ LHV}} \quad (22)$$

$$\omega = \frac{\dot{W}_{GT}\eta_{M+G,GT} + \dot{W}_{ST}\eta_{M+G,ST} - \dot{W}_{\text{AUX}}}{\dot{M}_{co,\text{inlet}}} \quad (23)$$

The thick lines in the diagrams are for constant pressure ratio and varying turbine inlet temperature (1000–1400° C) while the thin lines are for constant turbine inlet temperature and varying pressure ratio (5 or 10 to 20 or 30).

The results of the computational model for the simple cycle are in agreement with known simple cycle gas turbines. Current design practice is obviously a compromise between high efficiency and high specific power. The results of the steam-injected cycles reveal both higher efficiency and specific power compared to known systems like the aeroderivative steam-injected cycles. The reason for this is that in the present work the rate of steam injection is limited by the pinch-point constraint, while for existing systems the limita-

Downloaded 02 Jun 2010 to 171.66.16.102. Redistribution subject to ASME license or copyright; see http://www.asme.org/terms/Terms_Use.cfm

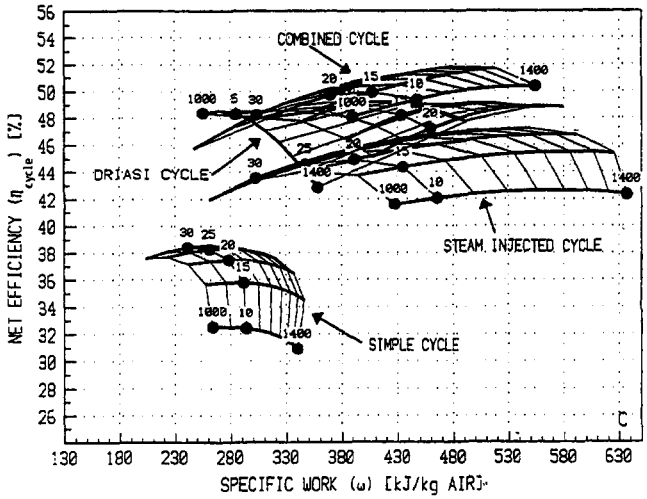

Fig. 10 Computational results for machine class C (aeroderivatives)

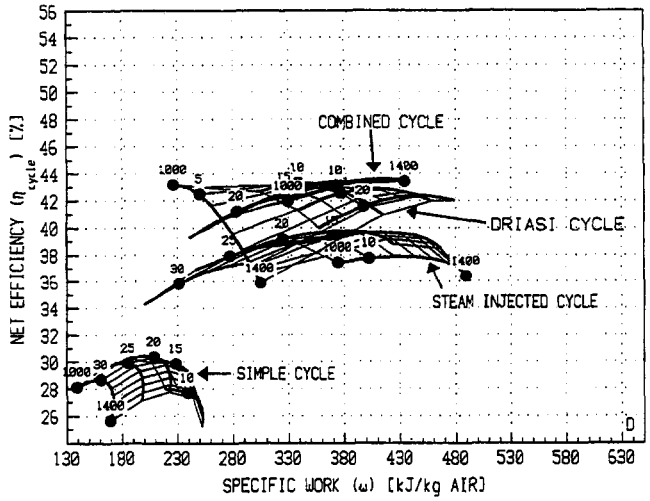

Fig. 11 Computational results for machine class D (small industrial)

tion may typically be gas generator speed (Hånde, 1992). The results for combined cycles are in accord with current design practice.

The steam-injected cycle is superior to the simple cycle in both efficiency and specific work. The difference in efficiency is typically in the range of 8–10 percentage points when considering typical pressure ratios and turbine inlet temperatures for the different machine classes. A characteristic difference between the simple cycle and the steam-injected cycle is that the increase in specific power per increase in turbine inlet temperature is much larger for the steam-injected cycle. Another characteristic difference is that for a given pressure ratio the efficiency peaks at a higher turbine inlet temperature for the steam injected cycle.

The DRIASI cycle is typically 3–4 percentage points more efficient compared to the steam-injected cycle, while specific work is slightly lower for the DRIASI cycle. The efficiency for the DRIASI cycle peaks over a broad range of pressure ratios and turbine inlet temperatures. This is a remarkable characteristic of the DRIASI cycle, which means that high efficiency is obtainable for moderate pressure ratios and rather low turbine inlet temperatures. For the class D gas turbines it is impractical to have pressure ratios exceeding 12–15 and the cooling technology is not developed to the same level as for larger gas turbines. Therefore, the class D gas turbines are especially suited to this type of cycle arrangement, when high efficiency is wanted. Even for gas turbines with very advanced cooling technology, high efficiencies may be obtainable at rather moderate turbine inlet temperatures.

The large combined cycles are superior to the other systems with respect to efficiency. Typical values for the efficiency of the combined cycle with class A gas turbines are in the range of 52–55 percent, while the DRIASI and the steam-injected cycles are at 49 and 45–46, respectively. For the combined cycles with gas turbines from classes B, C, and D, the differences in efficiency compared to the DRIASI cycle are much smaller. The combined cycle efficiency is reduced as a function of gas turbine technology level and steam cycle power output. For the gas turbine classes B, C, and D, the condenser pressure is higher because the use of a cooling tower is assumed. The steam turbine is less efficient because it is smaller, and the steam cycle level of technology is typically reduced as power output is decreased. For the smallest machines (class D), the DRIASI cycle provides comparable or superior efficiencies to the combined cycle.

Medium and small combined cycles are, in most cases, designed for cogeneration of power and heat, and extraction and/or backpressure systems offer the possibility of having a high degree (up to 90 percent) of fuel utilization as well as a certain flexibility between the heat and power generation. The DRIASI cycle has some of the same advantageous capabilities of the combined cycle in cogeneration applications (Elmasri, 1988a, b; Bolland, 1990).

Conclusions

A detailed, general model that represents the gas turbine with turbine cooling has been developed. The model is intended for use in cycle analysis applications. Suitable choice of a few technology description parameters enables the model to represent accurately the performance of actual gas turbine engines of different technology classes.

A characterization of 16 existing gas turbines has been carried out with the developed gas turbine model, resulting in descriptions of "average" gas turbine technology levels of four different classes.

A parametric study (pressure ratio and turbine inlet temperature) has been carried out for four types of power cycle including four classes of gas turbine technology level. For the small systems, the proposed development of the gas turbine cycle, the DRIASI cycle, are found to provide comparable or superior efficiencies to combined cycles, and superior to steam-injected cycles. For the medium systems, combined cycles provide the highest efficiencies but can be challenged by the DRIASI cycle. For the largest systems, the combined cycle was found to be superior to all of the alternative gas turbine based cycles considered in this study.

The DRIASI type of cycle, with its special characteristics, points toward another direction in gas turbine design development. The current trend in gas turbine technology development is toward higher pressure ratios and turbine inlet temperatures for medium and small machines, and toward mainly higher turbine inlet temperatures for large machines. The DRIASI cycle opens up for improved gas turbine performance without any further increases in the turbine inlet temperature or pressure ratio. Instead, emphasis is on developing heat exchanger and water evaporation units. It has been shown that high efficiencies are attainable with redesigned gas turbines with a low or moderate level of technology.

Acknowledgments

The discussions held with Dr. Maher Elmasri were invaluable during the course of this work.

Downloaded 02 Jun 2010 to 171.66.16.102. Redistribution subject to ASME license or copyright; see http://www.asme.org/terms/Terms_Use.cfm

References

Bolland, O., 1990, "Analysis of Combined and Integrated Gas Turbine Cycles," Dissertation, Norwegian Institute of Technology, University of Trondheim, Norway.

Bolland, O., 1991, "A Comparative Evaluation of Advanced Combined Cycle Alternatives," ASME JOURNAL OF ENGINEERING FOR GAS TURBINES AND POWER, Vol. 113, pp. 190–197.

Boyle, R. J., 1979, "Effect of Steam Addition on Cycle Performance of Simple and Recuperated Gas Turbines," NASA Technical Paper 1440.

Elmasri, M. A., 1986a, "GASCAN—An Interactive Code for Thermal Analysis of Gas Turbine Systems," presented at the ASME Winter Annual Meeting, Anaheim, CA.

Elmasri, M. A., 1986b, "On Thermodynamics of Gas Turbine Cycles: Part 2—A Model for Expansion in Cooled Turbines," ASME JOURNAL OF ENGINEERING FOR GAS TURBINES AND POWER, Vol. 108, pp. 151–159.

Elmasri, M. A., and Pourkey, F., 1986, "Prediction of Cooling Flow Requirements for Advanced Utility Gas Turbines, Part 1: Analysis and Scaling of the Effectiveness Curve," ASME Paper No. 86-WA/HT-43.

Elmasri, M. A., 1988a, US patent 4,753,068.

Elmasri, M. A., 1988b, "A Flexible, Efficient Gas Turbine Cogeneration Cycle With a Novel Dual-Mode Heat Recovery System," presented at ASME Cogen-Turbo, 2nd International Symposium on Turbomachinery, Combined-Cycle Technologies and Cogeneration, Montreux, Switzerland.

GTPRO, 1992, "GTPRO User's Manual," Thermoflow, Inc., Wayland, MA.

Hånde, B., 1992, "Simulation of Steam Injected Gas Turbines," Dissertation, Norwegian Institute of Technology, University of Trondheim, Norway.

Kunz, F., 1982, "VISUM; Benutzer-Handbuch Version 2.0 (1967 IFC)," Siemens/KWU, Erlangen, Germany.

Louis, J. F., 1977, "Systematic Studies of Heat Transfer and Film Cooling Effectiveness," AGARD CP 2291.

Louis, J. F., Hiraoka, K., and Elmasri, M. A., 1983, "A Comparative Study of the Influence of Different Means of Turbine Cooling on Gas Turbine Performance," ASME Paper No. 83-GT-180.

Olikara, C., and Borman, G. L., 1975, "A Computer Program for Calculating Properties of Equilibrium Combustion Products With Some Applications to I.C. Engines," SAE Paper No. 750468.

Rohsenow, W. M., 1955, "Effect of Turbine-Blade Cooling on Efficiency of a Simple Gas Turbine Power Plant," ASME Paper No. 55-A-120.

Shapiro, A. H., 1953, *The Dynamics and Thermodynamics of Compressible Fluid Flow*, Vol. I, The Ronald Press Company, New York.

Staudt, J. E., Birkholz, D., Jansen, W., and Tuzson, J. J., 1989, "Intercooled and Recuperated Dresser-Rand DC990 Gas Turbine Engine," ASME Paper No. 89-GT-3.

Thomas, W. J. R., and Higson, A. J., 1985, "An Intercooled Regenerative Rolls-Royce Spey Gas Turbine," ASME Paper No. 85-IGT-59.

Valland, H., and Pedersen, E., 1988, "User's Manual for the In-House Version of the Olikara & Borman Property Data Computer Code," Institute of Technology, Trondheim, Norway.

APPENDIX

Assumptions used in the present work are given below. If four different numbers are given, these refer to gas turbine classes A–D, respectively.

Ambient: 15°C, 1.013 bar, 60 percent RH
Cooling water temperature: 15°C
Fuel: CH_4, LHV = 50056 kJ/kg, T = 25°C

Gas Turbine Cycle

Combustion efficiency (percent): 99.7, 99.7, 99.5, 99.0
Total pressure losses (percent):
air filter: 1.0, combustor: 4.0, diffuser, 1.0, pipe to recuperator: 0.6, pipe from recuperator: 0.6, recuperator hot and cold side: 0.6, intercooler: 2.5, aftercooler: 2.5, superheater, boiler, economizer and feedwater preheater cold side (each): 5.0, superheater, boiler, economizer, and feedwater preheater hot side (each): 0.6, steam injection steam pipe: 10.0,
Heat losses:
pipe to recuperator: 1.0 K, pipe from recuperator: 1.0 K, recuperator (HTR) and superheater (each): 0.2 percent, recuperator (LTR), boiler, economizer, and feedwater preheater (each): 0.1 percent, steam injection steam pipe: 0.5 K, from turbine to HRSG inlet: 1.0 K.
Minimum recuperator temperature difference: 30 K
Exhaust gas-superheated steam temperature difference: 30 K
Minimum steam generator pinch point: 10 K
Economizer approach temperature: 5 K
Mechanical and generator efficiency (percent):
(average values including gear box when used) (percent): 98.2, 96.9, 98.1, 94.9
Auxiliary power requirement: 200 kW (per 100 kg/s of compressor air)
Maximum turbine blade metal temperature: 850°C
Minimum pressure difference between compressor bleed point and the cooled turbine stage: $p_{\text{bleed}} = p_{\text{turbine stage}} * 1.25$
Intercooler and aftercooler: the amount of water injected is such that the exit air is 15 K above the dew point temperature. Water injection temperature is 15°C.
Intercooler location in compressor: It is optimized in each cycle calculation.

Steam Cycle

Class A: Triple pressure reheat steam cycle, p_{steam}: HP = 120 RH = 30 IP = 16 LP = 3 bar
Class B: Dual pressure steam cycle, p_{steam}: HP = 80 LP = 5 bar
Class C: Dual pressure steam cycle, p_{steam}: HP = 60 LP = 5 bar
Class D: Single pressure steam cycle, p_{steam}: HP = 45 bar

HRSG

Pinch point: 10 K
Exhaust gas-superheated steam temperature difference: 20–30 K (30 for the hot end)
Economizer approach temperature: 5 K
Pressure drop steam pipes to turbine (percent): HP = 5, RH = 6, IP = 7, LP = 10
Heat loss steam pipes to turbine: 1 K
Pressure drop superheater, reheater, boiler, economizer, and feedwater preheater (cold side): 5 percent
HRSG pressure drop exhaust gas: 40 mbar
Deaerator pressure: 1.2 bar
Maximum steam temperature: 550°C

Steam Turbine

Pressure drop throttle/control valves: 2 percent
Pressure drop reheat return pipe: 3 percent
Isentropic efficiencies (percent) (before correction for moisture):
Class A: HP = 92 RH = 92 IP = 92 LP = 89
Class B: HP = 90 LP = 87
Class C: HP = 88 LP = 85
Class D: HP = 83
LP section leaving loss: 30 kJ/kg
Wilson line steam quality: 0.975 [kg/kg], below this steam quality the steam turbine efficiency is corrected for moisture (Bolland, 1990, 1991)
Auxiliary power fraction: 0.25 percent
Mechanical and generator efficiency (percent): 98.2, 97.0, 96.0, 95.0
Condenser pressure (bar): 0.04, 0.07, 0.07, 0.07
Pumps: mechanical efficiency: 92 percent, isentropic efficiency: 80 percent

Downloaded 02 Jun 2010 to 171.66.16.102. Redistribution subject to ASME license or copyright; see http://www.asme.org/terms/Terms_Use.cfm

W. Tabakoff

M. Metwally

A. Hamed

Department of Aerospace Engineering
and Engineering Mechanics,
University of Cincinnati,
Cincinnati, OH 45221

High-Temperature Coatings for Protection Against Turbine Deterioration

In this research, an investigation was conducted to study the fly ash particles associated with the erosion behavior of alloys and coatings that are widely used in gas and steam turbines. The erosion behavior of many alloys and protective coatings has been investigated experimentally at high temperatures using a specially designed wind erosion tunnel. The erosion results show the effect of velocity, temperature, and impact angle on the erosion rate.

Introduction

Gas and steam turbines operate in environments where the ingestion of solid particles is inevitable. In industrial applications and power generation, such as coal-burning boilers, fluidized beds, and gas turbines, solid particles are produced during the combustion of heavy oils, synthetic fuels, and pulverized coal. In commercial and military aircraft and naval installations, some of the mechanisms that cause solid particle ingestion are vortices generated during landing and takeoff, sand storms, volcanic ash, and thrust reverser efflux at low speed, which blows sand, ice, and dust into the engines. In steam turbines, the solid particles are principally boiler scale, mainly iron oxide, that break off and become entrained in the steam. Filters and separators can remove a large percentage of the solid particles, but significant amounts of small particles still pass through and enter the engines.

Due to their higher inertia, the solid particles deviate from the flow streamlines, impact the blade surfaces, and cause severe erosion damage. This damage is manifested by pitting and cutting of the blade leading and trailing edges and an increase in the blade surface roughness. The overall effects of these phenomena are to increase the pressure loss and to change the blade geometry. Continued operation under particulate flow conditions adversely affects the performance of the engines, as well as their lives, and can be detrimental to their reliability.

Gas turbine materials have developed rapidly beyond the conventional ferrous alloys consisting of steels and stainless steels of various compositions, physical, thermal, and mechanical history, and microstructure. Several nickel and cobalt base alloys have been developed and have been used widely in the hot section of gas turbines in order to meet complex high-temperature corrosion phenomena. Chromium additions have been used and they contribute to an improvement in high-temperature strength and oxidation resistance. Protective coatings have been used to enhance superalloy resistance to hot erosion–corrosion. Some of the most widely used coatings are diffusion coatings, overlay coatings, plasma-sprayed coatings, and ion implantation coatings. Chromium, platinum, radium, and silicon additions have been used in order to improve the erosion–corrosion resistance of the coatings.

Although physical, chemical, and mechanical properties of turbine alloys and coatings are documented satisfactorily, there are insufficient data about their rebound and erosion behavior, especially at high temperatures. Therefore, an experimental investigation has been conducted to study coal ash particle rebound characteristics and associated erosion behavior of many alloys and coatings subjected to particulate flow at high temperature. In this paper only the erosion behavior of alloys and protective coatings is reported. The experiments were performed at high temperature in a specially designed erosion wind tunnel. The experimental results show the effects of the main erosion parameters, namely velocity, temperature, and impact angle, on the erosion rates. Erosion models have been developed for the tested materials based on the experimental erosion data and restitution parameters.

Erosion Wind Tunnel

The high-temperature erosion test facility was designed to provide erosion and rebound data in the range of operating temperatures experienced in compressors and turbines. In addition to the high temperature, the facility properly simulates the erosion parameters that were determined to be important from an aerodynamic point of view. These parameters include particle velocity, angle of impact, particle size, particle concentration, and sample size. Close attention was given to the aerodynamic effects to insure that important parameters, such as the angle of impact, are not masked or altered.

A schematic of the erosion test facility is shown in Fig. 1. It consists of the following components: particle feeder (A),

Contributed by the International Gas Turbine Institute and presented at the 38th International Gas Turbine and Aeroengine Congress and Exposition, Cincinnati, Ohio, May 24–27, 1993. Manuscript received at ASME Headquarters March 3, 1993. Paper No. 93-GT-200. Associate Technical Editor: H. Lukas.

Copyright © 1995 by ASME

Downloaded 02 Jun 2010 to 171.66.16.102. Redistribution subject to ASME license or copyright; see http://www.asme.org/terms/Terms_Use.cfm

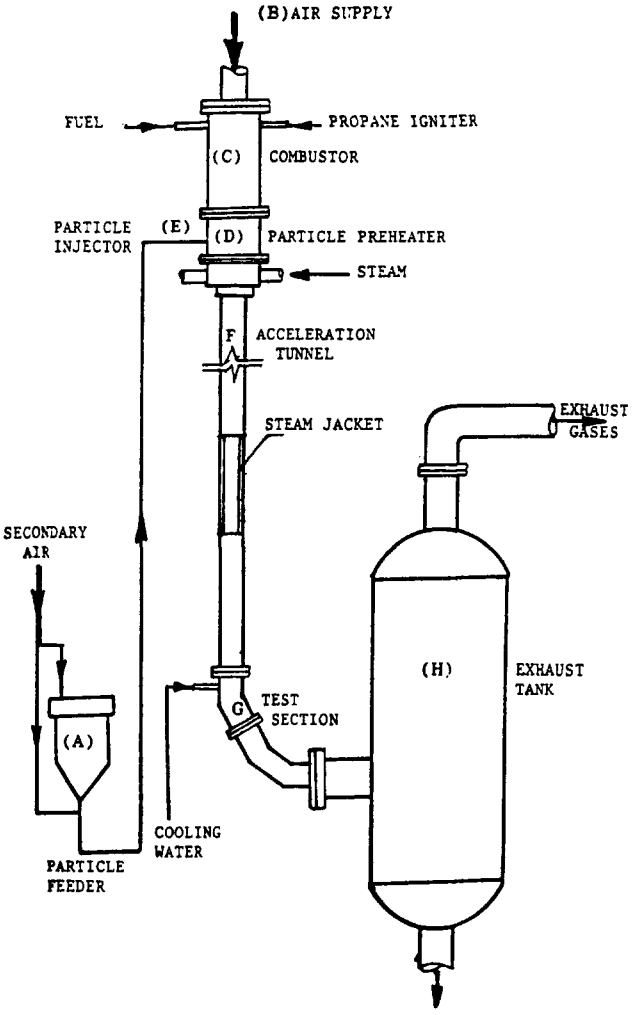

Fig. 1 Schematic of erosion test facility

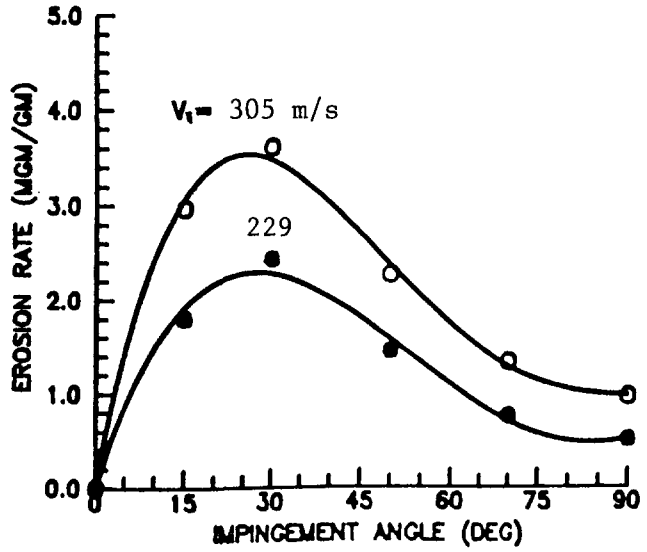

Fig. 2 410 stainless steel erosion rate variation with impingement angle: T = 550°C chromite particles

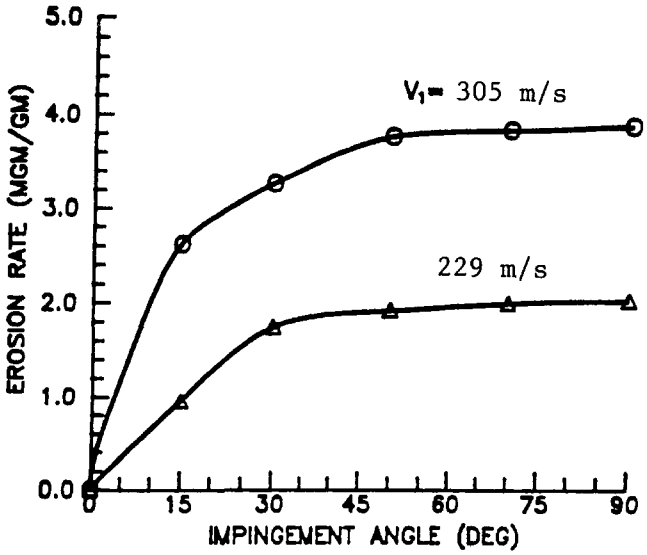

Fig. 3 LC-1B coating erosion rate variation with impingement angle: T = 550°C, chromite particles

Table 1 Typical chromite powder analysis

Constituent	Typical Range (Weight, %)
Chromium Oxide (Cr_2O_3)	45.5 - 46.5
Iron Oxide (FeO)	19.5 - 20.5
Alumina (Al_2O_3)	13.5 - 15.5
Magnesia (MgO)	9.3 - 10.5
Calcium Oxide (CaO)	0.2 - 0.4
Free Silica	0.8 - 1.5

main air supply pipe (B), combustor (C), particle preheater (D), particle injector (E), acceleration tunnel (F), test section (G), and exhaust tank (H).

The equipment functions as follows. A measured amount of abrasive grit of a given mixture of constituents is placed into the particle feeder (A). The particles are fed into a secondary air source and blown up to the particle preheater (D), and then to the injector (E), where they mix with the main air supply (B), which is heated by the combustor (C). The particles are then accelerated by the high-velocity air in a constant-area steam-cooled duct (F) and impact the specimen in the test section (G). The particulate flow is then mixed with the coolant and dumped in the exhaust tank. Figure 1 shows that the tunnel geometry is uninterrupted from the acceleration tunnel into the test section. In this manner the particle-laden flow is channeled over the specimen and the aerodynamics of the fluid passing over the sample are preserved.

A detailed description of the wind tunnel and the particle feeder is given by Tabakoff and Wakeman (1979).

Erosion Test Results

The erosion tests were conducted to obtain the erosion rate, which is defined as the ratio between the change in the sample mass and the mass of the impacting particles. In each test, the specimen was impacted by a preweighed dose of particles. After each particle dose had impacted the sample, it was taken out from the erosion tunnel and its surface was cleaned with air, then the specimen was weighed, and the change in specimen weight was recorded. The erosion rate was determined from the relation:

$$\text{erosion rate} = \frac{\text{change in mass of sample}}{\text{mass of impacting particles}}$$

The experimental results show the effect of the main erosion

Downloaded 02 Jun 2010 to 171.66.16.102. Redistribution subject to ASME license or copyright; see http://www.asme.org/terms/Terms_Use.cfm

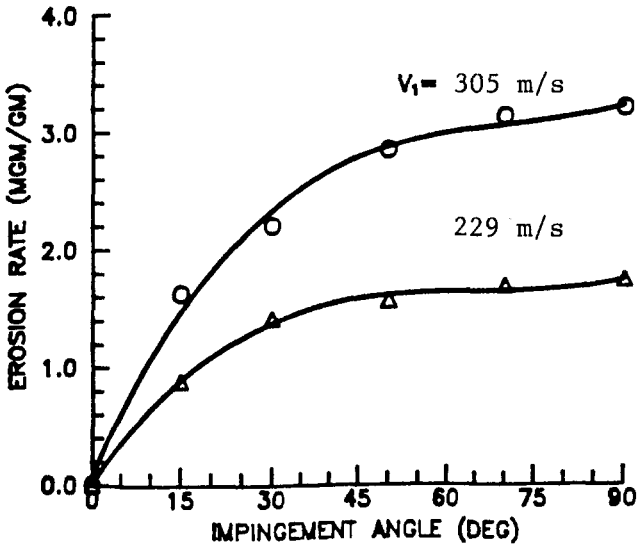

Fig. 4 LC-1H coating erosion rate variation with impingement angle: T = 550°C, chromite particles

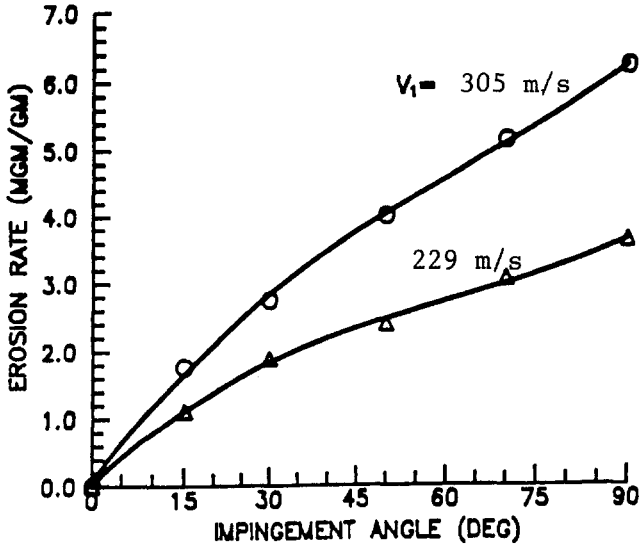

Fig. 5 Plasma spray coating erosion rate variation with impingement angle: T = 550°C, chromite particles

parameters, namely, impact velocity, impact angle, and sample temperature on the material erosion rate. Super alloys and coatings are widely used in gas turbine components. In the present investigation, the erosion behavior of coatings and alloys intended for steam turbine components have been studied. The experimental data for 410 stainless steel and LC1-1B, LC-1H, SDG-2207 and plasma spray coatings are presented. Since the solid particles in steam turbines are mainly boiler scales, chromite particles have been used in the present investigation. The chromite particle chemical analysis is listed in Table 1, and the particle distribution is from 2 μm to 176 μm. Erosion testing for all samples was performed for impact velocities of 304.8 m/s and 228.6 m/s at a temperature of 550°C.

Impingement Angle Effect on the Erosion Rate. It is well known that the erosion rate is a function of particle impingement angle. For a ductile material, the erosion rate increases from zero at 0 deg particle impact angle to a maximum as impact angle is increased. After reaching a maximum, the erosion rate decreases to a minimum value at 90 deg. On the other hand, the erosion rate of a brittle material increases from zero at 0 deg impact angle to a maximum value at 90 deg. All four coatings have INCO 718 as substrate and were supplied by Union Carbide Company.

410 Stainless Steel. AISI Type 410 is a hardenable 12 percent chromium stainless steel. It offers a wide range of mechanical properties and has good resistance to corrosion and oxidation. Among its many applications are steam turbine components. Therefore, it has been included in the test program.

The variation of 410 stainless steel erosion rate with impingement angle is shown in Fig. 2 for two velocities. The test results indicate that 410 stainless steel has ductile erosion behavior with maximum erosion rate at 25 deg impact angle. This figure also illustrates qualitatively the strong effect of particle impact velocity on the erosion rate.

LC-1B Coating. LC-1B is a detonation gun coating containing about 65 percent chromium carbide with the balance 80 Ni/20 Cr alloy (nichrome). The nichrome powder size was 44 μm fraction. It was developed for steam turbine components. The impingement angle effect on the erosion rate of LC-1B coating exhibits a brittle erosion pattern with maximum erosion rate at 90 deg as shown in Fig. 3. Initially the erosion rate increases rapidly with impingement angle, reaching a maximum in the 30 deg–45 deg impingement angle range, after which it remains approximately constant.

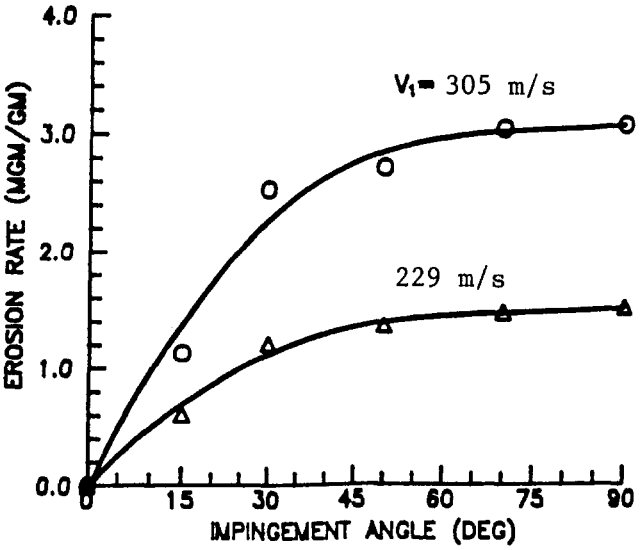

Fig. 6 SDG-2207 coating erosion rate variation with impingement angle: T = 550°C, chromite particles

LC-1H Coating. LC-1H is a detonation gun coating containing 80 percent chromium carbide, of Cr_7C_3 composition, and 20 percent nichrome. The nichrome powder used for LC-1H is of finer size than the powder used for LC-1B, being a 20 μm fraction. This coating was developed for steam turbines. Figure 4 presents the variation of LC-1H erosion rate with impingement angle. The erosion rate reaches its maximum value at 90 deg which indicates the brittle nature of LC-1H coating. Inspection of Figs. 3 and 4 reveals that LC-1H coating has better erosion resistance than LC-1B coating at both test velocities. The superiority of LC-1H over LC-1B, which employs powders mixed in the same ratio, is attributed to the finer particle size powders (20 μm) used for LC-1H. In the range of 45 deg–90 deg impingement angle, LC-1H shows only a small increase in the erosion rate with increasing impingement angle.

Plasma Spray Coating. This coating is a plasma deposit of 85 percent Cr_3C_2 and 15 percent FeCrAlY powder, and it

Downloaded 02 Jun 2010 to 171.66.16.102. Redistribution subject to ASME license or copyright; see http://www.asme.org/terms/Terms_Use.cfm

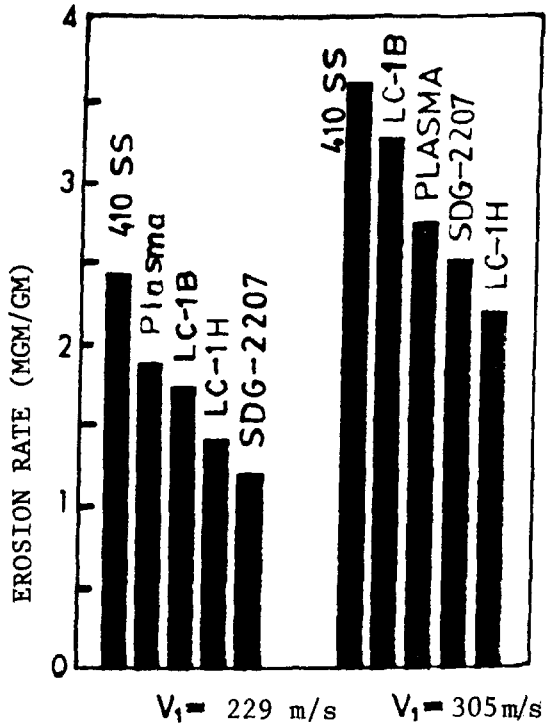

Fig. 7 Comparison of erosion rates of coatings and 410 stainless steel alloy: β_1 = 30 deg, chromite particles

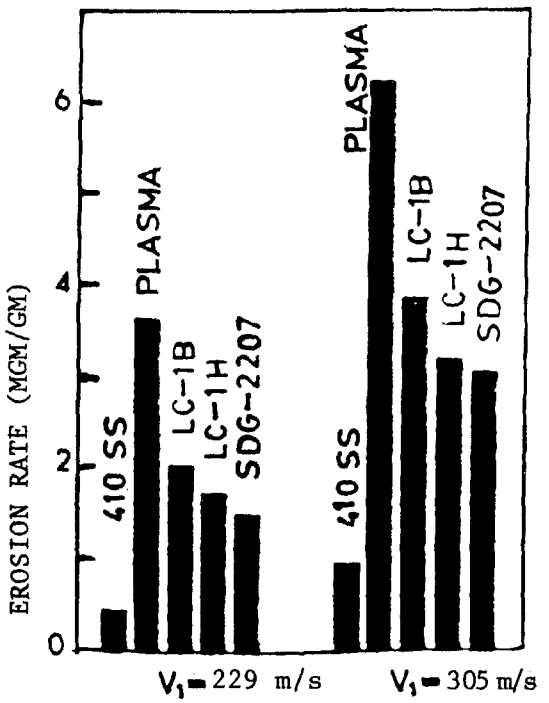

Fig. 8 Comparison of erosion rates of coatings and 410 stainless steel alloy: β_1 = 90 deg chromite particles

was given a 72 hour exposure at 550°C before testing. The erosion test results show a continuous increase of plasma-coating erosion rate with increasing impingement angle, as shown in Fig. 5. The figure indicates that the erosion rate curves follow the familiar form of brittle erosion with maximum at 90 deg. The velocity effect on the erosion rate can be clearly observed in Fig. 5.

SDG-2207 Coating. SDG-2207 is a super D-Gun coating

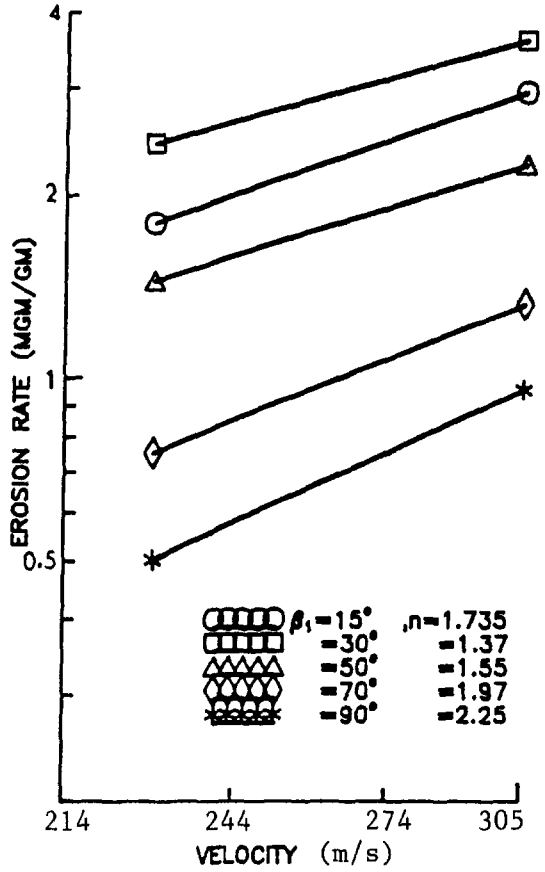

Fig. 9 Velocity effect on 410 stainless steel erosion rate at different angles: T = 550°C, chromite particles

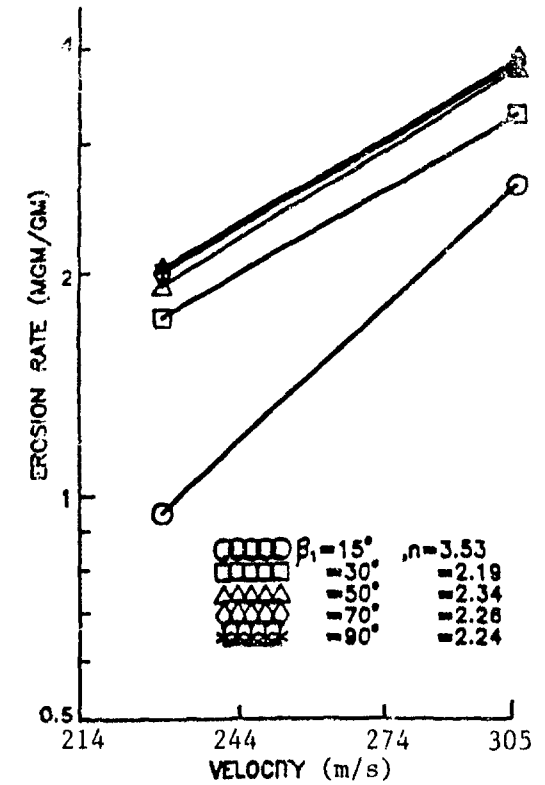

Fig. 10 Velocity effect on LC-1B coating erosion rate at different angles: T = 550°C, chromite particles

Downloaded 02 Jun 2010 to 171.66.16.102. Redistribution subject to ASME license or copyright; see http://www.asme.org/terms/Terms_Use.cfm

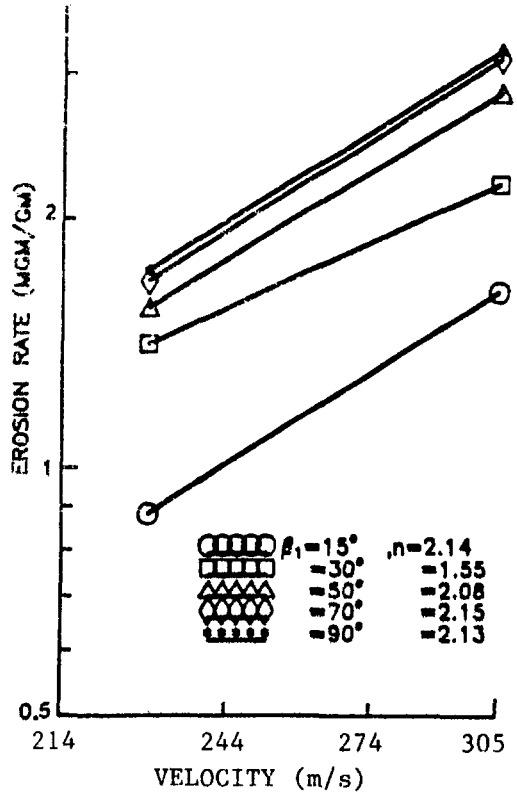

Fig. 11 Velocity effect on LC-1H coating erosion rate at different angles: T = 550°C, chromite particles

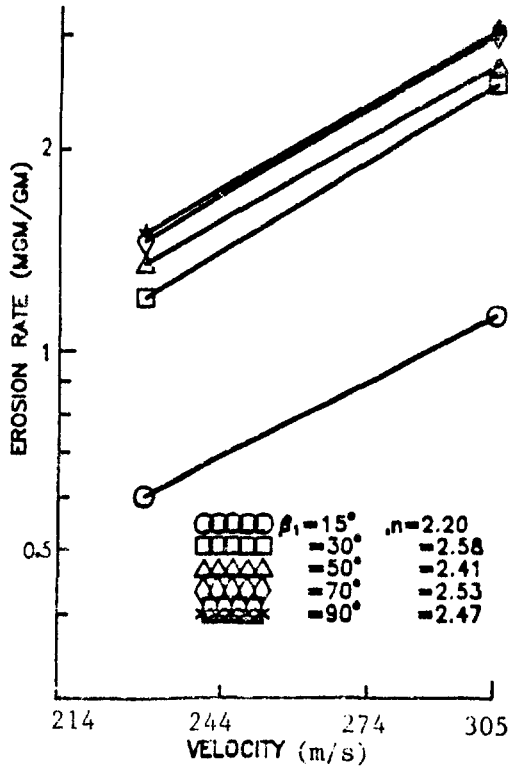

Fig. 13 Velocity effect on SDG-2207 coating erosion rate at different angles: T = 550°C, chromite particles

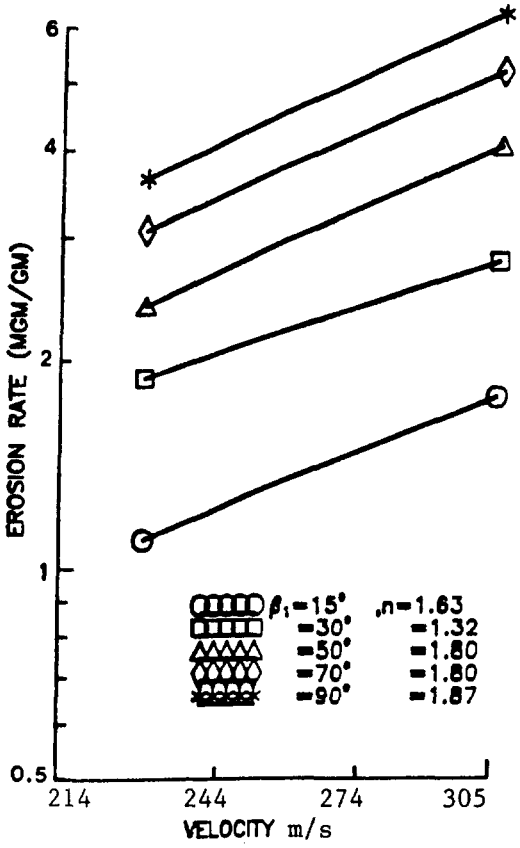

Fig. 12 Velocity effect on plasma spray coating erosion rate at different angles: T = 550°C, chromite particles

made from a powder mix containing 89 percent Cr_3C_2 and 11 percent Inconel 718 powder. The influence of the impingement angle on the erosion rate of SDG-2207 coating is presented in Fig. 6 for 228.6 m/s and 304.8 m/s particle impact velocity. The figure illustrates that the coating exhibits brittle erosion pattern with maximum erosion at 90 deg. The erosion rate shows only a small variation with impingement angle in the 45 deg–90 deg range.

Comparison Between 410 Stainless Steel and Coating Erosion Rates. Figures 7 and 8 present erosion rates for 410 stainless steel, LC-1B, LC-1H, SDG-2207 and plasma coatings at oblique (30 deg) and normal (90 deg) impact angles for 228.6 m/s and 304.8 m/s impact velocities. At small impact angle ($\leq$ 30 deg), the tested coatings showed better erosion resistance than 410 stainless steel. Therefore, at small impact angles, these coatings provide good erosion resistance and significantly prolong the life of the steam turbine components. SDG-2207 coating, whose erosion rate is one half the erosion rate of 410 stainless steel, offers the best erosion resistance at 30 deg impact angle and 228.6 m/s impact velocity as shown in Fig. 7. However, at an impact velocity of 304.8 m/s, LC-1H coating exhibits the lowest erosion rate (40 percent less than 410 stainless steel erosion rate) compared to the other coatings.

At large impact angle ($>$ 35 deg), the coating erosion rates were much higher than stainless steel erosion rate due to the coating brittleness. Figure 8 indicates that the 410 stainless steel erosion rate is less than one third the erosion rate of the best coating (SDG-2207) at 90 deg.

Velocity Effect on Erosion Rates. The influence of particle impact velocity on 410 stainless steel and the coatings is shown in Figs. 9–13 for different impact angles at a sample temperature of 1022°F. In these figures, the solid lines represent the power law curve fit of the experimental data at each angle. The velocity exponent, n, obtained by curve fitting is listed in the figures for each impingement angle. For 410

Downloaded 02 Jun 2010 to 171.66.16.102. Redistribution subject to ASME license or copyright; see http://www.asme.org/terms/Terms_Use.cfm

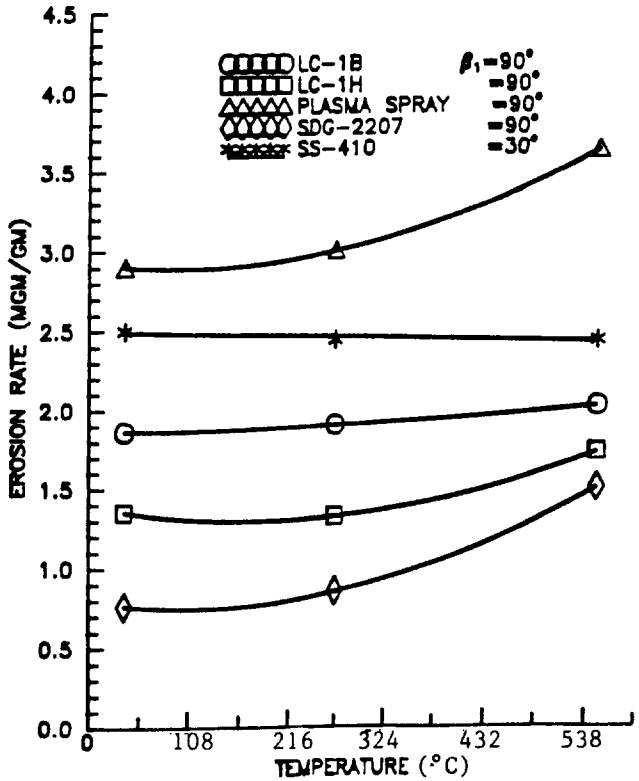

Fig. 14 Variation of erosion rate with temperature for LC-1B, LC-1H, SDG-2207, and plasma spray coatings and 410 stainless steel

stainless steel, the velocity exponent varies from 1.37 to 2.25 (Fig. 9). Figure 10 shows that LC-1B erosion rate is proportional to particle impact velocity to power ranging from 3.53 to 2.19. The velocity exponent obtained for LC-1H coating is in the vicinity of 2 (Fig. 11), while the plasma spray coating (Fig. 13) shows a velocity exponent less than 2 (n = 1.32–1.87). Figure 13 reveals that SDG-2207 coating has a velocity exponent of about 2.5. The different values of the velocity exponents for the different coatings for the same test conditions indicate the material properties effect on the erosion behavior. The variation of the exponent, n, for each coating reveals that n is dependent on the impact angle. The strong effect of the velocity on the material erosion rate is manifested by the high value of the velocity exponent.

Temperature Effect on the Erosion Rate. To study the temperature effect on erosion rates, the investigated materials were tested at ambient, 260°C and 550°C sample temperatures for particle velocity of 228.6 m/s and maximum erosion angles (90 deg for coatings and 30 deg for 410 stainless steel). The experimental results are presented in Fig. 14. This figure shows that the temperature has a similar effect on the tested coatings. The coating erosion rates continuously increase with increasing temperature. Stainless steel 410 shows a weak temperature effect in the testing temperature range. Increasing the temperature from 21.1°C to 550°C, doubled the erosion rate of SDG-2207 coating, and increased the erosion rate of the other coatings by 20 percent as can be observed in Fig. 14. Additional information for the same coating is reported by Walsh and Tabakoff (1990). A theoretical model developed for superalloys and coating erosion rates is reported by Tabakoff et al. (1992).

Conclusions

1 Different coatings, which can be used as erosion protection in steam turbines, were tested in an erosion wind tunnel, which simulates the velocity, temperature, and particle impacting angle.
2 Of the coatings tested, SDG-2207 exhibited the lowest erosion rates at low angles of incidence and LC-1H was next lowest.
3 At high impact angles (greater than 35 deg), all the coatings exhibited erosion rates that were higher than 410 stainless steel.
4 The improvements that these coatings provide over uncoated substrates allow them to find wide application in steam and gas turbines.

Acknowledgments

This research was sponsored by the U.S. Department of Energy, Contract No. 19X-89628C, Oak Ridge National Laboratory, Oak Ridge, Tennessee. Dr. Rod Judkins, Technical Monitor, is most gratefully acknowledged. The coatings were prepared by Union Carbide, and we would like to thank Dr. Patrick Walsh for his assistance.

References

Tabakoff, W., Hamed, A., Metwally, A., and Yeuan, J., 1992, "Study of Particle Rebound Characteristics and Material Erosion at High Temperature," DOE Report ORNL/Sub/84-89628/04, Apr.

Tabakoff, W., and Wakeman, T., 1979, "Test Facility for Material Erosion at High Temperature," ASTM Special Publication 664, pp. 123–135.

Walsh, P. N., and Tabakoff, W., 1990, "Comparative Erosion Resistance of Coatings Intended for Steam Turbine Components," *Advances in Steam Turbine Technology for Power Generation*, ASME PWR-Vol. 10, pp. 1–8.

Downloaded 02 Jun 2010 to 171.66.16.102. Redistribution subject to ASME license or copyright; see http://www.asme.org/terms/Terms_Use.cfm

Coatings for the Protection of Turbine Blades From Erosion

P. N. Walsh

J. M. Quets

R. C. Tucker, Jr.

Praxair Surface Technologies, Inc.
Indianapolis, IN 46224

Many types of turbines, including aircraft gas turbines, steam turbines, and power recovery turbines, suffer from solid particle erosion caused by a variety of materials ingested into the machines. Utilization of various laboratory erosion tests tailored to the specific application by using various erodents, temperatures, velocities, and angles of impact, have been shown to be effective in the development and selection of coatings for the erosion protection of turbine blades and other components. Detonation gun coatings have demonstrated their efficacy in providing substantial protection in many situations. It has now been shown that several tungsten carbide and chromium carbide Super D-Gun™ coatings not only have better erosion resistance than their D-Gun analogs, but cause little or no degradation of the fatigue properties of the blade alloys. Nonetheless, caution should be employed in the application of any laboratory data to a specific situation and additional testing done as warranted by the turbine designer.

Introduction

Erosion by solid particles is a problem common to the operation of many types of turbines. For example, aircraft gas turbine compressors ingest a variety of debris from runways [1], the initial stages of steam turbines suffer from scale that spalls from the heat exchanger tubing [2], and power recovery turbines are subjected to entrained process materials such as catalyst particles or blast furnace effluent [3]. The resulting erosion causes a loss in efficiency due to a reduction in chord width, tip recession, or surface roughening. It may also reduce service life, increase down time, cause unscheduled shut downs, and increase replacement or repair costs. The overall cost to industry is extremely large.

Typical blade and vane alloys, whether they are aluminum, titanium, steel, or superalloys, do not have adequate erosion resistance. Moreover, because of structural, mechanical, and thermal property requirements, it is unlikely they ever will have. A solution to the problem for many applications has been the use of coatings. For a coating to be useful, however, it must not only be substantially more erosion resistant than the bare blade alloy, but it must also be stable in the service environment (i.e., be thermally stable, corrosion resistant, etc.) and not detrimentally affect the performance of the substrate (e.g., not significantly reduce the fatigue strength of the blade). Detonation gun and Super D-Gun coatings based on tungsten and chromium carbides have been shown to satisfy these requirements for a variety of applications. Several of these coatings and applications are described in this paper.

Coatings

Detonation gun coatings [4] are produced by introducing a small amount of powder as a pulse into an explosive gas mixture of oxygen and acetylene in a long gun barrel and then detonating the gas. The resulting detonation wave moving down the barrel heats the powder particles to near their melting point and accelerates them to a velocity of about 750 m/s. The molten or nearly molten particles impacting on the surface to be coated form a very dense, well bonded coating. For more than three decades detonation gun (D-Gun) coatings have been the hallmark of thermal spray coatings, largely because of the extremely high velocity and well-controlled temperature imparted to the powder particles. Recently, a new family of coatings has been developed using Super D-Gun [4] technology. By changing the gases used in the detonation process and other modifications, the powder particle velocity has been increased to about 1000 m/s with a concomitant near doubling of the kinetic energy. The result is coatings that are even more dense and more strongly bonded. An additional benefit achieved with Super D-Gun coatings is a unique control of the residual stress in the coatings. While most thermal spray coatings have an as-deposited residual tensile stress as the result of the thermal contraction of the cooling particles on a cold substrate, well-controlled compressive residual stresses can be developed in Super D-Gun coatings.

A wide variety of ceramic, metallic and cermet coatings have been made; those of primary interest here are tungsten carbide–cobalt, (tungsten, titanium) carbide–nickel, chromium carbide–nickel chromium, and chromium carbide–Alloy 718. The compositions and some selected properties of these coatings are shown in Table 1. Representative micrographs are shown in Fig. 1. As noted earlier, of particular concern are the effects of a coating on the properties of the substrate, especially the fatigue properties when rotating turbine components are to be coated. The effects of several D-Gun coatings are compared with their Super D-Gun

[1]Super D-Gun™ is a trademark of Praxair S. T. Technology, Inc.

Contributed by the International Gas Turbine Institute and presented at the 38th International Gas Turbine and Aeroengine Congress and Exposition, Cincinnati, Ohio, May 24–27, 1993. Manuscript received at ASME Headquarters March 10, 1993. Paper No. 93-GT-291. Associate Technical Editor: H. Lukas.

Copyright © 1995 by ASME

Downloaded 02 Jun 2010 to 171.66.16.102. Redistribution subject to ASME license or copyright; see http://www.asme.org/terms/Terms_Use.cfm

Table 1 Characteristics of coatings

Coating	Deposition Method	Composition	Density g/cc	% Strain [5] to fracture
UCAR WT-1	D-Gun	17 Ni + 83[(W, Ti)C]	8.6	0.24
SDG 2002	Super D-Gun	86W-12Co-2c	14.2	0.64
UCAR LC-1H	D-Gun	20 [80Ni20Cr] +80 [Cr_7C_3]	6.3	0.30
SDG 2207	Super D-Gun	15[IN 718] +85 [Cr_5C_3]	6.3	0.37

Table 2 Characteristics of erosion tests

Erodent	Temp °C	Velocity m/s	Test Site	Target Application	Ref.
− 120μm chromite	550	305	Univ. of Cincinnati	Steam Turbine	8
50μm alumina	25	49	PSTI Lab	Aircraft Compressor	7
27μm alumina	25	91	PSTI Lab	Power Recovery	9

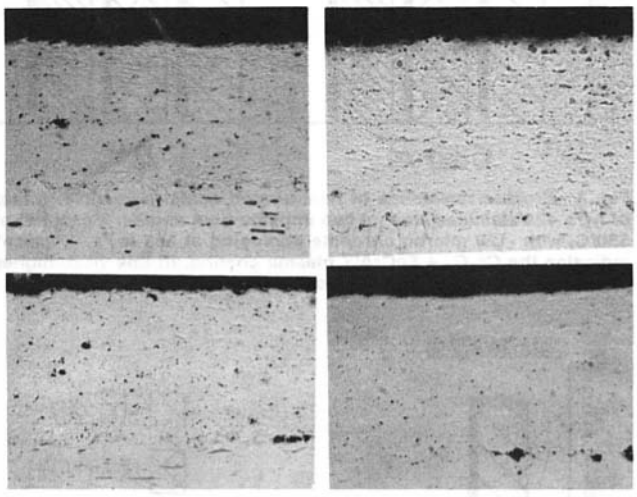

Fig. 1 Microstructures of coatings: clockwise from top left: UCAR WT-1, SDG 2002, SDG 2207, UCAR LC-1H. The SDG 2207 is 300 μm thick.

counterparts in Figs. 2–4 [6]. In these figures, the number of cycles to failure in a tension-tension fatigue test is plotted against the maximum tensile stress applied, in conventional S/N plots. It can readily be seen that while the D-Gun coatings caused a significant reduction in the fatigue properties of the titanium and steel substrates tested, a characteristic that had to be taken into account in the use of these coatings, the Super D-Gun coatings caused no such degradation, in fact improving performance in a few instances. (It should be kept in mind that coatings on test specimens may differ somewhat from those of actual parts due to geometry and other effects so additional testing by users may be needed.)

Testing for Specific Erosion Applications

A major problem in any practical materials development program is the simulation of the service environment in the laboratory with sufficient accuracy to rank materials at least relatively in a meaningful manner. This problem seems to be particularly acute in the field of erosion. Materials react differently, not only as a function of the angle of impact, but also as a function of temperature and the composition, size and shape of the erodent. This issue was explored extensively by Walsh [7] with regard to the erosion of steam turbines and

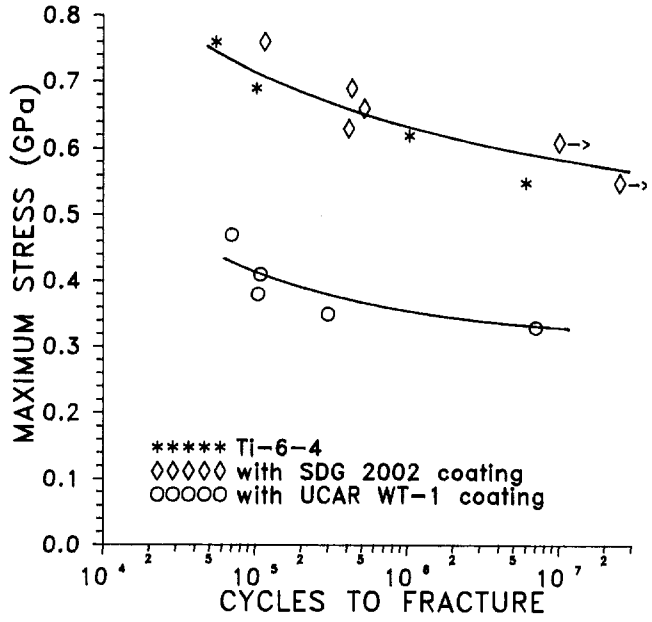

Fig. 2 High cycle tension-tension (R = 0.1) fatigue S/N curves for stress relieved Ti-6-4 specimens coated with SDG 2002 and UCAR WT-1 coatings

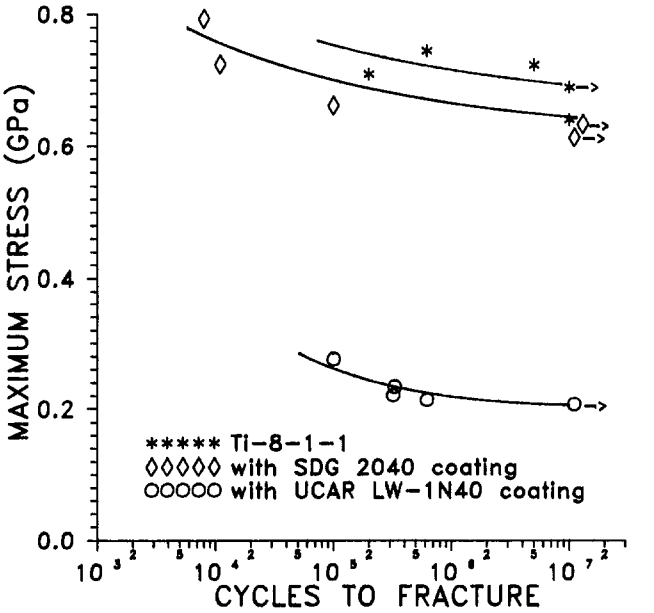

Fig. 3 High cycle tension-tension (R = 0.1) fatigue S/N curves for stress relieved Ti-8-1-1 specimens coated with SDG 2040 and UCAR LW-1N40 coatings

noted by Gill and Quets [8] with regard to aircraft gas turbine compressors. Table 2 contains the parameters for the erosion testing used here as well as the target applications. Greater detail on the test procedures can be found in the references listed in Table 2.

Steam Turbine Solid Particle Erosion. The most relevant testing to simulate the erosion caused by the exfoliation of magnetite boiler scale in steam turbines was found [7] to be that using sub-120 micron iron chromite ($Fe_2Cr_2O_4$) particles at impact angles of 15 to 30 deg. Tests at 550° C and 305 m/s (close to the turbine conditions) were run in a test apparatus at the University of Cincinnati under the direction of Prof. W. Tabakoff. Coatings consisting of a mixture of chromium

Downloaded 02 Jun 2010 to 171.66.16.102. Redistribution subject to ASME license or copyright; see http://www.asme.org/terms/Terms_Use.cfm

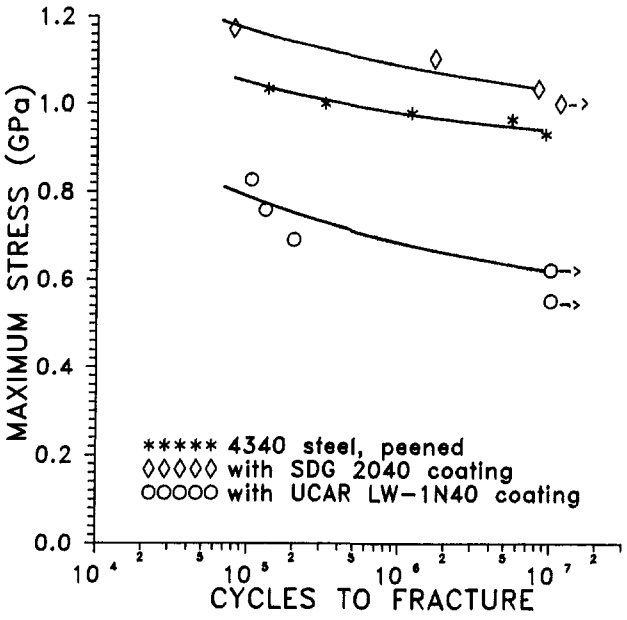

Fig. 4 High cycle tension-tension (R = 0.1) fatigue S / N curves for peened 4340 steel specimens coated with SDG 2040 and UCAR LW-1N40 coatings

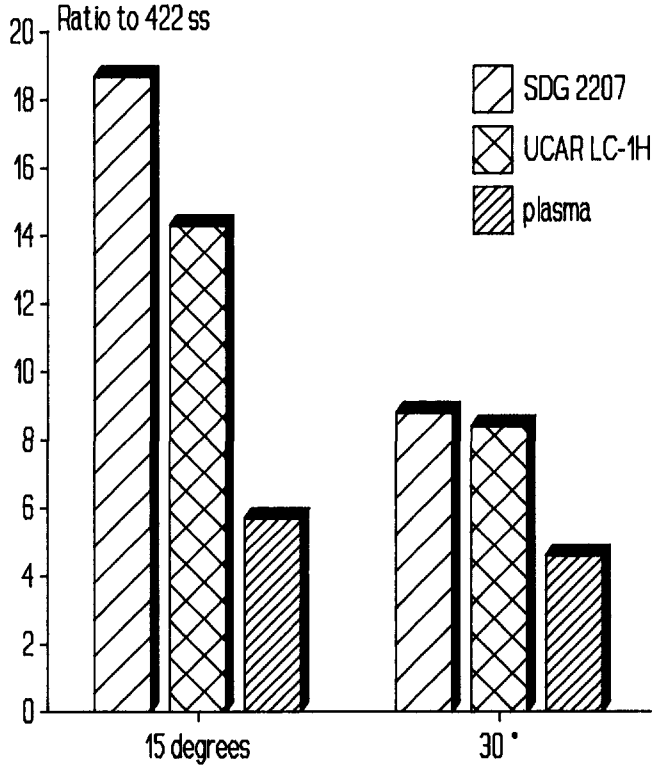

Fig. 5 Erosion resistance of heat-treated coatings *relative to that of type 422 stainless steel* at two impingement angles. Measured at 550°C, with -120 micron chromite impinging at 305 m / s. "Plasma" indicates the Cr_3C_2 + FeCrAlY plasma coating. In this view, higher values correspond to greater erosion resistance.

carbide with a nickel chromium alloy (D-Gun) or Alloy 718 (Super D-Gun) were compared with bare Type 422 stainless steel, the blade alloy, and a plasma-deposited composition developed by General Electric Company under contract to the Electric Power Research Institute (EPRI) [10]. The coatings were tested as deposited and after heat treatment in air for 72 h at 550° C, a temperature close to the turbine operating temperature and required in the EPRI coating prescription. The results for the heat-treated coatings are shown in Fig. 5. In-house room temperature tests at 49 m/s with the same erodent were also run, Fig. 6. The lower erosion rate measured for the D-Gun coating, UCAR LC-1H, is consistent with service experience of its effectiveness. The even better performance indicated for the Super D-Gun coating, SDG 2207, is currently being evaluated in field tests.

Aircraft Gas Turbine Compressor Erosion. The erosion caused by runway debris in the compressor section of aircraft gas turbine engines can be reasonably simulated using nominally 50-μm-dia alumina particles at low angles of impact. A D-Gun coating of tungsten, titanium carbide–nickel (UCAR WT-1) has been extensively used on titanium compressor blades in the lower temperature stages of compressors and was compared with a new Super D-Gun coating of tungsten carbide–cobalt (SDG 2002) in a laboratory test at 49 m/s at room temperature. The results are shown in Fig. 7. Based on these results and similar results in engine testing, combined with the very favorable fatigue benefits described previously, the new coating has supplanted the old in some applications.

In the higher temperature stages of compressors, the oxidation resistances of the tungsten carbide based coatings may be inadequate. The chromium-carbide-based coating UCAR LC-1H, discussed earlier in connection with steam turbines, has been shown to be very effective in this regime.

Power Recovery Turbine Erosion. The coating required for a given power recovery turbine is, of course, a function of the erodent and the environment. An example is the use of UCAR LC-1C, a D-Gun chromium carbide–nickel, chromium analog of LC-1H, already described. Here, however, the erodent is better simulated by a fine alumina, Fig. 8. Even though this coating continues to provide excellent service, an improvement is being sought with a Super D-Gun analog, also shown in Fig. 8.

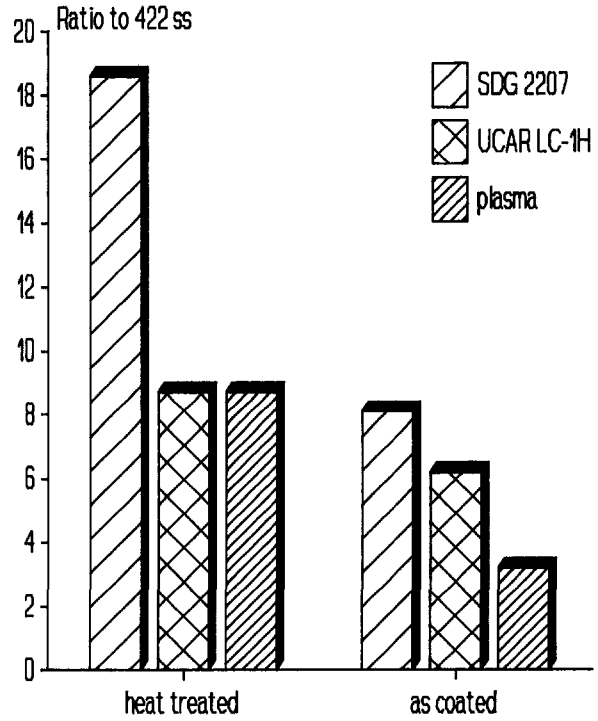

Fig. 6 Erosion resistance of coatings *relative to that of type 422 stainless steel* at 20 deg impingement angle. Measured at room temperature with -120 μm chromite impinging at 49 m / s. "Plasma" indicates the Cr_3C_2 + FeCrAlY plasma coating.

In another power recovery turbine application, turbines

Downloaded 02 Jun 2010 to 171.66.16.102. Redistribution subject to ASME license or copyright; see http://www.asme.org/terms/Terms_Use.cfm

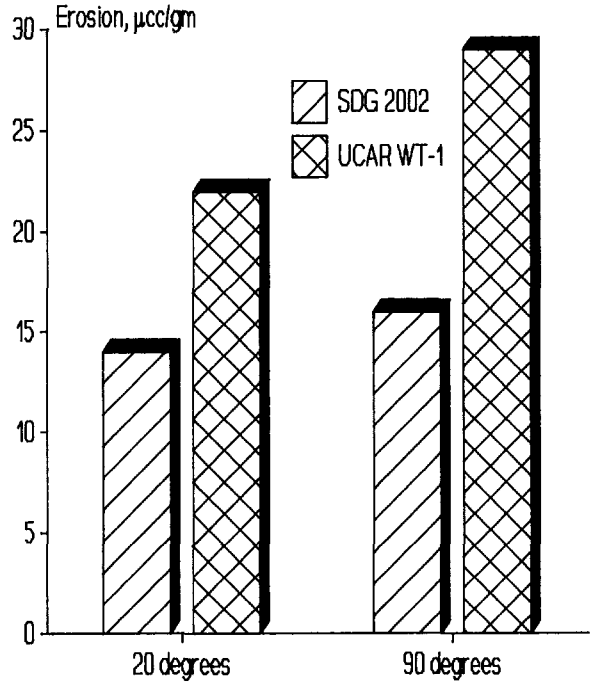

Fig. 7 Erosion rates of coatings for aircraft gas turbine compressor protection. Measured at room temperature with 50 μm alumina impinging. In this view, lower values correspond to greater erosion resistance.

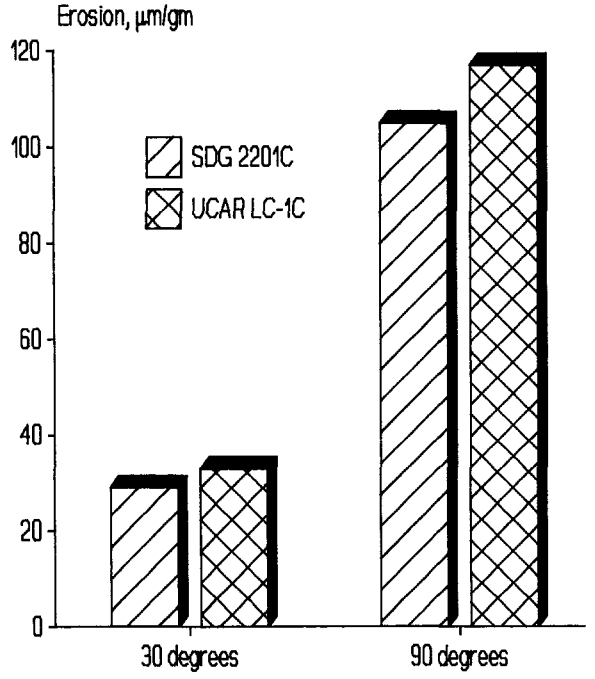

Fig. 8 Erosion rates of chromium carbide coatings for power recovery turbine protection. Measured at two angles at room temperature with 27 μm alumina impinging.

extracting energy from blast furnace off-gas, a tungsten carbide–cobalt coating (UCAR LW-1N40) has proven effective. Nonetheless, Fig. 9 indicates that further improvement might be obtained by using SDG 2040, a Super D-Gun analog.

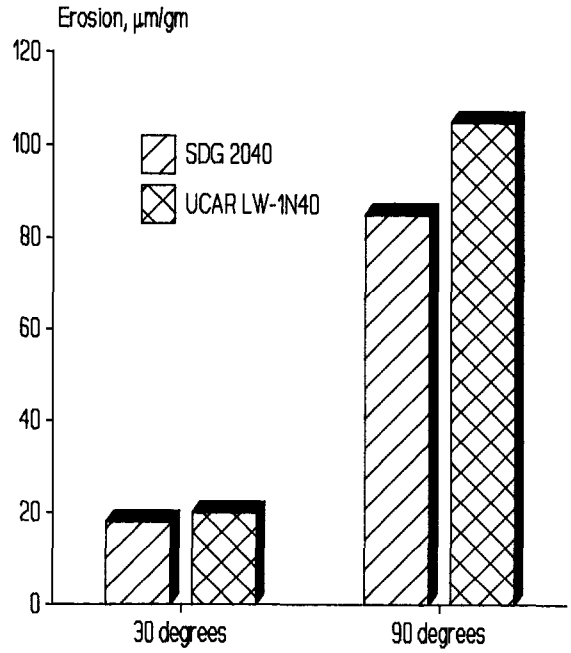

Fig. 9 Erosion rates of tungsten carbide coatings for power recovery turbine protection. Measured at two angles at room temperature with 27 μm alumina impinging.

Conclusions

The utilization of various laboratory erosion tests tailored to the specific application by using various erodents, temperatures, velocities, and angles of impact, has been shown to be effective in the development and selection of coatings for the erosion protection of turbine components. Examples have included coatings for blades in steam turbines, the compressor sections of aircraft gas turbines, and power recovery turbines.

It has been shown that several tungsten carbide and chromium carbide Super D-Gun coatings not only have better erosion resistance than their D-Gun analogs, but cause little or no degradation of the fatigue properties of the blade alloys. Caution should be used in the application of any laboratory data to specific hardware designs and additional testing done if warranted by the turbine designer.

References

1 Tucker, R. C., Jr., and Nitta, H., "Detonation Gun Coatings—Coating Characteristics and Applications," ATTAC'88, Osaka, Japan, May 1988.

2 McCloskey, T. H., and Bellanca, C., "Minimizing the Effects of Solid Particle Erosion in Utility Steam Turbines," in: *Solid Particle Erosion of Steam Turbine Components: 1989 Workshop*, EPRI GS-6535, 1989.

3 Wolektarski, W., *Proceedings of the 11th Turbomachinery Symposium*, Texas A & M University, College Station, TX 1982.

4 Tucker, R. C., Jr., and Nitta, H., "Detonation Gun and Super D-Gun Coating Processes," *J. High Temp. Soc. Japan*, Vol. 18 Supplement, p. 204, 1992.

5 Cox, L. C., "The Four Point Bend Test as a Tool for Coating Characterization," *Surface and Coatings Technology*, Vol. 36, 1988, pp. 807–815.

6 Gill, B. J., and Quets, J. M., "Wear and Fatigue Resistant Coatings From the New Super Detonation Gun Process," presented at SURFAIR, France, 1992.

7 Walsh, P. N., "Erosion Resistance of Coatings at Steam Turbine Temperatures," in: *Steam Turbine-Generator Developments for the Power Turbine Industry*, ASME PWR-Vol. 18, 1992.

8 Tabakoff, W., and Wakeman, T., "Test Facility for Material Erosion at High Temperature," ASTM Special Publication 664, 1979, p. 129.

9 ASTM G76-83, "Practice for Conducting Erosion Tests by Solid Particle Impingement Using Gas Jets."

10 Wlodek, S. T., 1987, "Erosion Resistant Coatings for Steam Turbines," EPRI CS-5415, Electric Power Research Institute, Palo Alto, CA.

Downloaded 02 Jun 2010 to 171.66.16.102. Redistribution subject to ASME license or copyright; see http://www.asme.org/terms/Terms_Use.cfm

Processing Methods for High Reliability Silicon Nitride Heat Engine Components

V. K. Pujari

D. M. Tracey

Northboro Research and Development Center, Saint-Gobain / Norton Industrial Ceramics, Northboro, MA 01532

The paper discusses highlights of a silicon nitride processing methodology that has been developed in the course of a major four-year DoE funded program in processing for reliability. The program focused on the attainment of high strength and reliability through the identification and subsequent control of strength-degrading flaws introduced during processing unit operations. Process control and NDE methods applied to achieve an optimized process with the potential to produce high-reliability advanced heat engine components are discussed. Concluding remarks are directed to the extensive tensile strength database that has been generated through testing of over 300 tensile rods produced by the optimized process.

Introduction

This paper discusses aspects of an optimized process, which has resulted from an extensive R & D program on silicon nitride processing for reliability. The material produced by this process has been designated NCX-5102 and consists of a silicon nitride–4 percent yttria composition, which is densified by use of glass encapsulation HIPing.

The program was conducted in three stages, namely: (1) baseline process definition, (2) process optimization, and (3) large-scale production demonstration. In Stage I, two distinct processing routes—injection molding and colloidal consolidation (CC)—were evaluated and the CC route was found to offer the best potential for quality and cost-effective manufacturing. In Stage II, the CC process was optimized relative to stringent mechanical property targets. The program focused on net shape forming of the buttonhead tensile rod, which allowed a convenient, direct means (tensile testing) to assess the quality of the processed material. The overall program goal was to achieve a mean room temperature tensile strength of 900 MPa with a Weibull modulus of 20, a mean 1370°C tensile strength of 500 MPa, and a mean 1230°C, 350 MPa tensile stress rupture life of 100 hours.

The process optimization strategy involved a series of process iterations each starting with Si_3N_4–4 percent Y_2O_3 mill batches capable of yielding approximately 75 net shape cast buttonhead tensile rods. The rods were tested to determine the tensile strength distribution representative of the iteration. Each iteration served as an experiment in a test matrix, which was designed with the critical process parameters as variables. Extensive NDE and fractography data were generated to establish the nature of failure precursors for guidance on the process improvements necessary for strength and reliability enhancement in subsequent iterations. The resulting data for the set of experiments were used to define the optimum total process control variable levels.

To ensure process repeatability, a comprehensive standard operating procedure (SOP) was established for each subtask of each unit operation. The Stage III demonstration provided over 300 samples and a corresponding mechanical properties database. Fabricability of large cross-sectional components was assessed by forming a 50-mm-dia sample. Mechanical properties of these samples were assessed by testing specimens machined from locations across the samples.

Colloidal Process Method

Powder Processing. Several large ($\approx$ 30 kg) batches were prepared using a closed-loop aqueous milling procedure. The aqueous closed-loop process is compared with the conventional alcohol milling approach in Fig. 1. Various physical

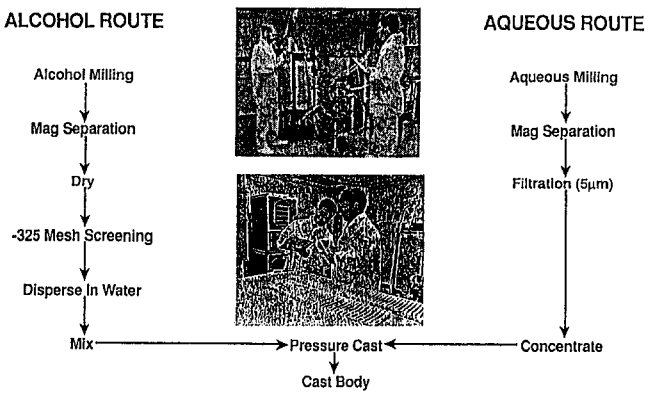

Fig. 1 Comparison of aqueous and alcohol-based powder processing

Contributed by the International Gas Turbine Institute and presented at the 38th International Gas Turbine and Aeroengine Congress and Exposition, Cincinnati, Ohio, May 24–27, 1993. Manuscript received at ASME Headquarters March 17, 1993. Paper No. 93-GT-319. Associate Technical Editor: H. Lukas.

Copyright © 1995 by ASME

Downloaded 02 Jun 2010 to 171.66.16.102. Redistribution subject to ASME license or copyright; see http://www.asme.org/terms/Terms_Use.cfm

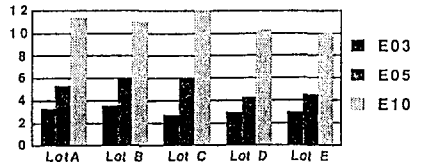

Fig. 2(*a*) Surface area for various grades and lots of UBE silicon nitride powder

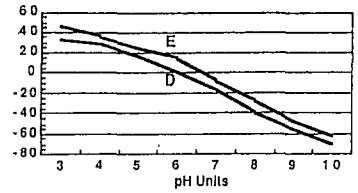

Fig. 2(*b*) Zeta potential versus pH for Si_3N_4 lots D and E

Fig. 2 Powder processing control: surface characterization

and chemical characterization techniques were employed both for the raw material and the milled powder. Although x-ray diffraction of the starting Ube powder found very little variation in α phase from lot to lot, measurable variations in surface area (shown in Fig. 2*a*), particle size, and oxygen content were found. In most cases, milling conditions were adjusted to bring the powder properties within the specified control limits. However, the fifth lot of powder, "Lot E," in spite of meeting all physical property specifications, showed very different colloidal casting behavior. Further surface chemical examinations (courtesy Dr. S. Malghan, N.I.S.T.) suggested significant shift in the iso-electric point (IEP) for the Lot E powder (as compared to Lot D) as shown in Fig. 2(*b*). Other lots of powder showed similar behavior to that of Lot D. Various surface treatments have been developed to control the IEP and hence the casting behavior. IEP was also included as a process control parameter.

Slurry Development and Characterization. A comprehensive slurry characterization methodology was developed using such measurements as viscosity, pH, and centrifuge packing density in combination with the NMR (Nuclear Magnetic Resonance) spin-lattice parameter (T_1). Slurry characterization was further refined to predict casting behavior. A "Casting Rate Slope" parameter was defined and developed as a process control measure. The procedure is briefly described as follows: A fixed amount of slurry is cast at a constant pressure on an established porous material. Cast thickness is monitored at fixed time intervals. Thickness squared is plotted as a function of casting time and the slope of the line is defined as the "Casting Rate Slope" (CRS). An upper control limit for CRS is defined by UCL as shown in Fig. 3(*a*). Slurries having CRS values above UCL are rejected, as high CRS correlates with unacceptable density gradient levels in the cast body as described in the next section.

Casting of Net Shape Formed (NSF) Tensile Bars. The casting of concentrated ceramic suspensions is influenced by the mold design and the slurry properties, especially the CRS as described in the previous section.

The effect of mold design on the cast density variation has been addressed by Pujari et al. (1991a) previously. The effect of total mold filtration surface area was analyzed using Computed Tomography (CT). From that analysis, an optimum mold design was established. In the present investigation the optimum design defined in the above-mentioned reference was utilized.

Various slurry batches for which CRS was defined previously were utilized to cast NSF bars using the optimized

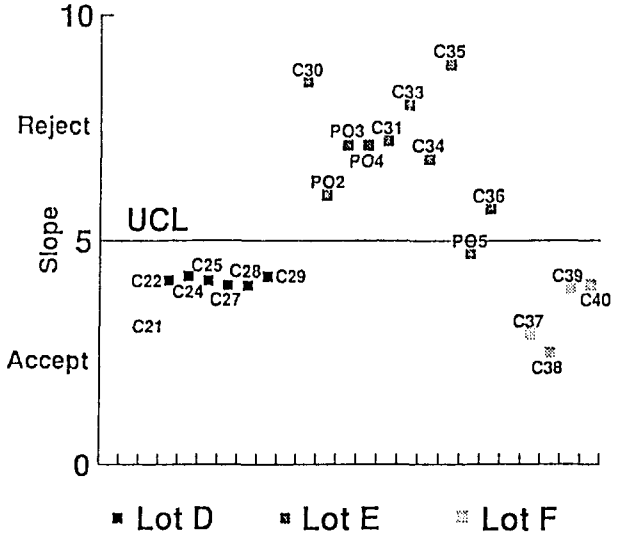

Fig. 3(*a*) Slope of casting rate curves for various lots of powder

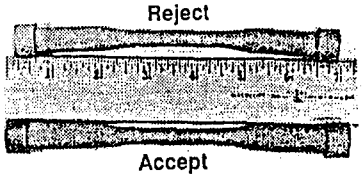

Fig. 3(*b*) Density gradient effect on part tolerance

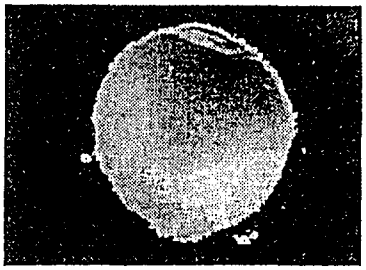

Fig. 3(c) UT image of green tensile bar showing density gradient

Fig. 3 Shape forming (casting) control: casting rate effect

mold. The effect of slurry CRS is illustrated in Fig. 3(*b*) by the bent shape of a HIPed tensile rod. This rod was cast from a slurry, which had a CRS value above UCL. Bending during the HIP process results from the radial green density gradient shown by the ultrasonics C-scan in Fig. 3(*c*). The correlation of CRS with the cast density gradient was established in this program and apparently has not been previously recognized considering the lack of discussion of the concept in the literature. The correlation follows from the fact that excessive casting rates provide inadequate time for the optimum packing of powder particulates during filtration.

All test bars for testing and reliability demonstration were fabricated from slurry batches showing CRS below CL level. The process yield at casting unit operation was computed to be upward of 90 percent.

Hot Isostatic Pressing. The cast NSF bars were hot isostatically pressed (HIPed) using ASEA glass encapsulation technology. The HIP process was optimized using pressure, time, and temperature parameters to assure full densification and development of an elongated microstructure (Fig. 4) for desired fracture toughness (K_{IC}). Control limits for density and fracture toughness were defined as > 99.5 percent TD and $5.8 < K_{IC} < 6.2$ MPa$\sqrt{\text{m}}$, respectively. It was imperative

Downloaded 02 Jun 2010 to 171.66.16.102. Redistribution subject to ASME license or copyright; see http://www.asme.org/terms/Terms_Use.cfm

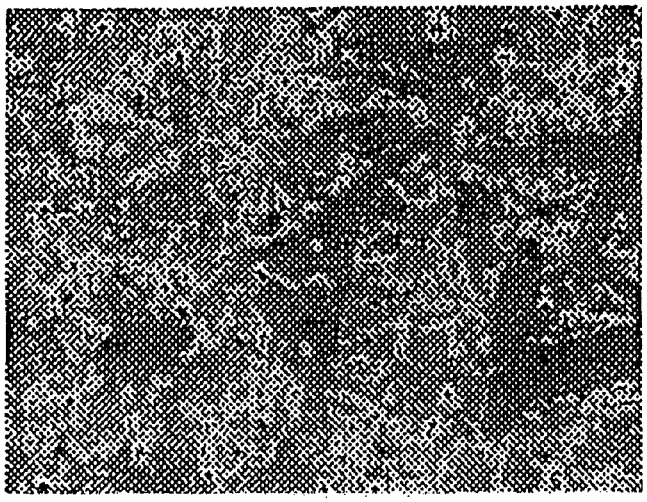

K_{1C} = 6.26 MPa√m

Fig. 4 SEM micrograph showing high-toughness elongated microstructure

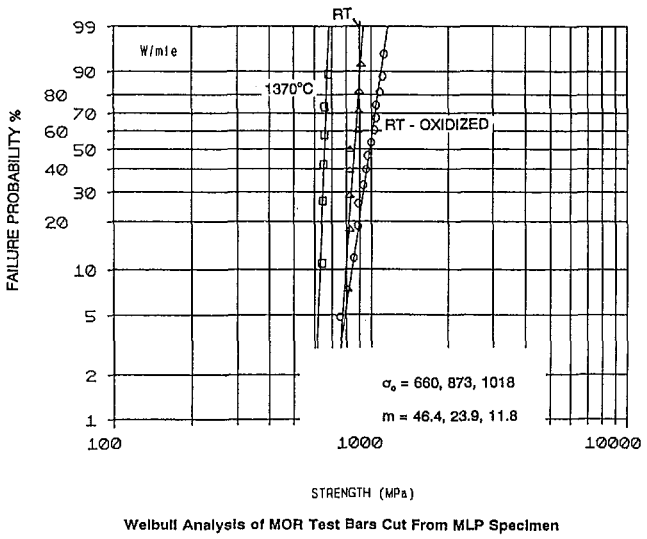

Fig. 5 Fabrication of "MLP" (machined from large piece) component

to reproduce K_{IC} within specified control limits in order to examine the process improvement due to the flaw reduction, a key objective of this program. It was, however, found that the HIP process contributed to the process variability by nature of its being a batch process. Better understanding of the thermal profiles during the HIP cycle and/or incorporation of a continuous sintering cycle will further enhance the reliability of this improved process. A limited effort has been launched toward understanding the temperature gradients during sintering in general and in the HIP cycle in particular.

Fabrication of Large Cross-Sectional Specimens. Fabricability of a 50-mm-dia cylindrical specimen using the colloidal consolidation technique was demonstrated during the investigation. These specimens were also fully densified using the HIP process. To examine the uniformity through the cross section, MOR bars (3 × 4 × 50 mm) were machined from various sections of the specimen for room temperature and 1370°C fast fracture flexure strength and fracture toughness (four-point indentation strength) measurements.

The fast fracture flexure strength data are presented in a

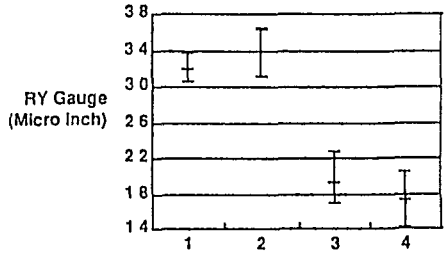

Fig. 6(*a*) Effect of machining procedure on the surface finish

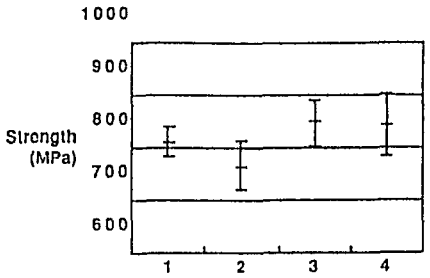

Fig. 6(*b*) Effect of machining procedure on the tensile strength

Fig. 6 Finish machining: process optimization

Weibull plot in Fig. 5. Room temperature tests were performed on a group of specimens that were oxidized and on a group given no heat treatment. Similar to previous experience in testing NSF tensile bars, the oxidation treatment was found to enhance the characteristic strength, but diminish the Weibull modulus: (1018 MPa, 12) versus (873 MPa, 24). Excellent 1370°C strength was measured (660 MPa, 46) especially in view of the fact that these specimens were not given a post-HIP crystallization heat treatment. Seven fracture toughness tests were performed and these provided an average toughness of 6.8 ± 0.36 MPa√m .

Machining Process Optimization. Four distinct machining procedures were evaluated for their influence on tensile strength. Consistent with the focus on machining damage effects, the specimens were not given heat treatments for the purpose of this study. A total of 72 specimens from 3 HIP runs were machined and tested in the study.

Customary practice expresses surface finish specification in terms of the average roughness R_a. Early Stage II work resulted in a reduction of the R_a spec from 16 μin. (0.4 m) to 10 μin. at the buttonhead radius and to 8 μin. along the gage length. The current study maintained these R_a specs but varied the rough grinding procedure including intermediate grinding steps, diamond wheel type, and depths of cut. On the basis of the grinding parameters employed, the machining procedures would be ranked according to operational precision from #1 to #4, with #4 being the most precise procedure.

In spite of the major differences in operational precision, the resultant tensile strength data showed no statistically significant dependence on procedure, Fig. 6, even though R_y (maximum peak to valley) Talysurf surface finish values were significantly higher for procedures #1 and #2 when compared to procedure, #3 and #4.

The mean strengths found in this study are consistent with the 900 MPa room temperature target, given the absence of strength enhancing heat treatment. Therefore the primary consideration in choosing a machining procedure for Stage III was attaining a minimum variability of strength and high Weibull modulus. Since procedure #1 had the smallest standard deviation, it was chosen as SOP for Stage III demonstration.

Downloaded 02 Jun 2010 to 171.66.16.102. Redistribution subject to ASME license or copyright; see http://www.asme.org/terms/Terms_Use.cfm

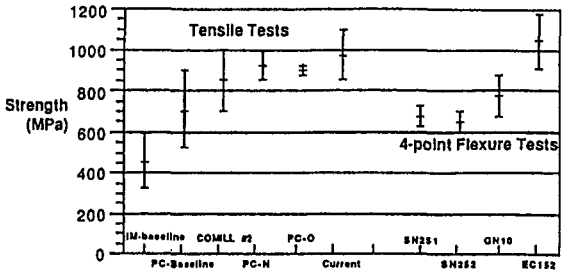

Fig. 7(*a*) Tensile strength improvement: NCX5102

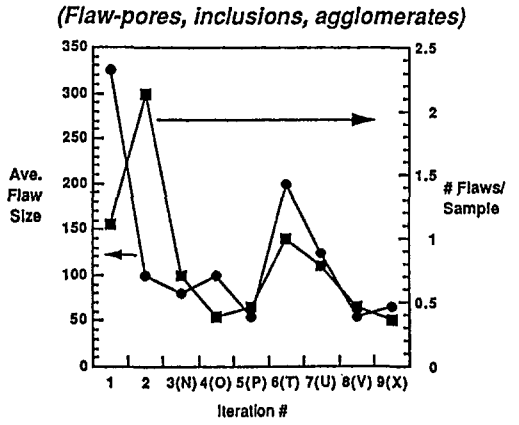

Fig. 7(*b*) Flaw reduction

Fig. 7 Chronology of process improvement

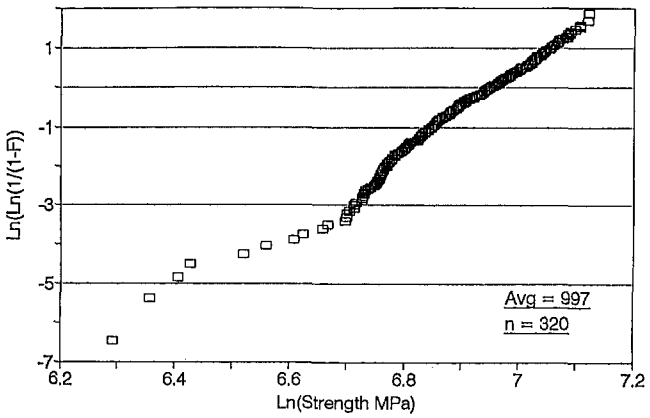

Fig. 8 Cumulative probability of failure plot of entire strength database

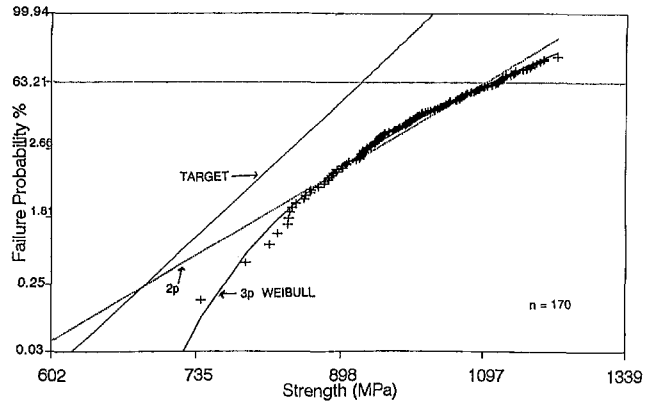

Fig. 9 Cumulative probability of failure plot of intrinsic strength data from competing risk analysis

Tensile Strength Database

The buttonhead tensile bars were tested on an Instron Model 8562 utilizing the Instron "Super-grip" and straight copper collet system. A double ramp loading procedure was used to test all specimens. First, the specimen is loaded to 6666 N (1500 lb) at 39 MPa/min (250 lb/min) . This allows time for the copper collets to deform to the buttonhead radius of the specimen. After the initial ramp to 6666 N, the specimen is then loaded to failure at a stressing rate of 600 MPa/min (equivalent to ASTM STD. C1161 for type B flexure specimens).

Over the course of the four-year program, hundreds of tensile rods were fabricated and tested. The final Stage III demonstration involved over 300 samples, which were tested to establish the room temperature fast fracture tensile strength distribution characteristics of the optimized process. In addition, more than 25 elevated temperature fast fracture (1370°C) and stress rupture (1230°C) tensile tests were completed as discussed below.

The chronology of process improvement of NCX-5102 in terms of mean tensile strength is summarized in Fig. 7(*a*). As can be seen, average tensile strength has been increased from 500 MPa to 1 GPa, suggesting substantial reduction in the inherent defect sizes, as indicated in Fig. 7(*b*). Tensile strengths at the 1 GPa level have rarely been reported for any other silicon nitride material. NCX-5102 data is also benchmarked against other competitive materials as shown in Fig. 7(*a*).

The tensile test database from the Stage III demonstration set includes fractography results on location, type, and size of the failure origins obtained using optical and scanning electron microscopy. The majority of the room temperature specimens had failure origins at the surface within the uniformly stressed 6-mm-dia gage length. Two types of surface failure origins were identified, namely: machining flaws and glass blisters that developed during postmachining oxidation heat treatment. Also, two distinct types of volume flaws were observed. One was a microstructural flaw characterized by a zone of microporosity. The other involved inclusions from titanium contamination traced to wear of a casting filter.

At this writing, only preliminary statistical analysis of the Stage III data has been done. Exploratory statistical analysis has considered fractography, NDE, and toughness data as well as trends/variations attributable to batch processing through the unit operations of the production cycle. The strength data have been examined with the goal of establishing the best fit using available parametric models. The study includes the investigation of mixture models and competing risk analysis. This work has been conducted in collaboration with Dr. Mark Vangel of the Army Materials Technology Laboratory.

The database includes a total of 320 valid tensile tests with failure origins of the four types described above. The 320 strength data are presented in a cumulative probability of failure plot using standard Weibull coordinates in Fig. 8. The data range from 540 to 1237 MPa and have a mean value of 997 MPa. The nonlinear character of the distribution with multiple inflections suggests that a two-parameter Weibull fit of these data (σ_0 = 1038 MPa, m = 10.4) would be inappropriate and that the multimodal nature of the data should be represented using competing risk analysis.

The multimodal analysis was pursued by considering the group of 320 strength data as being composed of two sets, with one set (n = 170) representing strengths of intrinsic defects and the other (n = 150) representing strengths of extrinsic defects. The surface glass blister and the volume microstructural flaw were considered to comprise the set of intrinsic flaws, since they occur randomly within the standard processing cycle. On the other hand, the machining damage

Downloaded 02 Jun 2010 to 171.66.16.102. Redistribution subject to ASME license or copyright; see http://www.asme.org/terms/Terms_Use.cfm

and inclusion flaws were classified as being extrinsic flaws, subject to control by means unrelated to the silicon nitride process per se.

Competing risk analysis reveals that the extrinsic strength data dominate the nonlinear low strength tail of the overall distribution. A plot of their distribution is similar to that of Fig. 8. The intrinsic strength data on the other hand have a distinctly different character, which is well represented by a three-parameter Weibull model with a threshold stress of 665 MPa, a scale value of 444 MPa and a shape value of 3.92. The intrinsic strength data are plotted in Fig. 9 along with this three parameter model and also with a two-parameter fit, which is clearly a poor representation of the data. The line to the left of the data represents the program target material having a mean tensile strength of 900 MPa and a two-parameter Weibull modulus of 20.

From a reliability perspective, the important feature of the three-parameter Weibull distribution is the existence of a threshold stress below which there is a zero probability of failure. Physically this corresponds to a processing methodology that has succeeded in truncating the upper tails of the critical flaw size distributions. A threshold at the level indicated clearly has direct impact on design systems used in fielding reliable ceramic components. For instance, NCX-5102 with the three-parameter distribution on Fig. 9 would provide higher reliability at all stress levels when compared to the program target material.

In comparison to the quantity of room temperature tests, minimal elevated temperature testing was pursued. A mean tensile strength of 396 MPa (n = 15) was found at 1370°C. Stress rupture testing at 1230°C was conducted at stress levels from 250 to 350 MPa. Stress rupture life in excess of 100 hours was found at 250 MPa but at higher stress levels shorter lifetimes were determined.

Numerous processing steps were optimized to produce superior room temperature properties to demonstrate that flaw control can result in significant advances in the quality of silicon nitride. Additional processing optimization can be expected to provide improved high-temperature properties beyond what has been accomplished in this program.

Conclusions

Using an iterative processing approach, each unit operation of the colloidal process and the process as a whole has been optimized. Closed-loop aqueous processing incorporating powder comminution, slurry concentration, and casting has been the key to the successful completion of the program with desired reliability objectives.

Equally significant has been the implementation of various powerful NDE techniques both for in-process control and for the identification of critical strength limiting defects. Use of NMR spectroscopy for slurry aging behavior characterization (Pujari et al., 1991b), computed tomography (CT) for density gradient evaluation leading to optimum mold design (Pujari et al., 1991a,b), ultrasonic (UT) technique for in-situ monitoring of the casting process (Pujari et al., 1992), and density gradient evaluation in cast NSF bars, microfocus radiography for volume flaw detection both in green and dense specimens, and lastly liquid dye penetrant (LDP) approach for the detection of machining related damage as a few salient examples.

A comprehensive data base has been generated through fabrication, testing, and postmortem fractography of a large population (> 300) of net shape formed tensile bars. Analysis of the data suggests a significant reduction in both the flaw size and the frequency of their occurrence. As shown in Fig. 7(b), microfocus radiography data from a large population of tensile bars suggests a fivefold reduction in flaw size (from 250 μm to below 50 μm) and frequency of detection of flaws (2.5/bar to less than 0.5/bar). These data agree very well with the 100 percent increase in average tensile strength realized in the program.

Statistical analysis suggests that the truncation of large failure precursors affected by the processing strategy results in a three-parameter Weibull strength distribution with threshold stress near 665 MPa. It follows that NCX-5102 is both stronger and more reliable than the targeted material, which is characterized by a mean tensile strength of 900 MPa and two-parameter Weibull shape factor (modulus) of 20.

Acknowledgments

This research was sponsored by the U.S. Department of Energy, Assistant Secretary for Conservation and Renewable Energy, Office of Transportation Technologies, as part of the Ceramic Technology Project of the Materials Development Program, under contract DE-AC05-840R21400 with Martin Marietta Energy Systems, Inc.

References

Pujari, V. K., Amin, K. E., and Tewari, P. H., 1991a, "Development of Improved Processing and Evaluation of Silicon Nitride," ASME Paper No. 91-GT-317.

Pujari, V. K., et al., 1991b, "Reliability Improvements of High Strength Silicon Nitride Through Process Optimization and Control," *Proceedings of the Annual Automotive Technology Development Contractors' Coordination Meeting*, Dearborn, MI, Oct. 28–31.

Pujari, V. K., Sales, L. C., Wang, J. S., and Fraser, J., 1992, "Precision Casting Process Control by Ultrasonic Technique," *Ceramic Engineering and Science Proceedings*, Vol. 13, M7–8.

Downloaded 02 Jun 2010 to 171.66.16.102. Redistribution subject to ASME license or copyright; see http://www.asme.org/terms/Terms_Use.cfm

Soft Computing in Design and Manufacturing of Advanced Materials

K. J. Cios
University of Toledo,
Toledo, OH 43606

G. Y. Baaklini

A. Vary

NASA Lewis Research Center,
Cleveland, OH 44135

The goal of this paper is to show the potential of fuzzy sets and neural networks, often referred to as soft computing, for aiding in all aspects of manufacturing of advanced materials like ceramics. In design and manufacturing of advanced materials it is desirable to find which of the many processing variables contribute most to the desired properties of the material. There is also interest in real-time quality control of parameters that govern material properties during processing stages. This paper briefly introduces the concepts of fuzzy sets and neural networks and shows how they can be used in the design and manufacturing processes. These two computational methods are alternatives to other methods such as the Taguchi method. The two methods are demonstrated by using data collected at NASA Lewis Research Center. Future research directions are also discussed.

Introduction

In this paper our intent is to show the potential of soft computing methods, namely fuzzy sets and neural networks, in design and fabrication of ceramics. Soft computing in our framework is utilized to identify trends indicating which input variable contributes most to the increase of a desired output parameter, say strength. Such identification can potentially speed up the process of designing a new material. Human designers can easily notice such trends for a few variables but it becomes very difficult to do so for a large number of variables.

Initially, we shall briefly introduce fuzzy sets and neural networks. Then, we shall illustrate the power of soft computing for fabrication of new materials by showing some of the results obtained in our previous work [1, 2] in which we utilized the data originally collected by Sanders and Baaklini [3]. Results on the data from 273 NASA 6Y silicon nitride [1–3] modulus of rupture bars tested at room temperature will be given.

Three input variables, namely milling time of the composition powder, the sintering time of the modulus of rupture test bars, and the nitrogen pressure employed during sintering, are considered. The relationship between the above-listed input variables and the flexural strength and density as output variables, found by soft computing methods, will be shown and commented on.

Background

The reason for choosing silicon nitride is that it is an important material for heat engine applications due to its high operating temperature, reduced weight, resistance to oxidation, thermal shock resistance, and good high-temperature strength [4]. Estimates of potential efficiency improvements for automotive engines with structural ceramic components range from 30 to 50 percent over current engine technology. Ceramics consist of nonstrategic materials that are relatively inexpensive. Their scatter in strength and low toughness is generally attributed to discrete defects such as voids, inclusions, and cracks introduced during processing [3]. Current cost-effective fabrication procedures also frequently produce ceramics containing bulk density variations and microstructural anomalies that can adversely affect performance [4].

Scatter in mechanical properties of ceramics is a great drawback from a design/reliability stand point. This scatter is attributed to defects and inhomogeneities occurring during processing of silicon nitride powder compositions and during part fabrication. From the research work on silicon nitride composition at the National Aeronautics and Space Administration Lewis Research Center it was evident that density gradients were strongly dependent upon sintering conditions [5]. The results of an investigation of one silicon nitride composition involving sintering trials of 21 batches of material are described in [3], and these particular data are utilized here to show that soft computing is a useful tool, which can be used either on its own or in a hybrid system to provide much needed information to advanced materials designers.

Soft Computing Methods

Basics of Fuzzy Sets. Fuzzy sets were developed by Zadeh as means for dealing with vague information, in everyday language represented by linguistic variables like high, low, more or less, etc. [16]. Fuzzy set theory provides a natural approach to problems in which objects change their member-

Contributed by the International Gas Turbine Institute and presented at the 38th International Gas Turbine and Aeroengine Congress and Exposition, Cincinnati, Ohio, May 24–27, 1993. Manuscript received at ASME Headquarters February 12, 1993. Paper No. 93-GT-1. Associate Technical Editor: H. Lukas.

Copyright © 1995 by ASME

Downloaded 02 Jun 2010 to 171.66.16.102. Redistribution subject to ASME license or copyright; see http://www.asme.org/terms/Terms_Use.cfm

ship in classes gradually. Fuzzy sets allow us to deal with phenomena that are vague, imprecise, too complex or too ill defined to be analyzed by conventional mathematical tools [7]. Definitions essential for subsequent explanation of the used methods follow.

Let R be the set of real numbers and U be the conventional (crisp) set. Let u be a generic element of U. A fuzzy subset A of U is defined by a membership function μ_A: $U \rightarrow [0, 1]$. The fuzzy subset A of U can be expressed as:

$$A = \{ \mu_A(u) \mid u; u \in U, \mu_A(u) \in [0, 1] \} \quad (1)$$

where μ_A is referred to as the grade of membership of u in A.

The support of A is the set of elements in U whose memberships in fuzzy subset A, $\mu_A(u)$, are positive:

$$\text{Supp}(A) = \{u \mid u \in U, \mu_A(u) > 0\} \quad (2)$$

As an example, let us define a fuzzy subset "old" on a crisp set of people of different ages. The support of "old" may be defined on nine points for ages 10 through 100 (in steps of ten). Grades of membership for these points can be assigned as .01/10, .05/20, .1/30, .5/40, .7/50, .8/60, .9/70, 1/80, 1/90, 1/100; where μ_{old}/u means that μ_{old} is a grade of membership of element u in a fuzzy subset "old." Thus, say, .7/50 means that a person who is 50 years old belongs to a fuzzy subset "old" with the grade of membership equal to 0.7.

Aggregation of fuzzy sets is an operation by which several fuzzy sets are combined into a single set. In general, any aggregation operation is defined by the function

$$h:[0, 1]^n \rightarrow [0, 1] \quad (3)$$

for some $n >= 2$. When applied to n fuzzy sets defined on U, h produces an aggregate fuzzy set A by operating on the grades of membership of each element of U in the sets being aggregated. From the several classes of averaging operations we chose generalized means, which is defined as follows:

$$h_\alpha(a_1, a_2, \ldots a_n) = \left(\frac{a_1^\alpha + a_2^\alpha + \ldots + a_n^\alpha}{n} \right)^{1/\alpha} \quad (4)$$

where $\alpha \neq R$ ($\alpha \neq 0$) is a parameter by which different means are distinguished; $\alpha = 2$ was used.

Radial Basis Functions. The other type of soft computing comprises neural networks. A neural network can be made to approximate any given function provided that the network has a sufficient number of processing units, called neurons. In this paper we shall briefly describe a neural network algorithm called radial basis function (RBF) network [9]. It is a three-layer network with "locally tuned" processing units in the hidden layer. RBF neurons are centered at the training data points, or some subset of it, and each neuron only responds to an input that is closest to its center. The output layer neurons are linear or sigmoidal functions and their weights may be obtained by using a supervised learning method, such as a gradient descent method.

Figure 1 shows a general RBF network with n inputs and one linear output. This network performs a mapping $f:R^n \rightarrow R$ given by the following equation [10]:

$$f(x) = \lambda_0 + \sum_{i=1}^{n_r} \lambda_i \phi(\| x - c_i \|) \quad (5)$$

where $x \in R^n$ is the input vector, $\phi(.)$ is a function from $R^n \rightarrow R$, $\| \ \|$ denotes the Euclidean norm, λ_i ($0 <= i <= n_r$) are the weights of the output node, c_i ($0 <= i <= n_r$) are the RBF centers, and n_r is the number of the so-called RBF centers.

One of the most common functions used for $\phi(.)$ is the Gaussian function:

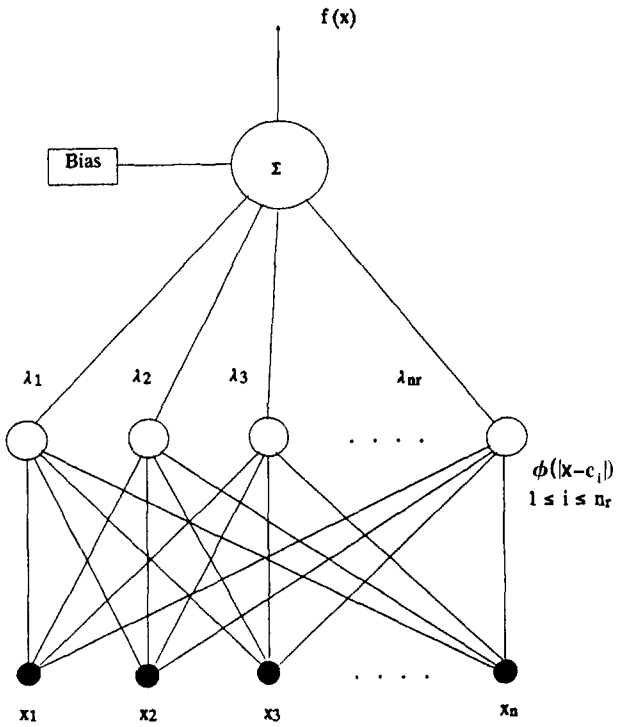

Fig. 1 Radial basis function network with single output

$$\phi(\| x - c_i \|) = \exp\left(- \frac{\| x - c_i \|^2}{\sigma_1^2} \right) \quad (6)$$

where σ_1 is a constant that determines the width of the ith node. This function has a maximum value of 1 when $\| x - c_i \|$ is 0, and drops off to 0 as $\| x - c_i \|$ approaches infinity.

The centers of the RBF functions, c_i, are usually chosen from the training data points x_i ($1 <= i <= N$). This method is known as the "neurons at data points" method [11]. For larger data sets, it is not practical to have an RBF center at each data point, so other methods were developed to reduce the number of RBF centers. Some of them are the random selection of centers, clustering of data points, and orthogonal least-squares reduction [10].

The random selection method simply uses a random selection of n_r centers from N data points, where $n_r < N$. If the desired outputs are discrete and represent, say, C different classes, then clustering methods such as k-means clustering [11] may be used to cluster the data points within each class. A very effective method of choosing a set of RBF centers from the training data is the orthogonal least-squares reduction method [10], which enables the selection of the most significant RBF centers from a given training data set.

Method of Making Predictions and Data Used

For room temperature, 18 different combinations of milling time, sintering time, and nitrogen pressure yielded the composition strengths and densities shown in Table 1.

In order to validate the soft computing method predictions, we needed to test the system using known test vectors to evaluate the error of predictions. We were particularly interested in the ability of the network to predict the output values for batch number 6Y25, as this batch number represented the optimum combination for the input variables [3]. Thus, batch number 6Y25 was first removed from the data. The data were then pseudo-randomly divided into two parts: 70 percent for training and the remaining 30 percent for

Downloaded 02 Jun 2010 to 171.66.16.102. Redistribution subject to ASME license or copyright; see http://www.asme.org/terms/Terms_Use.cfm

Table 1 Strength and density at room temperature for different processing and sintering conditions

Batch #	No. of specimen	Milling time [hr]	Sintering time [hr]	Nitrogen pressure [MPa]	Actual Strength [MPa]	Actual density [g/cm³]
6Y1B	30	24	1	2.5	556	3.12
6Y2B	30	24	1	2.5	532	3.18
6Y11	15	100	1	2.5	490	3.23
6Y12	15	300	1	2.5	579	3.25
6Y13	15	100	1	2.5	684	3.24
6Y14	14	300	1	2.5	746	3.24
6Y1516	19	24	2	5	664	3.22
6Y17	10	100	2	5	646	3.23
6Y18	10	100	1.5	5	608	3.21
6Y19	10	100	1.5	5	570	3.22
6Y20	10	100	2	5	650	3.22
6Y23	15	100	1.25	5	631	3.24
6Y24A	15	100	1.25	3.5	586	3.26
6Y24B	15	100	2	3.5	619	3.26
6Y25	10	300	2	5	714	3.28
6Y26A	15	100	1	3.5	479	3.20
6Y26B	15	100	1	5	503	3.18
6Y28	10	100	2	5	671	3.21

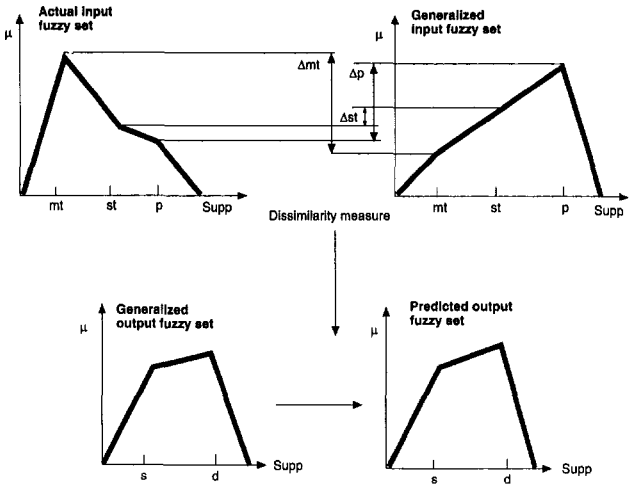

Fig. 2 Explanation of the fuzzy prediction method

testing. Batch number 6Y25 was then inserted into the test data set.

Next, we wanted to see whether it was possible to find combinations of input variables, other than those used in [3], that would result in the strength and density values close to the optimal (6Y25) value. Thus, a training data set consisting of all the batch numbers (100 percent) except 6Y25 was created. Batch number 6Y25 was then placed in the training data set and we made predictions for different, not tried by experiments in [3], combinations of the input vectors.

For the fuzzy sets, the collected data were used to define fuzzy sets for each batch for both input and output variables. The input fuzzy sets were defined for three values of support (nitrogen pressure, sintering time, and milling time) while the output fuzzy sets had support of two elements (flexural strength and density). The grades of memberships were normalized elementwise, and the normalization was repeated for every step of prediction. The resulting membership grades were combined by means of generalized mean operation. After that, a dissimilarity measure (a modified Hamming

Table 2 Overall results for strength and density for room temperature

Strength - average % error for all test vectors and (6Y25)	Density - average % error for all test vectors and (6Y25)
5.7 (4.4)	2.4 (0)

Table 3 Prediction of input variables for highest strength and density, for entire training data from Table 1

Milling time [hr]	Sintering time [hr]	Nitrogen Pressure [MPa]	Predicted Strength [Mpa]	Predicted Density [g/cm³]
150	1.5	3	596	3.15
175	1.5	3	604	3.18
200	1.5	3	611	3.21
200	1.75	4	634	3.28
250	1.5	3	619	3.25
250	1.5	4	634	3.28
250	1.75	4	649	3.28
300	1.5	4	649	3.28
300	1.75	4	656	3.28
300	2	5	686	3.28

distance [2]) was used to calculate the difference between the actual and generalized fuzzy sets of input parameters. Next, the k-fraction of the measure, where $k \in (0, 1)$ was either added to or subtracted from the generalized grades of memberships of the output parameters. The graphic explanation of the method is shown in Fig. 2. It shows the 6Y12 test batch. The generalized input fuzzy set consists of grades of membership obtained by generalized mean operation performed on normalized values of input parameters: milling time (mt), sintering time (st), and pressure (p). The actual input fuzzy set represents normalized values of 6Y12 batch input. The dissimilarity measure was then used to calculate the sum of the elementwise differences between grades of membership of actual and generalized input fuzzy sets. The k-fraction of the measure was then added to the grades of membership of the generalized output fuzzy set. The generalized output fuzzy set was obtained by generalized mean operation performed on normalized values of output parameters, strength (s) and density (d). Addition of k-fraction of dissimilarity measure results in the predicted fuzzy set. The latter is then compared with the actual grades of membership obtained by normalization of the values of the 6Y12 batch output thus yielding a measure of error for strength and density.

Results

Utilization of Fuzzy Sets. The method described above for fuzzy sets was used to predict, for randomly chosen values of input variables, the values for output variables, namely, flexural strength and density of batch samples at room temperatures. This was done in order to estimate the error. The overall results are shown in Table 2. Since the errors were reasonably small, we made predictions for selected new, not tried in [3], combinations of processing and sintering variables. Table 3 shows the results. We can notice that the resultant strengths and densities are lower than the one for the optimum batch (6Y25 was the optimum because of low scatter, not shown in Table 1).

Utilization of Neural Networks. The RBF networks were trained using the same training data as described above. The "neurons at data points" method was used to set up the hidden layer. The gradient descent method was used to train

Downloaded 02 Jun 2010 to 171.66.16.102. Redistribution subject to ASME license or copyright; see http://www.asme.org/terms/Terms_Use.cfm

Table 4 Overall results for strength and density for room tempera-

Strength - average % error for all test vectors and (6Y25)	Density - average % error for all test vectors and (6Y25)
10.54 (10.17)	0.98 (2.50)

Table 5 Prediction of input variables for highest strength and density, for entire training data from Table 1

Milling time [hr]	Sintering time [hr]	Nitrogen Pressure [MPa]	Predicted Strength [MPa]	Predicted Density [g/cm^3]
150	1.5	3	692	3.28
175	1.5	3	700	3.28
200	1.5	3	706	3.28
200	1.75	4	689	3.27
250	1.5	3	709	3.28
250	1.5	4	705	3.28
250	1.75	4	705	3.28
300	1.5	4	711	3.28
300	1.75	4	713	3.28
300	2	5	712	3.28

the output layer neurons that use sigmoidal function. The RBF networks consisted of three input neurons and two output neurons, which corresponds to the number of input and output variables, respectively. The number of neurons in the hidden layer depended on the number of the training vectors. The overall results are shown in Table 4. Table 5 shows predictions made for selected, not previously tried [3], combinations of processing and sintering variables that resulted in strengths and densities similar to that of the optimum batch (6Y25).

The information in Table 5 suggests that there may have been other, than those tried in [3], combinations of sintering and processing variables that would have produced results almost as good as that obtained for 6Y25 [3] but more efficiently. For example, in Table 5, using a milling time of 250 hours, a sintering time of 1.5 hours, and a nitrogen pressure of 3 MPa, the network predicts that a strength of 709 MPa can be obtained. This is only slightly less than the optimal value for 6Y25 but with a reduction in milling time of 50 hours. A word of caution here. Although the confidence in prediction results for strength and density lies within 11 and 2.5 percent (from Tables 2 and 4), respectively, these predictions need to be confirmed by fabrication of ceramics using the input parameters suggested in Table 5. From the theoretical point of view, if the relation between the input and output variables is a smooth function, either increasing or decreasing, then RBF predictions will be accurate and valid for sufficiently large training data set.

Discussion

If in the process of designing new ceramics the designers were to use soft computing in order to notice the correlations between the input and output variables, it might greatly shorten the fabrication cycle. We have shown that this was true for even the small number of input variables. If larger number of input variables could be used that would certainly improve the reliability of predictions and their accuracy. Soft computing can be also seen as an alternative to the Taguchi method [12].

Predicting bulk density of ceramics was more successful than predicting strength. This may be explained by noticing that bulk density is more directly related to milling time,

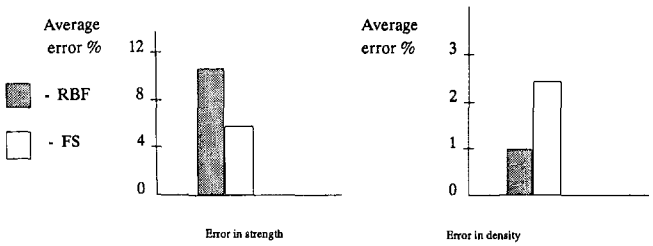

Fig. 3 Average errors in predicting strength and density

sintering time, and pressure, whereas the flexural strength is additionally dependent on pore morphology, on microstructure, and on the presence of failure causing defects.

Comparison of results obtained by using fuzzy sets [2] with those obtained by using neural networks [1] indicates that both were successful in modeling relationships existing between the processing variables and output variables. This is shown graphically, based on Tables 2 and 4, in Fig. 3. As can be seen, small differences exist in terms of errors. Fuzzy sets were slightly better than neural networks in predicting strength, which is statistically varied as a result of the fabrication process. On the other hand, the more precise relationship between the input variables and density was modeled better using neural networks.

When we tried to predict the untried combinations of input variables that might yield the highest ("optimum") values for strength and density, Tables 3 and 5, the results were again slightly different. Now, however, in order to make a state about which method gives more accurate predictions, the real experiments will need to be performed and errors calculated. In an absence of such an experiment we cannot compare the two methods of predictions. We can only say, from Tables 2 and 4, that our confidence in predicting strength is larger for fuzzy sets, while for predicting density it is larger for neural networks.

Conclusions

We have shown that soft computing, if it were the part of the design process, could help in optimizing the process of fabricating ceramics with high strength, accompanied by low scatter. We approached the problem by concentrating on three input variables and two output parameters. The available data set was divided into training and test parts. The former was used for training neural networks and defining fuzzy sets, and the second to validate them on the test part as to how accurately they can predict the strength and density of the test set given new "unknown" inputs.

Then, we have shown that it was possible to indicate other, than those tried, combinations of input variables that resulted in material at least as strong as the one from the known training data (6Y25), but more "optimal" in terms of either shorter milling and sintering times, or lower pressure.

Soft computing methods may not necessarily yield the optimal solution, but most of the time they will give an acceptable, low-cost solution. In many situations, a robustly obtained "good" solution is preferred to an optimal solution, which may take a lot of time to compute.

The results obtained indicate that soft computing can be a powerful tool for both process modeling and process control. It can speed the development and fabrication of emerging ceramic materials. Thus, soft computing might help to capture imprecise relationships between the input variables and output parameters. In turn, these learned relationships can be used for predicting strength and density for new combinations of the input variables. The reliability of our predictions was validated by calculating the errors on the test data

Downloaded 02 Jun 2010 to 171.66.16.102. Redistribution subject to ASME license or copyright; see http://www.asme.org/terms/Terms_Use.cfm

encompassing 30 percent of available data. The maximum combined error, for both methods, for the strength was less than or equal to 10.54 percent, and for density it was less than or equal to 2.4 percent. However, between the two methods, the combined minimum error was less than or equal to 5.7 percent for strength, and 0.98 percent for density. The latter clearly shows that by using a hybrid approach one can achieve better results.

Future Research Directions

In the future we envision a more versatile and powerful hybrid system, which will combine the two soft computing methods with genetic algorithms and numerical optimization methods. Genetic algorithms will enable exploration of the entire design space in search for global optimum. Such a system would rapidly optimize the process of ceramics fabrication as a function of input variables and process parameters. The hybrid system should also incorporate the existing knowledge of the ceramics fabrication experts. After such a system has been developed, the next step would be to move to the problem of optimal design of other composite materials such as ceramic- and metal-matrix composites.

Soft computing, however, is not a panacea for solving problems. It should not be used in situations where mathematically sound models are known. However, since the two soft computing methods are inherently parallel, and thus easily implementable in hardware, they might prove advantages for real-time applications.

References

1 Cios, K. J., Baaklini, G. Y., Vary, A., and Tjia, R. E., "Radial Basis Function Network Learns Ceramic Processing and Predicts Related Strength and Density," *Journal of Testing and Evaluation*, Vol. 22, No. 4, 1994, pp. 343–350.

2 Cios, K. J., Sztandera, L., Baaklini, G. Y., and Vary, A., "Using Fuzzy Sets in the Prediction of Flexural Strength and Density of Silicon Nitride Ceramics," *Materials Evaluation*, Vol. 52, No. 5, 1994, pp. 600–606.

3 Sanders, W. A., and Baaklini, G. Y., "Correlation of Processing and Sintering Variables With the Strength and Radiography of Silicon Nitride," *Ceramic Engineering and Science Proceedings*, Vol. 7, No. 7–8, 1986, pp. 839–860.

4 Klima, S. J., and Baaklini, G. Y., "Nondestructive Characterization of Structural Ceramics," *SAMPE Quarterly*, Vol. 17, No. 3, 1986, pp. 13–19.

5 Baaklini, G., "NDE Reliability and Process Control for Structural Ceramics," ASME JOURNAL OF ENGINEERING FOR GAS TURBINES AND POWER, Vol. 109, 1987, pp. 263–266.

6 Zadeh, L., "Fuzzy Sets," *Information Control*, Vol. 8, 1965, pp. 338–353.

7 Cios, K. J., Shin, I., and Goodenday, L., "Using Fuzzy Sets to Diagnose Artery Coronary Stenosis," *IEEE Computer Magazine*, Vol. 24, No. 3, 1991, pp. 57–63.

8 Klir, G. J., and Folger, T. A., *Fuzzy Sets, Uncertainty and Information*, Prentice Hall, Englewood Cliffs, NJ, 1988.

9 Moody, J., and Darken, C., "Fast Learning Networks of Locally-Tuned Processing Units," *Neural Computing*, Vol. 1, No. 2, 1989, pp. 281–294.

10 Chen, S., Cowan, C. F. N., and Grant, P. M., "Orthogonal Least Squares Learning Algorithm for Radial Basis Function Networks," *IEEE Trans. Neural Networks*, Vol. 2, No. 2, 1991, pp. 302–309.

11 Zahirniak, D. R., Chapman, R., Rogers, S. K., Suter, B. W., Kabrisky, M., and Pyati, V., "Pattern Recognition Using Radial Basis Function Networks," *Conf. Aerospace Application of AI*, Dayton, 1990, in press.

12 McEntire, B. J., Tagliavore, A. P., Heichel, D. N. Bright, E., Yeckley, R. L., Holowczak, J. E., and Quackenbush, C. L., "Silicon Nitride Component Development for Advanced Gas Turbine Engines," *Proceedings of the 27th Automotive Technology Development Contractors' Coordination Meeting*, Society of Automotive Engineers, Inc., Warrendale, PA, 1990, pp. 341–349.

Downloaded 02 Jun 2010 to 171.66.16.102. Redistribution subject to ASME license or copyright; see http://www.asme.org/terms/Terms_Use.cfm

A Novel Method for Refurbishing Used Hot Section Gas Turbine Blades

A. Kempster
Diffusion Alloys Limited,
Hatfield,
Hertfordshire, United Kingdom

N. Czech
TVWTI,
Siemens AG, KWU,
Mulheim a.d. Ruhr,
Federal Republic of Germany

During the normal operation of a land-based gas turbine, attack will occur of the gas-washed surfaces of the rotating stationary blades in the turbine hot section. This attack and its intensity can be variable depending on the blade's position in the turbine hot section. This attack will progressively degrade these gas-washed surfaces even if these surfaces have been previously coated with a protective layer. During the service period of the turbine, it will be necessary to refurbish the blades from the hotter section of the turbine. One of the refurbishment steps will be to provide the blades with a suitable replacement coating to afford protection until the next service period. Conventional refurbishment techniques used to clean the blade surface rely on abrasive cleaning and / or chemical pickling. These processes may be capable of removing superficial oxidation and any residual coating but are not able consistently to remove the substrate material that has suffered from corrosive attack. It is important that this attacked substrate layer be removed completely, otherwise any residual corrosion products, particularly the presence of deeply penetrated sulfides in grain boundaries, could significantly reduce the life of any subsequent coating. The technique described in this paper essentially activates the surface layer of the substrate that is corroded, thus rendering it more easily removed by chemical and physical means. It is possible by this method to remove up to 400 μm of the substrate material and provided that all the corrosion products are contained within this zone, it is demonstrated how this produces a clean unattacked surface that is necessary for any subsequent welding, brazing, or recoating operation.

Introduction

Today, in modern power generation plants, the high-efficiency gas turbine plays an important and versatile role. Recently, most gas turbines of this type have found application in combined cycle systems where the high temperature of the turbine inlet yields hitherto unachievable efficiencies in the combustion of fossil fuels. Figure 1 shows a photograph of a typical power generation gas turbine. Such units can be used to generate up to 200 MW of power. Figure 2 is a longitudinal section through a turbine showing the general arrangement of the compressor, hot section, and combustion chamber. These modern gas turbines are designed to operate with almost all types of gaseous and liquid fuels.

The efficiency of the process is raised by increasing the temperature of the gases entering the turbine section. For example, on heavy-duty gas turbines, like the Siemens type V84.2, the gas inlet temperature at the first stator row is about 1125° C, while for newly developed and "advanced" gas turbines like the Siemens type V64.3 and the V84.3, the inlet temperature is higher than 1300° C. Clearly, the rotating blades and stationary vanes (both made from high strength Nickel Super Alloys) in the hot section are vulnerable to degradation. Various approaches have been adopted to reduce the high-temperature degradation of these nickel superalloy substrates.

Methods for Improving Component Life

Firstly, the substrate alloy may be provided with a protective surface coating, the aim of which is effectively to restrict the high-temperature attack to within this layer. Typical coatings that are used for this purpose are the platinum aluminide type (Lehnert, 1968), chromium-diffused coatings applied by a thermochemical treatment (Goward and Cannon, 1988), and MCRAIY coatings applied by low-pressure plasma spraying (Goward, 1979). The latter is also used in combination with aluminide coatings (Wood et al., 1989). The design life of the component is usually three to four times longer than the life of the coating, which is eventually consumed by the loss of the protective elements.

Second, the alloy may be modified (for example, by directional solidification or using single crystals) so that the mechanical properties (e.g., creep strength) allow higher metal temperatures to be used. Third, the turbine blade and vanes

Contributed by the International Gas Turbine Institute and presented at the 38th International Gas Turbine and Aeroengine Congress and Exposition, Cincinnati, Ohio, May 24–27, 1993. Manuscript received at ASME Headquarters March 10, 1993. Paper No. 93-GT-281. Associate Technical Editor: H. Lukas.

Copyright © 1995 by ASME

Downloaded 02 Jun 2010 to 171.66.16.102. Redistribution subject to ASME license or copyright; see http://www.asme.org/terms/Terms_Use.cfm

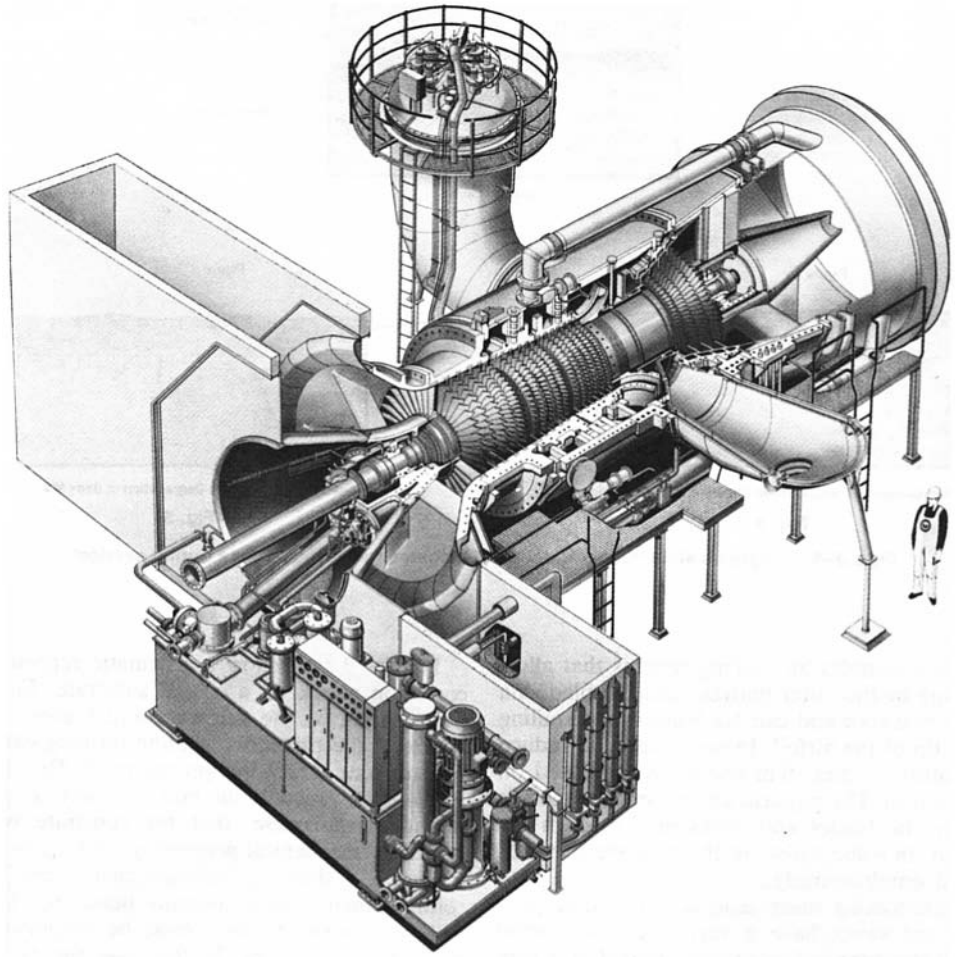

Fig. 1 Siemens heavy-duty gas turbine V94.2

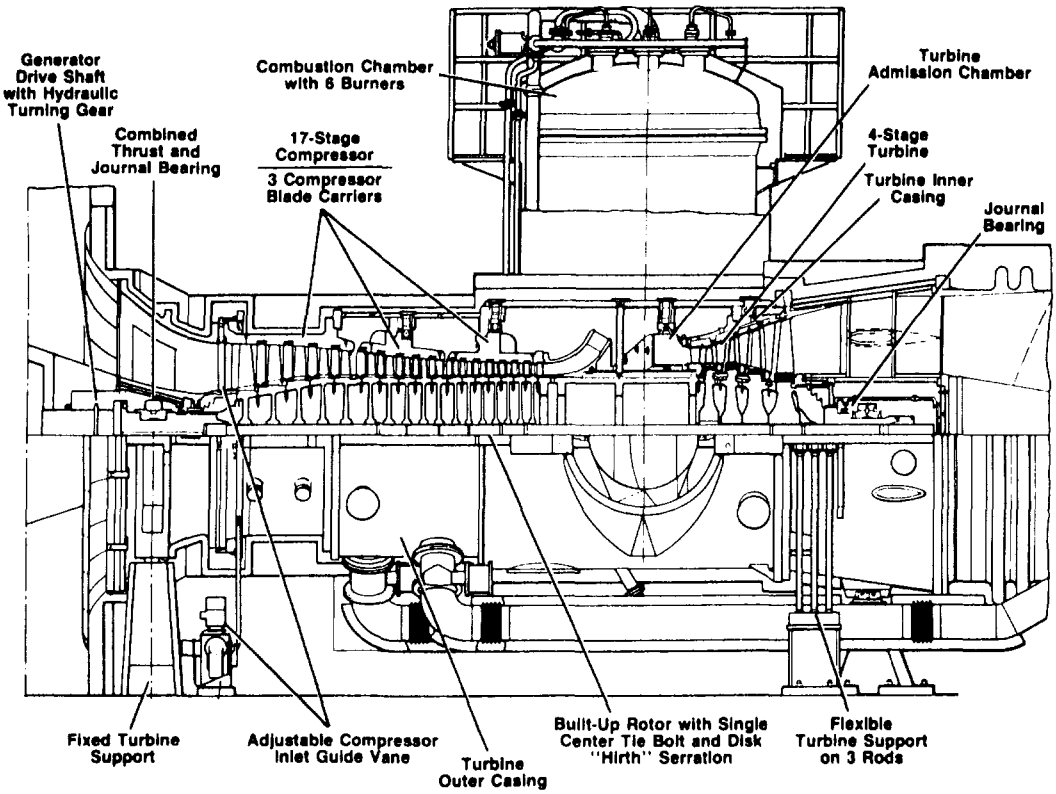

Fig. 2 Longitudinal section of V84 gas turbine

Downloaded 02 Jun 2010 to 171.66.16.102. Redistribution subject to ASME license or copyright; see http://www.asme.org/terms/Terms_Use.cfm

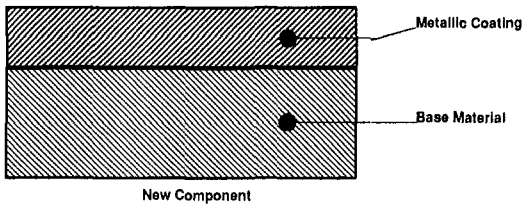

Fig. 3

Figure 4

Figure 5

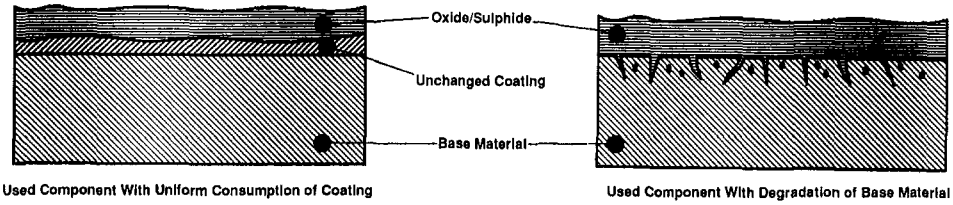

Fig. 4 Fig. 5

Figs. 3–5 Diagrams showing degradation of a coated gas turbine blade during service

can be provided with complex air cooling systems that allow air to enter the vane by the outer buttress and the blade via the base of the fir tree root and exit via holes in the trailing edge or the blade tip of the airfoil. In some cases, to reduce the metal temperature further, film cooling is employed on some areas of the airfoil. The physical and chemical demands that are placed on the blades and vanes in a modern gas turbine dictate that, in some cases, all three of the methods above may be used simultaneously.

Consequently, considering these aspects, it is not surprising these blades and vanes have a very high commercial value. Naturally, at the appropriate service interval, it is very desirable for the turbine user that a route exist to refurbish these high-value components to an "as new" standard rather than have the greater expense of replacing the used blades and vanes with new components (Burgel et al., 1990; Deblon and Keienburg, 1985; Czech et al., 1990).

High-Temperature Corrosion

The nature of the corrosive attack on the coated alloy will depend on the following factors:

(*i*) The type and concentration of aggressive chemical species present in the gas stream (e.g. NaCl, Na_2SO_4 and V_2O_5).
(*ii*) The composition of the coating and, after its consumption, on the composition of the substrate.
(*iii*) The temperature of the gas/coating interface and the length of time this temperature is achieved.

Although the blade system is designed to avoid any base material attack, in many cases this does occur, particularly in areas that are highly stressed by thermal and/or chemical influences. In general, an outer oxide scale will form that protects the metal underneath it. However, in some cases the scale can be porous or mechanically degraded by cracks through which corrosive compounds can enter. This attack will eventually lead to a subsurface depletion of the scale-forming elements such as chromium, aluminum, and titanium and result in a more nonuniform attack of the coating and substrate, especially when the conditions are favorable for sulfidation. In equiaxed castings the grain boundaries are in general more prone to sulfidation than the grain itself. In some cases grain boundary degradation can exceed uniform consumption of the metal by an order of magnitude.

Figures 3 to 5 show a schematic representation of a hot corrosion attack on a coated substrate. Figure 3 shows the new coating on the substrate and Figure 4 a hot corrosion attack of the protective coating forming oxides and sulfides. No substrate attack has yet occurred. The situation shown in Fig. 4 is, in practice, the best for carrying out refurbishment provided, of course, that the substrate will maintain the necessary mechanical properties until the next service period.

Figure 5 shows a situation that is not so favorable for refurbishment where specially developed techniques, which will be described later, must be employed to remove all subsurface inclusions. In this case the protective layer has been totally consumed by hot corrosion reactions to produce a mixture of metal oxides and sulfides. Also, a nonuniform attack of the substrate has occurred and sulfide, oxide, and nitride inclusions are produced within the grains and at grain boundaries.

Figures 6–8 show scanning electron micrographs of an inadequately cleaned surface after applying a low-pressure plasma-sprayed CoCrAlY coating. It can be seen that considerable debris exists in the surface of the base material. X-ray analysis shows this material to be rich in aluminum and deficient in nickel.

Blade and Vane Refurbishment Techniques

It has been mentioned in the introduction that during the operation of a gas turbine there will be steady and progressive attack of the components in its hot section by various aggressive chemicals present in the gas stream. Depending on the conditions of operation, an oxide layer of varying thickness may form on the component. Also, and most significantly, sulfur can penetrate into the base material, especially along grain boundaries, to form sulfides deep in the material. During refurbishment of these attacked surfaces it is necessary that all of these corrosion products be removed prior to carrying out any remedial work (i.e., coating, welding, or brazing). The removal of any superficial corrosion or oxidation products is easily achieved by pickling in hot acidic solutions. This is particularly effective if the component has the remains of a protective coating that is itself readily attacked by the acid being employed. Alternatively, abrasive blasting may be used where hard particles of, for example, silicon carbide or aluminum oxide are impacted on to the surface of the component, causing cutting and substrate removal. However, both of these methods, even when used in

Downloaded 02 Jun 2010 to 171.66.16.102. Redistribution subject to ASME license or copyright; see http://www.asme.org/terms/Terms_Use.cfm

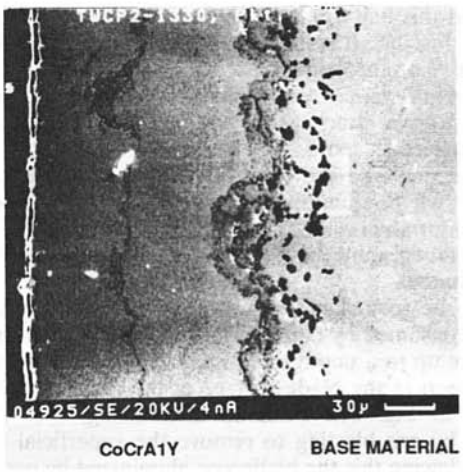

Fig. 6

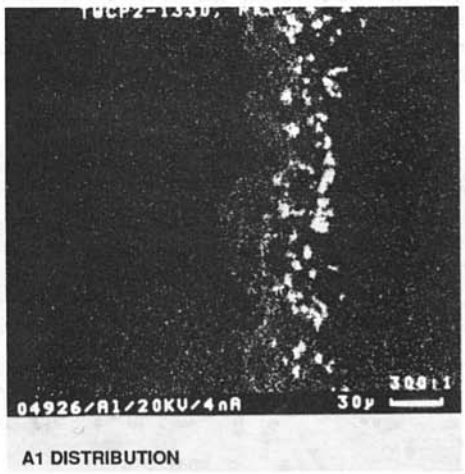

Fig. 7

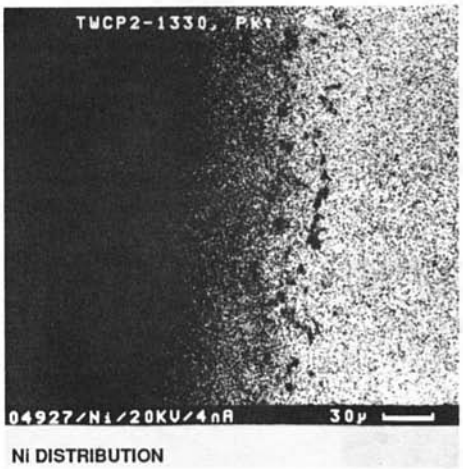

Fig. 8

Figs. 6–8 Photographs showing SEM analysis of CoCrAlY coating on an inadequately cleaned surface

combination, are not able to remove significant amounts of the substrate.

Hence, even following such a cleaning process as described above, the more deeply penetrated sulfides, oxides, and nitrides will still remain in the substrate. It is clearly important to remove these deeper lying inclusions because there is a possibility that during subsequent operation of the components, these inclusions will diffuse farther into the base material and have a deleterious effect on the alloy mechanical properties. Also, the presence of subcutaneous inclusions could markedly effect the application and performance of any new coating applied to such a contaminated surface. This is most important if recoating is carried out by Low Pressure Plasma Spraying. In this process, deposition of the new coating is very sensitive to this kind of contamination and can result in coating exfoliation.

During the refurbishment of used turbine blades and vanes, one common method used to remove corrosion/oxidation products from their surface is by hand grinding or linishing. In these cases use is made of rotary stones and also moving belts impregnated with ceramic materials. However, these methods are difficult to control and are also very operator dependent. The amount of material being removed from the component surface will therefore be variable and consequently, it is very difficult to predict when an uncontaminated and hence clean surface has been achieved.

Novel Method of Refurbishment

The technique described in this paper shows how it is possible to activate the surface layers of the corroded component to chemical and physical attack by introducing, in this case, aluminum by a chemical vapor deposition process (aluminizing). This process of aluminizing has been well studied and is commonly used to protect turbine components in the hot section of both aero and land-based turbines against corrosion and oxidation (Duret et al., 1982). The aluminide coatings used in these cases are typically 25–75 μm in thickness. It is the object of this paper to demonstrate that by using a modification of this technique it is possible to produce aluminide coatings up to a depth of 400 μm in one coating step that are capable of encapsulating the deep-lying inclusions in the substrate. The coatings formed by aluminizing are composed of essentially nickel aluminides that are readily attacked by mineral acids such as hydrochloric acid. Therefore the conversion of the surface layer of the substrate from a conventional nickel alloy to a nickel aluminide activates this zone of the surface to acid attack. Consequently, the removal of this aluminide layer will also remove the substrate that has been contaminated by corrosion products. Also, the aluminide coating is friable and is more readily removed by abrasive blasting than the original unaluminized surface.

Before aluminizing is carried out, it is necessary to clean the surface of the component to remove corrosion products, which mainly consist of bulky oxides. These oxides, if not removed, will impair the ability of the aluminum to diffuse into the substrate and ultimately reduce the depth of its penetration. This cleaning is accomplished either by abrasive blasting using alumina or by chemical attack using an aqueous acid pickle.

During aluminizing it is important to establish conditions that will result in the maximum diffusion zone in the coating. In this instance the diffusion zone is defined as the proportion of the aluminide coating that exists beneath the original surface of the alloy (i.e., the original base material into which aluminum has diffused). A high proportion of an additive zone in the coating is to be avoided as this will result in an ineffective encapsulation of the inclusions. The additive zone is this case is defined as the proportion of the coating that exists above the original surface (i.e., before coating) of the alloy. The examples given in this paper demonstrate the importance of effective cleaning of the substrate during refurbishment of a turbine blade when considering the performance of a low-pressure plasma-sprayed MCrAlY layer applied after two separate and different cleaning routes.

In the first case the turbine blade (IN738Lc) being refurbished was cleaned by using alternative acid pickling in 20

Downloaded 02 Jun 2010 to 171.66.16.102. Redistribution subject to ASME license or copyright; see http://www.asme.org/terms/Terms_Use.cfm

percent hydrochloric acid at 85° C and abrasive blasting with 30-40 mesh alumina particle with an air pressure of 100 psi (690×10^3 Pascals). In this case the turbine blade was subjected to three alternative cycles of acid pickling and blasting. After the final blasting operation the turbine blade was coated with an MCrAlY layer approximately 150 μm in thickness using low-pressure plasma spraying. The blade was then heat treated in a vacuum furnace to achieve the necessary mechanical properties for the substrate alloy. After 2000 operational hours a turbine inspection revealed that the low-pressure plasma-sprayed coating was suffering from catastrophic exfoliation (Fig. 9). A section taken through this area of the turbine blade revealed that substantial quantities of corrosion products were still present beneath the new VPS layer and this had dramatically reduced its adhesion properties (see Fig. 10). It is implicit that during a coating failure of this type that the complete coating exfoliates in this area. There are, of course, serious implications for the substrate as rapid corrosive attack will immediately start on the unprotected surfaces.

The second case shows an example of a satisfactory refurbishment where aluminizing is used to remove the deep-lying corrosion products substantially. Figure 11 shows an example of a metallographic microsection of a turbine vane before refurbishment.

It can be seen that the protective coating has been completely consumed by corrosion and the blade material shows corrosion up to a depth of 300 μm. The sulfide particles are visible deep in the blade surface at the grain boundaries (as marked in Fig. 11). Prior to aluminizing, the blade was cleaned by grit blasting to remove the superficial bulky oxides. Following this the blade was aluminized by pack cementation using a time and temperature necessary to achieve a coating thickness of circa 300 μm in on operation. Figure 12 shows the blade section for aluminizing. It can be seen that the aluminide coating has encapsulated the particles produced by corrosion including the sulfide particles. During

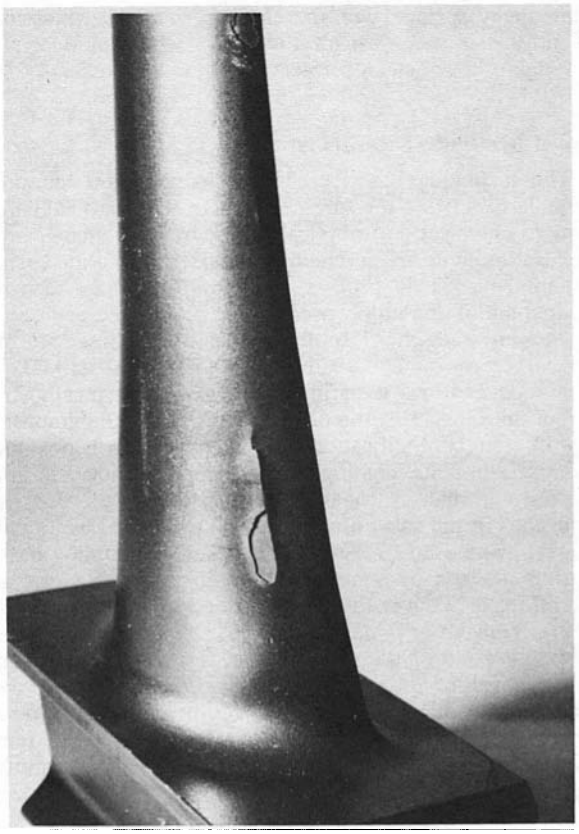

Fig. 9 Refurbished first-stage rotor blade with exfoliated LPPS coating due to inadequate cleaning

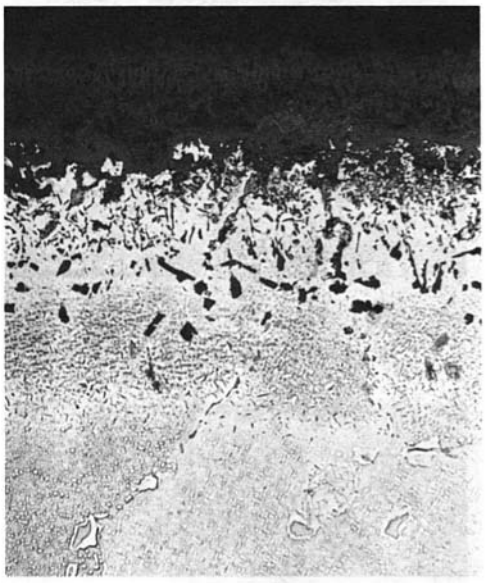

Fig. 11 Micrograph showing corroded material surface

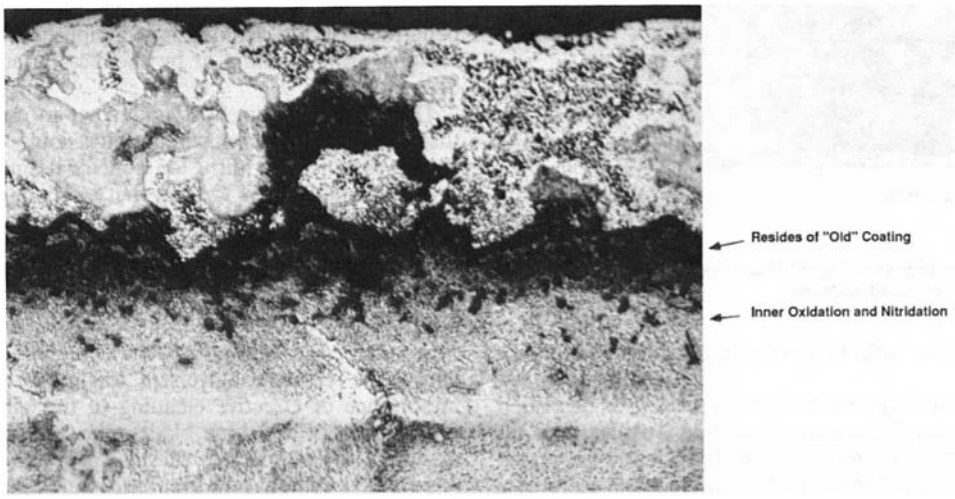

Fig. 10 LPPS coating applied to an inadequately cleaned surface: Micrograph shows both poor adhesion and microstructure on blade after 2000 h service

Downloaded 02 Jun 2010 to 171.66.16.102. Redistribution subject to ASME license or copyright; see http://www.asme.org/terms/Terms_Use.cfm

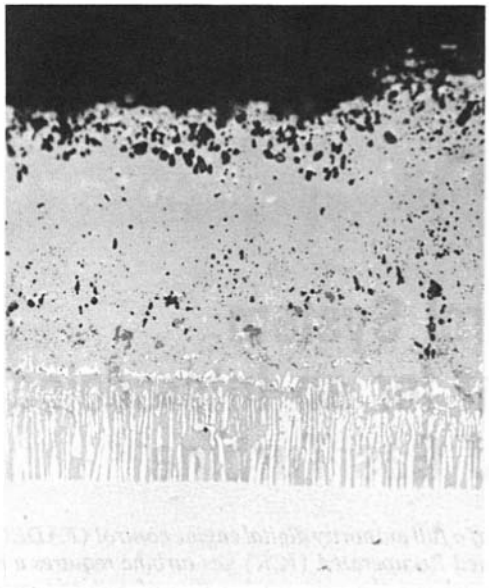

Fig. 12 Micrograph showing aluminized surface

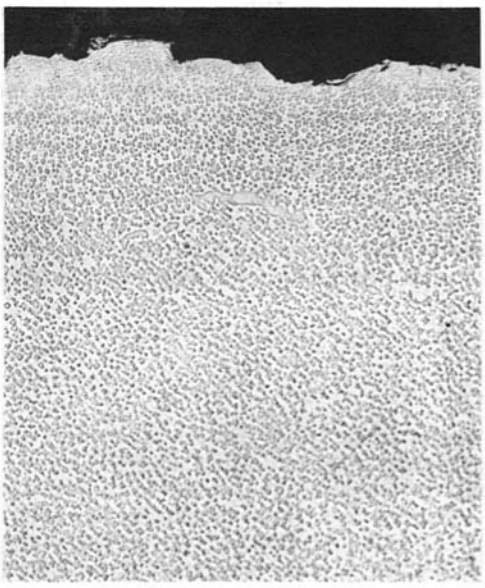

Fig. 13 Micrograph of blade after removal of aluminizing; all photographs 500:1

this aluminizing it is necessary to protect any machined surfaces from aluminum diffusion using solid shields, otherwise during acid pickling undesirable metal removal would occur. Figure 13 shows the same blade section after removal of the aluminide layer. This was carried out by blasting with alumina particles followed by acid pickling in 20 percent hydrochloric acid at 85° C. It can be seen that a clean surface is produced using this technique with no observable sulfide particles present. This surface is now in a satisfactory condition to receive the new protective coating, which may be a diffusion coating such as produced by chromizing or a low-pressure plasma-sprayed coating of the MCrAlY type. Alternatively the method above is equally effective in producing a clean substrate surface that is satisfactory for refurbishment by welding or brazing.

Conclusion

In service, the rotating and stationary blades in the land-based generator hot section are subject to deep and aggressive chemical attack. These components are expensive to produce and are therefore ideal candidates for refurbishment at appropriate service periods. Special techniques are necessary to ensure that the new coating or other refurbishment technique is applied to an essentially clean surface. The technique described above (designated as "SICLEAN" in Siemens processing nomenclature (Czech and Kempster, 1991)) illustrates how this provides a solution to the removal of deep subcutaneous sulfide penetration.

An important advantage of the refurbishment technique described above is that a uniform layer is removed from the surface of the blade or vane irrespective of the components contours. What is more, the amount removed is the same for each component treated in this manner. This is not the case for other types of surface cleaning (e.g., hand grinding or linishing) where it is difficult to quantify the amount removed from specific areas of the component or in fact to reproduce the depth removed from one component to another.

Protective coatings such as those produced by low-pressure plasma spraying or chromium diffusion when applied to surfaces cleaned using the technique above are able to afford the same protection as that experienced on new components.

References

Burgel, R., Koromzay, and Redecker, 1990, "Refurbishment Procedures for Stationary Gas Turbine Blade," *Proceedings, International Conference on Life Assessment and Repair Technology for Combustion Turbine Hot Section Components*, Viswanathan and Allan, eds., Phoenix, AZ, Apr. 17–19.

Czech, N., Deblon, B., and Esser, W., 1990, "Refurbishment of Gas Turbine Blade—Concept, Development and Experience," *Proceedings, International Conference on Life Assessment and Repair Technology for Combustion Turbine Hot Section Components*, Viswanathan and Allan, eds., Phoenix, AZ, Apr. 17–19.

Czech, N., and Kempster, A., 1991, Siemens AG/Diffusion Alloys Ltd., British Patent Application No. 91163329.

Deblon, B., and Keienburg, K. H., 1985, "Refurbishing Gas Turbine Blades," *Turbomachinery International*, Oct., pp. 28–56.

Duret, C., Davin, A., Marijnissen, G., and Pichoir, R., 1982, "Recent Approaches to the Development of Corrosion Resistant Coatings," *Proceedings, High Temperature Alloys for Gas Turbines*, R. Brunetaud et al., eds., D. Reidel Publishing Co., Dordrecht, Federal Republic of Germany, pp. 53–77.

Goward, G. W., 1979, *Source Book on Materials for Elevated Temperature Application*, E. F. Bradley, ed., ASM Metals Park, OH, p. 369.

Goward, G. W., and Cannon, L. W., 1988, ASME JOURNAL OF ENGINEERING FOR GAS TURBINES AND POWER, Vol. 110, p. 150.

Lehnert, G., 1968, T. E. W., German Patent No. P17.96,175.0.

Wood, J. W., Foster, A. D., and Schilke, P. W., 1989, "High Temperature Coating for Improved Oxidation/Corrosion Protection," ASME Paper No. 89-GT-239.

Downloaded 02 Jun 2010 to 171.66.16.102. Redistribution subject to ASME license or copyright; see http://www.asme.org/terms/Terms_Use.cfm

Digital Control System Development for an Intercooled Recuperated Gas Turbine

R. J. Carlson
Westinghouse Electric Corporation,
Sunnyvale, CA 94088

P. M. West
Rolls-Royce, Inc.,
Sunnyvale, CA 94088

D. E. Azouz
CAE Electronics, Ltd.,
Saint-Laurent, Quebec, Canada

The on-going development of a full authority digital engine control (FADEC) system for the US Navy's Intercooled Recuperated (ICR) gas turbine requires a high level of system coordination to achieve the primary benefits of reduced specific fuel consumption and improved specific output power relative to a simple cycle engine. This paper describes the system requirements analysis and the implementation of control algorithms leading to the preliminary ICR control system design. The ICR control system is required to coordinate the actions of over 30 actuators using data taken from over 150 sensors. Primary control of the engine output power is provided by regulation of the fuel metering valve. Thermal management of the intercooler, recuperator, and variable area power turbine nozzle results in maximum cycle efficiency within safe operating limits. The new electronic engine controller (EEC) is based on a new open architecture Futurebus+ backplane and is fully redundant in all operationally critical control functions. The EEC also features an operating panel and video display for local operation and maintenance of the control system. The graphic display and function keys provide access to control functions as well as assisting maintenance activities with built-in test diagnostics to trouble shoot failed circuitry.

I Introduction

The goal of the first phase of the US Navy's ICR gas turbine program is to design and produce an advanced development (AD) version of a new main propulsion engine that can be readily adapted to a fully qualified version of the engine for fleet use. The new ICR engine is based on Rolls-Royce's RB211 series aero engine, modified to include both intercooling and recuperation, providing a nearly flat efficiency profile (Todman, 1992; Bowen and Groghan, 1984; Thomson et al., 1987). Greater detail on the engine features and configuration is provided in a companion paper by Crisalli and Parker (1993).

In a joint effort by the authors' companies, the new control system for the ICR engine is being developed based on an advanced prototype version of the final, tactical FADEC system. The parallel development of a new engine, sensors, and control actuators by Westinghouse and Rolls-Royce and a new EEC by CAE Electronics is quite challenging and requires a high degree of flexibility in establishing requirements, as well as planning and allocating hardware and software resources. The design approach selected for the prototype EEC will result in a controller that embraces the final hardware architecture, but is implemented using low-cost commercial equivalent components.

The controller is configured for either local or remote operation. Local operating capability is enhanced through the use of a graphic display monitor with menu pages and iconically based system mimic pages. The remote control capability is effected through a standard digital interface, which allows the controller to both send condition status and receive commands over a serial link to a remote monitoring and control system (RMCS). Alternate interface cards can be custom designed and added to the EEC to make integration of the ICR engine into backfit options with established interfaces attractive.

The controller is being developed using a new open architecture based on IEEE Specification P896 (Futurebus+). The control system includes redundant sensors and actuators for all key functions as well as redundancy of controller circuitry.

The EEC software will be developed to MIL-STD-1815 in Ada, and compliant with all the methodologies and requirements of DOD-STD-2167A. Updated by actual prototype and rig test data developed during the AD program, the software will continue to evolve as the engine design and operating cycles firm up.

A key part of the development of the EEC is to test it against a real-time computer simulation model of the ICR engine. The stimulator-simulator computer runs the engine model, using analog-to-digital converters to take the controller's outputs, and digital-to-analog outputs to send back signals mimicking the engine behavior in the sensors. The stimulator-simulator computer can test the entire envelope of controller operation as it simulates engine transient or steady-state performance in response to the actions of the FADEC system.

II EEC Hardware Architecture

The EEC is packaged in a standard shock-mounted drip-

Contributed by the International Gas Turbine Institute and presented at the 38th International Gas Turbine and Aeroengine Congress and Exposition, Cincinnati, Ohio, May 24-27, 1993. Manuscript received at ASME Headquarters March 17, 1993. Paper No. 93-GT-326. Associate Technical Editor: H. Lukas.

Copyright © 1995 by ASME

Downloaded 02 Jun 2010 to 171.66.16.102. Redistribution subject to ASME license or copyright; see http://www.asme.org/terms/Terms_Use.cfm

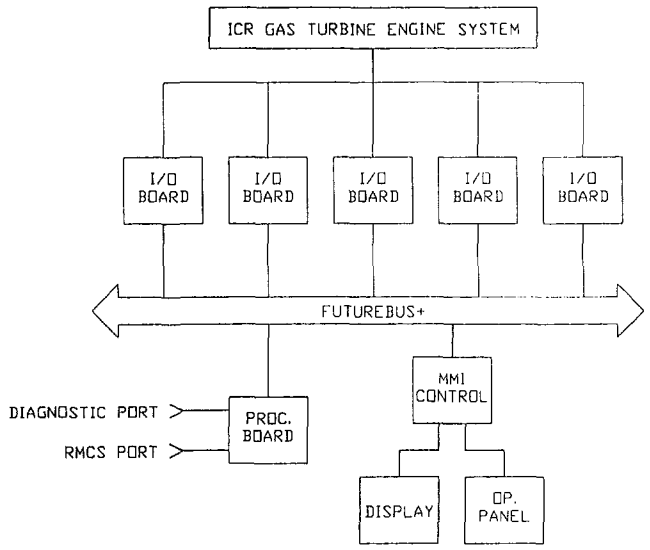

Fig. 1 ICR engine control system architecture

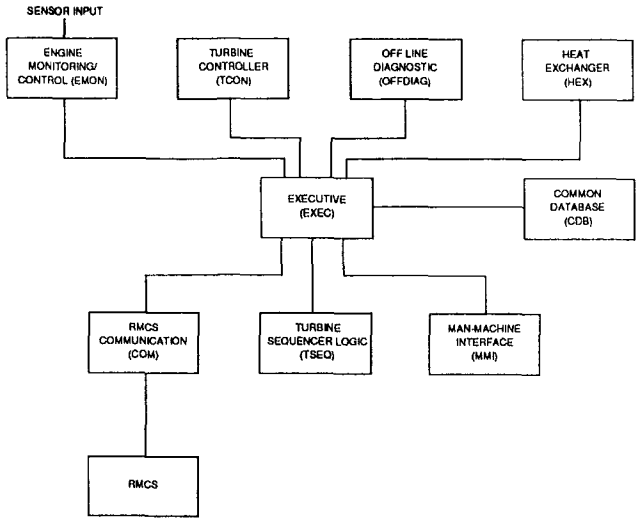

Fig. 2 ICR engine control software functional capabilities

proof front-access enclosure. This enclosure houses the Futurebus+ chassis assembly, power conditioning and distribution, and the cooling fan assembly. Additionally, a man-machine interface (MMI) in the form of a display monitor, entry devices, and annunciators is mounted on the enclosure. The EEC outline and architectural concept is shown in Fig. 1.

The EEC processes engine system control commands received from either the RMCS or the local MMI and data signals from the engine sensors to provide control and monitoring of the ICR engine. The EEC performs all data transfers between I/O and main processor memory, performs the local control functions, and transfers data and commands between the EEC, the RMCS, and the local MMI. Closed-loop digital servo control and signal processing is also provided for proportional controls and for continuous engine vibration monitoring.

The EEC also incorporates hardware and software to provide built-in-test capability to detect and isolate control system faults. Critical engine control and protection functions are fully redundant with instrumentation circuits routed independently and brought to separate I/O boards within the EEC. All I/O channels are load short-circuit, spike voltage, reverse voltage, and overvoltage protected. EMI filtering is also provided for I/O channels within the EEC.

III ICR Control Algorithms

The control system software is functionally modular and consists of the following capabilities:

- (*a*) Executive capability (EXEC).
- (*b*) Man-machine interface capability (MMI).
- (*c*) Engine monitoring and control capability (EMON).
- (*d*) Off-line diagnostic capability (OFFDIAG).
- (*e*) Turbine controller capability (TCON).
- (*f*) Turbine sequencer capability (TSEQ).
- (*g*) Heat exchange logic capability (HEX).
- (*h*) RMCS communication capability (COM).

Figure 2 shows the conceptual arrangement of these capabilities.

Operational modes, conditions, and states can be selected from two locations. The primary control location will be the RMCS, and the secondary location will be the MMI at the EEC assembly.

Nomenclature

AD = advanced development
BIT = built-in test
BOV = bleed-off valve
BOVCO = bleed-off valve control
CO_2 = carbon dioxide
CPU = central processing unit
EEC = electronic engine controller
EMI = electromagnetic interference
EMON = engine monitoring
EXEC = executive capability
FADEC = full authority digital engine controller
FMV = fuel metering valve
GT = gas turbine
HEX = heat exchanger
HP = high pressure
HPC = high pressure compressor
HWG = highest wins gate
I/O = input/output
ICR = intercooled recuperated gas turbine engine system
IEEE = Institute of Electrical and Electronic Engineers
IP = intermediate pressure
IPC = intermediate pressure compressor
LWG = lowest wins gate
mm = millimeters
MMI = man-machine interface
NH = high-pressure shaft speed
NI = intermediate pressure shaft speed
NPT = power turbine shaft speed
OFFDIAG = off-line diagnostics
P3 = high-pressure compressor delivery pressure
PT = power turbine
PTET = power turbine entry temperature
R = gas constant
RMCS = remote monitoring & control system
SFC = specific fuel consumption
T26 = high-pressure compressor inlet temperature
T31 = combustor inlet temperature
T601 = recuperator inlet temperature
T9 = exhaust temperature
TCON = turbine controller
TSEQ = turbine sequencer
UPS = uninterruptable power supply
US = United States
VAN = variable area nozzle
°C = degrees Celsius

Downloaded 02 Jun 2010 to 171.66.16.102. Redistribution subject to ASME license or copyright; see http://www.asme.org/terms/Terms_Use.cfm

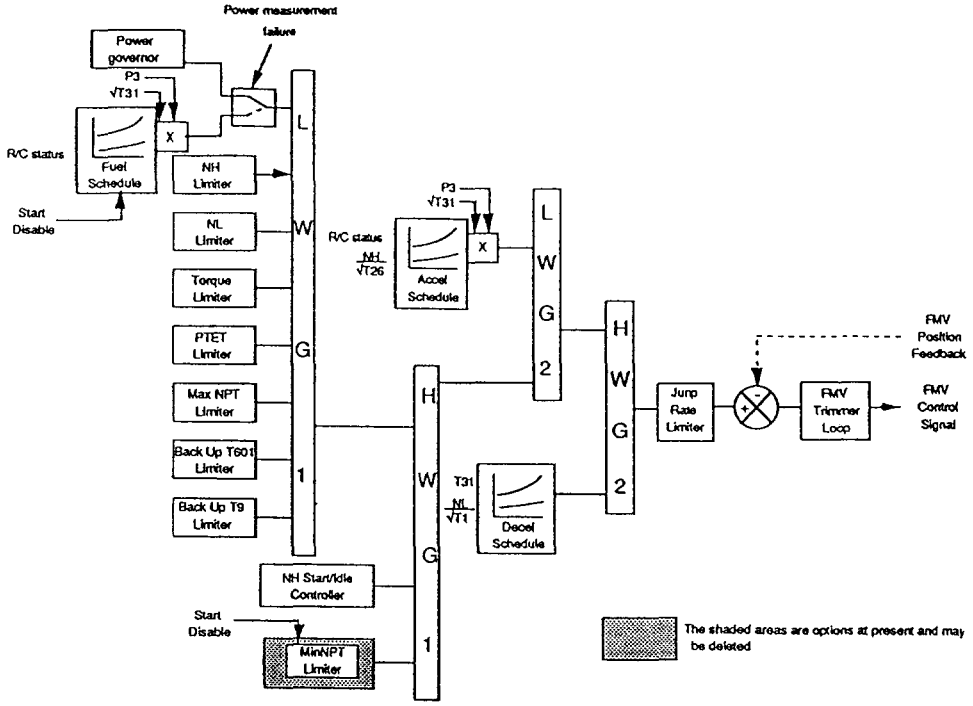

Fig. 3 ICR engine power and fuel control

Executive Capability. The purpose of the EXEC component is to provide an environment to execute control system tasks. It provides a mechanism for concurrent process synchronization and communication as well as allocation of resources to a particular task. In addition to the above, EXEC is also responsible for initialization of the system, event logging and database management. All requests for data by a software component from the other components are coordinated by EXEC.

Man-Machine Interface Capability. The presentation of overview information and detailed status information to the operator is by means of integrated dynamic graphics displays. These displays are a collection of related information displayed as pages on the MMI screen. A page has two basic purposes:

(*a*) To convey information about status of engine systems;
(*b*) To provide a means of controlling the engine operation.

The page window area of the screen is used to display the system mimic pages. All pages contain portions of text and graphics, which do not change once the page is displayed. These static data serve to identify the dynamic elements and to tie them together. Transfer of electrical energy, gas, or fluid is represented by lines interconnecting machinery components. Flow direction in each transfer path is indicated by an arrowhead symbol. Graphic symbols displayed on pages can be either dynamic or static; the static graphic is given a distinctly different appearance. The dynamic data comprise all information that may change after the page is initially displayed.

The message area of the screen is used to provide textual information about events, alarms, and device errors.

The menu area occupies the bottom of the screen. This area is subdivided into seven menu option rectangles and one graphic area located at the right of the menu window area. Menu options can scroll horizontally so that a menu that has more than seven options can have all its options made available to the operator.

Engine Monitoring and Control Capability. EMON directly accesses the engine sensors to acquire plant data as well as controlling the output signals of all auxiliary subsystems. EMON consists of three subcapabilities, namely engine monitoring (EMONM), engine control (EMONC) and gas turbine protection (GT-PROTECTION). The data acquired are checked against the applicable limits and deadbands before recording in the signal database. Alarm and warning deadbands are used to limit reporting of state changes around the alarm and warning thresholds.

The GT-PROTECTION component is responsible for initiating safe stop of the ICR upon detecting an abnormal engine condition. It detects abnormal conditions by comparing selected parameters against predefined safe limits; any abnormal condition is declared when a parameter value is outside the safe limit.

Off-Line Diagnostic Capability. The OFFDIAG component provides a means of detection and isolation of FADEC hardware faults. OFFDIAG starts at the power-up (or resets) of the system without operator intervention.

OFFDIAG is capable of identifying faults to the lowest replaceable unit (circuit card) level in order to enable the operator to replace the identified unit and bring the system to fully operational state.

The detectable errors are categorized as follows:

(*a*) Fatal Errors—The errors that can cause serious effect on the operation of the EEC. Upon detecting errors of this severity OFFDIAG does not transfer the control to the application software.
(*b*) Nonfatal Errors—These errors may cause the loss of facility provided by a circuit card or the software, but are not severe enough to prevent the EEC from running in a degraded mode.

Turbine Control Capability. The TCON component is responsible for the control of the fuel metering valve, the variable area power turbine nozzle (VAN), and the compressor handling bleed valves.

The primary fuel control loop attempts to regulate power turbine output power. However, the power control is limited by companion control loops that limit engine speeds, temperatures, and torque. There are also loops for controlled acceleration and deceleration. The control loops are compared through cascaded lowest wins/highest wins gates (LWG/HWG)

Downloaded 02 Jun 2010 to 171.66.16.102. Redistribution subject to ASME license or copyright; see http://www.asme.org/terms/Terms_Use.cfm

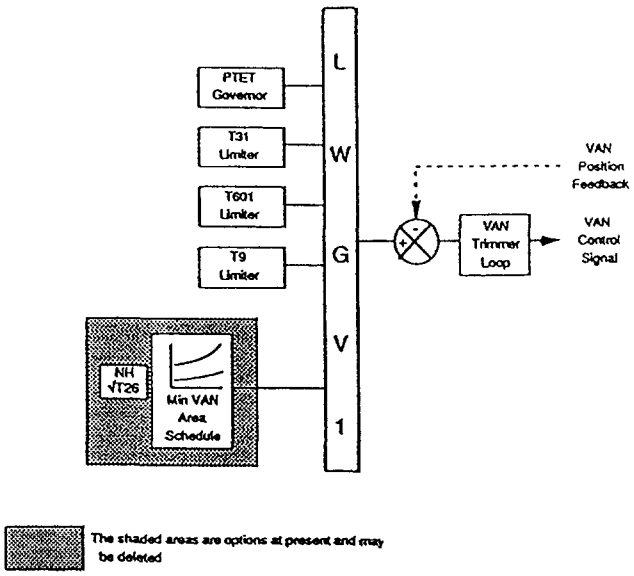

Fig. 4 ICR engine variable area nozzle control

to select the appropriate fuel flow schedules. A back-up primary control based on fuel flow is used in the event of power measurement loss. The overall fuel control system block diagram is shown in Fig. 3.

The power reference, or set point, received from the RMCS is provided to the power governor via a rate limiter. This provides several benefits:

(*a*) The fuel governor can have high gains to keep tight control, and a fast response.

(*b*) The initial rate of change of fuel during large positive transients is limited so that excessive power turbine entry temperature (PTET) and compressor running line excursions are avoided.

(*c*) The fuel flow increase is restricted at the start of the transient, which allows the VAN time to respond to its control loop.

Stability at a commanded power level is required to be better than ±2 percent power fluctuations from idle to 50 percent power and ±1 percent above 50 percent power. Power measurement is provided by measuring the PT shaft speed and torque.

The VAN control attempts to regulate the power turbine entry temperature to maximize recuperator heat recovery. The VAN control is also restrained by companion temperature control loops that limit combustor inlet temperature, recuperator temperature, and exhaust gas temperature. The control loops are compared through a LWG to ensure that the lowest temperature control loop governs the VAN opening. The overall VAN control system block diagram is shown in Fig. 4.

The bleed-off/valve (BOV) control capability (BOVCO) opens and shuts four intermediate-pressure compressor (IPC) and three high-pressure compressor (HPC) BOVs to avoid compressor surge during transient or light load conditions.

Three of the four IPC bleed valves are 6 percent bleeds (i.e., they will flow 6 percent of the IPC inlet mass flow, at the point for which they are needed). The fourth bleed valve is a 10 percent bleed, which will mainly be used for bypassed intercooler operation. Each bleed will be switched at a nondimensional speed. There must be a degree of hysteresis in the bleed operation to prevent teetering on a switching point.

Two of the three HPC bleed valves are 5 percent bleeds. These will be taken from the third stage of the compressor. Each bleed will be switched at a HP compressor nondimensional speed and are controlled in a fashion similar to the IPC bleed valves. The third HPC bleed valves is also 5 percent and will close on the acceleration to idle during starting.

Turbine Sequencer Capability. The turbine sequencer (TSEQ) component is responsible for start and stop sequences of the ICR engine system. TSEQ has two modes of operation: ONLINE and OFFLINE. ONLINE operation provides the capability to start and stop the ICR manually or automatically, while OFFLINE operation provide the means of individually verifying the operation of the primary engine control actuators to assist in engine maintenance activities.

Heat Exchange Logic Capability. The HEX capability is responsible for the thermal management of the intercooler and recuperator systems.

Control of the temperature of the fresh water entering the intercooler is necessary to avoid condensation in the HPC entry air. Condensation is avoided by controlling the temperature of the water entering the intercooler to be above the dew point of the air at IPC delivery pressure.

Since there is a potential for boiling the intercooler fresh water when the circulating pumps have stopped, the EEC automatically takes action to remove the water from the intercooler cores. HEX is responsible for drain and isolation valve sequencing for intercooler bypass operation.

At recuperator core operating temperatures below approximately 140°C, sulfuric acid in the exhaust gas could condense on the metal surfaces of the recuperator, leading to corrosion problems and reduction of service life. HEX maintains recuperator temperature above 170°C by controlling a bypass valve between the air side entry and exit to divert a portion of the HPC delivery air directly to the combustor inlet manifold, reducing the heat extracted from the exhaust gas, and maintaining a minimum recuperator core temperature.

RMCS Communication Capability. The COM component is responsible for formating the engine status data for transmission to and for the interpreting the commands received from the RMCS. The engine status data is updated for transmission at a rate of four times per second.

IV Conclusion

The development of the new ICR gas turbine main propulsion engine for US navy surface combatants is paralleled by the development of a modern electronic engine controller. The decision to base the controller on a standard, commercial open architecture results in a system that will be easy to maintain, support, and upgrade throughout the service life of the ICR engine. The incorporation of the graphically based control interface and built-in-test capability provides the operator with easily understood status, alarm conditions, and system faults.

Acknowledgments

The authors wish to thank Mr. R. G. Ricket of Westinghouse, Mr. Lynn Steward of Rolls-Royce Marine and Industrial Gas Turbines, Ltd., and Mr. M. Allard of CAE Electronics, Ltd. for their assistance and contributions to this paper.

References

Bowen, T. L., and Groghan, D. L., 1984, "Advanced Cycle Gas Turbines for Naval Ship Propulsion," *Naval Engineers Journal*, Vol. 96, No. 2.

Crisalli, A. J., and Parker, M. L., 1993, "Overview of the WR21 Intercooled Recuperated Gas Turbine Engine System—A Modern Engine for a Modern Fleet," ASME Paper No. 93-GT-231.

Thomson, G. A., Pratley, D. J., and Owen, D. A., 1987, "Intercooling and Regenerating the Modern Marine Gas Turbine Propulsion System," SAE Paper No. 871379.

Todman, M. T., 1992, "The ICR Gas Turbine—An Introduction to the Future," INEC 92, Paper 35.

Downloaded 02 Jun 2010 to 171.66.16.102. Redistribution subject to ASME license or copyright; see http://www.asme.org/terms/Terms_Use.cfm

Active Vibration Control of Rotating Machinery Using Piezoelectric Actuators Incorporating Flexible Casing Effects

T. S. Barrett

A. B. Palazzolo

Department of Mechanical Engineering,
Texas A & M University,
College Station, TX 77840

A. F. Kascak

U.S. Army at NASA Lewis
Research Center,
Cleveland, OH 44135

The modern trend toward lighter and more flexible designs in rotating machinery brings with it increasing demands for ways to dissipate the excess energy transferred to such structures by the action of dynamic forces. The present study incorporates the use of active feedback control mechanisms to suppress this unwanted vibration. The basic active damping scheme involves the introduction of a control force on the structure from a feedback network whose input is dictated by the motion of the structure. The control force is applied to the rotor bearing support housing via a piezoelectric actuator attached to the rotor casing. The current research extends previous electromechanical simulations by incorporating a flexible finite element shell model of the casing to support the actuator and sensors. Actuator and feedback loop dynamics are included in the stability and response simulation.

Introduction

In many cases, passive devices are inadequate or impractical, and unable to provide the required amount of damping to reduce vibration to acceptable levels. In cases such as this, a class of dampers known as active dampers, whose performance relies on the availability of external power, can be used. Active dampers generally incorporate a feedback control mechanism, which senses the motion of the structure, and responds with a corrective force to oppose the unwanted vibration. Thus, the output force is dependent on each successive motion of the structure. The main advantage of active control over passive control is the ease with which active control can adjust to varying loading conditions. Other advantages of active vibration control include low weight, compact size, and versatile operating conditions.

Literature Review

Lin et al. (1993) developed an optimal control method using proportional/derivative control techniques utilizing piezoelectric actuators. This research extends the model developed, adding flexible rotor casing effects.

Rouch et al. (1986) investigated modeling of rotor/foundation interaction using frequency response functions in a special purpose finite element code. This analysis was done using frequency response functions to form a matrix of functions, which include interaction between support locations and coupling of horizontal and vertical effects. This research determined that the addition of foundation flexibility tends to lower the frequency of the first critical speed, increase the amplification factor, and can change the system stability. Active vibration control was not utilized in this system.

Kramer et al. (1976) proposed a method to simplify the solution of large degree of freedom rotor models while still including foundation effects; however, the technique was not incorporated with active vibration controls. Balas (1978) developed a feedback control scheme for flexible systems using the generalized wave equation with damping. The control spillover due to the residual modes was treated and the effect on system stability examined.

Salm and Schweitzer (1984) examined modal space–output feedback–optimal control in a reduced order model. Spillover effects were discussed, and the authors show how stability of the closed-loop system is assured if the sensors and actuators are collocated, and if the stiffness and damping feedback matrices are positive definite. The control strategy used was addition of modal stiffness and damping values, and only steady-state response was discussed. Reinig and Desrochers (1986) developed an approach to identify and counteract the imbalance force in a Jeffcott rotor with rigid bearings. Foundation and casing flexibility was not discussed. The controlled vibrations were steady state.

Contributed by the International Gas Turbine Institute and presented at the 38th International Gas Turbine and Aeroengine Congress and Exposition, Cincinnati, Ohio, May 24–27, 1993. Manuscript received at ASME Headquarters March 10, 1993. Paper No. 93-GT-293. Associate Technical Editor: H. Lukas.

Copyright © 1995 by ASME

Downloaded 02 Jun 2010 to 171.66.16.102. Redistribution subject to ASME license or copyright; see http://www.asme.org/terms/Terms_Use.cfm

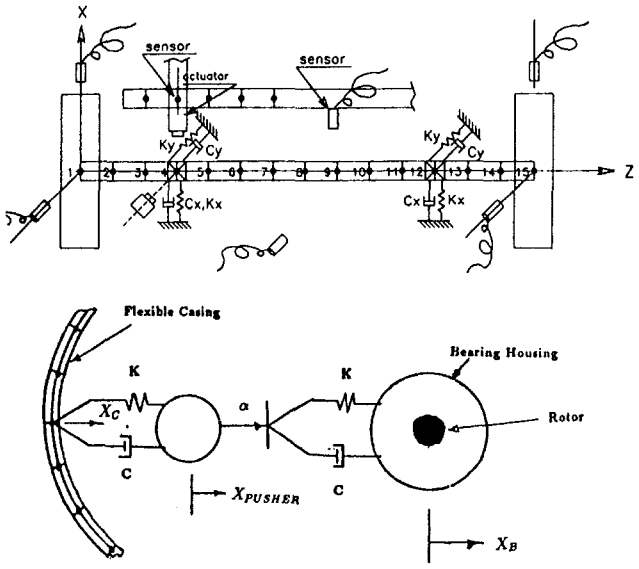

Fig. 1 Fourteen mass rotor model and actuator connection

The unique contribution of this work is to develop a generic active vibration control modeling procedure including flexible casing effects.

Theoretical Development

Bearing / Actuator Equations of Motion. Figure 1 depicts the 14 mass rotor model used in this research to represent a test rig at NASA Lewis Research Center, Cleveland, Ohio. The piezoelectric actuators are applied at each of the two bearings (nodes 4 and 12), and the corresponding motion sensors are located as close to the actuators as physically possible. Typically four orthogonal pushers are used at each bearing, but the number of actuators can be modified as desired.

Figure 2 shows a two pusher model with an equivalent electrical circuit representing the feedback loop. Note that each pusher is shown attached to a flexible casing instead of "ground" as in previous models. This circuit represents what is termed throughout this research as one "module." One module represents a circuit containing two opposing pushers, and their electrical degrees of freedom. Each pusher acts equal and opposite of the other, since the pushers do not

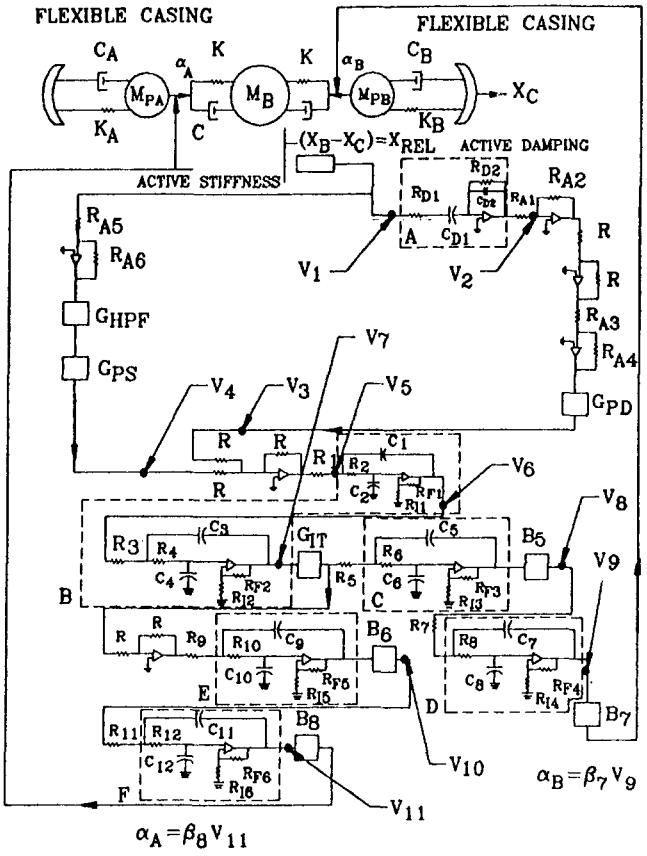

Fig. 2 Pusher model with equivalent electrical circuit

have the capability to "pull" the squirrel cage support in any one direction, thus pushers must always be used in opposing configurations for proper vibration suppression. Figure 3 shows a single pusher mounted to a flexible casing and its method of attachment along with an internal diagram of the actuator. The motion of the bearing and pushers is best described with the free body diagrams shown in Figs. 4–6. Summing forces of the bearing according to Newton's second law for the bearing (Fig. 4)

$$M_B\ddot{X} = -K_{PB}(X - X_B + \alpha_B) - K_{PA}(X - X_A - \alpha_A) - KX - C\dot{X} + F(t)$$

Nomenclature

A = low pass filter constant
$[C]$ = damping matrix
$[E]$ = material property matrix
$F(t)$ = forcing function (function of time)
G_{PD} = equivalent gain to match original and new circuit
G_{PS} = active stiffness loop gain
i_c = current flow from capacitor
I_{T_j} = translatory moment of inertia of inertia station
k = attachment spring
$[K]$ = stiffness matrix
K_j = internal zero frequency gain of low pass filter
K_{PA} = stiffness of pusher A
K_{PB} = stiffness of pusher B
K_{RA} = absorber stiffness at pusher A
K_{RB} = absorber stiffness at pusher B
K_s = piezoelectric stack stiffness
$[M]$ = mass matrix
M_B = mass of bearing
M_PA = mass of pusher A
M_PB = mass of pusher B
$[N]$ = shape function matrix
$\text{NDOF}_{\text{CLOOP}}$ = number of degrees of freedom (closed loop)
$\text{NDOF}_{\text{OLOOP}}$ = number of degrees of freedom (open loop)
R = resistance
u, v, w = nodal displacements
V_C = voltage across a capacitor
V_R = voltage drop across a resistor
V_{in} = voltage into low pass filter
V_{out} = voltage out of low pass filter
X = displacement of bearing
X_A = displacement of pusher A
X_B = displacement of pusher B
$X_{\text{REL}} = X_{\text{ROTOR}} - X_{\text{CASING}}$
$[Z]$ = displacement vector
α = prescribed displacement
ζ = sensitivity of displacement probe
ν = Poisson ratio
ω_j = cut-off frequency of low pass filter (undamped)

Downloaded 02 Jun 2010 to 171.66.16.102. Redistribution subject to ASME license or copyright; see http://www.asme.org/terms/Terms_Use.cfm

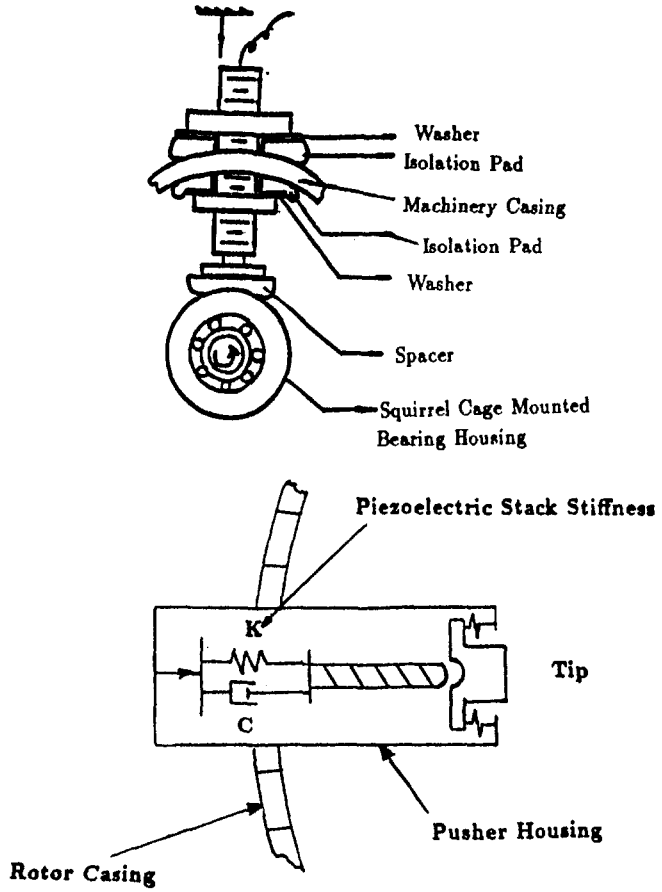

Fig. 3 Actuator mounted to flexible housing and its internal diagram

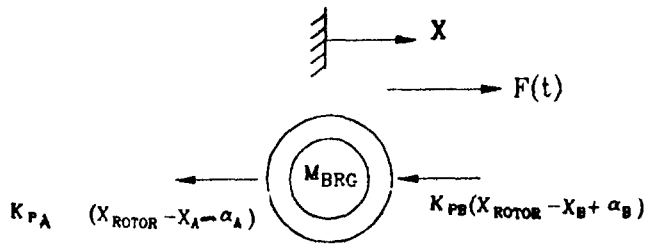

Fig. 4 Free body diagram of rotor bearing mass

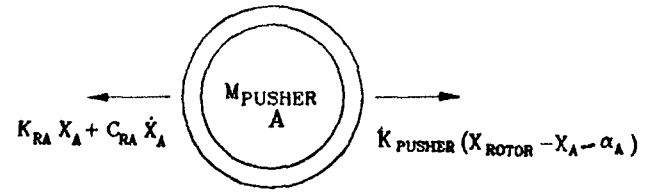

Fig. 5 Free body diagram of pusher *A*

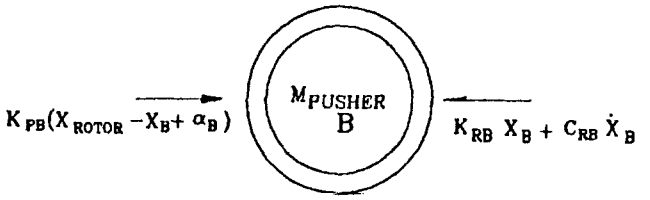

Fig. 6 Free body diagram of pusher *B*

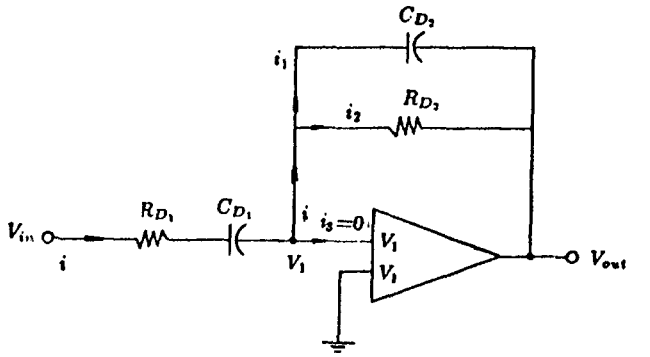

Fig. 7 Diagram of inverting differentiator

where α represents the prescribed displacement the prescribed displacement of the pusher. Simplifying, the equation becomes:

$$M_B\ddot{X} + C\dot{X} + (K + K_{PB} + K_{PA})X + K_{PB}\alpha_B - K_{PA}\alpha_A - K_{PA}X_A - K_{PB}X_B = F(t) \quad (1)$$

Similarly for pusher A (shown in Fig. 5):

$$M_{PA}\ddot{X}_A = K_{PA}(X - X_A - \alpha_A) - K_{RA}X_A - C_{RA}\dot{X}_A$$

and

$$M_{PA}\ddot{X}_A + (K_{PA} + K_{RA})X_A + C_{RA}\dot{X}_A - K_{PA}X + K_{PA}\alpha = 0 \quad (2)$$

and pusher B (Fig. 6),

$$M_{PB}\ddot{X}_B = K_{PB}(X - X_B - \alpha_B) - K_{RB}X_B - C_{RB}\dot{X}_B$$

Again simplifying, this becomes:

$$M_{PB}\ddot{X}_B + (K_{PB} + K_{RB})X_B + C_{RB}\dot{X}_B - K_{PB}X - K_{PB}\alpha_B = 0 \quad (3)$$

Equations (1)–(3) describe the fundamental equations of motion for the pushers and bearing, and are used in conjunction with the electrical circuit shown in Fig. 2 to simulate the system.

Electromechanical Equations of Motion. The electrical circuit is divided into two main branches: an active damping loop and an active stiffness loop. Each module consists of two pusher degrees of freedom and seven voltage degrees of freedom, corresponding to the construction of the circuit in Fig. 2.

The active damping loop serves to reduce unbalance response at a resonant frequency, while the active stiffness loop is used primarily to shift the location of the natural frequency. Starting with the active damping loop, the equations for each component of the circuit will be derived and the matrix form of the equations shown. The first component in the active damping loop is an inverting differentiator (see Fig. 7), which takes the displacement signal on input, and differentiates to yield velocity. The entire circuit has one differentiator and six noninverting second-order low pass filters, resulting in equations for the seven voltage degrees of freedom. Referring to Fig. 7, the equation describing the differentiator is:

$$\dot{V}_{IN} + R_{D1}C_{D2}\ddot{V}_{OUT} + \frac{R_{D1}}{R_{D2}}\dot{V}_{OUT} + \frac{C_{D2}}{C_{D1}}\dot{V}_{OUT} + \frac{1}{C_{D1}R_{D2}}V_{OUT} = 0 \quad (4)$$

But, $V_{IN} = \zeta_1 X$, where ζ_1 is the sensitivity of the displacement probe in volts/meter. Denoting V_{OUT} as V_1 and substi-

Downloaded 02 Jun 2010 to 171.66.16.102. Redistribution subject to ASME license or copyright; see http://www.asme.org/terms/Terms_Use.cfm

tuting the sensitivity relation, the final expression for the inverting differentiator becomes:

$$(R_{D1}C_{D2})\ddot{V}_1 + \left(\frac{R_{D1}}{R_{D2}} + \frac{C_{D2}}{C_{D1}}\right)\dot{V}_1 + \frac{1}{C_{D1}R_{D2}}V_1 + \zeta_1\dot{X}_{REL} = 0 \quad (5)$$

Referring to Fig. 8, the equation for the second-order low pass filter is:

$$V_1\left(\frac{K}{R_1R_2C_1C_2}\right) = \ddot{V}_2 + \left(\frac{1}{C_1C_2} + \frac{1}{R_2C_2} - \frac{K}{R_2C_2} + \frac{1}{R_2C_1}\right)\dot{V}_2 + \frac{1}{R_1R_2C_1C_2}V_2 \quad (6)$$

Defining

$$A = \left(\frac{1}{R_1C_1} + \frac{1}{R_2C_2} - \frac{K}{R_2C_2} + \frac{1}{R_2C_1}\right) \quad (7)$$

The first portion of the feedback loop shown in Fig. 2 is composed of an inverting differentiator (Block *A*), followed by two second-order noninverting low pass filters after the summing junction to simulate a fourth-order low pass filter (Block *B*). The second portion of the loop, again the gain G_{IT}, similarly uses two second-order noninverting low pass filters to simulate pusher driver *B* (Block *C*), pusher *B* (Block *D*), pusher driver *A* (Block *E*), and pusher *A* (Block *F*). The nonideal characteristics of the feedback elements (differentiator, filter, and actuator) due to phase lag and actuator roll off can be examined with this model as discussed by Lin et al. (1993). This figure depicts the feedback displacement X_{REL}, which represents the relative displacement between the rotor and casing.

Using Eq. (5) for the inverting differentiator, expanding the generalized relation (Eq. (9)) for the six low pass filters), and recalling the equations of motion for the bearing and pushers (Eqs. (1)–(2)), the nine electromechanical equations in matrix form representing one module, are shown below in Eq. (11).

$$\begin{pmatrix} M_B & 0 & 0 & 0 & 0 & 0 & 0 & 0 & 0 & 0 \\ 0 & M_{PA} & 0 & 0 & 0 & 0 & 0 & 0 & 0 & 0 \\ 0 & 0 & M_{PB} & 0 & 0 & 0 & 0 & 0 & 0 & 0 \\ 0 & 0 & 0 & R_{D1}C_{D2} & 0 & 0 & 0 & 0 & 0 & 0 \\ 0 & 0 & 0 & 0 & 1 & 0 & 0 & 0 & 0 & 0 \\ 0 & 0 & 0 & 0 & 0 & 1 & 0 & 0 & 0 & 0 \\ 0 & 0 & 0 & 0 & 0 & 0 & 1 & 0 & 0 & 0 \\ 0 & 0 & 0 & 0 & 0 & 0 & 0 & 1 & 0 & 0 \\ 0 & 0 & 0 & 0 & 0 & 0 & 0 & 0 & 1 & 0 \\ 0 & 0 & 0 & 0 & 0 & 0 & 0 & 0 & 0 & 1 \end{pmatrix} \begin{pmatrix} \ddot{x} \\ \ddot{x}_A \\ \ddot{x}_B \\ \ddot{V}_1 \\ \ddot{V}_2 \\ \ddot{V}_3 \\ \ddot{V}_4 \\ \ddot{V}_5 \\ \ddot{V}_6 \\ \ddot{V}_7 \end{pmatrix} + \begin{pmatrix} c & 0 & 0 & 0 & 0 & 0 & 0 & 0 & 0 & 0 \\ 0 & C_{RA} & 0 & 0 & 0 & 0 & 0 & 0 & 0 & 0 \\ 0 & 0 & C_{RB} & 0 & 0 & 0 & 0 & 0 & 0 & 0 \\ \zeta_1 & 0 & 0 & B & 0 & 0 & 0 & 0 & 0 & 0 \\ 0 & 0 & 0 & 0 & A_1 & 0 & 0 & 0 & 0 & 0 \\ 0 & 0 & 0 & 0 & 0 & A_2 & 0 & 0 & 0 & 0 \\ 0 & 0 & 0 & 0 & 0 & 0 & A_3 & 0 & 0 & 0 \\ 0 & 0 & 0 & 0 & 0 & 0 & 0 & A_4 & 0 & 0 \\ 0 & 0 & 0 & 0 & 0 & 0 & 0 & 0 & A_5 & 0 \\ 0 & 0 & 0 & 0 & 0 & 0 & 0 & 0 & 0 & A_6 \end{pmatrix} \begin{pmatrix} \dot{x} \\ \dot{x}_A \\ \dot{x}_B \\ \dot{V}_1 \\ \dot{V}_2 \\ \dot{V}_3 \\ \dot{V}_4 \\ \dot{V}_5 \\ \dot{V}_6 \\ \dot{V}_7 \end{pmatrix}$$

$$+ \begin{pmatrix} k_{11} & k_{22} & k_{13} & 0 & 0 & 0 & 0 & k_{18} & 0 & k_{110} \\ k_{11} & k_{22} & 0 & 0 & 0 & 0 & 0 & 0 & 0 & k_{210} \\ k_{31} & 0 & k_{33} & 0 & 0 & 0 & 0 & k_{38} & 0 & 0 \\ 0 & 0 & 0 & k_{44} & 0 & 0 & 0 & 0 & 0 & 0 \\ k_{51} & 0 & 0 & k_{54} & k_{55} & 0 & 0 & 0 & 0 & 0 \\ 0 & 0 & 0 & 0 & k_{65} & k_{66} & 0 & 0 & 0 & 0 \\ 0 & 0 & 0 & 0 & 0 & k_{76} & k_{77} & 0 & 0 & 0 \\ 0 & 0 & 0 & 0 & 0 & 0 & k_{87} & k_{88} & 0 & 0 \\ 0 & 0 & 0 & 0 & 0 & k_{96} & 0 & 0 & k_{99} & 0 \\ 0 & 0 & 0 & 0 & 0 & 0 & 0 & 0 & k_{109} & k_{1010} \end{pmatrix} \begin{pmatrix} x \\ x_A \\ x_B \\ V_1 \\ V_2 \\ V_3 \\ V_4 \\ V_5 \\ V_6 \\ V_7 \end{pmatrix} = \begin{pmatrix} F(t) \\ 0 \\ 0 \\ 0 \\ 0 \\ 0 \\ 0 \\ 0 \\ 0 \\ 0 \end{pmatrix} \quad (11)$$

and

$$\omega = \sqrt{\frac{1}{R_1R_2C_1C_2}} \quad (8)$$

the equation becomes:

$$\ddot{V}_2 + A\dot{V}_2 + \omega^2V_2 = \omega^2KV_1 \quad (9)$$

Generalizing Eq. (9) for the *j*th low pass filter model:

$$V_{1j}\left(\frac{K_j}{R_{2j-1}R_{2j}C_{2j-1}C_{2j}}\right) = \ddot{V}_{2j} + \left(\frac{1}{C_{2j-1}C_{2j}} + \frac{1}{R_{2j}C_{2j}} - \frac{K_j}{R_{2j}C_{2j}} + \frac{1}{R_{2j}C_{2j-1}}\right)\dot{V}_{2j} + \frac{1}{R_{2j-1}R_{2j}C_{2j-1}C_{2j}}V_{2j} \quad (10)$$

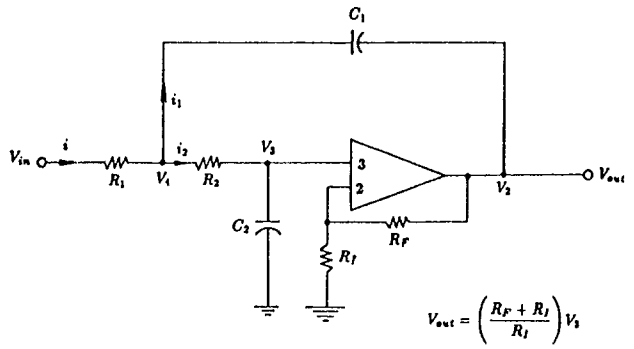

Fig. 8 Second-order low pass filter

Downloaded 02 Jun 2010 to 171.66.16.102. Redistribution subject to ASME license or copyright; see http://www.asme.org/terms/Terms_Use.cfm

where

$$k_{11} = k_j + k_{PA} + k_{PB} \qquad k_{12} = -k_{PA}$$
$$k_{13} = -k_{PB} \qquad k_{18} = k_{PB}\beta_7$$
$$k_{110} = -k_{PA}\beta_8 \qquad k_{21} = -k_{PA}$$
$$k_{22} = k_{RA} + k_{PA} \qquad k_{210} = k_{PA}\beta_8$$
$$k_{31} = -k_{PB} \qquad k_{33} = k_{RB} + k_{PB}$$
$$k_{38} = -k_{PB}\beta_7 \qquad k_{44} = 1/C_{D1}R_{D2}$$
$$k_{51} = \gamma_1 K_1 \omega_1^2 \qquad k_{54} = -K_1\gamma_2\omega_1^2$$
$$k_{55} = \omega_1^2 \qquad k_{65} = -\omega_2^2 K_2$$
$$k_{66} = \omega_2^2 \qquad k_{76} = \omega_3^2 K_3 G'_{IT}$$
$$k_{77} = \omega_3^2 \qquad k_{87} = -\omega_4^2 K_4 \beta_5$$
$$k_{88} = \omega_4^2 \qquad k_{96} = -\omega_5^2 K_5 G'_{IT}$$
$$k_{99} = \omega_5^2 \qquad k_{109} = -\omega_6^2 K_6 \beta_6$$
$$k_{1010} = \omega_6^2$$

In this formulation, K_j is the internal zero frequency gain of the individual filter, defined by:

$$K_j = \frac{R_{I_j} + R_{F_j}}{R_{I_j}}$$

and ω_j is the undamped natural frequency of the filter:

$$\omega_j = \sqrt{\frac{1}{R_{2j-1}R_{2j}C_{2j-1}C_{2j}}}$$

The constants A_j and B are defined as:

$$A_i = \left(\frac{1}{C_{2i-1}}\left(\frac{1}{R_{2i-1}} + \frac{1}{R_2 i}\right) + \frac{1 - K_i}{R_{2i}C_{2i}}\right)$$
$$B = \left(\frac{R_{D1}}{R_{D2}} + \frac{C_{D2}}{C_{D1}}\right) \tag{12}$$

Note that the β coefficients are scale factors used to match the amplitudes of the frequency response functions to those of the equivalent electrical circuit for the pusher driver and pusher, i.e.:

$$\alpha_A = \beta_8 V_7$$
$$\alpha_B = \beta_7 V_5$$

The equations shown in Eq. (11) represent the electromechanical degrees of freedom, and are assembled into the structural finite element model of the rotor and casing.

Using the equations developed above for the electrical components, expressions can be written for each voltage in the circuit. Starting with the active damping loop, V_1 is the displacement signal (X_{REL}) multiplied by the sensor sensitivity (ζ)

$$V_1 = \zeta X_{REL} \tag{13}$$

V_2 and the subsequent voltages can be expressed with the transfer functions of each electrical component, thus:

$$V_2 = \frac{-R_{D2}C_{D1}SV_1}{R_{D1}R_{D2}C_{D1}C_{D2}S^2 + [(R_{D1}C_{D1} + R_{D2}C_{D2})S + 1]} \tag{14}$$

$$V_4 = -V_1 G_{HPF} G_{PS} \tag{15}$$

$$V_5 = -(V_3 + V_4) \tag{16}$$

$$V_6 = \frac{\frac{K_6}{R_1R_2C_1C_2}V_5}{S^2 + \left[\frac{1}{C_1}\left(\frac{1}{R_1} + \frac{1}{R_2}\right) + \frac{1 - K_6}{R_2C_2}\right]S + \frac{1}{R_1R_2C_1C_2}} \tag{17}$$

where K_i represents the zero frequency gain, or

$$K_i = \frac{R_{Fi} + R_{Ii}}{R_{Ii}} \tag{18}$$

In similar fashion,

$$V_7 = \frac{\frac{K_7}{R_3R_4C_3C_4}V_6}{S^2 + \left[\frac{1}{C_3}\left(\frac{1}{R_3} + \frac{1}{R_4}\right) + \frac{1 - K_7}{R_4C_4}\right]S + \frac{1}{R_3R_4C_3C_4}} \tag{19}$$

$$V_8 = \frac{\frac{K_8}{R_5R_6C_5C_6}G_{IT}\beta_5 V_7}{S^2 + \left[\frac{1}{C_5}\left(\frac{1}{R_5} + \frac{1}{R_6}\right) + \frac{1 - K_8}{R_6C_6}\right]S + \frac{1}{R_5R_6C_5C_6}} \tag{20}$$

$$V_9 = \frac{\frac{K_9}{R_7R_8C_7C_8}V_8}{S^2 + \left[\frac{1}{C_7}\left(\frac{1}{R_7} + \frac{1}{R_8}\right) + \frac{1 - K_9}{R_8C_8}\right]S + \frac{1}{R_7R_8C_7C_8}} \tag{21}$$

$$\alpha_B = \beta_7 V_9 \tag{22}$$

$$V_{10} = \frac{-\frac{K_{10}}{R_9R_{10}C_9C_{10}}\beta_6 V_{10}}{S^2 + \left[\frac{1}{C_9}\left(\frac{1}{R_9} + \frac{1}{R_{10}}\right) + \frac{1 - K_{10}}{R_{10}C_{10}}\right]S + \frac{1}{R_9R_{10}C_3C_{10}}} \tag{23}$$

$$V_{11} = \frac{\frac{K_{11}}{R_{11}R_{14}C_{11}C_{12}}\beta_8 V_{10}}{S^2 + \left[\frac{1}{C_{11}}\left(\frac{1}{R_{11}} + \frac{1}{R_{12}}\right) + \frac{1 - K_{11}}{R_{12}C_{12}}\right]S + \frac{1}{R_{11}R_{12}C_{11}C_{12}}} \tag{24}$$

and,

$$\alpha_A = \beta_8 V_{11} \tag{25}$$

Structural Rotor Bearing Development. Consider the lumped mass rotor bearing model shown in Fig. 1. The equation of motion, from Newton's second law, is (in matrix form):

$$[M]_n\{\ddot{Z}\}_{(n\times 1)} + [C]_{(n)}\{\dot{Z}\}_{(n\times 1)} + [K]_{(n\times n)}\{Z\}_{(n\times 1)} = \{F(t)\}_{(n\times 1)} \tag{26}$$

where $[M]$, $[C]$, and $[K]$ represent the rotor bearing mass, damping, and stiffness matrices, n represents the number of degrees of freedom, and $\{F\}$ represents the external forces acting on the system.

Downloaded 02 Jun 2010 to 171.66.16.102. Redistribution subject to ASME license or copyright; see http://www.asme.org/terms/Terms_Use.cfm

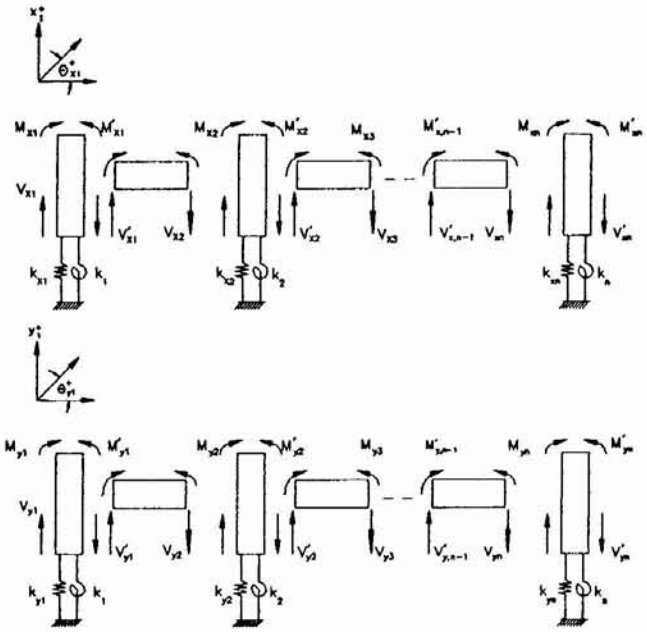

Fig. 9 Free body representation of the rotor elements

The structural model discretizes the rotor into a series of lumped inertia stations connected by massless beam segments, and the equilibrium equation of a disk is determined by consideration of the external forces resulting from adjoining beam segments and bearing stiffness forces. The reader is referred to Barrett (1992) for development of the beam mass, damping, and stiffness matrices of the element shown in Fig. 9.

The AVC simulation can be done either "open loop," i.e., without feedback, or "closed loop," in which the feedback circuit is enabled. The matrix structure of the electromechanical matrix is slightly different for each due to the location of the pusher degrees of freedom. In the open loop case, the pusher DOF's (1 DOF per pusher) are located directly after the rotor degrees of freedom, resulting in augmented matrices of the form:

$$\begin{pmatrix} [M]_{n\times n} & \vdots & \\ \cdots & \cdots & \cdots \\ & \vdots & [M]_{npsh\times 1} \end{pmatrix}\{\ddot{Z}\} + \begin{pmatrix} [C]_{n\times n} & \vdots & \\ \cdots & \cdots & \cdots \\ & \vdots & [C]_{npsh\times 1} \end{pmatrix}\{\dot{Z}\} + \begin{pmatrix} [K]_{n\times n} & \vdots & \\ \cdots & \cdots & \cdots \\ & \vdots & [K]_{npsh\times 1} \end{pmatrix}\{Z\} = \{F(t)\}_{(n+npsh\times 1)} \tag{27}$$

where $\{Z\}$ is a vector having dimension $(n + npsh \times 1)$.

For the closed-loop case the pusher degrees of freedom are contained within each module, and the total number of DOF's becomes:

$$\text{NDOF}_{\text{CLOOP}} = N_{\text{ROTORNODES}} * 4 + \frac{N_{\text{PUSHERS}}}{2} * 9 + N_{\text{CASINGDOF}} \tag{28}$$

For the open-loop case:

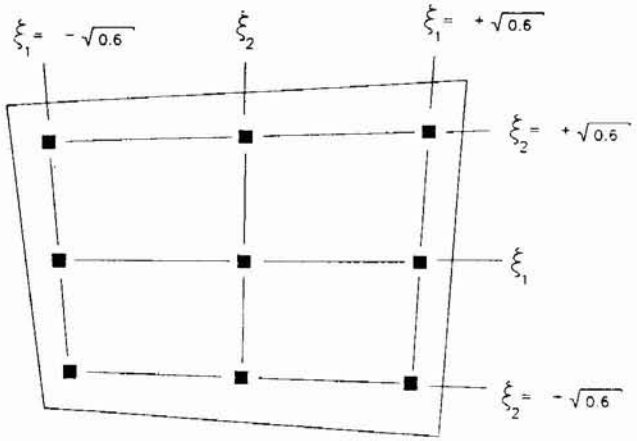

Fig. 10 Elemental cross section showing Gauss point locations

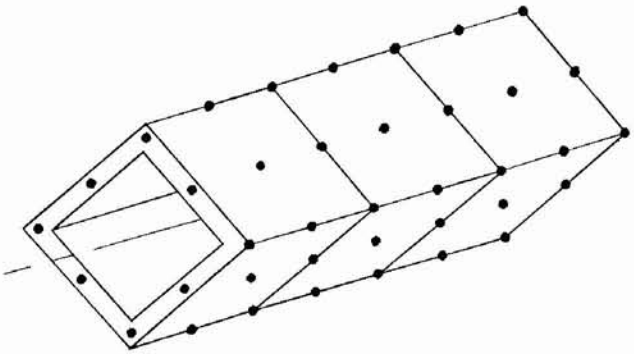

Fig. 11 Casing model; 12 plate elements

$$\text{NDOF}_{\text{OLOOP}} = N_{\text{ROTORNODES}} * 4 + N_{\text{PUSHERS}} + N_{\text{CASINGDOF}} \tag{29}$$

Note that for the examples of this research, the closed-loop case is used as a basis of comparison to Lin (1990).

Casing Finite Element Model. The rotor casing is modeled using nine noded isoparametric finite elements based on standard isoparametric theory. The shape factors used in the formulation produce quadratic interpolation of the element displacements and coordinates. The formulation employs third-order Gauss quadrature as the integration scheme over the volume of the element for a total of 27 integration points (nine in cross section, three through the thickness). Figure 10 depicts an elemental cross section showing the Gauss point locations.

The general form of the stiffness matrix then becomes:

$$[K] = \int_V [B]^T[E][B]dV \tag{30}$$

where $[E]$ is the (6×6) material property matrix, $[B]$ contains derivatives of the shape functions, and V is the volume of the element.

The casing model is shown in Fig. 11, and is composed of 12 isoparametric plate elements arranged in cylindrical fashion. This arrangement was used as an approximation of a rotor casing. Four pushers are attached to orthogonal nodes of the casing at the outboard bearing, and pushers at the inboard bearing are attached in a similar fashion. For the purposes of the research presented here, the pushers at the outboard bearing were inoperative, functioning simply as passive springs to ground and lumped masses. Note also that the casing model is cantilevered, or rigidly constrained at one end and free on the other end.

Downloaded 02 Jun 2010 to 171.66.16.102. Redistribution subject to ASME license or copyright; see http://www.asme.org/terms/Terms_Use.cfm

The casing model contains 288 degrees of freedom, including the cantilever constraints, and the rotor/electromechanical model has an additional 96 degrees of freedom, for a total of 384 degrees of freedom. The augmented system solved by the computer code becomes $2N \times 2N$, or 768 degrees of freedom. This eigenvalue problem is solved using a Cray YMP supercomputer, with a vectorized IMSL mathematical library, and the resulting CPU time for each run was approximately 1 minute.

The matrix assembly procedure is a simple addition of the three models (rotor, electromechanical, and casing) developed in this research. The matrices are joined along their diagonals, and the stiffness matrices coupled via a 4×4 matrix representing a spring connection. An assumption of very small rotational mass was used in the matrix of the casing. This was done in the shell model due to the difficulty in calculating a proportionate mass for the rotational degrees of freedom.

Equation (31) shows the form of the composite mass matrix for the system, and similarly, Eq. (32) shows the form of the stiffness matrix.

$$[M] = \begin{pmatrix} & \vdots & & & & \\ M_{\text{ROTOR}} & \vdots & & & & \\ & \vdots & & & & \\ \cdots \quad \cdots & \cdots & \cdots & & & \\ & \vdots & & \vdots & & \\ & \vdots & M_{\text{ELECTMECH}} & \vdots & & \\ & \vdots & & \vdots & & \\ & \cdots & \cdots & \cdots & \cdots & \cdots \\ & & & & \vdots & \\ & & & & M_{\text{CASING}} & \\ & & & & \vdots & \\ & & & & \vdots & \end{pmatrix} \tag{31}$$

and

$$[K] = \begin{pmatrix} & \vdots & & & & \\ K_{\text{ROTOR}} & \vdots & & & & \\ & \vdots & & & & \\ \cdots \quad \cdots & \cdots & \cdots & & & \\ & \vdots & k & \vdots & & -k \\ & \vdots & K_{\text{ELECTMECH}} & \vdots & & \\ & \vdots & & \vdots & & \\ & \cdots & \cdots & \cdots & \cdots & \\ & & -k & & & k \\ & & & & K_{\text{CASING}} & \\ & & & & \vdots & \\ & & & & \vdots & \end{pmatrix} \tag{32}$$

The coupling connection springs, k, in Eq. (32) are used to attach the casing to the pushers.

The value of k was chosen to be equal to the pusher absorber stiffness, or 0.657E7 N/m. The absorber is a rubberlike material for which the stiffness has been determined to be the value stated above, and the absorber is assumed to have no damping value. The previous research of Lin had the pushers attached to an infinitely rigid "ground" connection. The coupling used here eliminates the ground connection and softens the effective stiffness by connecting to a flexible casing.

Results

Although the main purpose of the study is the investigation of casing effects on predicted response of a rotor bearing system, a reliable method for assuring the integrity of the computer model had to be found. A simple test used in the case of this research was to examine graphically the resulting eigenvalues of the model for a varying range of E (modulus of elasticity), while holding thickness of the casing constant. In other words, the isoparametric plate thickness was held constant at 1/4 in. while the material modulus was varied. To depict stability graphically, the real portion of the eigenvalue is plotted versus the imaginary part for the frequency range of 0 to 10,000 Hz, the frequency range in which instability of the rotor system is a concern. Note that if the real portion of the eigenvalue is negative, then the system is considered unstable. The rationale behind this test is that as the stiffness of the casing increases, the natural frequencies will tend to move upward out of the frequency range, eventually leaving only the eigenvalues of the rotor model alone, which can then be compared to the baseline model with no flexible casing.

Figure 12 shows the baseline eigenvalues of the rotor system alone, without the casing attached. This is the baseline set of eigenvalues, which will be compared to each subsequent set of eigenvalues as casing stiffness is increased. Figures 13 and 14 show corresponding graphs with increased stiffness of 0.207E12 Pa, and 0.207E18 Pa, respectively. Note that these stability checks have been done with an open-loop simulation, or with a very small feedback gain. One can easily see that as the stiffness of the casing is increased, the eigenvalues of the system approach the baseline graph, Fig. 12.

The computer code used to simulate the system, ACTCON.RESP, models the system based on the equations shown derived from Fig. 9 for the structural model and Eq. (11) for the electromechanical model. The parameters are read in via an input file and the code evaluates an eigenvalue/eigenvector solution for either the open or closed-loop solution as

Downloaded 02 Jun 2010 to 171.66.16.102. Redistribution subject to ASME license or copyright; see http://www.asme.org/terms/Terms_Use.cfm

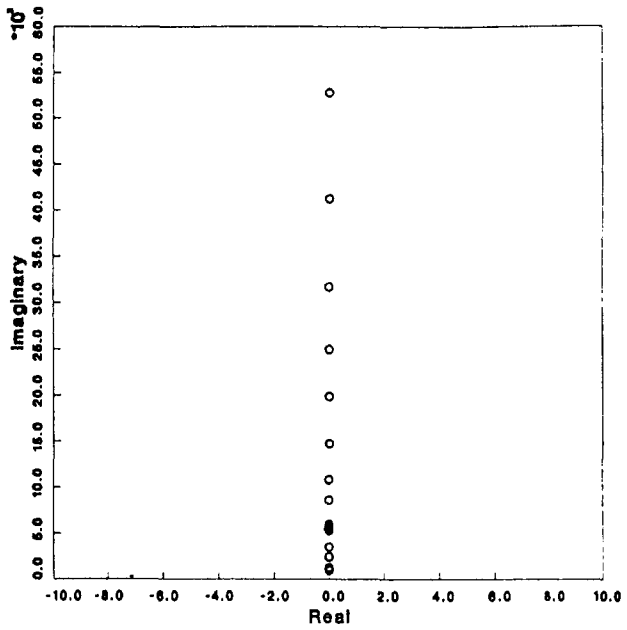

Rotor Only/No Casing
Open Loop Simulation
Beta4=0.00

Fig. 12 Baseline eigenvalues rotor model only (open loop)

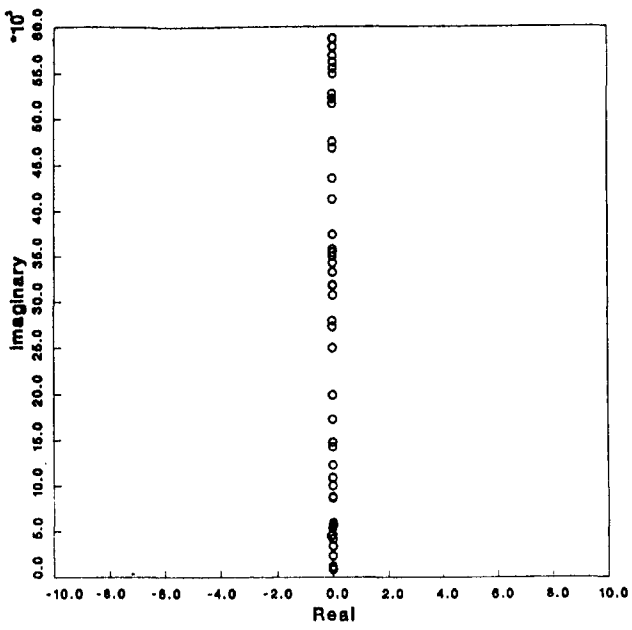

Casing Modulus = .207E12 Pa (30.0 E+6 PSI)
Open Loop Simulation
Beta4=0.00 Thickness = 0.25 in.

Fig. 13 Open-loop predicted eigenvalues; E = 0.207E12 Pa

required. The modeshapes corresponding to each eigenvalue can subsequently be viewed and plotted utilizing DI3000 graphics software package.

Closed-Loop Response. The method presented here to evaluate the effect of a flexible casing is a simple comparison of eigenvalues and modeshapes before and after the addition of the casing. Each mode of the system with the casing attached will have components of both the rotor and casing;

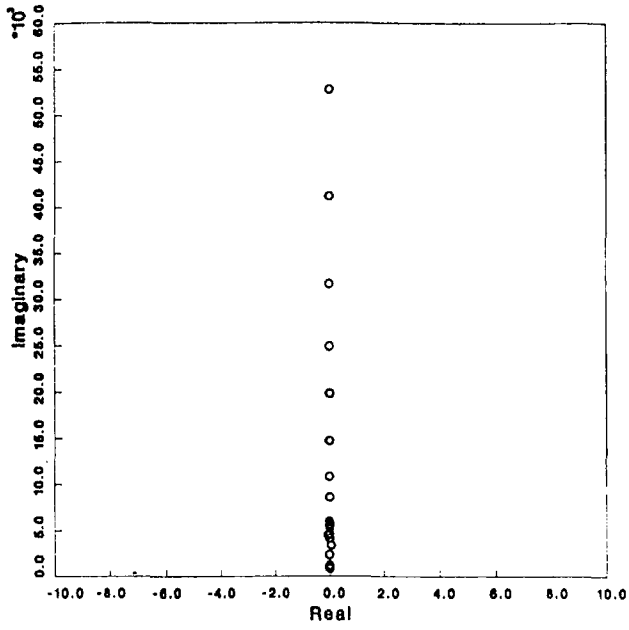

Casing Modulus = .207E18 Pa (30.0E+12 PSI)
Open Loop Simulation
Beta4=0.00 Thickness = 0.25 in.

Fig. 14 Open-loop predicted eigenvalues; E = 0.207E18 Pa

thus the modeshapes generated will not necessarily be the same modeshapes of the baseline case. Since the eigenvalues of the casing are known, the "casing only" eigenvalues can be separated from the output, and comparison of the remaining eigenvalues will show the net effect of the casing. In the case of the NASA test rig, the lowest three modes will be used as an example. In addition, the research by Lin predicted an unstable mode at approximately 2400 Hz, which in reality occurred in the actual tests at 2100 Hz. The effect of the casing on this unstable mode will also be shown.

Figures 15–17 show the first three modeshapes of the baseline rotor model with a feedback gain of 0.25. The lowest three eigenvalues are:

Mode	Eigenvalue
1	$0 + 976i$
2	$-2.201 + 1096.97i$
3	$0 + 1128.3i$

The value of feedback gain was chosen such that the unstable mode at 2400 Hz would be unstable so the effect of the casing on the instability could be seen. The unstable mode is shown in Fig. 18, and matches the shape predicted by Lin.

Figures 19–21 show the modeshape of the first combined rotor/casing mode for a 1/4 in. thick casing. The general modeshapes are unaffected as thickness of the casing is increased, but the eigenvalues do change considerably.

Effect of Casing on System Stability. The effect of the casing on system stability is best presented in much the same fashion as was the verification cases of the ACTCON computer code used for this research. Graphic representations of the eigenvalues for several thicknesses of casings will be compared for trends in stability, and investigated for possible methods of casing thickness optimization. This investigation can be generalized to all rotor bearing systems.

Given a rotor bearing system with piezoelectric actuators as used in this study, fundamental vibration theory suggests that the effect of a flexible casing will be to lower the predicted critical speeds of the system. Since the casing

Downloaded 02 Jun 2010 to 171.66.16.102. Redistribution subject to ASME license or copyright; see http://www.asme.org/terms/Terms_Use.cfm

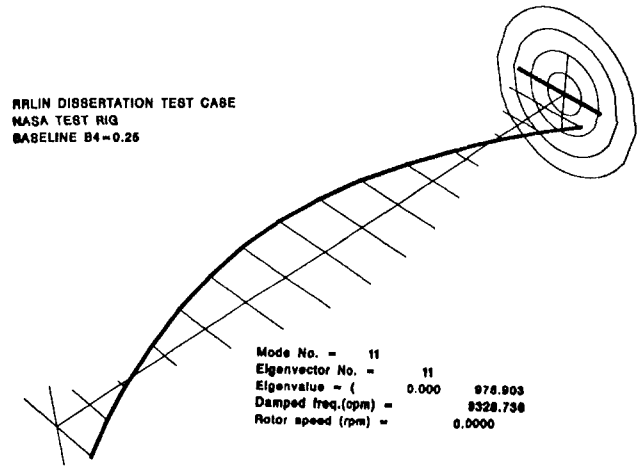

Fig. 15 Predicted first mode rotor only, no casing

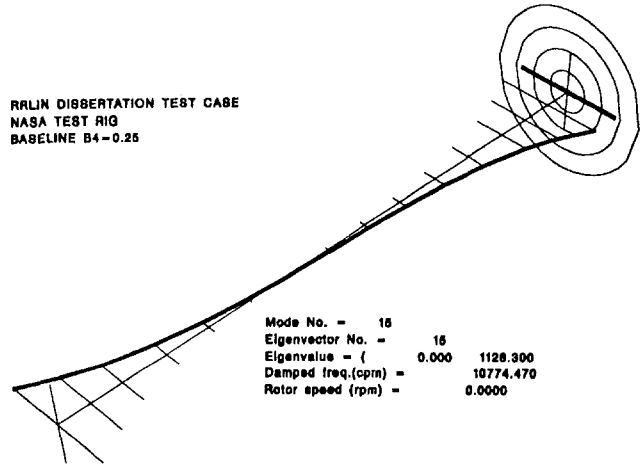

Fig. 16 Predicted second mode rotor only, no casing

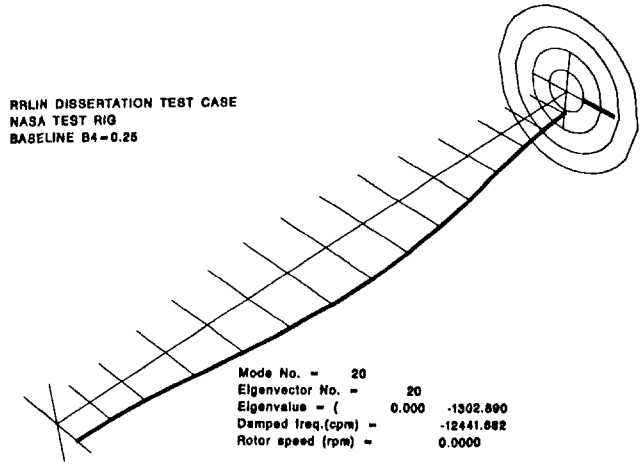

Fig. 17 Predicted third mode rotor only, no casing

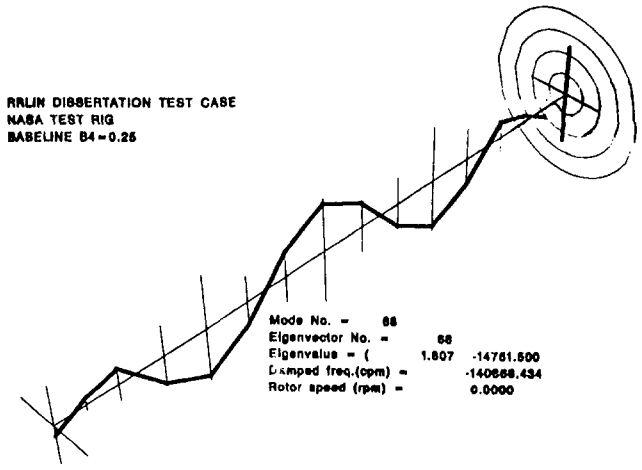

Fig. 18 Predicted unstable mode rotor only, no casing

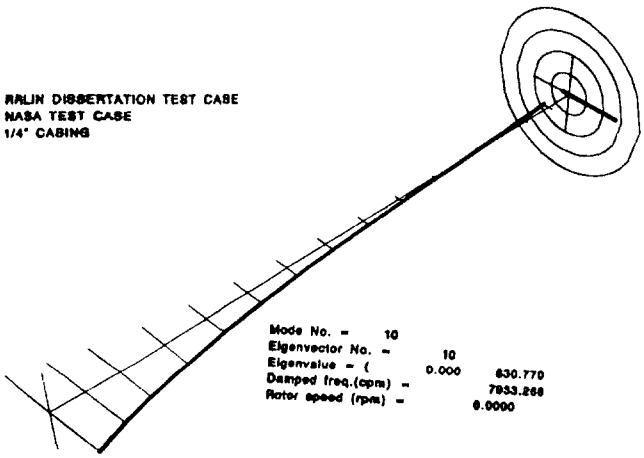

Fig. 19 First mode of combined rotor/casing model (1/4 in. casing)

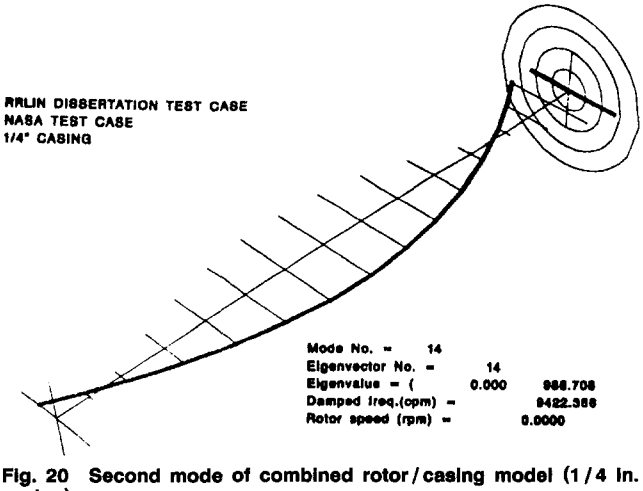

Fig. 20 Second mode of combined rotor/casing model (1/4 in. casing)

stiffness is in series with the pusher stiffness, and the effective casing stiffness decreases, overall stiffness should decrease, provided the pusher stiffness remains constant. This can be rationalized from the fact that in the baseline condition, the piezoelectric pushers are attached to "ground," creating the effect of an infinitely stiff case. Thus, the introduction of a flexible casing effectively lowers the stiffness of the system, and subsequently, the natural frequencies of the system should decrease. The examples discussed will be open-loop examples with the following parameters:

Feedback gain (β_4) = 0.25

Casing modulus (Pa) = 0.207E12 (30.0E6 psi)

Pusher attachment spring (N/m) = 0.657E7 (37516 lb/in.)

These parameters were chosen for study as they produce predicted instabilities in the operating range; thus the study will center around eliminating or minimizing the instabilities.

Downloaded 02 Jun 2010 to 171.66.16.102. Redistribution subject to ASME license or copyright; see http://www.asme.org/terms/Terms_Use.cfm

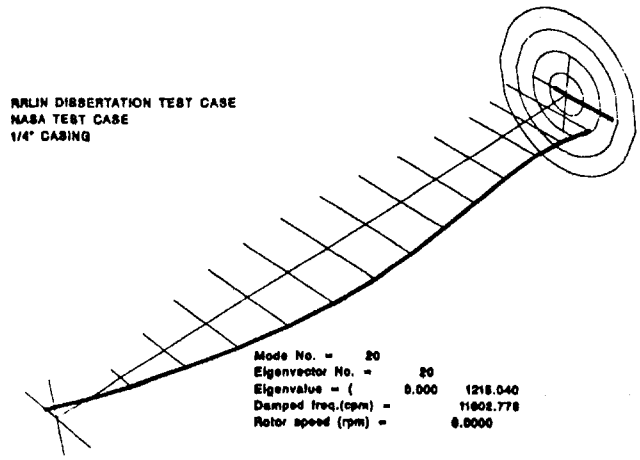

Fig. 21 Third mode of combined rotor/casing model (1/4 in. casing)

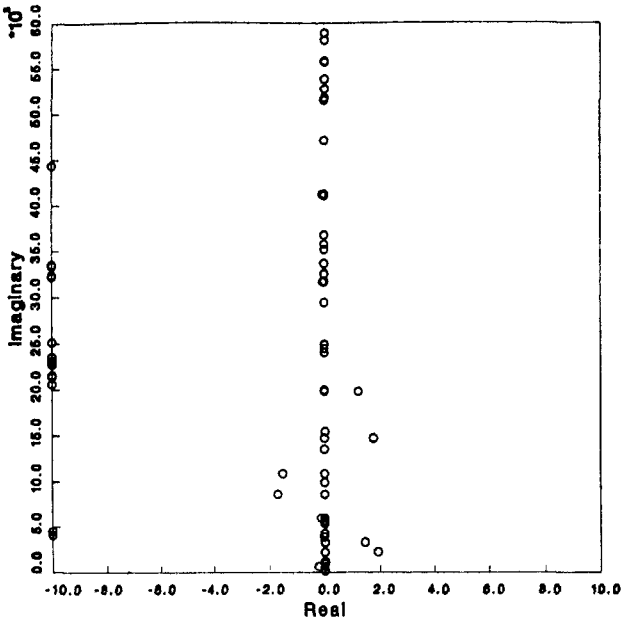

Casing Modulus = .207E12 Pa (30.0E+6 PSI)
Closed Loop Simulation
Beta4=0.25 Thickness = 1/128 in.

Fig. 22 1/128 in. casing wall thickness eigenvalue stability graph

Table 1 Summary of eigenvalues from combined model mode

Thickness	1	2	3
$\frac{1}{128}$"	(-.23,658.38)	(0,982.26)	(0,1201.80)
$\frac{1}{64}$"	(0,562.40)	(0,983.31)	(0,1206.47)
$\frac{1}{32}$"	(0,727.27)	(0,984.48)	(0,1210.25)
$\frac{1}{16}$"	(0,788.66)	(0,985.52)	(0,1212.76)
$\frac{1}{8}$"	(0,817.08)	(0,986.25)	(0,1214.24)
$\frac{1}{4}$"	(0,830.77)	(0,986.71)	(0,1215.04)
$\frac{3}{8}$"	(0,835.27)	(0,986.88)	(0,1215.32)

Casing thicknesses ranging between 1/128 in. and 1/8 in. will be presented for illustration.

Figures 22–26 show stability graphs for the eigenvalues resulting from the casing thicknesses listed above. In looking at the progression of casing thickness, one can see that as the

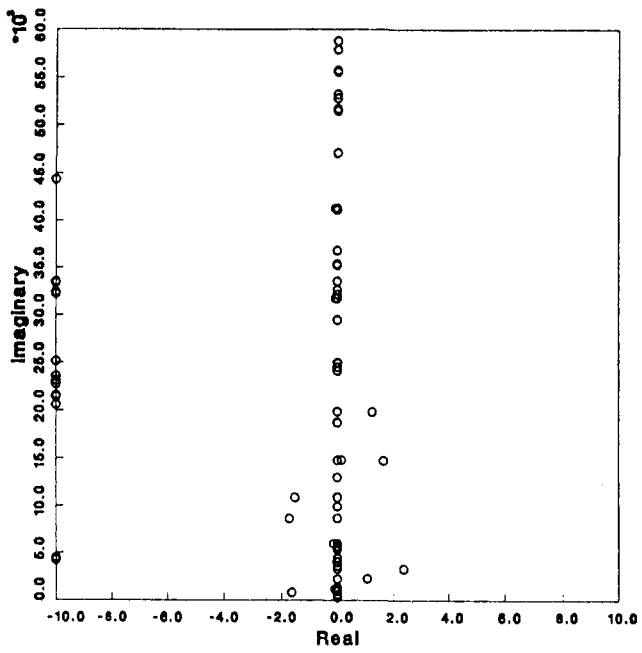

Casing Modulus = .207E12 Pa (30.0E+6 PSI)
Closed Loop Simulation
Beta4=0.25 Thickness = 1/64 in.

Fig. 23 1/64 in. casing wall thickness eigenvalue stability graph

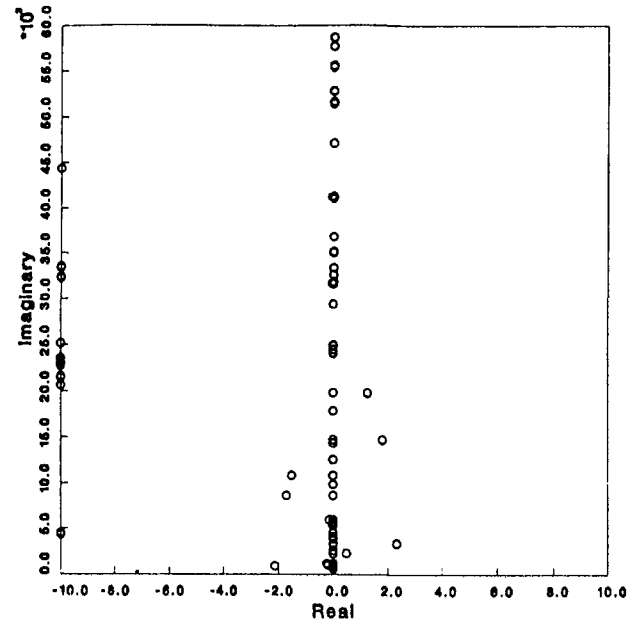

Casing Modulus = .207E12 Pa (30.0E+6 PSI)
Closed Loop Simulation
Beta4=0.25 Thickness = 1/32 in.

Fig. 24 1/32 in. casing wall thickness eigenvalue stability graph

wall thickness of the casing becomes thicker, certain unstable eigenvalues tend to migrate to the left (stable) portion of the graph. Figure 23 shows that at a casing thickness of 1/64 in. four unstable eigenvalues appear, and are denoted by the real portion of the eigenvalue being positive. Table 2 tracks each unstable mode as casing thickness is increased. Looking at the lowest of the unstable modes shows that increasing casing thickness lessens the instability, until the mode is

Downloaded 02 Jun 2010 to 171.66.16.102. Redistribution subject to ASME license or copyright; see http://www.asme.org/terms/Terms_Use.cfm

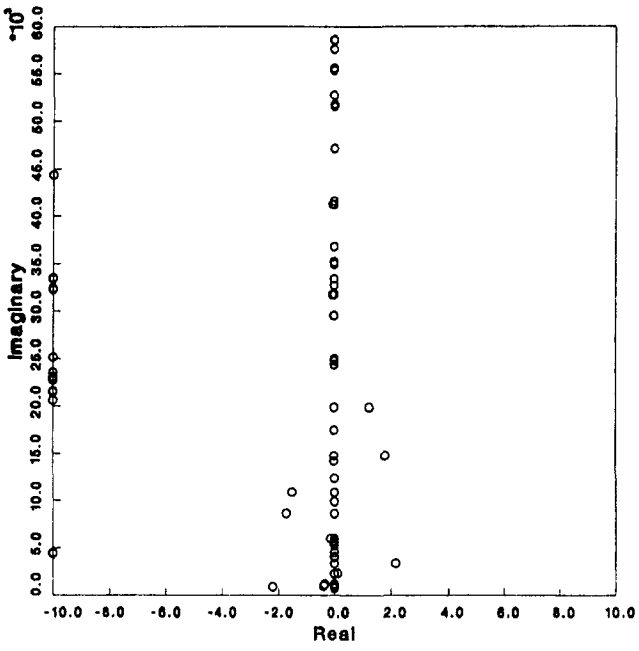

Casing Modulus = .207E12 Pa (30.0E+6 PSI)
Closed Loop Simulation
Beta4=0.25 Thickness = 1/16 in.

Fig. 25 1 / 16 in. casing wall thickness eigenvalue stability graph

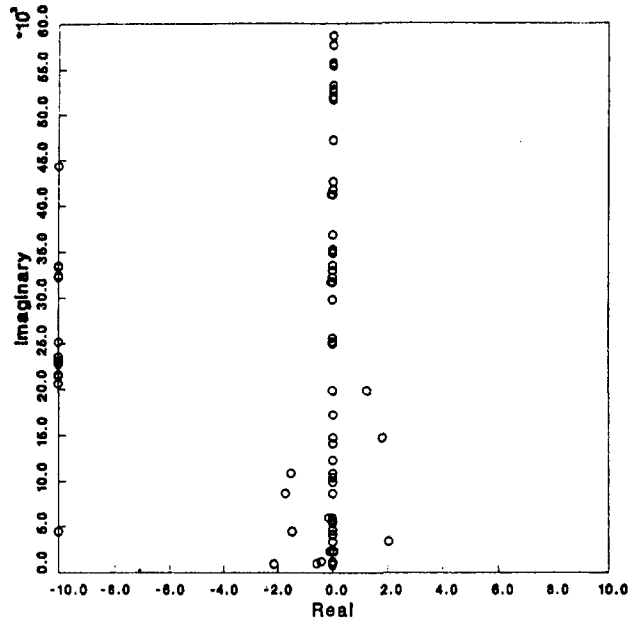

Casing Modulus = .207E12 Pa (30.0E+6 PSI)
Closed Loop Simulation
Beta4=0.25 Thickness = 1/8 in.

Fig. 26 1 / 8 in. casing wall thickness eigenvalue stability graph

stable at 1/4 in. casing thickness (stability graph not shown). The second unstable mode exhibits a similar effect, but the instability never completely disappears as casing thickness increases. The third and fourth unstable modes appear insensitive to casing effects.

Effect of Flexible Casing on Unstable Modes. In the research and tests of Lin, the unstable mode predicted at 2400 Hz, which appeared in actual tests at 2100 Hz, has been

Table 2 Unstable eigenvalue summary unstable mode

Thickness	1	2	3	4
$\frac{1}{128}$"	(1.93,2260)	(1.47,3282)	(1.78,14751)	(1.25,19680)
$\frac{1}{64}$"	(1.07,2306)	(2.38,3350)	(1.66,14750)	(1.25,19680)
$\frac{1}{32}$"	(0.47,2330)	(2.32,3383)	(1.81,14752)	(1.25,19680)
$\frac{1}{16}$"	(0.13,2342)	(2.16,3400)	(1.80,14751)	(1.25,19680)
$\frac{1}{8}$"	(0.05,2344)	(2.04,3409)	(1.80,14751)	(1.25,19680)
$\frac{1}{4}$"	—	(1.98,3412)	(1.80,14751)	(1.25,19680)
$\frac{3}{8}$"	—	(1.95,3414)	(1.80,14751)	(1.25,19680)

Table 3 Summary of baseline eigenvalues with decreased absorber stiffness; baseline model (no casing); unstable mode

Abs. Stiffness (N/m)	1	2	3	4
0.100E6	(1.47,2101)	(2.33,3044)	(1.80,14751)	(1.25,19680)
0.800E6	(0.97,2169)	(2.61,3158)	(1.80,14751)	(1.25,19680)
0.200E7	—	(2.09,3298)	(1.80,14751)	(1.25,19680)
0.400E7	—	(0.37,3429)	(1.80,14751)	(1.26,19680)
0.657E7	—	—	(1.80,14752)	(1.26,19680)

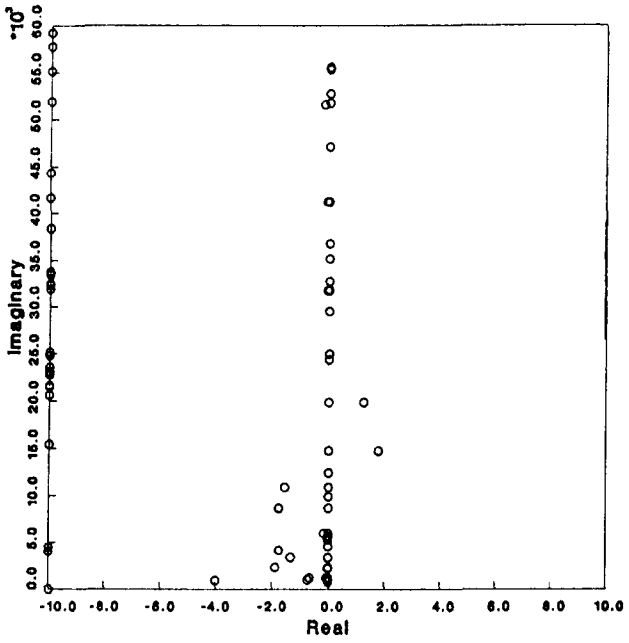

Casing Modulus = .207E12 Pa (30.0E+6 PSI)
Closed Loop Simulation (modified x)
Beta4=0.25 Thickness = 1/16 in.

Fig. 27 Uncoupled sensor (1 / 16 in. casing)

a subject of intense study. It was hoped that the introduction of a flexible casing into the system would help explain the mechanism of this mode, and perhaps lead to a better understanding of its cause.

Table 2 shows that the unstable mode at 2400 Hz is unaffected by the flexible casing. Comparison of baseline eigenvalues in Table 3 verifies this condition, as the mode is insensitive to changes in the absorber stiffness. This mode is believed to be due to electrical component effects. It is important to note that this does not mean that the absorber has no effect on response of the rotor, as it does affect the lower critical speeds and suppresses some unstable modes seen in the actual tests. This finding suggests that the mode is due primarily to the rotor geometry, the mass distribution of the rotor, and electrical effects.

Downloaded 02 Jun 2010 to 171.66.16.102. Redistribution subject to ASME license or copyright; see http://www.asme.org/terms/Terms_Use.cfm

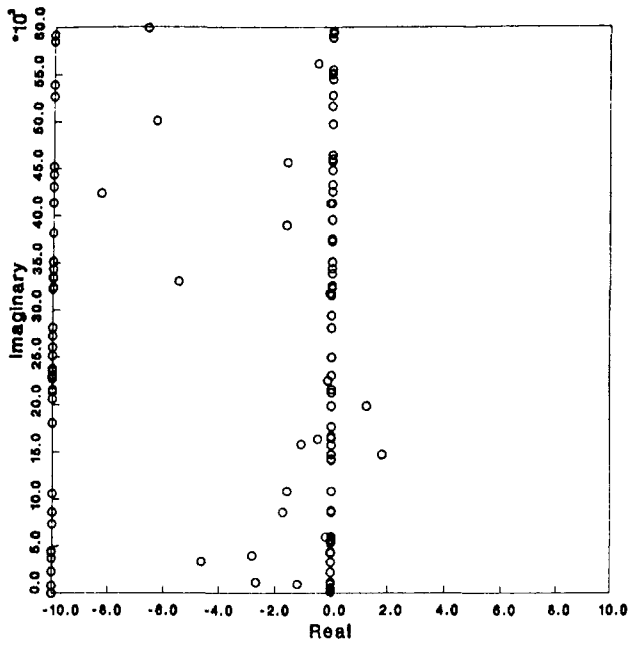

Casing Modulus = .207E12 Pa (30.0E+6 PSI)
Closed Loop Simulation (modified x)
Beta4=0.25 Thickness = 1/64 in.

Fig. 28 Uncoupled sensor (1 / 64 in. casing)

Effect of Sensor Location. In all the simulations up to now, the sensors were attached to the flexible casing, and thus moved with each displacement of the casing. In this configuration, the sensors sensed a relative displacement, or the difference between the casing and rotor displacements. Two simulations were performed with the sensor uncoupled from the casing, or attached to ground, sensing only the rotor displacement. Simulations were performed for casing thicknesses of 1/64 in. and 1/16 in. with this uncoupling of the sensors. Stability graphs for the two cases are shown in Figs. 27 and 28, respectively. With this sensor configuration, the simulation no longer predicts the lower unstable modes predicted with the other sensor configuration. The higher unstable modes, however, remain unaffected. The failure to predict the lower modes occurs because the displacement fed back into the circuit is not an accurate representation of the system behavior.

Conclusions. This paper has presented a new method of active vibration control simulation, using piezoelectric actuators and incorporating a flexible rotor casing into the simulation. The modeling tool used was a FORTRAN computer code, ACTCON, which assembled the structural and electromechanical matrices, and solved the eigenvalue problem. The combined modeling tool predicts rotordynamic stability of a rotor system based on a given casing geometry and thickness. It was seen that the addition of the casing lowers the first predicted mode of the system. As casing thickness increases, unstable eigenvalues tend to migrate toward the stable side of the graph, and at a certain thickness becomes completely stable. The location of the sensor was found to affect the predicted response, with the sensor fixed to ground being unable to predict the lower unstable modes. The sensor attached to the flexible casing was able to predict the lower unstable modes successfully.

Acknowledgments

The authors wish to acknowledge the Air Force Office Of Scientific Research for their funding of this research, and NASA Lewis Research Center for their assistance in completing this study.

References

Balas, M. J., 1978, "Feedback Control of Flexible Systems," IEEE Short Paper No. 0018-9286/78/0800-673.

Barrett, L. E., and Queitzsch, G. K., 1985, "Forced Response Analysis of Multi-level Rotor Systems With Substructure," University of Virginia, Department of Mechanical and Aerospace Engineering, Report UVA/643092/MAE85/320.

Barrett, T. S., 1992, "Active Vibration Control of Rotating Machinery Utilizing Piezoelectric Pushers," Texas A & M University, MS Thesis, Department of Mechanical Engineering.

Bathe, K., 1982, *Finite Element Procedures in Engineering Analysis*, Prentice Hall, Inc., Englewood Cliffs, NJ.

Cook, R., 1981, *Concepts and Applications of Finite Element Analysis*, Wiley, New York.

Heinzman, J. D., Flack, R., and Lewis, D., 1980, "The Implementation of Automatic Vibration Control in a High Speed Rotating Test Facility," Univ. of Virginia Report UVA/464761/MAE80/160.

Kaya, F., and Roberts, J., 1984, "Optimum Vibration Control of Flexible Transmission Shafts," Institute of Mechanical Engineering, C298/84, pp. 525–534.

Kramer, E., Nordman, R., and Klement, H. D., 1976, "The Solution of Vibration Problems With Simple Models," Institute of Mechanical Engineering.

Lin, R., 1990, "Active Vibration Control of Rotorbearing Systems Utilizing Piezoelectric Pushers," Texas A & M University, PhD Dissertation, Department of Mechanical Engineering.

Lin, R., Palazzolo, A., Kascak, A. F., and Montague, G. T., 1993, "Electromechanical Simulation and Testing of Actively Controlled Rotordynamic Systems With Piezoelectric Actuators," ASME JOURNAL OF ENGINEERING FOR GAS TURBINES AND POWER, Vol. 115, pp. 324–335.

MacNeal, R., 1976, "A Simple Quadrilateral Shell Element," *Computers and Structures Journal*, Vol. 8, pp. 175–183.

Palazzolo, A., 1991, Class Notes for MEMA 647, Texas A & M University, Department of Mechanical Engineering.

Palazzolo, A., 1981, "Vibrations of Locally Modified Mechanical and Structural Systems," University of Virginia, PhD Dissertation, Department of Mechanical Engineering.

Reinig, K. D., and Desrochers, A. A., 1986, "Disturbance Accommodating Controllers for Rotating Mechanical Systems," ASME *Journal of Dynamic Systems, Measurement, and Control*, Vol. 108, pp. 24–31.

Roorda, J., 1971, "Active Damping in Structures," Cranfield Institute of Technology, Structural and Aerospace Dynamics Group, Cranfield Report Aero. No. 8.

Rouch, K., McMains, T., and Stephenson, R., 1986, "Modeling of Rotor-Foundation Systems Using Frequency-Response Functions in a Finite Element Approach," copies may be obtained from T. S. Barrett.

Salm, J., and Schweitzer, G., 1984, "Modeling and Control of a Flexible Rotor With Magnetic Bearings," I.Mech.E. *Conference on Rotordynamics*, Paper C277/84, pp. 553–561.

Vance, J., 1988, *Rotordynamics of Turbomachinery*, Wiley, New York.

Zheng, Zhao-chang, Ding, Kui-yuan, and Zhang, Ruo-jing, "Dynamic Analysis of Large Rotor-Fluid Film Bearing-Elastic Foundation Systems Using Component Mode Synthesis," Tsinghua University, Peking, China.

Downloaded 02 Jun 2010 to 171.66.16.102. Redistribution subject to ASME license or copyright; see http://www.asme.org/terms/Terms_Use.cfm

Magnetic Bearing Control of Flexible Shaft Vibrations Based on Multi-access Velocity-Displacement Feedback

G. Petela

K. K. Botros

Nova Husky Research Corp.,
Calgary, Alberta, Canada

A model of the forced vibrations of a flexible, asymmetric, and unbalanced shaft, supported by two magnetic bearings, is derived to simulate the effect of different schemes of active control on shaft dynamic behavior. Simulation results were compared for several cases of single and multi-access bearing controls, rigid-body mode only and rigid with flexible mode control, and linear and nonlinear bearing responses. It is shown that the multi-access bearing response, calculated from the known equation of the stable ROCL (Reduced Order Closed Loop) and based on the direct velocity-displacement feedback, provided the most precise shift in critical frequencies and also reasonable suppression of shaft vibration amplitudes. The nonlinear bearing design was also briefly discussed. The stability analysis showed that stability limits were influenced by more parameters in this case, but no particular advantages were observed in suppression of the vibration amplitudes as compared to the linear case.

1 Introduction

Magnetic bearings have been proven to be a novel and attractive form of shaft and rotor suspension. They possess some distinct advantages in that they do not generate wear and do not need lubrication. Their dynamic response can be designed and adjusted actively to control shaft vibrations in a wide range of operational speeds. They also have long life and great potential for shaft vibration suppression.

Disadvantages, however, include lack of sufficient field experience, unknown reliability over a long time, relatively high cost, and required advanced automatic control and complex design. The design of a control system for a magnetic bearing is difficult and constitutes a challenging task, which requires extensive experimental and theoretical efforts and investigations.

Dynamic models used to design the various components of the magnetic bearing and its controller are quite numerous. They comprise the classical problem of modeling the dynamic behavior of the shaft, where the presence of the bearing is simulated as an external component to the system, which has its own dynamic response. Complexity of the shaft models varies from the one-degree-of-freedom representation of spring-damper-mass to the multimass shaft described by matrix equations. Experimental work was mainly focused on testing different closed-loop configurations, which furnished proper selection, optimization, and tuning of the hardware parameters.

Some of the fundamental work done by Allaire, Humphris, et al. [1–4, 7–9, 11] gave useful experimental insight into the contribution of the bearing stiffness and damping to the general rotor dynamic behavior. Results of their experimental work with different circuit band widths were also compared in terms of the achieved stability regions. They have also proposed basic theoretical models for effective bearing stiffness and damping for a simple rotor configuration, with its mass lumped in a one-degree-of-freedom spring-mass system.

Quite extensive theoretical work, supported by experimental verification, has been developed by Schweitzer and Salm [20, 21, 23, 24], where a shaft-bearing system was represented in modal coordinates and a reduced order model was used to evaluate bearing response proportional to the direct velocity and displacement feedback. A similar approach has been presented in an excellent report by Strunce et al. [26] and by Lin et al. [14–16]. These papers gave also stability analysis and formulated stability conditions. Since the bearing force coefficients were calculated from the reduced-order model of the system, in order to ensure stability of the full-order rotor model, special requirements had to be satisfied by the coefficient matrices in terms of matrix structure and number of controlled modes. Other design methods suitable for control design are discussed in [5, 6, 10, 13, 16, 19, 27].

Generally, the level of complexity of the shaft model determines, to some extent, the design of the bearing response. However, freedom in design of bearing response

Contributed by the International Gas Turbine Institute and presented at the 38th International Gas Turbine and Aeroengine Congress and Exposition, Cincinnati, Ohio, May 24–27, 1993. Manuscript received at ASME Headquarters March 10, 1993. Paper No. 93-GT-294. Associate Technical Editor: H. Lukas.

Copyright © 1995 by ASME

Downloaded 02 Jun 2010 to 171.66.16.102. Redistribution subject to ASME license or copyright; see http://www.asme.org/terms/Terms_Use.cfm

constitutes one of the greatest advantages in magnetic bearing application. Design of bearing response starts with the acceptance of certain control rules, which specify how the control current responsible for the magnitude of the bearing force should react to signals measured by displacement and velocity sensors. Theoretically, any arbitrary function can be adopted as a design rule. The real limitations actually come from the capability and speed of the controller and cost of the required hardware. Also, highly sophisticated control strategy may not necessarily be the best solution to rotor vibration control. Therefore, the potential benefit resulting from the complicated bearing design has to be compromised and balanced with the cost of the proposed solution.

Review of the numerous reported experimental work on magnetic bearing concepts indicates that the linear bearing response, based on the direct velocity-displacement feedback, is the most popular technique employed in practical applications. Additionally, the linear bearing force is further restricted to only two terms: One contributes to the system stiffness (displacement feedback), and the second provides damping (velocity feedback). This suggests that difficulties associated with implementation of nonlinear bearing control were not worth the potential benefits of this type of control. However, the justification of linear systems given in the literature is often based on experiments and experience. Few authors even mentioned the possibility of other than linear design of a bearing response.

The present paper provides simple numerical verification of the linear bearing response and comparison of effects of several different control scenarios on shaft dynamic behavior. It also briefly discusses the influence of the nonlinear bearing response on the stability of shaft operation.

Two separate models are used to simulate the dynamic behavior of a shaft-bearing system. First, a general analytical model is derived for forced vibrations of an unbalanced, asymmetric, three-mass shaft supported by two magnetic bearings with collocated sensors. Second, for the assumed linear type of control, the stable, reduced-order-closed-loop (ROCL) equation is accepted as the bearing design algorithm. For this algorithm the design objectives are specified in terms of the required amount of damping and shift in shaft natural frequencies, which should result from the presence of the bearing, and, consequently, the corresponding bearing force coefficients, i.e., stiffness and damping gains, are calculated. This calculated bearing force is then used in the analytical model of the system to simulate behavior of shaft controlled by the designed bearing force. The results showing the actual amplitudes and critical frequencies of the shaft are compared with those specified as the objectives for the bearing force algorithm. Magnitudes of observed discrepancies can be recognized as quantitative measures of the spillover effects. Simulations are performed assuming single and multi-access bearing responses. Different modes are also selected for the direct control. Effectiveness of the considered types of control is compared in terms of suppression of shaft vibration and accuracy in the achieved shift in natural frequencies.

Finally, the nonlinear bearing force is introduced into the derived analytical shaft-bearing model and the shaft vibrations are simulated and compared to the linear control case. No apparent benefits are observed in vibration suppression. However, brief analysis of the stability of the system shows that the nonlinear type of control creates more possibilities to increase system stability limits, since they become dependent on a larger number of parameters, including rotational speed and shaft imbalance.

2 Linear Magnetic Bearing Response

In an active magnetic bearing system, the rotating shaft is suspended in the magnetic field created by stationary electromagnets. The position of the shaft is dynamically corrected when the sensors detect any shaft departures from equilibrium (centerline) position. Magnets are usually working in the attractive mode, i.e., the shaft displacement is corrected by the increased pull in the desired direction.

The electromagnetic force exerted on a mass located at the distance x from the magnet is a function of the mass position itself, x, and of the current I in the magnet coil:

$$F = \frac{\mu_0 A N^2 I^2}{2x^2} \tag{2.1}$$

If the shaft departs from its equilibrium position by a distance Δx, the control system should adjust the bearing response, by applying the proper correction ΔI to the magnet control current. Assuming that the shaft displacement is small, the resulting corrective force, ΔF, can be estimated from the linearized Eq. (2.1):

$$\Delta F = F(x_0 + \Delta x, I_0 + \Delta I) - F(x_0, I_0) = \frac{A\mu_0 N^2 I_0}{2x_0^2}\left(\Delta I - \frac{I_0}{x_0}\Delta x\right) \tag{2.2}$$

where $F(x_0, I_0)$ is the stationary force sufficient to support shaft weight in equilibrium position. The net force responsible for correction of shaft departure given by Eq. (2.2) is a

Nomenclature

μ_0 = magnetic permeability of the gap
A = area of magnet pole
N = number of coil turns (per pole) in magnet
I = current in magnet coil
$[Gd]$, $[Gv]$ = coefficient or gain matrices, which comprise stiffness and damping coefficients, respectively, for each bearing actuator
$[Cd]$, $[Cv]$ = position/influence matrices of displacement and velocity sensors
$\{q\}$ = vector of modal coordinates
$[\tilde{P}]$, $[P]$ = modal and weighted modal matrix, respectively (based on eigenvectors of undamped system)
$[A]$ = actuator position/influence matrix
$[c]$ = modal damping matrix of the system with no external forces
$[\Lambda]$ = eigenvalues of the undamped system
$\{F\}$ = vector of the external forces (magnetic bearing response)
m_i = discrete shaft mass concentrated at the ith location (i = 0, 1, 2)
$M \cdot r$ = shaft imbalance
K = shaft stiffness
D = external damping (usually negligibly small)
F_i = response of the respective bearing (i = 0, 2)
A_i, α_i = vibration amplitude and phase angle for the ith concentrated mass
z_k = modal damping ratio for the kth vibration mode
p = index that indicates the order of modal truncation (it is equal to the number of the primary modes)

Downloaded 02 Jun 2010 to 171.66.16.102. Redistribution subject to ASME license or copyright; see http://www.asme.org/terms/Terms_Use.cfm

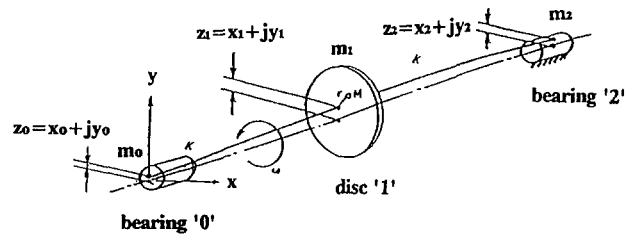

Fig. 1 Three mass shaft supported by two magnetic bearings with collocated sensors

function of two dependent variables: shaft displacement Δx, which can be only implicitly controlled, and the current ΔI, which can be changed directly and, therefore, becomes the subject of control design and optimization.

Assuming that changes in the magnet coil current are proportional to the local shaft displacements measured by all available sensors and also to the displacement velocities, which are either directly measured or calculated by differentiating the displacement signal in a controller, i.e.,

$$I \propto (\{z\}_{\text{meas}}, \{\dot{z}\}_{\text{meas}}) \tag{2.3}$$

and assuming negligible phase lags and rolloffs of the control circuit, it follows that the bearing response is proportional to the position and velocity feedbacks:

$$F \propto [Gd][Cd]\{z\}_{\text{meas}} + [Gv][Cv]\{\dot{z}\}_{\text{meas}} \tag{2.4}$$

Design of the bearing response, which is now reduced to the determination of both gain matrices, should satisfy the following goals: (*i*) to provide sufficient damping of the shaft vibrations; (*ii*) to cause the required shift in natural frequencies; and (*iii*) to ensure stable shaft operation in a specified range of rotational speed. One of the methods to achieve this is based on the modal representation of shaft vibration, with the bearing response acting as an external force [14, 24, 26]. Since this approach will be implemented further in the present model of shaft controlled vibrations, it is briefly summarized below:

The shaft equation in modal coordinates, suitable for the control design, has to be reduced to include only the primary vibration modes that are directly controlled:

$$\{\ddot{q}\}_p + [c]_p\{\dot{q}\}_p + [\Lambda]_p\{q\}_p = [P]_p^T[A]\{F\} \tag{2.5}$$

Substitution of the bearing force defined by Eq. (2.4) into this shaft model results in the reduced-order-closed-loop (ROCL) equation with the new overall stiffness and damping properties increased due to contribution of the bearing forces.

Once the new stiffness and damping of the system are specified as the design objectives, the resulting bearing gain matrices, $[Gd]$ and $[Gv]$, are calculated as follows [14, 24, 25]:

$$[Gd] = \left([P]_p^T[A]\right)^T\left\{[P]_p^T[A]\left([P]_p^T[A]\right)^T\right\}^{-1} \times([\Lambda]_{\text{req}} - [\Lambda]_{\text{exist}})\left\{([Cd][P]_p)^T[Cd][P]_p\right\}^{-1} \times([Cd][P]_p)^T \tag{2.6}$$

$$[Gv] = \left([P]_p^T[A]\right)^T\left\{[P]_p^T[A]\left([P]_p^T[A]\right)^T\right\}^{-1} \times([c]_{\text{req}} - [c]_{\text{exist}})\left\{([Cv][P]_p)^T[Cv][P]_p\right\}^{-1} \times([Cv][P]_p)^T \tag{2.7}$$

However, although the residual flexible modes of higher orders do not participate in gain calculation, they will obviously be affected, creating what is called *spill-over effects*, causing discrepancies between the required and achieved design objectives and also affecting system stability.

Therefore, in order to ensure stability of the full-order model, additional conditions have to be satisfied in the gain calculations. References [25–27, 38, 42] present a good review and justification of these conditions in more detail. What will be relevant to the present simulation is that, first, the reduced order model has to contain at least all rigid and undamped modes of vibration and, second, both augmented damping and stiffness matrices have to be positive definite. It follows that the total number of velocity/displacement sensors in the system has to be at least equal to the number of desired controlled modes.

3 Shaft-Magnetic Bearing Model

Consider the simple unbalanced asymmetric and flexible shaft supported by two magnetic bearings shown in Fig. 1. Each bearing consists of two actuators placed in the 0–x and 0–y planes with the corresponding collocated sensors. Shaft mass is concentrated at both ends, corresponding to the bearing locations, and at the midspan plane. The mathematical model of the unbalance-forced shaft vibration with no gyroscopic effects and negligible small cross-coupling, written in the complex coordinates $z = x + jy$, represents the classical balance of forces:

'1'-*disk*:

$$m_1\ddot{z}_1 + D\dot{z}_1 + K(z_1 - z_0) + K(z_1 - z_2) = Mr\omega^2 e^{(j\omega t)} \tag{3.1}$$

'0'-*mass*:

$$m_0\ddot{z}_0 + K(z_0 - z_1) = F_0 \tag{3.2}$$

'2'-*mass*:

$$m_2\ddot{z}_2 + K(z_2 - z_1) = F_2 \tag{3.3}$$

The following particular solution of the differential Eqs. (3.1)–(3.3) describes rotor synchronous forced vibrations:

$$z_i = A_i e^{(j\omega t + \alpha_i)} \quad \text{for } i = 0, 1, 2 \tag{3.4}$$

The bearing responses, F_0 and F_2, appear in the model (Eqs. (3.2) and (3.3)), and hence will obviously influence the solution, which determines both the amplitudes and phase angles of rotor vibration.

Assuming the linear, multi-access bearing design, based on the shaft displacement/velocity measured by both sensors in each plane, with no cross-coupling between 0–x and 0–y planes, the bearing response takes a similar form in both planes, i.e.,

$$\{F\} = \begin{bmatrix}\{F_x\}\\ \{F_y\}\end{bmatrix} = [Gd]\begin{bmatrix}x_0\\ x_2\\ y_0\\ y_2\end{bmatrix} + [Gv]\begin{bmatrix}\dot{x}_0\\ \dot{x}_2\\ \dot{y}_0\\ \dot{y}_2\end{bmatrix} \tag{3.5}$$

where the gain matrices $[Gd]$ and $[Gv]$ are defined as:

$$[Gd] = \left[\begin{array}{cc|cc} K_{Fx0,x0} & K_{Fx0,x2} & \multicolumn{2}{c}{[0]} \\ K_{Fx2,x0} & K_{Fx2,x2} & & \\ \hline \multicolumn{2}{c|}{[0]} & K_{Fy0,y0} & K_{Fy0,y2} \\ & & K_{Fy2,y0} & K_{Fy2,y2} \end{array}\right] \tag{3.6a}$$

$$[Gv] = \left[\begin{array}{cc|cc} D_{Fx0,x0} & D_{Fx0,x2} & \multicolumn{2}{c}{[0]} \\ D_{Fx2,x0} & D_{Fx2,x2} & & \\ \hline \multicolumn{2}{c|}{[0]} & D_{Fy0,y0} & D_{Fy0,y2} \\ & & D_{Fy2,y0} & D_{Fy2,y2} \end{array}\right] \tag{3.6b}$$

The first subscript of each term in the gain matrix denotes the location of the actuator to which the particular gain applies, and the second, the location of the sensor that

Downloaded 02 Jun 2010 to 171.66.16.102. Redistribution subject to ASME license or copyright; see http://www.asme.org/terms/Terms_Use.cfm

provides measurement multiplied by the given gain. For example, $K_{Fx2,x0}$ is the stiffness coefficient, which multiplied by the displacement measured by sensor located at x_0, will become part of the response of the actuator at x_2 location in the 0–x plane. It follows that for the single-access bearing design, only the terms on the main diagonal would be retained, since response of each actuator is proportional only to the signal measured by its own sensor. The [0] terms in the second and third quarters of each matrix indicate the lack of cross coupling between actuator forces in the 0–x and 0–y planes.

3.1 Synchronous Forced Vibrations of Unbalanced Shaft Supported by Two Multi-access Magnetic Bearings. Substituting the bearing response defined by Eqs. (3.5) and (3.6) into shaft dynamic model given by Eqs. (3.1)–(3.3) and solving it, the following relations are obtained for the amplitudes and phase angles for three concentrated shaft masses:

'2'-*mass*:

$$A_2 = \frac{KMr\omega^2}{T_6} \qquad \alpha_2 = -\gamma_6 \tag{3.7}$$

'0'-*mass*:

$$A_0 = T_4 A_2 \qquad \alpha_0 = \alpha_2 + \gamma_4 \tag{3.8}$$

'1'-*disk*:

$$A_1 = \frac{T_7}{K} A_2 \qquad \alpha_1 = \alpha_2 + \gamma_7 \tag{3.9}$$

where

$$T_6 = \sqrt{(T_4T_1)^2 + T_5^2 + 2T_1T_4T_5\cos(\gamma_1 + \gamma_4 - \gamma_5)} \tag{3.10}$$

$$T_5 = \sqrt{(X_1X_{20})^2 + K^4 - 2K^2X_1X_{20}\cos(\phi_1 + \phi_{20})} \tag{3.11}$$

$$T_4 = \sqrt{\frac{X_2^2 + X_{20}^2 - 2X_2X_{20}\cos(\phi_2 - \phi_{20})}{X_0^2 + X_{30}^2 - 2X_0X_{30}\cos(\phi_0 - \phi_{30})}} \tag{3.12}$$

$$T_1 = \sqrt{(X_0X_1)^2 + K^4 - 2K^2X_0X_1\cos(\phi_0 + \phi_1)} \tag{3.13}$$

$$\tan(\gamma_6) = \frac{T_4T_1\sin(\gamma_4 + \gamma_1) + T_5\sin(\gamma_5)}{T_4T_1\cos(\gamma_4 + \gamma_1) + T_5\cos(\gamma_5)} \tag{3.14}$$

$$\tan(\gamma_5) = \frac{X_1X_{20}\sin(\phi_1 + \phi_{20})}{X_1X_{20}\cos(\phi_1 + \phi_{20}) - K^2} \tag{3.15}$$

$$\tan(\gamma_3) = \frac{X_0\sin(\phi_0) - X_{30}\sin(\phi_{30})}{X_0\cos(\phi_0) - X_{30}\cos(\phi_{30})} \tag{3.16}$$

$$\tan(\gamma_2) = \frac{X_2\sin(\phi_2) - X_{20}\sin(\phi_{20})}{X_2\cos(\phi_2) - X_{20}\cos(\phi_{20})} \tag{3.17}$$

$$\tan(\gamma_1) = \frac{X_1X_0\sin(\phi_1 + \phi_0)}{X_1X_0\cos(\phi_1 + \phi_0) - K^2} \tag{3.18}$$

$$X_1 = \sqrt{(2K - m_1\omega^2)^2 + (D\omega)^2} \tag{3.19}$$

$$\tan(\phi_1) = \frac{\omega D}{2K - m_1\omega^2} \tag{3.20}$$

$$X_0 = \sqrt{(K + K_{Fz0,z0} - m_0\omega^2)^2 + (\omega D_{Fz0,z0})^2} \tag{3.21}$$

$$\tan(\phi_0) = \frac{\omega D_{Fz0,z0}}{K + K_{Fz0,z0} - m_0\omega^2} \tag{3.22}$$

$$X_2 = \sqrt{(K + K_{Fz2,z2} - m_2\omega^2)^2 + (\omega D_{Fz2,z2})^2} \tag{3.23}$$

$$\tan(\phi_2) = \frac{\omega D_{Fz2,z2}}{K + K_{Fz2,z2} - m_2\omega^2} \tag{3.24}$$

$$X_{20} = \sqrt{K_{Fz0,z2}^2 + (\omega D_{Fz2,z0})^2} \tag{3.25}$$

$$\tan(\phi_{20}) = \frac{\omega D_{Fz0,z2}}{K_{Fz0,z2}} \tag{3.26}$$

$$X_{30} = \sqrt{K_{Fz2,z0}^2 + (\omega D_{Fz2,z0})^2} \tag{3.27}$$

$$\tan(\phi_{30}) = \frac{\omega D_{Fz2,z0}}{K_{Fz2,z0}} \tag{3.28}$$

$$T_7 = \sqrt{(X_0T_4)^2 + X_{20}^2 + 2X_0X_{20}T_4\cos(\phi_0 + \gamma_4 - \phi_{20})} \tag{3.29}$$

$$\tan(\gamma_7) = \frac{T_4X_0\sin(\gamma_4 + \phi_0) + X_{20}\sin(\phi_{20})}{T_4X_0\cos(\gamma_4 + \phi_0) + X_{20}\cos(\phi_{20})} \tag{3.30}$$

$$\gamma_4 = \gamma_2 - \gamma_3 \tag{3.31}$$

The analytical solution given by Eqs. (3.7)–(3.31) describes the forced synchronous vibration of the unbalanced asymmetric shaft controlled by two multi-access bearings with collocated sensors. Bearing stiffness and damping coefficient appear explicitly in the model. Once the coefficient values are determined, shaft-controlled vibration can be simulated; the resulting magnitude of vibration amplitudes and critical frequencies will provide assessment of the quality of control achieved with the given bearing design, as will be shown in Section 3.3.

It is worth noting, that the analytical solution presented, although complex in nature, has a definite advantage as compared to a numerical solution, in that it demonstrates explicitly the effects of the shaft parameters such as mass, imbalance, stiffness, rotational speed, etc., and also the effects of bearing stiffness and damping, on the amplitudes and phase angles of the shaft concentrated masses. However, for a complex multimass shaft, the analytical solution is not attainable, and the numerical model is the only way to simulate shaft vibration. A numerical model can easily be developed based on the same principles as the existing numerous dynamic simulators for a shaft supported by conventional bearings, which comprise dynamic equations written in a matrix form for each of the shaft concentrated masses. The difference will be only in the magnetic bearing model, because while the stiffness and damping of the conventional bearing depend on the shaft deflection strictly at the bearing location, magnetic bearing response is modeled as proportional to the chosen local deflections at the sensor locations. However, since the numerical models are of a quantitative, not qualitative nature and do not provide the closed-form solution, the analytical model, showing a tangible relation among the important system parameters, seems to be better suited for the analysis and understanding of the problem.

3.2 Modal Analysis of the Shaft—Determination of the Linear Bearing Force Coefficients. Stiffness and damping gains for the linear, multi-access bearing response will be calculated from the gain algorithm, given by Eqs. (2.6) and (2.7).

For gain algorithm, the shaft eigenvectors and eigenvalues have to be known. Therefore, those parameters were estimated first from the free shaft model, represented by Eqs. (3.1)–(3.3), with no imbalance, damping, or external forces present.

For this shaft with three degrees of freedom in each plane, the three eigenvalues calculated (natural frequencies), identical for the 0–x and 0–y planes, and three corresponding eigenvectors (mode shapes) summarized in modal matrix $[\tilde{P}]$, are as follows:

Downloaded 02 Jun 2010 to 171.66.16.102. Redistribution subject to ASME license or copyright; see http://www.asme.org/terms/Terms_Use.cfm

$$\omega_1^2 = 0$$

$$\omega_2^2 = \frac{K}{2}\left[\frac{1}{m_0} + \frac{2}{m_1} + \frac{1}{m_2} - \sqrt{\left(\frac{1}{m_0} - \frac{1}{m_2}\right)^2 + \left(\frac{2}{m_1}\right)^2}\right]$$

$$\omega_3^2 = \frac{K}{2}\left[\frac{1}{m_0} + \frac{2}{m_1} + \frac{1}{m_2} + \sqrt{\left(\frac{1}{m_0} - \frac{1}{m_2}\right)^2 + \left(\frac{2}{m_1}\right)^2}\right] \tag{3.32}$$

$$[\tilde{P}] = \begin{bmatrix} 1 & 1 & 1 \\ 1 & Y1 & Y3 \\ 1 & Y2 & Y4 \\ 0 & 0 & 0 \\ 0 & 0 & 0 \\ 0 & 0 & 0 \end{bmatrix} \tag{3.33}$$

where:

$$Y1 = \frac{1}{2} - m_0\left[\frac{1}{2m_2} + \frac{1}{m_1} - \frac{1}{2}\sqrt{\left(\frac{1}{m_0} - \frac{1}{m_2}\right)^2 + \left(\frac{2}{m_1}\right)^2}\right]$$

$$Y2 = Y1\left\{1 - m_1\left[\frac{1}{2m_0} + \frac{1}{2m_2} - \frac{1}{2}\sqrt{\left(\frac{1}{m_0} - \frac{1}{m_2}\right)^2 + \left(\frac{2}{m_1}\right)^2}\right]\right\} - 1$$

$$Y3 = \frac{1}{2} - m_0\left[\frac{1}{2m_2} + \frac{1}{m_1} + \frac{1}{2}\sqrt{\left(\frac{1}{m_0} - \frac{1}{m_2}\right)^2 + \left(\frac{2}{m_1}\right)^2}\right]$$

$$Y4 = Y3\left\{1 - m_1\left[\frac{1}{2m_0} + \frac{1}{2m_2} + \frac{1}{2}\sqrt{\left(\frac{1}{m_0} - \frac{1}{m_2}\right)^2 + \left(\frac{2}{m_1}\right)^2}\right]\right\} - 1 \tag{3.34}$$

The first natural frequency and the mode shape are rigid mode parameters.

The numerical calculations carried out with the following shaft data: $m_0 = 1.8$ kg, m_1(disk) = 68.0 kg, $m_2 = 2m_0 = 3.6$ kg, $K = 24{,}000$ N/m, $Mr = 0.0036$ kgm, gave the natural frequencies of the shaft $\omega_2 = 83.67$ rad/s and $\omega_3 = 117.06$ rad/s, and the corresponding normalized mode shapes shown in Fig. 2.

The amplitudes of the shaft free vibration are presented in Fig. 3. It should be noted that each of the concentrated shaft masses experienced zero amplitude at a particular natural frequency, while the other two masses were acting as *absolutely effective undamped absorbers*.

With the calculated eigenvectors and eigenvalues, the design objectives for the bearing gains can now be specified in terms of the desired shifts in the natural frequencies and the required amount of damping.

Since the shaft-bearing system has only two position sensors in each plane, the number of controlled primary modes has to be reduced to the rigid mode and the first flexible mode. The third flexible mode, which is beyond control, will certainly be affected by the bearing force, but in an unpredictable way. This will be demonstrated by means of the following two examples.

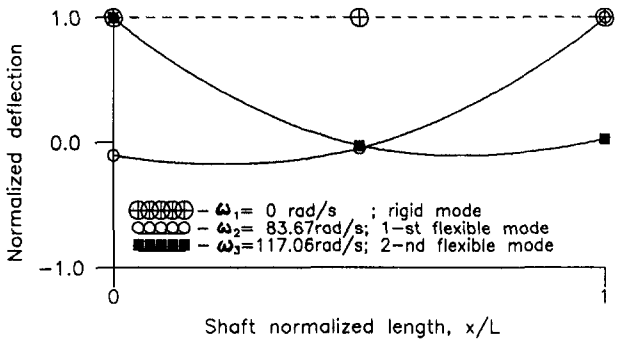

Fig. 2 Shaft modes of vibration

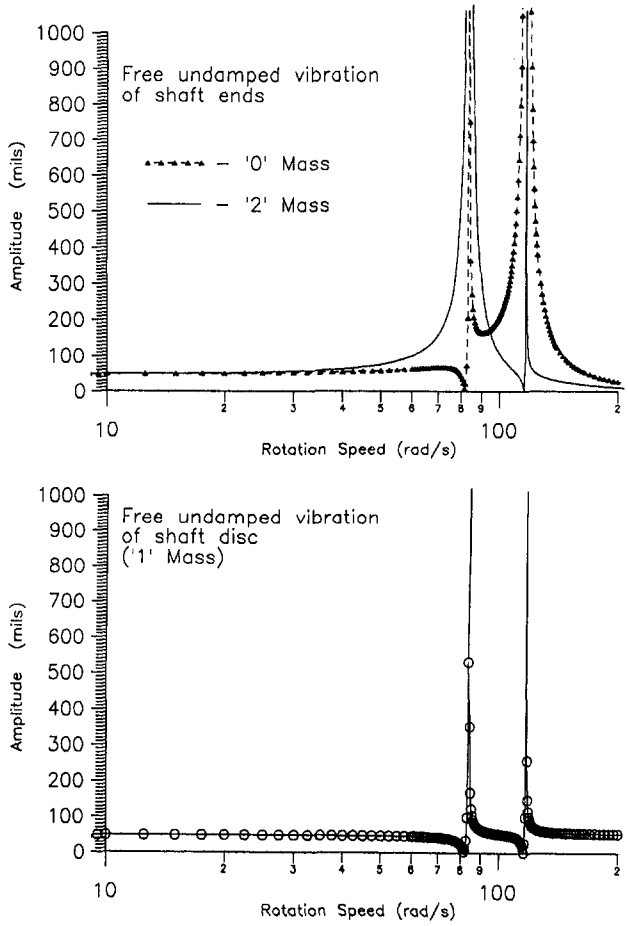

Fig. 3 Amplitudes of undamped vibration of free three mass shaft

Case I: It is required to achieve the following shift in frequencies and amount of damping for the controllable modes in each plane:

$$\left.\begin{matrix}\omega_1 = 0 \text{ rad/s} \\ \omega_2 = 83.67 \text{ rad/s}\end{matrix}\right\} \text{ should be shifted to } \begin{matrix}\omega_1' = 5 \text{ rad/s} \\ \omega_2' = 100 \text{ rad/s}\end{matrix}$$

It follows that the additional stiffness resulting from the magnetic bearing presence is determined as:

$$[\Lambda]^* = [\Lambda]_{\text{req}} - [\Lambda]_{\text{exist}} = \left[\omega_1'^2\right] - \left[\omega_1^2\right] = \begin{bmatrix} 25 & 0 \\ 0 & 3000 \end{bmatrix} \tag{3.35}$$

Downloaded 02 Jun 2010 to 171.66.16.102. Redistribution subject to ASME license or copyright; see http://www.asme.org/terms/Terms_Use.cfm

Additionally, the second design objective is equal modal damping ratio required for both controlled modes:

$$z_k = 0.707 \quad \text{for } k = 1, 2$$

Since the existing damping ratio is negligible, the entire damping is practically provided by the bearing force and is calculated as the product of the required ratios and the respective natural frequencies:

$$[c]^* = [c]_{\text{req}} - [c]_{\text{exist}} = 2([z]_{\text{req}} - [z]_{\text{exist}})[\omega'] = \begin{bmatrix} 7.07 & 0 \\ 0 & 141.4 \end{bmatrix} \quad (3.36)$$

With both design objectives given by Eqs. (3.35) and (3.36) and the reduced weighted modal matrix $[P]_p$ calculated from the known eigenvectors and eigenvalues of the free shaft, the following gain matrices were obtained from Eqs. (2.6) and (2.7):

$$[Gd] = \left[\begin{array}{cc|cc} 10815 & -9154 & \multicolumn{2}{c}{[0]} \\ -9154 & 9328 & & \\ \hline \multicolumn{2}{c|}{[0]} & 10815 & -9154 \\ & & -9154 & 9328 \end{array}\right]$$

$$[Gv] = \left[\begin{array}{cc|cc} 864.1 & -394.3 & \multicolumn{2}{c}{[0]} \\ -394.3 & 443.5 & & \\ \hline \multicolumn{2}{c|}{[0]} & 864.1 & -394.3 \\ & & -394.3 & 443.5 \end{array}\right] \quad (3.37)$$

Both the matrices are symmetric, as a consequence of the collocation condition. The fourth matrix quarters, which contain stiffness and damping coefficients for the actuators in the 0–y plane, are identical to those for the 0–x plane. This is an obvious consequence resulting from the assumed lack of cross-coupling and from the same design objectives required for both planes.

Case II: In this case, the same shift in natural frequencies and the same damping ratio for the rigid mode are required as in the first case. However, a lower damping ratio, $z_2 = 0.11545$, is assumed for the flexible mode. Therefore, while the stiffness matrix remains the same, given by Eq. (3.35), the new damping matrix becomes:

$$[c]^* = [c]_{\text{req}} - [c]_{\text{exist}} = \begin{bmatrix} 7.07 & 0 \\ 0 & 23.09 \end{bmatrix} \quad (3.38)$$

The resulting second set of bearing gain matrices is:

$$[Gd] = \left[\begin{array}{cc|cc} 10815 & -9154 & \multicolumn{2}{c}{[0]} \\ -9154 & 9328 & & \\ \hline \multicolumn{2}{c|}{[0]} & 10815 & -9154 \\ & & -9154 & 9328 \end{array}\right]$$

$$[Gv] = \left[\begin{array}{cc|cc} 496.9 & -27.1 & \multicolumn{2}{c}{[0]} \\ -27.1 & 76.3 & & \\ \hline \multicolumn{2}{c|}{[0]} & 496.9 & -27.1 \\ & & -27.1 & 76.3 \end{array}\right] \quad (3.39)$$

Comparison of the numerical results obtained in both examples shows no change in the calculated bearing stiffness coefficients, $[Gd]$, since the required shift in natural frequencies was the same in both cases; however, the different damping of the controlled modes specified for both cases resulted in substantial differences in the entries of $[Gv]$ matrices.

3.3 Verification of the Bearing Design Objectives. The calculation procedure of the bearing gains was based on the truncated modal representation of the shaft, with one elastic mode excluded from the control design. Therefore, the bearing design objectives specified as a required shift in the critical frequencies and damping of the primary modes will not be achieved precisely in the control of the full order shaft model. The highest uncontrollable elastic mode, truncated in this analysis, will be also affected by the active control, with its amplitude damped and its frequency shifted. This, in turn, affects the critical frequencies and damping of the primary modes, causing discrepancies between the designed and achieved dynamic behavior of the controlled modes, a phenomenon known as the *spillover effect*.

To estimate the magnitude of spillover effects and to verify the accuracy of bearing design, the bearing force coefficients $[Gd]$ and $[Gv]$ calculated in both cases were substituted into the analytical model of shaft vibration, given by Eqs. (3.7)–(3.31). The shaft vibration amplitudes were determined in the entire frequency range, which covered all three modes. Results show the final effect of the bearing control with the

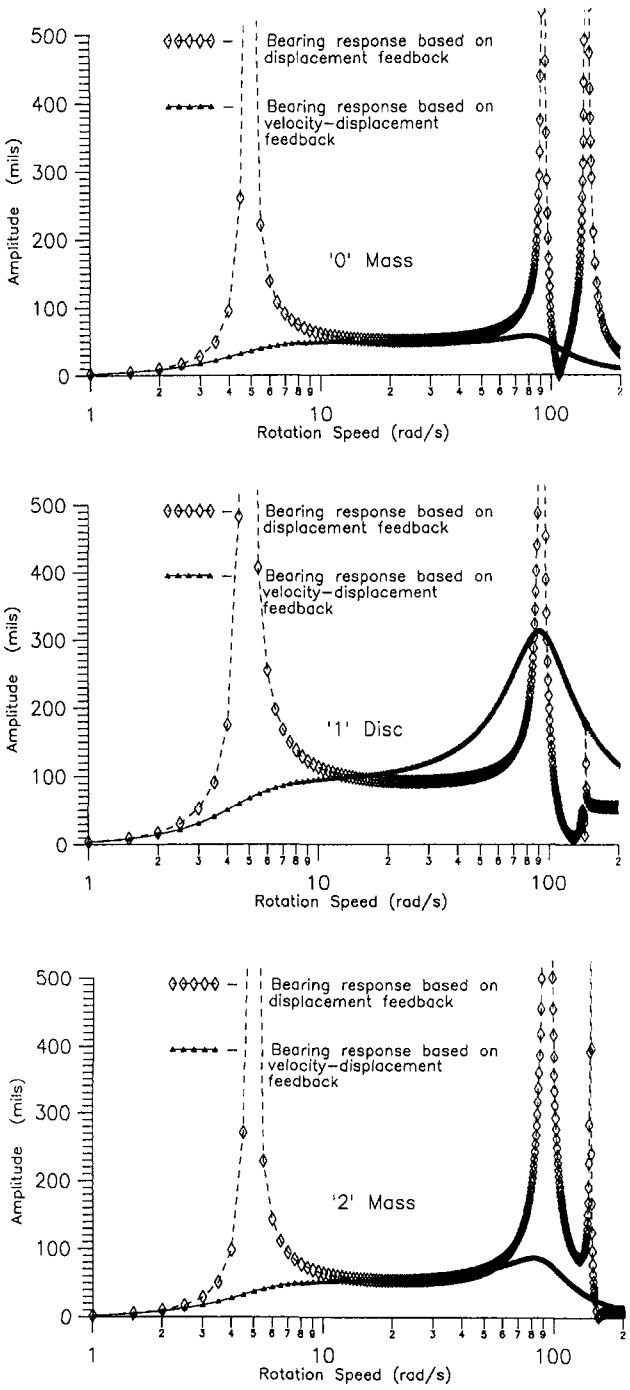

Fig. 4 Case I: shaft vibration controlled by multi-access bearings

Downloaded 02 Jun 2010 to 171.66.16.102. Redistribution subject to ASME license or copyright; see http://www.asme.org/terms/Terms_Use.cfm

visible discrepancies between the required and achieved design objectives (Figs. 4–7).

Figure 4 shows the results for the Case I. To observe precisely the actual shift in critical frequencies, first, no damping was introduced ($[Gv] = 0$); the dotted curves show vibration of all three shaft-concentrated masses controlled by the bearing force, which possessed only the designed stiffness. The achieved frequency shift for the first rigid mode is precisely as has been designed, i.e., from 0 to 5 rad/s; the second controlled frequency was shifted to 93 rad/s, instead of 100 rad/s, as was required by the design objective; the third uncontrolled frequency has been shifted from its natural value of 117.06 rad/s to 143 rad/s. The solid lines show shaft vibrations controlled by the complete bearing force, including stiffness and damping terms. Vibrations of the shaft at both ends have been significantly attenuated. The disk, however, still experienced large vibrations around the second critical frequency, but its amplitudes at the first and third criticals have been suppressed substantially.

Two other scenarios have also been considered and compared with the previously discussed full control results in Fig. 5. In the first scenario, the number of the primary modes had been reduced only to the rigid mode. For this mode the required frequency shift and a damping ratio were as in the both previous cases (i.e., $\omega_1' = 5$ rad/s, and $z_1 = 0.707$). Thus, the $[\Lambda]^*$ and $[c]^*$ matrices would be as follows:

$$[\Lambda]^* = \begin{bmatrix} 25 & 0 \\ 0 & 0 \end{bmatrix} \qquad [c]^* = \begin{bmatrix} 0.707 & 0 \\ 0 & 0 \end{bmatrix}$$

The second scenario was the single access control, where the actuator response was proportional to the signal measured only by its *own* sensor. The gain matrices for this single access case would contain only the terms on the main diagonals, obtained by summing all entries in rows in the respective multi-access matrices $[Gd]$ and $[Gv]$ in Eq. (3.37), i.e.,

$$[Gd] = \left[\begin{array}{cc|cc} 1661 & 0 & & \\ 0 & 174 & [0] & \\ \hline & & 1661 & 0 \\ [0] & & 0 & 174 \end{array}\right]$$

$$[Gv] = \left[\begin{array}{cc|cc} 469.8 & 0 & & \\ 0 & 49.2 & [0] & \\ \hline & & 469.8 & 0 \\ [0] & & 0 & 49.2 \end{array}\right]$$

This means that the corresponding magnet responses, e.g., in the 0–x plane, were:

$$F_{x0} = (K_{Fx0,x0} + K_{Fx0,x2})x_0 + (D_{Fx0,x0} + D_{Fx0,x2})\dot{x}_0$$
$$F_{x2} = (K_{Fx2,x0} + K_{Fx2,x2})x_2 + (D_{Fx2,x0} + D_{Fx2,x0})\dot{x}_2$$

The results presented in Fig. 5 indicated that the best suppression of amplitudes at both ends of the shaft as well as the most precise shift in critical frequencies was provided by the designed multi-access control. The rigid mode control ensured very good suppression of the shaft vibration except for the heavier end of the shaft.

A certain similarity can also be observed between the single access and rigid mode controls—both types of control resulted in good suppression of the disk vibration but the amplitude of the heavier end of the shaft was excessive.

Results for Case II are shown in Fig. 6. As expected, with the same bearing stiffness coefficients as Case I, the shift in critical frequencies was also similar. The only difference was shown in the suppression of shaft vibration, where the disk amplitude was more attenuated as compared to Case I, but the amplitude of the heavier end of the shaft became higher.

This case has also been compared with the results obtained with the rigid mode and the single access controls in

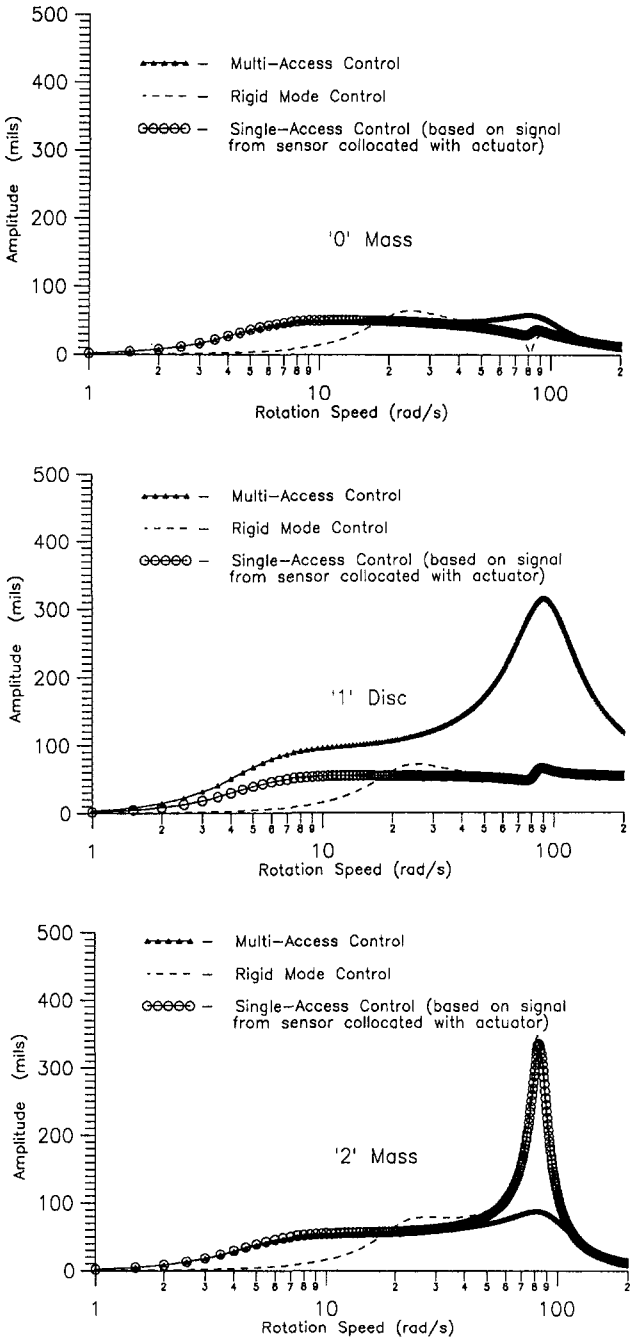

Fig. 5 Case I: comparison of different control scenarios

Fig. 7. The concept of the rigid mode control was the same as the one described in Case I. However, the single access control was rather a pure numerical exercise, where it was assumed that the actuator received displacement/velocity signals only from the sensor at the opposite end of the shaft, so the bearing forces, e.g., in the 0–x plane, become:

$$F_{x0} = (K_{Fx0,x0} + K_{Fx0,x2})x_2 + (D_{Fx0,x0} + D_{Fx0,x2})\dot{x}_2$$

and

$$F_{x2} = (K_{Fx2,x0} + K_{Fx2,x2})x_0 + (D_{Fx2,x0} + D_{Fx2,x2})\dot{x}_0$$

The gain matrices in this single-access scenario had only off-diagonal terms, which were obtained, analogously to the conventional single-access control considered in Case I, by summing all the entries in rows in the respective multi-access gain matrices given by Eq. (3.39).

The results shown in Fig. 7 also support conclusions drawn

Downloaded 02 Jun 2010 to 171.66.16.102. Redistribution subject to ASME license or copyright; see http://www.asme.org/terms/Terms_Use.cfm

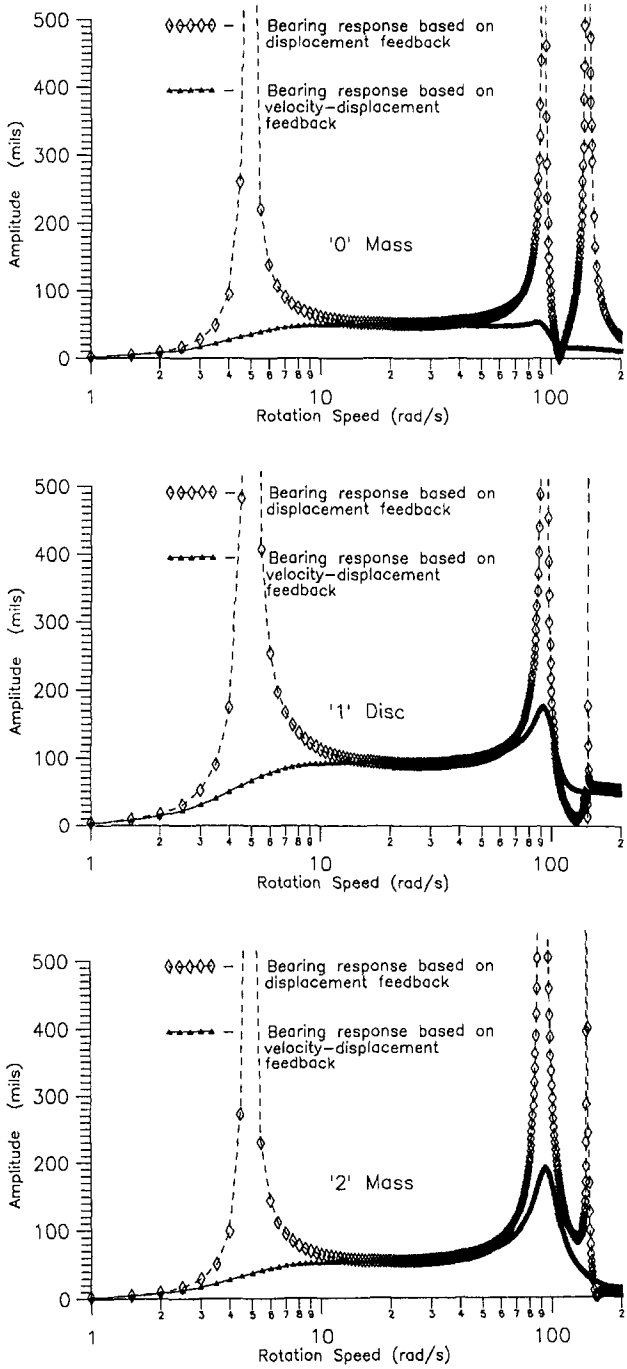

Fig. 6 Case II: shaft vibration controlled by multi-access bearings

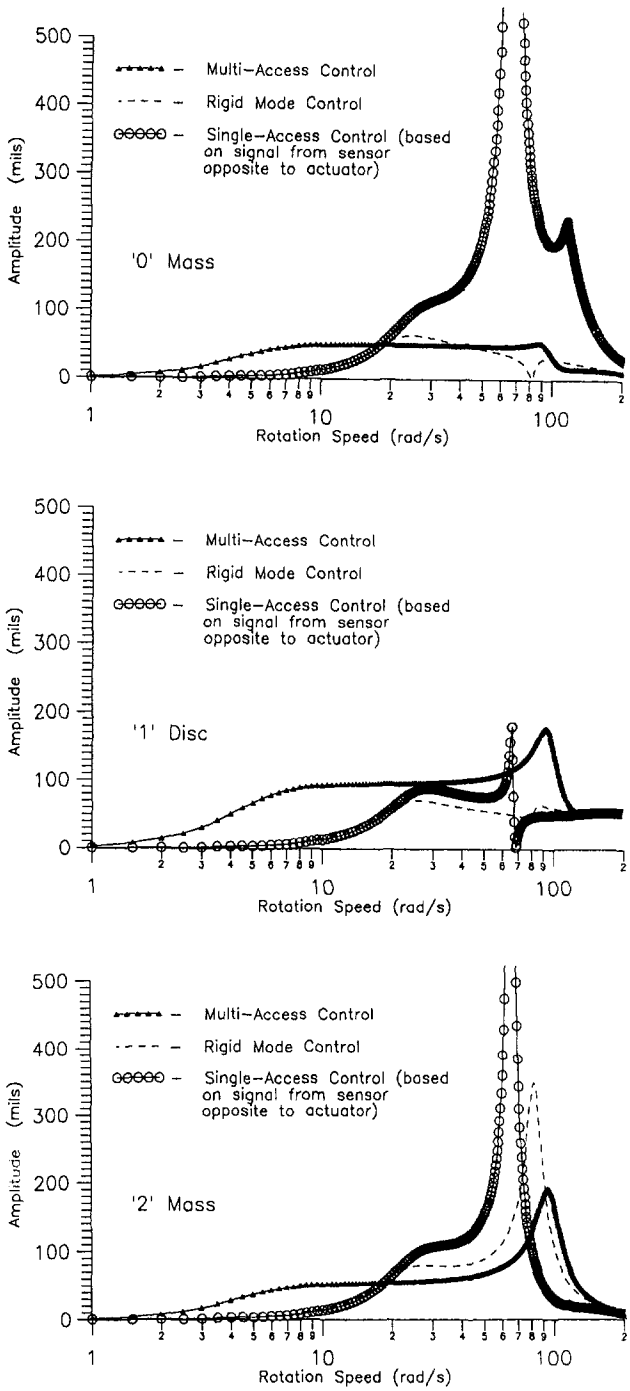

Fig. 7 Case II: comparison of different control scenarios

from the first case. The designed multi-access bearings provided the shift in critical frequencies that was the closest to the design objective and ensured good control of shaft end vibration; however, suppression of disk vibrations was not effective. Rigid mode control provided sufficient damping, but again, the heavier end of the shaft experienced higher vibrations. As may also be expected, the assumed single access control based on the measurement received from the sensor opposite to the actuator allowed for extreme amplitudes at both shaft ends; rather surprisingly, however, the disk maintained quite stable position in this purely hypothetical case.

4 Nonlinear Bearing Response and Stability Analysis

In all the simulated cases presented above, regardless of the number of controlled modes, single or multi-access type of control, the magnetic bearing response remained a linear function of displacement and velocity. As has already been mentioned in the introduction, the nonlinear bearing design rarely deserves attention, since it brings severe numerical and functional difficulties in the theoretical modeling and in the practical implementation.

To assess the characteristics of a nonlinear bearing system, the following numerical exercise was carried out introducing the nonlinear terms into the bearing force model derived analytically in Section 3.1.

Assume that the bearing force is single access and the damping term includes a nonlinear arbitrary function, φ, of the measured respective displacement amplitude, i.e.,

Downloaded 02 Jun 2010 to 171.66.16.102. Redistribution subject to ASME license or copyright; see http://www.asme.org/terms/Terms_Use.cfm

$$\{F\} = [Gd][z]_{\text{meas}} + ([Gv] + \{\varphi(|z|_{\text{meas}})\})[\dot{z}]_{\text{meas}} \quad (4.1)$$

Substitution of this force definition into the shaft vibration model given by Eqs. (3.1)–(3.3) complicates it to the extent that the explicit solution is impossible. Even with the further simplifying assumption of shaft symmetry, ($m_0 = m_2$), phase angles and shaft amplitudes had to be calculated implicitly from the model.

Sample calculations were carried out assuming two different nonlinear terms in the bearing response:

$$\varphi(|z|_{\text{meas}}) \propto \text{const}(|z|_{\text{meas}})^2 \quad \text{and}$$

$$\varphi(|z|_{\text{meas}}) \propto \text{const}(|z|_{\text{meas}})^4$$

Comparison of the results with the corresponding linear control case show similar shifts in critical frequencies for both bearing designs. It was rather expected, since the stiffness terms were identical. Nonlinear force was responding more effectively in the vicinity of the shaft critical frequencies, but no apparent benefits were observed in terms of amplitude suppression as compared to linear force. Generally, the character of the damping effects obtained was similar to the properly adjusted suppression due to the linear bearing force.

Contrary to the simulation results with no major differences in the achieved vibration suppression and shift in critical frequencies, analysis of shaft stability shows qualitative difference between stability regimes of shaft controlled by nonlinear and linear bearing force. The presence of a nonlinear damping term in the bearing response does not necessarily increase the stability limits, but it introduces new parameters into shaft motion characteristic equation, which can affect stability range. Those parameters were not able to alter the stability boundaries of shaft supported by bearing with linear response. This will be illustrated below.

Stability analysis of the synchronous rotor vibrations and derivation of the rotor characteristic equation was carried out, adopting the classical perturbation method [17]. The variational real variable $a(t)$ was introduced as the perturbation of rotor vibration amplitude in the following way:

$$z_i = [A_i + a_i(t)]e^{j(\omega t + \alpha_i)} \qquad i = 0, 1, 2 \quad (4.2)$$

Consequently, this perturbation had to appear also as an argument in the nonlinear part of the bearing response:

$$\varphi(|z|) = \varphi[A + a(t)] = \varphi(A) + \left(\frac{d\varphi}{dA}\right)_A a(t) \quad (4.3)$$

Substitution of these "perturbed" coordinates defined by Eqs. (4.2) and (4.3) into the shaft motion Eqs. (3.1)–(3.3) and omission of terms $e^{j\omega t}$ results in the following set of equations, which describes behavior of the perturbation in time:

'1'-*disk*:

$$m_1(\ddot{a}_1 + 2j\omega\dot{a}_1 - \omega^2 a_1) + D(\dot{a}_1 + j\omega a_1) + 2Ka_1 - Ka_0 e^{j(\alpha_0 - \alpha_1)} - Ka_2 e^{j(\alpha_2 - \alpha_1)} = 0 \quad (4.4)$$

'0'-*mass*:

$$m_0(\ddot{a}_0 + 2j\omega\dot{a}_0 - \omega^2 a_0) + [D_{Fz0,z0} + \varphi_0(A_0)](\dot{a}_0 + j\omega a_0) + \left(\frac{d\varphi_0}{dA_0}\right)_{A_0} j\omega A_0 a_0 + (K + K_{Fz0,z0})a_2 - Ka_1 e^{j(\alpha_1 - \alpha_0)} = 0 \quad (4.5)$$

'2'-*mass*:

$$m_2(\ddot{a}_2 + 2j\omega\dot{a}_2 - \omega^2 a_2) + [D_{Fz2,z2} + \varphi_2(A_2)](\dot{a}_2 + j\omega a_2) + \left(\frac{d\varphi_2}{dA_2}\right)_{A_2} j\omega A_2 a_2 + (K + K_{Fz2,z2})a_2 - Ka_1 e^{(\alpha_1 - \alpha_2)} = 0 \quad (4.6)$$

Solution of these perturbation equations takes the form:

$$a_i = E_i e^{(st - j\omega t - j\alpha_i)} \qquad i = 0, 1, 2 \quad (4.7)$$

where E = real or complex constant.

Substitution of Eq. (4.7) into Eqs. (4.3)–(4.6) leads to the following characteristic equation of shaft motion:

$$\begin{aligned}
&(m_1 s^2 + Ds + 2K)\left\{m_0 s^2 + [D_{Fz0,z0} + \varphi_0(A_0)]s + \left(\frac{d\varphi_0}{dA_0}\right)_{A_0} j\omega A_0 + K + K_{Fz0,z0}\right\}\left\{m_2 s_2 + [D_{Fz2,z2} + \varphi_2(A_2)]s + \left(\frac{d\varphi_2}{A_2}\right)_{A_2} j\omega A_2 + K + K_{Fz2,z2}\right\} \\
&-K^2\left\{m_2 s^2 + K + K_{Fz2,z2} + [D_{Fz2,z2} + \varphi_2(A_2)]s + \left(\frac{d\varphi_2}{dA_2}\right)_{A_2} j\omega A_2 + m_0 s^2 + K + K_{Fz0,z0} + [D_{Fz0,z0} + \varphi_0(A_0)]s + \left(\frac{d\varphi_0}{dA_0}\right)_{A_0} j\omega A_0\right\} = 0 \quad (4.8)
\end{aligned}$$

The numerical analysis of the roots of Eq. (4.8) defines the stability limits for the rotor synchronous vibrations controlled by the nonlinear bearing response. In the stable region all roots should have nonpositive real parts. This ensures time-decaying perturbation behavior, which is the sufficient condition for the stable shaft operation.

Analyzing the equation derived, it is worthwhile to notice that assuming the bearing force as linear, ($\{\varphi\} = 0$), and, accordingly, equating the nonlinear terms and their derivatives to zero, the characteristic Eq. (4.8) becomes the characteristic equation for the purely rotational shaft motion.

Without calculating the roots of Eq. (4.8), it is shown that the presence of the nonlinear terms in the bearing response introduced new parameters into the characteristic equation: rotational speed of shaft ω, and vibration amplitudes A_i ($i = 0, 1, 2$) of all concentrated masses, which, in turn, depend on the magnitude of shaft imbalance. It opens more possibilities to influence the stability limits as compared to the linear force case, where only stiffness, mass of the shaft, and bearing properties (stiffness and damping gains) could affect shaft stable operational range.

This observation is analogous to the one described for fluid bearing [17, 18], where the presence of the nonlinear components of fluid forces made rotor stability dependent on the imbalance and a wider region of shaft stable operation was obtained simply by increasing imbalance of the shaft.

5 Conclusions

A mathematical model of three mass shaft supported by two magnetic bearings with collocated sensors has been derived to simulate vibration control provided by the differently designed magnetic bearing force.

In this analysis, the linear bearing response has been assumed, with the stiffness and damping coefficients calculated from the stable ROCL equation. The multi-access bearing response was verified in terms of the precision in the achieved shift in critical frequencies and suppression of the amplitudes of rigid and flexible modes. Results were compared with the multi-access control of the rigid mode only, and with the single access control.

It was demonstrated that reasonable control of shaft end vibration and the most precise shift in critical frequencies was provided by multi-access bearings. This design also satisfied stability requirements in that the bearing gain matrices

Downloaded 02 Jun 2010 to 171.66.16.102. Redistribution subject to ASME license or copyright; see http://www.asme.org/terms/Terms_Use.cfm

must be positive definite and symmetric. Single access bearings gave good attenuation of the middle disk mass, but poor suppression of the amplitude of the heavier end of the shaft. Also, with the single access control considered, the desired shifts in critical frequencies were not attained. Finally, the effect of the single access control appeared to be similar to the case of multi-access control of the rigid mode only, with two other residual flexible modes beyond control.

Nonlinear control provided by the bearing force with the linear stiffness but nonlinear damping part was also briefly analyzed and compared to the linear control results. No apparent benefits were observed in suppression of shaft vibration or shift in frequencies. However, stability analysis showed that with the nonlinear type of control, the limits of stable shaft operation can be influenced by additional parameters such as imbalance and shaft rotational speed, which had no effect on stability of the shaft operating with the conventional linear bearings.

References

1 Allaire, P. E., Humphris, R. R., and Kelm, R. D., "Dynamics of Flexible Rotor in Magnetic Bearings," *Proc. of Rotordyn. Instability Problems in High-Performance Turbomach.*, NASA Conference Publication 2443, 1986.

2 Allaire, P. E., Humphris, R. R., and Kelm, R. D., "Magnetic Bearings for Vibration Reduction and Failure Prevention," *Proc. of the 45th Meeting of Mech. Failure Prevention Group*, NBS, Gaithersburg, MD, Apr. 16–18, 1985.

3 Allaire, P. E., Lewis, D. W., and Jain, V. K., "Feedback Control of a Single Mass Rotor on Rigid Supports," *J. of the Franklin Institute*, Vol. 312, No. 1, July 1981.

4 Allaire, P. E., Lewis, D. W., and Knight, J. D., "Active Vibration Control of a Single Mass Rotor on Flexible Supports," *J. of the Franklin Institute*, Vol. 315, No. 3, Mar. 1983.

5 Baruch, H., "A Recursive Pole Displacement Method for Large Flexible Structures," presented at the 1987 ASME Design Technology Conferences—11th Biennial Conference on Mechanical Vibration and Noise, Boston, MA, Sept. 1987.

6 Firoozian, S. R., "Modeling and Control of Turbomachinery Vibrations," presented at the 1987 ASME Design Technology Conf., Boston, MA, Sept. 1987.

7 Humphris, R. R., Allaire, P. E., and Lewis, D. W., "Design and Testing of Magnetic Bearings for Vibration Reduction," *Proc. of the 41st Meeting of Mech. Failure Prevention Group*, Maryland, Oct. 1986.

8 Humphris, R. R., Allaire, P. E., Lewis, D. W., and Barret, L. E., "Diagnostic and Control With Magnetic Bearing," *Proceedings of the 24th Intersociety Energy Conversion Eng. Conf.*, 1989.

9 Humphris, R. R., Kelm, R. D., Lewis, D. W., and Allaire, P. E., "Effect of Control Algorithms on Magnetic Journal Bearing Properties," ASME JOURNAL OF ENGINEERING FOR GAS TURBINES AND POWER, Vol. 108, Oct. 1986.

10 Joshi, S. M., and Groom, N. J., "Design of Reduced-Order Controllers for Large Flexible Structures," presented at the XVIth Annual Allerton Conf. on Communication, Control and Computing, Allerton House, Monticello, IL, 1978.

11 Kasarda, M., Allaire, P. E., Humphris, R. R., and Barret, L. E., "A Magnetic Damper for First Mode Vibration Reduction in Multimass Flexible Rotors," ASME JOURNAL OF ENGINEERING FOR GAS TURBINES AND POWER, Vol. 112, Oct. 1990.

12 Lewis, D. W., Moore, J. W., Bradley, P. L., and Allaire, P. E., "Vibration Limiting of Rotors by Feedback Control," *Proceedings of NASA/ARO Workshop on Rotor Dynamic Instability*, 1982.

13 Levine, W. S., and Athans, M., "On the Determination of the Optimal Constant Output Feedback Gains for Linear Multivariable Systems," *IEEE Trans. on Automatic Control*, Vol. AC-15, No. 1, Feb. 1970.

14 Lin, J. G., "Closed-Loop Asymptotic Stability and Robustness Conditions for Large Space Systems With Reduced Order Controllers," presented at the 20th IEEE Conf. on Decision and Control, San Diego, IEEE Control Systems Society, 1981.

15 Lin, J. G., Lin, Y. H., and Preston, R. B., "Stability Augmentation for Large Space Structures by Modal Dashpots and Modal Springs," presented at the VPI-SU/AIAA Symp., Dynamics and Control of Large Flexible Spacecraft, Blacksburg, VA, 1981.

16 Lin, J. G., Hegg, D. R., Lin, Y. H., and Keat, J. E., "Output Feedback Control of Large Space Structures: An Investigation of Four Design Methods," presented at the Sec. VPI-SU/AIAA Symp., Dynamics and Control of Large Flexible Spacecraft, Blacksburg, VA, 1979.

17 Muszynska, A., "Whirl and Whip-Rotor/Bearing Stability Problems," ASME *Journal of Sound and Vibration*, Vol. 110, No. 3, 1986.

18 Muszynska, A., "Improvements in Lightly Loaded Rotor/Bearing and Rotor/Seal Models," *Rotating Machinery Dynamics*, Vol. 1, ASME, New York, 1987.

19 Nonami, K., "Vibration Control of Rotor Shaft Systems by Active Control Bearings," NASA Technical Memorandum 87053, 1985.

20 Salm, J., and Schweitzer, G., "Modelling and Control of a Flexible Rotor With Magnetic Bearings," Inst. of Mech. Engrs., York, United Kingdom, 1984.

21 Schweitzer, G., "Magnetic Bearings," *Rotordynamics 2. Problems in Turbomachinery*, Springer-Verlag, 1988.

22 Schweitzer, G., and Ulbrich, H., "Magnetic Bearings—A Novel Type of Suspension," presented at the Sec. Int. Conf. on Vibrations in Rotating Machinery, Institution of Mechanical Engineers, London–Cambridge, 1980.

23 Schweitzer, G., "Characteristics of a Magnetic Rotor Bearing for Active Vibration Control," *Inst. Mech. Engrs.*, Vol. C239, 1976.

24 Salm, J., "Eine aktive magnetische Lagerung eines elastichen Rotors als Beispiel ordungsreduzierter Regelung grosser elasticher Systeme," VDI-Verlag GmbH, Dusseldorf, 1988.

25 Stanway, R., and O'Reilly, J., "State-Variable Feedback Control of Rotor-Bearing Suspension Systems," IMechE, C274, 1984.

26 Strunce, R. R., et al., "Active Control of Space Structures," Final Technical Report No. RADC-TR-81-289, C. S. Draoer Laboratory, Inc., Cambridge, MA, 1981.

27 Ulbrich, H., and Anton, E., "Theory and Application of Magnetic Bearings With Integrated Displacement and Velocity Sensors," Inst. Mech. Engrs., Vol. C299, 1984.

28 *Proceedings of the Second Int. Symposium on Magnetic Bearings*, Tokyo, Japan, July 12–14, 1990.

29 "Magnetic Bearings," *Proceedings of the First Int. Symposium ETH Zurich*, G. Schweitzer, ed., Switzerland, June 6–8, 1988.

Downloaded 02 Jun 2010 to 171.66.16.102. Redistribution subject to ASME license or copyright; see http://www.asme.org/terms/Terms_Use.cfm

Exploring How Shroud Constraint Can Affect Vibratory Response in Turbomachinery

M.-T. Yang

J. H. Griffin

Department of Mechanical Engineering,
Carnegie Mellon University,
Pittsburgh, PA 15213

Unusual resonant responses were observed during spin pit tests of shrouded blades. The unusual behavior consisted of blades that exhibited strong response over a broad range of frequencies. The frequencies of peak resonance were considerably lower than predicted and were also lower than those observed in other tests of nominally identical wheels. In addition, the tracking plots of blade amplitudes versus frequency were truncated rather than displaying the usual sharp peaks seen in other tests. The unusual response is potentially dangerous since high vibratory response could be excited over a broad range of operating speeds. The blades were designed to be free standing with gaps of approximately 0.25 mm between neighboring shrouds. It is hypothesized that shroud contact at the blade tips could cause the unusual vibratory response. A simple model of a blade with shroud contact is developed in order to determine if shroud contact could cause blades to vibrate in the observed manner. The model is unusual in that it seeks to explore how contact could cause the blade to respond at lower (rather than higher) frequencies since contact typically increases the constraints on a structure and raises its natural frequencies.

Introduction

The manufacturers of both steam and gas turbines design blading with integrally machined shrouds at the blade tips, Fig. 1. The shrouds serve to enclose the flow and increase the efficiency of the stage. Furthermore, integral shrouds can mitigate or even eliminate problems related to the connection of the shroud to the blade, such as rivet creep or accelerated corrosion at the interface. Often the shrouds are designed so that there are small gaps between the shrouds on neighboring blades. From the point of view of aerodynamic efficiency, the design is improved if the nominal gap distance is reduced. However, from the point of view of a structural engineer, very small gaps can lead to unusual vibratory response that may cause durability problems. As part of a technology development program, a series of spin-pit tests was conducted on turbo-pump stages in order to develop a better understanding of their dynamic response. Unusual results from the tests are depicted in Fig. 2. The figure shows strain gage data from tests of two nominally identical stages that were excited by 12 equally spaced jets. The horizontal axes correspond to the fundamental excitation frequency, which is 12 times the rotational speed. The vertical axes correspond to the twelfth engine-order frequency component of the vibratory responses of the blades (the $12N$ component). A number of lines are plotted in each of the graphs, each one of which corresponds to the vibratory response of an individual blade. In theory, both stages should exhibit the same trends, but it is apparent that the dynamic response of the two stages are very different, both in their frequency content and in the shape of the response curves. The purpose of this paper is to explore the possible causes of these differences.

In Fig. 2(a), stage A responds as a moderately "mistuned" bladed disk. Mistuning has been discussed in the literature for a number of years, for examples see [1–3]. Mistuning refers to the fact that blades have slightly different frequencies because of variations in the manufacturing process. The characteristics of a mistuned disk are that the vibratory response of the blades have multiple peaks and that, at a given peak, the amplitudes of the individual blades may vary

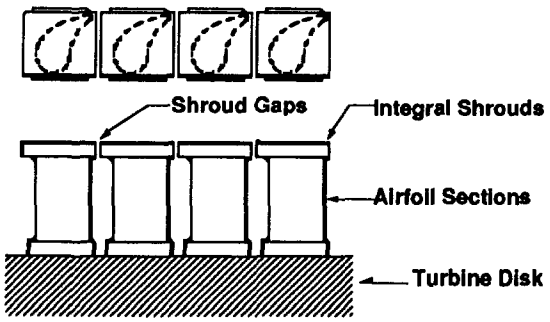

Fig. 1 Partial row of integrally shrouded blades

Contributed by the International Gas Turbine Institute and presented at the 38th International Gas Turbine and Aeroengine Congress and Exposition, Cincinnati, Ohio, May 24–27, 1993. Manuscript received at ASME Headquarters March 10, 1993. Paper No. 93-GT-285. Associate Technical Editor: H. Lukas.

Copyright © 1995 by ASME

Downloaded 02 Jun 2010 to 171.66.16.102. Redistribution subject to ASME license or copyright; see http://www.asme.org/terms/Terms_Use.cfm

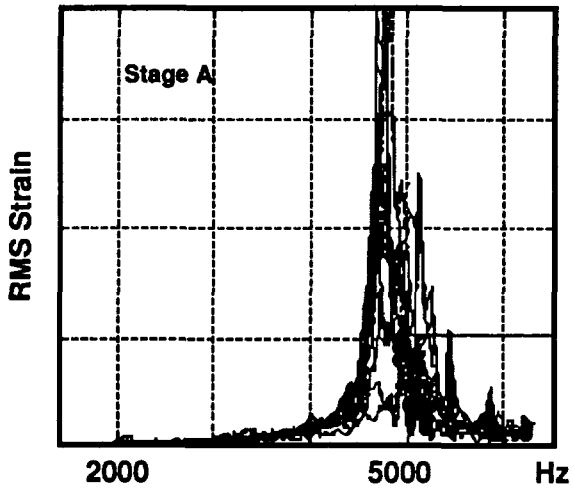

(a) Stage A: Moderately Mistuned Bladed Disk

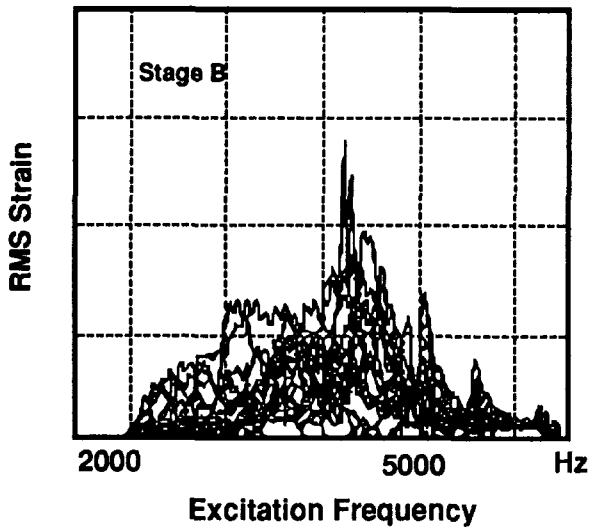

(b) Stage B: Severely Mistuned Bladed Disk

Fig. 2 Spin-pit test data

significantly. This classic mistuned behavior is apparent in the behavior of stage A. Note that while the blades respond at multiple peaks, the peaks are still grouped about the frequency of the theoretical first bending mode of a tuned bladed disk in which the shrouds do not touch (approximately 5000 Hz). The response of the bladed disk in Fig. 2(*b*), stage *B*, is very different and quite unusual in two respects: (1) The blades tend to have high vibratory response over a very broad frequency range where many of the frequencies are much lower than the theoretical frequency of the tuned bladed disk, and (2) the response curves tend to be flattened at the top.

The vibratory response of stage *B* is undesirable because it makes it difficult to design the stage so as to avoid resonance. When the stage has a strong response over a limited range of frequencies, as in Fig. 2(*a*), it is possible to modify the design so that resonance does not occur in the operating range. However, if a stage responds as in Fig. 2(*b*) there is no safe operating speed. Thus, it becomes important to understand the causes of stage B's response so that this type of behavior can be avoided in future designs.

To isolate the cause of the unusual vibratory response two additional tests were made on the blade set of stage *B*. In the first test, blade set *B* was put into disk *A*. The result was that the response was very similar to that displayed in Fig. 2(*b*). Consequently, it was concluded that the source of difference in spectrum lies in the blades and not in the disks. In the second test, the shrouds of blade set *B* were ground down in order to increase the size of the gaps between the blades. The stage was tested for a second time and blades responded more like stage *A*. This indicates that the cause of the unusual response was probably shroud contact.

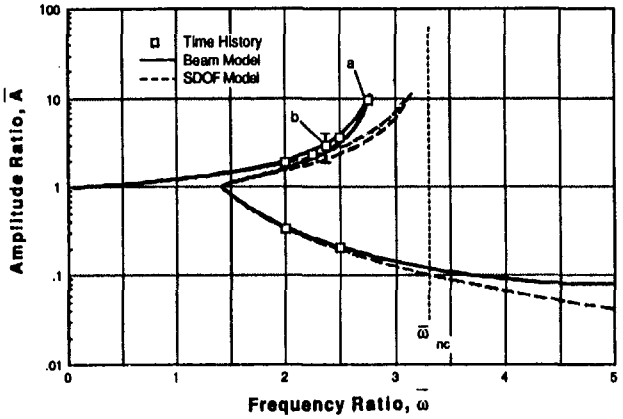

Fig. 3 Effect of an open gap between shrouds [4]

While it is clear from the tests that shroud contact caused the unusual response of stage *B* it is not clear why contact should produce flattened response curves over a broad frequency range that is lower than the tuned system frequency. Modeling shroud contact has been the subject of a number of papers; for example, see [4–6]. However, in these papers it has been shown that contact tends to increase the constraints on the blades and raise the frequencies at which they exhibit peak response. Thus, the goal of this paper is to explore how shroud contact could possibly cause the type of response exhibited by stage *B*.

In the next section, we will try to identify the mechanisms that could cause the low-frequency mistuned response of stage *B* and develop a simple model of the system. Then, the governing equations for the model problem will be derived and their solution investigated both numerically and analytically. The results will be discussed in the final section.

Formulation and Analysis

Model Development. First consider the classical response of a tuned bladed disk in which the blades have small, uniform gaps between their tip shrouds. If the excitation is sufficiently large so as to cause the blades to come in contact with their neighbors, then from [4] we know that the response is of the form depicted in Fig. 3. As might be expected, the nonlinear gap constraint acts like a hardening spring, which raises the frequency of the peak response. In the case of the turbo-pump blades such a model is not applicable for two reasons: (1) The blades are short and stiff and, as a result, the amplitudes of the vibrations are an order of magnitude lower than those that would cause a blade with nominal gaps to hit its neighbor; (2) the peak responses in the experimental data of stage *B* occur at lower frequencies than the blade would have if it was unconstrained at its tip.

Because the turbo-pump blade is so stiff, it is likely that any contact with its neighbor first occurs because of static loading, which causes it to lean against the adjacent blade. (If one examines the tolerances and the geometry of the design this is a possibility.) Then any nonlinear vibratory response would be associated with the loss of contact. However, a preloaded shroud and lift-off would still result in additional

Downloaded 02 Jun 2010 to 171.66.16.102. Redistribution subject to ASME license or copyright; see http://www.asme.org/terms/Terms_Use.cfm

constraints to the blades and, consequently, higher frequencies of peak response.

In order for a blade to respond at a lower frequency, the constraints acting on it have to be reduced by some mechanism. It is hypothesized that when a blade leans against its neighbor, the resulting moment causes the teeth of the fir tree attachment to seat improperly on one side. If the attachment is modeled as pinning the blade and providing a restoring moment in a manner equivalent to a torsional spring, then the unloading of the teeth causes the stiffness of the spring to be reduced. In fact, in the limit, the attachment would act as a simple pinned constraint.

A model of a blade with this type of constraint is depicted in Fig. 4. A number of models could have been developed. The specific model was chosen because of its simplicity, which allows us more readily to analyze its response. The blade is modeled as a beam with a reduced attachment stiffness K_r. It leans against a neighboring blade, which is represented by the spring of stiffness K_n. This model could correspond to two different physical cases: (1) The attachment of the neighboring blade is fully seated and it has a significantly higher natural frequency, and (2) the blade and its neighbor are identical but respond 180 deg out of phase. In the first case K_n represents the equivalent static stiffness of the neighboring blade and, in the second case, it represents the local stiffness of the shroud.

Formulation. The nondimensionalized equation of motion for a continuous beam under a centrifugal force field [7] is (Appendix A)

$$\frac{\partial^2\eta}{\partial\tau^2} - \frac{\partial}{\partial\xi}\left(f_a(\xi)\frac{\partial\eta}{\partial\xi}\right) + \frac{1}{\alpha_0^4}\frac{\partial^4\eta}{\partial\xi^4} = f_e(\xi,\tau) - f(\eta(\xi_n,\tau))\delta(\xi-\xi_n) \quad (1)$$

where τ is the time variable, ξ is the longitudinal coordinate, $\eta(\xi,\tau)$ is the transverse displacement, and α_0 is a constant related to how the time is nondimensionalized. $f_a(\xi)$ is the centrifugal force that acts in the axial direction, $f_e(\xi,\tau)$ the external excitation, $f(\eta(\xi_n,\tau))$ the nonlinear restoring force due to the shroud contact, and ξ_n is the location where the shrouds come into contact.

The nonlinear contact force can be expressed in terms of the transverse displacement at the contact point, i.e.,

$$f(\eta(\xi_n,\tau)) = \begin{pmatrix} \kappa_n(\eta(\xi_n,\tau)-\chi_d) & \text{for } \eta(\xi_n,\tau) > \chi_d \\ 0 & \text{for } \eta(\xi_n,\tau) < \chi_d \end{pmatrix} \quad (2)$$

where

$$\chi_d = \frac{d}{|d|} = \begin{pmatrix} 1 & \text{for } d > 0 \\ -1 & \text{for } d < 0 \end{pmatrix} \quad (3)$$

κ_n is the stiffness of the nonlinear constraint and d is the physical gap size.[1] Equation (2) states that when the displacement of the tip is greater than χ_d, the blade is subjected to a spring constraint and when it is less than χ_d it is unconstrained. (The shroud is statically preloaded when $\chi_d = -1$.)

The boundary conditions for the beam are

$$\eta(0,\tau) = 0 \quad (4)$$

$$\frac{\partial^2\eta(0,\tau)}{\partial\xi 2} = \kappa_r\frac{\partial\eta(0,\tau)}{\partial\xi} \quad (5)$$

[1]Since we are only interested in the vibration of blades with preloaded shrouds, the $d = 0$ case is intentionally ruled out.

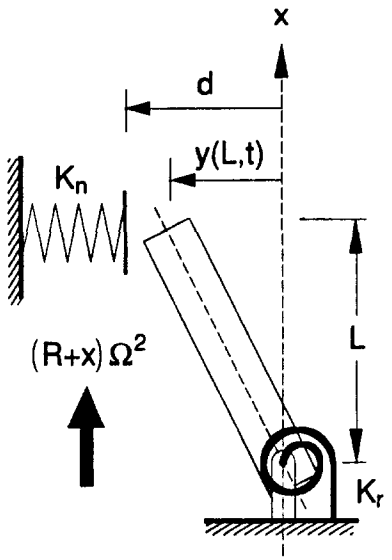

Fig. 4 A simplified model

$$\frac{\partial^2\eta(0,\tau)}{\partial\xi^2} = \kappa_r\frac{\partial\eta(0,\tau)}{\partial\xi} \quad (6)$$

$$\frac{\partial^3\eta(1,\tau)}{\partial\xi^3} - \alpha_0^4 f_a(1)\frac{\partial\eta(1,\tau)}{\partial\xi} = 0 \quad (7)$$

where κ_r is the stiffness of the root constraint.

It is assumed that the excitation force is constant along the length of the blade and that only its fundamental frequency component is important, i.e.,

$$f_e(\xi,\tau) = p_e\cos(\gamma_e\tau) \quad (8)$$

where, in the case discussed in the introduction, the excitation frequency, γ_e, is twelve times the rotational speed of the stage, γ. Except for the reduced attachment stiffness κ_r, the other parameters in the beam model can be estimated from the nominal specifications of the turbo-pump blade. Initially, as a limiting case, we assume that the torsional stiffness of the attachment is negligible ($\kappa_r = 0$) and that the attachment acts as a simple pinned constraint.

Modal Representation. It is assumed that the vibratory response of the blade can be represented as a linear combination of its modes, i.e.,

$$\eta(\xi,\tau) = \sum_i a_i(\tau)b_i(\xi) \quad (9)$$

where the $a_i(\tau)$ are the modal amplitudes that oscillate in time and $b_i(\xi)$ are the modes of a blade that is unconstrained at its shroud and subject to a centrifugal force field.

By substituting Eq. (9) into Eq. (1) we can obtain the modal equation of motion:

$$\mathbf{M\ddot{a}} + \mathbf{C\dot{a}} + \mathbf{Ka} = \mathbf{f}_e\cos(\gamma_e\tau) + \mathbf{b}_n f(\eta(\xi_n,\tau)) \quad (10)$$

where the ith elements of the vectors $\mathbf{f}_e$ and $\mathbf{b}_n$ are:

$$\{\mathbf{f}_e\}_i = p_e\int_0^1 b_i(\xi)d\xi \quad (11)$$

and

$$\{\mathbf{b}_n\}_i = b_i(\xi_n) \quad (12)$$

There are three observations that can be made about this modal representation. First, the modes are orthogonal [7]. Second, the modes and the natural frequencies change when the rotational speed changes since the centrifugal force $f_a(\xi)$ is proportional to γ^2. The first mode of the pinned blade in a

Downloaded 02 Jun 2010 to 171.66.16.102. Redistribution subject to ASME license or copyright; see http://www.asme.org/terms/Terms_Use.cfm

centrifugal force field is very similar to that of a pendulum and has a frequency that is almost proportional to γ (the square root of the effective gravitational constant). Third, within the operating frequency range, the γ_e is close to the natural frequency of the first pendulum-type mode. The natural frequency of the second mode is an order of magnitude higher. A consequence of this last observation is that in most cases the accuracy of the representation will be adequate if only the first mode (or at most the first few modes) is taken into account.

At this point the issue is whether or not the model problem will exhibit similar behavior to that observed in the spin-pit tests. In order to explore this issue we will need to develop solutions to Eq. (10). Since the equations are nonlinear and complicated they can be only solved either numerically or approximately using perturbation methods. A numerical solution is developed in the next section that will be used as a baseline for comparison with an approximate analytical solution that will be developed later.

Numerical Approach. In this investigation the Newmark method [8, 9] is used to develop numerical time integration solutions to Eq. (10). It employs a second-order implicit integration scheme. The Newmark method was chosen because it is computationally efficient for second-order systems and because higher order algorithms provide little or no increase in accuracy when dealing with intermittent contact problems, since the derivative of the contact force is discontinuous. The Newmark method assumes that the acceleration varies linearly between two instants of time. The basic expressions for the displacement and velocity vectors are

$$\dot{\mathbf{a}}^{(n+1)} = \dot{\mathbf{a}}^{(n)} + \left[(1-\beta)\ddot{\mathbf{a}}^{(n)} + \beta\ddot{\mathbf{a}}^{(n+1)}\right]\Delta\tau \tag{13}$$

$$\mathbf{a}^{(n+1)} = \mathbf{a}^{(n)} + \dot{\mathbf{a}}^{(n)}\Delta\tau + \left[\left(\frac{1}{2}-\alpha\right)\ddot{\mathbf{a}}^{(n)} + \alpha\ddot{\mathbf{a}}^{(n+1)}\right](\Delta\tau)^2 \tag{14}$$

where the superscript (n) denotes the quantities at the time level n. From [8], "the parameters α and β indicate how much the acceleration at the end of the interval enters into the velocity and displacement equations at the end of the interval $\Delta\tau$." In the resulting simulations, α was taken as 0.25 and β as 0.5 so that the numerical scheme would have no spurious damping and would be unconditionally stable [8]. This choice of α and β corresponds to the assumption of constant acceleration over the time step.

By combining these two equations with the equation of motion in numerical form, i.e.,

$$\mathbf{M}\ddot{a}^{(n+1)} + \mathbf{C}\dot{a}^{(n+1)} + \mathbf{K}\mathbf{a}^{(n+1)} = \mathbf{p}^{(n+1)} \tag{15}$$

we can obtain the expression for $\mathbf{a}^{(n+1)}$

$$\mathbf{a}^{(n+1)} = \left(\frac{1}{\alpha(\Delta\tau)^2}\mathbf{M} + \frac{\beta}{\alpha\Delta\tau}\mathbf{C} + \mathbf{K}\right)^{-1} \times \left\{\mathbf{p}^{(n+1)} + \mathbf{M}\left(\frac{1}{\alpha(\Delta\tau)^2}\mathbf{a}^{(n)} + \frac{1}{\alpha\Delta\tau}\dot{\mathbf{a}}^{(n)} + \left(\frac{1}{2\alpha}-1\right)\ddot{\mathbf{a}}^{(n)}\right) + \mathbf{C}\left(\frac{\beta}{\alpha\Delta\tau}\mathbf{a}^{(n)} + \left(\frac{\beta}{\alpha}-1\right)\dot{\mathbf{a}}^{(n)} + \left(\frac{\beta}{\alpha}-2\right)\frac{\Delta\tau}{2}\ddot{\mathbf{a}}^{(n)}\right)\right\} \tag{16}$$

The purpose of the simulation was to generate results in a manner that is consistent with those generated in the spin-pit tests. As a result, the procedure indicated in the flow chart of Fig. 5 was followed in order to simulate a slow accel in the spin-pit. First, the rotational speed of the stage, γ, was chosen and the modes of the beam calculated for this value

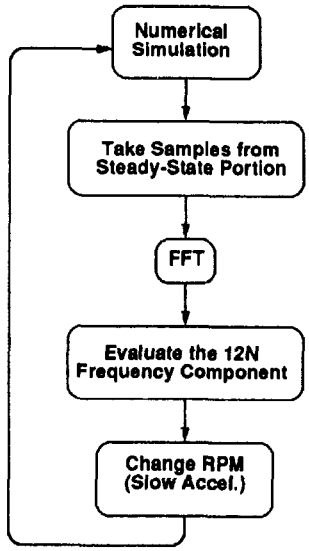

Fig. 5 Procedure to simulate the spin-pit tests

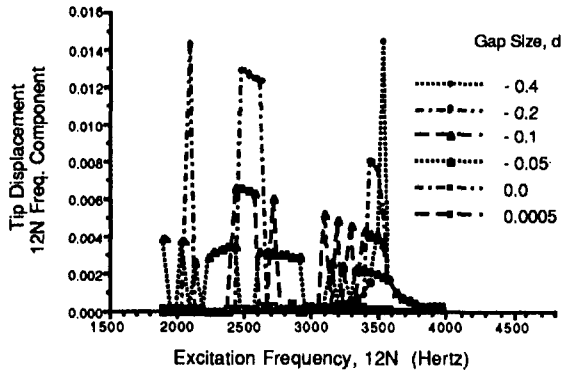

Fig. 6 Physical tip displacements computed numerically for initial conditions equal to zero

of γ. Then Eq. (16) was solved for a sufficiently long period of time so that the vibration essentially had reached its steady state (i.e., transients had died out). The output was then sampled and its Fast Fourier Transform [10] calculated so as to establish its frequency components. The rotational speed was then incremented and the process repeated so as to cover the operating range. The first four modes were included in the simulation. Including additional modes had no apparent affect on the results. Using this approach, the $12N$ component of the response was calculated as a function of the rotational speed; a representative result is depicted in Fig. 6. The numerical results have two characteristics that are similar to those in Fig. 2(*b*). First, the resonant peaks can occur over broad range of frequencies. Second, the vibratory responses often show flat (truncated) curves. These two features suggest the proposed model may capture the essential physics of the stage that was tested in the spin-pit.

Two additional characteristics of the response that can be observed from the numerical simulation should be noted. The first is the way in which the amplitude of the response tends to jump from a high level back to a low level and then back to a high level again, as though there were multiple peaks or as though the results might be unstable. If the initial conditions are slightly perturbed then it can be observed in Fig. 7 that the response at specific frequencies can shift between higher and lower values. This result suggests that the preloaded blade has multiple steady-state solutions that are sensitive to the initial conditions.

A second characteristic that can be ascertained from the

Downloaded 02 Jun 2010 to 171.66.16.102. Redistribution subject to ASME license or copyright; see http://www.asme.org/terms/Terms_Use.cfm

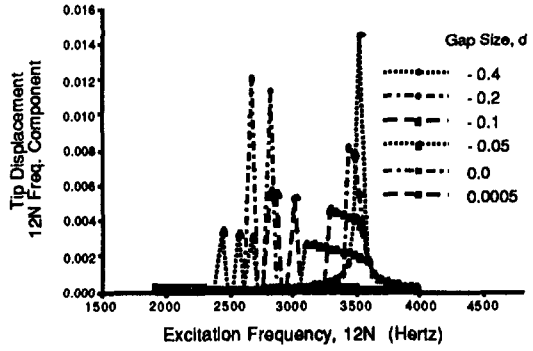

Fig. 7 Physical tip displacements computed numerically for slightly perturbed initial conditions

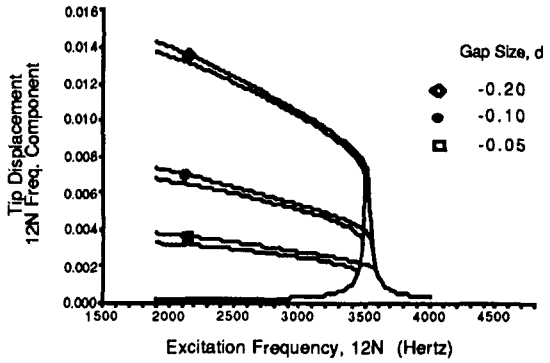

Fig. 8 Physical tip displacements predicted by harmonic balance

numerical results is that the FFT of the long time solution typically only contains two significant components: a zero frequency component induced by the static preload and a component that has the same frequency as the excitation. This result suggests that an approximate solution can be determined using the harmonic balance method; see for example [4, 11]. An analytical solution is desirable since it would shed some light on the presence of multiple solutions.

Analytical Approach (Harmonic Balance Method). The harmonic balance (HB) method is based on the observation that if the excitation is sinusoidal, then the response of the system is probably periodic[2] and has the same period as the excitation. The basic idea is that if the response is represented in terms of a Fourier series then the governing equations can be solved by equating the coefficients of terms that correspond to the same harmonic, thus "balancing" the harmonics. This approach is essentially exact if a large number of harmonic terms are included, see for example [12, 13]. When a large number of frequency components is included then the approach is essentially a numerical method since the resulting large system of nonlinear equations must be solved on the computer. However, the approach is used more often to develop relatively simple, approximate solutions by keeping only a few terms in the Fourier series. This latter approach will be employed here since we know from the results of the numerical simulation that the frequency content of the vibratory response is usually limited.

Thus, it is assumed that the response can be represented in terms of two components, one static and one dynamic, i.e.,

$$\eta(\xi_n, \tau) = \chi_0 + \chi \cos(\gamma_e \tau - \phi) \tag{17}$$

$$\mathbf{a}(\tau) = \mathbf{a}_0 + \mathbf{a}_c \cos(\gamma_e \tau) + \mathbf{a}_s \sin(\gamma_e \tau) \tag{18}$$

where

$$\eta(\xi_n, \tau) = \sum_i a_i(\tau) b_i(\xi_n) \tag{19}$$

By substituting Eq. (17) into Eq. (2), the nonlinear tip restoring force can be written as

$$f(\theta) = \begin{pmatrix} \kappa_n(\chi_0 + \chi \cos\theta - \chi_d) & \text{for } (\chi_0 + \chi \cos\theta) > \chi_d \\ 0 & \text{for } (\chi_0 + \chi \cos\theta) < \chi_d \end{pmatrix} \tag{20}$$

where $\theta = \gamma_e \tau - \phi$. If from Eq. (20), $f(\theta)$ is then expanded in a Fourier series, it may be approximated by the first two terms as

$$f(\theta) \cong \kappa_n \chi(z_0 + z \cos\theta) \tag{21}$$

where

$$z_0(\theta^*) = \frac{1}{\pi}(-\theta^* \cos\theta^* + \sin\theta^*) \tag{22}$$

$$z(\theta^*) = \frac{1}{\pi}(\theta^* - \sin\theta^* \cos\theta^*) \tag{23}$$

and

$$\theta^* = \begin{pmatrix} 0 & \text{no contact} \\ \cos^{-1}\left(\dfrac{\chi_d - \chi_0}{\chi}\right) & \text{lift - off} \\ \pi & \text{remains in contact} \end{pmatrix} \tag{24}$$

To obtain the solution, Eqs. (17), (18), and (21) are substituted into Eq. (10). After equating the linearly independent terms, the phase ϕ is eliminated by using the relation $\sin^2\phi + \cos^2\phi = 1$. This results in two nonlinear algebraic equations in the following form (see Appendix B):

$$\chi_0 = F_0(\theta^*) \tag{25}$$

$$\chi = F_1(\theta^*) \tag{26}$$

The procedures used to solve these equations are as follows. For the linear cases (continuous contact or no contact) θ^* is set equal to a constant value and χ_0 and χ determined by evaluating Eqs. (25) and (26). For the nonlinear case of blade lift-off, χ_0, χ, and θ^* are all unknowns and Eqs. (24), (25), and (26) must be solved simultaneously. This was accomplished by rewriting them in the form of a single equation in terms of θ^*, i.e.,

$$G(\theta^*) \equiv F_1(\theta^*) \cos\theta^* - \chi_d + F_0(\theta^*) = 0 \tag{27}$$

where $0 \le \theta^* \le \pi$. Since Eq. (27) involves only a single unknown with a limited range of values, it can be readily solved by a number of numerical methods. We solved Eq. (27) by evaluating it at a large number of evenly spaced points on the interval $(0, \pi)$ and then, when $G(\theta^*)$ changed signs, using the bi-section method to isolate its zeros. Once θ^* is computed then χ_0 and χ are calculated from Eqs. (25) and (26).

Some representative results for a statically preloaded interface are depicted in Fig. 8. Note that the system displays multiple solutions over a broad range of frequencies. Typically the lower solution corresponds to a linear solution in which there is no lift-off at the shroud. The solution with the highest value is a stable solution that corresponds to the nonlinear case of lift-off. The middle solution is unstable and corresponds to a stability limit that separates the two regimes. Note that the system displays a strong softening spring effect, i.e., the frequency of the higher amplitude solution tends to

[2]This assumption is not always true for nonlinear systems since under some conditions the response may contain subharmonics of the excitation frequency or even be chaotic.

Downloaded 02 Jun 2010 to 171.66.16.102. Redistribution subject to ASME license or copyright; see http://www.asme.org/terms/Terms_Use.cfm

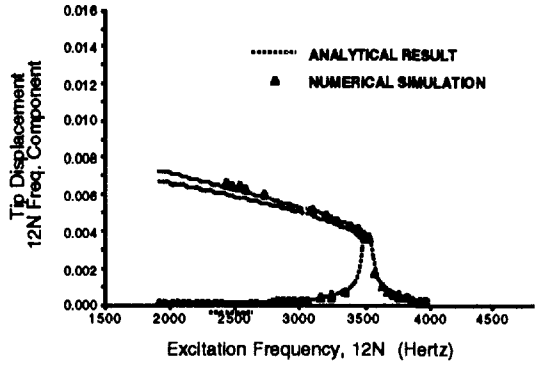

(a) High Pre-Load

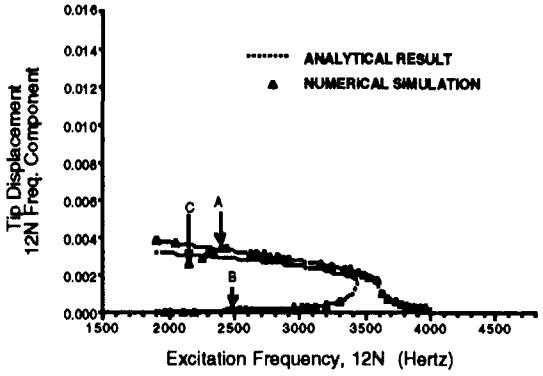

(b) Small Pre-Load

Fig. 9 Comparison of numerical and analytical results

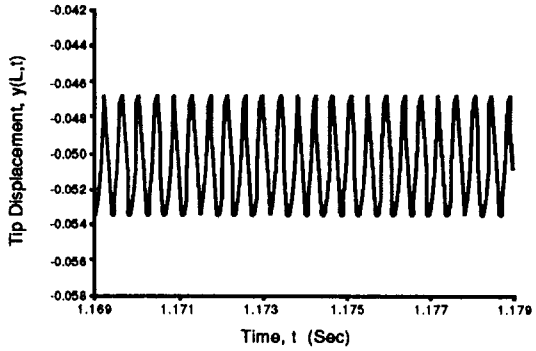

(a) Point A

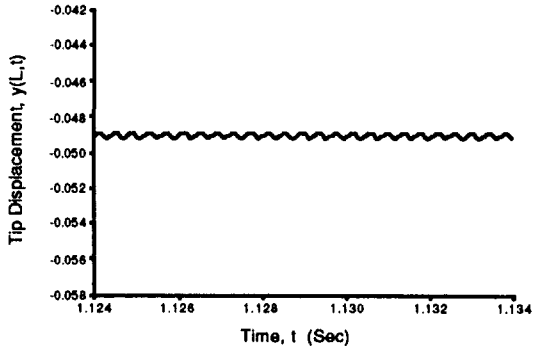

(b) Point B

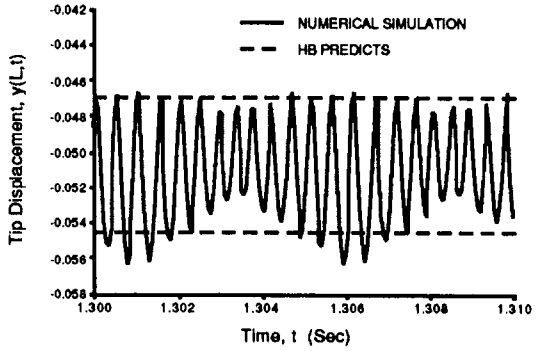

(c) Point C

Fig. 10 Time histories for various cases

decrease as the amplitude increases. This occurs for two reasons: As the amplitude increases the blade is in contact with its neighbor less of the time and, consequently, it is less constrained. Secondly, the pinned/free blade has a pendulum-like mode whose frequency decreases as the γ decreases. Thus, the higher amplitude solution occurs over an unusually wide range of amplitudes.[3]

Solutions from the HB method and from the numerical simulation will be compared in the next section.

Comparison of Numerical and Analytical Solutions

Both numerical and analytical solutions were found for a beam having properties that were similar to the turbo-pump blade that was tested in the spin-pit. Figure 9 shows the $12N$ frequency components of the numerical and analytical results for blades with preloaded shrouds. As can be seen, most of the numerical results lie near the upper and lower HB solutions. In general, the numerical and analytical results have good agreement for high preloads (or relatively low excitations) but poorer agreement for lower preloads (or relatively high excitations). In order to understand the correlation better, we examine in more detail the time histories and frequency spectra of some representative points in Fig. 9(b), points A, B, and C.

For points A and B there is good agreement between the analytical and numerical solutions. If one considers the corresponding time histories in Fig. 10(a, b) it is seen that they are "very" sinusoidal and their corresponding frequency spectra, Fig. 11(a, b), are dominated by their zero frequency and $12N$ components. On the other hand, for case C the long time numerical solution, Fig. 10(c), exhibits a beat phenomena and the frequency spectra, Fig. 11(c), has a number of components near $12N$ that have significant amplitudes. As a result, the HB method does not predict the $12N$ component nearly as well. However, note that the HB method does not do a bad job of predicting the average vibratory response (the dotted lines in Fig. 10c) even under these difficult conditions.

Several interesting results were observed when we plotted the solutions using the nondimensional variables. Figure 12 shows response curves predicted by the harmonic balance method as well as data points calculated from numerical simulations for three different ratios of the excitation to the preload. Consider, the effect of changing the ratio on each branch of the solution and what it means physically.

In Fig. 12(a) the excitation is large, in 12(b) it is moderate, and in 12(c) it is small. Since the lower branch of the solution

[3]The current analyses were performed under the assumption that the attachment acted as a pinned constraint and that the effective stiffness of the attachment, κ_r, was zero. If instead, κ_r was small but not equal to zero the response would be similar to that depicted in Fig. 8 except that there would be a lower bound on the range of frequencies that yield multiple solutions.

Downloaded 02 Jun 2010 to 171.66.16.102. Redistribution subject to ASME license or copyright; see http://www.asme.org/terms/Terms_Use.cfm

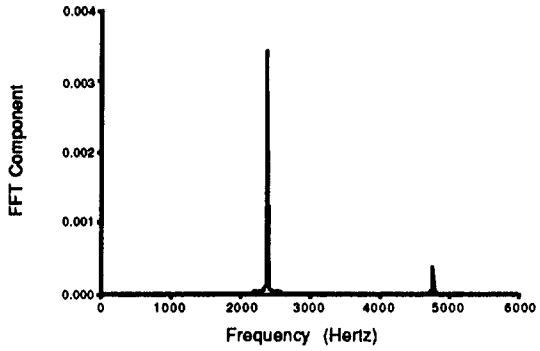

(a) Point A

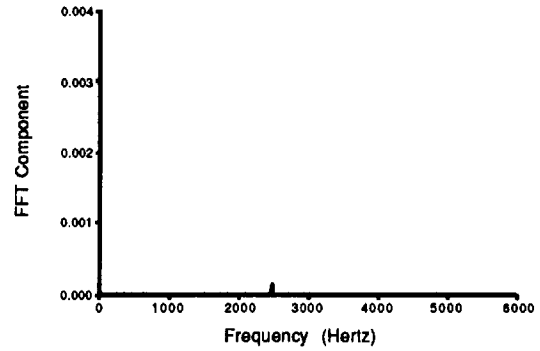

(b) Point B

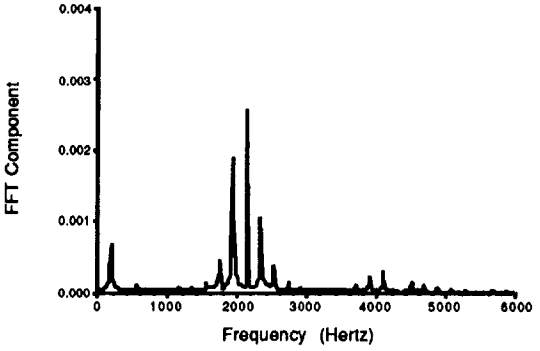

(c) Point C

Fig. 11 Frequency spectra for various cases

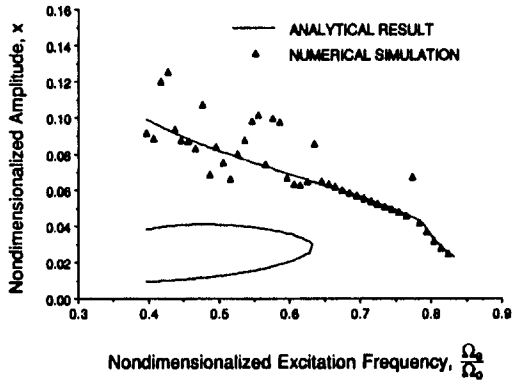

(a) High Excitation Force

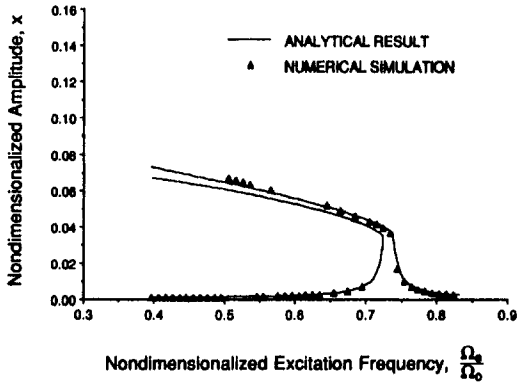

(b) Moderate Excitation Force

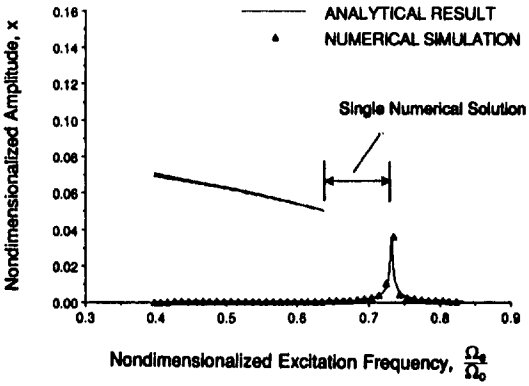

(c) Small Excitation Force

Fig. 12 Response curves for various ratios of excitation to preload

is the linear solution to the problem in which no lift-off occurs, it increases in each case in proportion to the magnitude of the excitation. It is essentially independent of the preload, except for the fact that the preload limits the frequency range over which this solution occurs.

The upper branch of the solution is approximately the same for each case and, consequently, is nearly independent of the magnitude of the excitation. However, because of the way in which we nondimensionalized the problem, this result implies that the actual vibration amplitude is almost directly proportional to the static preload in the shroud and independent of the magnitude of the excitation.

Lastly, note the behavior of the middle solution branch and its effect on the numerical simulation results. Recall that the middle branch corresponds to an unstable solution. When the excitation/preload ratio is small this branch is hardly distinguishable from the upper solution branch, Fig. 12(*c*). As a result, it was practically impossible to get the numerical simulation results to go to the upper branch. When the excitation was moderate, 12(*b*), the middle branch was more evenly spaced between the upper and lower solutions and it was relatively easy to numerically generate either solution. Lastly, when the excitation/preload ratio was high the middle branch of the solution was much closer to the lower branch and it was very difficult to numerically generate solutions corresponding to the lower branch.

Conclusions

Spin-pit tests on some turbo-pump stages with integrally shrouded blades exhibited unusually severe mistuning that was characterized by blades having high amplitudes of response over a very broad range of low frequencies and by many of the response curves having flattened peaks. The

Downloaded 02 Jun 2010 to 171.66.16.102. Redistribution subject to ASME license or copyright; see http://www.asme.org/terms/Terms_Use.cfm

tests indicated that the cause of the unusual response was shroud contact. Shroud contact by itself would tend to provide additional constraints on the blade that would raise its frequency of peak response. In this paper it has been hypothesized that the moment exerted by the shroud contact causes one side of the blade attachment to partially lose contact with the disk and reduce the effective stiffness of the attachment. A simple model of a blade with a preloaded shroud and with a reduced attachment constraint was developed and analyzed numerically. The simple model exhibited vibratory response, which was similar to the spin-pit data.

The numerical results seemed to indicate that under certain conditions there were multiple long time solutions (depending on the initial conditions). An approximate analytical solution was developed using the harmonic balance (HB) method and it was found that the HB solutions were, in fact, multivalued. The long time numerical solutions correlated reasonably well with the HB solutions.

From these results it is concluded that it is likely that the unusual vibratory response of the blades in the spin-pit test was caused by the mechanisms that were modeled, i.e., a statically preloaded shroud, a loss of constraint in the attachment, and shroud lift-off because of vibration. An interesting result that could be observed from the response of the model problem is that when the static preload was increased the peak vibratory response increased. Consequently, preloaded shrouds should be avoided, especially since the amount of preload depends on machining variations, which are very difficult to control.

Alternatively, if the shrouds are not preloaded and gaps exist then the gaps can be an effective means of reducing the vibratory response [4]. While we have limited information, the authors would make the following speculations on the advisability of small gaps. From the point of view of vibratory response, having a design that has very small nominal gaps between the shrouds may be a good or bad idea depending on the blade's design. If the blade is short and stiff (as in the case of the turbo-pump blade) then the shroud of the blade is more likely to lean against its neighbor since small misalignments in the attachment strongly affect the position of the shroud at the blade's tip. This condition should be avoided. However, if the blade is long and flexible (as in the case of stream turbines) then, even if the attachment is misaligned, the centrifugal forces will tend to cause the blades to straighten. Consequently, the shrouds should have open gaps that if properly designed may reduce the peak vibratory response.

Acknowledgments

This work was supported by NASA Contract NAS8-38348 under the direction of Mr. L. Kiefling of NASA Marshall Space Flight Center.

References

1 Griffin, J. H., and Hoosac, T. M., "Model Development and Statistical Investigation of Turbine Blade Mistuning," ASME *Journal of Vibration, Acoustics, Stress, and Reliability in Design*, Vol. 106, 1984, pp. 204–210.

2 Whitehead, D. S., "Effect of Mistuning on the Vibrations of Turbomachine Blades Induced by Wakes," *Journal of Mechanical Science*, Vol. 8, No. 1, 1966, pp. 15–21.

3 Ewins, D. J., "Vibration Modes of Mistuned Bladed Disks," ASME JOURNAL OF ENGINEERING FOR POWER, 1976, pp. 349–355.

4 Wagner, L. F., and Griffin, J. H., "Blade Vibration With Nonlinear Tip Constraint: Model Development," ASME *Journal of Turbomachinery*, Vol. 112, No. 4, 1990, pp. 778–785.

5 Watanabe, T., "Forced Vibration of Nonlinear System With Symmetrical Piecewise-Linear Characteristics," *Bulletin of JSME*, Vol. 27, No. 229, 1984, pp. 1493–1498.

6 Nguyen, D. T., Noah, S. T., and Kettleborough, C. F., "Impact Behavior of an Oscillator With Limiting Stops, Part I: A Parametric Study," *Journal of Sound and Vibration*, Vol. 109, No. 2, 1986, pp. 293–307.

7 Meirovitch, L., *Analytical Methods in Vibration*, Macmillan, New York, 1967.

8 Rao, S. S., *Mechanical Vibrations*, 2nd ed., Addison-Wesley, New York, 1990, pp. 548–549.

9 Hughes, T. J. R., "A Note on the Stability of Newmark's Algorithm in Nonlinear Structural Dynamics," *International Journal for Numerical Methods in Engineering*, Vol. 11, 1976, pp. 383–387.

10 Brigham, E. O., *The Fast Fourier Transform*, Prentice-Hall, New Jersey, 1974.

11 Gelb, A., and Vander Velde, W. E., *Multiple-Input Describing Functions and Nonlinear System Design*, McGraw-Hill, New York, 1968.

12 Dowell, E. H., "Component Mode Analysis of a Simple Non-linear, Non-conservative System," *Journal of Sound and Vibration*, Vol. 80, 1982, pp. 233–246.

13 Cameron, T. M., and Griffin, J. H., "An Alternating Frequency/Time Domain Method for Calculating the Steady-State Response of Nonlinear Dynamic Systems," *Journal of Applied Mechanics*, Vol. 56(1), 1989, pp. 149–154.

APPENDIX A

By neglecting the shear force and the rotary inertia, the equation of motion for the proposed model is [7],

$$\rho A\frac{\partial^2 y}{\partial t^2} - \frac{\partial}{\partial x}\left(P_a(x)\frac{\partial y}{\partial x}\right) + \frac{\partial^2}{\partial x^2}\left(EI\frac{\partial^2 y}{\partial x^2}\right) = P_e(x,t) - P(y(x_n,t))\,\delta(x-x_n) \quad \text{(A.1)}$$

with boundary conditions

$$y(0,t) = 0 \quad \text{(A.2)}$$

$$EI\frac{\partial^2 v(0,t)}{\partial x^2} = K_r\frac{\partial y(0,t)}{\partial x} \quad \text{(A.3)}$$

$$EI\frac{\partial^2 y(L,t)}{\partial x^2} = 0 \quad \text{(A.4)}$$

$$\frac{\partial}{\partial x}\left(EI\frac{\partial^2 y(L,t)}{\partial x^2}\right) - P_a(L)\frac{\partial y(L,t)}{\partial x} = 0 \quad \text{(A.5)}$$

where $y(x, t)$ denotes the transverse displacement, ρ is the density, A is the cross-sectional area, E is the Young's modulus, I is the moment of inertia, and K_r is the effective stiffness of the root constraint. $P_a(x)$ is the axial force, $P_e(x, t)$ is the external excitation, $P(y(x_n, t))$ is the nonlinear restoring force due to shroud contact, and x_n is the location where shrouds come into contact. The mathematical representations for $P_a(x)$ and $P(y(x_n, t))$ are

$$P_a(x) = \int_x^L \rho A(R+r)\Omega^2 dr = \frac{1}{2}\rho A\Omega^2(2R+L+x)(L-x) \quad \text{(A.6)}$$

$$P(y(x_n,t)) = \begin{pmatrix} K_n(y(x_n,t)-d) & \text{for } y(x_n,t) > d \\ 0 & \text{for } y(x_n,t) < d \end{pmatrix} \quad \text{(A.7)}$$

with Ω denoting the rotational speed of the turbine disk, R the radius of the turbine disk, L the length of the beam, K_n the stiffness of the nonlinear constraint, and d, the gap size.

The nondimensionalized equation of motion can be achieved by letting

$$\xi = \frac{x}{L} \quad \text{(A.8)}$$

$$\tau = \Omega_0 t \quad \text{(A.9)}$$

$$\eta = \frac{y}{|d|} \quad \text{(A.10)}$$

Downloaded 02 Jun 2010 to 171.66.16.102. Redistribution subject to ASME license or copyright; see http://www.asme.org/terms/Terms_Use.cfm

where Ω_0 is the reference frequency, which was chosen as the fundamental frequency of the beam with its root clamped, i.e.,

$$\Omega_0 = \alpha_0^2 \sqrt{\frac{EI}{\rho A L^4}} \tag{A.11}$$

and α_0 is approximately equal to 1.875.

It was further assumed that ρ, A, E, and I are constant and the external excitation is uniformly distributed along the x direction, i.e.,

$$P_e(x, t) = F_e \cos(\Omega_e t) \tag{A.12}$$

where Ω_e is the excitation frequency, which is 12 times the rotational speed, Ω, in our case. The nondimensionalized equation of motion (1) is thus obtained via some simple algebra by manipulating the previously listed equations.

In Eqs. (1), $f_a(\xi)$ denotes the nondimensionalized axial force which is, with $\gamma = \Omega/\Omega_0$,

$$f_a(\xi) = \frac{P_a}{\rho A \Omega_0^2 L^2} = \frac{\gamma^2}{2}\left(\frac{2R}{L} + 1 + \xi\right)(1 - \xi) \tag{A.13}$$

$f_e(\xi, \tau)$ denotes the nondimensionalized external excitation which is

$$f_e(\xi, \tau) = \frac{P_e}{\rho A \Omega_0^2 |d|} = p_e \cos(\gamma_e \tau) \tag{A.14}$$

where

$$p_e = \frac{F_e}{\rho A \Omega_0^2 |d|}$$

and $\gamma_e = \Omega_e/\Omega_0$. Finally, $f(\eta(\xi_n, \tau))$ denotes the nondimensionalized nonlinear force, which is

$$f(\eta(\xi_n, \tau)) = \frac{p}{\rho A \Omega_0^2 L |d|} \tag{A.15}$$

and is also described in Eq. (2) where the stiffness of the nonlinear constraint, κ_n, is given by

$$\kappa_n = \frac{K_n}{\rho A L \Omega_0^2} \tag{A.16}$$

In Eq. (5), κ_r denotes the stiffness of the root constraint, which is

$$\kappa_r = \frac{K_r L}{EI} \tag{A.17}$$

APPENDIX B

Expressions for functions $F_1(\theta^*)$ an $F_0(\theta^*)$ are

$$F_1(\theta^*) = \sqrt{\frac{\Sigma_{\kappa e}^2 + \Sigma_{\zeta e}^2}{\kappa_n^2\left(\Sigma_\kappa^2 + \Sigma_\zeta^2\right) z^2(\theta^*) + 2\kappa_n \Sigma_\kappa z(\theta^*) + 1}} \tag{B.1}$$

$$F_0(\theta^*) = -\kappa_n \Sigma_0 F_1(\theta^*) z_0(\theta^*) \tag{B.2}$$

where

$$\Sigma_{\kappa e} = \sum_i \frac{\left(\gamma_i^2 - \gamma_e^2\right)\{\mathbf{b_n}\}_i \{\mathbf{f_e}\}_i}{m_i\left(\left(\gamma_i^2 - \gamma_e^2\right)^2 + (2\zeta_i \gamma_i \gamma_e)^2\right)} \tag{B.3}$$

$$\Sigma_{\zeta e} = \sum_i \frac{(2\zeta_i \gamma_i \gamma_e)\{\mathbf{b_n}\}_i \{\mathbf{f_e}\}_i}{m_i\left(\left(\gamma_i^2 - \gamma_e^2\right)^2 + (2\zeta_i \gamma_i \gamma_e)^2\right)} \tag{B.4}$$

$$\Sigma_\kappa = \sum_i \frac{\left(\gamma_i^2 - \gamma_e^2\right)\{\mathbf{b_1}\}_i}{m_i\left(\left(\gamma_i^2 - \gamma_e^2\right)^2 + (2\zeta_i \gamma_i \gamma_e)^2\right)} \tag{B.5}$$

$$\Sigma_\zeta = \sum_i \frac{(2\zeta_i \gamma_i \gamma_e)\{\mathbf{b_n}\}_i}{m_i\left(\left(\gamma_i^2 - \gamma_e^2\right)^2 + (2\zeta_i \gamma_i \gamma_e)^2\right)} \tag{B.6}$$

$$\Sigma_0 = \sum_i \frac{\{\mathbf{b_n}\}_i^2}{m_i \gamma_i^2} \tag{B.7}$$

with m_i, γ_i, and ζ_i being the modal mass, the natural frequency, and the modal damping of the ith mode, respectively. The expressions for $\{\mathbf{f_e}\}_i$, $\{\mathbf{b_n}\}_i$, $z_0(\theta^*)$, and $z(\theta^*)$ are given by Eqs. (11), (12), (22), and (23), respectively.

Downloaded 02 Jun 2010 to 171.66.16.102. Redistribution subject to ASME license or copyright; see http://www.asme.org/terms/Terms_Use.cfm

Eigenvector Derivatives of Generalized Nondefective Eigenproblems With Repeated Eigenvalues

Y.-Q. Zhang

W.-L. Wang

Department of Applied Mechanics,
Fudan University,
Shanghai, People's Republic of China

A new method is presented for computation of eigenvalue and eigenvector derivatives associated with repeated eigenvalues of the generalized nondefective eigenproblem. This approach is an extension of recent work by Dailey and by Juang et al. and is applicable to symmetric or nonsymmetric systems. The extended phases read as follows. The differentiable eigenvectors and their derivatives associated with repeated eigenvalues are determined for a generalized eigenproblem, requiring the knowledge of only those eigenvectors to be differentiated. Moreover, formulations for computing eigenvector derivatives have been presented covering the case where multigroups of repeated first eigenvalue derivatives occur. Numerical examples are given to demonstrate the effectiveness of the proposed method.

Introduction

Eigenvector derivatives are very useful in many fields of structural dynamics, such as system identification, structural control, and optimization. Calculation methods for eigenvector derivatives associated with distinct eigenvalues have been developed by many researchers (Fox and Kapoor, 1968; Rogers, 1970; Rudisill and Chu, 1975; Nelson, 1976). The increased effectiveness of these methods has made it possible to calculate the sensitivity of eigendata to changes in system parameters.

The computation problem of eigenvalue and eigenvector derivatives associated with repeated eigenvalues is much more complicated and difficult due to the nonuniqueness of the eigenvectors. Mills-Curran (1988) and Lim et al. (1989) have presented two algorithms for computing the eigenvector derivatives with distinct eigenvalue derivatives. Wei (1992) proposed another method using generalized inverse, but a complete solution has not been presented. Juang et al. (1989) developed a novel approach to investigate the existence of differentiable eigenvectors for a nondefective matrix that may have repeated eigenvalues and provided the formulations for computation of the eigenvector derivatives of the standard eigenproblem using the modal expansion technique, which, therefore, requires the complete solution of the eigenproblem. However, the formulations for calculating the eigenvector derivatives for the case in which repeated first eigenvalue derivatives occur are incomplete since the eigenvector derivatives associated with the rest of the distinct eigenvalue derivatives have not been shown.

On the other hand, Dailey (1989) improved Ojalvo's method (1986) and provided a powerful method for analyzing and computing the eigenvector derivatives of generalized eigenvalue problems with symmetric matrices. Unfortunately, this method is partially incorrect. In the paper, Dailey stated that the eigenvector derivatives are not unique when repeated eigenvalue derivatives occur and that "this provides a free parameter to set arbitrarily." He further suggested that "the simplest choice is to set $c_{ij} = c_{ji} = 0.5q_{ij}$ whenever $\lambda_i^l = \lambda_j^l$." This is generally incorrect, except for the special case in which any higher eigenvalue derivatives are repeated, or in mechanical terminology as pointed out by Dailey (1989) "the parameter p affects the degenerate modes equally or not at all." In practice, however, it is also possible that one of the higher, but finite, derivatives of the eigenvalues becomes distinct when the first eigenvalue derivatives are repeated. It will be demonstrated in this paper that in this case the eigenvector derivatives are still unique.

A novel algorithm is provided in this paper for computing the derivatives of eigenvalues and eigenvectors for nondefective generalized eigenvalue problems with repeated eigenvalues. This algorithm requires the knowledge of only those eigenvectors that are to be differentiated. In this paper a new method is developed for calculating the particular solutions of the eigenvector derivatives based on the theory of linear algebraic equations, which leads to considerable mathematical simplification. Moreover, complete formulations are provided for computation of the eigenvalue and eigenvector derivatives for the case where different repeated first eigenvalue derivatives occur. The general formulations for higher

Contributed by the International Gas Turbine Institute and presented at the 38th International Gas Turbine and Aeroengine Congress and Exposition, Cincinnati, Ohio, May 24–27, 1993. Manuscript received at ASME Headquarters March 17, 1993. Paper No. 93-GT-340. Associate Technical Editor: H. Lukas.

Copyright © 1995 by ASME

Downloaded 02 Jun 2010 to 171.66.16.102. Redistribution subject to ASME license or copyright; see http://www.asme.org/terms/Terms_Use.cfm

derivatives of the eigenvectors are also provided, which makes it possible to deal with the case where more complicated patterns of eigenvalue derivatives occur.

Expression of the Problem

Consider the right and left nondefective eigenvalue problems for a structure with N degrees of freedom

$$\mathbf{K}(p)\mathbf{\Phi}_\mathbf{R}(p) = \mathbf{M}(p)\mathbf{\Phi}_\mathbf{R}(p)\Omega(p) \tag{1}$$

$$\mathbf{K}^T(p)\mathbf{\Phi}_\mathbf{L}(p) = \mathbf{M}^T(p)\mathbf{\Phi}_\mathbf{L}(p)\Omega(p) \tag{2}$$

with biorthonormalization relation

$$\mathbf{\Phi}_\mathbf{L}^\mathrm{T}(p)\mathbf{M}(p)\mathbf{\Phi}_\mathbf{R}(p) = \mathbf{I}_\mathbf{N} \tag{3}$$

where $\mathbf{K}(p)$ and $\mathbf{M}(p)$ are the stiffness and mass matrices, respectively, whose elements are analytic functions of the real scalar parameter p in a neighborhood of p_0. As is usually the case in structural dynamics, it is assumed that $\mathbf{M}(p)$ is symmetric and nonsingular. It may be noticed that on the nonsingularity assumption of the mass matrix the eigenproblems of Eqs. (1) and (2) can be transformed into the standard eigenvalue problems studied by Juang et al. (1989). However, calculations of the inverse of $\mathbf{M}(p)$ and the derivatives, especially higher derivatives, of $\mathbf{K}(p)\mathbf{M}(p)^{-1}$ are not easy tasks. Hence, it is considered to be convenient to develop computational methods for the eigenvector derivatives of generalized eigenvalue problems.

The right and left eigenvector matrices in Eqs. (1)–(3) are designated as

$$\mathbf{\Phi}_\mathbf{R}(p) = [\mathbf{Z}_\mathbf{R}(p)\ \mathbf{Y}_\mathbf{R}(p)] \qquad \mathbf{\Phi}_\mathbf{L}(p) = [\mathbf{Z}_\mathbf{L}(p)\ \mathbf{Y}_\mathbf{L}(p)]$$

and the eigenvalue matrix is defined as

$$\Omega(p) = \mathrm{diag}(\Lambda(p)\ \Delta(p))$$

It is further assumed that

$$\mathbf{K}(p) \to \mathbf{K}_0, \quad \mathbf{M}(p) \to \mathbf{M}_\mathbf{0}, \quad \Omega(p) \to \Omega_0 = \mathrm{diag}(\Lambda\ \Delta)$$
$$\mathbf{\Phi}_\mathbf{R}(p) \to \mathbf{\Phi}_\mathbf{R} = [\mathbf{Z}_\mathbf{R}\ \mathbf{Y}_\mathbf{R}],\ \mathbf{\Phi}_\mathbf{L}(p) \to \mathbf{\Phi}_\mathbf{L} = [\mathbf{Z}_\mathbf{L}\ \mathbf{Y}_\mathbf{L}]$$
$$\mathbf{K}^{(i)}(p) \to \mathbf{K}^{(i)}, \quad \mathbf{M}^{(i)}(p) \to \mathbf{M}^{(i)}$$
$$\mathbf{Z}_\mathbf{R}^{(i)}(p) \to \mathbf{Z}_\mathbf{R}^{(i)}, \quad \Lambda_R^{(i)}(p) \to \Lambda_R^{(i)}, \quad i = 1, 2, \cdots, \tag{4}$$

as $p \to p_0$. The superscript (i) here, and throughout the paper, represents the ith-order derivative with respect to parameter p.

In these formulations, $\mathbf{Z}_\mathbf{L}(p)$, $\mathbf{Z}_\mathbf{R}(p)$, and $\Lambda(p)$ are the solutions of the following right and left eigenvalue problems:

$$\mathbf{K}(p)\mathbf{Z}_\mathbf{R}(p) = \mathbf{M}(p)\mathbf{Z}_\mathbf{R}(p)\Lambda(p) \tag{5}$$

$$\mathbf{K}^T(p)\mathbf{Z}_\mathbf{L}(p) = \mathbf{M}(p)\mathbf{Z}_\mathbf{L}(p)\Lambda(p) \tag{6}$$

$$\mathbf{Z}_\mathbf{L}^\mathrm{T}(p)\mathbf{M}(p)\mathbf{Z}_\mathbf{R}(p) = \mathbf{I}_\mathbf{n} \tag{7}$$

which have an eigenvalue λ_0 at $p = p_0$ with multiplicity n, i.e., $\Lambda = \lambda_0\mathbf{I}_\mathbf{n}$. Here $\mathbf{I}_\mathbf{n}$ is an n by n identity matrix.

Note that since the eigenvectors for a repeated eigenvalue are not unique, it is not known whether the eigenvector solutions associated with λ_0, denoted as $\mathbf{X}_\mathbf{L}$ and $\mathbf{X}_\mathbf{R}$, which also satisfy

$$(\mathbf{K}_\mathbf{0} - \lambda_0\mathbf{M}_\mathbf{0})\mathbf{X}_\mathbf{R} = 0, \tag{8}$$

$$(\mathbf{K}_\mathbf{0} - \lambda_0\mathbf{M}_\mathbf{0})^T\mathbf{X}_\mathbf{L} = 0 \tag{9}$$

$$\mathbf{X}_\mathbf{L}^T\mathbf{M}_\mathbf{0}\mathbf{X}_\mathbf{R} = \mathbf{I}_\mathbf{n} \tag{10}$$

are continuous and differentiable. More generally they are not. However, since the column vectors of $\mathbf{X}_\mathbf{L}$ and $\mathbf{X}_\mathbf{R}$, respectively, span a left eigenspace and a right eigenspace for the eigenvalue λ_0, the differentiable eigenvectors can be expressed as

$$\mathbf{Z}_\mathbf{R} = \mathbf{X}_\mathbf{R}\alpha_\mathbf{R} \qquad \mathbf{Z}_\mathbf{L} = \mathbf{X}_\mathbf{L}\alpha_\mathbf{L} \tag{11}$$

Hence, it is of primary importance to find out the particular coefficient matrices $\alpha_\mathbf{R}$ and $\alpha_\mathbf{L}$ for determination of the differentiable eigenvectors and to verify the uniqueness of the column vectors in $\mathbf{Z}_\mathbf{R}$ and $\mathbf{Z}_\mathbf{L}$ that are independent on the choice of the eigenvectors of Eqs. (8)–(10).

Eigenvector Derivatives

Taking the partial derivatives of Eq. (5) with respect to parameter p and let $p \to p_0$, we obtain

$$\bar{\mathbf{K}}\mathbf{Z}_\mathbf{R}^{(\mathbf{i})} = \mathbf{F}_\mathbf{i}, \tag{12}$$

where

$$\bar{\mathbf{K}} = \mathbf{K}_\mathbf{0} - \lambda_0\mathbf{M}_\mathbf{0}, \quad \bar{\mathbf{K}}^{(i)} = \mathbf{K}^{(i)} - \lambda_0\mathbf{M}^{(i)} \tag{13}$$

$$\mathbf{F}_\mathbf{i} = \sum_{k=1}^{i} C_i^k \left[\sum_{j=1}^{k} C_k^j \mathbf{M}^{(k-j)}\mathbf{Z}_\mathbf{R}^{(i-k)}\Lambda^{(j)} - \bar{\mathbf{K}}^{(k)}\mathbf{Z}_\mathbf{R}^{(i-k)} \right] \tag{14}$$

$$C_i^k = \frac{i!}{k!(i-k)!} \tag{15}$$

It can be proved (see the appendix) that Eq. (12) is solvable if and only if

$$\mathbf{Z}_\mathbf{L}^T\mathbf{F}_\mathbf{i} = 0 \tag{16}$$

Substitution of Eq. (14) into Eq. (16) yields

$$\Lambda^{(i)} = -\mathbf{Z}^T\mathbf{g}_\mathbf{i}, \qquad i = 1, 2, 3, \cdots \tag{17}$$

where

$$\mathbf{g}_\mathbf{i} = \mathbf{F}_\mathbf{i} - \mathbf{M}_\mathbf{0}\mathbf{Z}_\mathbf{R}\Lambda^{(i)} \tag{18}$$

is called the ith-order source excitation. Premultiplying Eq. (17) by $\mathbf{M}_\mathbf{0}\mathbf{Z}_\mathbf{R}$ and substituting the resulting equation into Eq. (18) gives

$$\mathbf{F}_\mathbf{i} = (\mathbf{I} - \mathbf{M}_\mathbf{0}\mathbf{Z}_\mathbf{R}\mathbf{Z}_\mathbf{L}^T)\mathbf{g}_\mathbf{i} \equiv \mathbf{P}_\mathbf{R}\mathbf{g}_\mathbf{i}, \quad i = 1, 2, \cdots \tag{19}$$

where $\mathbf{P}_\mathbf{R}$, referred to as the right projection matrix (Craig, 1981), is invariant to the choice of the eigenvectors of Eqs. (8) and (9), that is,

$$\mathbf{P}_\mathbf{R} = \mathbf{I} - \mathbf{M}_\mathbf{0}\mathbf{Z}_\mathbf{R}\mathbf{Z}_\mathbf{L}^T = \mathbf{I} - \mathbf{M}_\mathbf{0}\mathbf{X}_\mathbf{R}\mathbf{X}_\mathbf{L}^T \tag{20}$$

Hence, a combination of Eqs. (12) and (19) results in

$$\bar{\mathbf{K}}\mathbf{Z}_\mathbf{R}^{(\mathbf{i})} = \mathbf{P}_\mathbf{R}\mathbf{g}_\mathbf{i}, \qquad i = 1, 2, \cdots \tag{21}$$

For convenience, we employ a frequency-shifted system, whose stiffness and mass matrices are $\bar{\mathbf{K}} = \mathbf{K}_\mathbf{0} - \lambda_0\mathbf{M}_\mathbf{0}$ and $\mathbf{M}_\mathbf{0}$. Then the shifted eigenvalues problems are

$$\bar{\mathbf{K}}\mathbf{\Phi}_\mathbf{R} = \mathbf{M}_\mathbf{0}\mathbf{\Phi}_\mathbf{R}\mathbf{\Xi}, \quad \bar{\mathbf{K}}^T\mathbf{\Phi}_\mathbf{L} = \mathbf{M}_\mathbf{0}\mathbf{\Phi}_\mathbf{L}\mathbf{\Xi} \tag{22}$$

$$\mathbf{\Phi}_\mathbf{L}^\mathrm{T}\bar{\mathbf{K}}\mathbf{\Phi}_\mathbf{R} = \mathbf{\Xi} \tag{22a}$$

The eigensolutions of this system can be written as

$$\mathbf{\Phi}_\mathbf{R} = [\mathbf{Z}_\mathbf{R}\ \mathbf{Y}_\mathbf{R}], \quad \mathbf{\Phi}_\mathbf{L} = [\mathbf{Z}_\mathbf{L}\ \mathbf{Y}_\mathbf{L}]$$
$$\mathbf{\Xi} = \mathrm{diag}(\mathbf{0}_{n\times n},\ \mathbf{\Delta} - \lambda_0\mathbf{I}_\mathbf{r}) \tag{23}$$

Here $r = N - n$, and is equal to the rank of $\bar{\mathbf{K}}$. It can be seen from Eq. (23) that the column vectors of matrix $\mathbf{Z}_\mathbf{R}$ become the zero frequency modes, or so-called *rigid body modes*, of the frequency-shifted system, and that the eigenspaces spanned by the column vectors of $\mathbf{Z}_\mathbf{R}$ and $\mathbf{Y}_\mathbf{R}$ are the nullspace, denoted as $N(\bar{\mathbf{K}})$, and the complementary space, denoted as $R(\bar{\mathbf{K}})$, of $\bar{\mathbf{K}}$.

Generally speaking, the eigenvector derivatives can be expressed as a linear combination of the complete set of the eigenvectors of the system

$$\mathbf{Z}_\mathbf{R}^{(\mathbf{i})} = [\mathbf{Z}_\mathbf{R}\ \mathbf{Y}_\mathbf{R}]\begin{pmatrix}\mathbf{s}_\mathbf{i}\\ \mathbf{q}_\mathbf{i}\end{pmatrix} \equiv \mathbf{W}_\mathbf{i} + \mathbf{Z}_\mathbf{R}\mathbf{s}_\mathbf{i}, \quad i = 1, 2, \cdots \tag{24}$$

where $\mathbf{s}_\mathbf{i}$ and $\mathbf{q}_\mathbf{i}$ are arbitrary coefficient matrices, and $\mathbf{W}_\mathbf{i}$, which is defined equal to $\mathbf{Y}_\mathbf{R}\mathbf{q}_\mathbf{i}$ represents the component of $\mathbf{Z}_\mathbf{R}^{(\mathbf{i})}$ in $R(\bar{\mathbf{K}})$. Such a representation of $\mathbf{W}_\mathbf{i}$ has been used by Juang et al. (1989) to determine the eigenvector derivatives.

Downloaded 02 Jun 2010 to 171.66.16.102. Redistribution subject to ASME license or copyright; see http://www.asme.org/terms/Terms_Use.cfm

Since for large structural systems usually only a truncated set of mode shapes are computed, it is more practical and reasonable to express $\mathbf{W}_i$ by $\mathbf{Z}_R$.

In mathematical terminology (Lancaster, 1985), the solution set of Eq. (21) has the form of $\mathbf{W}_i^* + N(\bar{\mathbf{K}})$, and the general solutions can be expressed as

$$\mathbf{Z}_R^{(i)} = \mathbf{W}_i^* + \mathbf{Z}_R \mathbf{c}_i \tag{25}$$

where $\mathbf{W}_i^*$ is a particular solution of Eq. (21) and $\mathbf{c}_i$ is any n by n matrix. Since rank $(\bar{\mathbf{K}}) = r$ for an eigenvalue λ_0 with multiplicity n, $\bar{\mathbf{K}}$ can then be reordered of the form

$$\mathbf{R}\bar{\mathbf{K}}\mathbf{Q} = \begin{pmatrix} \bar{\mathbf{K}}_{rr} & \bar{\mathbf{K}}_{rn} \\ \bar{\mathbf{K}}_{nr} & \bar{\mathbf{K}}_{nn} \end{pmatrix}$$

In this equation $\mathbf{R}$ and $\mathbf{Q}$ are the transition matrices, and $\bar{\mathbf{K}}_{rr}$ is a nonsingular submatrix of $\bar{\mathbf{K}}$ and should be selected to be well conditioned. By using this equation, $\mathbf{W}_i$ can be solved from Eq. (21)

$$\mathbf{W}_i^* = \mathbf{R}\begin{pmatrix} \bar{\mathbf{K}}_{rr}^{-1} & 0 \\ 0 & 0 \end{pmatrix}\mathbf{Q}\mathbf{P}_R\mathbf{g}_i \equiv \mathbf{G}\mathbf{P}_R\mathbf{g}_i \tag{26}$$

Observe that the particular solution determined by Eq. (26) depends on the choice of $\bar{\mathbf{K}}_{rr}$. Nevertheless, it is of great importance to note the fact that different selection of the particular solution of linear algebraic equations does not change the solution set. As a result, both Eqs. (24) and (25) are the formulations for the general solutions of Eq. (21). Hence, it is possible to determine the particular solution $\mathbf{W}_i$ in Eq. (24) through Eq. (25). In fact, such a solution can be obtained by imposing the biorthonormal condition

$$\mathbf{Z}_L^T\mathbf{M}_0(\mathbf{W}_i^* + \mathbf{Z}_R\mathbf{c}_i) = 0 \tag{27}$$

which will be satisfied if we choose

$$\mathbf{c}_i = -\mathbf{Z}_L^T\mathbf{M}_0\mathbf{W}_i^* \tag{27a}$$

In other words, if $\mathbf{c}_i$ is so chosen as in Eq. (27*a*), the solution given by Eq. (25) will be in $R(\bar{\mathbf{K}})$. It is clear that this solution is just the particular solution required in Eq. (24) since Eq. (27) has been used. Therefore, substituting Eq. (27*a*) into Eq. (25) yields

$$\mathbf{W}_i = \mathbf{P}_L^T\mathbf{W}_i^* = \mathbf{G}_e\mathbf{g}_i, \quad i = 1, 2, \cdots \tag{28}$$

where

$$\mathbf{G}_e \equiv \mathbf{P}_L^T\mathbf{G}\mathbf{P}_R \tag{28a}$$

$$\mathbf{P}_L = \mathbf{I} - \mathbf{M}_0\mathbf{Z}_L\mathbf{Z}_R^T = \mathbf{I} - \mathbf{M}_0\mathbf{X}_L\mathbf{X}_R^T \tag{28b}$$

The matrices $\mathbf{G}_e$ and $\mathbf{P}_L$ are referred to as the "elastic" flexibility matrix (Craig, 1981) and the left projection matrix. Note that although the matrix $\mathbf{G}$ given by Eq. (26) is arbitrary in the sense of its dependence on the choice of $\bar{\mathbf{K}}_{rr}$, it can be verified that the "elastic" flexibility matrix $\mathbf{G}_e$ is unique. Note also that the matrix $\mathbf{W}_i$ that is defined in Eq. (28) can be calculated by using only the eigenvectors of concern, without requiring the knowledge of any other eigenpairs of the structure.

On the other hand, it is not difficult to notice that substituting Eq. (22) into Eq. (21) will yield

$$\mathbf{G}_e = \mathbf{Y}_R(\mathbf{\Delta} - \lambda_0\mathbf{I}_r)^{-1}\mathbf{Y}_L^T \tag{29}$$

which indicates that $\mathbf{G}_e$ can also be calculated by $\mathbf{Y}_R$ and $\mathbf{Y}_L$, the "elastic" modes of the frequency-shifted system. As a matter of fact, it has been demonstrated (not shown in this paper) that substitution of Eq. (29) and unit mass matrix into the formulations in the next section for computing the eigenvalue and eigenvector derivatives will result in the same formulations as those given by Juang et al. (1989). However, calculation of $\mathbf{G}_e$ by Eq. (28) requires less computational time.

Formulations for Computation of Eigenvalue and Eigenvector Derivatives

From Eqs. (14), (17), and (18), we have

$$\Lambda^{(1)} = \mathbf{Z}_L^T\bar{\mathbf{K}}^{(1)}\mathbf{Z}_R \tag{30}$$

Since $\mathbf{Z}_L$ and $\mathbf{Z}_R$ are biorthonormalized such that $\alpha_L^T\alpha_R = \mathbf{I}$ and α_L is nonsingular, substitution of Eq. (11) into Eq. (30) yields

$$\mathbf{D}_1\alpha_R = \alpha_R\Lambda^{(1)} \tag{31}$$

where

$$\mathbf{D}_1 = \mathbf{X}_L^T\bar{\mathbf{K}}^{(1)}\mathbf{X}_R \tag{31a}$$

The first eigenvalue derivatives can be determined by eigenproblem Eq. (31). The formulations for calculation of $\mathbf{Z}_R^{(1)}$ will be discussed as follows.

Distinct Eigenvalue Derivatives. For distinct eigenvalue derivatives

$$\lambda_j^{(1)} \neq \lambda_k^{(1)} \quad j \neq k; \quad j, k = 1, 2, \cdots, n \tag{32}$$

The solution of Eq. (31) will give the unique eigenvector matrix α_R, which can further determine $\mathbf{Z}_R$ through Eq. (11). It can be proved that $\mathbf{Z}_R$ is also unique, independent of the choice of eigenvectors of Eqs. (8)–(10). Consequently, we obtain

$$\mathbf{Z}_L = \mathbf{X}_L\alpha_L = \mathbf{X}_L\alpha_R^{-T}$$

by using $\alpha_L^T\alpha_R = \mathbf{I}_n$. Thus, the component of $\mathbf{Z}_R^{(1)}$ in $R(\bar{\mathbf{K}})$ can be determined using Eqs. (28), (18) and (14)

$$\mathbf{W}_1 = -\mathbf{G}_e\bar{\mathbf{K}}^{(1)}\mathbf{Z}_R \tag{33}$$

To determine the coefficient matrix $\mathbf{s}_1$, the second derivatives of eigenvalues are used. Let $i = 2$ for Eqs. (14), (17), and (18), we get

$$\Lambda^{(2)} = -\mathbf{Z}_L^T\left[2\left(\mathbf{M}_0\mathbf{Z}_R^{(1)}\Lambda^{(1)} - \bar{\mathbf{K}}^{(1)}\mathbf{Z}_R^{(1)}\right) - \bar{\mathbf{K}}^{(2)}\mathbf{Z}_R + 2\mathbf{M}^{(1)}\mathbf{Z}_R\Lambda^{(1)}\right]$$

Substituting $\mathbf{Z}_R^{(1)} = \mathbf{W}_1 + \mathbf{Z}_R\mathbf{s}_1$ into this equation yields

$$\mathbf{s}_1\Lambda^{(1)} - \Lambda^{(1)}\mathbf{s}_1 + 0.5\Lambda^{(2)} = \mathbf{Z}_L^T\mathbf{J}\mathbf{Z}_R + \mathbf{L}_1\Lambda^{(1)} \equiv \mathbf{U}_1 = \left(u_1^{jk}\right) \tag{34a}$$

where

$$\mathbf{J} = 0.5\bar{\mathbf{K}}^{(2)} - \bar{\mathbf{K}}^{(1)}\mathbf{G}_e\bar{\mathbf{K}}^{(1)}, \quad \mathbf{L}_1 = -\mathbf{Z}_L^T\mathbf{M}^{(1)}\mathbf{Z}_R \tag{34b}$$

The scalar form of Eq. (34*a*) can be written as

$$\left(\lambda_j^{(1)} - \lambda_i^{(1)}\right)s_1^{ij} + 0.5\lambda_i^{(2)}\delta_{ij} = u_1^{ij} \tag{34c}$$

where the Kronecker delta is defined as

$$\delta_{ij} = \begin{cases} 1 & i = j, \\ 0 & \text{otherwise}. \end{cases}$$

Equation (34*c*) results in

$$\lambda_i^{(2)} = 2u_1^{ii} \tag{35a}$$

$$s_1^{ij} = \frac{u_1^{ij}}{\lambda_j^{(1)} - \lambda_i^{(1)}}, \quad i \neq j \tag{35b}$$

Thus, the off-diagonal elements of $\mathbf{s}_1$ have been determined in Eq. (35*b*). To determine further the diagonal elements of $\mathbf{s}_1$, the normalization constraint

$$\mathbf{Z}_{Ri}^T(p)\mathbf{M}(p)\mathbf{Z}_{Ri}(p) = 1 \tag{36}$$

is used. Taking a partial derivative of Eq. (36) with respect to parameter p and substituting $\mathbf{Z}_{Ri}^{(1)} = \mathbf{W}_1^i + \mathbf{Z}_R\mathbf{s}_1^i$ into the resulting equation gives

$$\mathbf{Z}_{Ri}^T\mathbf{M}_0\mathbf{Z}_R\mathbf{s}_1^i = -0.5\mathbf{Z}_{Ri}^T\mathbf{M}^{(1)}\mathbf{Z}_{Ri} - \mathbf{Z}_{Ri}^T\mathbf{M}_0\mathbf{W}_1^i \equiv b_{ii}$$

Here $\mathbf{s}_1^i$ and $\mathbf{W}_1^i$ indicate the ith column vector of $\mathbf{s}_1$ and $\mathbf{W}_1$,

Downloaded 02 Jun 2010 to 171.66.16.102. Redistribution subject to ASME license or copyright; see http://www.asme.org/terms/Terms_Use.cfm

respectively. Hence, the diagonal elements of $\mathbf{s}_1$ can be obtained

$$s_1^{ii} = b_{ii} - \sum_{j=1, j\neq i}^{n} \mathbf{Z}_{\mathbf{Ri}}^{\mathrm{T}} \mathbf{M}_0 \mathbf{Z}_{\mathbf{Rj}} s_1^{ji} \qquad i = 1, 2, \cdots, n \quad (37)$$

Note that for the eigenproblem with nonsymmetric stiffness matrix, $\mathbf{Z}_{\mathbf{Ri}}^{\mathrm{T}} \mathbf{M}_0 \mathbf{Z}_{\mathbf{Rj}} \neq 0$, $i \neq j$. Hence, the diagonal elements of $\mathbf{s}_1$ cannot be calculated before the off-diagonal elements are determined.

Repeated Eigenvalue Derivatives. In this section, we will consider the case in which repeated eigenvalue derivatives occur and are of the pattern

$$\Lambda^{(1)} = \mathrm{diag}\left(\Lambda_1^{(1)}, \Lambda_2^{(1)}, \cdots, \Lambda_h^{(1)}\right) \quad (38a)$$

where

$$\Lambda_k^{(1)} = \lambda_k^{(1)} \mathbf{I}_{\mathbf{m}_k}, \quad m_k \geq 1, \quad k = 1, 2, \cdots, h$$
$$\lambda_1^{(1)} < \lambda_2^{(1)} < \cdots < \lambda_h^{(1)} \quad (38b)$$

m_k ($k = 1, 2, \cdots, h$) is the multiplicity of the kth group of repeated first eigenvalue derivatives, and $\sum_{k=1}^{h} m_k = n$. The corresponding right and left eigenvectors of $\mathbf{D}_1$ are denoted as

$$\boldsymbol{\Gamma}_{\mathbf{R}} = [\boldsymbol{\gamma}_{\mathbf{R1}} \ \boldsymbol{\gamma}_{\mathbf{R2}} \ \cdots \ \boldsymbol{\gamma}_{\mathbf{Rh}}]$$
$$\boldsymbol{\Gamma}_{\mathbf{L}} = [\boldsymbol{\gamma}_{\mathbf{L1}} \ \boldsymbol{\gamma}_{\mathbf{L2}} \ \cdots \ \boldsymbol{\gamma}_{\mathbf{Lh}}]$$

where $\boldsymbol{\gamma}_{\mathbf{Rk}}$ and $\boldsymbol{\gamma}_{\mathbf{Lk}}$ represent the collections of the right and left eigenvectors associated with $\Lambda_k^{(1)}$ ($k = 1, 2, \cdots, h$). Due to the nonuniqueness of $\boldsymbol{\gamma}_{\mathbf{R}}$ and $\boldsymbol{\gamma}_{\mathbf{Lk}}$, for any matrices $\mathbf{a}_k$ and $\mathbf{b}_k$ ($k = 1, 2, \cdots, h$), $\boldsymbol{\gamma}_{\mathbf{Rk}}\mathbf{a}_k$ and $\boldsymbol{\gamma}_{\mathbf{Lk}}\mathbf{b}_k$ are also the right and left eigenvectors of $\mathbf{D}_1$. Hence, the differentiable eigenvectors cannot be identified yet. Clearly, only those $\mathbf{a}_k$'s and $\mathbf{b}_k$'s such that the eigenvectors of the initial system are differentiable at $p = p_0$ are of interest. Thus, Eq. (11) can be rewritten as

$$\mathbf{Z}_{\mathbf{R}} = [\mathbf{Z}_{\mathbf{R1}} \ \mathbf{Z}_{\mathbf{R2}} \ \cdots \ \mathbf{Z}_{\mathbf{Rh}}] \quad (39)$$

$$\mathbf{Z}_{\mathbf{L}} = [\mathbf{Z}_{\mathbf{L1}} \ \mathbf{Z}_{\mathbf{L2}} \ \cdots \ \mathbf{Z}_{\mathbf{Lh}}] \quad (40)$$

where

$$\mathbf{Z}_{\mathbf{Rk}} = \mathbf{X}_{\mathbf{R}} \boldsymbol{\gamma}_{\mathbf{Rk}} \mathbf{a}_k, \quad \mathbf{Z}_{\mathbf{Lk}} = \mathbf{X}_{\mathbf{L}} \boldsymbol{\gamma}_{\mathbf{Lk}} \mathbf{b}_k$$

Substituting Eqs. (39) and (40) into Eq. (34a) yields

$$\mathbf{B}_1 - \mathbf{B}_2 + 0.5\Lambda^{(2)} = \mathbf{U}_1 \quad (41)$$

where

$$\mathbf{B}_1 = \begin{pmatrix} \mathbf{s}_{11}\Lambda_1^{(1)} & \mathbf{s}_{12}\Lambda_2^{(1)} & \cdots & \mathbf{s}_{1h}\Lambda_h^{(1)} \\ \mathbf{s}_{21}\Lambda_1^{(1)} & \mathbf{s}_{22}\Lambda_2^{(1)} & \cdots & \mathbf{s}_{2h}\Lambda_h^{(1)} \\ \vdots & \vdots & \ddots & \vdots \\ \mathbf{s}_{h1}\Lambda_1^{(1)} & \mathbf{s}_{p2}\Lambda_2^{(1)} & \cdots & \mathbf{s}_{hh}\Lambda_h^{(1)} \end{pmatrix}$$

$$\mathbf{B}_2 = \begin{pmatrix} \Lambda_1^{(1)}\mathbf{s}_{11} & \Lambda_1^{(1)}\mathbf{s}_{12} & \cdots & \Lambda_1^{(1)}\mathbf{s}_{1h} \\ \Lambda_2^{(1)}\mathbf{s}_{21} & \Lambda_2^{(1)}\mathbf{s}_{22} & \cdots & \Lambda_2^{(1)}\mathbf{s}_{2h} \\ \vdots & \vdots & \ddots & \vdots \\ \Lambda_h^{(1)}\mathbf{s}_{h1} & \Lambda_h^{(1)}\mathbf{s}_{h2} & \cdots & \Lambda_h^{(1)}\mathbf{s}_{hh} \end{pmatrix}$$

$$\Lambda^{(2)} = \begin{pmatrix} \Lambda_1^{(2)} & & & \\ & \Lambda_2^{(2)} & & \\ & & \ddots & \\ & & & \Lambda_h^{(2)} \end{pmatrix}$$

$$\mathbf{U}_1 = \begin{pmatrix} \mathbf{u}_{11} & \mathbf{u}_{12} & \cdots & \mathbf{u}_{1h} \\ \mathbf{u}_{21} & \mathbf{u}_{22} & \cdots & \mathbf{u}_{2h} \\ \vdots & \vdots & \ddots & \vdots \\ \mathbf{u}_{h1} & \mathbf{u}_{h2} & \cdots & \mathbf{u}_{hh} \end{pmatrix}$$

In these equations

$$\mathbf{u}_{\mathbf{jk}} = \mathbf{Z}_{\mathbf{Lj}}^{\mathrm{T}}\left(\mathbf{J} - \lambda_k^{(1)}\mathbf{M}^{(1)}\right)\mathbf{Z}_{\mathbf{Rk}} \quad (42)$$

and $\mathbf{s}_{\mathbf{jk}}$ ($j, k = 1, 2, \cdots, h$) are the m_j and m_k submatrices of $\mathbf{s}_1$. Equation (41) can be rewritten in the submatrix form

$$\mathbf{s}_{\mathbf{kk}}\Lambda_{\mathbf{k}}^{(1)} - \Lambda_{\mathbf{k}}^{(1)}\mathbf{s}_{\mathbf{kk}} + 0.5\Lambda_{\mathbf{k}}^{(2)} = \mathbf{u}_{\mathbf{kk}} \quad (43)$$

$$\mathbf{s}_{\mathbf{jk}}\Lambda_{\mathbf{k}}^{(1)} - \Lambda_{\mathbf{j}}^{(1)}\mathbf{s}_{\mathbf{jk}} = \mathbf{u}_{\mathbf{jk}} \quad j \neq k \quad (44)$$

Noting that $\mathbf{s}_{\mathbf{kk}}\Lambda_{\mathbf{k}}^{(1)} = \Lambda_{\mathbf{k}}^{(1)}\mathbf{s}_{\mathbf{kk}}$, and that $\mathbf{b}_{\mathbf{k}}^{\mathbf{T}}\mathbf{a}_{\mathbf{k}} = \mathbf{I}$ and $\mathbf{b}_{\mathbf{k}}^{\mathrm{T}}$ is nonsingular, Eq. (43) can be rewritten as

$$\mathbf{D}_{2\mathbf{k}}\mathbf{a}_{\mathbf{k}} = \mathbf{a}_{\mathbf{k}}\Lambda_{\mathbf{k}}^{(2)} \quad k = 1, 2, \cdots, h \quad (45)$$

where

$$\mathbf{D}_{2\mathbf{k}} = 2\gamma_{Lk}^{T}\mathbf{X}_{\mathbf{L}}^{T}\left(\mathbf{J} - \lambda_k^{(1)}\mathbf{M}^{(1)}\right)\mathbf{X}_{\mathbf{R}}\gamma_{Rk} \quad (45a)$$

For the case in which all the eigenvalues of Eq. (45) are distinct, the corresponding eigenvectors of Eq. (45) are unique. Again, $\mathbf{Z}_{\mathbf{L}}$, $\mathbf{Z}_{\mathbf{R}}$, and $\mathbf{b}_{\mathbf{k}}$ can be obtained through a procedure similar to the case of distinct first eigenvalue derivatives. Also, it can be proved that the column vectors of $\mathbf{Z}_{\mathbf{L}}$ and $\mathbf{Z}_{\mathbf{R}}$ are unique.

Therefore, the off-diagonal blocks of $\mathbf{s}_1$ can be determined by Eq. (44):

$$\mathbf{s}_{\mathbf{jk}} = \frac{\mathbf{Z}_{\mathbf{Lj}}^{\mathrm{T}}\left(\mathbf{J} - \lambda_k^{(1)}\mathbf{M}^{(1)}\right)\mathbf{Z}_{\mathbf{Rk}}}{\lambda_k^{(1)} - \lambda_j^{(1)}} \quad j \neq k; \quad j, k = 1, 2, \cdots, h \quad (46)$$

It remains to determine the diagonal submatrices of $\mathbf{s}_1$. Clearly, the off-diagonal elements of the diagonal submatrices cannot be obtained by Eq. (43).

Now using Eq. (17) for $i = 3$ and combining terms yields

$$\left(\mathbf{s}_2\Lambda^{(1)} - \Lambda^{(1)}\mathbf{s}_2\right) + \frac{1}{3}\Lambda^{(3)} + \left(\mathbf{s}_1\Lambda^{(2)} - \Lambda^{(2)}\mathbf{s}_1\right)$$
$$= \mathbf{T} + 2\mathbf{L}_1\left(\mathbf{s}_1\Lambda^{(1)} - \Lambda^{(1)}\mathbf{s}_1\right) + 2\left(\mathbf{s}_1\Lambda^{(1)} - \Lambda^{(1)}\mathbf{s}_1\right)\mathbf{s}_1 \equiv \mathbf{U}_2 \quad (47)$$

where

$$\mathbf{T} = \mathbf{Z}_{\mathbf{L}}^{T}\Big[\overline{\mathbf{K}}^{(1)}\mathbf{W}_{22} + \overline{\mathbf{K}}^{(2)}\mathbf{W}_1 + \frac{1}{3}\overline{\mathbf{K}}^{(3)}\mathbf{Z}_{\mathbf{R}} - \left(2\mathbf{M}^{(1)}\mathbf{W}_1 + \mathbf{M}^{(2)}\mathbf{Z}_{\mathbf{R}}\right)\Lambda^{(1)}\Big] + \mathbf{L}_1\Lambda^{(2)}$$
$$\mathbf{W}_{22} = \mathbf{G}_{\mathbf{e}}\Big[2\left(\mathbf{M}^{(1)}\mathbf{Z}_{\mathbf{R}} + \mathbf{M}_0\mathbf{W}_1\right)\Lambda^{(1)} - \overline{\mathbf{K}}^{(2)}\mathbf{Z}_{\mathbf{R}} - 2\overline{\mathbf{K}}^{(1)}\mathbf{W}_1\Big] \quad (48)$$

$\mathbf{s}_2$ is the coefficient matrix of $\mathbf{Z}_{\mathbf{R}}^{(2)} = \mathbf{W}_2 + \mathbf{Z}_{\mathbf{R}}\mathbf{s}_2$. Partitioning Eq. (47), we get the diagonal submatrix equations. The only ones of interest here are:

$$\mathbf{s}_{\mathbf{kk}}\Lambda_{\mathbf{k}}^{(2)} - \Lambda_{\mathbf{k}}^{(2)}\mathbf{s}_{\mathbf{kk}} + \frac{1}{3}\Lambda_k^{(3)} = \mathbf{T}_{\mathbf{kk}}$$
$$+2\sum_{j=1, j\neq k}^{h}\left(\lambda_j^{(1)} - \lambda_k^{(1)}\right)\left(\mathbf{s}_{\mathbf{kj}} - \mathbf{L}_{\mathbf{1kj}}\right)\mathbf{s}_{\mathbf{jk}} \equiv \mathbf{U}_{2\mathbf{k}} = \left(u_{2k}^{ij}\right) \quad (49)$$

where $\mathbf{T}_{\mathbf{kk}}$ and $\mathbf{U}_{2\mathbf{k}}$ are, respectively, the kth diagonal blocks of $\mathbf{T}$ defined in Eq. (48) and $\mathbf{U}_2$ defined in Eq. (47). Equation (49) can be easily rewritten in the scalar form

$$\left(\lambda_{kj}^{(2)} - \lambda_{ki}^{(2)}\right)s_{kk}^{ij} + \frac{1}{3}\lambda_{ki}^{(3)}\delta_{ij} = u_{2k}^{ij} \quad (50)$$

which yields

Downloaded 02 Jun 2010 to 171.66.16.102. Redistribution subject to ASME license or copyright; see http://www.asme.org/terms/Terms_Use.cfm

$$\lambda_{ki}^{(3)} = 3u_{2k}^{ii} \tag{51}$$

$$s_{kk}^{ij} = \frac{u_{2k}^{ij}}{\lambda_{kj}^{(2)} - \lambda_{ki}^{(2)}} \quad j \neq i \tag{52}$$

Thus, all the off-diagonal elements of $\mathbf{s}_1$ have been determined; the diagonal ones can also be calculated using Eq. (37). It can be seen from Eqs. (46) to (52) and Eq. (37) that the coefficient matrix $\mathbf{s}_1$ is unique. As a result, the eigenvector derivatives are also unique, since $\mathbf{W}_1$ and $\mathbf{Z}_R$ are unique.

Summary of Computational Steps

The complete algorithm is summarized as follows:

1 Compute the eigenvalues and eigenvectors of the eigenproblem as $p = p_0$; determine the multiplicity of the repeated eigenvalues.

2 Calculate $\mathbf{G}_e$ using Eq. (28*a*).

3 Solve the eigenvalue problem, Eq. (31), to determine the first eigenvalue derivatives and the corresponding eigenvectors. If no repeated first eigenvalue derivatives occur, use Eq. (11) to determine the differentiable eigenvectors, and use Eq. (33) to determine $\mathbf{W}_1$. Then, calculate the coefficient matrix $\mathbf{s}_1$ by Eqs. (34), (35), and (37).

4 If repeated first eigenvalue derivatives occur, solve the eigenvalue problem, Eq. (45), to obtain the second eigenvalue derivatives. Determine the differentiable eigenvectors for distinct second eigenvalue derivatives case. Then determine $\mathbf{W}_1$ by Eq. (33) and compute $\mathbf{s}_1$ using Eqs. (46) to (52).

For the case in which some eigenvalue derivatives of second order are still repeated, the complete set of unique differentiable eigenvectors cannot be identified yet. Thus, the eigenproblems associated with the eigenvalue derivatives of higher orders have to be solved until one of the higher derivatives of the repeated eigenvalues becomes distinct. This is not very difficult to do since the general forms of the higher derivatives of the eigenvalues and eigenvectors have been presented in this paper, as shown in Eqs. (12) to (21).

Numerical Examples

Example 1. To check the validity of the present method, the three-order problem used by Juang et al. (1989) is re-examined, but only the eigenvector derivatives associated with the repeated eigenvalues are calculated. The left and right eigenvectors of concern are

$$\mathbf{X}_L = \mathbf{X}_R = \begin{pmatrix} 0 & 0 \\ 1 & 0 \\ 0 & 1 \end{pmatrix}$$

Then, using Eq. (28) we get

$$\mathbf{G}_e = \begin{pmatrix} 1 & 0 & 0 \\ 0 & 0 & 0 \\ 0 & 0 & 0 \end{pmatrix}$$

Solving the eigenvalue problem of Eq. (31), we obtain

$$\mathbf{\Lambda}^{(1)} = \begin{pmatrix} 1 & \\ & 1 \end{pmatrix}, \qquad \mathbf{\Gamma}_L = \mathbf{\Gamma}_R = \begin{pmatrix} 1 & 0 \\ 0 & 1 \end{pmatrix}$$

Since the eigenvalue derivatives are also repeated and $h = 1$, the differentiable eigenvectors cannot be identified yet. Hence, we solve the eigenproblem of Eq. (45) to get

$$\mathbf{\Lambda}^{(2)} = \begin{pmatrix} -2 & \\ & 2 \end{pmatrix}, \qquad a_1 = b_1 = \begin{pmatrix} 1 & 0 \\ 0 & 1 \end{pmatrix}$$

The second derivatives of the repeated eigenvalues are distinct. Hence, the differentiable eigenvectors can be determined as

$$\mathbf{Z}_R = \mathbf{X}_R \mathbf{\Gamma}_R a_1 = \mathbf{X}_R, \qquad \mathbf{Z}_L = \mathbf{X}_L$$

Then, from Eq. (33) we have

$$\mathbf{W}_1 = \begin{pmatrix} 1 & 0 \\ 0 & 0 \\ 0 & 0 \end{pmatrix}$$

Since all the first eigenvalue derivatives are repeated, the off-diagonal elements of $\mathbf{s}_1$ are directly calculated by using Eqs. (48) to (52). Combining Eq. (37), we get

$$\mathbf{s}_1 = \begin{pmatrix} 0 & 1 \\ 2 & 0 \end{pmatrix}$$

Finally, the derivatives of the eigenvectors under consideration are

$$\mathbf{Z}_R^{(1)} = \begin{pmatrix} 1 & 0 \\ 0 & 1 \\ 2 & 0 \end{pmatrix}$$

which is the same as given by Juang et al. (1989).

Example 2. Assume there exists a five-order problem where

$$\mathbf{M} = \begin{pmatrix} 1 & & & & \\ & 1 & & & \\ & & 1 & & \\ & & & 1 & \\ & & & & 4 \end{pmatrix}$$

$$\mathbf{K}(p) = \begin{pmatrix} k_1 & 0 & 0 & 0 & -k_1 \\ (p-1)^3 & p^2 & 0 & 0 & -p^2 \\ 0 & 0 & k_2 & 0 & -k_2 \\ 0 & 0 & 0 & p & -p \\ -k_1 & -p^2 & -k_2 & -p & k_3 \end{pmatrix}$$

where

$$k_1 = \frac{1}{3}(1 + 2p^3) \qquad k_2 = 2p^2 - 2p + 1$$

$$k_3 = \frac{1}{3}(1 + 2p^3) + 3p^2 - p + 7$$

The eigenvector derivatives are required at $p = p_0 = 1$. First, solving the generalized eigenvalue problem for $p_0 = 1$ gives the eigenvalues 0.5, 1, 1, 1, 3 and the normalized left and right eigenvectors associated with the repeated eigenvalues

$$\mathbf{X}_L^T = \mathbf{X}_R^T = \frac{1}{2\sqrt{6}} \begin{pmatrix} 2\sqrt{3} & -2\sqrt{3} & 0 & 0 & 0 \\ 2 & 2 & -4 & 0 & 0 \\ \sqrt{2} & \sqrt{2} & \sqrt{2} & -3\sqrt{2} & 0 \end{pmatrix}$$

Hence, we obtained

$$\mathbf{G}_e = -\frac{1}{8} \begin{pmatrix} 3 & 3 & 3 & 3 & 2 \\ 3 & 3 & 3 & 3 & 2 \\ 3 & 3 & 3 & 3 & 2 \\ 3 & 3 & 3 & 3 & 2 \\ 2 & 2 & 2 & 2 & 0 \end{pmatrix}$$

Solving Eq. (31), we get

$$\mathbf{\Lambda}^{(1)} = \text{diag}(2, 2, 1.25), \qquad \mathbf{\Gamma}_L = \mathbf{\Gamma}_R = \mathbf{I}_3$$

Since repeated first eigenvalue derivatives occur, Eq. (45) is further solved, which gives

$$\mathbf{\Lambda}_1^{(2)} = \text{diag}(1.6, 4), \qquad \mathbf{\Lambda}_2^{(2)} = \frac{31}{48}$$

$$\mathbf{a}_1 = \begin{pmatrix} -\sqrt{3}/2 & 1/2 \\ 1/2 & \sqrt{3}/2 \end{pmatrix}, \qquad a_2 = 1$$

Thus, the differentiable eigenvectors can be identified

Downloaded 02 Jun 2010 to 171.66.16.102. Redistribution subject to ASME license or copyright; see http://www.asme.org/terms/Terms_Use.cfm

$$\mathbf{Z}_L^T = \mathbf{Z}_R^T = \frac{1}{2\sqrt{6}} \begin{pmatrix} -2 & 4 & -2 & 0 & 0 \\ 2\sqrt{3} & 0 & -2\sqrt{3} & 0 & 0 \\ \sqrt{2} & \sqrt{2} & \sqrt{2} & -3\sqrt{2} & 0 \end{pmatrix}$$

and the particular solution is

$$\mathbf{W}_1^T = \frac{\sqrt{3}}{16} \begin{pmatrix} 0 & 0 & 0 & 0 & 0 \\ 0 & 0 & 0 & 0 & 0 \\ 1 & 1 & 1 & 1 & 2 \end{pmatrix}$$

The coefficient matrix can be obtained as

$$\mathbf{s}_1 = \begin{pmatrix} 0.00000 & 0.57735 & 0.31427 \\ 0.28868 & 0.00000 & 0.00000 \\ -0.31427 & 0.00000 & 0.00000 \end{pmatrix}$$

The eigenvector derivatives are

$$\mathbf{Z}_R^{(1)} = \begin{pmatrix} 0.11340 & -.23570 & -.27665 \\ -.09072 & 0.47140 & 0.36485 \\ -.29485 & -.23570 & -.02005 \\ 0.27717 & 0.00000 & 0.10825 \\ 0.00000 & 0.00000 & 0.21651 \end{pmatrix}$$

Conclusions

This paper has developed a new method for computation of the derivatives of eigenvalue and eigenvector derivatives associated with repeated eigenvalues of the generalized nondefective eigenproblem. This method requires the knowledge of only those eigenvectors to be differentiated. A complete set of formulations has been presented covering the case where some groups of repeated first eigenvalue derivatives occur. In addition, the proposed approach can be extended to deal with general cases in which repeated eigenvalue derivatives of higher, but finite, orders than that discussed in this paper occur. Also, if required, this approach can be used to compute the higher derivatives of the eigenvectors associated with repeated eigenvalues, since the general forms of the higher derivatives of the eigenvalues and eigenvectors have been presented in this paper, as shown in Eqs. (12) to (21). Moreover, it is not difficult to verify that the algorithm presented by Juang et al. (1989) is just a special case of that presented in this paper, since the formulations presented by Juang et al. (1989) for computation of eigenvector derivatives can be easily obtained by substituting Eq. (29) into the formulations presented in this paper.

References

Craig, R. R., Jr., 1981, *Structural Dynamics*, Wiley, New York.

Dailey, R. L., 1989, "Eigenvector Derivatives With Repeated Eigenvalues," *AIAA Journal*, Vol. 27, pp. 486–491.

Fox, R. L., and Kapoor, M. P., 1968, "Rate of Change of Eigenvalues and Eigenvectors," *AIAA Journal*, Vol. 6, pp. 2426–2429.

Juang, J.-N., Ghaemmaghami, P., and Lim, K. B., 1989, "Eigenvalue and Eigenvector Derivatives of a Nondefective Matrix," *Journal of Guidance, Control, and Dynamics*, Vol. 12, pp.480–486.

Lancaster, P., 1985, *The Theory of Matrices*, Academic Press, Orlando, FL.

Lim, K. B., Juang, J.-N., and Ghaemmaghami, P., 1989, "Eigenvector Derivatives of Repeated Eigenvalues Using Singular Value Decompositions," *Journal of Guidance, Control, and Dynamics*, Vol. 12, pp. 282–283.

Mills-Curran, W. C., 1988, "Calculation of Eigenvector Derivatives for Structures With Repeated Eigenvalues," *AIAA Journal*, Vol. 26, pp. 867–871.

Nelson, R. B., 1976, "Simplified Calculations of Eigenvector Derivatives," *AIAA Journal*, Vol. 14, pp. 1201–1205.

Ojalvo, I. U., 1986, "Gradients for Large Structural Models With Repeated Frequencies," SAE Paper No. 86-1789.

Rogers, L. C., 1970, "Derivatives of Eigenvalues and Eigenvectors," *AIAA Journal*, Vol. 8, pp. 943–944.

Rudisill, C. S., and Chu, Y., 1975, "Numerical Methods for Evaluating the Derivatives of Eigenvalues and Eigenvectors," *AIAA Journal*, Vol. 13, pp. 834–837.

Wei, F.-S., 1992, "Eigen Sensitivity Analysis With Repeated Eigenvalues," *Proc. 10th International Modal Analysis Conference*, San Diego, CA, pp. 596–600.

APPENDIX

Observe that Eq. (12) is solvable if and only if

$$\text{rank}(\bar{\mathbf{K}} \ \mathbf{F}_i) = \text{rank}(\bar{\mathbf{K}}) \tag{A1}$$

Hence, Eq. (16) can be proved as follows:

Proof. Necessity. If Eq. (A1) holds, then $\mathbf{F}_i$ is a linear combination of the column vectors of $\bar{\mathbf{K}}$, i.e.,

$$\mathbf{F}_i = \bar{\mathbf{K}}\mathbf{B}$$

Premultiplying both sides of this equation by $\mathbf{Z}_L^T$ with the aid of Eq. (2) gives

$$\mathbf{Z}_L^T\mathbf{F}_i = \mathbf{Z}_L^T\bar{\mathbf{K}}\mathbf{B} = 0 \tag{A2}$$

Sufficiency. If $\mathbf{Z}_L^T\mathbf{F}_i = 0$, using $\mathbf{Z}_L^T\bar{\mathbf{K}} = 0$, we get $\mathbf{Z}_L^T\hat{\mathbf{K}} \equiv \mathbf{Z}_L^T[\bar{\mathbf{K}} \ \mathbf{F}_i] = 0$, or $\hat{\mathbf{K}}^T\mathbf{Z}_L = 0$, which means $\dim N(\hat{\mathbf{K}}) \geq n$. Hence

$$\text{rank}(\hat{\mathbf{K}}) = \text{rank}(\hat{\mathbf{K}}^T) = N - \dim N(\hat{\mathbf{K}}^T) \leq N - n = r \tag{A3}$$

On the other hand, it is clear that $\bar{\mathbf{K}} \subset \hat{K}$, which implies

$$\text{rank}(\hat{\mathbf{K}}) \geq r = \text{rank}(\bar{\mathbf{K}}) \tag{A4}$$

Therefore, a combination of Eqs. (A3) and (A4) leads to

$$\text{rank}(\hat{\mathbf{K}}) = r \tag{A5}$$

This completes the proof.

Downloaded 02 Jun 2010 to 171.66.16.102. Redistribution subject to ASME license or copyright; see http://www.asme.org/terms/Terms_Use.cfm

Blade Erosion in Automotive Gas Turbine Engine

M. Metwally

W. Tabakoff

A. Hamed

Department of Aerospace Engineering and Engineering Mechanics, University of Cincinnati, Cincinnati, OH 45221

In this work, a study has been conducted to predict blade erosion and surface deterioration of the free power turbine of an automotive gas turbine engine. The blade material erosion model is based on three-dimensional particle trajectory simulations in the three-dimensional turbine flow field. The particle rebound characteristics after surface impacts were determined from experimental measurements of restitution ratios for blade material samples in a particulate flow tunnel. The trajectories provide the spatial distribution of the particle impact parameters over the blade surfaces. A semi-empirical erosion model, derived from erosion tests of material samples at different particulate flow conditions, is used in the prediction of blade surface erosion based on the trajectory impact data. The results are presented for the three-dimensional particle trajectories through the turbine blade passages, the particle impact locations, blade surface erosion pattern, and the associated erosion parameters. These parameters include impact velocity, impact angle, and impact frequency. The data can be used for life prediction and performance deterioration of the automotive engine under investigation.

Introduction

In the late seventies, the U.S. Department of Energy (DOE) conducted a program to develop a gas-turbine-powered automotive engine that meets the Federal Emissions Standards with acceleration characteristics and fuel economy that are competitive with current conventionally powered vehicles. The Chrysler Corporation Sixth Generation Gas Turbine Engine has served both as a baseline reference and as a test bed for the DOE automotive gas turbine engine. Baseline vehicles are intermediate size four-door sedans modified to accept the baseline gas turbine engine. The sixth generation Chrysler turbine engine is a low pressure ratio, regenerative, free power turbine design. The automotive engine is described in detail by Angell and Golec (1976). The cold clear air performance of the baseline free power turbine was evaluated experimentally in 1978 at NASA Lewis Research Center. The results were reported by Kofskey and Nusbaum (1978).

In general, the automotive gas turbine engines operate in environments where the ingestion of solid particles is inevitable. Engine inlet filters and separators can remove a large percentage of the damaging particles, but significant amounts of small particles still pass through and enter the engine. The impingement of particles on the turbine blade surfaces can cause erosion damage leading to a permanent loss of engine performance and structural failure of the blades. Continued operation under particulate flow conditions adversely affects the performance of these engines as well as their lives and can be detrimental to their reliability. A study of the free power turbine blade erosion under particulate flow conditions can provide important information that is required in the evaluation of engine performance and life prediction.

This work was conducted to predict particle dynamics and surface blade erosion in the free-power turbine designed for 112 kW automotive gas turbine engines. The results present the 15 μm particle trajectories through the turbine blade passages, the blade erosion pattern, and spatial distribution of blade surface particle impact parameters. Data are presented for coated (rhodium platinum aluminide coating) and uncoated (MAR-M246 alloy) blade surfaces to demonstrate the coating effect on particle trajectories and resulting blade erosion.

Analysis

The equations governing the particle motion in the turbomachinery flow field written in cylindrical polar coordinates relative to a frame of reference fixed with respect to the rotating blade are:

$$\frac{d^2r_p}{d\tau^2} = F_r + r_p\left(\frac{d\theta_p}{d\tau} + \omega\right)^2 \tag{1}$$

$$r_p\frac{d^2\theta_p}{d\tau^2} = F_\theta - 2\frac{dr_p}{d\tau}\left(\frac{d\theta_p}{d\tau} + \omega\right)^2 \tag{2}$$

$$\frac{d^2z_p}{d\tau^2} = F_z \tag{3}$$

where r_p, θ_p, z_p define the particle location in cylindrical polar coordinates, and ω is the blade angular velocity. The

Contributed by the International Gas Turbine Institute and presented at the 37th International Gas Turbine and Aeroengine Congress and Exposition, Cologne, Germany, June 1–4, 1992. Manuscript received by the International Gas Turbine Institute February 21, 1992. Paper No. 92-GT-344. Associate Technical Editor: L. S. Langston.

Copyright © 1995 by ASME

Downloaded 02 Jun 2010 to 171.66.16.102. Redistribution subject to ASME license or copyright; see http://www.asme.org/terms/Terms_Use.cfm

centrifugal force and Coriolis acceleration are represented by the last term on the right-hand side of Eqs. (1) and (2). The first term on the right-hand side of Eqs. (1) through (3) represents the force of interaction between the two phases, per unit mass of particles.

Under the particulate flow conditions in turbomachines, the effects of the forces due to gravity and interparticle interactions are negligible, compared to those due to the aerodynamic and centrifugal forces. The force of interaction between the two phases is dominated by the drag due to the relative velocity between the solid particles and the gas flow. The force of interaction per unit mass of solid particles is given by

$$\bar{F} = \frac{3}{4}\frac{\rho}{\rho_p}\frac{C_D}{d}\left[\left(V_r - \frac{dr_p}{d\tau}\right)^2 + \left(V_\theta - r_p\frac{d\theta_p}{d\tau}\right)^2 + \left(V_z - \frac{dz_p}{d\tau}\right)^2\right]^{1/2}\left(\bar{V} - \bar{V}_p\right) \quad (4)$$

where $\bar{V}$ and $\bar{V}_p$ are the gas and particle velocities relative to the blade, V_r, V_θ, V_z, represent the relative gas velocity components in the radial, circumferential, and axial directions, respectively, and ρ, ρ_p are the gas and solid particle material densities, d the particle diameter, and C_D the particle drag coefficient. This coefficient is dependent on the Reynolds number, which is based on the relative velocity between the particle and the gas. The empirical relations used to fit the drag curve over a wide range of Reynolds numbers were discussed by Tabakoff and Hamed (1986).

Particle Trajectories. The particle trajectory calculations consist of the numerical integration of Eqs. (1)–(3) in the flow field, up to the point of blade, hub, or tip impact. The magnitude and direction of particle rebounding velocity after these impacts are dependent on the impacting conditions and the particle and surface materials. The particle rebounding conditions are determined from empirical correlations based on the experimental measurements of the particle impact and rebound velocities, V_1 and V_2 correspondingly, near the metal surface, using laser-Doppler velocimetry. The LDV measurements are obtained near the material samples set at various angles relative to the particle-laden flow in a special tunnel described by Tabakoff and Hamed (1982). The restitution ratios were found to be mainly dependent upon the impingement angle (Tabakoff and Malak, 1987) for a given particle–material combination.

The following empirical correlations were obtained for mean values of fly ash particles restitution parameters in terms of the impingement angle (Tabakoff et al., 1990b).

For MAR-M246 Alloy

$$e_T = \frac{V_{T2}}{V_{T1}} = 1.00 - 0.00832249\beta_1 - 8.09523 \times 10^{-5}\beta_1^2 + 1.78601 \times 10^{-6}\beta_1^2 \quad (5)$$

$$e_N = \frac{V_{N2}}{V_{N1}} = 1.00 + 0.00809841\beta_1 - 0.00122611\beta_1^2 + 2.30864 \times 10^{-5}\beta_1^3 - 1.2922 \times 10^{-7}\beta_1^4 \quad (6)$$

where V_T and V_N are the tangential and the normal velocity components, and β_1 are particle impingement angles.

For Rhodium Platinum Aluminide Coating (RT22B)

$$e_T = \frac{V_{T2}}{V_{T1}} = 1.0 - 0.0217\beta_1 + 4.0459 \times 10^{-4}\beta_1^2 - 1.882 \times 10^{-6}\beta_1^3 \quad (7)$$

Table 1

	MAR-M246 alloy	Rhodium platinum aluminide coating (RT22B)
$C1$	0.044678	0.0795
$C2$	0.986610^{-3}	0.0045×10^{-4}
$N1$	2.32	3.70
$N2$	1.15	1.5
$N3$	2.15	4.3
$N4$	2.94	3.73

$$e_N = \frac{V_{N2}}{V_{N1}} = 1.0 - 0.03624\beta_1 + 8.0027 \times 10^{-4}\beta_1^2 - 5.5885 \times 10^{-6}\beta_1^3 \quad (8)$$

In the case of rotor blade impacts, the velocities and angles of impact and rebound are considered relative to the rotating blade. The particle trajectory after each blade impact and the particle distribution over the blade row are influenced by the rebound correlations and the local turbine blade geometry as reported by Hussein and Tabakoff (1973). The blade airfoil, hub, and casing geometry must therefore be accurately represented in the trajectory analysis as it strongly influences the predicted particle dynamics.

Turbine Blade Passage Flow Fields. The large flow turning angles generally encountered in turbine blading produce large pitchwise as well as radial and axial flow field variations. The description of the three-dimensional flow field in the blade passage is required for accurate prediction of the particle trajectories. In the present study, the flow field in a blade passage is synthesized from a number of blade-to-blade stream surface solutions using Katsanis' code (1965). The pitchwise and streamwise variations in the flow properties are reflected in each flow field solution on a blade-to-blade stream surface. The influence of the hub and tip contours and the hub-to-tip variation in the blade shapes, on the other hand, are represented in the stream surface shapes and stream filament thickness, as determined from a midchannel hub-to-tip stream surface solution by Katsanis and McNally (1977). The computed three-dimensional flow field data at the grid points in the blade-to-blade stream surfaces are used to interpolate for the flow properties at each time step during the numerical integration of the particle equations of motion.

Blade Erosion Model. The erosion model consists of a semi-empirical equation (Tabakoff et al., 1984) in which the values of the constants are determined from the experimental measurements. Sample coupons from the blade materials, which are tested in the erosion tunnel under different conditions, are shown in Fig. 1.

$$\epsilon = C_1\left(\frac{V_1}{100}\right)^{N1}\sin^{N2}\beta_1\cos^{N3}\beta_1\left[1 - e_T^2\right] + C_2\left(\frac{V_1}{100}\right)^{N4}\sin^2\beta_1\left[1 - e_N^2\right] \quad (9)$$

In the equation above, the erosion mass parameter, ϵ, represents the ratio of the eroded mass of target material to the mass of impinging particles; V_1 and β_1 represent the impact velocity (m/s) and impact angle (deg) respectively, and e_T and e_N are the tangential and normal restitution ratios given by Eqs. (5) and (6) for M246 and by Eqs. (7) and (8) for RT22B.

The values of constants $C1$ and $C2$ and the exponents $N1$, $N2$, $N3$, and $N4$ are given in Table 1 for fly ash particles impacting samples of the blade materials under investigation (Tabakoff et al., 1990a).

Figure 1 gives a graphic presentation of the erosion char-

Downloaded 02 Jun 2010 to 171.66.16.102. Redistribution subject to ASME license or copyright; see http://www.asme.org/terms/Terms_Use.cfm

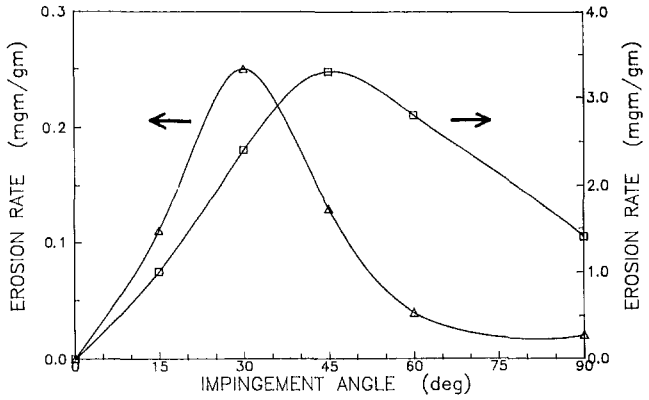

Fig. 1 Erosion rate variations with the impingement angles at V_1 = 366 m/s and T = 815°C

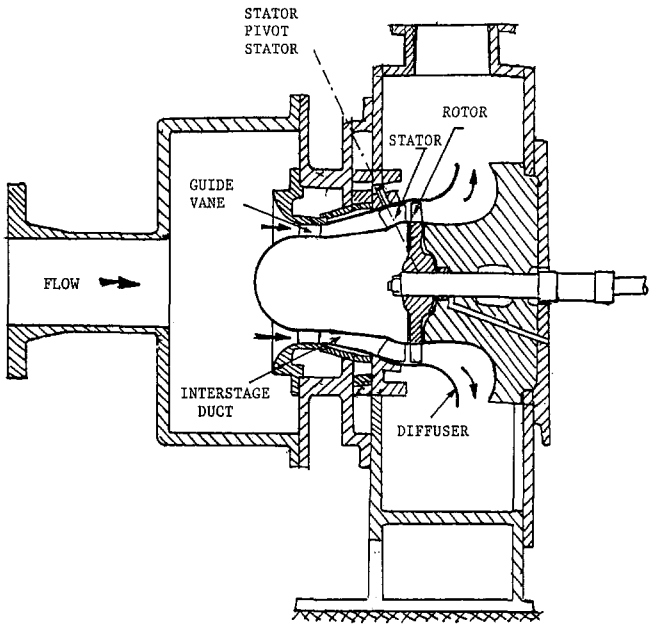

Fig. 2 Schematic of the auto turbine

acteristics of the blade material and coating under investigation. According to the experimental data, the coating reduces the erosion rate by an order of magnitude. Both curves exhibit typical ductile material erosion behavior, with maximum erosion rate of 35 · − 50 · for MAR-M246 and 30 · for RT22B. The computation of blade erosion combines the model for the mass erosion parameter (9) with the results of the particle trajectory calculations. The latter provides the impact velocities, impingement angles, and impact locations for a large number of particle trajectories.

Calculation Procedure

Two separate computer codes are used, one for calculating particle trajectories in the blade passages and another for predicting the blade erosion. The output of the particle trajectory code consists of three files. The first file provides the input for particle trajectory plots. The second file contains all particle exit conditions from a given blade row. It is used as input to provide the initial conditions for the particle trajectories in the following blade row. The data are first adapted to a new frame of reference, which is fixed in each blade row. The third file contains all computed particle impact data, including the impact locations, the impact velocity, and impingement angle relative to the blade surface.

The code for blade surface erosion computations uses as

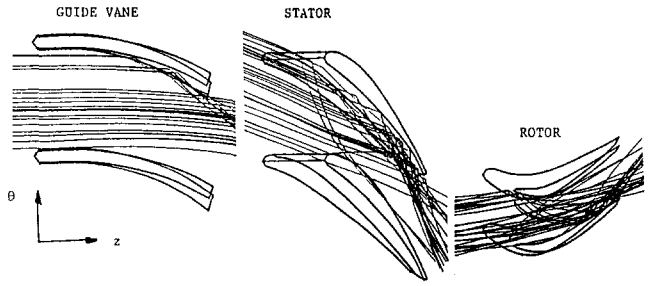

Fig. 3(*a*) Projection of particle trajectories in θ–z plane for M246 alloy

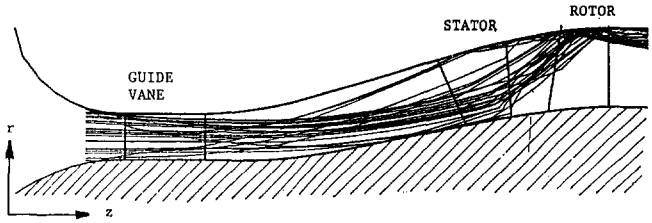

Fig. 3(*b*) Projection of particle trajectories in r–z plane for M246 alloy

input the third particle trajectory output file containing the blade impact data. The appropriate empirical equations for the blade material erosion and the blade surface geometry are also needed in the blade erosion simulations. The output from this program includes the blade erosion pattern, as well as the distribution of the impact velocity, impingement angles, and the frequency of particle blade surface impacts, over the blade pressure and suction surfaces.

Results and Discussion

The particle trajectory and blade erosion analysis were carried out through an automotive axial flow turbine, which was described by Kofskey and Nusbaum (1978) and shown schematically in Fig. 2. The blade impact data from the trajectories of 100,000 ingested 15 μm particles were used to obtain the erosion results. The trajectories were simulated in the gas turbine of standard inlet air equivalent conditions at 18,543 rpm and 1.075 kg/s weight flow. At the turbine inlet, the particles were assumed to enter axially at the same velocity as the gas, and they were distributed in proportion to the mass flux, using random number generators.

Typical particle trajectories for MAR-M246 blade material and blade erosion patterns are presented for the same blade material with and without RT22B (rhodium platinum aluminide) coating. In addition, the particle blade impact data that influence erosion, including the impact frequency, impact velocity, and impingement angle distribution over the blade, are presented to gain insight into the blade erosion phenomena.

Particle Trajectories. The particle trajectories were computed for both coated and uncoated blades, but no significant differences were observed between the two cases. Figure 3(*a*) shows projected particle trajectory samples in the z–θ plane in the relative frame of reference of each blade row. Due to their inertia, the particles deviate from the streamlines and some of them tend to impact the guide vane and stator blade pressure surfaces as shown in Fig. 3(*a*). Because of their lower absolute velocities at the stator exit, the particles enter the rotor blade row with a high negative incidence angle in its relative frame of reference. This causes many of the particles to impact the rotor blade suction surface near the

Downloaded 02 Jun 2010 to 171.66.16.102. Redistribution subject to ASME license or copyright; see http://www.asme.org/terms/Terms_Use.cfm

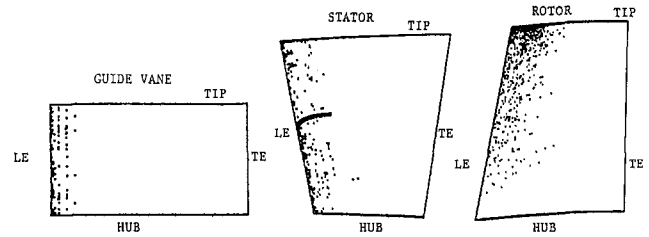

Fig. 4 Particle impact locations on the blade suction surfaces for M246 alloy

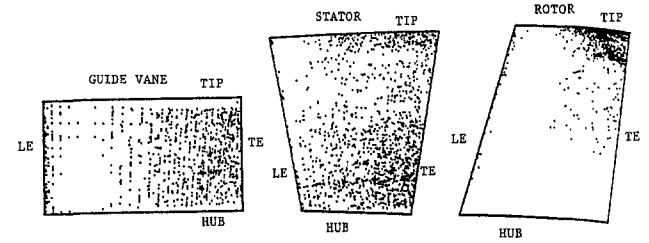

Fig. 5 Particle impact locations on the blade pressure surfaces for M246 alloy

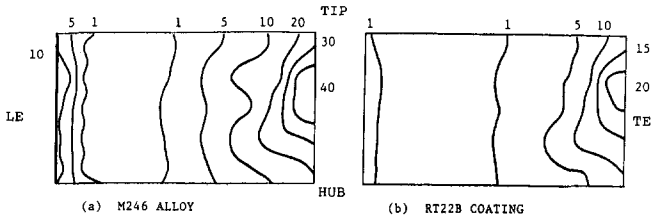

Fig. 6 Guide vane pressure surface erosion rate $\times$ 10^5 (mg / g / cm^2)

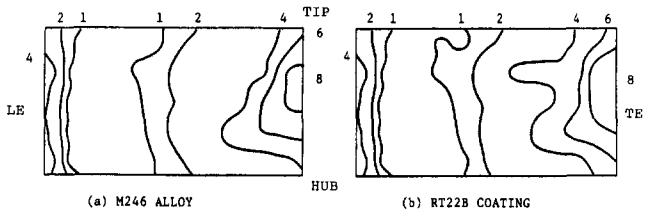

Fig. 7 Guide vane pressure surface impact frequency $\times$ 10^{-6} (g^{-1} cm^{-2})

leading edge as shown in Fig. 3(*a*). The same particles later impact the second half of the rotor blade pressure surface.

Figure 3(*b*) shows the projection of the particle trajectories in the meridional (z–r) plane throughout the turbine. The influence of the particle impacts with the stator and rotor blade surfaces on their radial migration can be clearly observed in this figure. The imparted circumferential rebounding particle velocities cause particle centrifugation away from the hub, especially after the rotor blade impacts.

Particle Impact Locations. The particle impact locations on the blade suction and pressure surfaces are shown in Figs. 4 and 5, respectively. Comparing the two figures, one can see that in general the stationary blade pressure surfaces are subjected to many more impacts than the suction surfaces. Figure 5 shows that in the guide vane, the blade pressure surface impacts increase toward the trailing edge with no radial variation in the impact pattern. The stator blade impacts are more evenly distributed over the pressure surface with the exception of a reduced impact zone near the leading

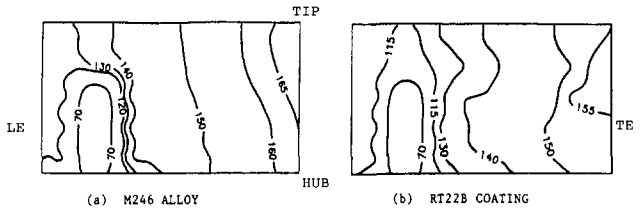

Fig. 8 Guide vane pressure surface impact velocity (m / s)

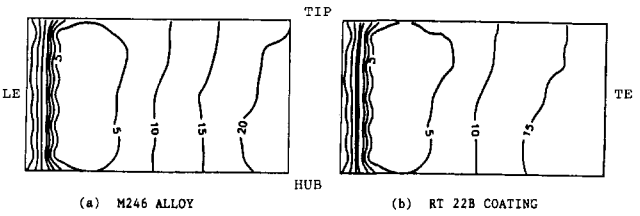

Fig. 9 Guide vane pressure surface impact angle (deg)

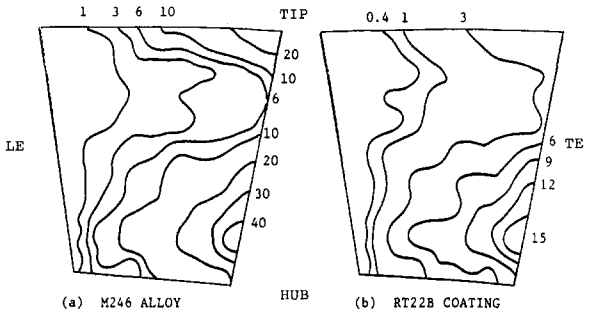

Fig. 10 Stator pressure surface erosion rate $\times$ 10^5 (mg / g / cm^2)

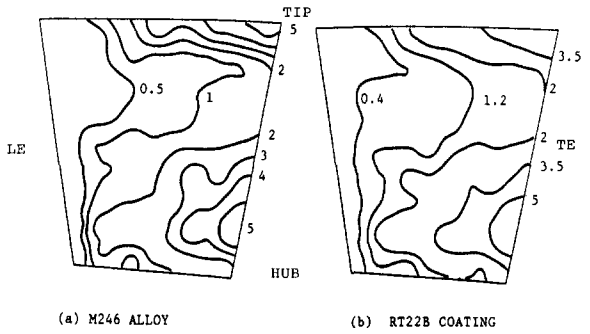

Fig. 11 Stator pressure surface impact frequency $\times$ 10^{-6} (g^{-1} cm^{-2})

edge. The stationary blades suction impacts are seen to be mostly restricted to the zone near the leading edge (Fig. 4), with most of the blade suction surface not subject to any particle impacts. The rotor blade suction surface is subjected to more impacts near the leading edge because of the negative incidence angle of the particles at the rotor inlet (Fig. 3*a*). The rotor pressure surface impacts are restricted to the corner of the tip trailing edge as seen in Fig. 5.

Blade Erosion. The blade erosion prediction is based on the particle computed impact data as determined from the particle trajectory calculations, and erosion model [Eq. (9)]. The blade mass erosion rate (in mg/m^{-2}/g^{-1}) is defined as the blade mass removal per unit area of the blade surface per unit mass of ingested particles. Since the stationary blade suction surfaces are subjected to fewer impacts, their erosion is insignificant. Thus, the erosion prediction results are presented only for pressure surfaces of the fixed blades.

Downloaded 02 Jun 2010 to 171.66.16.102. Redistribution subject to ASME license or copyright; see http://www.asme.org/terms/Terms_Use.cfm

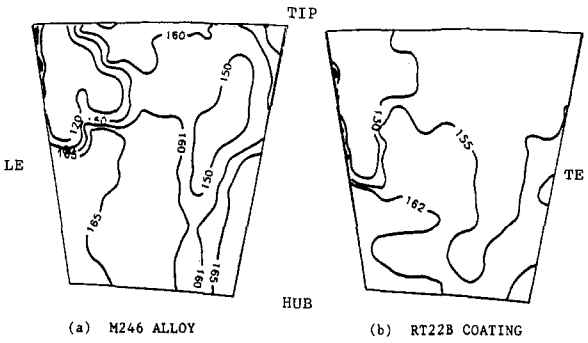

Fig. 12 Stator pressure surface impact velocity (m/s)

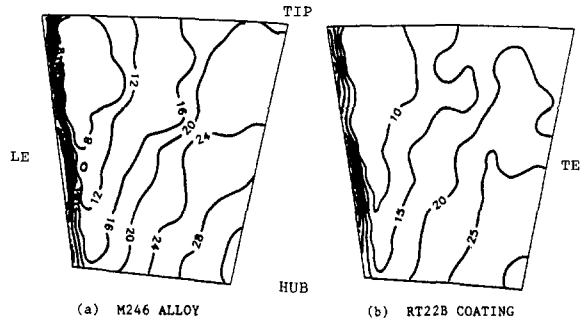

Fig. 13 Stator pressure surface impact angle (deg)

Figure 6 shows the distribution of the predicted guide vane pressure surface erosion for both uncoated and coated blades. According to this figure, the erosion is minimum at 25 percent of the chord and increases toward the leading and trailing edges with the maximum at midspan of the trailing edge in both cases. In spite of the similarity in blade erosion patterns, the coating is seen to reduce the erosion rate by 50 percent. The impact frequency pattern (Fig. 7) is very similar to the erosion pattern (Fig. 6). The surface impact frequency is defined as the number of particle impacts per unit area of blade surface per unit mass ingested particles (m^{-2}/g^{-1}). Figures 8 and 9 show that both the impact velocities and impingement angles are minimum at 25 percent of the chord and increase toward the leading and trailing edges, with maximum impact velocities near the trailing edges.

The erosion and its related parameters over the stator blade pressure surface are presented in Fig. 10–13. One can observe that the high impact frequencies at the trailing edge near the hub (Fig. 11) combined with high impact velocities (Fig. 12) produces maximum pressure surface erosion in this region (Fig. 10). The blade coating is found to reduce the stator blade pressure surface erosion by 60 percent.

The blade erosion and its related parameters over the rotor blade surfaces are presented in Figs. 14–21. Figure 14 shows that the rotor pressure surface erosion is mainly limited to about one-third of the blade surface area with a maximum at the trailing edge tip corner due to the radial centrifugation of the particles. On the other hand, Fig. 18 shows that suction surface blade erosion is limited to one-fourth of the blade surface at the leading edge tip. In general, the maximum erosion is much higher on the rotor blade pressure surface compared to the suction surface. This can be attributed to the fact that the erosion rate is much higher at the impingement angles between 20–30 · , than the 50–60 · that are the impingement angles ranges encountered at the regions of maximum impact frequencies over the pressure and suction surfaces respectively, as can be seen in Figs. 17 and 21. One can see from Figs. 14 and 18 that

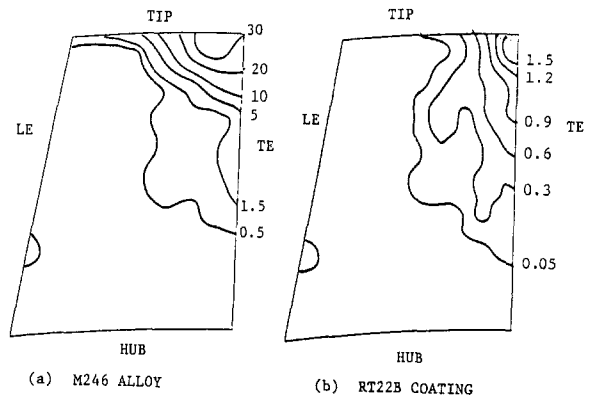

Fig. 14 Rotor pressure surface erosion rate $\times 10^{-5}$ ($mg/g/cm^2$)

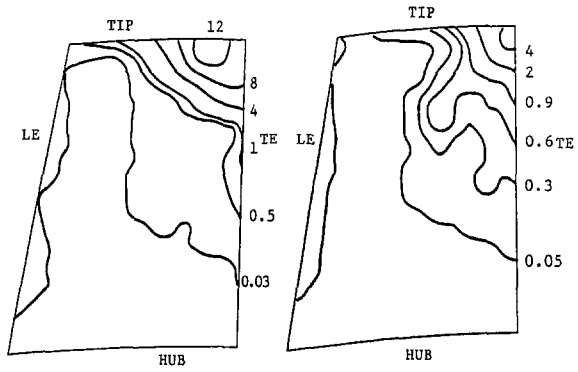

Fig. 15 Rotor pressure surface impact frequency $\times 10^{-6}$ (g^{-1}/cm^{-2})

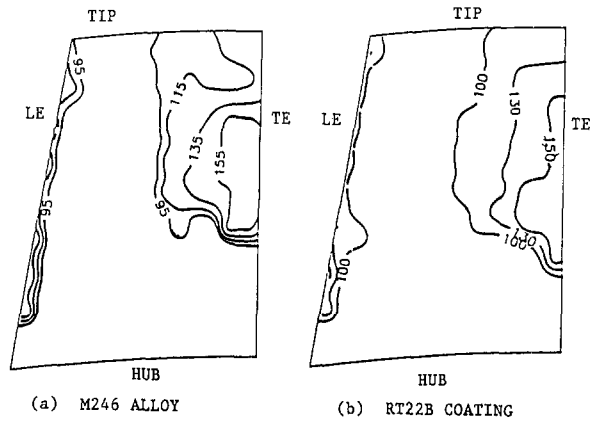

Fig. 16 Rotor pressure surface impact velocity (m/s)

coating reduces the magnitude of the rotor blades pressure surface erosion by 85 percent and the rotor suction surface erosion by 75 percent.

Coating Effect on the Blade Erosion. One can see from Figs. 6–21 that the blade impact frequency, impact angle, and impingement angle contours are very similar for both coated and uncoated surfaces. These similarities are attributed to the fact that these parameters are obtained directly from particle dynamics, which does not vary significantly with blade coating. Therefore, the blade erosion rate contours for the uncoated and coated blade surfaces are similar but the erosion rate levels are quite different, as shown in Figs. 6, 10, 14, and 18. These results demonstrate that the enhancement of the surface erosion resistance ob-

Downloaded 02 Jun 2010 to 171.66.16.102. Redistribution subject to ASME license or copyright; see http://www.asme.org/terms/Terms_Use.cfm

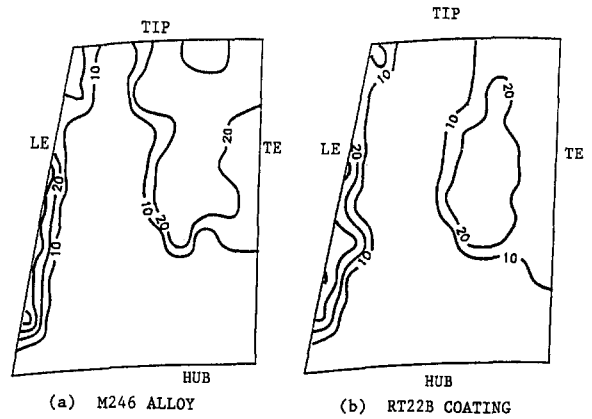

Fig. 17 Rotor pressure surface impact angle (deg)

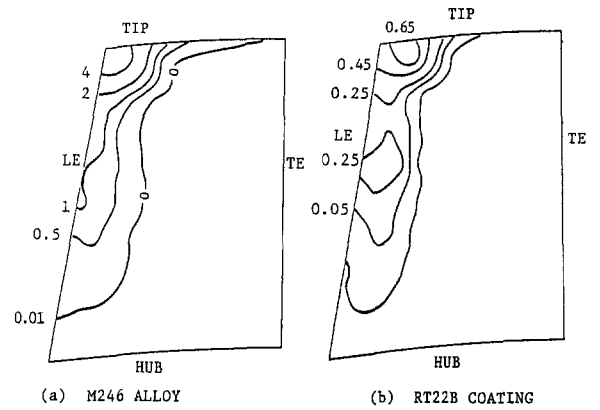

Fig. 18 Rotor suction surface erosion rate $\times 10^5$ (mg/g/cm^2)

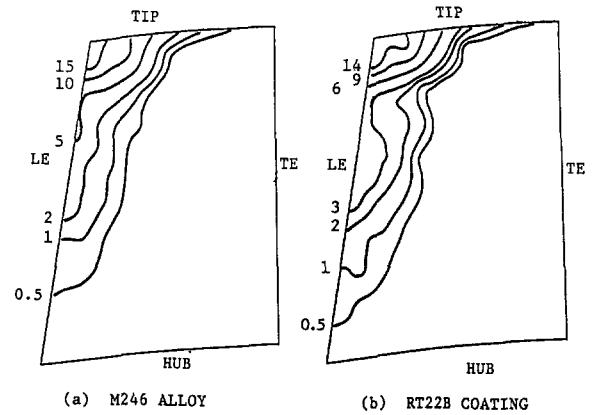

Fig. 19 Rotor suction surface impact frequency $\times 10^{-6}$ (g^{-1}/cm^{-2})

served in erosion tests would also be expected in an actual turbine because coating has little effect on the particle dynamics. As indicated in the previous discussion of the results, the predicted reduction in blade surface erosion due to coating is 50 percent, the stator pressure surface over 60 percent, and over 85 percent of the rotor blade pressure surface.

Conclusions

The results presented provide a detailed description of particle trajectories and blade surface erosion pattern through a power turbine of an automotive gas turbine engine for both coated and uncoated blade surfaces. The results of the particle trajectory computations show no significant variation in the computed three-dimensional trajectories for coated and uncoated blades. The blade surface erosion results indicate that the magnitude of the blade erosion, as well as the erosion pattern and location of maximum blade erosion, are different in the three blade rows. In the guide vanes, the maximum erosion is at the trailing edge near the middle of the blade span. The stator blade row suffers the maximum erosion at the leading and trailing edges near the hub. In the rotor blade row, maximum erosion is located at the outermost radial locations. Coating has very slight influence on the erosion patterns, but produces a substantial reduction in its magnitude that ranges between 50 and 75 percent for all blade surfaces. This improved blade surface erosion resistance through coatings would lead to longer blade lives and better performance.

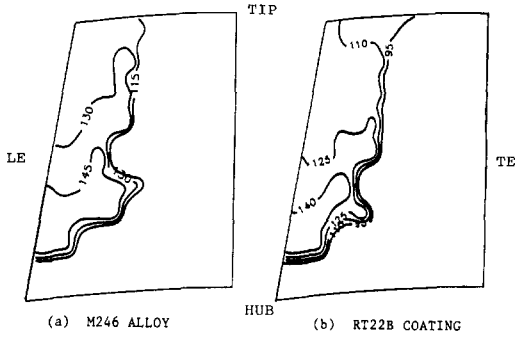

Fig. 20 Rotor suction surface impact velocity (m/s)

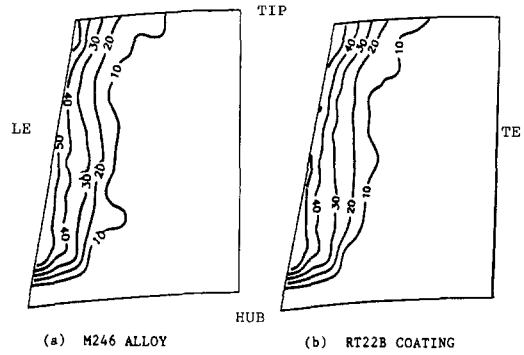

Fig. 21 Rotor suction surface impact angle (deg)

Acknowledgments

This research work was partially supported by the U.S. Department of Energy, Fossil Energy Advanced Research and Technology Development Materials Program under Contract No. 19X-89628C, Oak Ridge National Laboratory, Oak Ridge, TN. We offer special thanks to Dr. Rod Judkins, Fossil Energy Program Manager, for our useful discussions.

References

Angell, P. R., and Golec, T., 1976, "Upgrading Automotive Gas Turbine Technology: An Experimental Evaluation of Improvement Concepts," SAE Paper No. 760280.

Eroglu, H., and Tabakoff, W., 1990, "Effect of Inlet Flow Angle on the Erosion of Radial Turbine Guide Vanes," ASME *Journal of Turbomachinery*, Vol. 112, pp. 64–70.

Hussein, M. F., and Tabakoff, W., 1973, "Dynamic Behavior of Solid Particles Suspended by Polluted Flow in a Turbine Stage," *Journal of Aircraft*, Vol. 10, pp. 434–440.

Downloaded 02 Jun 2010 to 171.66.16.102. Redistribution subject to ASME license or copyright; see http://www.asme.org/terms/Terms_Use.cfm

Katsanis, T., 1965, "Fortran Program for Calculating Transonic Velocities on a Blade-to-Blade Stream Surface of a Turbomachine," NASA TND-2809, May.

Katsanis, T., and McNally, W. D., 1977, "Revised Fortran Program for Calculating Velocities and Streamlines in the Hub-Tip Mid Channel Stream Surface of an Axial, Radial, or Mixed Flow Turbomachine or Annular Duct, Vols. 1 and 2," NASA TND-8430 and NASA TND-8431.

Kofskey, M., and Nusbaum, W. J., 1978, "Cold-Air Performance of Free Power Turbine Designed for 112 Kilowatt Automotive Gas-Turbine Engine: I—Design Stator-Vane-Chord Setting Angle of 35°," NASA Technical Paper 1007.

Tabakoff, W., and Hamed, A., 1982, "Investigation of Gas Particle Flow in Erosion Wind Tunnel," presented at the 7th Annual Conference on Materials for Coal Conversion and Utilization, National Bureau of Standards, Gaithersburg, MD, Nov.

Tabakoff, W., Hamed, A., and Eroglu, H., 1984, "Study of Particle Rebound Characteristics and Material Erosion at High Temperature," Final Technical Report, Fossil Energy Materials Program, U.S. Department of Energy, ORNL/Sub/84-89628/01.

Tabakoff, W., and Hamed, A., 1986, "The Dynamics of Suspended Solid Particles in a Two-Stage Gas Turbine," ASME *Journal of Turbomachinery*, Vol. 108, pp. 298–302.

Tabakoff, W., and Malak, M. F., 1987, "Laser Measurements of Fly Ash Rebound Parameters for Use in Trajectory Calculations," ASME *Journal of Turbomachinery*, Vol. 109, pp. 535–540.

Tabakoff, W., Hamed, A., Metwally, M., Yeuan, J., and Pasin, M., 1990a, "Study of Particle Rebound Characteristics and Material Erosion at High Temperature," Final Technical Report, Fossil Energy Materials Program, U.S. Department of Energy, ORNL/Sub/84-89628/03, Oct.

Tabakoff, W., Hamed, A., Metwally, M., and Yeuan, J., 1990b, "Study of Particle Rebound Characteristics and Material Erosion at High Temperature," ORNL/FMP-902, AR&TD Fossil Energy Materials Semi-Annual Progress Report for the period ending Sept. 30, 1990, ORNL, Part IV, pp. 381–393.

ERRATA

To the paper "Performance Evaluation of Low Heat Rejection Engines," by X. Sun, W. G. Wang, R. M. Bata, and X. Gao, published in the ASME JOURNAL OF ENGINEERING FOR GAS TURBINES AND POWER, Vol. 116, October 1994, pp. 758–764:

The present address of the first author, X. Sun, was incorrectly given as Michigan State University. He is currently affiliated with the University of Michigan.

Downloaded 02 Jun 2010 to 171.66.16.102. Redistribution subject to ASME license or copyright; see http://www.asme.org/terms/Terms_Use.cfm

Katsanis, T., 1965, "Fortran Program for Calculating Transonic Velocities on a Blade-to-Blade Stream Surface of a Turbomachine," NASA TND-2809, May.

Katsanis, T., and McNally, W. D., 1977, "Revised Fortran Program for Calculating Velocities and Streamlines in the Hub-Tip Mid Channel Stream Surface of an Axial, Radial, or Mixed Flow Turbomachine or Annular Duct, Vols. 1 and 2," NASA TND-8430 and NASA TND-8431.

Kofskey, M., and Nusbaum, W. J., 1978, "Cold-Air Performance of Free Power Turbine Designed for 112 Kilowatt Automotive Gas-Turbine Engine: I—Design Stator-Vane-Chord Setting Angle of 35°," NASA Technical Paper 1007.

Tabakoff, W., and Hamed, A., 1982, "Investigation of Gas Particle Flow in Erosion Wind Tunnel," presented at the 7th Annual Conference on Materials for Coal Conversion and Utilization, National Bureau of Standards, Gaithersburg, MD, Nov.

Tabakoff, W., Hamed, A., and Eroglu, H., 1984, "Study of Particle Rebound Characteristics and Material Erosion at High Temperature," Final Technical Report, Fossil Energy Materials Program, U.S. Department of Energy, ORNL/Sub/84-89628/01.

Tabakoff, W., and Hamed, A., 1986, "The Dynamics of Suspended Solid Particles in a Two-Stage Gas Turbine," ASME *Journal of Turbomachinery*, Vol. 108, pp. 298–302.

Tabakoff, W., and Malak, M. F., 1987, "Laser Measurements of Fly Ash Rebound Parameters for Use in Trajectory Calculations," ASME *Journal of Turbomachinery*, Vol. 109, pp. 535–540.

Tabakoff, W., Hamed, A., Metwally, M., Yeuan, J., and Pasin, M., 1990a, "Study of Particle Rebound Characteristics and Material Erosion at High Temperature," Final Technical Report, Fossil Energy Materials Program, U.S. Department of Energy, ORNL/Sub/84-89628/03, Oct.

Tabakoff, W., Hamed, A., Metwally, M., and Yeuan, J., 1990b, "Study of Particle Rebound Characteristics and Material Erosion at High Temperature," ORNL/FMP-902, AR&TD Fossil Energy Materials Semi-Annual Progress Report for the period ending Sept. 30, 1990, ORNL, Part IV, pp. 381–393.

ERRATA

To the paper "Performance Evaluation of Low Heat Rejection Engines," by X. Sun, W. G. Wang, R. M. Bata, and X. Gao, published in the ASME JOURNAL OF ENGINEERING FOR GAS TURBINES AND POWER, Vol. 116, October 1994, pp. 758–764:

The present address of the first author, X. Sun, was incorrectly given as Michigan State University. He is currently affiliated with the University of Michigan.

Copyright © 1995 by ASME

Downloaded 02 Jun 2010 to 171.66.16.102. Redistribution subject to ASME license or copyright; see http://www.asme.org/terms/Terms_Use.cfm